

Shear Enhancement in RC Beams Loaded on the Tension Face

A thesis submitted in partial fulfilment of the requirements of the degree of Doctor of
Philosophy (PhD) and Diploma of Imperial College London (DIC)

Abobakr Elwakeel

Department of Civil & Environmental Engineering
Imperial College of Science, Technology and Medicine
London SW7 2AZ, United Kingdom

October 2019

*This work is dedicated to my parents, wife and
to my two sons (Abdelrahman and Kareem)*

إلى

ماما، بابا، هولاء، موني وكريم

جزاكم الله خيراً

DECLARATION

I, hereby, certify that the work reported in this thesis is solely my own work conducted at the Department of Civil Engineering of Imperial College London. Any work reported in this thesis from other sources has been properly cited inside the text and referenced.

The copyright of this thesis rests with the author. Unless otherwise indicated, its contents are licensed under a Creative Commons Attribution-Non Commercial 4.0 International Licence (CC BY-NC). Under this licence, you may copy and redistribute the material in any medium or format. You may also create and distribute modified versions of the work. This is on the condition that you credit the author and do not use it, or any derivative works, for a commercial purpose. When reusing or sharing this work, ensure you make the licence terms clear to others by naming the licence and linking to the licence text. Where a work has been adapted, you should indicate that the work has been changed and describe those changes. Please seek permission from the copyright holder for uses of this work that are not included in this licence or permitted under UK Copyright Law.

ABSTRACT

Shear strength of reinforced concrete beams significantly enhances when loads are applied closer to the support due to the arching action. This enhancement is widely investigated and has been included in the design codes. However, scarce resources are available in the literature regarding this enhancement for the case of multiple point loads applied within the enhancement zone; in addition, the available literature focuses on loads applied to the flexural compression face. Situations where multiple point loads are applied on the tension face are found in practice in structures like balanced-cantilever crosshead girders of bridges and transfer girders near the supports. Nevertheless, research considering this configuration has not been found in the available literature. The aim of this research is to study the effect of the loading arrangements on the shear strength enhancement of deep beams loaded on the compression or tension face with multiple point loads. This research was motivated by differences in the principal compressive stress trajectories obtained with nonlinear finite element analysis for the two different configurations.

The author conducted an experimental program to investigate the influence of loading face, the effect of varying the ratio between loads applied within the enhancement zone and the influence on shear enhancement of partly loading the beam outside the enhancement zone. Detailed measurements of the crack kinematics and global deformation were obtained during the tests using the digital images correlation system. These measurements were used to provide descriptive models of the deformed beams and to evaluate the shear transfer actions of the tested beams.

Strength of the tested beams was estimated using design codes (BS8110, EC2 2004 and MC2010) and non-linear finite element analysis. A novel practical strut-and-tie model was developed for the case of multiple point load applied to the tension face of the beams. This model correctly predicted the failure plane, fairly represented the stress field, and it is suitable for multiple loads applied entirely inside or partly outside the shear enhancement zone.

ACKNOWLEDGEMENT

It was such a delightful three-year journey at Imperial College London, surely to obtain my PhD but of course, plenty of good memories and milestones also happened. This epic journey would have been impossible to travel without the support of many people, whom I would like to thank. I know these words are not enough to express the gratitude that you deserve.

My sincere appreciation goes to my supervisor, Dr Robert Lars Vollum, who has been greatly supportive before and during my PhD. I would like to thank him for the knowledge, guidance, warm encouragement, patience and kindness. I appreciate the time invested in the very long meetings and the detailed revisions of the chapters and publications.

This work was funded by several bodies. I find myself indebted to the Islamic Development Bank, the Government of the Republic of Sudan, Dr Vollum, the department of Civil and Environmental Engineering at Imperial College and the Gordon Memorial Trust Fund. I would not be able to have this opportunity without their financial support.

I would also like to express my gratitude to the skilled and very helpful technicians at the Heavy Structures Laboratory at Imperial College London. Their dedication, advice and support were of important help to finish this work. I would like to offer my special gratitude to Les Clack and Delroy Hewitt (Bob). I also appreciate the support and feedback offered by Andy Pullen regarding his help in post-processing the digital images and to Dr Mohamed Mustafa and Dr Luis Soares for their help with the FEA.

I owe an important debt to the people at the Department of Civil and Environmental engineering, particularly Ms Fionnuala Donovan. Special gratitude goes to my mates in office 424 Cagatay, Bradley, Mariana, Bowen, Zhan, Izat, Kaidong, Sofi, Luke, Javier, and Chunyan and to my research group Marcus, Andri, Omar and Deema. I also would like to extend my thanks to the Sudanese community in the Du Cane Road for being my UK family.

Above all, I owe my deepest gratitude always to my parents, Elsadig and Hind Elwakeel, to whom I owe all my successes and achievements, to my lovely wife, Ibtihal, and to my two sons, Abdelrahman and Kareem, for their unconditional love, support and patience during this journey. To them, and to everyone else I have missed, I say thank you.

TABLE OF CONTENTS

Abstract	5
Acknowledgement	6
Table of Contents	7
List of Figures	13
List of Tables	28
Annotations	31
Chapter 1. Introduction.....	37
1.1. Background.....	37
1.2. Research Aim and Objectives	39
1.3. Thesis Outline	40
Chapter 2. Literature Review.....	43
2.1. Introduction.....	43
2.2. Shear Transfer Actions in Reinforced Concrete Beams	43
2.2.1. The contribution of aggregate interlock	45
2.2.2. The contribution of dowel action	53
2.2.3. The contribution of shear reinforcement	55
2.2.4. The contribution of the compression zone	58
2.2.5. Evaluation of crack kinematics using DIC.....	60
2.3. Provisions for Shear Strength in Different Codes of Practice	62
2.3.1. Shear Strength in EC2.....	64
2.3.2. Shear Strength in BS 8110-97.....	65
2.3.3. Shear Strength in FIB MC2010.....	66
2.3.4. Shear Strength Enhancement of RC beams	68
2.4. Essential Models for Shear in RC Beams	71

2.4.1.	The Modified Compression Field Theory (MCFT)	71
2.4.2.	The Tow-Parameter Kinematic Theory (2PKT)	76
2.5.	Introduction to Strut-and-Tie Models.....	84
2.5.1.	B and D regions	84
2.5.2.	Constructing a strut-and-tie model	85
2.5.3.	Model optimization.....	86
2.5.4.	Dimensioning strut-and-tie model	87
2.5.5.	Models for beams with horizontal and vertical shear reinforcement	90
2.5.6.	Codes provisions of the strut-and-tie models	94
2.5.7.	Problems in constructing strut-and-tie models.....	97
2.6.	Conclusions.....	97
Chapter 3.	Experimental program	100
3.1.	Overview.....	100
3.2.	General Test Description	101
3.2.1.	First series of beams (Series A).....	103
3.2.2.	Second series of beams (Series B)	105
3.2.3.	Third series of beams (Series C).....	107
3.3.	Manufacturing and Curing	109
3.4.	Beams setup and Test Configuration	111
3.4.1.	Setup for Series A.....	111
3.4.2.	Setup for Series B.....	116
3.4.3.	Setup for Series C.....	116
3.5.	Instrumentation	119
3.5.1.	General Aspects	119
3.5.1.	Digital Image Correlation (DIC) System.....	119
3.5.2.	Strain Gauges.....	127

3.5.3. Linear Variable Displacement Transducers (LVDT).....	132
3.6. Conclusions.....	134
Chapter 4. Experimental Results.....	135
4.1. Introduction.....	135
4.2. Material Properties.....	135
4.2.1. Concrete material properties.....	135
4.2.2. Reinforcement material properties.....	146
4.3. Results of Series A.....	148
4.3.1. Summary of the results.....	148
4.3.2. Modes of failure and development of cracks.....	149
4.3.3. Concrete surface strains and crack kinematics.....	151
4.3.4. Load-deflection response.....	158
4.3.5. Reinforcement strains.....	162
4.4. Results of Series B.....	165
4.4.1. Summary of test results.....	165
4.4.2. Modes of failure and development of cracks.....	166
4.4.3. Concrete surface strains and crack kinematics.....	169
4.4.4. Load-deflection response.....	174
4.4.5. Reinforcement strains.....	175
4.5. Results of Series C.....	179
4.5.1. Summary of the results.....	179
4.5.2. Modes of failure and development of cracks.....	180
4.5.3. Concrete surface strains and crack kinematics.....	182
4.5.4. Load-deflection response.....	187
4.5.5. Reinforcement strains.....	189
4.6. Conclusions.....	193

Chapter 5. Cracks Kinematics and Shear Transfer Mechanisms	195
5.1. Introduction	195
5.2. Description of Beams Deformation Using 2PKT	195
5.2.1. Deformation of beams loaded on the compression face	196
5.2.2. Deformation of beams loaded on the tension face.....	200
5.2.3. Modification of the 2PKT's description of the deformation for the double cantilever beams	203
5.3. Assessing Beam Strength and Shear Transfer Actions Using the Five – Spring Model220	
5.4. Validation of Crack Kinematics Assumed in the 2PKT and the Five – Spring Model230	
5.5. Shear Transfer Actions Based on Other Models in the Literature	243
5.5.1. S-w curves of the tested beams	246
5.5.2. Results of the shear transfer actions	250
5.5.3. Shear transfer actions based on equilibrium	254
5.6. Conclusions.....	257
Chapter 6. Non-linear Finite Element (NLFE) Methodology	259
6.1. Introduction.....	259
6.2. Discrete and Smeared Crack Modelling	259
6.3. Smeared Crack Model	260
6.3.1. Fixed smeared crack model.....	261
6.3.2. Multi-directional fixed smeared crack model	261
6.3.3. Rotating smeared crack model.....	263
6.4. NLFEA Using DIANA.....	264
6.4.1. Compressive behaviour of concrete	264
6.4.2. Tensile behaviour of the concrete	270

6.4.3.	Shear behaviour of the concrete	274
6.4.4.	Reinforcement modelling.....	276
6.4.5.	Solution procedures for non-linear systems	278
6.4.6.	Elements and mesh considerations	282
6.5.	Model Calibration and Baseline Parameters.....	283
6.5.1.	Description of NLFEA performed by Fang.....	284
6.5.2.	Challenges faced Fang and model enhancements	285
6.5.3.	Enhanced results and baseline model parameters	286
6.6.	Constructing the FE Models for the Tested Beams	289
6.7.	Modelling of the Loading Plates	290
6.8.	Sensitivity Analysis of the Model.....	292
6.8.1.	Element size.....	292
6.8.2.	Fixed and rotating crack model	293
6.8.3.	Compressive behaviour of the concrete	295
6.8.4.	Compressive fracture energy	296
6.8.5.	Shear retention model	297
6.9.	Finally Adopted Parameters	298
6.10.	Results of the FEA	301
6.11.	Conclusions.....	304
Chapter 7.	Analysis of Experimental Results	305
7.1.	Introduction.....	305
7.2.	Assessment of Beam Strength Using Codified Sectional Methods	306
7.3.	Evaluation of the Shear Strength Using Strut-and-tie Models.....	311
7.3.1.	STM for beams loaded in the tension face (STM3)	315
7.3.2.	Solution procedure for STM3	320
7.3.3.	Results of the STM	320

7.3.4.	The geometry of the STM of the tested beams	323
7.4.	Comparison between STM, Test Behaviour and NLFEA.	325
7.4.1.	Comparison of the stress fields and crack patterns	326
7.4.2.	Comparison of measured, STM and NLFEA reinforcement strains	330
7.4.3.	The effect of the transfer compression on the bond force	337
7.4.4.	Prediction of critical failure plane for tested beams	343
7.4.5.	Influence of tension face loading on shear resistance	346
7.5.	Conclusions	351
Chapter 8.	Conclusions and Recommendations	354
8.1.	Background Overview	354
8.2.	Description of the Experimental Program and Summary of the Test Results	356
8.3.	Analysis of the Results and Shear Transfer Actions	358
8.4.	Design Observations and Recommendations	361
8.5.	Suggestions for Further Work	363
References	365
Appendix I	371
Appendix II	381

LIST OF FIGURES

Figure 1.1: History of research in shear in the past 60 years(Collins et al., 2008). Figure reproduced with permission of the rights holder, Magazine of Concrete Research.	39
Figure 2.1: Shear transfer actions in reinforced concrete beams	44
Figure 2.2: Walraven two-phase model: a) Push-off test specimen, b) Aggregate interlock in the shear crack plane and c) Contact area during shear displacement (Walraven and Reinhardt, 1981)	46
Figure 2.3: Comparing the Walraven two-phase model with the test results Walraven and Reinhardt, 1981).	47
Figure 2.4: Modifications to Walraven (1980) kinematics and their effect on the direct and shear strength (Campana et al., 2013). Figure reproduced with permission of the rights holder, Magazine of Concrete Research.	47
Figure 2.5: Comparing the Walraven and Reinhardt model with the test results for a) Normal concrete and b) Lightweight concrete, Walraven and Reinhardt (1981).	49
Figure 2.6: Test results compared to the rough crack model (BAZANT and GAMBAROVA, 1980). Figure reproduced with permission of the rights holder, Journal of Structural Engineering.	50
Figure 2.7: Beam in elastic foundation theory for the dowel mechanism (Walraven, 1980).	53
Figure 2.8: behaviour of the shear reinforcement in cracked concrete and bond stress according to Sigrist's model (Campana et al., 2013). Figure reproduced with permission of the rights holder, Magazine of Concrete Research.	56
Figure 2.9: Sigrist stepped bond behaviour. Figure reproduced with permission of the rights holder, Magazine of Concrete Research.	57

Figure 2.10: Park et al model (2003) for compression zone contribution. a) Mohr's circle for the Rankine's failure mode. b) loading stages c) compression and tension controlled shear capacity. Figure reproduced with permission of the rights holder, ACI Structural Journal....	59
Figure 2.11: Results obtained using DIC for a) crack kinematics (Huber et al., 2019) and b) concrete surfaces strains (Cavagnis et al., 2017). Figure reproduced with permission of the rights holder, a) Structural Concrete and b) Engineering Structures.	62
Figure 2.12: Background in shear research of members without shear reinforcement (Collins et al., 2008). Figure reproduced with permission of the rights holder, Magazine of Concrete Research.	63
Figure 2.13: Shear enhancement in Kani's Valley (regenerated from (Kani, 1964))	69
Figure 2.14: Expected failure planes for beams loaded with two points within $2d$ (Fang, 2013)	70
Figure 2.15: Strain conditions in the MCFT (Vecchio and Collins, 1986). Figure reproduced with permission of the rights holder, ACI Structural Journal.	73
Figure 2.16: Stress-strain relationship in the MCFT (Vecchio and Collins, 1986). Figure reproduced with permission of the rights holder, ACI Structural Journal.	74
Figure 2.17: Details of the 2PKT (Mihaylov et al., 2013). Figure reproduced with permission of the rights holder, ACI Structural Journal.	77
Figure 2.18: describing the full displacement using the 2PKT DoF (Mihaylov et al., 2013). Figure reproduced with permission of the rights holder, ACI Structural Journal.	77
Figure 2.19: Geometry of the critical loading zone in the 2PKT (Mihaylov et al., 2013). Figure reproduced with permission of the rights holder, ACI Structural Journal.	78
Figure 2.20: 2PKT for beams with multiple point loads within the shear span	80
Figure 2.21: Different locations of the centre of rotation of the rigid body(Kueres et al., 2018). Figure reproduced with permission of the rights holder, Engineering Structures.....	81

Figure 2.22: Five-spring model for deep beams (Mihaylov, 2015). Figure reproduced with permission of the rights holder, Structural Concrete.	82
Figure 2.23 Equilibrium of the rigid block in the five-spring model (Mihaylov, 2015). Figure reproduced with permission of the rights holder, Structural Concrete.	82
Figure 2.24: Stress trajectories in B and D regions (Schlaich et al., 1987), Permission requested on 10/10/2019.	85
Figure 2.25: Examples of B and D regions in different structures (James K. Wight, 2012). Figure reproduced with permission of the rights holder, Pearson.	87
Figure 2.26: Concentrated and smeared nodes (Schlaich et al., 1987) - regenerated, Permission requested on 10/10/2019.	88
Figure 2.27: Examples of basic types of nodes (Schlaich et al., 1987) – regenerated, Permission requested on 10/10/2019.	88
Figure 2.28: Basic compression fields (Schlaich et al., 1987) –regenerated, permission requested on the 10/10/2019.	89
Figure 2.29: Load carrying mechanisms in the strut-and-tie model.....	90
Figure 2.30: Idealised crack band zone and stress relief strip in a strut (Yang and Ashour, 2010). Figure reproduced with permission of the rights holder, Journal of Structural Engineering. 91	91
Figure 2.31: Use of nodal sub-division to estimate the contribution of a) vertical, b) horizontal shear reinforcement and c) longitudinal tensile force in STM (James K. Wight, 2012)- figure reproduced with permission of the rights holder, Pearson.	92
Figure 2.32: Sagaseta and Vollum model for deep beams with vertical shear reinforcement (Sagaseta and Vollum, 2010). Figure reproduced with permission of the rights holder, Magazine of Concrete Research.	93
Figure 2.33: STMs proposed by Fang for beams with four-point loads (Fang, 2013)	93

Figure 2.34: Details of transverse tensile force in smeared reinforcement for bottle stress field (BSI, 2004).....	95
Figure 3.1. Shear force and bending moment diagrams of beams in series A	102
Figure 3.2: Cross section of the series A of test beams a) beams loaded in the compression face and b) beams loaded in the tension face.....	103
Figure 3.3: Geometry and reinforcement details of series A of test beams (Beams a) AC0 (0.5/0.5), b) AC200 (05/0.5), c) AT0 (0.5/0.5) and d) AT200 (0.5/0.5)	105
Figure 3.4: Geometry and reinforcement details of series B of test beams.....	107
Figure 3.5: Geometry and reinforcement details of the series C of test beams. a) CT0 (1.0/0), b) CT200 (1.0/0), c) CT0 (0.6/0.4) and d) CT200 (0.6/0.4)	108
Figure 3.6: Rebar cage for beams a) without b) with shear reinforcement	109
Figure 3.7: Reinforcement cages inside the moulds before casting.....	110
Figure 3.8: Pouring of the concrete	111
Figure 3.9: Beams and air cured specimens wrapped for curing	112
Figure 3.10: Test configurations for the series A a) Config -1 and b) Config -2.	114
Figure 3.11: Load cells (Left) and Seating ball (Right) in series A of beams.....	115
Figure 3.12: Test configuration Config. – 3	117
Figure 3.13: Test configurations for series C (Config. - 4).....	118
Figure 3.14: Spreader beam and loading plate in the LHS of the third series	119
Figure 3.15: Typical speckle pattern for DIC.....	120
Figure 3.16: DIC System used on the experimental program	121
Figure 3.17: Calibration board for DIC calibration.....	121

Figure 3.18: Typical virtual gauges along the critical crack (Beam BT200 (0.5/0.5)).....	122
Figure 3.19: Measurements for calculation of crack kinematics.....	123
Figure 3.20: Sensitivity Analysis for DIC gauge length	126
Figure 3.21: Typical measurements for full and reduced crack kinematics - Beam AC0(0.5/0.5)	127
Figure 3.22: Fixing and coating of a strain gauge	127
Figure 3.23: Positioning strain gauges on the a) sides or b) ribs of the rebar.	128
Figure 3.24: Location of strain gauges for beams loaded in the compression and tension faces.	128
Figure 3.25: Locations of stain gauges in all of the test beams (Dimensions in mm)	132
Figure 3.26: Locations of LVDTs for the different configurations	133
Figure 4.1: Strength development using cube strength – series A.....	137
Figure 4.2: Compressive strength for beams in series A.....	139
Figure 4.3: Strength development using cube strength – Series B.	141
Figure 4.4: Compressive strength for beams in series B.....	142
Figure 4.5: Strength development using cube strength – series C.....	144
Figure 4.6: Compressive strength for beams in series C.....	146
Figure 4.7: Stress-strain curves for the different reinforcement diameters (D)	148
Figure 4.8: Development of the cracks during the test – Series A	150
Figure 4.9: Crack patterns (post-peak) for Series A	151
Figure 4.10: Typical virtual gauges along the critical crack (Beam BT200 (0.5/0.5)).....	152

Figure 4.11: a) Crack opening and b) sliding along the beam heights at failure for series A	153
Figure 4.12: Crack Kinematics for beam AC0 (0.5/0.5)	154
Figure 4.13: Crack Kinematics for beam AC200 (0.5/0.5)	155
Figure 4.14: Crack Kinematics for beam AT0 (0.5/0.5)	156
Figure 4.15: Crack Kinematics for beam AT200 (0.5/0.5)	157
Figure 4.16: Crack patterns for comparable beams in Series A a) beams AC0 (0.5/0.5) and AT0 (0.5/0.5), b) beams AT200 (0.5/0.5) and AC200 (0.5/0.5).	158
Figure 4.17: Location of the transducer (LVDT#5) in series A	158
Figure 4.18: Vertical end displacement due to the rotation of the beam	159
Figure 4.19: Load-deflection response for beams of series A	161
Figure 4.20: Influence of shear reinforcement on the behaviour of series A for beams loaded on the a) compression and b) tension face.	161
Figure 4.21: Influence of Comparison of load-displacement response for beams a) without and b) with shear reinforcement.	162
Figure 4.22: Strain gauges locations and labelled for beams series A	162
Figure 4.23 Flexural reinforcement strains for beams of series A	163
Figure 4.24 Dowel effect on the reinforcement strains for beams in series A	164
Figure 4.25 Reduction in the longitudinal reinforcement strain due to the presence of transverse confinement in series A	165
Figure 4.26: Shear reinforcement strains for series A	165
Figure 4.27: Development of the cracks during the test – series B	167
Figure 4.28: Failure modes and crack patterns (post-peak) for series B	168

Figure 4.29: Critical shear cracks for series B a) at 95% of V_{max} and b) post failure	169
Figure 4.30: Crack Kinematics for beam BT200 (0.5/0.5)	170
Figure 4.31: Crack Kinematics for beam BT200 (1.0/0)	171
Figure 4.32: Crack Kinematics for beam BT200 (0/1.0)	172
Figure 4.33 Crack Kinematics for beam BT20 (0.3/0.7)	173
Figure 4.34: Location of LVDT#5 in series B	174
Figure 4.35: Load-deflection response for beams of series B (a) RHL vs deflection and b) Critical plane load vs deflection)	175
Figure 4.36: Strain gauges locations and labels for beams series B	176
Figure 4.37: Longitudinal reinforcement strains series B	176
Figure 4.38: Reinforcement strains at dowel locations – Series B	177
Figure 4.39: Reduction in the longitudinal reinforcement strain due to the presence of transverse confinement in series B.....	178
Figure 4.40: Shear reinforcement strains for series B	179
Figure 4.41: Development of the cracks during the test – series C.....	180
Figure 4.42: Modes of failure for beams of series C.....	181
Figure 4.43: Crack Kinematics for beam CT0 (1.0/0)	183
Figure 4.44: Crack Kinematics for beam CT200 (1.0/0)	184
Figure 4.45: Crack Kinematics for beam CT0 (0.6/0.4)	185
Figure 4.46: Crack Kinematics for beam CT200 (0.6/0.4)	186
Figure 4.47: Overlapped crack patterns for beams in series C	187

Figure 4.48: Location of the transducer (LVDT#7) in series C	187
Figure 4.49: Load-deflection response for beams of series C	188
Figure 4.50: Effect of partially applying the load partially outside ($2d$) for beams a) without shear reinforcement and b) with shear reinforcement.	188
Figure 4.51: Effect shear reinforcement in beams loaded a) inside ($2d$) and b) partially outside ($2d$)	189
Figure 4.52: Strain gauges locations and labels for beams series C	190
Figure 4.53: the flexural tensile and compressive strains of series C of beams	190
Figure 4.54 Reinforcement strains at dowel locations – series C.....	191
Figure 4.55: Reduction in the longitudinal reinforcement strain due to the presence of transverse confinement in series C.....	192
Figure 4.56: Shear reinforcement strains for series C	192
Figure 5.1: Instrumentation used to calculate parameters of the 2PKT for beams loaded on a) the compression face and b) the tension face.	196
Figure 5.2: Correction of the rotation for beams loaded on the compression face	197
Figure 5.3: Comparison between the 2PKT and the measured deformation for beam AC0 (0.5/0.5) – Deformation X30.....	199
Figure 5.4: Comparison between measured and predicted maximum deformation at location (0,-500) of beams loaded on the compression face	200
Figure 5.5: Block rotation calculated using LVDTs and DIC for beams AT0 (0.5/0.5)	201
Figure 5.6: Calculations of the degrees of freedom for double cantilever beams (Kueres, 2018). Figure reproduced with permission of the rights holder, KUERES, D. A.....	202
Figure 5.7: Calculation of the shear displacement for corrected double cantilever beams.	202

Figure 5.8: The Deformed shape of beam CT0 (0.6/0.4) obtained with original 2PKT at 0.95 V_{max} (deformation X30)	203
Figure 5.9: Location of the centre of rotation based on measured deformation (Kueres, 2018). Figure reproduced with permission of the rights holder, KUERES, D. A.....	204
Figure 5.10: CoR for beams loaded as double cantilever beams	207
Figure 5.11: The variation of corrected horizontal displacement along the height of beam CT0 (1.0/0).....	208
Figure 5.12: Corrected deformation of beam CT0 (0.6/0.4) calculated using actual CoR at 0.95 V_{max} (deformation X30)	209
Figure 5.13: Suggested deformation of beams with two-point loads on the tension face ..	210
Figure 5.14: Variation of vertical deformation in the shear span with the height of double cantilever beams with two-point loads	211
Figure 5.15: Final corrections for the deformed shaped of beam CT0 (0.6/0.4) at 0.95 V_{max} calculated using modified 2PKT (deformation X 3).....	212
Figure 5.16: Comparison between the 2PKT and the measured deformation (X30) for beams loaded on their tension face at 0.95 V_{max}	217
Figure 5.17: Comparison between measured and predicted maximum deformation of beams loaded as a double cantilever.....	219
Figure 5.18: Solution procedures for estimating the ultimate shear strength using the five-spring model	224
Figure 5.19: Shear transfer mechanisms evaluated using the five-spring model	228
Figure 5.20: Predictions of the load-deflection response of the test beams using the five-spring model.....	230

Figure 5.21: Comparison between the measured and estimated rotation of the rigid body in the 2PKT.....	232
Figure 5.22: Rotation of the rigid body of beams in series A obtained (a) experimentally and (b) from the 2PKT.....	233
Figure 5.23: Rotation of the rigid body of beams in series C obtained (a) experimentally and (b) from the 2PKT.....	234
Figure 5.24: Rotation of the rigid body of beams in series B obtained (a) experimentally and (b) from the 2PKT.....	235
Figure 5.25: Comparison between the measured and estimated shear displacement in the 2PKT.....	237
Figure 5.26: Comparison between measured and estimated kinematic using the 2PKT for the test beams.....	239
Figure 5.27: Comparison of the orientation of the actual critical crack and the 2PKT assumed critical crack – Beam BT200 (0.5/0.5).....	240
Figure 5.28: Sensitivity of the crack kinematics at mid height to the selection of the crack angle for beam BT200 (0.5/0.5) at $0.8V_{max}$	241
Figure 5.29: Variation of the crack kinematics along the height of the critical crack of beam BT200 (0.5/0.5) at $0.8V_{max}$	242
Figure 5.30: Shear stress along the crack calculated using variable and mid-height crack kinematics at $0.8V_{max}$ – Beam BT200 (0.5/0.5).....	243
Figure 5.31: Aggregate interlock and dowel contributions estimated using different models.....	245
Figure 5.32: Shear transfer actions in a free body diagram of a beam with two-point loads.....	246
Figure 5.33: s-w curves for beam AC0 (0.5/0.5) and AT200 (0.5/0.5).....	247

Figure 5.34: s-w curves for the test beams based on average readings.....	249
Figure 5.35: Contribution of the aggregate interlock calculated using provisions suggested by Walraven, Guidotti and Ulaga for a) beam AC0 (0.5/0.5) and b) BT200 (1.0-0).	250
Figure 5.36: Shear transfer actions for test beams	253
Figure 5.37: Shear transfer actions at failure based on equilibrium	255
Figure 5.38: Comparison of the crack kinematics for beams failing in outer shear plane inside (2d)	256
Figure 5.39: The contribution of the aggregate interlock for beams in series B during the test.	257
Figure 6.1: Nodal separation in Smearred crack model	260
Figure 6.2: Hognestad compression curve in DIANA (DIANA, 2017) - figure reproduced with permission of the rights holder, TNO-DIANA.	265
Figure 6.3: Thorenfeldt compression curve in DIANA (DIANA, 2017) - figure reproduced with permission of the rights holder, TNO-DIANA.	266
Figure 6.4: Feenstra parabolic curve in DIANA (DIANA, 2017) - figure reproduced with permission of the rights holder, TNO-DIANA.	266
Figure 6.5: influence of lateral confinement (DIANA, 2017) - figure reproduced with permission of the rights holder, TNO-DIANA.	268
Figure 6.6: Lateral reduction model - JSCE(DIANA, 2017) - figure reproduced with permission of the rights holder, TNO-DIANA.	269
Figure 6.7: Lateral reduction model - (Vecchio and Collins, 1986). . Figure reproduced with permission of the rights holder, ACI Structural Journal.....	269
Figure 6.8: tensile behaviour of the concrete (Hordijk, 1992)	270

Figure 6.9: predefined tension softening for Total Strain crack models (DIANA, 2017) - figure reproduced with permission of the rights holder, TNO-DIANA.	273
Figure 6.10: Constant shear retention for total strain crack model (DIANA, 2017) - figure reproduced with permission of the rights holder, TNO-DIANA.	274
Figure 6.11: Smearred and discrete models for reinforcement (Sagaseta, 2008) . Figure reproduced with permission of the rights holder, Sagaseta J.....	277
Figure 6.12: Bond-slip reinforcement models (DIANA, 2017) - figure reproduced with permission of the rights holder, TNO-DIANA.	278
Figure 6.13: Strain predictions in the reinforcement using the Von Mises plasticity model (Fang, 2013)	278
Figure 6.14: Typical iterative process in NLFEA (DIANA, 2017) - figure reproduced with permission of the rights holder, TNO-DIANA.	279
Figure 6.15: Difference between the actual behaviour and Newton's solution	281
Figure 6.16: Arc-length control (DIANA, 2017) - figure reproduced with permission of the rights holder, TNO-DIANA.	281
Figure 6.17: The effect of introducing the arc-length technique to the analysis of beam AT200 (0.5/0.5)	282
Figure 6.18: 2D Plane stress element used in the FEM (DIANA, 2017) - figure reproduced with permission of the rights holder, TNO-DIANA.	283
Figure 6.19: The topology of a reinforcement bar (DIANA, 2017) - figure reproduced with permission of the rights holder, TNO-DIANA.	283
Figure 6.20: Geometry, mesh, boundary conditions and loading of beam S1-1 (Fang, 2013)	285
Figure 6.21: Replication and comparison of Fang's beams FEA.....	288

Figure 6.22: Finite element mesh, loading and boundary conditions of beam	289
Figure 6.23: Vertical displacement of beam AT200 (0.5/0.5)	290
Figure 6.24: Stress concentration below loading plates a) no strength enhancement b) strength enhanced c) load-deflection response (Fang, 2013)	291
Figure 6.25: Enhancement of the response of beam B2-25 due to the interface element..	292
Figure 6.26: Stress variation under the loading plate with the use of an interface element.	292
Figure 6.27: Sensitivity of the FEA to the element size (Beam AC200 (0.5/0.5))	293
Figure 6.28: Crack patterns obtained using FEA with a) fixed, b) rotating and c) fixed to rotating crack modelsS	294
Figure 6.29: Sensitivity of the FEA to the crack model	295
Figure 6.30: Comparison of the different compressive models in FEA for the concrete in predicting the failure.....	295
Figure 6.31: The sensitivity of the FE analysis to the compressive fracture energy for beams without shear reinforcement	296
Figure 6.32: Sensitivity of the FEA to the shear retention models for beams without shear reinforcement (Beam AC0 (0.5/0.5))	297
Figure 6.33: Sensitivity of the analysis to the constant shear retention value	298
Figure 6.34: Effect of introducing the arc-length technique to the analysis of the beams in series A	300
Figure 6.35: Prediction of the load-deflection using FEA.....	303
Figure 7.1: Expected failure planes for beams loaded with two points within $2d$	307

Figure 7.2: Control section for cases where a) $av < d$ and b) control section at d from the face of the concentrated load.	308
Figure 7.3: Sagaseta and Vollum model for deep beams with vertical shear reinforcement (Sagaseta and Vollum, 2010)	312
Figure 7.4: STM for beams with a single point load (Mihaylov et al., 2013). Figure reproduced with permission of the rights holder, ACI Structural Journal.	313
Figure 7.5: Comparison of the strength calculated using STM1 and the model provided by Mihaylov (2013) for beams with single-point load.....	314
Figure 7.6: STMs proposed by Fang for beams with four-point loads (Fang, 2013): a) $P2 < Ts1 + Ts2$, b) $P2 < Ts1 + Ts2$, c) no shear reinforcement and d) stress fields of beam AC0 (0.5/0.5)	315
Figure 7.7: STM3 for beams loaded in the tension face. a) Geometry, b) bottom CCC node and c) top outer CCT node	316
Figure 7.8: Comparison of STM results obtained using the MCFT and EC2 with $\alpha = 0.85$. ..	322
Figure 7.9: STM3 adopted for beam AC0 (0.5/0.5) loaded on the compression face	323
Figure 7.10: Overlay of the STMs on the major crack pattern for test beams	325
Figure 7.11: FEA principal stress, STMs and experimental cracks for the test beams	327
Figure 7.12: Plastic strain at failure for beams a) AC200 (0.5/0.5) and b) BT200 (0.5/0.5)..	328
Figure 7.13: FEA principal strains, STMs and experimental cracks for the test beams	330
Figure 7.14: Maximum flexural tensile strains obtained from the experimental program, STM3 (EC2 and MCFT) and FEA	332
Figure 7.15: Locations and names of stirrups in the tested beams.....	334
Figure 7.16: Comparison between FE and experimentally obtained shear reinforcement strain	337

Figure 7.17: The influence of transverse pressure on the bond strength during loading – adapted from MC2010	338
Figure 7.18: Measurement of reduction in axial force along the support/load plates	339
Figure 7.19: Effect of transverse pressure on the bond strength for the tested beams	342
Figure 7.20: Influence of $P1/P$ on normalised failure loads a) $P2$ and b) P for Series B	345
Figure 7.21: Influence of failure plane for series A and B according to a) BS8110 and b) EC2	345
Figure 7.22: Influence of loading face on measured and predicted shear resistance for beams a) without and b) with shear reinforcement	347
Figure 7.23: The effect of varying the load ratio within the shear enhancement zone for beams loaded on the tension face predicted using several models	349
Figure 7.24: The effect of changing $Lb1e$ on the strength of a beam with $P1/P = 1$	350
Figure 7.25: Change of the effective width and the contribution of the CLZ with the change of the failure plane	351

LIST OF TABLES

Table 3.1: Geometry and reinforcement details of the series A of test beams	104
Table 3.2: Geometry and reinforcement details of the series B of test beams	106
Table 3.3: Geometry and reinforcement details of the series C of test beams	109
Table 4.1: Strength development using cubes strength (100mm x 100mm) – series A.....	135
Table 4.2: Compressive cylinder strength (100mm dia. x 250mm Height) – series A.....	136
Table 4.3: Compressive cube strength (100mm) – series A.....	137
Table 4.4: Tensile strength (150 diameter x 300 Height) – series A.....	138
Table 4.5: Compressive and tensile strength for series A.....	138
Table 4.6: Strength development using cubes compressive strength – Series B.....	139
Table 4.7: Compressive cube strength (100mm) – Series B.....	140
Table 4.8: Compressive cylinder strength (100mm diameter x 200mm height) – Series B..	140
Table 4.9: Tensile cylinder strength (150mm diameter x 300mm height) – Series B.....	141
Table 4.10: Compressive and tensile strength for series B	142
Table 4.11: Strength development using cubes compressive strength – Series C.....	143
Table 4.12: Compressive cube strength (100mm) – Series C.....	143
Table 4.13: Compressive Cylinders Strength (100mm diameter x 200mm Height) – Series C.	144
Table 4.14: Tensile cylinders strength (150mm diameter x 300mm height) – Series C.	145
Table 4.15: Compressive and tensile strength for the series C.....	146
Table 4.16: Reinforcement properties for the experimental program.....	147

Table 4.17: Summary of the results for series A.....	148
Table 4.18: Maximum crack opening and sliding for the beams in series A at peak load.	152
Table 4.19: Summary of the results for the series B.....	166
Table 4.20: Maximum crack opening and sliding for the beams in the series B at peak load	174
Table 4.21: Summary of the results for series C.....	180
Table 4.22: Maximum crack opening and sliding for the beams in series C at peak load	182
Table 5.1: Modification of the five-spring model to account for beams with multiple point loads	222
Table 5.2: Predictions of the shear strength and failure plane for test beams using the five- spring models.....	225
Table 6.1: Properties of materials used in the FEA for beams tested by Fang (Fang, 2013)	285
Table 6.2: Comparison of the FE results obtained by Fang (2013) and in this work	287
Table 6.3: Material models and properties used in the FEA	299
Table 6.4: Material properties used in the NLFEA	299
Table 6.5: Summary of the results of the FEA	301
Table 7.1: Predictions of the shear strength of the test beams calculated with different design codes	309
Table 7.2: Assessment of code predictions of the strength of beams tested in this program	310
Table 7.3: Height and width of struts 2 and 4	319
Table 7.4: Experimental failure load and estimations of P_{calc}/P_{test} using STMs and FEA ..	321

Table 7.5: Location and number of stirrups yielded in the test and NLFEA.....	334
Table 7.6: Predicted and actual failure plane for different models	344

ANNOTATIONS

$A_{c,eff}$	Effective area of the concrete
a_1	Centreline distance between the inner load and the support plate
a_2	Centreline distance between the outer load and the support plate
A_{sw}	Cross sectional area of the shear reinforcement
a_v	Clear shear span
a_{v1}	Clear shear span of the inner load plate
a_{v2}	Clear shear span of the outer load plate
A_x	Projected contact areas for a unit crack area in the x directions
A_y	Projected contact areas for a unit crack area in the y directions
b_w	Width of the beam for shear
c	Concrete cover
d	Effective depth of the beam
d'	Concrete cover (STM)
d_{agg}	Mean aggregate size
d_g	Maximum aggregate size(MC2010)
D_{max}	Maximum aggregate size(Walraven model)
d_p	Diameter of bottom longitudinal bars. (2PKT)
$dy(\theta)$	Vertical displacement caused by a global rotation of the beam around the roller support
$dy_{corrected}$	Corrected vertical displacement of transducer #5
E'	Post peak stiffness of reinforcement bar
E_c	Concrete elastic modulus
E_s	Steel elastic modulus
E'_s	post-peak stiffness of the reinforcement
f_{bd}	Design value of the ultimate bond strength
F_{bd}	Bond force available along the design length
$f_{bd,0}$	Basic bond strength
f'_c	Concrete compressive strength
f_{cc}	Concrete cubic compressive strength
f_{cdt}	Design concrete tensile strength
f_{ck}	Characteristic compressive strength of the concrete
f_{cm}	Mean concrete compressive strength
f_{ct}	Concrete tensile strength
f_{cu}	Concrete cubic compressive strength (Walraven,1980)

F_d	Dowel force
F_{du}	Ultimate dowel force
f_r	Modulus of rupture for the concrete
f_t	Reduced tensile strength of the concrete (FEA)
f_y	Yielding strength of the reinforcement
f_{ywd}	Yielding strength of the stirrups
G_{12}	Tangential shear modulus
G_f	Foundation modulus for concrete (Millard and Johnson, 1984)
G_{fc}	Compressive fracture energy
G_{ft}	Tensile fracture energy
h	Height of the beam
h	Crack band width (FEA)
H_i	Horizontal component of force in strut (STM)
I_s	Second moment of area for a reinforcement bar
K_c	Foundation modulus for concrete (Soroushian, 1987)
k_c	Concrete strength reduction factor (MC2101)
k_{dg}	Aggregate size factor (MC2010)
K_i	Initial dowel stiffness
k_s	Reduction factor due to the state of strain in the web (MC2010)
k_v	Reduction factor of the design shear resistance attributed to the concrete (MC2010)
L	Effective bond length
l	horizontal projections of the strut-node interface
L_0	Length of the heavily cracked zone
L_1	Bond length of the plastic zone (Sigrist, 1995)
L_2	Bond length of the elastic zone (Sigrist, 1995)
L_{b1e}	Effective width of the loading plate
l_{bd}	Design anchorage length
L_{comp}	Length over which the transfer pressure is spread
L_g	DIC gauge length
L_h	Vertical distance between the two RHS transducers at the edge of the beam
L'_h	Vertical distance between the two DIC at the centre of the beam
L_k	Length between the kinks in the flexural reinforcement
L_{SG}	Length between strain gauges before and after the support/load plates
l_t	Width of the top loading plate

M_{Ed}	Design moment at the critical section
M_{max}	Maximum beam moment
n	Number of stirrups within the central $\frac{3}{4}$ of the clear shear span (BS8110)
n_{avi}	Number of stirrups in the shear span i
P_1	Load applied at the inner loading plate
P_2	Load applied at the outer loading plate
P_{tr}	Transfer pressure near the load/support plate
r	Ratio of the sliding displacement to the crack opening (CDM)
R_1	Ratio of the inner load to the total RHS load
R_2	Ratio of the outer load to the total RHS load
R_{eff}	Percentage of the load on the right-hand side of the rig applied to the load/ support
s	Crack sliding
S_{CR}	Distance travelled by the corner of the beam during the test
S_{max}	Spacing of the radial cracks at the bottom of the section (2PKT)
S_{mx}	Crack spacing in the longitudinal reinforcement directions
S_{my}	Crack spacing in the transverse reinforcement directions
s_v	Stirrup spacing
S_{xe}	Effective crack spacing
S_θ	Crack spacing (MCFT)
T	Tensile force in the flexural reinforcement
t_{CR}	Distance between the bottom corner and the centre of rotation of the rigid body
T_{si}	Force in stirrups set i
u	Vertical projection of the strut-node interface
V_a	Contribution of aggregate interlock
V_c	Contribution of the compression zone
v_{ci}	Shear stress on the crack
V_{CLZ}	Contribution of the critical loading zone
V_d	Contribution of the dowel action
V_{Ed}	Design shear force
V_{flex}	Shear force resulting from flexural equilibrium (five -spring mode)
V_r	Contribution of the residual tensile strength
V_{Rd}	Design shear resistance
$V_{Rd,c}$	Design shear resistance attributed to the concrete
$V_{Rd,max}$	Maximum strength corresponding to the minimum inclination of the compressive stress field (MC2010)

$V_{Rd,s}$	The design shear resistance provided by shear reinforcement
V_{RHS}	Shear force in the right-hand side of the beam
V_s	Contribution of stirrups
v_u	Shear strength of the beam
w	Crack opening
w	Strut width, normal to its centreline, at the strut-node interface (STM)
w_{min}	Crack opening corresponding to the maximum concrete tensile strain
w_o	Initial crack opening
X_{CR}	X ordinate of the centre of rotation
X_i	Horizontal projection of the width of strut i at the node
x	Flexural compression zone depth
X_{out}	X ordinate of the RHS bottom corner of the beam
X'_{out}	X ordinate of the deformed RHS bottom corner of the beam
$x_{w,out}$	X ordinate of the bottom horizontal transducer
$x_{\Delta c}$	Distance from the origin of the 2PKT to the location where vertical displacement is measured
Y_i	Vertical projection of the width of strut i at the node
z	Effective shear depth
Z_{CR}	Z ordinate of the centre of rotation
Z_{out}	Z ordinate of the RHS bottom corner of the beam
Z'_{out}	Z ordinate of the deformed RHS bottom corner of the beam
γ	Slope of the crack opening and sliding curve (Ulaga,2003)
γ_c	Material factor of the concrete
γ_{cr}	Crack shear strain
$\gamma_{cr,ult}$	Limiting value of the crack shear strain
\emptyset	Bar diameter
\emptyset_{block}	Rotation of the rigid body
\emptyset'_{block}	Difference between the rigid block rotation and the global rotation of the beam
\emptyset_{global}	Global rotation of the beam
α	Ratio of the axial stress to the yielding strength of a bar (Millard and Johnson,1984)
α	Inclination of the critical crack
α	Concrete compressive strain (FE)
α_1	Stress field angle given by the (MCFT)
α_p	Strain corresponding to the maximum compressive stress (FE)
β	Shear retention factor (FEA)

β	Shear enhancement factor
β	Compressive strength softening parameter (MCFT)
β_1	Shear enhancement factor for the inner load
β_2	Shear enhancement factor for the outer load
β_i	Ratio of the horizontal component of the force in strut (i) to the total compression force in the flexural compression zone
$\beta_{\sigma cr}$	Concrete strength reduction factor due to lateral cracking (FEA)
δ	Crack Sliding (Ulaga, 2003)
Δ	Total displacement of the shear span (2PKT)
δ_{bottom}	Horizontal displacement at the bottom edge of the beam
Δ_c	Shear displacement (2PKT)
Δ'_c	Shear displacement of the intermediate zone of the beam
Δ_s	Crack sliding (Walraven and Reinhardt, 1981)
Δ_t	flexural displacement of the shear span
δ_{top}	Horizontal displacement at the top edge of the beam
δ_{total}	Total measured vertical displacement
$\delta_{w, out}$	Vertical displacement near the bottom edge of the beam
δ_x	Deformation of points in the x direction
δ_z	Deformation of points in the z direction
ε^{con}	Solid strain (concrete strain) (FEA)
ε_{nn}^{cr}	Crack strain (FEA)
$\varepsilon_{nn,ult}^{cr}$	Ultimate crack strain (FEA)
ε_0	Concrete ultimate strain
ε_1	Principal tensile strain
ε_{11}	Initial maximum principal strain
ε_2	Principal compressive strain
ε_{22}	Initial minimum principal strain
$\varepsilon_{ct,max}$	Maximum concrete tensile strain
ε_{cx}	Concrete strains in the x directions (MCFT)
ε_{cy}	Concrete strains in the y directions (MCFT)
ε_s	Strain in the reinforcement bar
ε_{sx}	Reinforcement strains in the x directions (MCFT)
ε_{sy}	Reinforcement strains in the y directions (MCFT)
$\varepsilon_{t,1}$	Reinforcement strain in section 1 (2PKT)
$\varepsilon_{t,2}$	Reinforcement strain in section 2 (2PKT)

$\varepsilon_{t,avg}$	Average tensile strain in the reinforcement
$\varepsilon_{t,min}$	Minimum average tensile strain in the reinforcement
ε_x	Longitudinal strain at the mid-depth of the effective shear depth
η_{fc}	Reduction factor for the brittle behaviour of concrete with higher strength
θ	Inclination of the compressive stress field
θ_{min}	Minimum inclination of the compressive stress field (MC2010)
μ	Coefficient of friction
ρ	Percentage of shear reinforcement
σ	Normal stress on the crack surface
σ_{nm}^{cr}	Crack stress (FEA)
σ_{11}	Initial maximum principal stress
σ_{22}	Initial minimum principal stress
σ_{avg}	Average stress in the critical loading zone
σ_{pu}	Matrix yielding strength
$\sigma_{(Rd,max)}$	Strength of the strut/node (EC2 2004)
τ	Shear stress on the crack surface
τ^{cr}	Crack shear stress (FEA)
τ_0	The bond stress of the stirrups and surrounding concrete (Sigrist, 1995)
τ_u	Maximum shear stress (Gambarova and Karakoç, 1983)

CHAPTER 1. INTRODUCTION

1.1. Background

Despite extensive research, there is still little consensus on an adequate theory to describe the shear behaviour of reinforced concrete (RC) elements, particularly for elements without shear reinforcement. The importance of the study of the shear arises from the nature of shear failure, which can be brittle occurring with little or no warning. Consequently, shear failure can lead to disastrous loss of infrastructure and associated casualties. A famous example of structural concrete shear failure is the collapse under self-weight of the roofs of two U.S. air force bases in 1955 (Stamenkovic, 1977) and 1956 (Delatte Jr, 2008). Key milestones in research into shear include the 1962 report of the joint ACI-ASCE Committee 326 (ACI-ACSE326), the work of Kani (Kani, 1964) and the CEB-FIB model code introduced in 1978. A noticeable milestone in the modelling of shear behaviour was the Modified Compression Field Theory (MCFT) of Vecchio and Collins (Vecchio and Collins, 1986). This theory forms the basis of the shear provisions in the AASTHO-LRFD (AASHTO-LRFD, 2012), CSA (CSA, 2004) as well as fib MC2010 (fib, 2010). Recent developments in this field include the critical shear crack theory (Muttoni and Fernández Ruiz, 2008), the two parameter kinematic theory (Mihaylov et al., 2013) and the five-spring model (Mihaylov, 2015). A noticeable milestone in the modelling of deep beams is strut-and-tie modelling (Schlaich et al., 1987).

The shear strength of reinforced concrete beams is enhanced by arching action when loads are applied to the top face of the beam within around twice the beam effective depth (d) of supports. The strain distribution in these so-called “disturbed” regions is not uniform. Consequently, the hypothesis that plane sections remain plane does not apply. Considerable effort has been expended in the experimental and numerical study of shear enhancement as outlined by Reineck and Todisco (2014) and Todisco et al. (2016). Despite this, the vast majority of pertinent laboratory tests are on simply supported beams with single point loads applied within $2d$ of supports. Such tests are unrepresentative of the typical design scenario where beams are continuous and top loaded on the tension face near supports. Experimental investigation is essential for the development of improved design methods but is expensive, time-consuming and subject to adequate selection of loading and boundary conditions. Nonlinear finite element analysis (NLFEA), on the other hand, can be used to predict

behaviour before tests if correctly calibrated. Consequently, NLFEA can be used to inform the choice of critical parameters to be investigated in the laboratory, which significantly reduces cost as well as enhancing the usefulness of test results. NLFEA can also be refined after testing to conduct parametric studies on non-investigated parameters.

With the exception of the tests of Brown and Bayrak (2007) and Vollum and Fang (2014, 2015), which considered beams loaded on their flexural compression face, little attention has been given to the behaviour of beams with multiple point loads applied either entirely within or partly within $2d$ of supports. Design codes typically provide simplified methods for modelling shear enhancement in beams loaded on their top face within $2d$ of supports. Most codified design methods relate shear resistance to either the flexural reinforcement strain or the flexural reinforcement ratio. Of these, only strain-based formulations (e.g. fib Model Code 2010 (fib, 2013)) are sensitive to the beam support conditions (e.g. simply supported or continuous) and hence whether or not loads are applied to the flexural tension or compression face. The author is unaware of any previous tests investigating the shear resistance of either continuous or cantilever beams with two point loads applied within $2d$ of supports. Furthermore, very low priority has been given to the case of beams loaded on their flexural tension face in the past 60 years with only 1% of the research directed to such cases as demonstrated by (Collins et al., 2008).

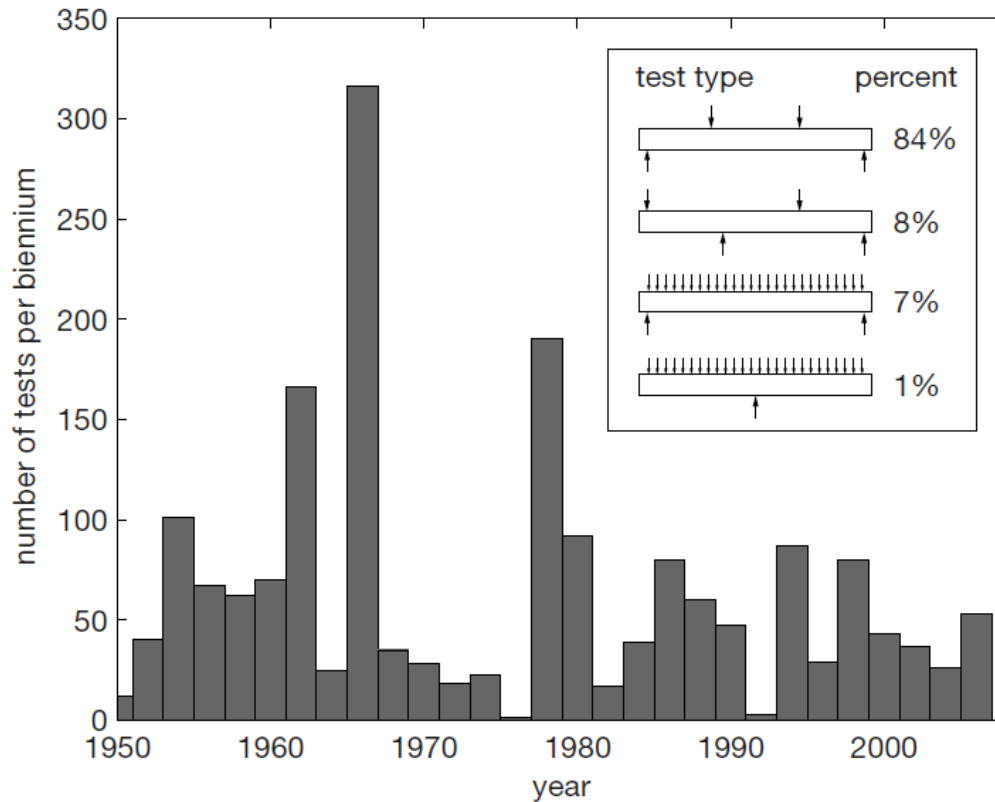


Figure 1.1: History of research in shear in the past 60 years (Collins et al., 2008). Figure reproduced with permission of the rights holder, Magazine of Concrete Research.

Beams loaded with multiple point loads on their tension face are commonly found in structures like bridges cross head girders and the internal supports of continuous transfer girders. Although very common, the code design methods do not differentiate between tension and compression loading face in design methods for shear resistance.

1.2. Research Aim and Objectives

This research aims to study the effect of loading arrangement, and sign of bending moment, on shear enhancement in RC beams loaded on their top face. This will be achieved through experimental investigation, non-linear finite element analysis, strut and tie modelling and analysis of the test results using available models and design codes. The research will shed light on the influence of the sign of bending moment (i.e. hogging/sagging) on the shear resistance and deformation of beams loaded on their top face with multiple point loads. In addition, a practical strut-and-tie model will be developed for the latter case, which is suitable for use, by practitioners.

The main objectives of this research are:

1. To develop and calibrate a nonlinear finite element modelling procedure using pertinent test results. The resulting modelling procedure is used to inform the design of the experimental campaign.
2. To conduct an experimental program to investigate the influences of loading beams on the tension and compression face, varying the ratio of pairs of loads applied within $2d$ from the face of the support and the effect of partly loading the beam outside $2d$ from the support.
3. To describe the deformation of beams loaded on the tension face with multiple point loads using displacements obtained with Digital Image Correlation (DIC).
4. To evaluate and compare the contributions of the shear transfer mechanisms (i.e. contributions of aggregate interlock, residual tensile stress, dowel action, flexural compression zone and shear reinforcement) of beams loaded on the tension and compression face. The individual contribution of the shear resisting mechanisms will be assessed using cracks kinematics obtained from DIC.
5. To examine the applicability of the shear strength provisions in codes of practice for short shear span beams with loads applied on the flexural tensile face, namely the former British Standard BS8110 (BSI, 1997), the current Eurocode (BSI, 2004) and fib Model code 2010 (fib, 2010).
6. To construct strut and tie models (STM) for beams loaded on the tension face with pairs of loads applied within $2d$ of supports.
7. To carry out parametric studies using NLFEA to evaluate the effect of parameters not investigated in the experimental program.

1.3. Thesis Outline

This work is spread over eight chapters. The outline of each chapter is as follows:

Chapter 1: Introduction

This current chapter provides a brief background to the research, addresses the research question, states the research aim and objectives and outlines the description of the thesis chapters.

Chapter 2: Literature Review

The available literature in the research topic is explored in this chapter; this includes the different models of shear transfer mechanisms and recent advances in this field, provisions for the shear strength in different codes of practice, a review of various design models of shear strength of deep beams and introduction to strut and tie modelling.

Chapter 3: The Experimental Program

This chapter describes the experimental program carried out by the author in the heavy structures laboratory at Imperial College London. Three sets of four short shear span beam specimens were tested. Each set investigates one of the variables described in objective (2). This chapter also describes the manufacturing process of the beams, the loading configurations, instrumentation and procedures used to obtain crack kinematics with DIC.

Chapter 4: The Experimental Results

This chapter presents the material properties of the concrete and reinforcement used in the beams as well detailed results of the beam tests (i.e. the global load-deflection response, failure modes and crack patterns, the surface strain of the concrete and reinforcement strain gauge readings).

Chapter 5: Crack kinematics and Shear Transfer Actions

This chapter provides a description of deformation and ultimate load for beams loaded on the compression and tension face based on the two parameters kinematic theory (Mihaylov et al., 2013) and the five-spring model (Mihaylov, 2015). These theories are modified in this chapter to account for the load configuration and boundary conditions. Shear transfer actions are evaluated using the five-spring model as well as in terms of crack displacements determined with the aid of the DIC system.

Chapter 6: Non-linear Finite Element Methodology

This chapter comprises three parts. The first part reviews the main features of the NLFEA and defines the basic constitutive models and solution procedure available on the software used (TNO Diana v10.2). The experimental results obtained in Chapter 4 are used in the second part to calibrate the FEM and to assess the sensitivity of the model to several parameters. Finally, the selected models and solution procedures are decided and the load-deflection response of the adopted parameters are compared with the test results.

Chapter 7: Analysis of the Experimental Results

Results obtained from the experimental program are used in this chapter to assess the provisions of current design codes regarding the shear strength of short shear span beams. A novel STM is developed for cantilever beams loaded with pairs of point loads on the tension face. The model is validated using the author's test results and refined NLFEM. NLFEM is used in this chapter to carry out parametric studies to investigate other aspects such as prediction of critical failure plane, the influence of tension face loading on shear resistance and the effect of the transfer compression on the bond force near the load/support plates. Comparisons are also made with the predictions of the five-spring model.

Chapter 8: Conclusions and Recommendations

This chapter provides a summary of the research, highlights key conclusions and recommends further work.

CHAPTER 2. LITERATURE REVIEW

2.1. Introduction

Shear failure in reinforced concrete structure has been subject to investigation since the early 20th century. The significance of the shear failure in reinforced concrete structures arises from its brittle nature and its limited capacity of deformation. The truss analogy was the first and basic model proposed to simulate the shear behaviour in reinforced concrete structures (Mörsch, 1922). Since then, extensive research has been conducted to understand shear behaviour, particularly shear transfer actions.

RC deep beams are shear critical members. As such, their behaviour in shear has been widely investigated both experimentally and theoretically (Mihaylov et al., 2013, Mihaylov, 2015, Mihaylov et al., 2015, Kyoung-Kyu Choi and Hong-Gun, 2016, Vollum and Fang, 2015).

This chapter briefly reviews the relevant literature, which includes:

1. Shear transfer actions in RC beams.
2. Essential models for shear in RC beams (Modified compression field theory (MCFT), the simplified MCFT, Two-parameter kinematic theory (2PKT) and Park's model).
3. Shear strength predictions in some design codes.
4. Strut-and-tie models (STM).

2.2. Shear Transfer Actions in Reinforced Concrete Beams

Shear failure is characterised by the formation of a critical shear crack (Muttoni and Fernández Ruiz, 2008). After the critical shear crack is formed, concrete can still transfer force through the crack via different shear transfer actions. There is a growing consensus about the main actions for shear transfer in reinforced concrete beams, which are (Figure 2.1):

- Aggregate interlock mechanism (V_a),
- Contribution of the compression zone (V_c),
- Dowel action mechanism (V_d),
- Shear reinforcement mechanism (V_s) – if present, and.
- Residual tensile stress mechanism (V_r)

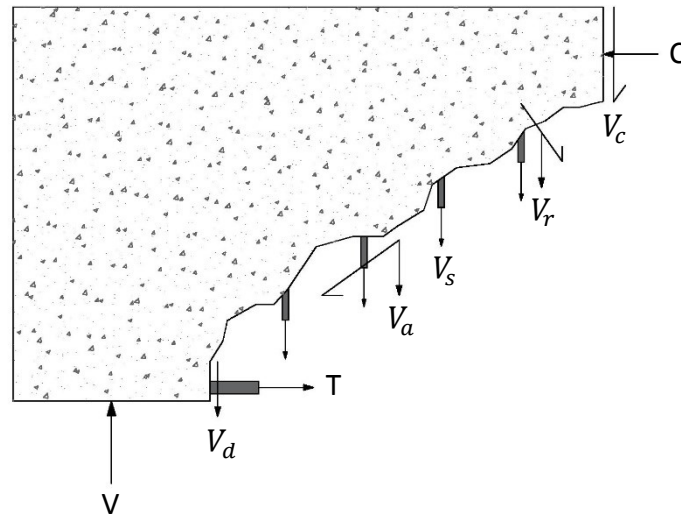


Figure 2.1: Shear transfer actions in reinforced concrete beams

Although considerable research has gone into studying these actions in isolation, the interaction between actions, as well as their individual contributions to overall shear resistance, are still the subject of much research (Campana et al., 2013, Cavagnis et al., 2015, Fang, 2013, Elwakeel et al., 2018).

Up to recently, quantitative studies into the relative contributions of each shear resisting action have been based on manual measurements of crack kinematics that were stopped prior to failure, for reasons of safety (Campana et al., 2013, Cavagnis et al., 2015, Fang, 2013, Elwakeel et al., 2018). Recently, the development of advanced Digital Image Correlation (DIC) methods has opened up the possibility of measuring crack kinematics up to and beyond peak load.

In the following sections, shear transfer actions in RC deep beams are reviewed and available models to evaluate them are discussed. Residual tensile strength contributes significantly to the shear strength of slender but not short shear span beams. This is due to differences in the shape and kinematics of the critical shear crack. In slender beams, the critical shear crack has an almost horizontal upper branch along which shear is resisted by residual tensile strength (Yang 2014). The contribution of residual tensile strength to shear resistance is much less in short shear span beams where the critical shear crack typically runs diagonally between the loading plate and support (Fang 2013). Consequently, the contribution of residual tensile strength is not be discussed further in this thesis.

2.2.1. The contribution of aggregate interlock

The contribution of aggregate interlock to the shear resistance of cracked reinforced concrete beams is widely acknowledged (Campana et al., 2013, Fang, 2013, Fernández Ruiz et al., 2015, Walraven and Reinhardt, 1981). Previous studies show that the shear force transferred through aggregate interlock depends on parameters including the crack slip, crack width, maximum aggregate size, concrete strength and crack normal stress.

Constitutive models for aggregate interlock can be classified into two categories:

1. Physical crack models which are based on the shape of the crack surface and have rational formation (e.g. (Walraven, 1980, Li, 1989))
2. Empirical crack models where the crack stress relationships are derived from experimental test results (e.g. (Walraven and Reinhardt, 1981, Hamadi and Regan, 1980, BAZANT and GAMBAROVA, 1980, Gambarova and Karakoç, 1983)).

The physical models are based on mechanical, geometric, material and statistical considerations and are consequently more complicated than empirical models derived from curve fitting test results.

Walraven two-phase model

Walraven (1980) developed a physical model of aggregate interlock as part of a wider investigation into the shear behaviour of pre-cracked push-off shear specimens - Figure 2.2. The Walraven two-phase model is widely used to estimate the contribution of aggregate interlock (Cavagnis et al., 2017).

The model treats concrete as a two-phase material consisting of aggregate (with diameter > 2.5 mm) and mortar (cement + fine aggregate with diameter < 2.5 mm). Walraven linked the normal and the shear resistance developed on the aggregate surface to several parameters including crack width and crack slip, the maximum aggregate size and the total aggregate volume of the concrete. Direct and shear force are given as:

$$\sigma = \sigma_{Pu}(A_x - \mu \times A_y) \quad \text{Equation 2.1}$$

$$\tau = \sigma_{Pu}(A_y + \mu \times A_x) \quad \text{Equation 2.2}$$

Where A_x and A_y are the projected contact areas (as in Figure 2.2 – a) for a unit crack area in the x and y directions, σ_{Pu} is the matrix yielding strength (given as $6.39 \times f_{cc}^{0.56}$ MPa) and μ is the coefficient of friction.

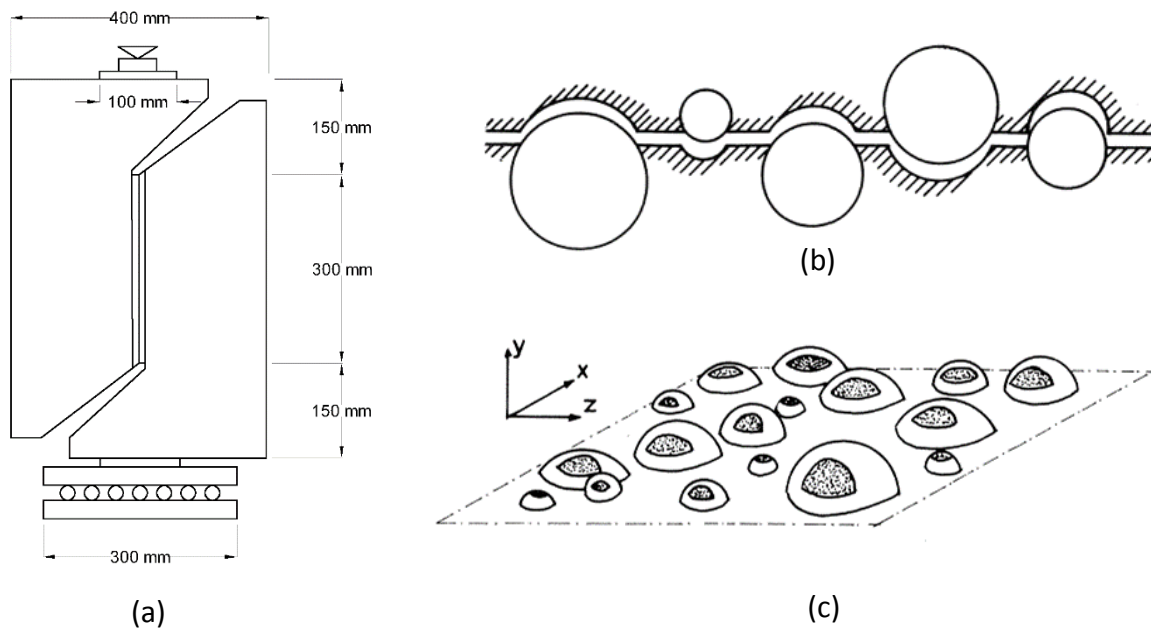


Figure 2.2: Walraven two-phase model: a) Push-off test specimen, b) Aggregate interlock in the shear crack plane and c) Contact area during shear displacement (Walraven and Reinhardt, 1981)

Walraven's two-phase model gives good predictions of the response of his push-off tests. This is illustrated in Figure 2.3, which shows good agreement for a wide range of crack opening and sliding displacements for both shear and normal stresses.

In terms of the crack kinematics, the model assumes all crack sliding (δ) occurs after the full development of the crack opening (w_0). The reliability of this assumption has been questioned by several researchers (Guidotti, 2010 and Ulaga, 2003). Guidotti (2010) suggested that only part of the crack opening (w_0) is necessary for the sliding (δ) to initiate, after that both the crack opening and sliding increase at an angle ($\gamma = \arctan(w_f/\delta)$) where $w_f = w - w_0$. Ulaga (2003), on the other hand, stated that cracks initiate at an angle (γ) with $w_0 = 0$. The Modifications to the Walraven (1980) kinematics and their effect on the direct and shear strength are presented in Figure 2.4.

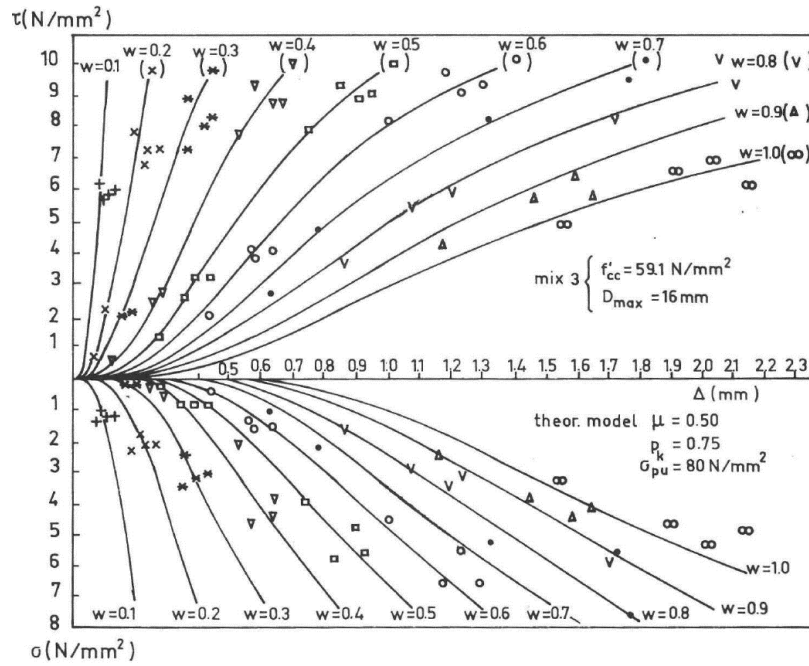


Figure 2.3: Comparing the Walraven two-phase model with the test results Walraven and Reinhardt, 1981).

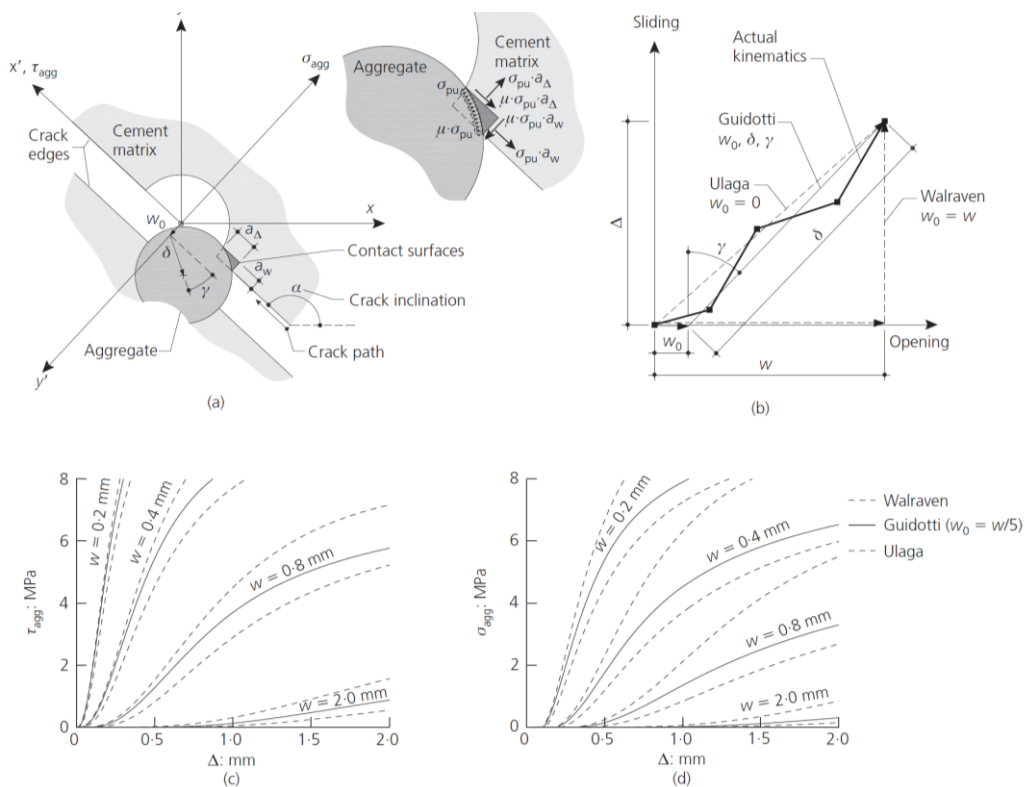


Figure 2.4: Modifications to Walraven (1980) kinematics and their effect on the direct and shear strength (Campana et al., 2013). Figure reproduced with permission of the rights holder, Magazine of Concrete Research.

The interaction between the crack kinematics (w and δ) depends on the type, location and orientation of the critical shear crack. In slender beams, the critical crack can be separated into a quasi-horizontal part with no sliding and an inclined part with the opening and sliding (Muttoni and Fernández Ruiz, 2008). In deep beams, however, the critical crack is inclined between the load and the support and mainly governed by shear displacement (Kueres and Hegger, 2018). The selection of the appropriate models hence is a case dependent and needs experimental verification.

Walraven and Reinhardt linear regression (1981)

Walraven and Reinhardt (Walraven and Reinhardt, 1981) used linear regression to develop a widely used aggregate interlock model which accounts for the effect of several parameters considered in their push-off tests. This model has widely been used to evaluate the contribution of aggregate interlock due to its simplicity and acceptable results. The investigated parameters included the flexural reinforcement ratio, bar diameter, concrete strength and crack plane roughness. The model provides two sets for normal and lightweight concrete in which the crack shear (τ_{cy}), and direct (σ_{cy}) stresses are expressed by the crack opening and sliding only. For normal concrete, the equations are as follows:

$$\tau_{cr} = -\frac{f_{cu}}{30} + [1.8 \cdot w^{-0.8} + f_{cu} \cdot (0.234 \cdot w^{-0.707} - 0.2)] \cdot s \quad \text{Equation 2.3}$$

$$\sigma_{cr} = -\frac{f_{cu}}{20} + [1.35 \cdot w^{-0.63} + f_{cu} \cdot (0.191 \cdot w^{-0.552} - 0.15)] \cdot s \quad \text{Equation 2.4}$$

Where for lightweight concrete:

$$\tau_{cr} = -\frac{f_{cu}}{80} + [1.495w^{-1.233} - 1] \cdot s \quad \text{Equation 2.5}$$

$$\sigma_{cr} = -\frac{f_{cu}}{40} + [1.928w^{-0.87} - 1] \cdot s \quad \text{Equation 2.6}$$

In which s is the crack sliding. Predictions obtained from this model have been verified by Walraven and Reinhardt as shown in Figure 2.5 for both normal and lightweight concrete. However, this model ignores contributions of parameters known to influence the aggregate contribution like the aggregate size and the strength of the mortar.

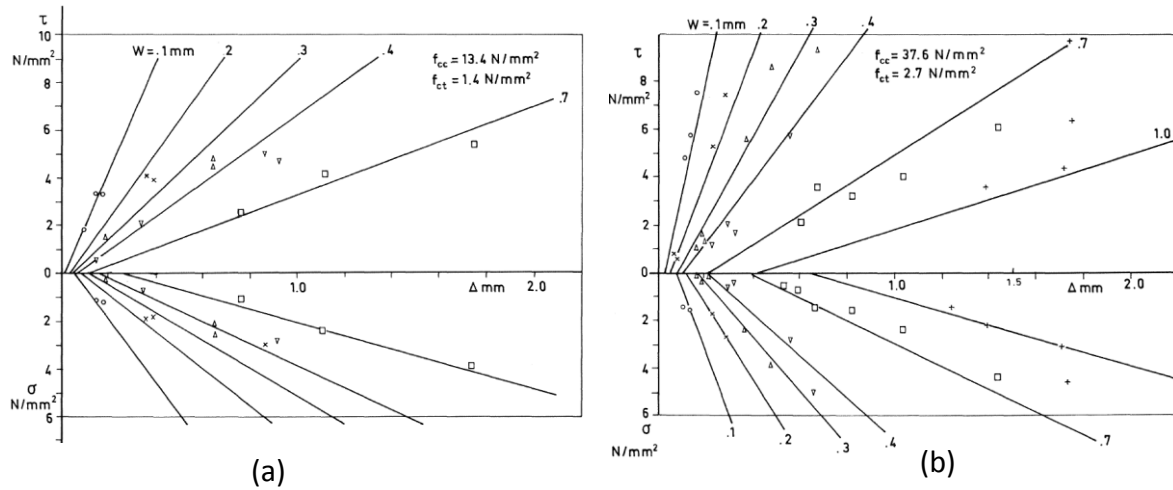


Figure 2.5: Comparing the Walraven and Reinhardt model with the test results for a) Normal concrete and b) Lightweight concrete, Walraven and Reinhardt (1981).

The Rough Crack model (BAZANT and GAMBAROVA, 1980) and (Gambarova and Karakoç, 1983)

Bazant and Gambarova (1980) developed the semi-empirical rough crack model by considering the crack surface as a regular array of trapezoidal asperities. The model was influenced by a series of tests into aggregate interlock performed by Paulay and Loeber in un-reinforced concrete/reinforced concrete (Paulay and Loeber, 1974). The main observations they concluded from these results, which became model assumptions, were:

1. The shear stress-displacement increases up to a horizontal plateau at a ratio $r=1.2$ (where r is the ratio of the sliding displacement to the crack opening i.e.: $r = s/w$)
2. The effect of the crack opening on the maximum shear stress is negligible.
3. The shear stress-displacement curve is proportional to the ratio of the sliding displacement to the crack opening.

The curve that best fits the results for the un-reinforced concrete obtained by Paulay and Loeber (1974) relates the shear and normal stress to the ratio of the sliding displacement to the crack opening, the concrete strength (f_c) and the maximum particle diameter (D_{max}).

The equations of the rough crack model are as follows:

$$\tau = \tau_u \cdot r \cdot \frac{a_3 + a_4 \cdot |r|^3}{1 + a_4 \cdot r^4} \tag{Equation 2.7}$$

$$\sigma = -\frac{a_1}{w} \cdot (a_2 \cdot |\tau|)^p \tag{Equation 2.8}$$

In which:

$$\tau_u = \tau_0 \cdot \frac{a_0}{a_0 + w^2}, \quad \tau_0 = 0.245 \cdot f', \quad p = 1.3 \left(1 - \frac{0.231}{1 + 0.185 \cdot w + 5.63 \cdot w^2} \right)$$

$$a_0 = 0.01 \cdot D_{max}; \quad a_1 = 5.34 \times 10^{-4} \frac{N}{mm}; \quad a_2 = 145 \frac{mm^2}{N}; \quad a_3 = \frac{2.45}{\tau_0} \frac{N}{mm^2};$$

$$a_4 = 2.44 \cdot \left(1 - \frac{4}{\tau_0} \frac{N}{mm^2} \right)$$

τ_u is the maximum shear strength when r tends to infinity and τ_0 is the limiting shear stress. Additionally, Bazant and Gambarova suggested a more complicated numerical model for use in finite element software. In this model, a smeared crack approach was adopted assuming the reinforced concrete to be divided into a reinforcement net and cracked concrete (solid concrete + cracks) with strain decomposition. The prediction of this model, as well as the model for unreinforced concrete, are shown in Figure 2.6 below.

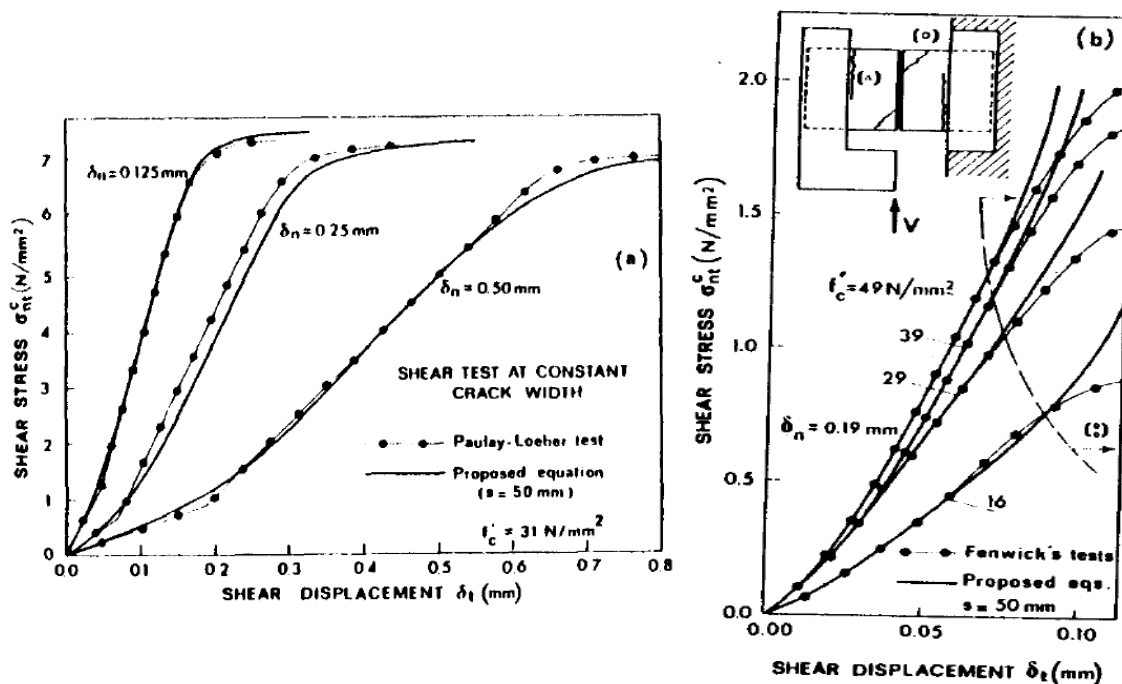


Figure 2.6: Test results compared to the rough crack model (BAZANT and GAMBAROVA, 1980). Figure reproduced with permission of the rights holder, *Journal of Structural Engineering*.

This model was later modified, to take into account the effect of the aggregate size and the confinement condition, by Gambarova and Karakoç (Gambarova and Karakoç, 1983) as follows:

$$\tau = \tau_0 \cdot \left(1 - \sqrt{\frac{2 \cdot w}{D_{max}}}\right) \cdot r \cdot \frac{(a_3 + a_4 \cdot |r|^3)}{(1 + a_4 \cdot r^4)} \quad \text{Equation 2.9}$$

$$\sigma = -a_1 \cdot a_2 \cdot \frac{r}{(1 + r^2)^{0.25}} \cdot \tau \quad \text{Equation 2.10}$$

$$a_1 \cdot a_2 = 0.62, \quad a_3 = \frac{2.45}{\tau_0}, \quad a_4 = 2.44 \cdot \left(1 - \frac{4}{\tau_0}\right), \quad \tau_0 = 0.25 \cdot f'$$

This model accounts for the aggregate size and boundary conditions. However, for reasons discussed earlier, it is more realistic to express the shear and direct stresses in terms of the crack opening and sliding rather than the ratio between them.

The Contact Density Model (CDM)

The contact density model, which have been developed by Li et al. (1989), describes the aggregate interlock resistance using contact density probability functions $\Omega(\theta)$. A crack plane is assumed here to consist of contact units with different inclinations in the range of $-\pi/2$ to $\pi/2$. The mathematical expression for this model is given by the following equations

$$\tau_{cr} = \int_{-\pi/2}^{\pi/2} \sigma_{con} K(w) A_t \Omega(\theta) \sin \theta d\theta \quad \text{Equation 2.11}$$

$$\sigma_{cr} = \int_{-\pi/2}^{\pi/2} \sigma_{con} K(w) A_t \Omega(\theta) \cos \theta d\theta \quad \text{Equation 2.12}$$

$K(w)$ is the effective ratio of contact area that presents the contact stage along the crack when w is large enough compared with the roughness of the crack surface. The density function $\Omega(\theta)$ is proposed as a trigonometric formula which is independent of the size, strength, type of the aggregate and the grading (Li, 1989). A_t (which represent the surface area) is proposed to be 1.27 time of the section area of crack plane.

Later work Li, Maekawa, Okamura & Soltani established a simplified formula based on their original model in which the stress depends on $r = s/w$, which is similar to the rough crack model.

$$\tau_{cr} = \frac{3.83 f' \left(\frac{1}{3}\right) r^2}{1 + r^2} \quad \text{Equation 2.13}$$

$$\sigma_{cr} = 3.83 f' \left(\frac{1}{3}\right) \left[\frac{\pi}{2} - \cot^{-1} r - \frac{r}{1 + r^2} \right] \quad \text{Equation 2.14}$$

Hamadi and Regan model (1980)

Hamadi and Regan conducted a series of 27 push-off tests and developed an empirical crack dilatancy model for aggregate interlock based on their test results (Hamadi and Regan, 1980). The model relates shear stress to the crack displacements, normal stress and aggregate type. Natural gravel aggregates and expanded clay aggregate were considered with the principal difference between the two being crack roughness. The main difference between the two types of concrete is that the crack surface for the natural aggregate concrete is rougher than that of the clay aggregate. The shear and direct stresses are given by the following expressions:

$$\tau = \frac{k}{w} \cdot s \quad \text{Equation 2.15}$$

$$\tau_u = c + \mu \cdot \sigma \quad \text{Equation 2.16}$$

The values for k , c and μ for the natural gravel are given as 5.4 N/mm^2 , 4.0 N/mm^2 and 0.7 respectively (Hamadi and Regan, 1980).

Discussion

There are some significant differences between the underlying assumptions of these models which can result in large differences in predictions between them as shown by Elwakeel et al. (Elwakeel et al., 2018). The mechanical model of Walraven (1980) accounts for aggregate type, maximum aggregate size, concrete strength, the coefficient of friction and the ratio between the total volume of the aggregate and the volume of concrete. The model also assumes no crack sliding occurs prior to crack opening which is not always the case as shown by Campana (Campana et al., 2013). The linear regression model of Walraven and Reinhardt (1981) is simple and widely used but it does not take into account the effect of the maximum aggregate size or type. The Gambarova and Karakoç (1983) model considers maximum aggregate size as well as the crack path $r = s/w$ and has been reported as giving reasonable predictions of shear transfer in deep beams (Fang, 2013, Sagaseta, 2008). The Hamadi and Regan model (1980) is a simple model for aggregate interlock; however, it has been reported to overestimate this contribution (Fang, 2013, Sagaseta and Vollum, 2011). In this research, the contribution of the compression zone is calculated using the Walraven two-phase model (Walraven, 1980) and for consistency with the five-spring model, the CDM (reference) (Li, 1989) is used in the calculation of the strength as seen in Chapter 5

2.2.2. The contribution of dowel action

Dowel action depicts the shear force transferred through cracks by combined shear and flexure in the reinforcement bars. Dowel action is commonly analysed using a beam on an elastic foundation analogy – Figure 2.7. The main parameters which influence dowel action are vertical displacement, bar diameter, concrete strength, shear reinforcement if present, and the concrete cover (Campana et al., 2013).

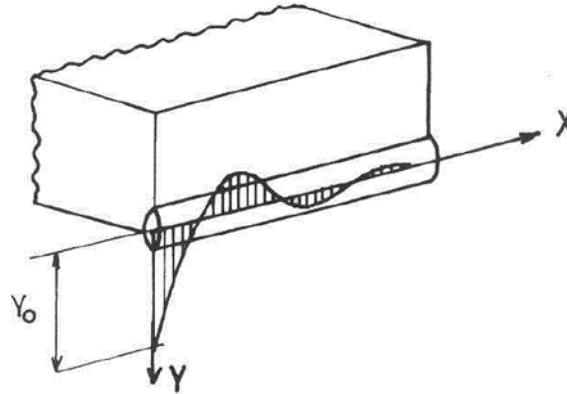


Figure 2.7: Beam in elastic foundation theory for the dowel mechanism (Walraven, 1980)

Three models for the contribution of the dowel action are discussed here: Walraven and Reinhardt model (Walraven and Reinhardt, 1981), Millard and Johnson model (Millard and Johnson, 1984) and He and Kwan model (He and Kwan, 2001).

Walraven and Reinhardt model (1980)

According to Walraven and Reinhardt, the dowel force depends on the bar diameter, crack opening and sliding displacements and concrete strength. This can be expressed based on the theory of a beam in an elastic foundation as follows:

$$F_d = \beta^3 EI \cdot 2s \quad \text{with } \beta = \sqrt[4]{\frac{\phi G_f}{4EI}} \quad \text{Equation 2.17}$$

Where s is the crack-sliding equivalent to the vertical displacement of the bar and G_f is the foundation modulus of the concrete. The value of G_f depends on the concrete quality under the bar, direction of the bar relative to the casting direction and the concrete cover. There is noticeable scatter in the literature regarding the value of G_f (Walraven, 1980). A value of $G_f = 34\sqrt{f_{cc} \cdot s^{-0.85}}$ was adopted by Walraven and Reinhardt where f_{cc} is the concrete cube

strength. Assuming no axial force exists in the bar ignoring the influence of the crack width on as a free length, the dowel force can be given as:

$$F_d = 50. s^{0.36} \cdot \phi^{1.75} \cdot f_c'^{0.38} \quad \text{Equation 2.18}$$

F_d is multiplied by ξ (Eleiott, 1974) to account for the reduction in the dowel strength caused by the presence of the tension force in the reinforcement:

$$\xi = 0.2 \cdot (w + 0.2)^{-1} \quad \text{Equation 2.19}$$

Millard & Johnson model (1984)

Millard & Johnson (1984) also based their model for the shear resistance provided by dowel reinforcement on the analysis of a beam on an elastic foundation. The dowel contribution in this model depends on the foundation modulus for the concrete (G_f) which was given as $G_f = 126.26 \times \sqrt{f_{cu}}$ where f_{cu} is the concrete cube compressive strength.

In the elastic stage, the initial dowel stiffness is expressed in this model as:

$$K_i = 0.166 \cdot G_f^{0.75} \cdot \phi^{1.75} \cdot E_s^{0.25} \quad \text{Equation 2.20}$$

Where E_s is the elastic modulus of the bar. However, due to the high-stress concentration beneath the bar, the assumption of elastic behaviour is not valid. This non-linear behaviour may occur due to concrete crushing/splitting or plastic yielding of the bar.

The dowel resistance is assumed to depend on the ratio (α) between the axial stresses in the bar and its yield strength. The dowel resistance is expressed as:

$$F_d = F_{du} \cdot \left(1 - \exp\left(\frac{-K_i s}{F_{du}}\right) \right) \quad \text{Equation 2.21}$$

F_{du} is the ultimate dowel force given by $F_{du} = 1.3 \cdot \phi^2 \cdot f_{cu}^{0.5} (f_y \cdot (1 - \alpha^2))^{0.5}$ and α is the ratio between the reinforcement stress and yield strength.

He and Kwan model (2001)

The He and Kwan (2001) model is based on the analysis of a beam on an elastic foundation. The dowel force in this model is given by:

$$F_d = E_s \cdot I_s \cdot \lambda^3 \cdot s \quad \text{Equation 2.22}$$

In which E_s is the modulus of elasticity of the flexural reinforcement. I_s is the moment of inertia of the bar and λ is a parameter signifies the foundation relative stiffness and has been stated as:

$$\lambda = \sqrt[4]{\frac{K_c \cdot \phi}{4 \cdot E_s \cdot I_s}} \quad \text{Equation 2.23}$$

In which K_c is the foundation modulus of the concrete around the reinforcement bar which is calculated using the formula recommended by Soroushian et al. (Soroushian et al., 1987) as $K_c = \frac{127 \cdot C_1 \cdot f_c'^{1/2}}{\phi^{2/3}}$. (C_1 is 0.6 for a clear bar spacing of 25mm and 1.0 for larger bar spacing).

The ultimate dowel action in this model was obtained using regression analysis on the test results of Dulacska (Dulacska, 1972) and is given by:

$$F_{du} = 1.27 \cdot \phi^2 \cdot (f_c \cdot f_y)^{1/2} \quad \text{Equation 2.24}$$

Discussion

The Walraven and Reinhardt model relates dowel resistance to the crack opening and sliding displacements, unlike the other two presented models, which relate the dowel force to the crack sliding displacement. Selection of an appropriate model for the dowel contribution depends on the stress state of the reinforcement and the required level of accuracy. The Walraven and Reinhardt model accounts for the influence of the tensile force in the reinforcing bar through the crack width. On the other hand, the Millard and Johnson model relates the dowel resistance to the ratio between the tensile stresses in the bar and reinforcement yield strength. The model proposed by He and Kwan is often used in finite element analysis as it adopts a linear response for the doweling action but this is not generally observed in experiments (Millard and Johnson, 1984). There are other models in the literature, which were not discussed here and can be found elsewhere ((Baumann and Rüschi, 1970, Campana et al., 2013), etc.).

Failure of dowel action can result from loss of concrete cover, longitudinal splitting of the concrete, concrete crushing, and formation of plastic hinges in the reinforcement or a combination of these. The upper limit of the dowel contribution based on the mentioned failure mechanisms is defined empirically in these models.

2.2.3. The contribution of shear reinforcement

Extensive research has been carried out to formulate the relationship between crack opening and the stresses induced in shear reinforcement crossing the crack. The model of Sigrist and Marti (1998) has been adopted by several researchers (Sigrist, 1995, Muttoni and Fernández Ruiz, 2007, Ruiz et al., 2010, Huber et al., 2016, Campana et al., 2013). The model is based on

a stepped rigid plastic behaviour for the bond between the shear reinforcement and surrounding concrete. Once the crack opens, the shear reinforcement is assumed to resist all the tensile stress previously resisted by concrete. Hence, the tensile force is maximized in the shear reinforcement at intersections with cracks and reduced in between cracks.

The bond strength between the shear reinforcement and the surrounding concrete is assumed constant and equals to twice the tensile strength of the concrete before yielding. After reinforcement yields, the bond strength reduces to the concrete tensile strength and plastic strains localize in stirrups in the zone near the crack. Figure 2.8 demonstrates the model behaviour of the shear reinforcement and its associated bond stress.

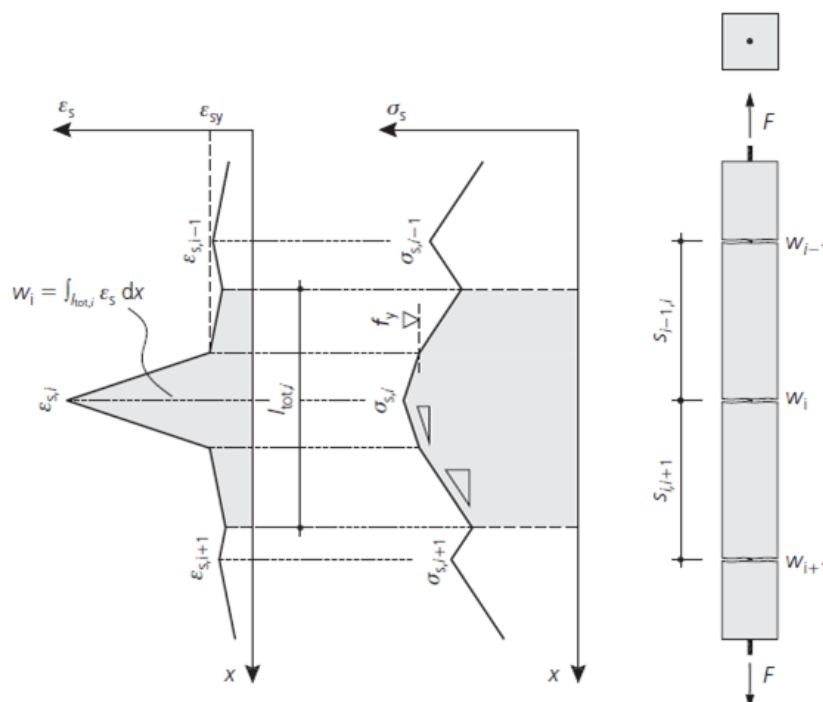


Figure 2.8: behaviour of the shear reinforcement in cracked concrete and bond stress according to Sigrist's model (Campana et al., 2013). Figure reproduced with permission of the rights holder, Magazine of Concrete Research.

According to this model, the stepped bond behaviour may be modelled in two phases before and after yielding - as shown in Figure 2.9.

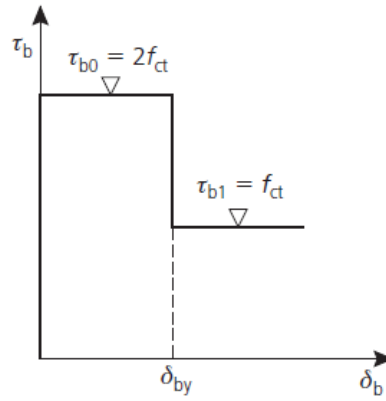


Figure 2.9: Sigrist stepped bond behaviour. Figure reproduced with permission of the rights holder, Magazine of Concrete Research.

The relationship between the stress in the bar (σ_s) and the crack opening (w) is derived using the strain-crack width relationship below:

$$w = 2 \cdot \int_0^L \varepsilon_s \cdot dx \quad \text{Equation 2.25}$$

In which L is the effective bond length.

Stirrups in the elastic stage

Before stirrups yield, the bond stress is assumed constant ($\tau_{b0} = 2 \cdot f_t$) and the effective bond length over which the slip occurs can be expressed as:

$$L = \frac{\sigma_s \cdot A_{sw}}{\pi \cdot \phi \cdot \tau_{b0}} \quad \text{Equation 2.26}$$

For a known crack opening (w), the stress in the stirrups (σ_s) can be found as:

$$\sigma_s = \sqrt{\frac{2 \cdot \pi \cdot E_s \cdot \phi \cdot f_t}{A_{sw}} \cdot w} \quad \text{Equation 2.27}$$

Stirrups in the elasto-plastic stage

After stirrups yield, the constant bond stress reduces to $\tau_{b1} = f_{ct}$. The bond length of the elastic zone (L_2) and that of the plastic zone (L_1) can be expressed as:

$$L_1 = \frac{(\sigma_s - f_y)}{\pi \cdot \phi \cdot \tau_{b1}} \cdot A_{sw} \quad \text{Equation 2.28}$$

$$L_2 = \frac{f_y}{\pi \cdot \phi \cdot \tau_{b0}} \cdot A_{sw} \quad \text{Equation 2.29}$$

As stated earlier, the crack width (w) can be obtained by the integration of the steel strains.

In this case, the crack width (w) can be expressed as follows:

$$w = 2A_{sw} \left(\frac{f_y^2}{2 \cdot E_s \cdot \pi \cdot \Phi \cdot \tau_{b0}} + \frac{(\sigma_s - f_y)^2}{2 \cdot E' \pi \cdot \Phi \cdot \tau_{b1}} + \frac{\sigma_s \cdot f_y}{E_s \pi \cdot \Phi \cdot \tau_{b1}} - \frac{f_y^2}{E_s \pi \cdot \Phi \cdot \tau_{b1}} \right) \quad \text{Equation 2.30}$$

Where $\sigma_s > f_y$ and E' is the post-peak stiffness of the reinforcement, which can be obtained from bar tests. Consequently, σ_s can be estimated in terms of the known crack width (w).

Aside from the model proposed by Sigrist, several researchers have also proposed other models to evaluate the contribution of the shear reinforcement (Shima et al., 1987, Maekawa and Qureshi, 1996, Soltani et al., 2003, Ruiz et al., 2007). However, the model proposed by Sigrist is widely used due to its simplicity and accepted outcomes (Campana et al., 2013, Fang, 2013).

2.2.4. The contribution of the compression zone

Numerous studies have been carried out to determine the contribution of the compression zone to shear resistance ((Tureyen and Frosch, 2003), (Choi et al., 2007), (Park et al., 2006) and (Mihaylov et al., 2015)). These studies show that the contribution of the compression zone depends on the acting normal and shear stresses and the depth of the compression zone at the failure location, which cannot be reliably predicted.

Park et al (Park et al., 2006) developed a strain based shear model for slender beams without shear reinforcement in which shear stress is assumed to be resisted by the compression zone of the intact concrete. The compression zone is subject to combined normal and shear stress resulting from the flexural moment and shear force. Although this model is applicable for slender beams where the stress distribution in the compression zone is assumed linear, it is presented here as it gives good background to the contribution of the compression zone for different load levels. In their study, the shear resistance of the compression zone is directly related to the normal stress and depends on the applied moment. The model adopts Rankin's failure criteria (Figure 2.10 (a)).

Four load stages are defined in this model as shown in Figure 2.10 (b). Before flexural cracking (AB), shear is resisted by the entire cross-section and the shear capacity is not significantly affected by micro-cracks. In the flexural cracks initiation stage (BC), the shear stress rapidly decreases as the effective depth resisting shear decreases. Stage (CD) applies once the cracks

reach the neutral axis when the shear force is assumed taken by the compression zone only. In the softening stage (DE), the effective compression zone of the intact concrete that resists the shear stress reduces since the softened extreme fibres do not contribute to the shear resistance.

According to Rankine's failure criteria, the material fails when its tensile stress reaches or exceeds its tensile strength or when its compressive stress reaches or exceeds its compressive strength. In concrete, the tensile strength is significantly less than the compressive strength; therefore, failure is governed by the tensile strength of the concrete.

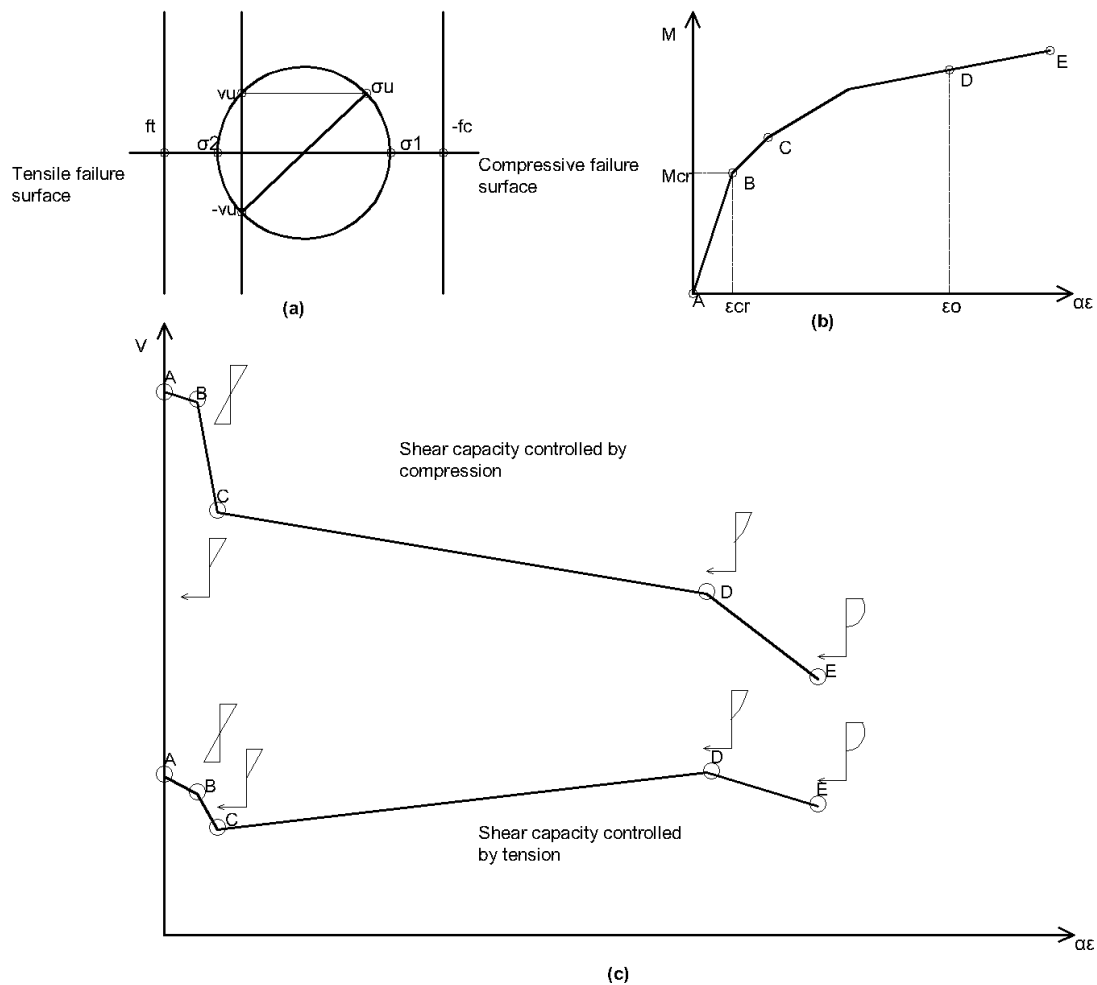


Figure 2.10: Park et al model (2003) for compression zone contribution. a) Mohr's circle for the Rankine's failure mode. b) loading stages c) compression and tension controlled shear capacity. Figure reproduced with permission of the rights holder, ACI Structural Journal.

As seen in Figure 2.10 (c), due to the low tensile strength of the concrete and regardless of the magnitude of the flexural deformation, the shear capacity controlled by tension is

significantly less than that controlled by compression. Equations for shear failure controlled by tension are given by (Park et al., 2006):

$$V = b \int_0^c v_u(z). dz \approx \sqrt{f'_t [f'_t + \bar{\sigma}]} \cdot b \cdot c \quad f_r/E_c < \alpha \varepsilon_0 < \varepsilon_0 \quad \text{Equation 2.31}$$

$$V = b \int_0^{c/\alpha} v_u(z). dz \approx \sqrt{f'_t [f'_t + \bar{\sigma}]} \cdot b \cdot c/\alpha \quad \alpha \varepsilon_0 > \varepsilon_0 \quad \text{Equation 2.32}$$

Where $\bar{\sigma} =$

$$\left. \begin{array}{l} \left(\alpha - \frac{\alpha^2}{3} \right) f_r/E_c < \alpha \varepsilon_0 < \varepsilon_0 \\ \frac{2}{3} f'_c \quad \alpha \varepsilon_0 > \varepsilon_0 \end{array} \right\} \quad \text{Equation 2.33}$$

$$f_r = 0.625 \cdot \sqrt{f'_c} \quad \text{Equation 2.34}$$

f'_t is the tensile strength of the concrete, v_u is the shear strength at failure, α is the ratio of the current strain to the ultimate strain ε_0 , $\bar{\sigma}$ is the average normal stress in the section, c is the depth of the compression zone and f_r is the modulus of rupture for the concrete.

Calculations of the depth of the compression zone and concrete compressive strain are complicated for non-linear behaviour and usually requires an iterative procedure. It is common to assume an elastic behaviour of the compression zone particularly for slender beams where the behaviour is governed by the flexural capacity. This is not the case in shear critical elements like deep beams where the behaviour is non-linear and the contribution of the compression zone is critical. Hence, several models for the shear transfer actions of deep beams have been developed with particular emphasis on the contribution of the compression zone as discussed in the next sections.

2.2.5. Evaluation of crack kinematics using DIC

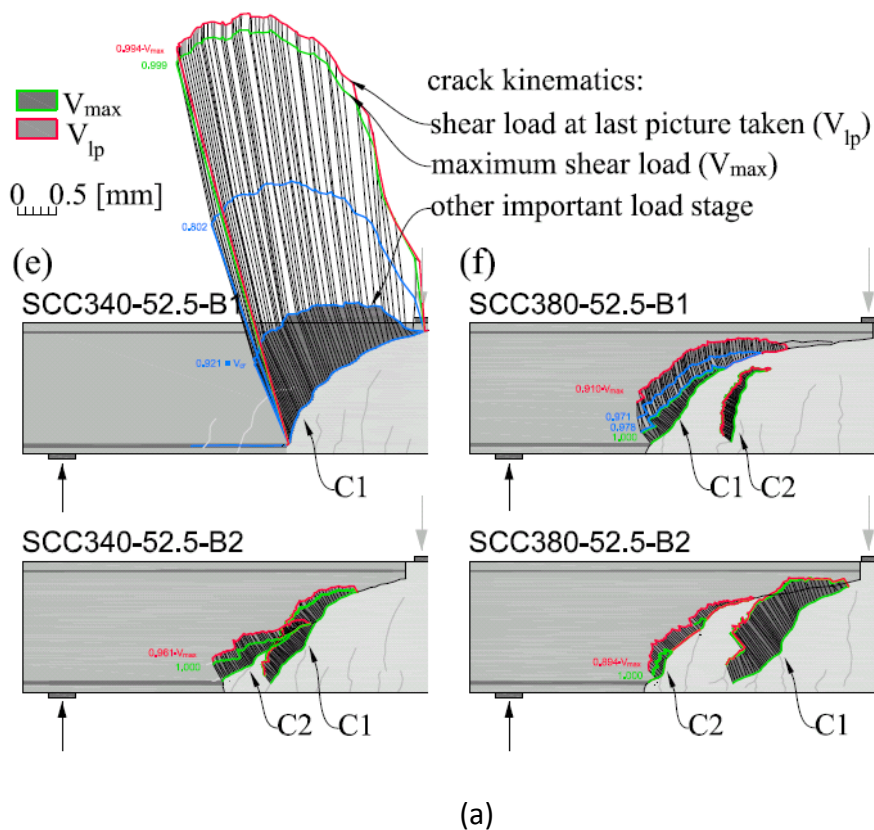
The shear transfer actions mentioned earlier are highly dependent on the kinematics and shape of the critical shear crack. Evaluation of these contributions includes two levels of uncertainties: the accuracy of the obtained crack kinematics and the validity of the models used. The first uncertainty has recently been limited with the use of the Digital Image Correlation (DIC) system while the latter is still an undergoing debate.

DIC is a non-contact tool used to obtain the displacement of samples during tests by means of digital photogrammetry. It has several advantages over conventional instruments like mechanical extensometers and cross transducers. The use of mechanical extensometers is

both tedious and potentially hazardous near failure. Furthermore, they do not provide continuous reading and can only gather information at discrete predetermined locations. Conversely, DIC systems provide continuous remote strain reading throughout the monitored area.

The use of DIC has recently been introduced to evaluate crack kinematics and orientation in the calculation of the shear transfer actions by several researchers (De Wilder et al., 2015, Cavagnis et al., 2015, Cavagnis et al., 2017, Huber et al., 2016, Huber et al., 2019).

The user needs to post-process the data gathered by the DIC system to obtain crack kinematics at selected load steps and the post-failure response (Figure 2.11- a) as described in Chapter 3. For certain DIC software packages, the user may also be able to directly obtain concrete surface strains (Figure 2.11- b). Further details about the processing of DIC and its accuracy can be found in Chapter 3.



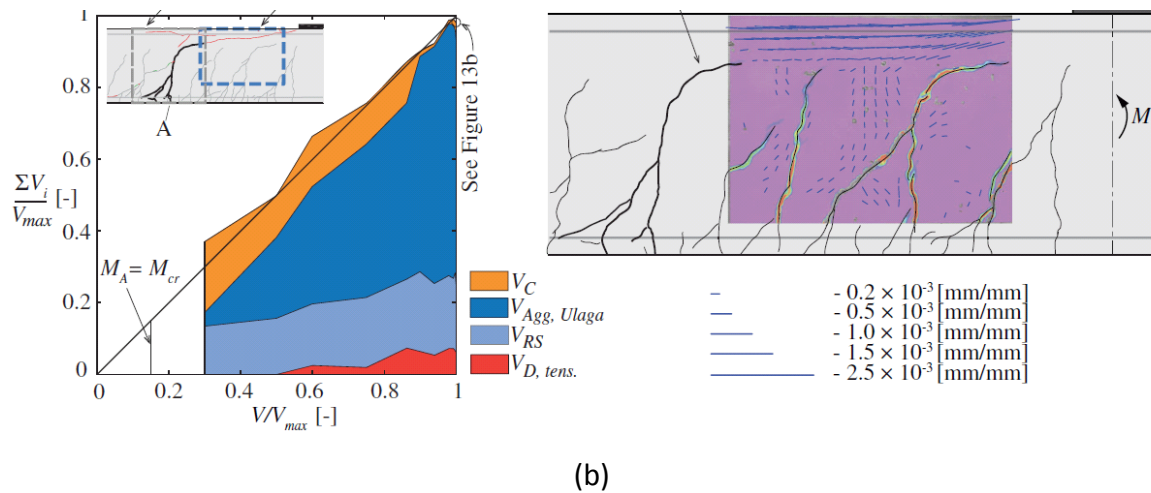


Figure 2.11: Results obtained using DIC for a) crack kinematics (Huber et al., 2019) and b) concrete surface strains (Cavagnis et al., 2017). Figure reproduced with permission of the rights holder, a) Structural Concrete and b) Engineering Structures.

2.3. Provisions for Shear Strength in Different Codes of Practice

Design approaches for shear in national and international design codes can be classified into empirical, semi-empirical and mechanically based approaches. Influential milestones in code development include the 1962 report of the joint ACI-ASCE Committee 326 (ACI-ACSE326), the work of Kani (Kani, 1964) as shown in Figure 2.12. The CEB-FIB model was introduced in 1978 about the same time Kani's book was published (in the late 1970s) followed by adoption of the Strut-and-tie-model by the Canadian Standards Association CSA. A noticeable milestone in the modelling of shear behaviour was the Modified Compression Field Theory (MCFT) presented in 1986 by Vecchio and Collins (Vecchio and Collins, 1986). This theory formed the basis of the shear provisions later in the AASTHO-LRFD (AASHTO-LRFD, 2012), CSA (CSA, 2004) and in some levels of approximations of the FIB MC2010 (fib, 2010).

Despite much time and effort spent in codifying shear capacity in design codes, there are still clear differences in code strength predictions, especially for deep beams. Several researchers have reported noticeable variance and sometimes very conservative/unsafe estimations of shear capacity of deep beams (Mihaylov et al., 2013, Mihaylov et al., 2015, Fang, 2013, Sagaseta, 2008). This is partly due to differences in underlining assumptions and variations in the approaches adopted to account for the various associated parameters.

This section reviews design code provisions for estimating the shear strength of reinforced concrete beams, namely: Eurocode 2 (BSI, 2004), British standards 8110-97 (BSI, 1997) and Model Code 2010 (fib, 2010). This section also compares the provisions provided in each code to take into account the shear strength enhancement when the load is applied close to the support. In the last part of this section: approaches to estimating the shear resistance of beams loaded with multiple point loads are also discussed.

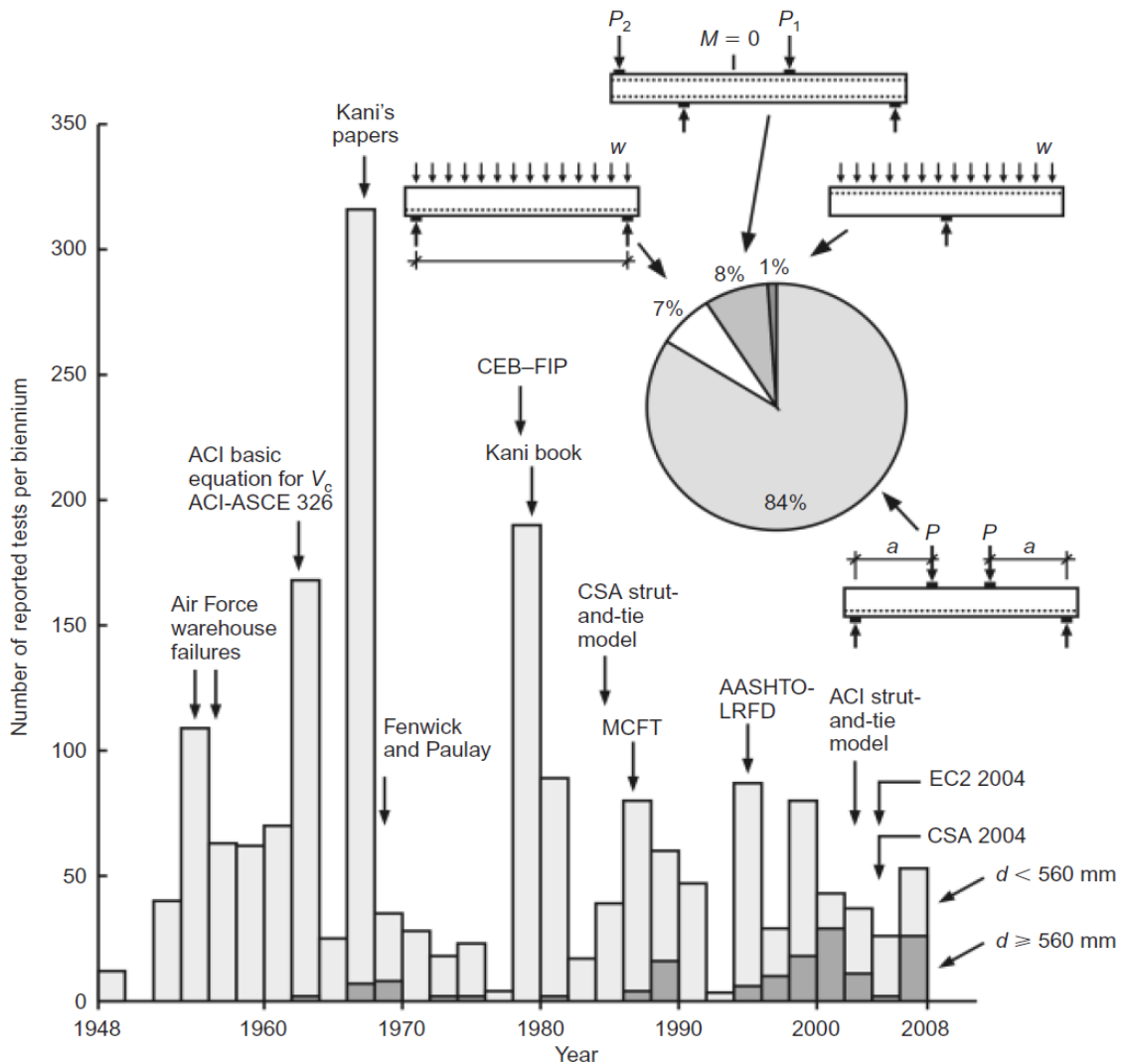


Figure 2.12: Background in shear research of members without shear reinforcement (Collins et al., 2008). Figure reproduced with permission of the rights holder, Magazine of Concrete Research.

2.3.1. Shear Strength in EC2

Beams not requiring design shear reinforcement

EC2 uses an empirical formula to calculate the shear strength of reinforced concrete members without shear reinforcement. The shear strength is a function of the compressive strength of the concrete, longitudinal reinforcement, size effect and dowel action. Shear strength is given by:

$$V_{Rd,c} = \left(C_{Rd,c} k (100 \rho_l f_{ck})^{1/3} + k_1 \sigma_{cp} \right) b_w d \geq (v_{min} + k_1 \sigma_{cp}) b_w d \quad \text{Equation 2.35}$$

The recommended values of $C_{Rd,c}$, k_1 and v_{min} are $\frac{0.18}{\gamma_c}$, 0.15 and $0.35 k^{3/2} f_{ck}^{1/2}$ respectively. Where A_l is the area of the longitudinal reinforcement, b_w is the least width of the section in the tensile zone, d is the effective depth, γ_c is the material factor (taken as 1.5 for the concrete) and σ_{cp} is the axial stress in the section $= \frac{N_{Ed}}{A_c} \leq 0.2 f_{cd}$ (BSI, 2004). $k = \left(1 + \sqrt{200/d} \right) \leq 2.0$ (D in mm) and $\rho_l = \frac{A_l}{b_w d} \leq 0.02$.

The shear stress at failure reduces with increasing beam depth due to the so called “size effect”. The above equation of the EC2 takes into account the size effect using the factor k . Several explanations of the size effect are available in the literature. Bažant (1985) relates the size effect to the fracture mechanics and the residual tensile strength of concrete (Bažant, 1985). On the other hand, Collins et al. link the reduction of shear strength to the crack spacing rather than the absolute element size (Collins et al., 2008).

Beams requiring design shear reinforcement

EC2 uses a variable angle truss model to calculate the shear resistance of beams with shear reinforcement. The inclination of the struts depicted as θ where $1 \leq \cot \theta \leq 2.5$. In this model, the shear strength of beams with shear reinforcement is assumed to depend on the shear reinforcement alone and is given by:

$$V_{Rd,s} = \frac{A_{sw}}{s} z f_{yw} \cot \theta \leq V_{Rd,max} = \alpha_{cw} b_w v_1 f_{cd} / (\cot \theta + \tan \theta) \quad \text{Equation 2.36}$$

In the above expression, A_{sw} is the area of stirrups, s is the spacing between stirrups, f_{yw} is the yield strength of the stirrups. The strength reduction factor for cracked concrete v_1 is given as:

$$\left. \begin{array}{ll} 0.6 & f_{ck} \leq 60\text{MPa} \\ 0.9 - \frac{f_{ck}}{200} & f_{ck} > 60\text{MPa} \end{array} \right\} \text{Equation 2.37}$$

The coefficient α_{cw} reflects the state of stress in the compression chord, it can be found using the expressions:

$$\left. \begin{array}{ll} \left(1 + \frac{\sigma_{cp}}{f_{cd}}\right) & 0 < \sigma_{cp} \leq 0.25f_{cd} \\ 1.25 & 0.25f_{cd} < \sigma_{cp} \leq 0.5f_{cd} \\ 2.5 \left(1 - \frac{\sigma_{cp}}{f_{cd}}\right) & 0.5f_{cd} < \sigma_{cp} \leq 0.25f_{cd} \end{array} \right\} \text{Equation 2.38}$$

In RC beams with low amounts of shear reinforcement, ignoring the contribution of concrete to shear resistance can underestimate resistance (Sagasetta 2008). For example, Equation 2.36 may give a lower resistance for beams with light shear reinforcement than Equation 2.35 for beams without shear reinforcement. This is misleading, since in reality even light shear reinforcement can significantly increase shear resistance as shown by Collins et al. (2008).

2.3.2. Shear Strength in BS 8110-97

Beams not requiring design shear reinforcement

BS8110 gives the shear strength of beams without shear reinforcement as:

$$V_{Rd,c} = \frac{0.79}{\gamma_m} \left(\frac{100A_l}{b_w d}\right)^{1/3} \left(\frac{400}{d}\right)^{1/4} b_w d \quad \text{Equation 2.39}$$

In which A_l is the area of the longitudinal reinforcement, b_w is the least width of the section in the tensile zone, d is the effective depth, γ_m is the material factor (taken as 1.5 for the concrete). The value of $\left(\frac{100A_l}{b_w d}\right)$ should be less than or equal to 3.0 and $\left(\frac{400}{d}\right)^{1/4}$ should be greater than or equal to 0.67. The shear strength here also reduces as the element size increases. It is affected also by the concrete strength and the reinforcement ratio. The strength given by this equation should be multiplied by a factor of $\left(\frac{f_{cu}}{25}\right)^{1/3}$ for concrete strengths greater than 25MPa. The maximum concrete cube strength in Equation 2.35 is limited to 40 MPa.

Beams requiring design shear reinforcement

For beams with shear reinforcement, when the applied shear stress v is greater the concrete shear strength v_c , shear reinforcement is required to carry out the rest of the force. The required area of reinforcement A_{sw} is given as:

$$A_{sw} \geq b_v s_v (v - v_c) / 0.87 f_{yv} \quad \text{Equation 2.40}$$

In which s_v is the spacing of the shear reinforcement and b_v is the width of the beam for the shear calculations.

2.3.3. Shear Strength in FIB MC2010

The determination of design shear resistance in MC2010 depends on the level of accuracy required. MC2010 provides two levels of approximation for beams without shear reinforcement and four levels of approximation for beams with shear reinforcement of which level IV involves numerical modelling. The effort and complexity required to estimate the shear strength are proportional to the level of approximation.

The analysis and design of structural members in shear using MC2010 requires determination of the longitudinal strain at mid-height of the effective shear depth of the element z (taken as $0.9d$).

Beams not requiring design shear reinforcement

The design shear strength of beams without shear reinforcement is given by:

$$V_{Rdc} = k_v \frac{\sqrt{f_{ck}}}{\gamma_c} \cdot z \cdot b_w \quad \text{Equation 2.41}$$

In which f_{ck} is the concrete compressive strength with $\sqrt{f_{ck}} \leq 8 \text{ MPa}$. b_w is the web width and γ_c is the concrete material factor (recommended as 1.5). k_v is determined based on the level of approximation required as follows:

For Level I Approximation:

$$k_v = \frac{180}{1000 + 1.25z} \quad (z \text{ in mm}) \quad \text{Equation 2.42}$$

For Level II Approximation:

$$k_v = \frac{0.4}{1 + 1500 \cdot \varepsilon_x} \cdot \frac{1300}{1000 + k_{dg} \cdot z} \quad (z \text{ in mm}) \quad \text{Equation 2.43}$$

If the maximum aggregate size $d_g \geq 16 \text{ mm}$; k_{dg} can be taken as 1.0. Otherwise:

$$k_{dg} = \frac{32}{16 + d_g} \geq 0.75 \quad \text{Equation 2.44}$$

In order to determine the shear capacity of a beam, one must first determine the longitudinal strain (ε_x) at the middle of the effective shear depth. This may require an iterative solution of the following equation to obtain the relevant strain:

$$\varepsilon_x = \frac{1}{2E_s A_s} \cdot \left(\frac{M_{Ed}}{z} + V_{Ed} \right) \quad \text{Equation 2.45}$$

Beams requiring design shear reinforcement

The design shear resistance of beams with shear reinforcement in level III approximation is given as the summation of the contribution of the concrete shear resistance and stirrups resistance, while in level I and II only the stirrups are assumed to resist the shear force (i.e. $V_{Rd} = V_{Rd,s}$). The concrete shear resistance is the same as for beam without shear reinforcement whereas the shear resistance provided by the stirrups is:

$$V_{Rd,s} = \frac{A_{sw}}{S_w} z \cdot f_{ywd} \cdot \cot \theta \quad \text{Equation 2.46}$$

The angle of strut inclination (θ) and k_v are defined based on the level of approximation required as follows:

For Level I Approximation:

$$\begin{aligned} \theta &= 30^\circ \\ k_v &= 0 \end{aligned} \quad \text{Equation 2.47}$$

For Level II Approximation:

$$\begin{aligned} \theta &= 20^\circ + 10,000 \cdot \varepsilon_x \\ k_v &= 0 \end{aligned} \quad \text{Equation 2.48}$$

For Level III Approximation:

$$\begin{aligned} \theta &= 29^\circ + 10,000 \cdot \varepsilon_x \\ k_v &= \frac{0.4}{1 + 1500 \cdot \varepsilon_x} \left(1 - \frac{V_{Ed}}{V_{Rd,max}(\theta_{min})} \right) \quad (z \text{ in mm}) \end{aligned} \quad \text{Equation 2.49}$$

$$V_{Rd,max} = k_c \frac{f_{ck}}{\gamma_c} b_w z \sin \theta_{min} \cos \theta_{min} \quad \text{Equation 2.50}$$

$$\theta_{min} = 20^\circ + 10000 \cdot \varepsilon_x \quad \text{Equation 2.51}$$

$$k_c = k_\varepsilon \eta_{fc} \quad \text{Equation 2.52}$$

$$\eta_{fc} = \left(\frac{30}{f_{ck}}\right)^{1/3} \quad \text{Equation 2.53}$$

$$k_\varepsilon = \frac{1}{1.2 + 55 \cdot \varepsilon_1} \leq 0.65 \quad \text{Equation 2.54}$$

$$\varepsilon_1 = \varepsilon_x + (\varepsilon_x + 0.002) \cot^2 \theta \quad \text{Equation 2.55}$$

The provisions given in MC2010 are based on the simplified MCFT presented by Bentz et al (2006) which takes into account the effect of multiple parameters and most importantly the state of the strain of the member. Furthermore, MC2010 allows the user to decide the level of approximation needed based on the desired design or analysis accuracy. Indeed, higher levels of approximations involve more calculations when compared to other provisions given in EC2 or BS8110.

2.3.4. Shear Strength Enhancement of RC beams

The shear strength of reinforced concrete beams is increased when load is applied within a distance of $2d$ from supports. This is due to the direct transfer of the load to the support through concrete in compression (arching action). The increase in the shear strength is linked to the ratio of the shear span to the effective depth of the beam (a_v/d) as can be seen in Kani's valley in Figure 2.13. In the context of this research, the shear span is the clear distance between the support and the loading plates.

Design codes model this enhancement in various ways. For instance, EC2 2004 (BSI, 2004) reduces the contribution of the loads applied within a distance $d/2 \leq a_v \leq 2d$ on the upper side by a factor $\beta = \frac{a_v}{2d}$. For members with $a_v < d/2$, a_v should be taken as $0.5d$. However, the shear force V_{Ed} without reduction should be less than $0.5v f_{cd} b_w d$. For cases of continuous beam, the shear enhancement zone can be taken up to $\frac{a_v}{3d}$.

The FIB MC2010 (fib, 2010) reduces the contribution to the design shear force of the loads applied within a distance $a_v \leq 2d$ from the face of the support by a factor $\beta = a_v/2d$.

The shear capacity should be checked at a control section located at a distance d from the support face. If the load is applied in a distance less than d ; then the shear capacity is calculated with $a_v/d = 1$ (i.e. the load is assumed to be applied at $a_v = d$).

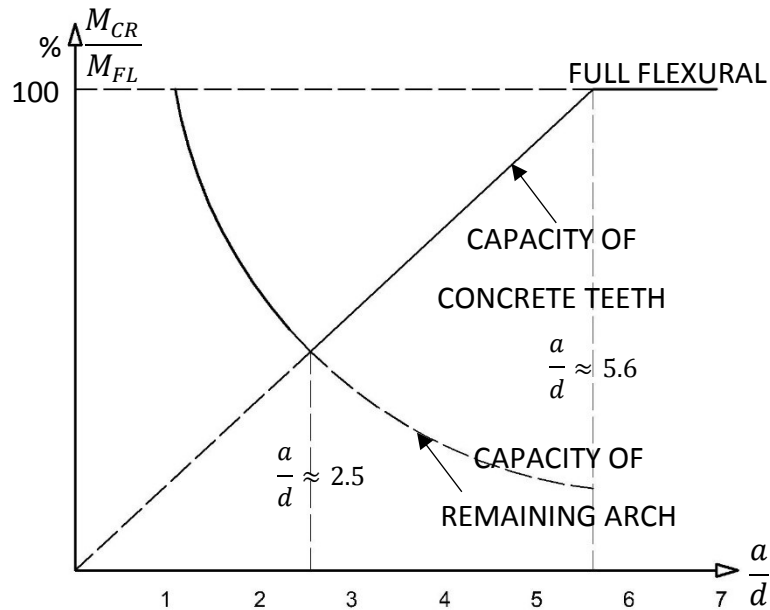


Figure 2.13: Shear enhancement in Kani's Valley (regenerated from (Kani, 1964))

Unlike EC2 and MC2010, the BS 8110-97 (BSI, 1997) enhances the shear strength of the concrete $v_{Rd,c}$ for beams loaded within a distance a_v less than $2d$ from the face of the support by a multiple of $\frac{2d}{a_v}$. The enhanced shear stress is limited to a maximum of $0.8\sqrt{f_{cu}} \leq 5 \text{ N/mm}^2$.

In the case of load application within $2d$ of the support, BS8110-97 gives the enhanced shear strength as:

$$V_{Rd} = (0.87nA_{sw}f_{yw})\frac{d}{a_v} + v_c\frac{2d}{a_v} \quad \text{Equation 2.56}$$

Although these codes capture the enhancement of shear resistance of RC beams due to arching action, the methods of shear enhancement are only equivalent subject to two conditions: i) a single load is applied within a distance of $2d$ from the support and ii) the member does not contain shear reinforcement. The latter condition is pertinent to slabs but not beams which codes require to have at least minimum shear reinforcement. Moreover, the application of these codes provisions regarding the shear strength enhancement in beams with multiple point loads applied within a distance of $2d$ from the support is unclear and conditional on the user's interpretation.

Fang (Fang, 2013) introduced modifications to the equations of shear capacity provided in EC2, BS8110 and MC2010 to account for the case of two points load applied within $2d$ from

the support. The basic assumption was to investigate two different failure planes explained in Figure 2.14. For instance, the design shear force for the EC2 was given as:

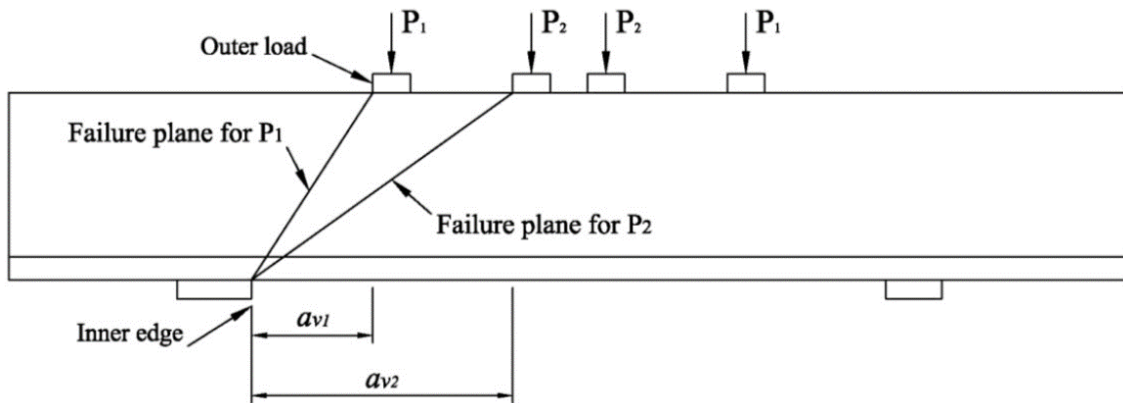


Figure 2.14: Expected failure planes for beams loaded with two points within $2d$ (Fang, 2013)

$$\frac{\beta_1 P_1}{\max(V_{Rd,c}; n_{av1} A_{sw} f_{yd})} + \frac{\beta_2 P_2}{\max(V_{Rd,c}; n_{av2} A_{sw} f_{yd})} \leq 1.0 \quad \text{Equation 2.57}$$

Where β_1 and β_2 correspond to the position of the load-application points and n_{avi} is the number of stirrups within the shear span a_{vi} .

In cases where stirrups provide greater shear resistance than $V_{Rd,c}$, the shear resistance according to Equation 2.53 is entirely governed by stirrups without any concrete contribution. Similarly, Vollum and Fang (2015) derived equations for estimating shear resistance with BS8110 and MC2010 when two points load are applied within $2d$ of the support. For BS8110, the failure load is governed by the least of the following:

$$P_1 + P_2 \leq V_{Rd,c} \cdot \frac{2d}{a_{v1}} + n_{av1} A_{sw} f_{yd} \frac{d}{a_{v1}} \quad \text{Equation 2.58}$$

$$P_2 \leq V_{Rd,c} \cdot \frac{2d}{a_{v2}} + n_{av2} A_{sw} f_{yd} \frac{d}{a_{v2}}$$

For MC2010:

$$\beta_1 P_1 + \beta_2 P_2 \leq V_{Rd} = V_{Rd,c} + V_{Rd,s} \quad \text{Equation 2.59}$$

Equation 2.59 assumes that failure occurs at the failure control section irrespective to the ratio between P_1 and P_2 .

In the context of the present research, it is pertinent to note that none of the considered approaches take into consideration whether the load is applied on the tension or compression face of the beam.

2.4. Essential Models for Shear in RC Beams

Many models are proposed in the literature for estimating the shear strength of RC beams (Collins et al., 2008, Zararis, 2003, Vecchio, 2000, Mihaylov et al., 2013, Mihaylov, 2015, Bentz et al., 2006, Vecchio and Collins, 1986). Of these, the Modified Compression Field Theory (MCTF) (Vecchio and Collins, 1986) and the Two Parameters Kinematic Theory (2PKT) (Mihaylov et al., 2013) are discussed in this thesis.

The MCTF is described since it is one of the most comprehensive models used to predict the shear behaviour of reinforced concrete elements. It forms the basis of the design equations for shear in MC2010 and it is incorporated into several commonly used computer programs (VecTor2 and Response-2000). The 2PKT is described since it provides good estimates for the shear strength of deep beams as well as the full displacement field at any point in the shear span during loading.

2.4.1. The Modified Compression Field Theory (MCFT)

Introduction

The MCFT and the simplified MCFT form the basis of shear calculations in several international design standards as well as the provisions of the strut-and-tie models (CSA, 2004, fib, 2010, AASHTO-LRFD, 2008). The MCFT can also be implemented as a smeared rotating crack model in NLFEA.

The earliest design procedures for shear in beams with shear reinforcement were very conservative since shear was assumed to be resisted by a 45-degree truss without any contribution from the tensile strength of the concrete (Mörsch, 1922). In 1986, Vecchio and Collins (Vecchio and Collins, 1986) proposed an analytical model to predict the behaviour of rectangular reinforced concrete elements subject to shear and axial loads (membrane stress). The model was calibrated using the results of a series of membrane panels tested under various combinations of shear and axial force. It is an extension of the previous compression field theory (CFT) proposed earlier by Mitchell and Collins (1974). Both models defined cracked concrete as a new material and developed its equilibrium conditions, compatibility conditions and stress-strain relationship in terms of average stress and strain. However, unlike the compression field theory, the modified compression field theory takes into account

the tension in the concrete between cracks. The model also considers the shear stress required for equilibrium at cracks.

Assumptions of the MCFT

The main assumptions of the MCFT are as follows:

1. The direction of average principal stresses and strains coincides and cracks develop perpendicular to the direction of the principal tensile strain. This co-axiality assumption did not exactly match the test results but has generally been found reasonable (Vecchio, 2000).
2. Only one stress state exists for each strain state with no account taken of previous loading history.
3. The bond between the concrete and reinforcement is perfect.
4. Reinforcement (longitudinal and transverse) is uniformly distributed along the element.
5. Reinforcement does not resist shear stress applied perpendicular to its cross section.

Compatibility conditions

According to the perfect bond assumption, the compatibility condition requires any deformation accrues in the concrete to be accompanied by the same deformation in the reinforcement, i.e.:

$$\begin{aligned}\varepsilon_x &= \varepsilon_{sx} = \varepsilon_{cx} \\ \varepsilon_y &= \varepsilon_{sy} = \varepsilon_{cy}\end{aligned}\quad \text{Equation 2.60}$$

In which: ε_{cx} and ε_{cy} are the concrete strains in the x and y directions. ε_{sx} and ε_{sy} are the reinforcement strains in the x and y directions. Recalling from Mohr's strain circle Figure 2.15 below:

$$\gamma_{xy} = \frac{2(\varepsilon_x - \varepsilon_y)}{\tan\theta} \quad \text{Equation 2.61}$$

$$\varepsilon_x + \varepsilon_y = \varepsilon_1 + \varepsilon_2 \quad \text{Equation 2.62}$$

$$\tan^2\theta = \frac{\varepsilon_x - \varepsilon_2}{\varepsilon_y - \varepsilon_2} = \frac{\varepsilon_1 - \varepsilon_y}{\varepsilon_1 - \varepsilon_x} = \frac{\varepsilon_1 - \varepsilon_y}{\varepsilon_y - \varepsilon_2} = \frac{\varepsilon_x - \varepsilon_2}{\varepsilon_1 - \varepsilon_x} \quad \text{Equation 2.63}$$

Where ε_1 and ε_2 are the principal tensile and compressive strains respectively.

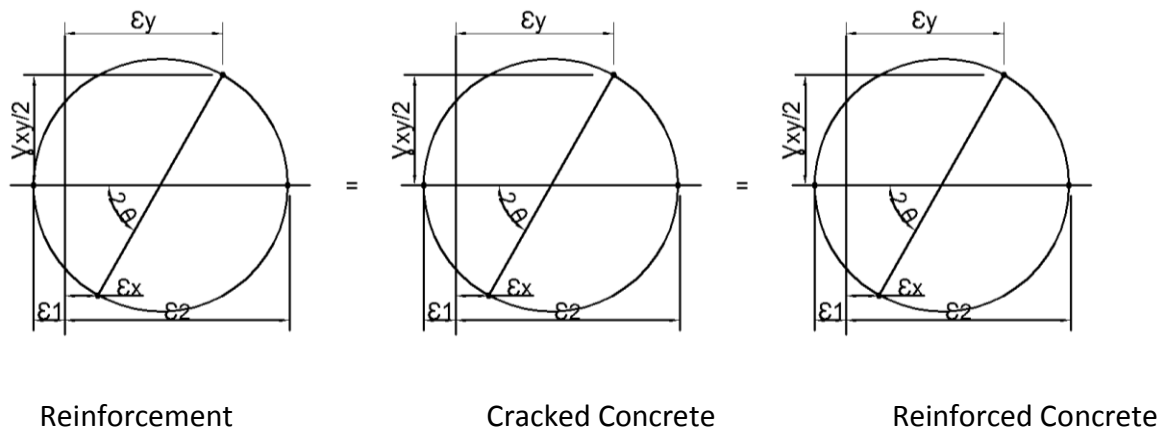


Figure 2.15: Strain conditions in the MCFT (Vecchio and Collins, 1986). Figure reproduced with permission of the rights holder, ACI Structural Journal.

Equilibrium conditions

The applied force develops stresses in both the concrete and the reinforcement. The equilibrium equations can be derived from Figure 2.15 as follows

$$\begin{aligned}
 f_x &= f_{cx} + \rho_{sx} \cdot f_{sx} \\
 f_y &= f_{cy} + \rho_{sy} \cdot f_{sy} \\
 v_{xy} &= v_{cx} + \rho_{sx} \cdot v_{sx} \\
 v_{yx} &= v_{cy} + \rho_{sy} \cdot v_{sy}
 \end{aligned}
 \tag{Equation 2.64}$$

In which f_{cx} , f_{cy} , f_{sx} and f_{sy} are the stresses in the concrete and the steel in the x and y directions respectively. The stress state of the concrete can be obtained as follows:

$$\begin{aligned}
 f_{cx} &= f_{c1} - v_{cxy} / \tan \theta_c \\
 f_{cy} &= f_{c1} - v_{cxy} \cdot \tan \theta_c \\
 f_{c2} &= f_{c1} - v_{cxy} \cdot (\tan \theta_c + 1/\theta_c)
 \end{aligned}
 \tag{Equation 2.65}$$

Stress-strain relationship

The MCFT relates the average principal compressive and tensile strains in the concrete to the corresponding mean strains. An elastic-perfectly plastic stress-strain relationship is assumed for reinforcement as follows:

$$\begin{aligned}
 f_{sx} &= E_s \cdot \epsilon_{sx} \leq f_{yx} \\
 f_{sy} &= E_s \cdot \epsilon_{sy} \leq f_{yy}
 \end{aligned}
 \tag{Equation 2.66}$$

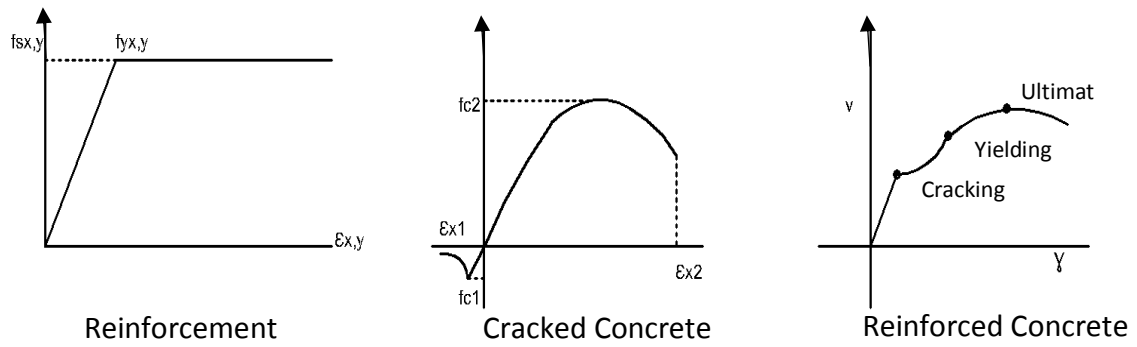


Figure 2.16: Stress-strain relationship in the MCFT (Vecchio and Collins, 1986). Figure reproduced with permission of the rights holder, ACI Structural Journal.

The MCFT also assumes that the compressive strength of cracked concrete is reduced by transverse principal tensile strain. The relationship between stress and the strain in the cracked concrete is given in terms of a softening parameter β :

$$f_{c2} = \beta \cdot \left[2 \cdot \left(\frac{\varepsilon_2}{\varepsilon'_c} \right) - \left(\frac{\varepsilon_2}{\varepsilon'_c} \right)^2 \right] \cdot f'_c \quad \text{Equation 2.67}$$

$$\beta = \frac{1}{0.8 - 0.34 \cdot \left(\frac{\varepsilon_1}{\varepsilon'_c} \right)} \leq 1.0 \quad \text{Equation 2.68}$$

Subsequently, these expressions for the softening parameter β and the compression curve were modified by Vecchio and Collins (Vecchio and Collins, 1993). In their research, the Thorenfeldt compression curve was adopted (Thorenfeldt et al., 1987), β was defined in terms of the average principal tensile strain ε_1 and the concrete cylinder strain at peak load ε_o as follows (Vecchio and Collins, 1993):

$$\beta = \frac{1}{1 + K_c} \leq 1.0 \quad \text{Equation 2.69}$$

$$K_c = 0.27 \cdot \left(\frac{\varepsilon_1}{\varepsilon_o} - 0.37 \right) \quad \text{Equation 2.70}$$

Prior to cracking, the average principal tensile stress is assumed proportional to the average principal tensile strain. After cracking, the stress reduces with increasing strain as follows:

$$f_{c1} = E_c \cdot \varepsilon_1 \quad \text{for } \varepsilon_1 < \varepsilon_{cr} \quad \text{Equation 2.71}$$

$$f_{c1} = \frac{f_{cr}}{1 + \sqrt{200 \cdot \varepsilon_1}} \quad \text{for } \varepsilon_1 > \varepsilon_{cr} \quad \text{Equation 2.72}$$

f_{cr} and ε_{cr} are stress and the strain of the concrete at cracking.

Shear stress on the crack

The tensile stress in the concrete is greatest at mid-way between cracks and reduces to zero at cracks, where the tensile stress in the reinforcement is greatest. In order to satisfy equilibrium, shear stresses v_{ci} are assumed to develop along cracks leading subsequently to yielding of the most highly stressed reinforcement. The shear stress v_{ci} is theoretically accompanied by a small normal stress f_{ci} . The values for the shear and normal stresses was adopted from Walraven and Reinhardt model (1981)

$$v_{ci} = 0.18 \cdot v_{ci,max} + 1.64 \cdot f_{ci} - 0.82 \cdot \frac{f_{ci}^2}{v_{ci,max}} \quad \text{Equation 2.73}$$

Where

$$v_{ci,max} = \frac{\sqrt{-f'_c}}{0.31 + 24 \cdot \frac{w}{a + 16}} \quad \text{Equation 2.74}$$

$$w = \varepsilon_1 \cdot S_\theta \quad \text{Equation 2.75}$$

$$S_\theta = \frac{1}{\sin \theta / S_{mx} + \cos \theta / S_{my}} \quad \text{Equation 2.76}$$

In which (w) is the crack width, S_θ is the crack spacing with S_{mx} and S_{my} are the crack spacing in the longitudinal and transverse reinforcement directions.

The simplified MCFT

The MCFT can predict the complete load-deflection response of cracked membrane panels. However, implementation of the model using hand calculations is tedious and time-consuming. A simplified version of the model has been introduced in 2006 (Bentz et al., 2006) with simpler calculations which only give the shear strength of the cracked concrete elements. Unlike the MCFT, the simplified model takes into account the size effect and the aggregate size in estimating the softening parameter. The shear strength can be obtained using the following equations

$$v = v_c + v_s = \beta \cdot \sqrt{f'_c} + \rho_y \cdot f_y \cdot \cot \theta \quad \text{Equation 2.77}$$

$$\beta = \frac{0.4}{1 + 1500 \cdot \varepsilon_x} \cdot \frac{1300}{1000 + S_{xe}} \quad \text{Equation 2.78}$$

$$\theta = (29^\circ + 7000 \cdot \varepsilon_x) \cdot \left(0.88 + \frac{S_{xe}}{2500}\right) \leq 75^\circ \quad \text{Equation 2.79}$$

$$S_{xe} = \frac{35 \cdot S_{mx}}{a + 16} \leq 0.85 \cdot S_x \quad \text{Equation 2.80}$$

S_{xe} is the effective crack spacing that considers the aggregate size. The crack width will be controlled in the presence of the shear reinforcement that meets the crack width

requirements, in such case S_{xe} should be taken as 300mm (BENTZ, 2008). The equation for the inclination of the strut is set to avoid crushing of the concrete, while its upper limit into ensuring that the shear reinforcement yields.

The MCFT and the SMCFT are remarkable developments in the science of estimating the shear capacity of structural elements. The MCFT refines the compression field theory by considering the stiffening effect of tensile stress in the concrete between cracks. The greatest merits of the MCFT are its relative simplicity and ability to predict the full load-deflection response along with ultimate shear capacity. However, some of its underlying assumptions are questionable and its use is theoretically restricted to applications where the reinforcement is evenly distributed. Like most NLFEA approaches, it neglects dowel action. On the other hand, SMCFT is simple and can easily be used by engineers. Nevertheless, it fails to predict the full load displacement response.

2.4.2. The Two-Parameter Kinematic Theory (2PKT)

Among the various shear models of deep beams, the 2PKT (Mihaylov et al., 2013) provides a detailed description of the deformed shape of deep beams during tests including crack opening and sliding, shear and flexural displacements, maximum deflection, flexural and shear reinforcement strains and a complete displacement field. It also calculates the ultimate shear resistance in terms of the different shear transfer actions.

Description of Beams Deformation Using 2PKT

The model considers concrete above the critical shear crack to behave as a rigid body subject to a vertical translation Δ_c and a rotation φ_{block} about the top of the crack in the compression zone. Concrete beneath the critical crack is modelled as a series of rigid radial struts as shown in Figure 2.17. The rotation is associated with the average tensile strain in the reinforcement $\varepsilon_{t,avg}$, and hence, this model is fully described using only two parameters: Δ_c and $\varepsilon_{t,avg}$. To describe the full displacement field, the following sets of equations can be used with the aid of Figure 2.18:

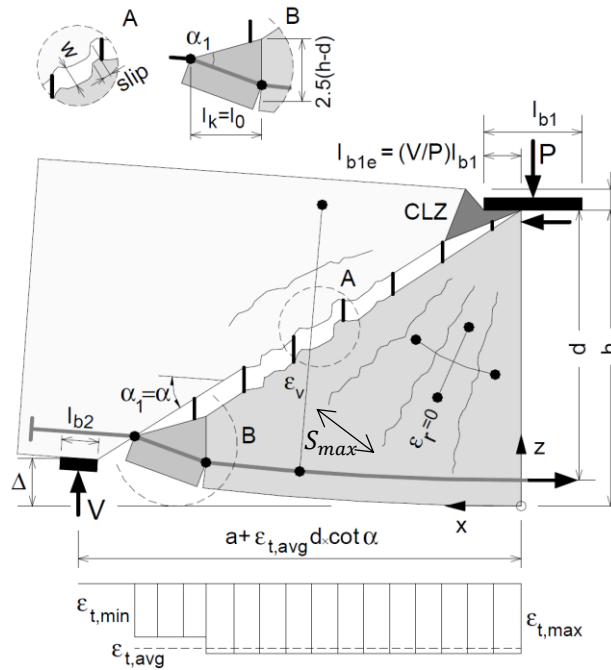


Figure 2.17: Details of the 2PKT (Mihaylov et al., 2013). Figure reproduced with permission of the rights holder, ACI Structural Journal.

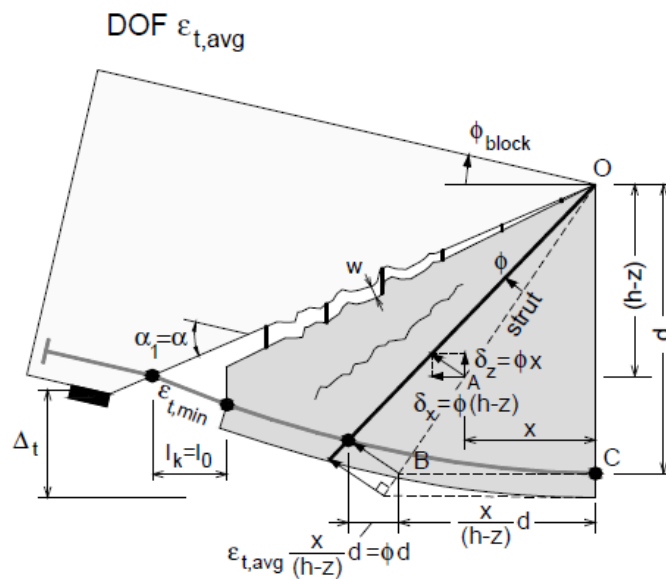


Figure 2.18: describing the full displacement using the 2PKT DoF (Mihaylov et al., 2013). Figure reproduced with permission of the rights holder, ACI Structural Journal.

- For points below the crack

$$\delta_x(x, z) = \epsilon_{t,avg} \cdot x \quad \text{Equation 2.81}$$

$$\delta_z(x, z) = \frac{\epsilon_{t,avg} \cdot x^2}{h - z} \quad \text{Equation 2.82}$$

- For points above the crack

$$\delta_x(x, z) = \varepsilon_{t,avg} \cdot (h - z) \cot \alpha \quad \text{Equation 2.83}$$

$$\delta_z(x, z) = \varepsilon_{t,avg} \cdot x \cot \alpha + \Delta_c \quad \text{Equation 2.84}$$

Where α is the angle of the critical crack and h is the height of the beam. The angle α is defined by the crack extending from the inner edge of the support to the end of the effective width of the loading plate l_{b1e} , which depends on the loading arrangement. To obtain the vertical translation Δ_c , the geometry of the critical loading zone (CLZ) adopted in the theory is used, which simulates the compression zone as a varying width cantilever.

$$\Delta_c = \frac{0.0035 \times 3l_{b1e} \cos \alpha}{\sin \alpha} = 0.0105l_{b1e} \cot \alpha \quad \text{Equation 2.85}$$

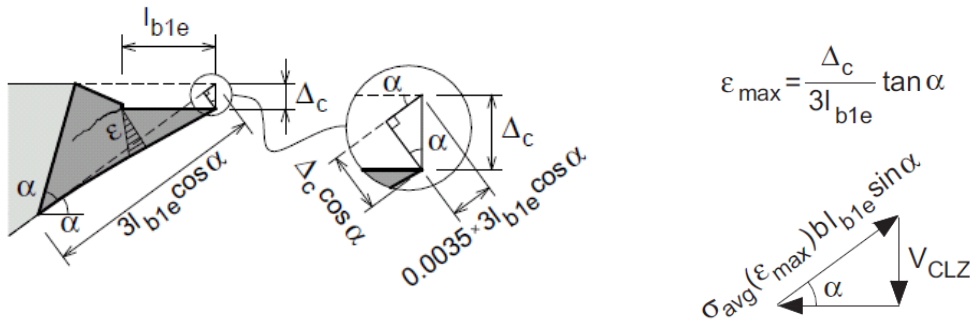


Figure 2.19: Geometry of the critical loading zone in the 2PKT (Mihaylov et al., 2013). Figure reproduced with permission of the rights holder, ACI Structural Journal.

The value of 0.0035 represents the concrete crushing strain; further details of the critical loading zone are given later. l_{b1e} is the effective width of the loading plate and equals to $(V/P) \cdot l_{b1}$. It shall not be taken as less than three times the maximum aggregate size.

To obtain the second parameter of the model ($\varepsilon_{t,avg}$), the following formula can be used.

$$\varepsilon_{t,avg} = \left[\varepsilon_{t,max} (d \cot \alpha - l_k) + \varepsilon_{t,min} l_k \right] \frac{\tan \alpha}{d} \quad \text{Equation 2.86}$$

The minimum strain $\varepsilon_{t,min}$ can be taken as the moment under the load (i.e. $\varepsilon_{t,min} = \varepsilon_{t,max}$) yet, more accurate results can be obtained if the contributions of the stirrups and dowel action are evaluated. The length l_k is the length between the kinks in the flexural reinforcement. Length l_k is given by the expression:

$$l_k = l_0 + d(\cot \alpha - \cot \alpha_1) \quad \text{Equation 2.87}$$

$$l_0 = 1.5(h - d) \cot \alpha_1 \geq S_{max} \quad \text{Equation 2.88}$$

Angle α_1 is the stress field angle given by the MCFT (Vecchio and Collins, 1986), l_0 is the length of the heavily cracked zone and S_{max} is the spacing of the radial cracks at the bottom of the section expressed as (see Figure 2.17):

$$S_{max} = \frac{0.28 d_b}{\rho_l} \frac{2.5(h-d)}{d} \quad \text{Equation 2.89}$$

In which d_b is the diameter of bottom longitudinal bars.

Although the crack opening is only given at mid-depth of the beam height in this theory, crack opening at different heights can be obtained using similar triangles as the opening varies linearly from zero at the crack tip to a maximum value near flexural reinforcement in this model. Crack opening at mid-depth is given as:

$$w_{l/2} = \Delta_c \cos \alpha + \frac{\varepsilon_{t,min} l_k}{2 \sin \alpha} \quad \text{Equation 2.90}$$

Equation 2.90 gives the crack opening at mid-height of the beam; the first term of the crack opening is constant (referred to as w_0) over the crack length resulting from the vertical translation Δ_c . The second term is due to the rotation and linearly varies depending on the length l from the crack tip. The vertical translation Δ_c results in a constant crack slip of a value ($\Delta_c \sin \alpha$) along the crack length.

In order to obtain the crack kinematics along the crack, Equation 2.90 can be written as (Kueres and Hegger, 2018):

$$w_l = w_0 + \frac{\varepsilon_{t,min} l_k \cdot l}{2d \sin \alpha} \quad \text{Equation 2.91}$$

$$s_l = (\Delta_c \sin \alpha) \quad \text{Equation 2.92}$$

Equation 2.81 to Equation 2.92 can be used to describe the full displacement field of the shear span area and the crack kinematics numerically. The predictions of the deformed shape have been assessed by the developers of the theory using a grid of targets in the experiment. According to the authors, 27 out of 28 targets were very accurately modelled (Mihaylov et al., 2013). Furthermore, from Figure 2.18 and using appropriate instrumentation, it can be seen that the two degrees of freedom of this model can be obtained experimentally. For example, if the rotation of the rigid body ϕ_{block} is measured using either two side transducers or an inclinometer, then the value of the average strain can be determined as follows:

$$\phi_{block} = \frac{\delta_{x,d}}{d} = \varepsilon_{t,avg} \cdot \left(\frac{d \cdot \cot(\alpha)}{d} \right) = \varepsilon_{t,avg} \cdot \cot(\alpha) \quad \text{Equation 2.93}$$

Also, if two vertical transducers are placed on the two sides of the effective width of the plate, the shear displacement Δ_c can be evaluated.

This model is based on a single point load applied on the compression face of the support and does not take into account if an additional force is applied within $2d$ from the face of the support either if the load was in the tension or the compression face. Application of additional point load between the initial load of the model and the support may affect the rotation of the rigid block (or the average strain $\varepsilon_{t,avg}$) for beams loaded in the compression face, while in beams loaded in the tension face, it may influence the vertical translation (Δ_c).

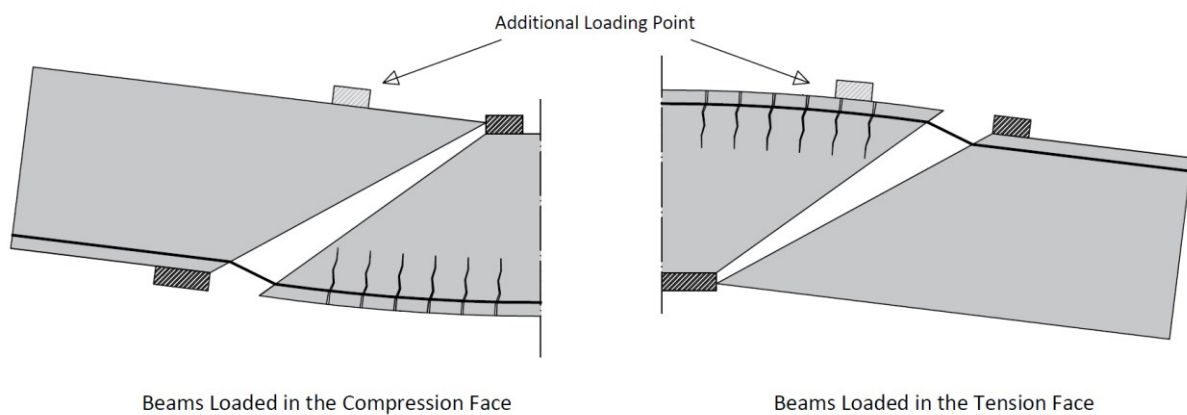


Figure 2.20: 2PKT for beams with multiple point loads within the shear span

Fang (2013) estimated the shear strength of beams loaded with single and two-point loads within the shear span of deep beams using the 2PKT. The predictions for the beams with two point loads (5 beams) were less accurate compared to those of single point loads (7 beams) (Fang, 2013) raising questions about its accuracy in beams with multiple point loads. This inaccuracy can be investigated better if the full displacement field of the deformed shape is available. The introduction of the DIC system allows detailed measurements of the deformation and can provide a better assessment of the model for beams with multiple point loads within the shear span.

Another assumption that has been made in the model is that the rigid body above the crack rotates around the intersection between of the crack and the loading plate. The validity of this assumption has been investigated by Kueres (2018) who found that the location of the centre of rotation and the deformation are affected by the span to effective depth ratio (see Figure 2.21). For very compact slabs, the deformation is governed by the vertical

translation (Δ_c) and the centre of rotation is located further away from the root of the shear crack. In slender slabs, the deformation is governed by the flexural rotation (or the average strain $\varepsilon_{t,avg}$) and the centre of rotation is located close to the crack tip as assumed in the 2PKT.

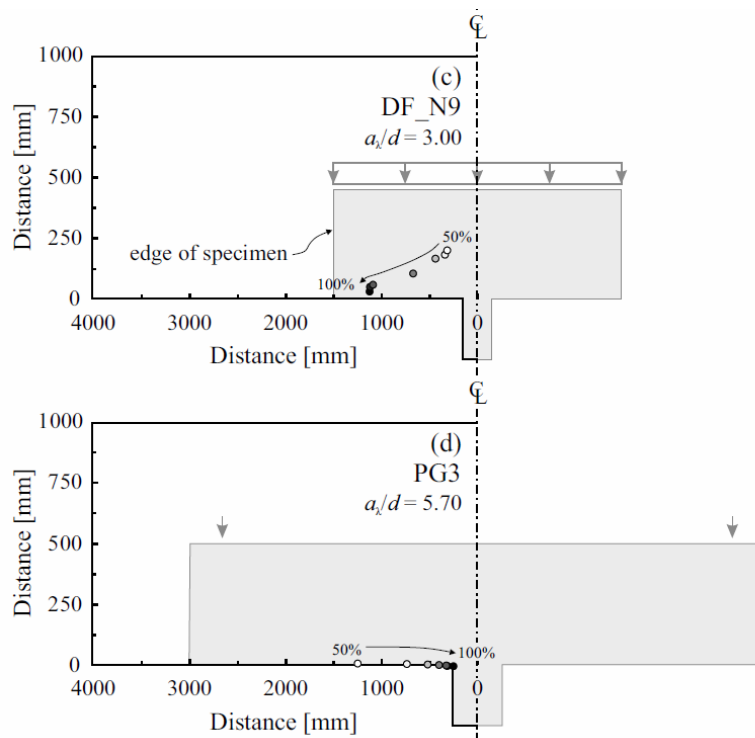


Figure 2.21: Different locations of the centre of rotation of the rigid body (Kueres et al., 2018). Figure reproduced with permission of the rights holder, Engineering Structures.

Strength prediction and the Five-spring model

The shear strength in the 2PKT is given as the summation of the shear transfer actions, namely: Aggregate interlock (V_{ci}), dowel action (V_d), stirrups (V_s) and the compression zone depicted as the critical loading zone CLZ (V_{CLZ}). Failure is governed in the model by crushing of the concrete in the CZL. The description of these contributions and the solution criteria was extended later to the Five-spring model (Mihaylov, 2015).

In the five-spring model, the shear span is characterised by two series of springs, a set of four parallel springs representing the shear transfer actions mentioned earlier and deforms by the shear displacement Δ_c and a fifth spring representing the flexural behaviour of the beam and deforms by the flexural displacement Δ_t . The total displacement of the beam Δ is given as:

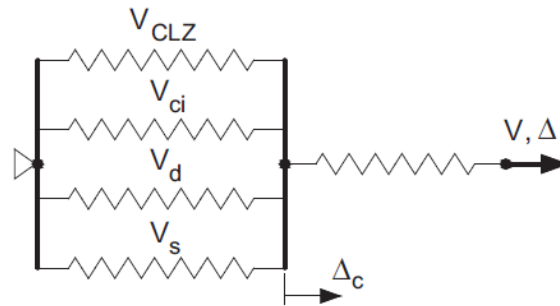


Figure 2.22: Five-spring model for deep beams (Mihaylov, 2015). Figure reproduced with permission of the rights holder, Structural Concrete.

$$\Delta = \Delta_t + \Delta_c = \frac{\varepsilon_{t,avg} \cdot l_t \cdot a}{d} + \Delta_c \tag{Equation 2.94}$$

At equilibrium, the summation of the shear transfer actions of the rigid block shown in Figure 2.23 is equal to the vertical force derived from the moment equilibrium of the shear span as described by Figure 2.23 below.

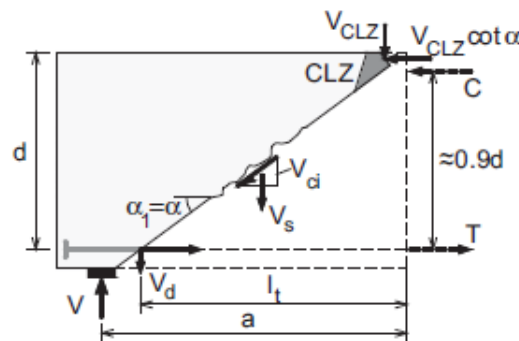


Figure 2.23 Equilibrium of the rigid block in the five-spring model (Mihaylov, 2015). Figure reproduced with permission of the rights holder, Structural Concrete.

$$V = \frac{T(0.9d)}{a} = V_{CLZ} + V_{ci} + V_d + V_s \tag{Equation 2.95}$$

The tensile force in the flexural reinforcement T takes into account the tension stiffening effect of the concrete. The tensile force T is expressed as a function of the average strain in the reinforcement $\varepsilon_{t,avg}$ as

$$T = \varepsilon_{t,avg} \cdot E_s A_s + \frac{0.33 \sqrt{f_c}}{\sqrt{1 + 200 \varepsilon_{t,avg}}} A_{c,eff} \tag{Equation 2.96}$$

The effective area of the concrete $A_{c,eff}$ is the area width of the beam b times the minimum of $2.5(h - d)$ and $h/2$.

From Figure 2.19 the triangular CLZ is described using the crack angle α and the effective width of the loading plate l_{b1e} . The average stress (σ_{avg}) in the CLZ is diagonal and relates to the linear strain in the CLZ (ε_c). The max concrete strain $\varepsilon_{c,max}$ can be obtained for a given shear displacement Δ_c as follows:

$$\varepsilon_{c,max} = \frac{\Delta_c}{3l_{b1e}} \tan(\theta) \quad \text{Equation 2.97}$$

The contribution of the CLZ (V_{CLZ}) is then expressed in terms of the average concrete stress σ_{avg} as:

$$V_{CLZ} = \sigma_{avg} \cdot (l_{b1e} \sin(\alpha) \cdot b) \cdot \sin(\alpha) \quad \text{Equation 2.98}$$

The contribution of the CLZ depends on the size of the zone or in other words of the effective width of the loading plate. This length is defined by the exact path of the crack and may sometimes need correction based on visual inspection of the CLZ in the test (Mihaylov, 2015). The contribution of the aggregate interlock in this model is taken from the contact density model (Li et al., 1989) in terms of the average shear stress (v_{ci}) as follows

$$v_{ci} = 3.83 f_c^{\frac{1}{3}} \frac{\varphi^2}{1 + \varphi^2} \quad \varphi = \frac{s}{w} \quad \text{Equation 2.99}$$

$$V_{ci} = 0.18 v_{ci} b d \quad \text{Equation 2.100}$$

The contribution of dowel action is calculated assuming the reinforcement behaves as an elastic built in beam with support settlement Δ_c with an upper limit corresponding to the formation of plastic hinges at the support. The expression given below also reduces the upper limit based on the stress state at the reinforcement bar:

$$V_d = \frac{12 E_s \pi d_b^4}{64 l_k^3} \Delta_c \leq \frac{n_b f_y d_b^3}{3 l_k} \left[1 - \left(\frac{T}{A_s f_y} \right)^2 \right] \quad \text{Equation 2.101}$$

The last component of the shear transfer actions (the stirrups contribution V_s) is given as a function of the average strain of the reinforcement given as:

$$\varepsilon_v = 2 \cdot \frac{\Delta_c + 0.25 \varepsilon_{t,avg} d \cot^2 \alpha_1}{0.9 d} \quad \text{Equation 2.102}$$

$$V_s = (\varepsilon_v E_{sv}) \rho_v b (d \cot \alpha_1 - l_0 - 1.5 l_{b1e}) \quad \text{Equation 2.103}$$

Plotting the load-displacement curves

The load-displacement curve is defined in this model by several polylines followed by a nonlinear response. The first linear response of the beam is from the start of the test up to the cracking load $V_{cr,fl}$ after which, the second linear response until the load forming the first

diagonal crack $V_{cr,sh}$. The last linear response is the sectional capacity V_{sect} given by MC2010 LoA III. After the load exceeds the sectional capacity, the shear transfer actions (according to this model) are activated and the behaviour is no longer linear. To obtain this nonlinear part of the response, a trial and error procedure is suggested as below.

The total displacement Δ is given by Equation 2.94 consists of two components. Imposing a total displacement Δ and assuming one component (Δ_t) yields the two DoF of the model Δ_c and $\varepsilon_{t,avg}$. These parameters are used to obtain the different shear actions and to solve Equation 2.95. An iterative solution may be required to obtain the DoF corresponding to the imposed displacement, which satisfies the equilibrium condition.

The 2PKT and the five-spring model are powerful tools to predict the shear strength and deformation during the test. The accuracy of the models has been proven very accurate in terms of both strength and deformation. However, the uncertainties associated with the size of the CLZ in these models and the need to inspect the zone visually during the test raise questions regarding the applicability of these models to predict the behaviour prior to testing. Bearing in mind that the failure of beams in shear in these models is triggered by the failure of the CLZ. Moreover, the average strain $\varepsilon_{t,avg}$ depends on the loading arrangement in the shear span. For cases of multiple loads where shear failure is not identified, the equilibrium equations need modifications to account for these cases.

2.5. Introduction to Strut-and-Tie Models

2.5.1. B and D regions

The Bernoulli hypothesis of plane strain assumes a linear strain distribution over the depth of the section allowing internal stresses to be determined easily. Regions in which plane sections remain plane are referred to as B regions, where B stands for Bernoulli.

For regions where the strain distribution is not linear (e.g. corners, openings, near concentrated loads, etc. – see Figure 2.24) the Bernoulli hypothesis is not applicable and other design methods like the strut-and-tie method (STM) should be used. D regions can occur due to either geometrical discontinuity (e.g. presence of holes, change in cross-section or direction) or due to static discontinuity (e.g. regions near concentrated loads/reactions). In certain cases (e.g. corbels, dapped ends and joints) D regions form due to both static and geometrical discontinuities.

The STM was first introduced in the middle of the last century as a development of the truss analogy method proposed by Morsch in 1908 (Leondardt, 1965). The method was further developed and brought to widespread attention by Schlaich et al. in 1987 (Schlaich et al., 1987).

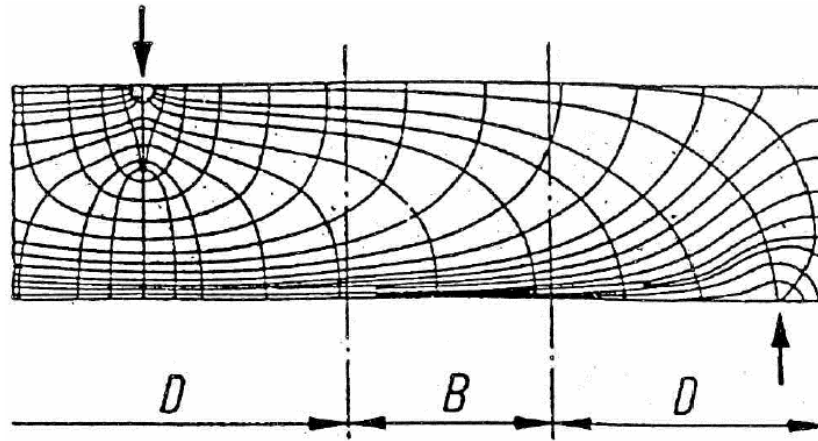


Figure 2.24: Stress trajectories in B and D regions (Schlaich et al., 1987), Permission requested on 10/10/2019.

The STM is based on the lower bound theorem of plasticity, which states that a structure will not collapse if the applied loads are in equilibrium with an internal stress distribution in which material strengths are not exceeded. For the theorem to be applicable, sufficient ductility should be available in the member.

In the early stages of loading, an elastic stress distribution exists prior to concrete cracking. After concrete cracks, the elastic state is disturbed due to the re-orientation of the internal force and the structure can be modelled using strut-and-tie model (STM). In an STM, concrete struts carry the compressive force and reinforcement ties transmit the tensile force. Concrete struts and reinforcement ties meet at virtual nodal zones referred to as nodes. More details about components of the STM and their dimensions will follow in section 2.5.4.

2.5.2. Constructing a strut-and-tie model

STMs are appealing to design engineers since load paths are clearly defined making it easy to check that equilibrium is satisfied. STM can be used for both design and assessment. It can be constructed in the iterative procedure described below:

1. Define the B and D regions within the studied structure. The definition of the D regions is based on the presence of static or geometrical discontinuities. A structure can

comprise both B and D regions. Saint Venant's Principle is used as a quantitative guide to decide the extension of the D regions, although it is a conceptual estimation. Figure 2.25 shows the definition of B and D regions in some structures.

2. Propose a model based on the force path and stress fields. Struts can be aligned with the direction of the elastic principal compressive stress and up to $\mp 15^\circ$ (James K. Wight, 2012).
3. Determine the forces in STM members using equilibrium equations.
4. In design, calculate the area of reinforcement required to resist tensile forces in the ties obtained from (3). Ties can be aligned either in the direction of the principal tensile stress or orthogonal to the member edges for convenience. However, there is less restriction on the conformance of ties with the direction of the principal tensile stress as ties should be positioned to give practical reinforcement layout.
5. Dimension nodes and struts based on codes provisions for limiting the strength of struts, ties and nodes. The selected dimensions should yield internal stresses in the model elements lower than the assumed strength of the elements.

2.5.3. Model optimization

The STM is based on a lower bound theory of plasticity in which a stress field satisfying equilibrium conditions is assumed. This suggests that more than one model satisfying equilibrium can be assumed; arising doubts of whether the selected model is the optimum model.

Optimization techniques are used to distinguish between a "good" and a "bad" model. The main concept is that loads tend to select the path with the least forces and deformations (the path with the least strain energy). Since reinforcement bars are much ductile than concrete, generally, the model with the least and shortest ties is the best. This criterion is established from the principle of the minimum strain energy for the elastic behaviour after cracking and has been formulated as follows (Schlaich and Schafer, 1991)

$$\sum F_i \cdot l_i \cdot \varepsilon_i = \text{Minimum} \quad \text{Equation 2.104}$$

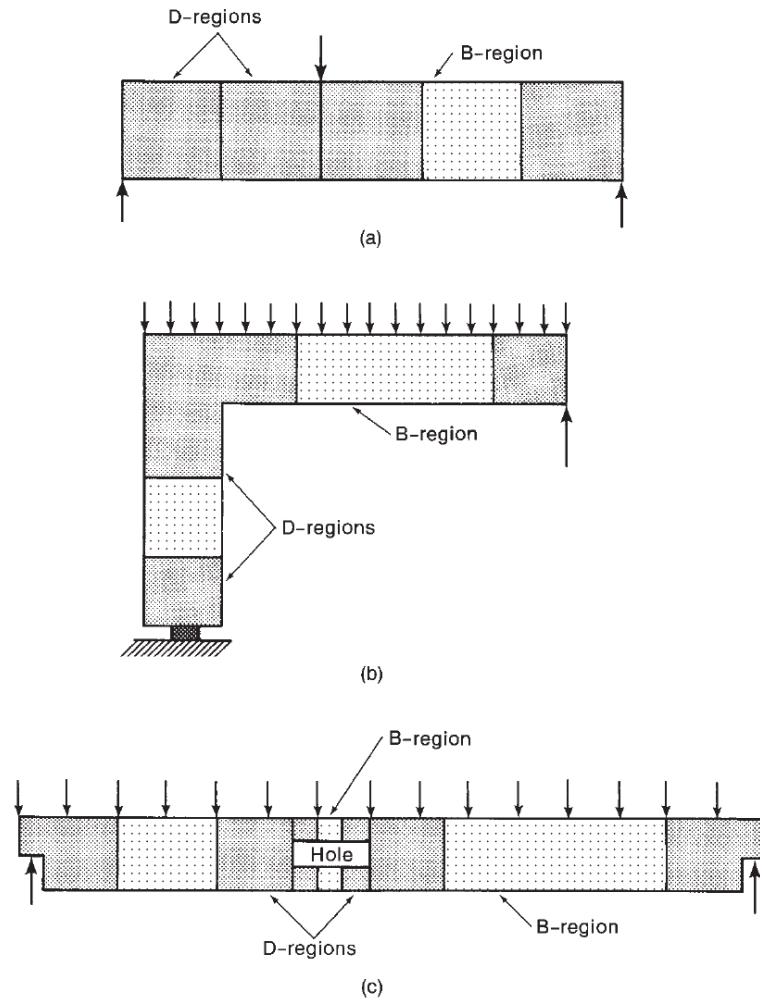


Figure 2.25: Examples of B and D regions in different structures (James K. Wight, 2012).
Figure reproduced with permission of the rights holder, Pearson.

Where F_i is the force in the model member (a strut or tie i), l_i is the length of the member and ε_i is the mean strain in the member. Ties are much deformable than concrete struts, thus, struts contribution in the strain energy can be neglected.

2.5.4. Dimensioning strut-and-tie model

Dimensioning of an STM involves sizing individual elements of the model (struts and ties) and detailing of the nodes. There is a strong relationship between the strength of the model elements and the nodal dimensions, which govern the strut width.

Nodes

Nodes are defined in STM as regions of the intersection of three or more elements i.e. struts or ties. Nodes may also reflect a change in the direction of forces. They can be classified into concentrated (or singular) nodes; where a strut or a tie represents a concentrated stress field

(typically under loading or support plates) or smeared (continuous) nodes; where a spread stress fields join each other or join a tensile tie consists of smeared reinforcement. Examples of concentrated and smeared nodes are shown in Figure 2.26 below.

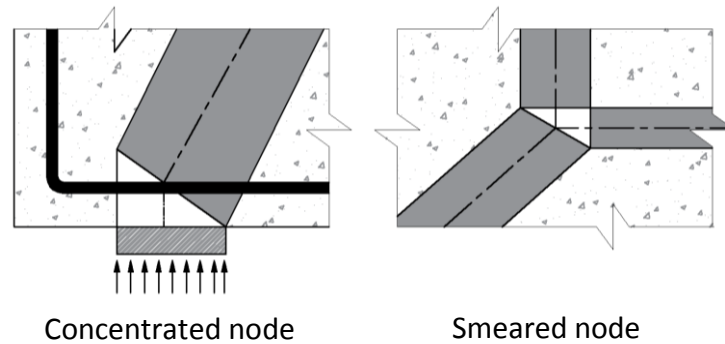


Figure 2.26: Concentrated and smeared nodes (Schlaich et al., 1987) - regenerated, Permission requested on 10/10/2019.

Nodes are commonly dimensioned using the width of the loading or support plates and the cover to the reinforcement for nodes with reinforcement ties, especially in tests. Yet, in case of concrete joints and real structures, dimensioning nodes can be more problematic.

Nodes are also defined according to the force in its associated elements as three-compression elements node (CCC), two compressive strut and a tie (CCT), a compressive strut and two ties (CTT) and three ties node (TTT) (see Figure 2.27). A CCC node is defined as hydrostatic if the stresses are equal in all the node sides (Schlaich et al., 1987). However, they are not common in real problems due to geometrical constraints and, hence, non-hydrostatic nodes are usually adopted in solving design problems.

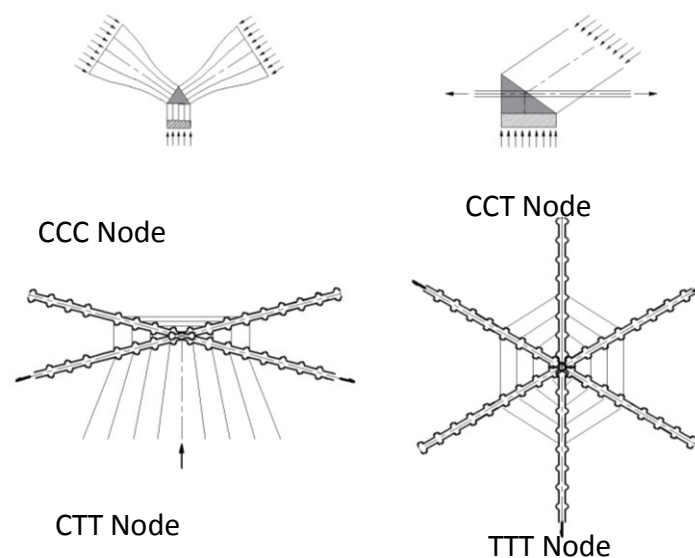


Figure 2.27: Examples of basic types of nodes (Schlaich et al., 1987) – regenerated, Permission requested on 10/10/2019.

Struts

Concrete struts, whether compressive or tensile struts, are two or three-dimensional stress fields, unlike reinforcement ties that are usually one-dimensional elements. The stress field in struts is typically depicted as fan-shaped, bottle-shaped or prismatic (i.e. parallel sided - Figure 2.28).

Transverse tension does not develop in the prism and fan stress fields (Schlaich et al., 1987). Consequently, concrete in the fan and prism stress fields can develop the full uniaxial compressive concrete strength, unlike concrete in a bottle stress field where transverse tension develops away from the nodes (Vecchio and Collins, 1986). The presence of transverse tensile stress accompanied by the compressive stress reduces the strength of the strut significantly which may result in early failure (Vecchio and Collins, 1986). Apart from the stress field in the strut, the strut strength is influenced by several factors such as disturbance due to cracking or transverse reinforcement, the angle between the strut and the adjacent reinforcement and the confinement effect.

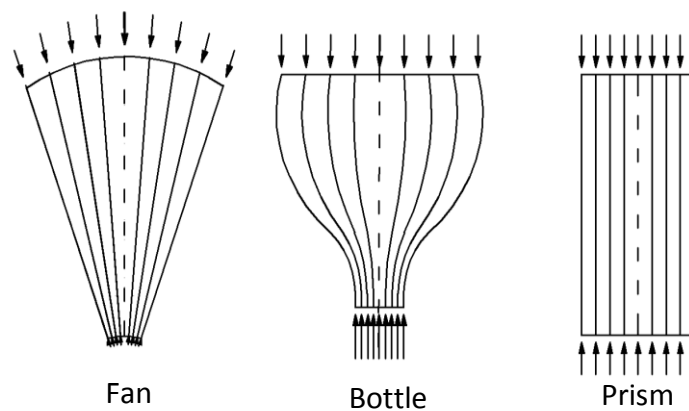


Figure 2.28: Basic compression fields (Schlaich et al., 1987) –regenerated, permission requested on the 10/10/2019.

Reinforcement ties

Ties are designed to resist tensile forces in STM and may consist of either concentrated or smeared reinforcement bars. Pre-stressed reinforcements are also considered as a part of ties resisting the tensile force. The tie force is generally associated with the yielding capacity of its reinforcement and sometimes is given as a fraction of the yielding capacity of the

reinforcement. Anchorage of ties is crucial and should be designed and checked according to the designated codes.

2.5.5. Models for beams with horizontal and vertical shear reinforcement

The STM is the most common tool in estimating the strength of deep beams (Liu and Mihaylov, 2016). It includes three load carrying mechanism (See Figure 2.29) depending on the load, beam geometry and shear reinforcement: direct strut mechanism, vertical truss mechanism and a horizontal truss mechanism. However, ways of estimating the proportion of each of these actions are still not widely agreed upon. Hwang et al. (2000) assumed that the proportion of force taken by these actions depends on the strut angle and whether or not shear reinforcement yield. Other authors ((Matamoros and Wong, 2003) and (Russo et al., 2005)) have proposed semi-empirical models with correction factors to estimate the forces resisted by each mechanism.

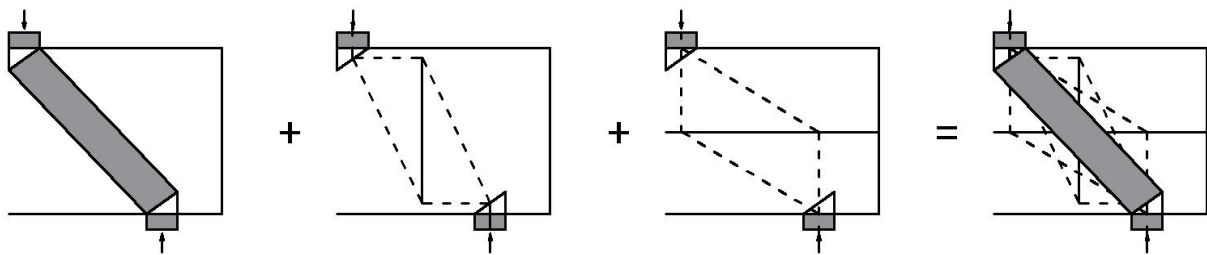


Figure 2.29: Load carrying mechanisms in the strut-and-tie model

Yang and Ashour (2010) proposed an STM for deep beams that takes into account the size effect based on the crack band theory. The model divides the diagonal strut into a crack band zone and a stress relief strip and uses energy equilibrium in the two zones - Figure 2.30.

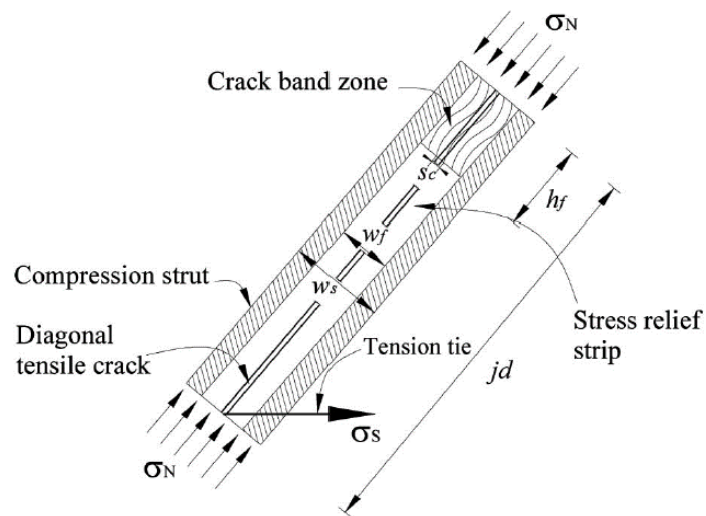


Figure 2.30: Idealised crack band zone and stress relief strip in a strut (Yang and Ashour, 2010). Figure reproduced with permission of the rights holder, *Journal of Structural Engineering*.

While the models in Figure 2.29 depend on direct super-position, other models (Amini Najafian et al., 2013, Sagaseta and Vollum, 2010, Vollum and Fang, 2014, James K. Wight, 2012) have been developed using the stress field method. Wight and Mac Gregor (2012) used the principle of nodal subdivision to divide the load applied to the nodes into several components. This can be utilised to estimate the load carried out by the direct strut, vertical and horizontal shear reinforcement as in Figure 2.31. This nodal sub-division allow the consideration of distributed loads (Dead loads of deep beams for instance) in the STM. The tensile force develops in the longitudinal reinforcement due to the distribution of the vertical shear reinforcement simulate better the force developed in the simple beam elastic theory.

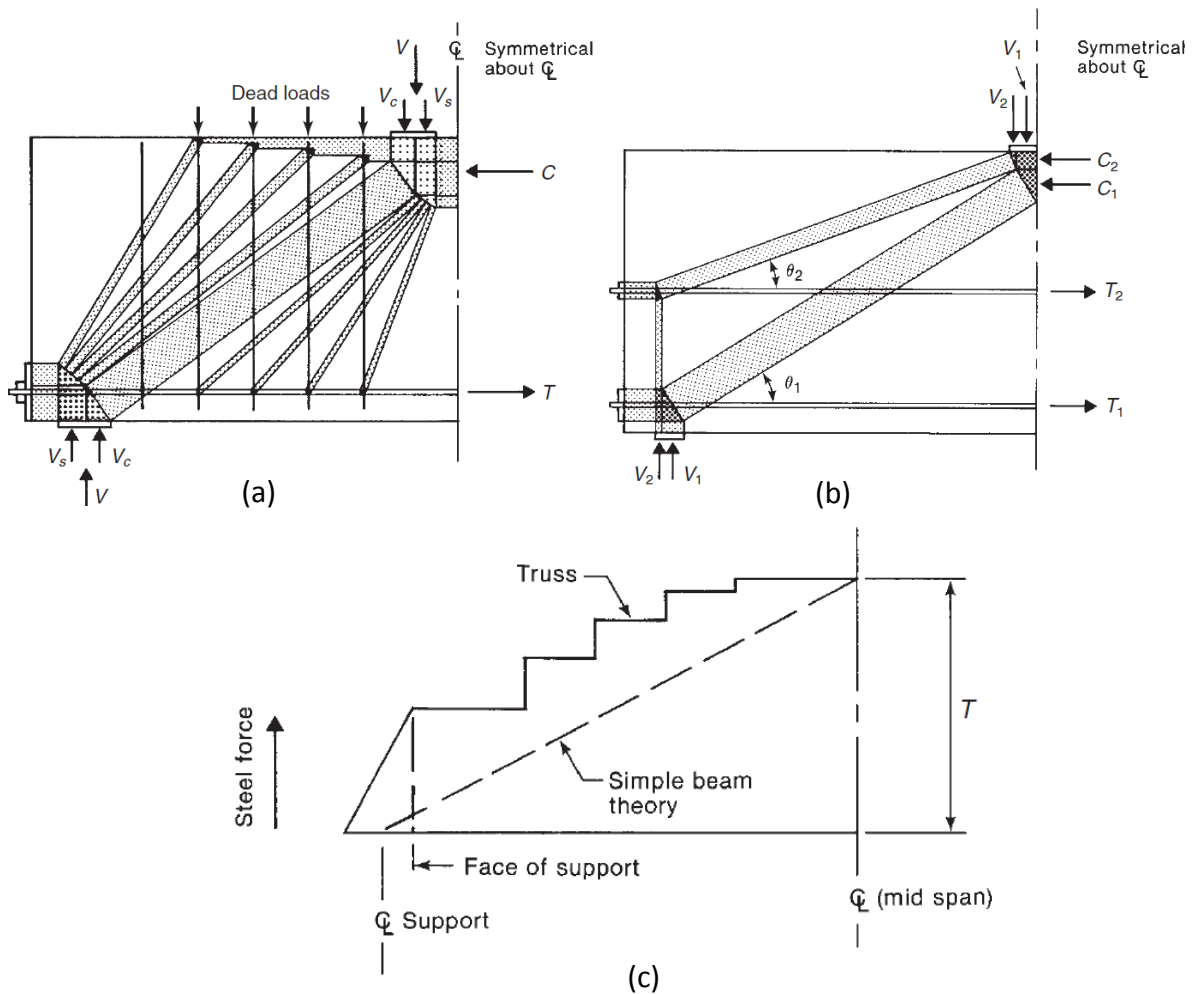


Figure 2.31: Use of nodal sub-division to estimate the contribution of a) vertical, b) horizontal shear reinforcement and c) longitudinal tensile force is STM (James K. Wight, 2012)- figure reproduced with permission of the rights holder, Pearson.

While the model shown in Figure 2.31 simulates the actual forces and evaluates the element forces individually, solving such a system can be time-consuming and not practical for engineers. The Sagaseta and Vollum model (2010) for beams with vertical shear reinforcement also uses the principle of nodal sub-division. However, the vertical reinforcements have been treated as a single bar at the centroid of the stirrups set with an equivalent area. This model has been used and modified by several researchers (Amini Najafian et al., 2013, Vollum and Fang, 2015) Figure 2.32.

The above-mentioned model calculates the strength of beams with/without shear reinforcement for symmetrical one/two points loads applied on the compression face of the beam. Shear strength is typically governed by simultaneous yielding of shear reinforcement

and crushing of strut I at the CCT node. However, this model fails to estimates the shear strength in the case of multiple points load applied to the compression face.

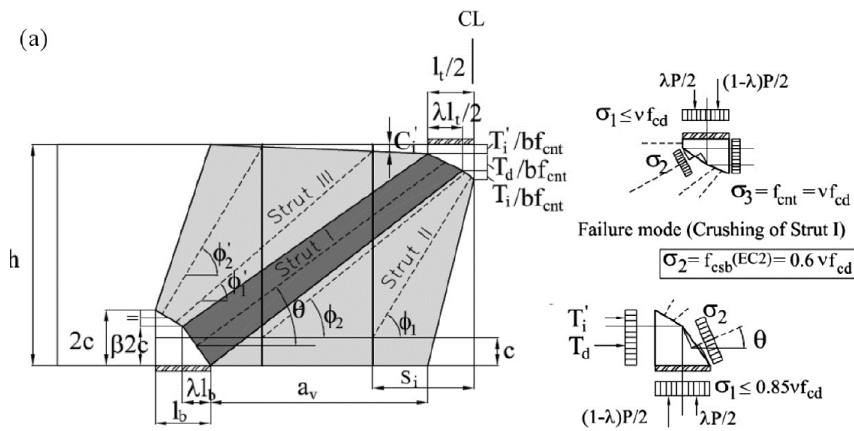


Figure 2.32: Sagaseta and Vollum model for deep beams with vertical shear reinforcement (Sagaseta and Vollum, 2010). Figure reproduced with permission of the rights holder, Magazine of Concrete Research.

Vollum and Fang (2013) used a similar approach to develop an STM for deep beams with and without shear reinforcement loaded with four-point loads as described in Figure 2.33. The selection of the model depends on whether the shear force resisted by the stirrups is greater than the applied force (P_2).

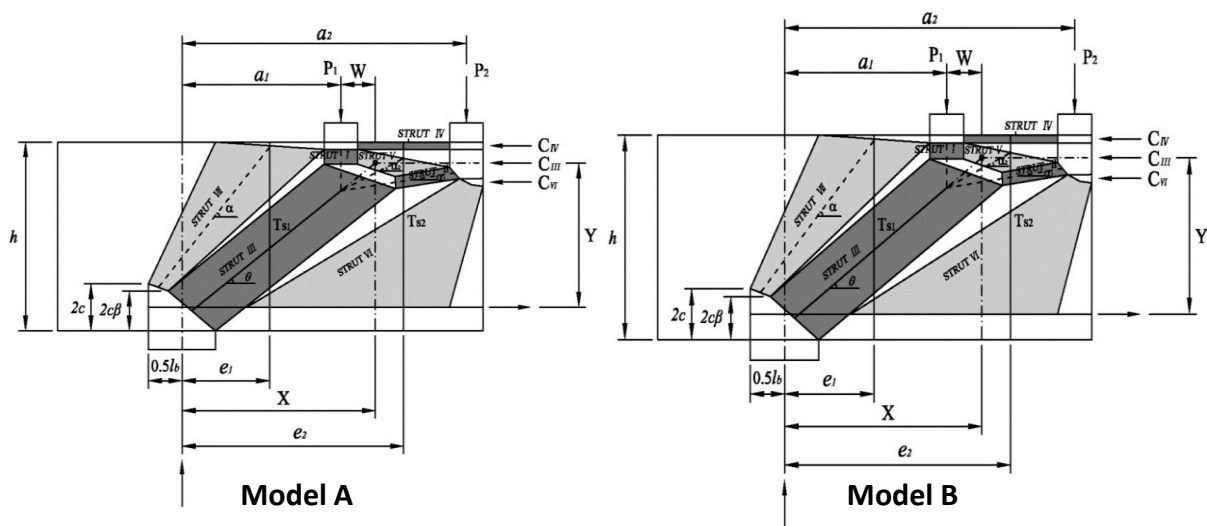


Figure 2.33: STMs proposed by Fang for beams with four-point loads (Fang, 2013).

The above model transmits the load through a combination of strut and truss model. This model was developed making use of stress fields derived using nonlinear finite element analysis. The horizontal component of the loads at the support is carried by the flexural reinforcement while strut IV on top carries the horizontal compression force between the two loading points. However, this is not always the case. For instance, beams loaded in the tension face with multiple loads (e.g. cantilevers, continuous beams, etc.) behave differently and tension reinforcement is placed on the top face. Accordingly, the need for an STM that considers such load configuration arises.

2.5.6. Codes provisions of the strut-and-tie models

The STM is codified in most modern design standards. Whilst there is a certain degree of consensus on estimating the strength of ties, various approaches are adopted for estimating the strength of nodes and struts. Several codes specifications for the strut-and-tie model are presented here in this regards.

Euro Code 2 (BSI, 2004)

EC2 allows the use of STM if a non-linear strain distribution develops. The strength of struts, nodes and ties are evaluated as follows:

Strength of struts

1. In the presences of transverse compressive stresses or the absence of the tensile stress, the strength of the strut is calculated using the expression: $\sigma_{Rd,max} = f_{Ecd}$
2. In the presence of transverse tension, the compressive strength is calculated by the expression:

$$\sigma_{Rd,max} = 0.6 \cdot v' \cdot f_{Ecd}, v' = 1 - f_{ck}/250 \quad \text{Equation 2.105}$$

Strength of nodes

Based on the node types as described in section 2.5.4, EC2 gives the following provision regarding the strength of nodes

1. In CCC nodes where no ties are associated with the node, the strength is obtained using:

$$\sigma_{Rd,max} = k_1 \cdot v' \cdot f_{Ecd} \quad \text{Equation 2.106}$$

2. In CCT nodes where ties are provided in only one direction, the strength is given using:

$$\sigma_{Rd,max} = k_2 \cdot v' \cdot f_{Ecd} \tag{Equation 2.107}$$

3. In CTT nodes where ties are provided in more than one direction, the strength is given using:

$$\sigma_{Rd,max} = k_3 \cdot v' \cdot f_{Ecd} \tag{Equation 2.108}$$

Where:

$v' = 1 - f_{ck}/250$, k_1, k_2 and k_3 are nationally determined parameters with recommended values of 1.0, 0.85 and 0.75 respectively. EC2 also gives provisions for transverse reinforcement in bottle stress fields. Two compression regions are defined here Figure 2.34: partial or full discontinuity. The tensile force (T) can be obtained using the following formulae:

$$\left. \begin{aligned} \text{Partial discontinuity } & \frac{1}{4} \frac{b-a}{b} \cdot F, \quad b \leq \frac{H}{2} \\ \text{Full discontinuity } & \frac{1}{4} \left(1 - 0.7 \frac{a}{h}\right) \cdot F, \quad b > \frac{H}{2} \end{aligned} \right\} \tag{Equation 2.109}$$

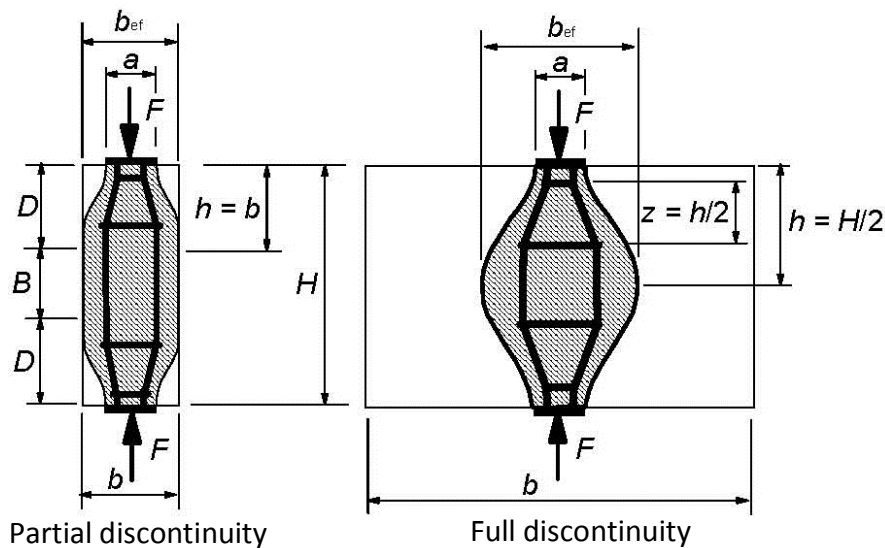


Figure 2.34: Details of transverse tensile force in smeared reinforcement for bottle stress field (BSI, 2004)

FIB Model Code 2010 (fib, 2010)

The strength of model elements in MC2010 is related to the direction of the reinforcement in the model. A reduction factor, K_c is applied to the concrete design strength to evaluate the strength of the elements as follows:

Strength of struts

1. For struts with undisturbed uniaxial stress field, or with transverse compression, $k_c = 1.0 \cdot \eta_{fc} \cdot \eta_{fc}$, where η_{fc} a factor takes into account the more brittle failure behaviour of concrete with a compressive strength greater than 30 MPa, $\eta_{fc} = \left(\frac{30}{f_{ck}}\right)^{\frac{1}{3}}$.
2. For struts with cracks in the direction of the compression stress field and tension reinforcement perpendicular to it $k_c = 0.75 \cdot \eta_{fc}$.
3. For struts with reinforcement running obliquely with the direction of the compression stress field $k_c = 0.55 \cdot \eta_{fc}$.

Strength of nodes

1. For nodes with only compression struts are associated, $k_c = 1.0 \cdot \eta_{fc}$.
2. For nodes with one or two ties anchored to it $k_c = 0.75 \cdot \eta_{fc}$.

Canadian Standards Association (CSA, 2004)Strength of struts

Provisions for the strength of struts in the Canadian code are obtained from the MCFT described earlier in section 2.4.1. The MCFT relates strut strength to the strain in the connected tie at the node and its angle of inclination as follows:

$$f_{cu} = \frac{f'_c}{0.8 + 170 \cdot \varepsilon_1} \leq 0.85 \cdot f'_c \quad \text{Equation 2.110}$$

$$\varepsilon_1 = \varepsilon_s + (\varepsilon_s + 0.002) \cdot \cot^2(\theta) \quad \text{Equation 2.111}$$

ε_s is the strain in the adjoining tie and θ is the smallest angle between the strut and the adjoining ties. In struts with longitudinal compression reinforcement, parallel to the strut, CSA 2004 allows the strut strength to be enhanced by the reinforcement capacity in compression.

Strength of nodes

The strength of the node is given as:

1. $f_{cu} = 0.85 f'_c$ for nodes with struts and bearing plates only.
2. $f_{cu} = 0.75 f'_c$ for nodes anchoring one tie.
3. $f_{cu} = 0.65 f'_c$ for nodes anchoring more than one tie.

2.5.7. Problems in constructing strut-and-tie models

Despite its simplicity and rationality, researchers have reported difficulties in constructing strut-and-tie models ((Schlaich and Schafer, 1991), (Sagasetta, 2008), (Fang, 2013) among others). The main drawback of the STM is that its geometry depends on the loading as well as the structure geometry. Consequently, the designer needs to propose a unique model for each different geometry or load arrangement. Obtaining the optimum model needs engineering experience, which could be subjective and usually involves iterative adjustment for the model. Although STM was first introduced in the 1960s (Leondardt, 1965), there are still uncertainties regarding the dimensioning of model elements, particularly nodes, and estimating the strength of the elements. Moreover, STM is typically statically indeterminate. Consequently, their solution includes assuming a yield condition or a failure criterion.

Although considerable efforts have been invested to optimise STMs for beams with web reinforcement, there is still a gap in estimating the proportions of the different mechanisms (direct strut, vertical and horizontal shear reinforcement). The direct super-positioning of the mechanisms provides a quick estimation, nevertheless, does not provide an accurate detailing of nodes and struts dimensions. The use of semi-empirical correction factors helps to estimate the total shear resistance easily but is data driven where STM is ultimately a case dependent solution. A better tactic is to use the stress field approach with nodes sub-division. Although this procedure is lengthier than the two previous approaches, it gives acceptable predictions and simulates the stress patterns when compared to FEM (Sagasetta, 2008, Fang, 2013).

2.6. Conclusions

Despite many years of effort, research into the shear strength of RC deep beams continues to be the subject of considerable research. This chapter reviewed some relevant literature on the shear strength of RC deep beams.

Early 20th century researchers assumed that, the shear resistance of diagonally cracked reinforced concrete members could be calculated using a 45-degree truss model neglecting any tensile contribution from the concrete. Subsequent research has shown that diagonally cracked concrete can resist shear through a variety of different shear transfer actions. These actions (aggregate interlock, dowel contribution, residual tensile strength, the contribution of the compression zone and stirrups) are highly dependent on the kinematics and shape of

the shear cracks. Evaluation of these contributions includes two levels of uncertainties: the accuracy of the obtained crack kinematics and the validity of the models used. The first uncertainty has recently been limited with the use of the Digital Image Correlation system while the latter is still an undergoing debate.

Calculation of the shear strength of RC beams has been codified in design codes since the 1960s. While the majority of code provisions are based on empirical equations (e.g. EC2 for members without shear reinforcement, BS8110 and ACI-318), a few have recently adopted physical models for the prediction of the shear strength (EC2 for members with shear reinforcement, MC2010 and AASHTO _LRFD). For beams loaded with concentrated load near the support, design codes allow the utilization of the shear strength enhancement resulting from arching action. These methods apply to beams loaded on the top face within $a_v \leq 2d$. BS 8110 enhances the shear resistance provided by concrete $v_{Rd,c}$ for beams loaded within $a_v \leq 2d$ by the multiple $\frac{2d}{a_v}$. Conversely, EC2 and MC2010 reduce the contribution to the design shear force of loads applied within $a_v \leq 2d$ by the multiple $\beta = \frac{a_v}{2d}$ where β is limited to a minimum of 0.25 in EC2 and 0.5 in MC2010. Although these approaches appear similar, there can be significant differences between the enhanced shear resistances given by EC2, MC2010 and the BS8110. Moreover, application of the EC2 shear enhancement design provisions are unclear for beams with shear reinforcement and multiple point loads applied within $a_v \leq 2d$ as discussed by Vollum and Fang (2015). These sectional methods are also not sensitive to the load application face or the boundary conditions.

In terms of shear prediction models, several models are available in the literature but two of them were discussed here, namely: the modified compression field theory MCFT (and its successor the simplified MCFT In this section) and the two parameters kinematics theory (and its successor the five-spring model). The MCFT is one of the earliest and most comprehensive theories for describing the behavior of RC panels under membrane action. It forms the essence of sectional shear prediction in design codes like MC2010 and its strength strain equations are used in several software (VecTor2 and Response-2000). However, it is lengthy and difficult to solve using hand calculations. The simplified MCFT is a simpler version of the MCFT and has been adopted in the calculations of the shear capacity of MC2010. The 2PKT (and the five-spring model) is pertinent to deep beams. It can predict the full displacement

field of the shear span during loading, yet, is case sensitive, and needs modifications to account for variations in load arrangements and boundary conditions.

Another popular method for estimating the shear capacity of members with discontinuity regions is the strut-and-tie model. Several design codes suggest using STM to account for the shear strength enhancement in deep beams.

STM for beams with shear reinforcement can be constructed assuming direct superposition, semi-empirical formulae, or more conveniently using stress field method based on the principal of nodal subdivisions. The model developed by Sagaseta and Vollum (Sagaseta and Vollum, 2010) simplified the principal of nodal sub-division suggested by Wight and Mac Gregor (James K. Wight, 2012). This model has been used and modified by several researchers (Amini Najafian et al., 2013, Vollum and Fang, 2015) to account for different loading arrangements. However, when loads are applied in the tension face instead of the compression face, these models will not be valid due to changes in the stress fields. This observation was supported by the differences in behaviour and failure load for the identical beams loaded on the tension and compression faces based on an initial FE investigation.

CHAPTER 3. EXPERIMENTAL PROGRAM

3.1. Overview

Shear failure in reinforced concrete structures is hard to predict realistically due to its brittle nature and limited deformation at failure. This thesis is concerned with shear enhancement in reinforced concrete (RC) beams. Shear enhancement arises due to arching action when loads are applied to the top surface of beams within around twice the beam effective depth ($2d$) of supports. The shear behaviour of RC deep beams has intensively been studied in the past decades (Liu and Mihaylov, 2016, Boyan et al., 2013, Yang and Ashour, 2008, Fernández Ruiz et al., 2015, Sagaseta and Vollum, 2011, Cavagnis et al., 2017).

Many studies have investigated shear enhancement in single span simply supported beams with a single point load applied to their compression face within $2d$ of supports. However, very little research has been carried out into shear enhancement in beams with several point loads applied within $2d$ of supports. This situation can occur in practice in structures like bridge crosshead girders where multiple point loads can be applied to either the flexural tension or the compression face dependent on the structural arrangement. Previous research into this problem has focussed on the situation where pairs of equal point loads are applied to the flexural compressive face of the beam. (Brown and Bayrak, 2007, Vollum and Fang, 2014). Furthermore, the effect of the shear enhancement in beams partly loaded outside $2d$ from the support has received virtually no attention apart from the work of Filiagi Pastore and Vollum (Pastore and Vollum, 2019a, Pastore and Vollum, 2019b).

This research considers the case of pairs of concentrated loads applied to the tension face of cantilever beams both within and partly within $2d$ from the face of the support. This chapter describes the experimental program carried out by the author in the Heavy Structures Laboratory at Imperial College London to investigate these issues. The main objectives of the experimental program were to investigate the effect of the following parameters on shear enhancement in RC beams:

1. The influence of loading face and structural arrangements on shear enhancement in top loaded RC beams.
2. The effect of varying the ratio between loads applied within $2d$ of the face of the support.

3. The effect on shear enhancement of partly loading the beam outside $2d$ from the face of the support.

A recent technical development in laboratory testing of RC beams is the use of the digital image correlation (DIC) systems to measure crack kinematics and the full displacement field during testing. The use of DIC improves the quality of surface strain measurements, captures the full displacement field of the specimen throughout the load displacement response including post-peak behaviour and produces continuous reading without the need to interrupt the test (Huber et al., 2016, Cavagnis et al., 2015, Sas et al., 2012, De Wilder et al., 2015, Cavagnis et al., 2017). In these tests, a two-camera DIC system supplied by LaVision GmbH (LaVision, 2017) was used to measure crack kinematics throughout the tests. Further description of the DIC system used is provided in Section 3.5.1 of this chapter.

3.2. General Test Description

A total of 12 beams were tested in the experimental program (three sets of four beams, depicted series A to C). All the beams measured 2800 mm long by 250mm wide by 500mm deep. Four test configurations were adopted in this program to accommodate the different loading conditions as described in Section 3.4. Series A was designed to investigate the influence on shear enhancement in top loaded beams of loading either the flexural tension or compression face of otherwise identical beams without and with shear reinforcement. Two simply supported beams were loaded on their compression face within $2d$ of supports while the remaining two beams were loaded as balanced cantilevers on their tension face. These two configurations are comparable in terms of the shear span to effective depth ratio, flexural and shear reinforcement, cross sectional dimensions and moment lever arms. However, the shear force and bending moment diagrams are different, as shown in Figure 3.1. In each case, the maximum shear force occurs at the support but the bending moment at the support is zero for the simply supported beam and a maximum for the cantilever. This difference is only addressed in MC2010, where the shear strength is related to the reinforcement strain at the critical section.

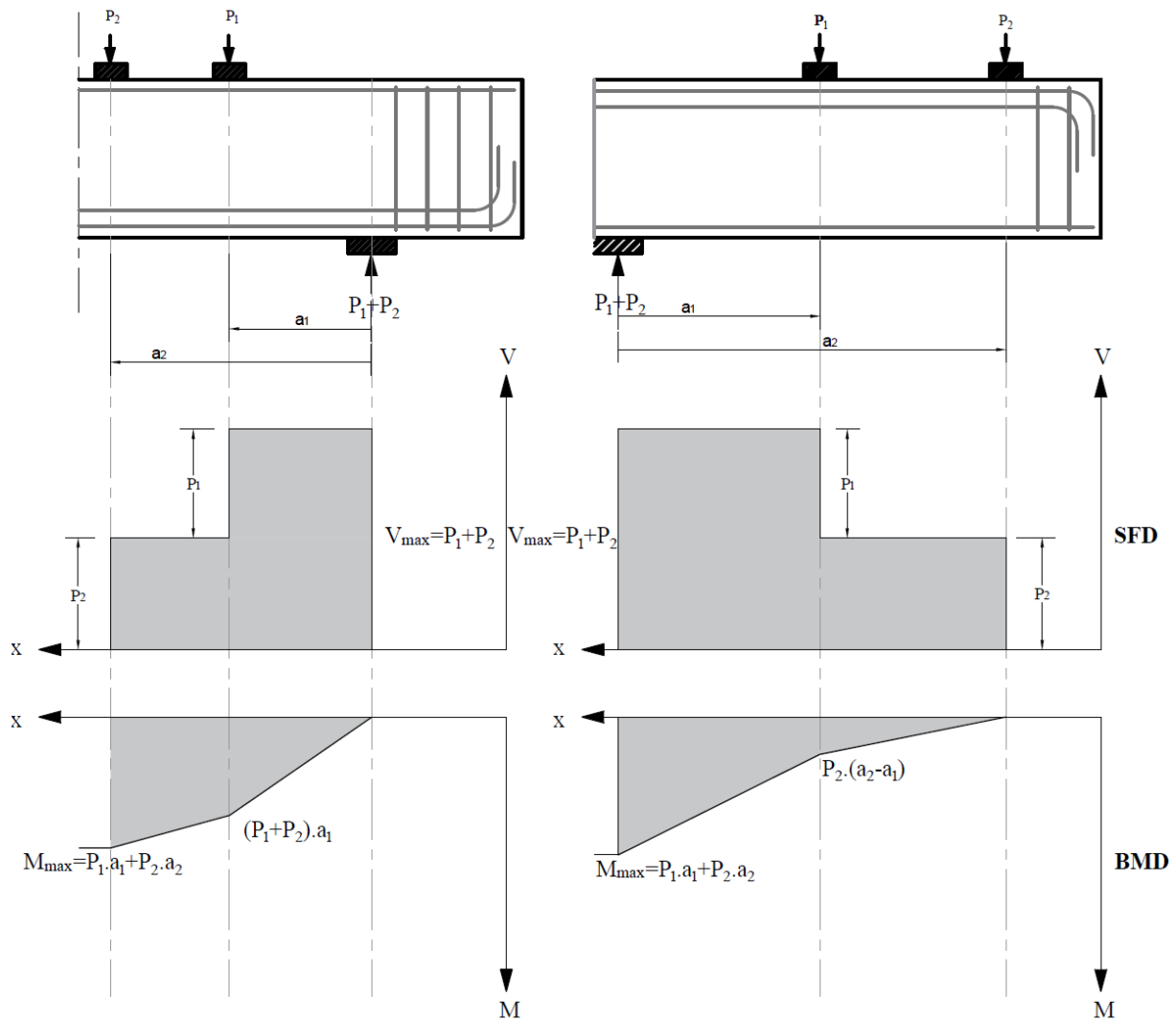


Figure 3.1. Shear force and bending moment diagrams of beams in series A

Series B considered the influence of varying the ratio between the inner and outer loads on the shear resistance of balanced cantilever beams with stirrups positioned at 200 mm centres. The third set (Series C) compared the shear strengths of beams loaded entirely within and partially outside $2d$ of supports. Series C included beams with and without shear reinforcement.

Where provided, shear reinforcement in the critical shear span consisted of 8 mm diameter links at 200 mm centres. The left-hand sides of all of the beams were reinforced with B10mm stirrups. This was done to ensure that failure occurred on the right-hand side of the beams, which was monitored by DIC. The test ID describes the test series, loading face, shear reinforcement and loading ratio. For example, BT200 (0.3/0.7):“B” – test Series, “T” – loaded

on tension face, “200” spacing of 8 mm diameter stirrups in critical shear span and “0.3/0.7” ratio of inner (P_1) (closest to support) and outer loads (P_2) to total load (P).

3.2.1. First series of beams (Series A)

This series consisted of four beams. Beams AC0 (0.5/0.5) and AC200 (0.5/0.5) were simply supported and loaded on their flexural compression face while beams AT0 (0.5/0.5) and AT200 (0.5/0.5) were balanced cantilevers loaded on their tension face. Each shear span was loaded with two equal point loads positioned at $0.76d$ and $1.63d$ from the centreline of the adjacent support. The shear span to effective depth ratio, shear reinforcement ratio and lever arms between the loads and the centre of the support were similar for beams loaded on tension and compression faces to obtain comparable results. The flexural reinforcement in all beams consisted of two layers of 3B25mm ($\rho=2.36\%$) and one layer of 2B16mm as a compression reinforcement ($\rho=0.322\%$). The concrete cover to the shear reinforcement was 25mm. The cross-sectional dimensions and reinforcement detailing are shown in Figure 3.2, Figure 3.3 and Table 3.1.

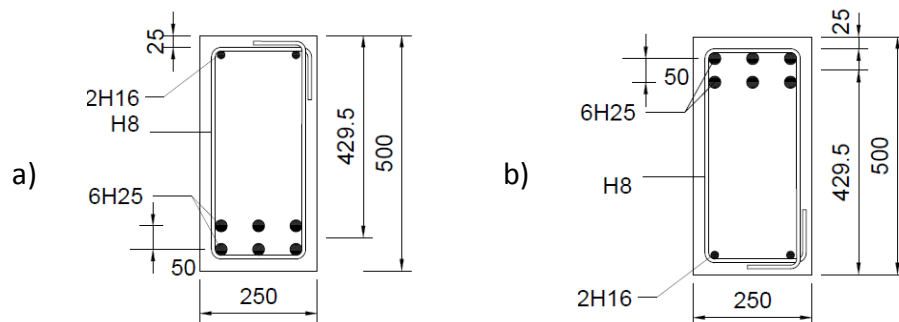
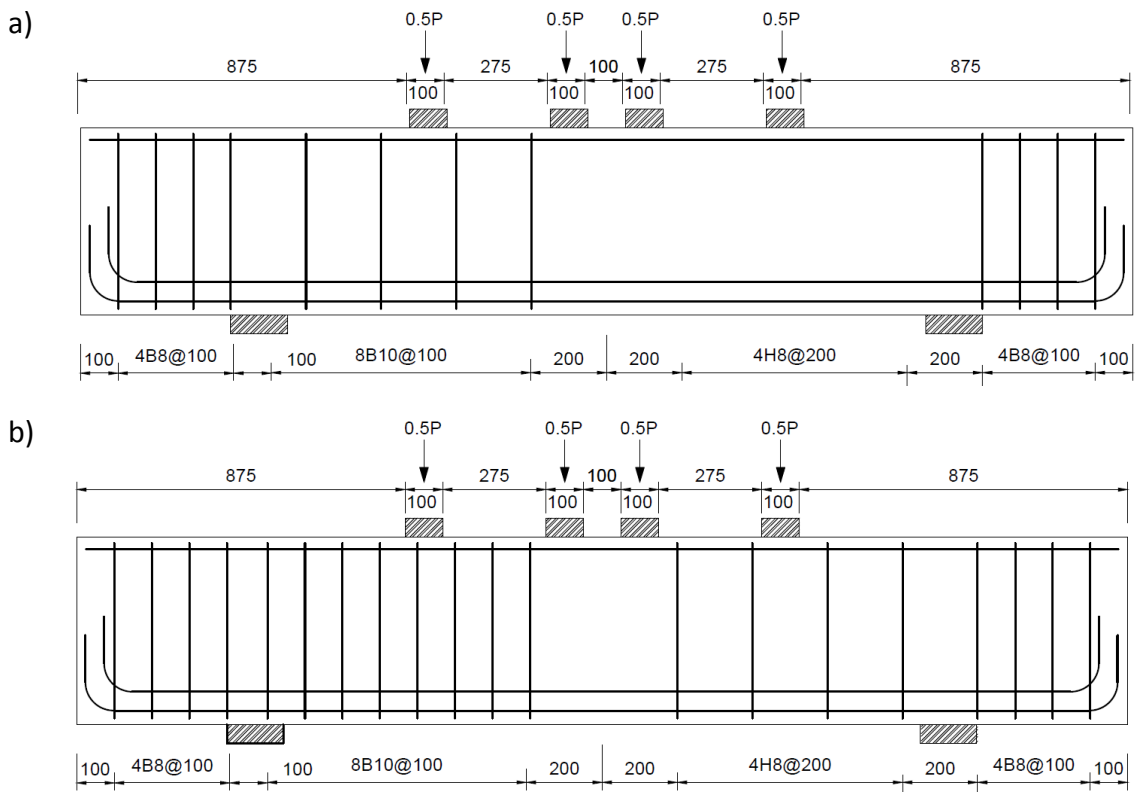


Figure 3.2: Cross section of the series A of test beams a) beams loaded in the compression face and b) beams loaded in the tension face.

The test setup and configuration of the first series are described in detail in Section 3.2.13.4.1. In summary, loads were applied using two actuators connected to two hydraulic jacks. The loading plates were 100 mm long with the same width as the beams. The length of support plates was 150 mm for beams loaded in the compression face and 300 mm for beams loaded on the tension face.

Table 3.1: Geometry and reinforcement details of the series A of test beams

Beam	Loading Face	Reinforcement Ratio %		Centreline distance to the support		Span to depth ratio	
		Flexure	Shear	a_1 (mm)	a_2 (mm)	a_{v1}/d	a_{v2}/d
AC0 (0.5/0.5)	Compression	2.36	0	450	825	0.76	1.63
AC200 (0.5/0.5)	Compression	2.36	0.201	450	825	0.76	1.63
AT0 (0.5/0.5)	Tension	2.36	0	525	900	0.76	1.63
AT200 (0.5/0.5)	Tension	2.36	0.201	525	900	0.76	1.63



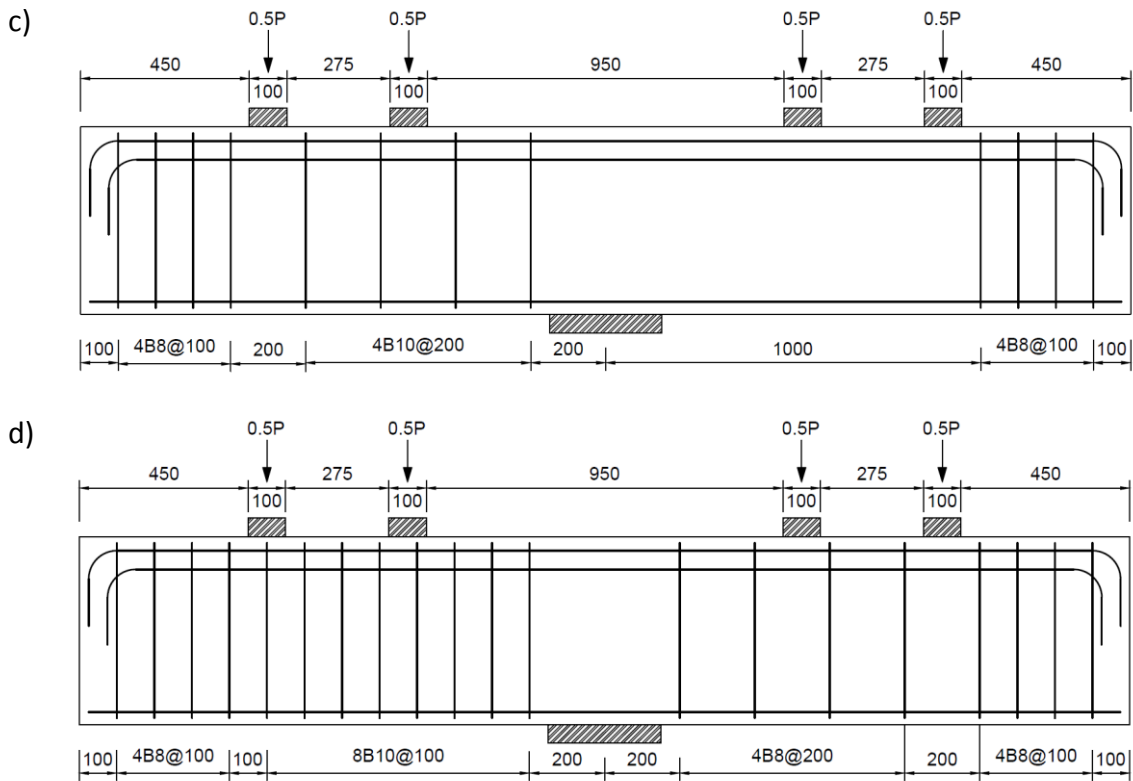


Figure 3.3: Geometry and reinforcement details of series A of test beams (Beams a) AC0 (0.5/0.5), b) AC200 (0.5/0.5), c) AT0 (0.5/0.5) and d) AT200 (0.5/0.5)

3.2.2. Second series of beams (Series B)

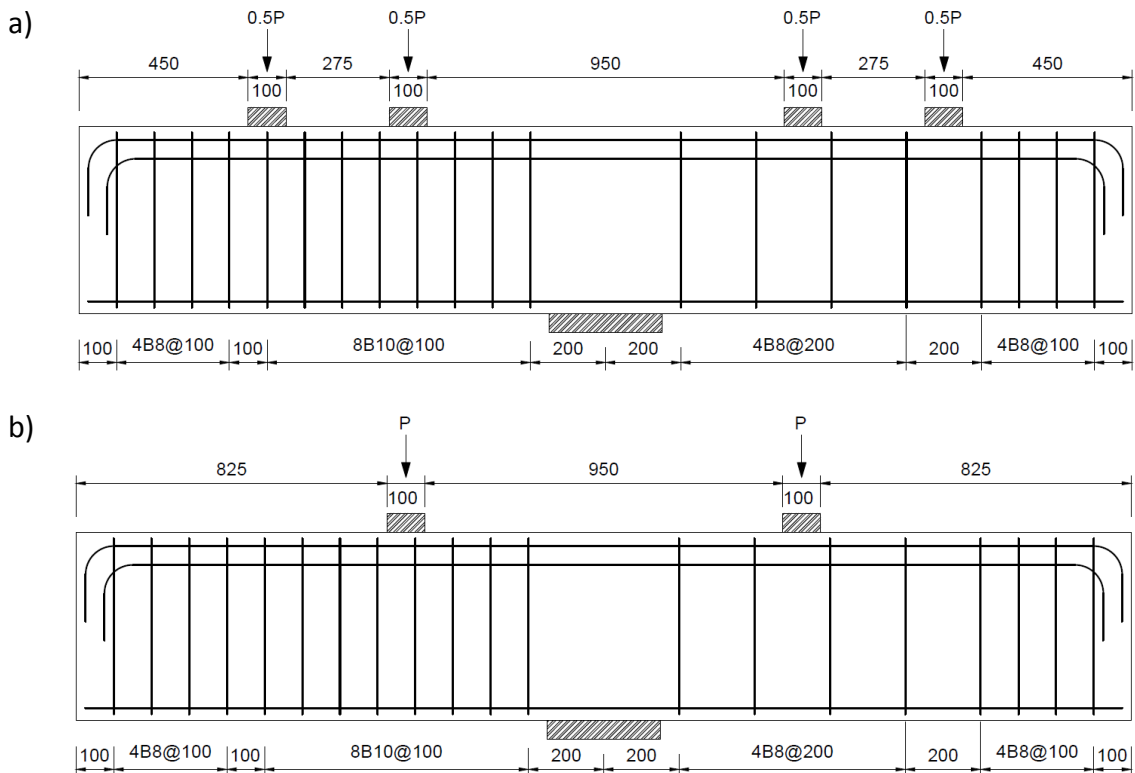
This series consisted of four beams all with the same length and cross-sectional dimensions as the first series. The beams were tested as balanced cantilevers and loaded on the tension face at the same positions as in Series A. The objective was to examine the effect on shear strength of varying the ratio between pairs of loads applied within $2d$ from the face of the support. The reinforcement arrangement for all the beams in Series B was the same as that for beam AT200 (0.5/0.5) of Series A (see Figure 3.2 – b).

The control beam of series B (beam BT200 (0.5/0.5)) was notionally a duplicate of beam AT200 (0.5/0.5) of the first series but the applied loading ratios differed slightly for reasons explained subsequently. Loading ratios were varied as follows: pairs of equal point loads (beam BT200 (0.5/0.5)), 30% of the load on the inner plate and 70% of the load at the outer plate (beam BT200 (0.3/0.7)), single load in the inner plate (beam BT200 (1.0/0)) and single load in the outer plate (beam BT200 (0/1.0)) as demonstrated in Figure 3.4 and Table 3.2.

Table 3.2: Geometry and reinforcement details of the series B of test beams

Beam	Reinforcement Ratio		Distance $a = b^*$	Centreline distance to the support (mm)		Span to depth ratio		Load ratio	
	Flexure	Shear		a_1	a_2	a_{v1}/d	a_{v2}/d	At a_1	At a_2
BT200 (0.5/0.5)	2.36	0.201	712.5	525	900	0.76	1.63	0.5	0.5
BT200 (1.0/0)	2.36	0.201	525	525	0	0.76	0	1	0
BT200 (0/1.0)	2.36	0.201	900	0	900	0	1.63	0	1
BT200 (0.3/0.7)	2.36	0.201	787.5	525	900	0.76	1.63	0.3	0.7

*Distance (a) and (b) are shown in Figure 3.10.



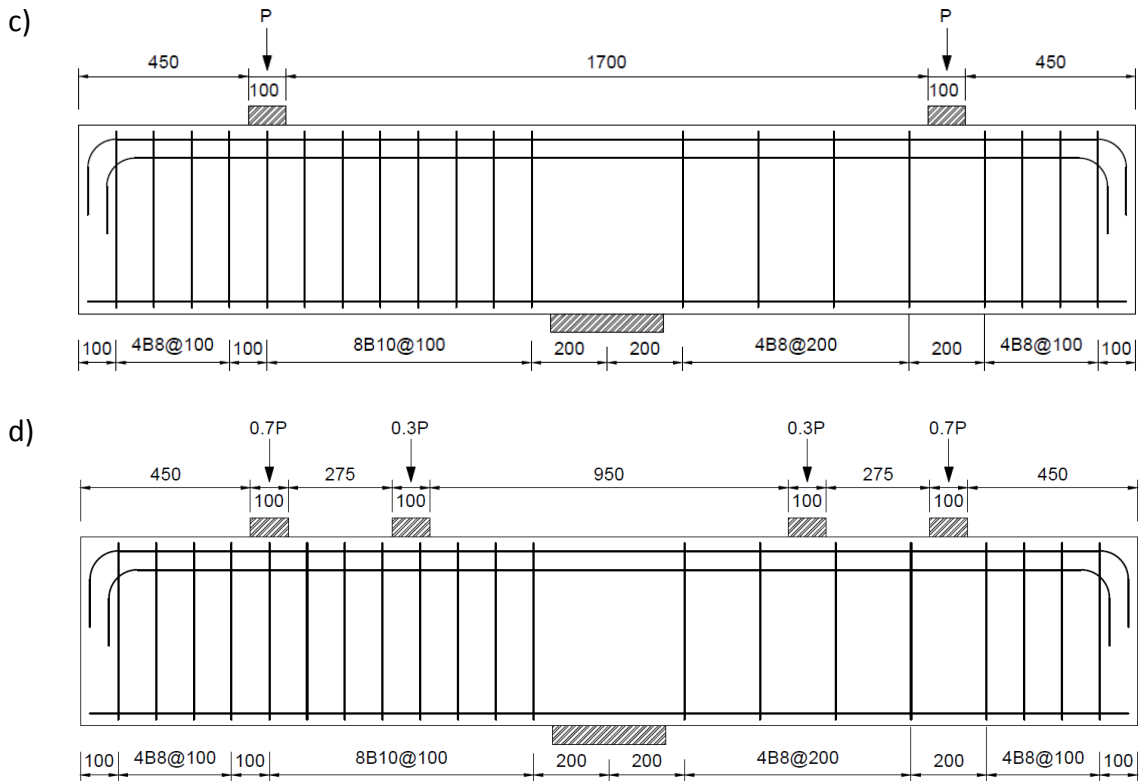


Figure 3.4: Geometry and reinforcement details of series B of test beams

3.2.3. Third series of beams (Series C)

This series consisted of two pairs of beams with and without shear reinforcement. The tests investigated the effect on shear strength of applying loads both within and outside $2d$ from the face of the support. Beams CT0 (1.0/0) and CT200 (1.0/0), without and with shear reinforcement respectively, were loaded with a single point load at $1.66d$ from the centreline of the support. An additional load was applied at $3d$ from the centreline of the support in tests CT0 (0.6/0.4) and CT200 (0.6/0.4). It was not possible to load the final two beams symmetrically since the required length of the beams was greater than the available width within the loading rig. Hence, beams CT0 (0.6/0.4) and CT200 (0.6/0.4) were loaded asymmetrically as shown in Figure 3.5. Details of the loading arrangement, beam geometry and reinforcement are given in Figure 3.5 and Table 3.3.

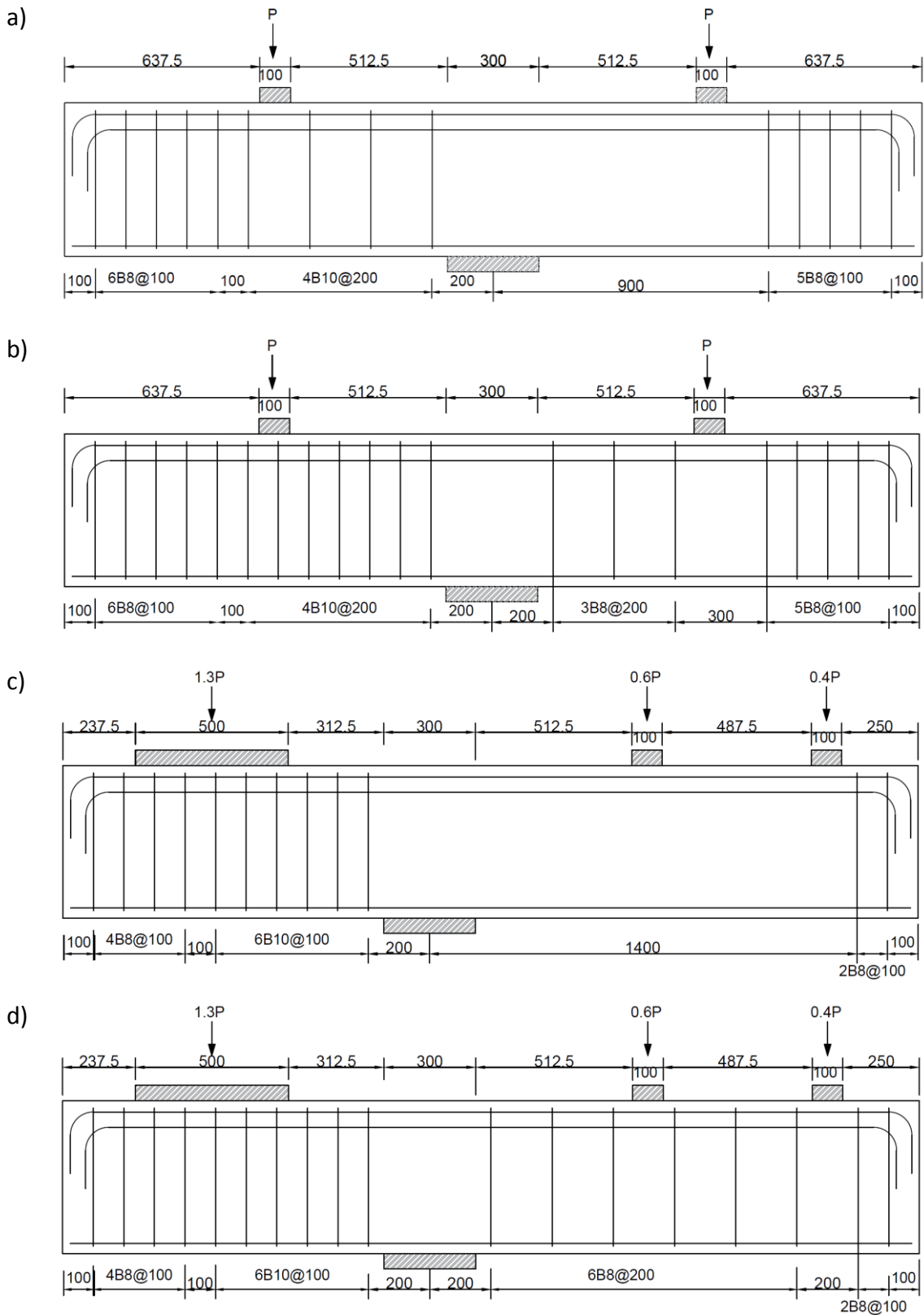


Figure 3.5: Geometry and reinforcement details of the series C of test beams. a) CT0 (1.0/0), b) CT200 (1.0/0), c) CT0 (0.6/0.4) and d) CT200 (0.6/0.4)

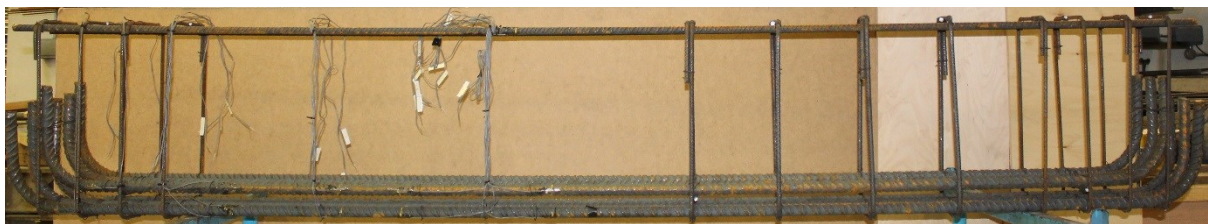
Table 3.3: Geometry and reinforcement details of the series C of test beams

Beam	Reinforcement Ratio %		Centreline distance to the support (mm)				Span to depth ratio		Load ratio	
	Flexure	Shear	b (LHS)	RHS			a_{v1}/d	a_{v2}/d	a_1	a_2
				a	a_1	a_2				
CT0 (1.0/0)	2.36	0.201	712.5	712.5	712.5	0	1.19	0	1	0
CT200 (1.0/0)	2.36	0.201	712.5	712.5	712.5	0	1.19	0	1	0
CT0 (0.6/0.4)	2.36	0.201	712.5	947.5	712.5	1300	1.19	2.56	0.6	0.4
CT200 (0.6/0.4)	2.36	0.201	712.5	947.5	712.5	1300	1.19	2.56	0.6	0.4

3.3. Manufacturing and Curing

Beams preparation included four main operations: fixing of reinforcement cages, attaching the strain gauges to the reinforcement, moulds manufacture and concrete casting. The three series of the experimental program were prepared in sequence to allow for modifications if needed.

The assembled reinforcement cages are shown in Figure 3.6, which also shows the locations of strain gauges. The reader is referred to Section 3.5.2 for further details regarding fixing of the strain gauges.



(a)

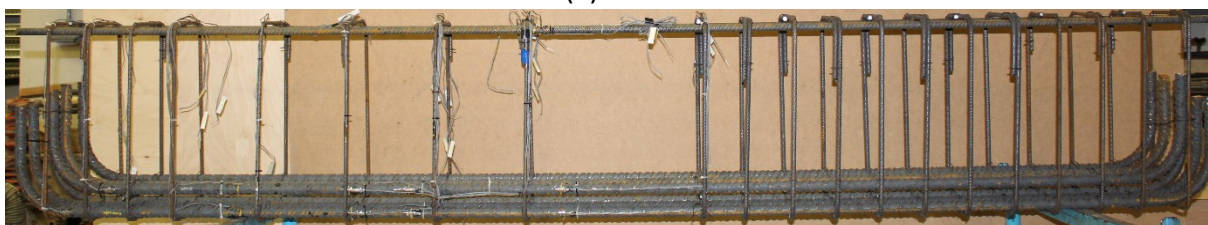


Figure 3.6: Rebar cage for beams a) without b) with shear reinforcement

After fixing the strain gauges into position, the reinforcement cages were placed in the formwork, which was constructed from 19mm plywood. The moulds were oiled to ease the de-moulding process and to prevent concrete bonding with the plywood – see Figure 3.7. Strain gauge lead wires were securely fixed to the top face of the moulds inside plastic bags as shown in Figure 3.7. Positions of anchorage links and shear reinforcement bars were marked on the moulds as well.



Figure 3.7: Reinforcement cages inside the moulds before casting.

Beams were cast in three groups of four with each group cast from a single batch of ready-mixed concrete supplied by CEMEX. The concrete was specified to have strength class C25/30, consistency class S3 and limestone aggregate with a maximum size of 20mm. The concrete was loaded into an upright concrete skip with a central discharge hose and then poured vertically into the moulds. An internal vibrator was used to compact the concrete.

For Series A, a total of 36 cubes (100mm), 12 cylinders (100mm diameter and 200mm height) for compressive strength and 12 cylinders (150mm diameter and 300mm height) for split cylinder tensile strength were cast. Half the control specimens were cured in water at 20° C with the remainder cured in air alongside the beams. The cube strengths were used to determine the development of concrete strength with time. Cylinders were used to evaluate the compressive and tensile strength of the concrete at the time of the first and last beam

tests. The strength of the remaining two beams was evaluated by interpolation using the strength development curve derived from the cube tests. The concrete beams and air cured control specimens were stored under a plastic cover. The specimens were sprayed with water every other day (Figure 3.9) apart from in the summer when specimens were sprayed daily on account of the warmer weather.



Figure 3.8: Pouring of the concrete

3.4. Beams setup and Test Configuration

3.4.1. Setup for Series A

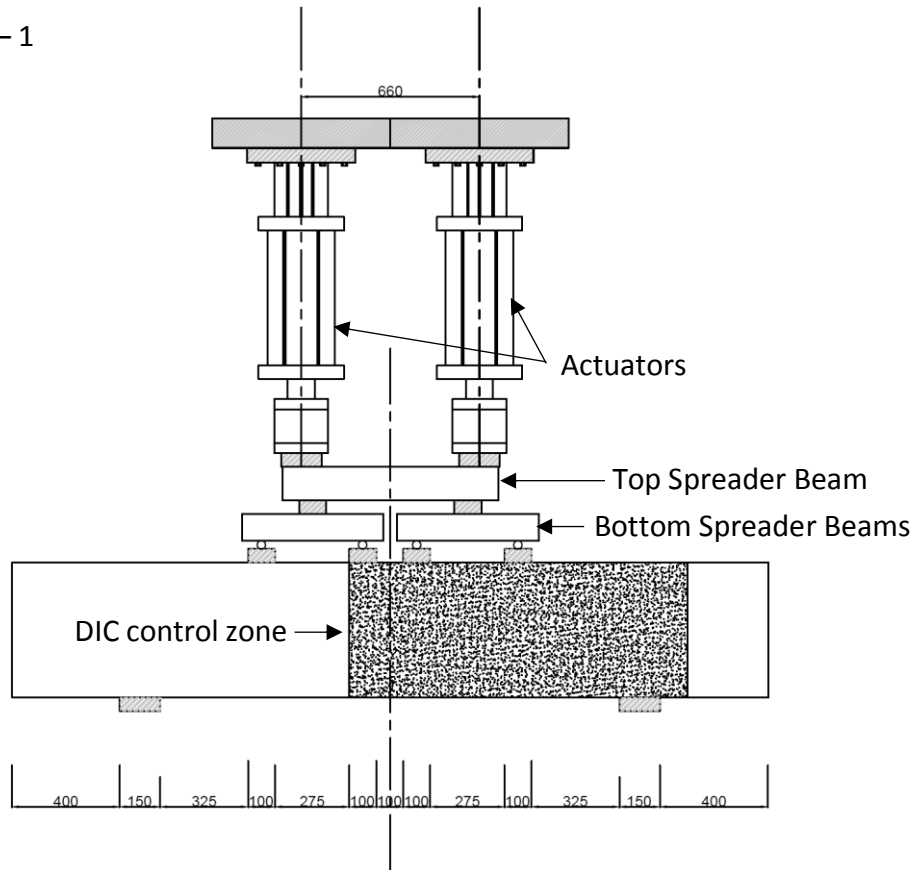
The aim of Series A was to compare the shear strengths of otherwise identical beams loaded on the flexural tension and compression face. Two different test configurations (defined as Config-1 and Config-2) were adopted in this series (Figure 3.10). The beams were loaded with two 1000 kN Instron actuators since the estimated failure loads exceeded the maximum capacity of a single actuator.



Figure 3.9: Beams and air cured specimens wrapped for curing

For beams loaded on the compression face (Config-1), three spreader beams were needed to transfer the load from the actuators to the four loading plates as demonstrated in Figure 3.10 a-b. This was the case because the minimum possible spacing between the two actuators of 660 mm was greater than the distance between the centreline of the pairs of loads in each shear span. Therefore, a top spreader beam was introduced to transfer the load from the actuators to the bottom spreader beams as shown in Figure 3.10 a-b. The spreader beams were fabricated from mild steel cross sections measuring 125 mm wide by 150 mm deep.

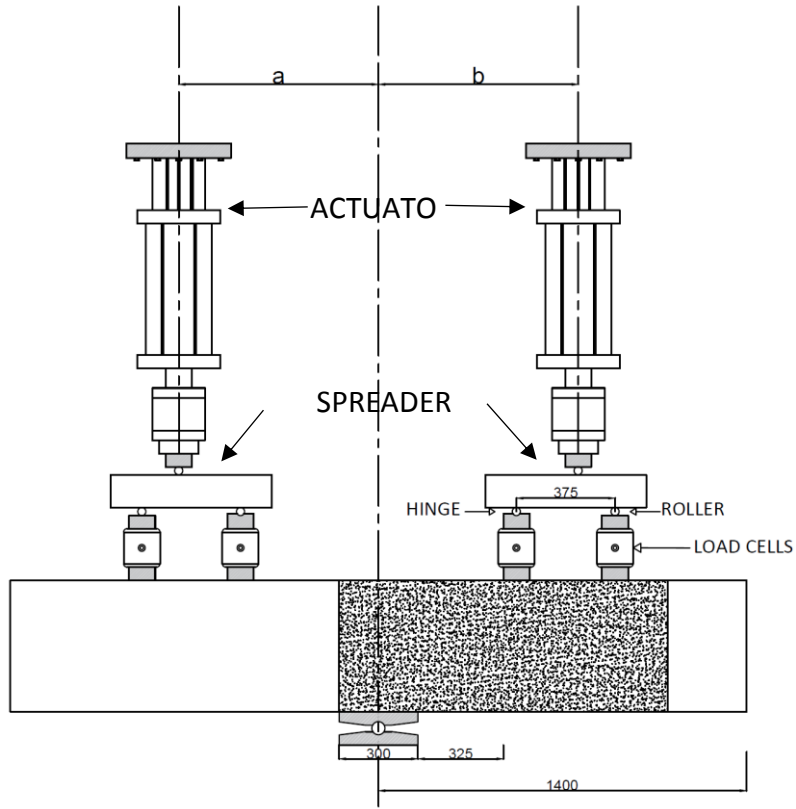
(a) Config. - 1



(b)



(c) Config. – 2



(d)



Figure 3.10: Test configurations for the series A a) Config -1 and b) Config -2.

For beams loaded on the tension face with 4-point loads (Figure 3.10 c-d), the required actuator spacing was sufficiently large for the actuators to directly load the spreader beams. Distances (a) and (b) in Config-2 (Figure 3.10 c) equalled 712.5 mm for tension face loaded beams in Series A. The bottom supporting plate rested on a captured roller to allow rotation but not translation (Figure 3.11 – right).

The load was applied in displacement control to capture the post-failure behaviour. Marginally different displacement rates were required in each actuator of the simply supported beams to maintain similar loads in each. This was the case due to each shear span having different stiffness due to the differing amounts of shear reinforcement.

For beams loaded on the tension face, the left actuator was kept fixed in place with zero-displacement while loading the right actuator in displacement control. This resulted in similar but not exactly equal loads in both actuators. To investigate the cause of this discrepancy, load cells were inserted between each loading plate and the spreader beam as shown in Figure 3.9-c. The load cell readings showed that due to unintended rotational friction in the loading arrangement, the split between the inner (P_1) and outer loads (P_2) was 0.58/0.42 in Series A rather than the intended 0.5/0.5. This unintended difference between P_1 and P_2 was eliminated in subsequent tests by inserting a roller between the actuator and spreader beam as shown in Figure 3.11.



Figure 3.11: Load cells (Left) and Seating ball (Right) in series A of beams

3.4.2. Setup for Series B

The second series was tested to examine the effect of varying the ratio between the inner (P_1) and outer (P_2) loads. The loading ratios in Series B were (1.0/0), (0.3/0.7), (0.5/0.5) and 0/1.0). Consequently, two beams were loaded with 4-point loads and two with 2-point loads.

For beams loaded with 4-point loads, Config. – 2 (Figure 3.10– b) was used with distances $a = b = 712.5$ mm for beams with 0.5/0.5 load split and $a = b = 787.5$ mm for beams with load split of 0.3/0.7. For beams loaded with one point load in each shear span, load was applied directly to the loading plates as shown in Config. – 3 in Figure 3.12.

3.4.3. Setup for Series C

The four beams in Series C were designed to investigate the effect of partly loading beams within and outside $2d$ from the support. These tests were motivated by the very different strength predictions given for this loading case by the shear enhancement methods of the superseded UK code BS8110 and (BSI, 1997) EC2 (BSI, 2004). The critical shear span of beams CT0 (1.0/0) and CT200 (1.0/0) was loaded within $2d$ of the support by a single point similar to Config – 3 with distances $a = b = 712.5$ mm ($a/d = 1.66$). The loading arrangement in test CT0 (1.0/0) and CT200 (1.0/0) is statically equivalent to that in test beam BT200 (0.5/0.5). The critical shear span of beams CT0 (0.6/0.4) and CT200 (0.6/0.4) was also loaded with an additional concentrated load positioned at $a = 1300$ mm ($a/d=3.0$) where shear enhancement is minimal. An asymmetric loading arrangement was adopted due to the beam length constraints of the rig (see Config. – 4 in Figure 3.13). A 500 mm long loading plate was used on the LHS of the beam to enhance its shear resistance sufficiently that shear failure occurred in the RHS of the beam. Details of the spreader beam and the loading arrangements are given in Figure 3.14 below.

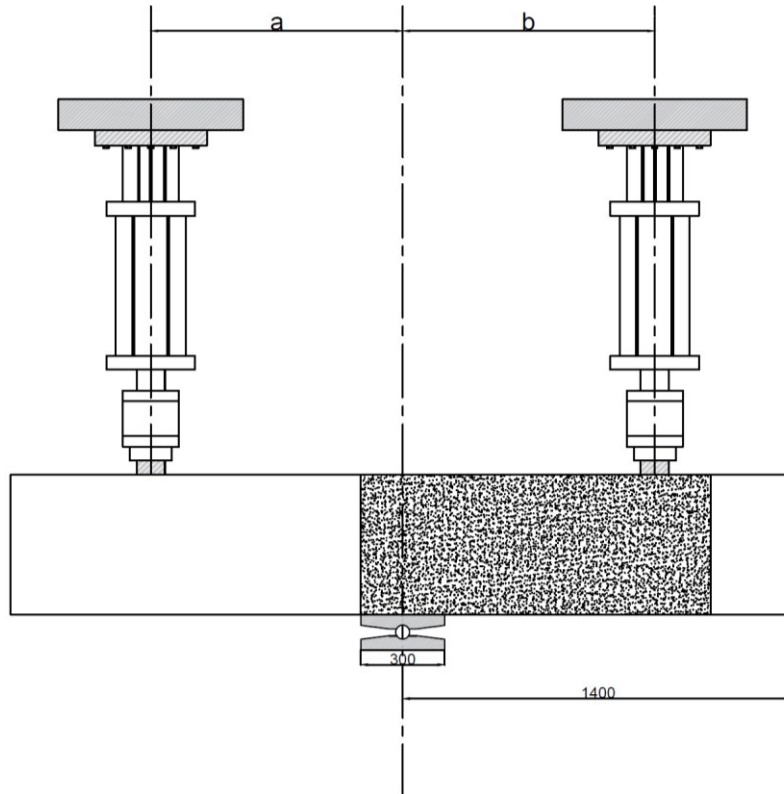


Figure 3.12: Test configuration Config. – 3

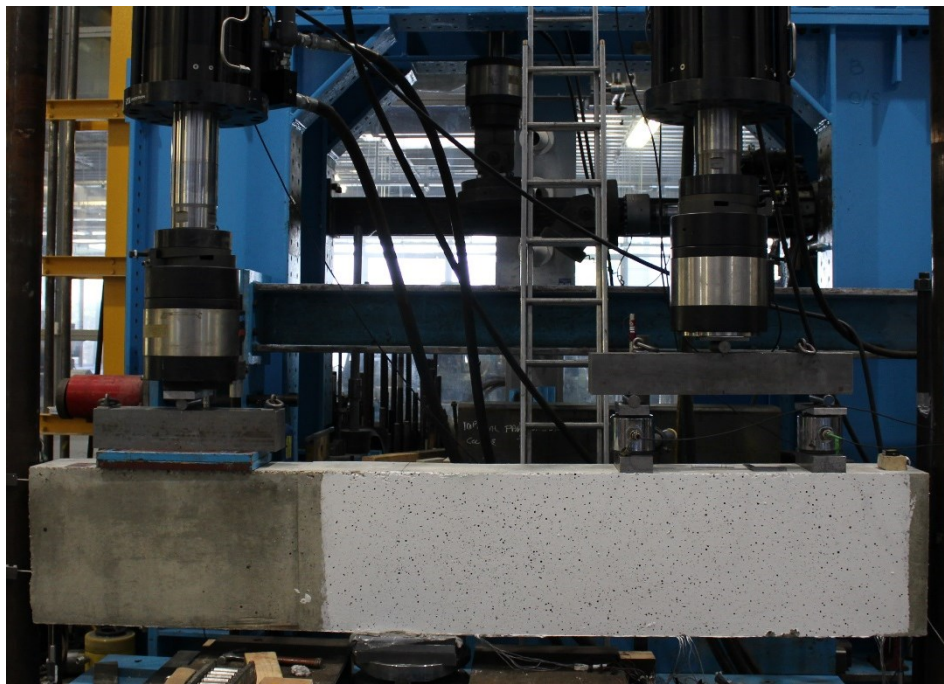
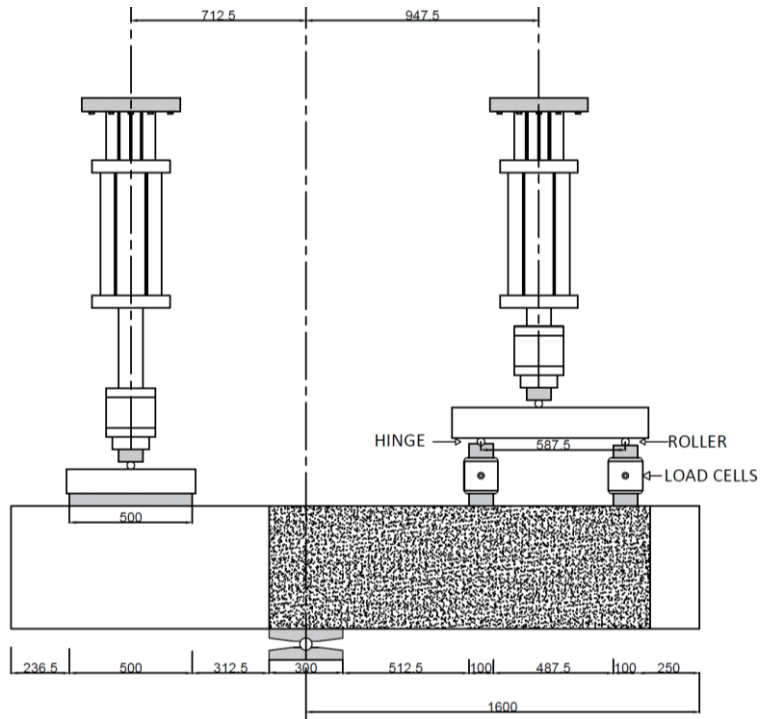


Figure 3.13: Test configurations for series C (Config. - 4)

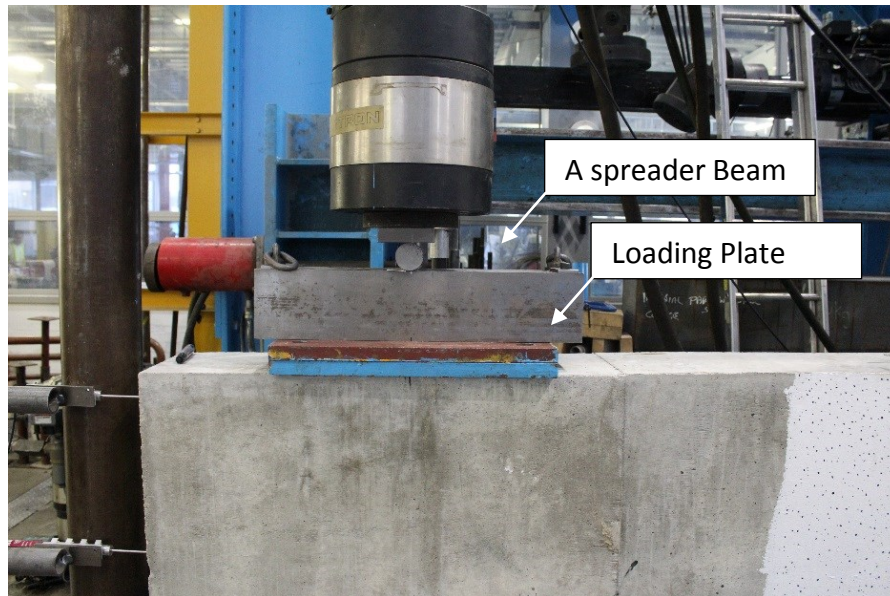


Figure 3.14: Spreader beam and loading plate in the LHS of the third series

3.5. Instrumentation

3.5.1. General Aspects

Measurements during the tests included concrete surface strains, crack displacements, reinforcement strains, global displacements and rotation of the beams. The instruments used were:

- a) Digital image correlation (DIC) system.
- b) Reinforcement strain gauges.
- c) Linear variable displacement transducers (LVDT).
- d) An inclinometer.

Specifications and setup of each of the above mentioned are discussed separately below.

3.5.1. Digital Image Correlation (DIC) System

DIC is a non-contact experimental technique used to obtain displacement fields of samples during tests. The principle of the DIC is to record and analyse series of images captured during the test with high-resolution cameras. DIC algorithms trace a random pattern on the surface of the specimen and calculate its displacement field using a correlation between deformed and un-deformed images.

DIC has several advantages over conventional instruments like manual extensometers (DEMCs) and cross transducers. Manual extensometers are both tedious to use and potentially hazardous towards failure. Furthermore, they do not provide continuous readings and like cross transducers can only gather information at predefined discrete locations. Conversely, DIC systems provide continuous remote strain readings throughout the test without user intervention.

In cases, where there are no visible features on the surface of the sample, a speckle pattern can be applied to a painted surface on the specimen. This is typically the case for concrete beams instrumented with DIC. In this research, the speckle pattern was applied using paintbrush and refined with a marker with a dot size equals to the recommended spackle pattern size. The optimum diameter of the speckle pattern depends on the size of the pixels and the monitored area. The quality of DIC results is affected by choosing the correct optimum size of the speckle pattern and the subset size (Pan et al., 2008). For this program, the optimum diameter of the pattern ranged between 0.3 – 0.4 mm based on the area of interest. A typical speckle pattern is demonstrated in Figure 3.15.



Figure 3.15: Typical speckle pattern for DIC

The 3D DIC system used for this program consisted of a programmable timing unit, two high-resolution cameras and two illumination lights all connected to a CPU – Figure 3.16. The system can import also force or displacement inputs from the test data logger.

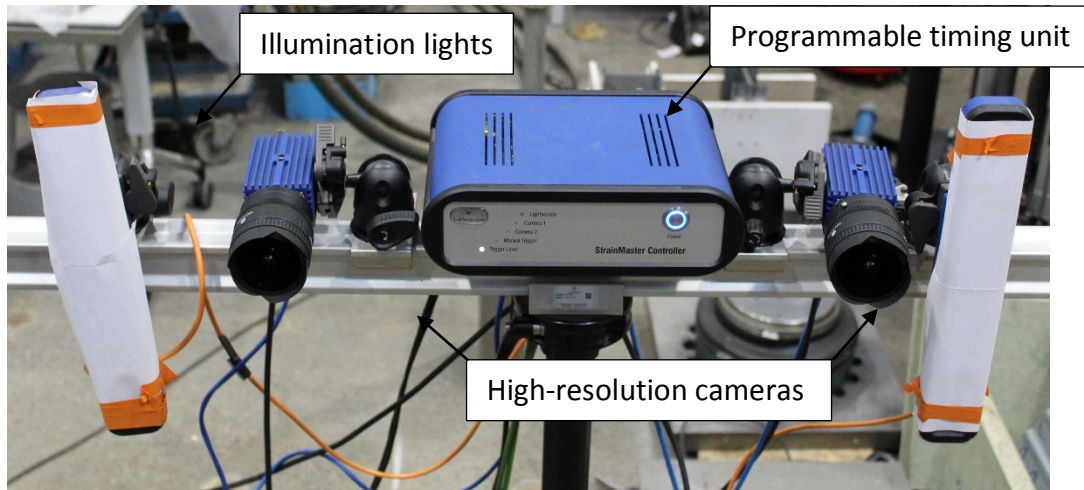


Figure 3.16: DIC System used on the experimental program

Calibration of the system is necessary to remove lens distortions and to scale images. Calibration was performed using a calibration plate Type 1000 Figure 3.17. The plate was placed in front of the beam and five images with different plate positions were obtained for calibration. Automatic calibration and scaling were performed by the software and calibrated images were calculated and corrected. Actuator load and displacement were imported into the system with data recorded at a frequency of 1 Hz.

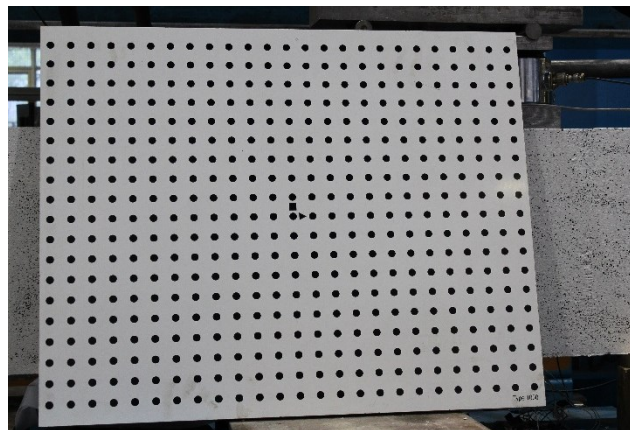


Figure 3.17: Calibration board for DIC calibration

Calculations of crack kinematics

The main purpose of using the DIC system was to measure crack propagation and crack kinematics during the test. DIC software can generate displacement and strains in different directions. However, calculations of crack kinematics needs to be performed outside the software using provisions from literature (Campana et al., 2013, Hamadi and Regan, 1980), as these kinematics are not given by the software.

Two virtual gauges were placed perpendicular to each other at steps of 25mm along the height of the crack (Figure 3.18). Gauges limits were checked visually to ensure that each gauge intersected only the critical crack and no gauge end was located outside beam boundaries. Gauges limits at the top and bottom of the crack were also checked to ensure that the end-points were within the beam. Gauge length or location was changed if the gauge intersected more than one crack or if its limits exceeded the beam boundaries. The sensitivity of the measurements to the gauge length is discussed later in this section. A MATLAB code was developed to extract the horizontal and vertical displacements of the gauge end-points. Using the provisions given by Campana (Campana et al., 2013) and described below, the crack opening and sliding were calculated.

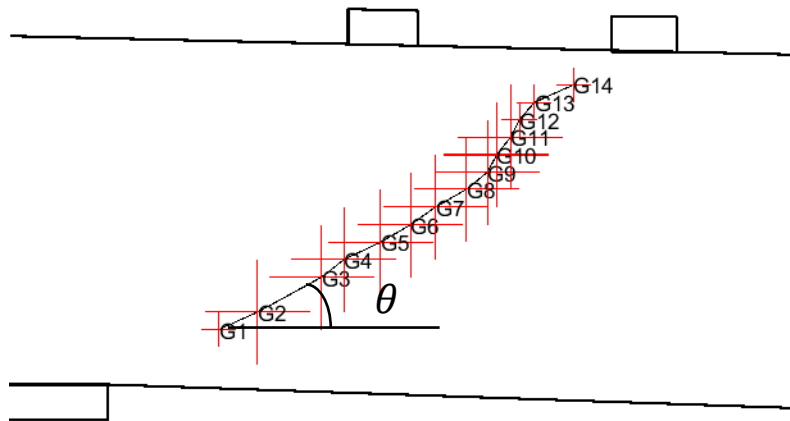


Figure 3.18: Typical virtual gauges along the critical crack (Beam BT200 (0.5/0.5))

To calculate the displacement fields of two rigid bodies located at different sides of a crack, the displacement of two reference points at each side can be used as follows:

The displacement field of each segment was obtained by tracking two points at each segment.

Assuming the initial positions of the points are $(P_1^i, P_2^i, P_3^i \text{ and } P_4^i)$ and the final positions after deformation were $(P_1^f, P_2^f, P_3^f \text{ and } P_4^f)$, the displacement fields can be described by

$$w_1(x, y) = \begin{cases} a_1 - e_1 \cdot y \\ b_1 + e_1 \cdot x \end{cases} \quad \text{Equation 3.1}$$

$$w_2(x, y) = \begin{cases} a_2 - e_2 \cdot y \\ b_2 + e_2 \cdot x \end{cases} \quad \text{Equation 3.2}$$

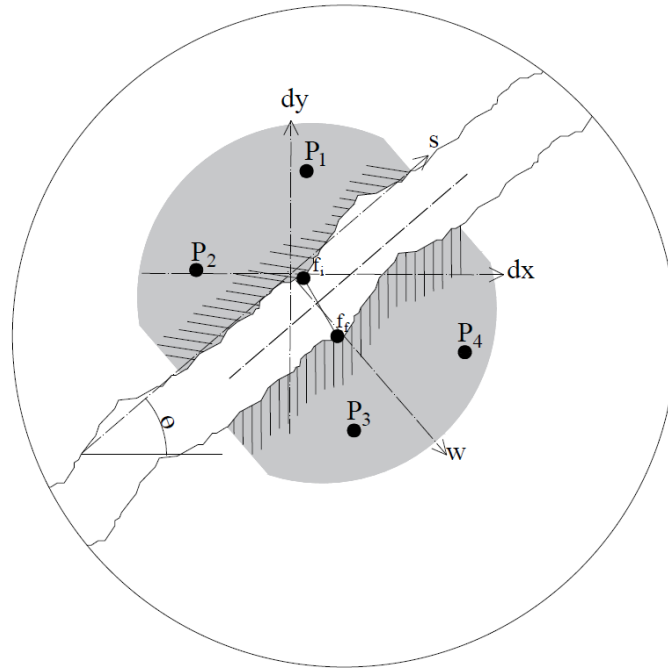


Figure 3.19: Measurements for calculation of crack kinematics

In which:

$$\begin{bmatrix} a_1 \\ b_1 \\ e_1 \end{bmatrix} = (A_1^T \cdot A_1)^{-1} \cdot (A_1^T \cdot c_1) \quad \text{Equation 3.3}$$

$$\begin{bmatrix} a_1 \\ b_1 \\ e_1 \end{bmatrix} = (A_1^T \cdot A_1)^{-1} \cdot (A_1^T \cdot c_1) \quad \text{Equation 3.4}$$

$$A_1 = \begin{bmatrix} 1 & 0 & -P_{1,y}^i \\ 0 & 1 & P_{1,x}^i \\ 1 & 0 & -P_{2,y}^i \\ 0 & 1 & P_{2,x}^i \end{bmatrix} \text{ and } A_2 = \begin{bmatrix} 1 & 0 & -P_{3,y}^i \\ 0 & 1 & P_{3,x}^i \\ 1 & 0 & -P_{4,y}^i \\ 0 & 1 & P_{4,x}^i \end{bmatrix} \quad \text{Equation 3.5}$$

$$c_1 = \begin{bmatrix} P_{1,x}^f - P_{1,x}^i \\ P_{1,y}^f - P_{1,y}^i \\ P_{2,x}^f - P_{2,x}^i \\ P_{2,y}^f - P_{2,y}^i \end{bmatrix} \text{ and } c_2 = \begin{bmatrix} P_{3,x}^f - P_{3,x}^i \\ P_{3,y}^f - P_{3,y}^i \\ P_{4,x}^f - P_{4,x}^i \\ P_{4,y}^f - P_{4,y}^i \end{bmatrix} \quad \text{Equation 3.6}$$

The relative displacements $w_f(d_{x,f}, d_{y,f})$ of a point (f) located in the crack path can be found as the difference between the two displacements $w_1(x_f, y_f)$ and $w_2(x_f, y_f)$

$$w_f(d_{x,f}, d_{y,f}) = w_2(x_f, y_f) - w_1(x_f, y_f) \quad \text{Equation 3.7}$$

To obtain the crack opening (w) and sliding (s) for a beam as described in Figure 3.18 with a crack inclination angle of (θ), the axis rotation matrices in Equation 3.8 and Equation 3.9 can be used. Because the crack propagates in different orientations (from right bottom to left top in beams loaded on the compression face and from left bottom to right top for beams loaded in the tension face), two rotation matrices were used based on the loading face.

For beams loaded in the tension face (similar to Figure 3.18):

$$\begin{bmatrix} w \\ s \end{bmatrix} = \begin{bmatrix} -\sin \theta & \cos \theta \\ \cos \theta & \sin \theta \end{bmatrix} \cdot w_f(d_{x,f}, d_{y,f}) \quad \text{Equation 3.8}$$

For beams loaded in the compression face:

$$\begin{bmatrix} w \\ s \end{bmatrix} = \begin{bmatrix} \cos \theta & \sin \theta \\ -\sin \theta & \cos \theta \end{bmatrix} \cdot w_f(d_{x,f}, d_{y,f}) \quad \text{Equation 3.9}$$

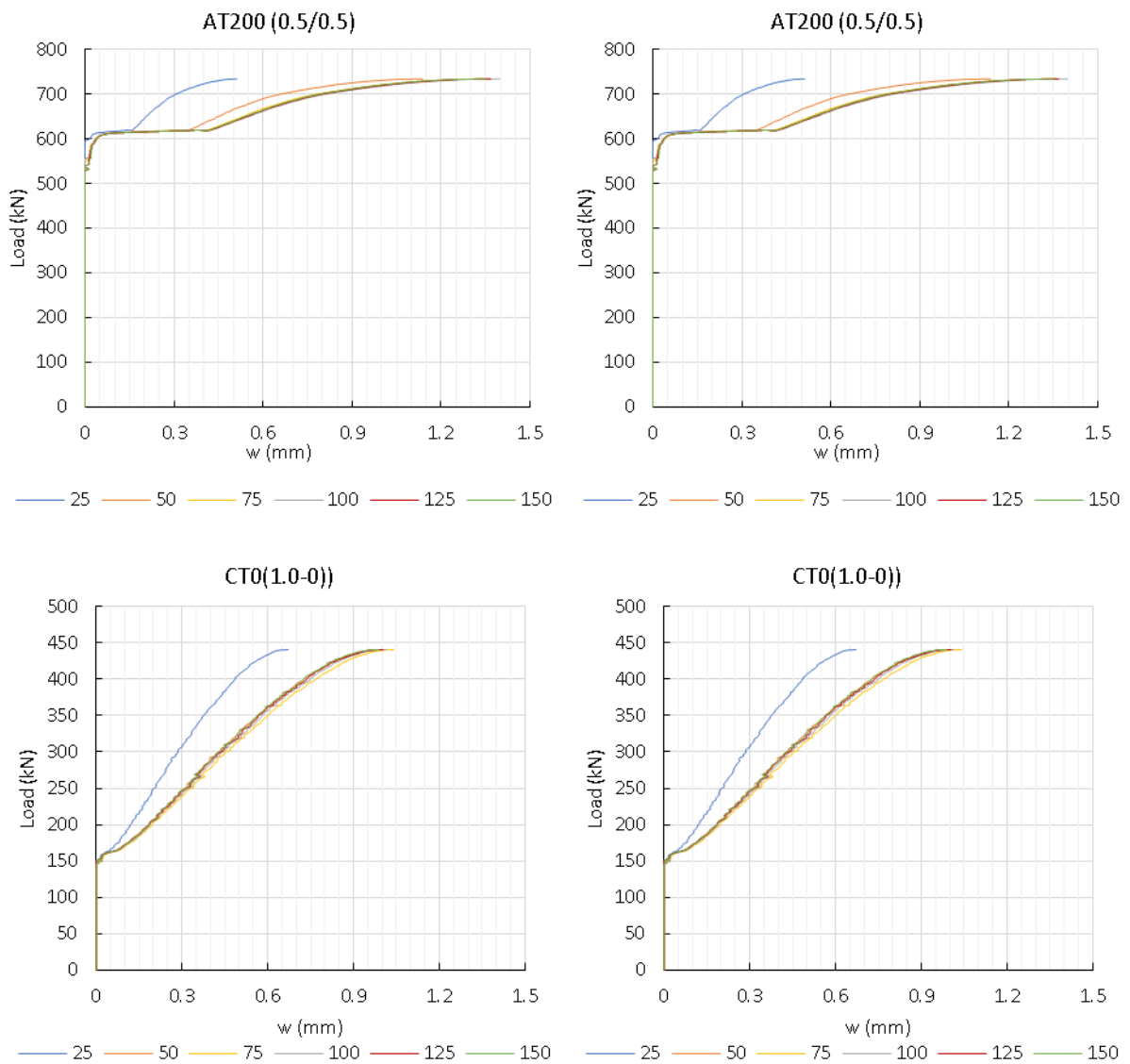
The above equations give the crack opening and sliding if these four points are crossed only by a single crack and the two sides are rigid bodies. Detailed description of the procedures and the MATLAB code are provided in Appendix I.

DIC accuracy and result refinement

Images are processed in DIC systems in windows of pixels called subsets. The accuracy of the results depends on the sizes of the subset (LaVision, 2018). A small subset size increases the spatial resolution but decreases vector accuracy and large subset size increases the accuracy of the associated vector but decreases spatial resolution. In this work, a subset size of 30 pixels was used with a step size (specifies the evaluation window overlap in pixel) of 10 as recommended for similar cases (LaVision, 2018).

The accuracy of the DIC results is also related to the length of the strain gauge and the magnitude of the developed strains (Acciaoli et al., 2018, Lee et al., 2011). To obtain accurate results, the length of the strain gauge needs to be maximized (Lee et al., 2011). However, using a long gauge in varying strain field zones is inaccurate; in addition, longer strain gauges may cross more than one crack particularly for micro-cracks. Hence, in this program, a sensitivity analysis of the crack opening and sliding with variable gauge lengths was

conducted. The gauge length was varied from 25mm to 150mm in steps of 25mm in several locations to investigate the effect of the gauge length on the accuracy of the results. The results (as shown in Figure 3.20) showed negligible or no sensitivity for gauges lengths ranging between (75 -150) mm. The calculated crack opening and sliding were similar when the gauge length was varied between 75-150mm. However, for shorter gauges (25 and 50 mm), the results appeared to deviate particularly for gauges with a length of 25mm. samples of results are presented below.



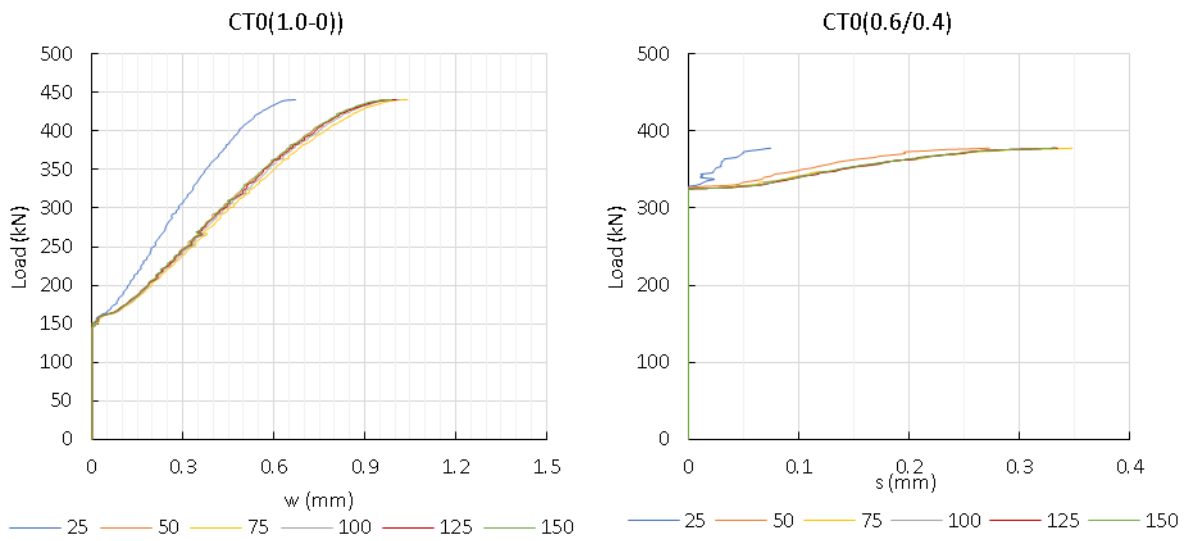


Figure 3.20: Sensitivity Analysis for DIC gauge length

Refined crack measurements

DIC measurements for small magnitude strains of homogenous materials may contain inherited errors (Acciaiolli et al., 2018). Furthermore, rather than being rigid as assumed in the calculation of crack displacements, concrete deforms in tension prior to cracking. Hence, a minimum crack opening (w_{min}) corresponding to the maximum concrete tensile strain ($\varepsilon_{ct,max}$) was calculated for different gauge lengths (L_g) as demonstrated in Equation 3.10. Any opening less than the minimum crack opening was taken as zero with relevant sliding also set to zero.

$$w_{min} = \varepsilon_{ct,max} \cdot L_g \quad \text{Equation 3.10}$$

Images were taken in a frequency of (1) Hz. However, for calculations of the shear transfer actions, crack kinematics were obtained at load steps of $0.1V_{max}$. To obtain crack kinematics at steps of $0.1V_{max}$ it was necessary to average the number of images. Because the number of frames captured for each beam was high (≈ 2500 -3500 frames/beam), it was common to find several frames corresponding to each load step of $0.1V_{max}$. A MATLAB code was developed to extract frames corresponding to each load step of $0.1V_{max}$ and to average their crack opening and sliding in order to use it for the calculations of the shear transfer actions. Figure 3.21 confirms that the averaged kinematics (the ten values of the crack opening and sliding corresponding to each load step of $0.1V_{max}$) fits well with the full response of the crack kinematics of the beam obtained using all the frames and the average kinematics can be used to calculate the shear transfer actions.

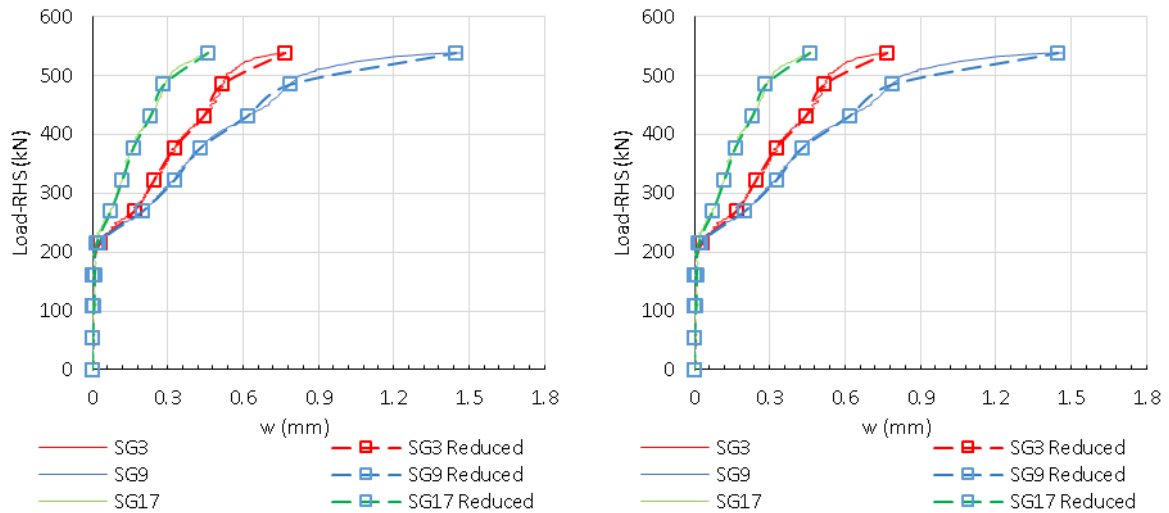


Figure 3.21: Typical measurements for full and reduced crack kinematics - Beam AC0(0.5/0.5)

3.5.2. Strain Gauges

Strains in longitudinal and shear reinforcement were measured using strain gauges. Strain gauges type (YFLA-5-F-1LJC-F) provided by Tokyo Sokki Kenkyujo Co. Ltd was used with a gauge length of 5mm, electric resistance of $119.8 \pm 0.5 \Omega$ and a gauge factor of $2.11 \pm 2\%$. Operations on rebar surface preparation included grinding of the rebar to provide a flat surface, cleaning the surface with acetone to remove any dirt or grease and neutralizing the acid using MNA5-2 neutralizer. Gauges were fixed with a glue on the rebar and coated with epoxy to protect it during concreting. A typical strain gauge is shown in Figure 3.22 below.



Figure 3.22: Fixing and coating of a strain gauge

To maintain the bond between concrete and the rebar and to minimize loss of cross-sectional area due to grinding the strain gauge positions, the strain gauges were typically fixed on the sides of the rebar where the ribs vanish (Figure 3.23 a). However, depending on the purpose of the strain gauges, the gauges were also placed in a few cases on the top and bottom of the rebar, where part of the ribs and rebar section was ground (Figure 3.23 –b). Several gauges

were lost in Series A and B in locations where strain gauges were placed over the ribs of the bar. Accordingly, an additional third gauge was placed to the side to evaluate strains in case one of the gauges was lost in series C.

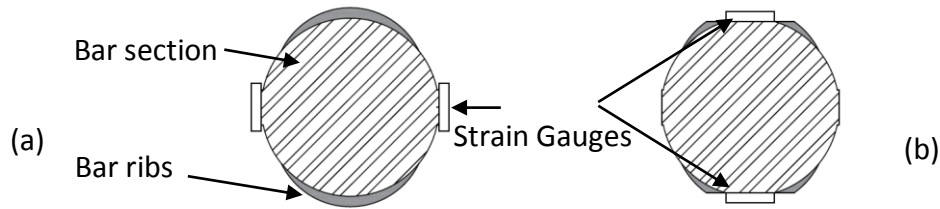


Figure 3.23: Positioning strain gauges on the a) sides or b) ribs of the rebar.

Strain gauges were used to measure strains in locations where: (see Figure 3.24 below) a) the flexural stresses are greatest, b) to capture the dowel effect (strain gauges were placed on the top and bottom of the bar as in Figure 3.23 –b), c) to confirm adequate anchorage of reinforcement and d) NLFEA predicted shear reinforcement stresses to be greatest.

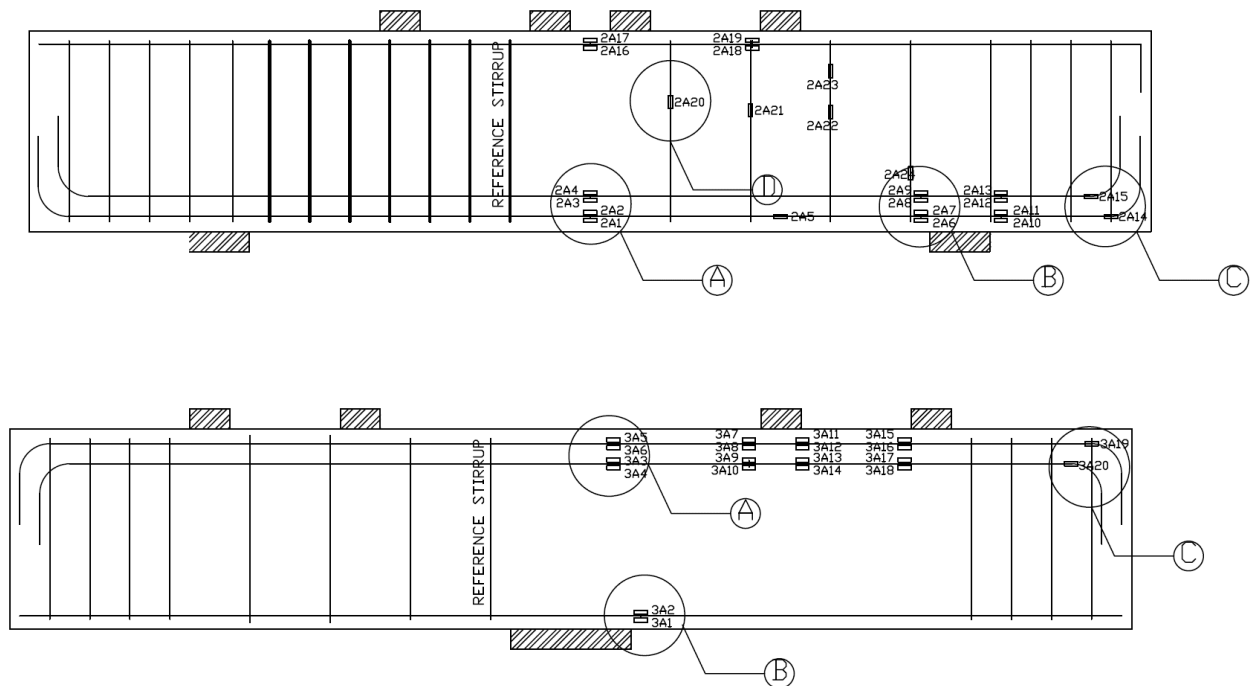
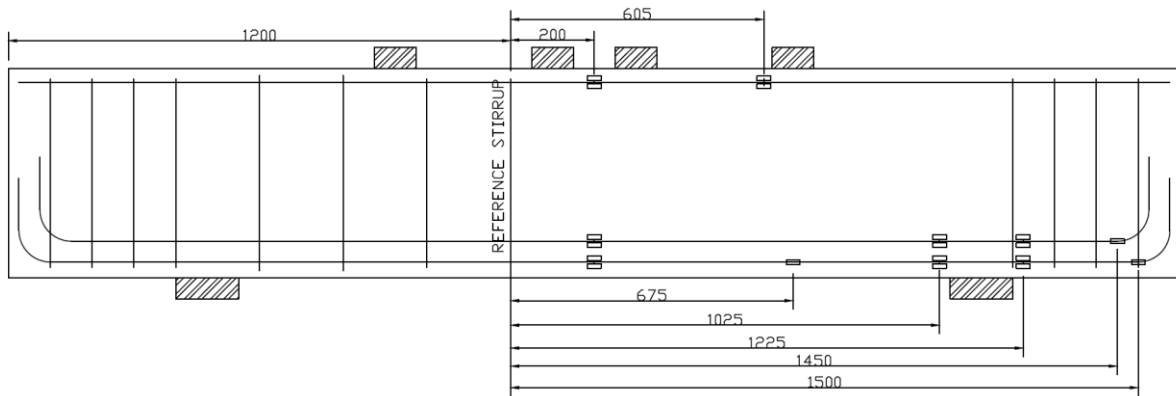


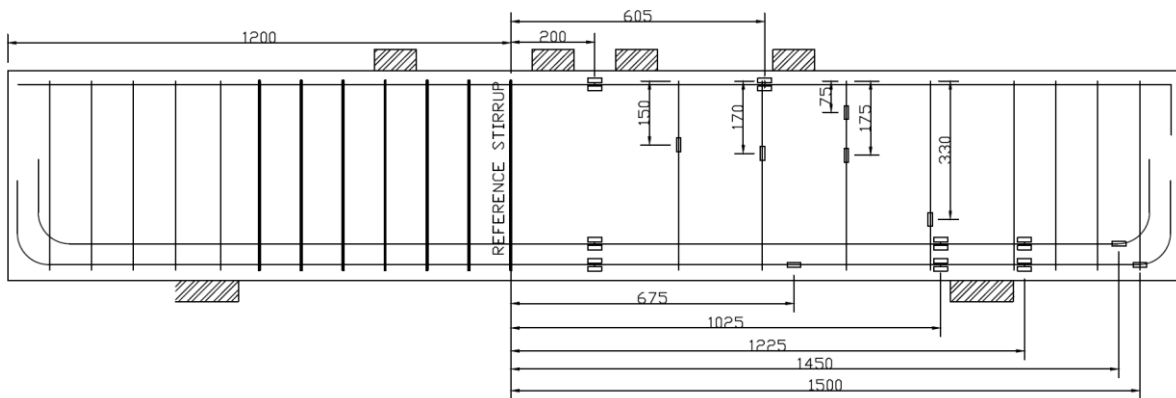
Figure 3.24: Location of strain gauges for beams loaded in the compression and tension faces.

The locations of the strain gauges were measured from a reference stirrup. This stirrup was then located in its exact position in the wooden moulds to insure the reinforcement cage (and hence strain gauges as well) were positioned correctly. Locations of strain gauges in all of the test beams are shown in Figure 3.25.

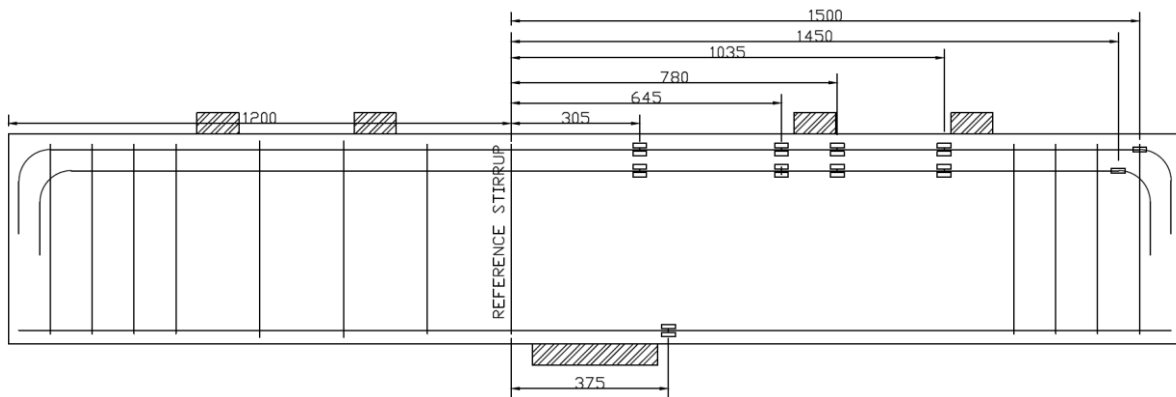
a) AC0 (0.5/0.5)



b) AC200 (0.5/0.5)

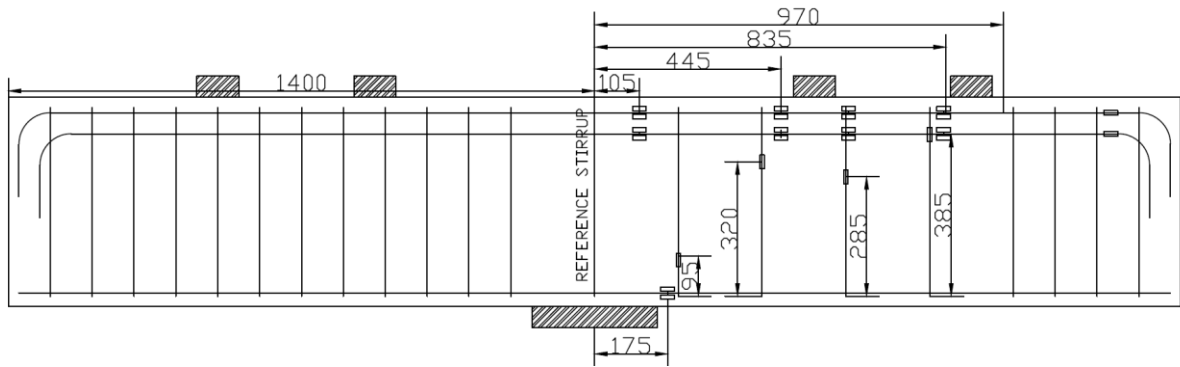


c) AT0 (0.5/0.5)

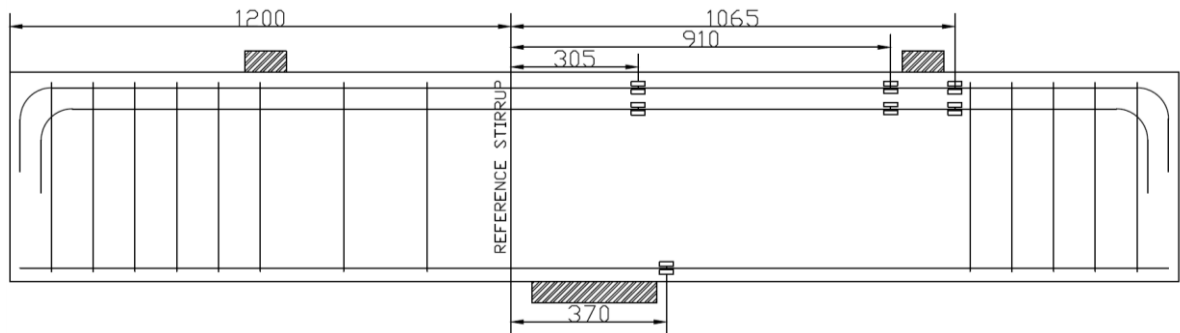


d) AT200 (0.5/0.5)

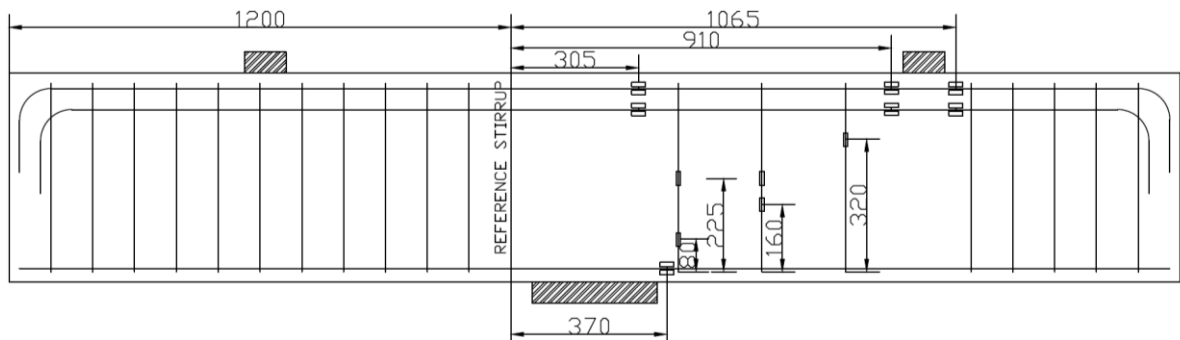
h) BT200 (0.3/0.7)



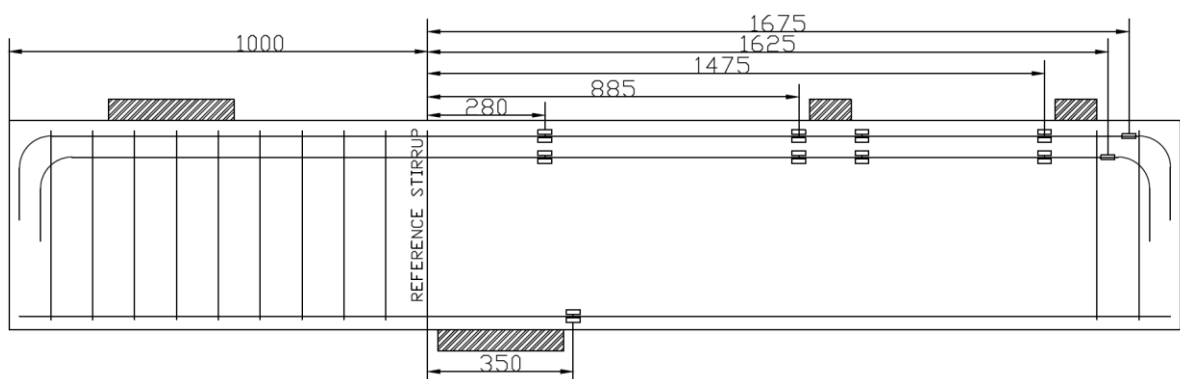
i) CT0 (1.0/0)



j) CT200 (1.0/0)



k) CT0 (0.6/0.4)



I) CT200 (0.6/0.4)

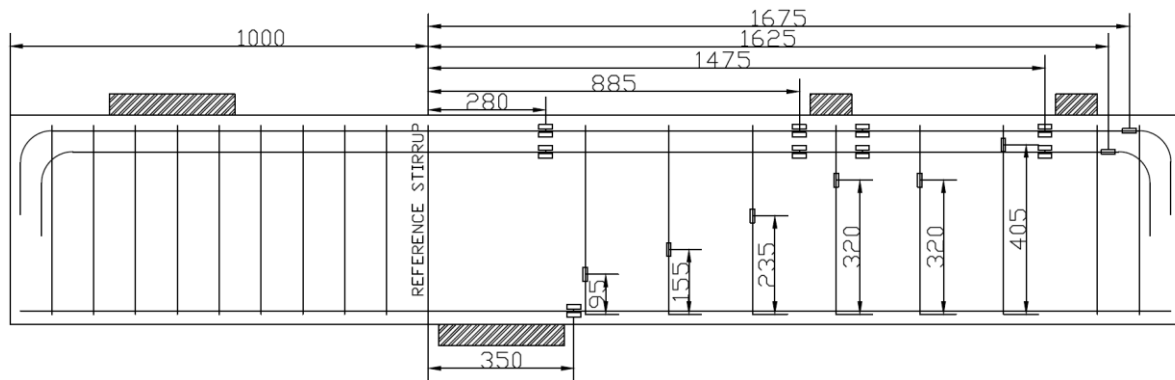


Figure 3.25: Locations of strain gauges in all of the test beams (Dimensions in mm)

3.5.3. Linear Variable Displacement Transducers (LVDT)

The global deformation of the beams was recorded using LVDTs located as shown in Figure 3.26. LVDT#1, LVDT#2, LVDT#3 and LVDT#4 were located at the ends of the beams to measure horizontal displacement and rotation. The length L_h between pairs of LVDTs was recorded for each test and used to evaluate the rotation along with the inclinometer. For Config. – 1, vertical transducers LVDT#6 and #7 were placed 150mm away from the support plate to evaluate the vertical displacement near the crack. Transducers LVDT#8 and #9 were placed vertically in the centreline of the beam to measure maximum vertical deflection.

For beams tested in Config. – 2, vertical transducers LVDT#6 and #7 were placed on the RHS loading plates to evaluate the vertical deflection beneath the load. LVDT#8 was placed in the location of the fixed LHS actuator. This transducer evaluates the vertical difference between the imposed zero actuator displacement and the vertical displacement due to upward load from the actuator onto the internal reaction rig. Transducer LVDT#5 was placed 50 mm from the RHS edge of the beam to evaluate the maximum vertical displacement.

Similar arrangements were applied to transducers in Config. – 3 and Config – 4 with the exception of transducer LVDT#8 which was at the bottom corner of the LHS for Config. – 3.

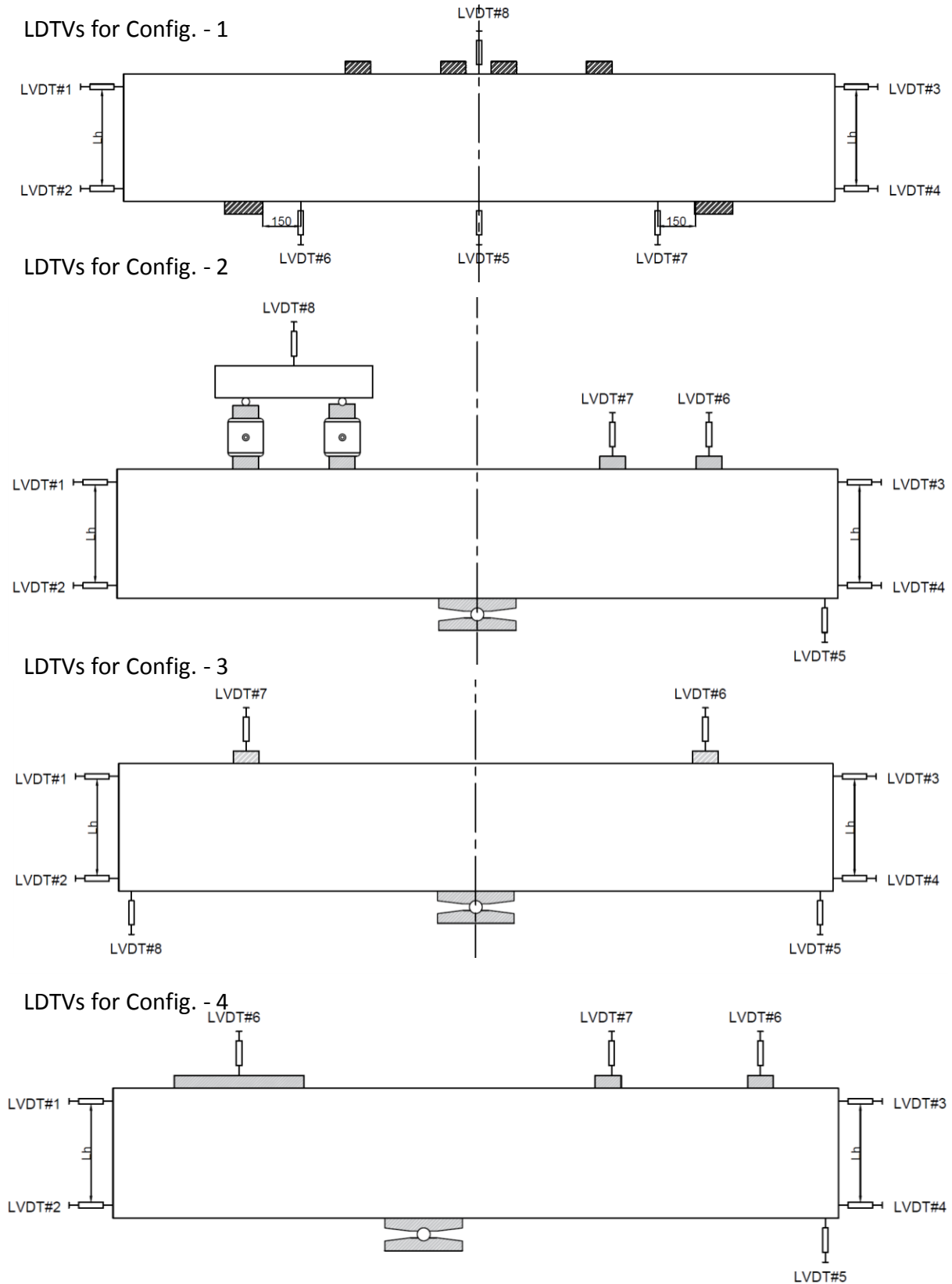


Figure 3.26: Locations of LVDTs for the different configurations

3.6. Conclusions

This chapter gives details of the 12 beams tested in this research as well as the experimental methodology. The experimental campaign was designed to investigate the effect of loading arrangement and loading face on shear enhancement in top loaded beams. All the beams measured 2800 mm long by 250mm wide by 500mm deep. The beams were tested in three series of four, depicted A to C. Each series of four tests had separate objectives. Series A was designed to investigate the influence of loading the tension or compression face of otherwise identical beams without and with shear reinforcement. Series B examined the effect of varying the ratio between the inner and outer loads on the shear strength of balanced cantilever beams with stirrups. Series C compared the shear resistance of beams loaded inside and partly outside the shear enhancement zone.

Details are given of the beam construction, material control tests, beam instrumentation and loading procedure. Measurements during beam testing included concrete surface strains (using DIC system), crack displacements (also using DIC system), reinforcement strains (strain gauges), global displacements of the beams (using linear variable displacement transducers (LVDT)) and the rotation of the beams (with an inclinometer). Results of the experimental campaign are presented in Chapter 4.

CHAPTER 4. EXPERIMENTAL RESULTS

4.1. Introduction

The results of the experimental program described in the previous chapter are presented and discussed here. The first part of the chapter describes the material properties of the concrete and the reinforcement. The second part provides a detailed description of the behaviour of the beams during testing comprising the global load-deflection response, failure modes and crack patterns and reinforcement strain.

4.2. Material Properties

4.2.1. Concrete material properties

Concrete was ready-mix concrete supplied by CEMEX. The concrete in all the beams was specified as Consistency Class S3, strength class C25/30 with limestone coarse aggregate of maximum size 20 mm. The concrete strengths for each set of beams are presented below.

Series A

All the beams in Series A were cast from a single batch of concrete. As described in Chapter 4, a total of 36 cubes (100mm), 12 cylinders (100mm diameter by 200mm height) for compressive strength and 12 cylinders (150mm diameter by 300mm height) for split cylinder tensile strength were cast. The tensile splitting test was used to evaluate concrete tensile strength in the experimental program. These strengths are used in the FEA presented in this thesis based on calibration studies presented in Chapter 6. The splitting strength is generally greater than direct tensile strength and lower than the flexural strength (ASTM, 2017). The strength development of the cubes is given in Table 4.1 below.

Table 4.1: Strength development using cubes strength (100mm x 100mm) – series A

Testing Date	Age at Testing	Curing Condition	Density* (Kg/m ³)	Strength (MPa)
16-Mar	9	air	2525.5	22.96
		Water	2547.5	23.11
21-Mar	14	air	2547.5	26.22
		Water	2547.5	26.05
28-Mar	21	air	2498.2	33.80
		Water	2563.9	30.00

Half the control specimens were cured in water at 20° C with the remainder cured in air alongside the beams. The cube readings were used to monitor the development of the concrete strength and to obtain the cube compressive strength of the concrete at each test date.

Due to technical issues in the grinding machine, cylinders were tested alongside cubes on the day of testing the second and fourth beams of Series A instead of the first and fourth beams as follows in series B and C. The resulting cylinder and cube strengths are presented in Table 4.2 and Table 4.3 respectively. The water cured 40-day cube and cylinder strengths were unexpectedly less than the corresponding 34-day strengths. The reason for the lower 40-day water cured strengths is unknown but is not considered representative of the in-situ strength of the beams. The development of the cube compressive strength with time is plotted in Figure 4.1.

Table 4.2: Compressive cylinder strength (100mm dia. x 250mm Height) – series A.

Testing Date	Age at Testing	Curing Condition	Density (Kg/m ³)	Strength (MPa)	Average strength (MPa)
10-Apr	34	air	2358.5	30.42	30.32
			2365.1	30.98	
			2371.7	29.55	
		water	2434.3	32.02	29.32
			2434.3	28.00	
			2421.1	27.93	
16-Apr	40	air	2308.2	31.92	31.15
			2315.6	31.04	
			2342.1	30.49	
		water	2394.0	27.69	27.47
			2397.3	27.86	
			2390.6	26.85	

Table 4.3: Compressive cube strength (100mm) – series A.

Testing Date	Age at Testing	Curing Condition	Density (Kg/m ³)	Strength (MPa)	Average strength (MPa)
10-Apr	34	air	2443.4	38.3	37.58
			2448.9	37.55	
			2476.2	36.9	
		water	2547.5	35.95	35.26
			2498.2	36.43	
			2542.0	33.39	
16-Apr	40	air	2503.6	38.08	38.34
			2514.6	37.92	
			2459.8	39.02	
		water	2514.6	33.03	32.43
			2525.5	32.54	
			2563.9	31.73	

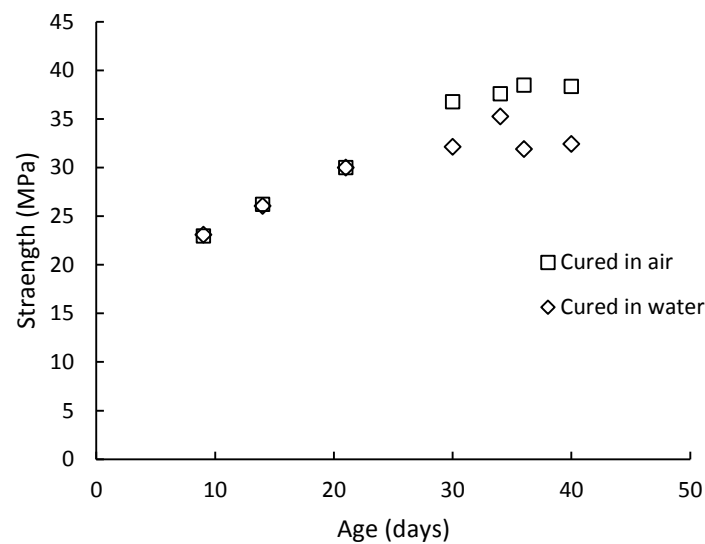


Figure 4.1: Strength development using cube strength – series A

The tensile strength of the concrete was found from split cylinder tests. The tensile strength (f_t) was calculated using the formula $f_t = 2P/\pi LD$ where P is the splitting force, L and D are the diameter and length of the cylinder respectively. The tensile strength was established on days of testing of the first and fourth beams. The results are shown in Table 4.4.

Table 4.4: Tensile strength (150 diameter x 300 Height) – series A.

Testing Date	Age at Testing	Curing Condition	Density (Kg/m ³)	Strength (MPa)	Average strength (MPa)
06-Apr	30	air	2552.9	2.361	2.505
			2308.3	2.524	
			2314.0	2.629	
		water	2300.7	2.340	2.401
			2373.1	2.227	
			2360.7	2.636	
16-Apr	40	air	2366.4	2.7639	2.764
			2280.7	2.824	
			2290.2	2.122	
		water	2366.4	2.582	2.419
			2372.1	2.262	
			2359.8	2.412	

The air cured control specimens are considered most representative of the in-situ concrete strength of the beams. Based on the strength development of the air-cured cubes, the in-situ compressive strength of the concrete in the first and third beams was estimated by linear extrapolation/interpolation from the air cured cylinder strengths of the second and fourth beams as shown in Figure 4.2. A similar approach was adopted for tensile strength. The values of the compressive and tensile strength of the beams are summarized in Table 4.5.

Table 4.5: Compressive and tensile strength for series A

Beam ID	Casting Day	Testing Day	Age at testing	f'_c (MPa)	f_t (MPa)
AC0 (0.5/0.5)	07-Mar	06-Apr	30	29.76	2.505
AC200 (0.5/0.5)		10-Apr	34	30.32	2.608
AT0 (0.5/0.5)		12-Apr	36	30.59	2.660
AT200 (0.5/0.5)		16-Apr	40	31.15	2.764

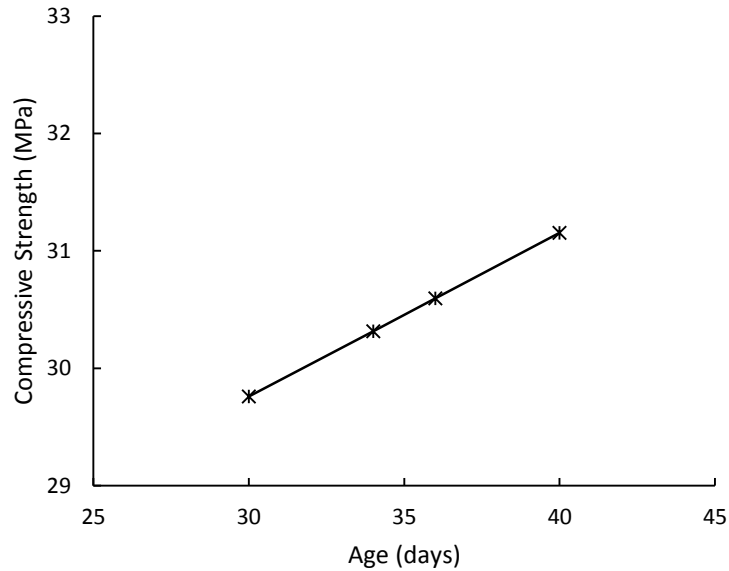


Figure 4.2: Compressive strength for beams in series A

Series B

As described in Chapter 4, a total of 18 cubes (100mm), 12 cylinders (100mm diameter and 200mm height) for compressive strength and 12 cylinders (150mm diameter and 300mm height) for split cylinder tensile strength were cast. Half of the specimens were cured in water and the other half were cured in the room temperature. Table 4.6 shows the strength development of the cubes.

Table 4.6: Strength development using cubes compressive strength – Series B.

Testing Date	Age at Testing	Curing Condition	Density* (Kg/m ³)	Strength (MPa)
09-May	7	water	2342	21.14
		air	2323	20.80
16-May	14	water	2314	23.81
		air	2353	25.23
23-May	21	water	2349	35.75
		air	2350	25.00

The cube, compressive cylinder and split cylinder tensile strengths are presented in Table 4.7, Table 4.8 and Table 4.9 respectively. The in-situ concrete strengths of the second and third beams were derived from the strengths of the first and last beams using linear interpolation.

Table 4.7: Compressive cube strength (100mm) – Series B.

Testing Date	Age at Testing	Curing Condition	Density (Kg/m ³)	Strength (MPa)	Average strength (MPa)
04-Jun	33	air	2261.20	33.13	33.17
			2257.50	33.05	
			2223.00	33.32	
		Water	2342.00	27.79	27.94
			2347.00	27.95	
			2330.00	28.09	
11-Jun	40	air	2261.70	35.39	35.10
			2262.50	35.34	
			2270.00	34.58	
		Water	2349.50	27.73	28.28
			2343.00	26.90	
			2362.00	30.22	

Table 4.8: Compressive cylinder strength (100mm diameter x 200mm height) – Series B.

Testing Date	Age at Testing	Curing Condition	Density (Kg/m ³)	Strength (MPa)	Average strength (MPa)
04-Jun	33	air	2291.50	26.66	28.43
			2304.43	28.36	
			2302.28	30.28	
	33	Water	2280.61	23.39	24.11
			2279.69	25.17	
			2291.18	23.76	
11-Jun	40	air	2379.70	28.25	29.24
			2356.55	29.17	
			2358.42	30.30	
	40	Water	2379.70	26.70	26.97
			2356.55	26.61	
			2358.42	27.60	

The in-situ compressive strength of the concrete in the second and third beams was estimated by linear interpolation from the air cured cylinder strengths of the first and fourth beams. This

approach is consistent with the strength development of the air-cured cubes shown in Figure 4.3. A similar approach was adopted for the tensile strength of the concrete.

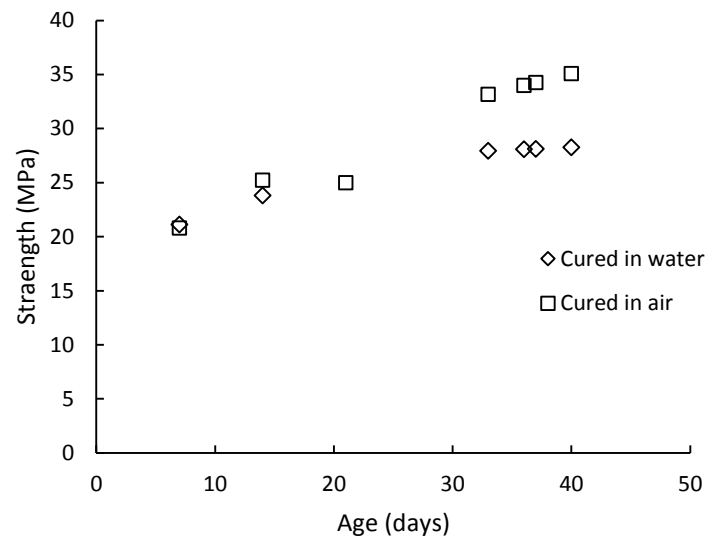


Figure 4.3: Strength development using cube strength – Series B.

Table 4.9: Tensile cylinder strength (150mm diameter x 300mm height) – Series B.

Testing Date	Age at Testing	Curing Condition	Density (Kg/m ³)	Strength (MPa)	Average strength (MPa)
04-Jun	33	air	2298.18	2.84	2.58
			2275.33	2.01	
			2313.57	2.89	
		Water	2338.55	2.65	2.52
			2374.22	2.58	
			2374.42	2.32	
11-Jun	40	air	2286.17	2.54	2.82
			2281.14	3.17	
			2328.59	2.76	
		Water	2353.36	2.78	2.78
			2357.53	2.90	
			2350.42	2.66	

The values of the compressive and tensile strength of the beams are summarised in Table 4.10 below.

Table 4.10: Compressive and tensile strength for series B

Beam ID	Casting Day	Testing Day	Age at testing	f'_c (MPa)	f_t (MPa)
BT200 (0.5/0.5)	02-May-18	02-Jun-18	33	28.43	2.58
BT200 (0.3/0.7)		07- Jun-18	34	28.78	2.68
BT200 (1.0/0)		08- Jun-18	36	28.89	2.72
BT200 (0/1.0)		11- Jun-18	40	29.24	2.82

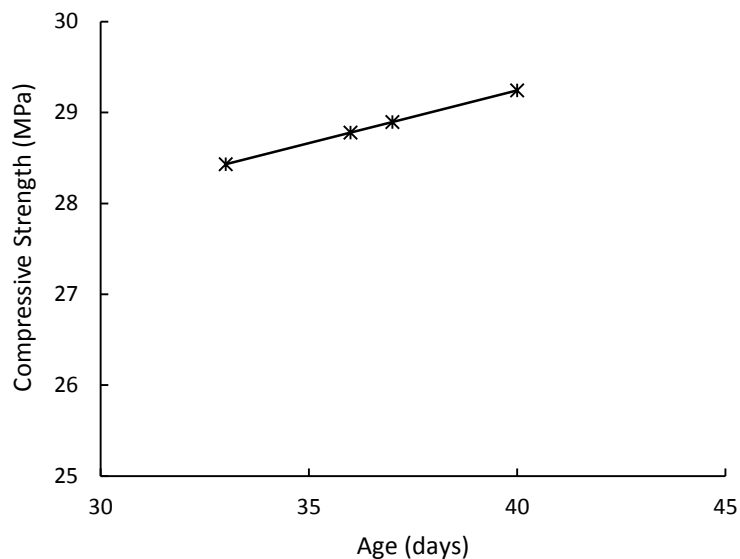


Figure 4.4: Compressive strength for beams in series B

Series C

As described in Chapter 3, a total of 18 cubes (100mm), 12 cylinders (100mm diameter and 200mm height) for compressive strength and 12 cylinders (150mm diameter and 300mm height) for split cylinder tensile strength were cast. Half of the specimens were cured in water and the other half were cured in the room temperature. The development of compressive cube strength with time is shown in Table 4.11. Compressive cube, cylinder and split cylinder tensile strengths are presented in Table 4.12, Table 4.13 and Table 4.14 respectively. The strength development is plotted in Figure 4.5. The difference between the cube strength of the first and last beam was less than 0.3 MPa, and hence, all the beams had almost similar

cubes strength. This was also the case for the tensile strength of the beams. However, the difference between the compressive cylinder strength of the first and last beam was 2 MPa.

Table 4.11: Strength development using cubes compressive strength – Series C.

Testing Date	Age at Testing	Curing Condition	Density (Kg/m ³)	Strength (MPa)
07-Jul	8	Water	2334.90	24.03
		Air	2313.10	24.76
13-Jul	14	Water	2303.10	25.90
		Air	2302.00	29.50
20-Jul	21	Water	2328.20	31.09
		Air	2323.00	32.56

Table 4.12: Compressive cube strength (100mm) – Series C.

Testing Date	Age at Test	Curing Condition	Density (Kg/m ³)	Strength (MPa)	Average strength (MPa)
01-Aug	33	air	2272	36.19	37.12
			2286	38.19	
			2251	36.98	
		Water	2316	32.02	32.13
			2364	31.11	
			2333	33.26	
08-Aug	40	air	2277	37.27	37.37
			2226	37.47	
		Water	2360	32.51	33.02
			2349	33.13	
			2332	33.43	

Table 4.13: Compressive Cylinders Strength (100mm diameter x 200mm Height) – Series C.

Testing Date	Age at Testing	Curing Condition	Density (Kg/m3)	Strength (MPa)	Average strength (MPa)
01-Aug	33	air	2283.63	26.81	26.90
			2275.10	26.85	
			2277.72	27.02	
		Water	2300.52	27.12	25.10
			2317.23	24.79	
			2309.18	23.38	
08-Aug	40	air	2337.12	29.23	28.90
			2342.76	29.40	
			2332.07	28.06	
		Water	2337.12	22.59	24.13
			2342.76	24.04	
			2332.07	25.76	

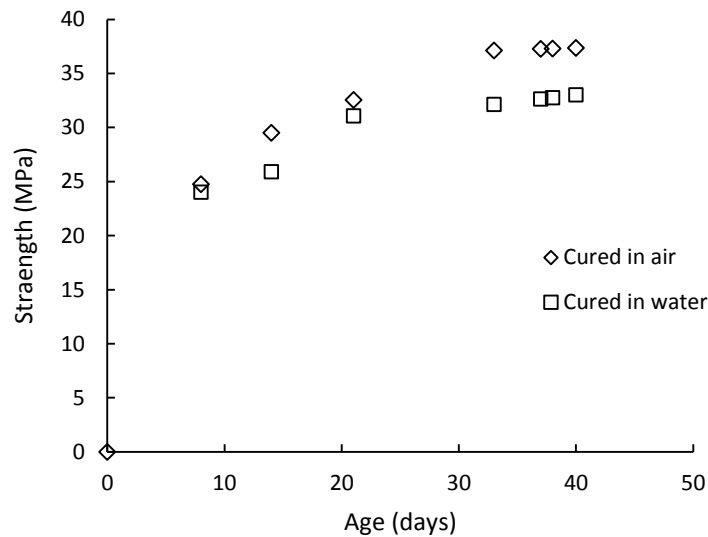


Figure 4.5: Strength development using cube strength – series C

Table 4.14: Tensile cylinders strength (150mm diameter x 300mm height) – Series C.

Testing Date	Age at Testing	Curing Condition	Density (Kg/m ³)	Strength (MPa)	Average strength (MPa)
01-Aug	33	air	2328.62	2.35	2.59
			2286.82	2.77	
			2296.96	2.65	
		Water	2333.18	1.63	1.82
			2330.59	1.76	
			2309.36	2.08	
08-Aug	40	air	2284.85	2.48	2.60
			2282.85	2.37	
			2263.92	2.95	
		Water	2339.85	2.04	1.93
			2339.21	1.84	
			2312.98	1.91	

For consistency with Series A and B, the in-situ compressive strength of the concrete in the second and third beams was estimated by linear interpolation from the air cured cylinder strengths of the first and fourth beams. The resulting cylinder compressive strengths are presented in Figure 4.6. Values of the compressive and tensile strength of the beams are summarised in Table 4.15. There were noticeable differences between the air and water cured strength. In the analysis of the results, the air-cured strength was used as it represents the curing condition of the beams.

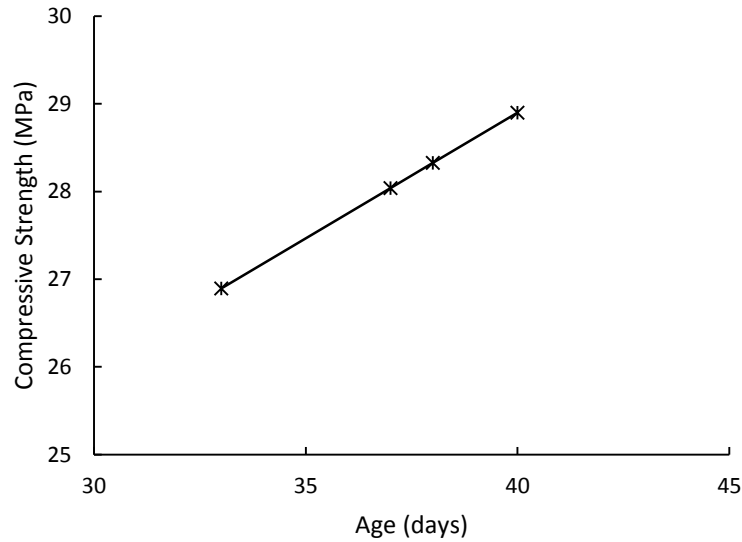


Figure 4.6: Compressive strength for beams in series C

Table 4.15: Compressive and tensile strength for the series C

Beam ID	Casting Day	Testing Day	Age at testing	f'_c (MPa)	f_t (MPa)
CT0 (1.0/0)	29-Jun-18	01-Aug-18	33	26.90	2.59
CT200(1.0/0)		05-Aug-18	37	28.04	2.59
CT0 (0.6/0.4)		06-Aug-18	38	28.33	2.60
CT200 (0.6/0.4)		08-Aug-18	40	28.90	2.60

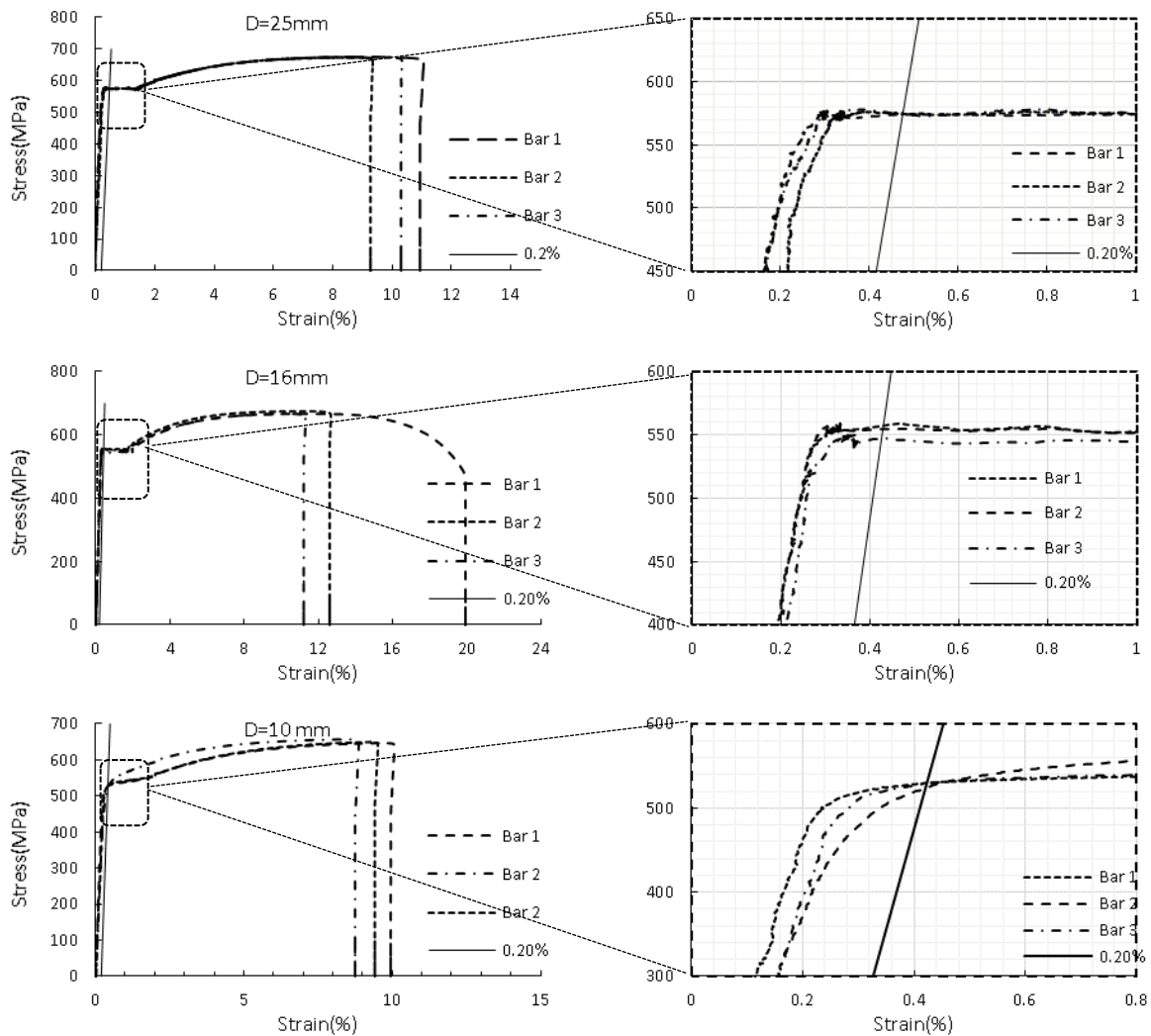
4.2.2. Reinforcement material properties

Grade 500 deformed reinforcement with different sizes was used for longitudinal and shear reinforcement in these tests. This comprised four different bar sizes (25mm, 16mm, 10mm and 8mm). The properties of the reinforcement were obtained from tensile tests on 400mm offcuts of each bar diameter. A digital video extensometer was used to measure axial strains. Stress-strain curves for the different sizes are shown in Figure 4.7. Average yield strength ($f_{yk,0.2}$) obtained by the 0.2% strain rule, modulus of elasticity (E_s), maximum tensile strength (f_{tk}) and corresponding strain (ϵ_1) were calculated with the aid of Figure 4.7 as in Table 4.16.

Table 4.16: Reinforcement properties for the experimental program

Size	$f_{yk,0.2}$ (MPa)	E_s (GPa)	f_{tk} (MPa)	ϵ_1 (%)
25 mm	570	235*	670	8.89
16 mm	550	200	670	10.81
10 mm	520	205	650	9.15
8 mm	560	200	689	5.36

*This value was discarded as it was above the code limit and a value of 200 MPa was assumed.



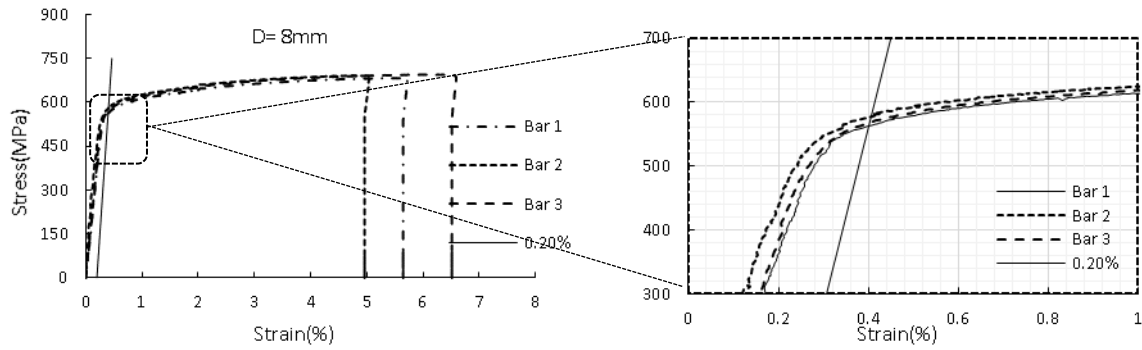


Figure 4.7: Stress-strain curves for the different reinforcement diameters (*D*)

4.3. Results of Series A

4.3.1. Summary of the results

Series A consisted of four beams (AC0 (0.5/0.5), AC200 (0.5/0.5), AT0 (0.5/0.5), and AT200 (0.5/0.5)). Beams AC0 (0.5/0.5) and AC200 (0.5/0.5) were loaded on the flexural compression face while beams AT0 (0.5/0.5) and AT200 (0.5/0.5) were loaded on the flexural tension face. Details of the beam geometry, reinforcement and loading arrangement are given in section 3.2.1. All four beams in series A failed in shear due to the formation of a shear crack which extended between the inner edges of the support and furthest (outer) loading plate. Table 4.17 summarizes the results of the first series of the beams. Beams AT0 (0.5/0.5) and AT200 (0.5/0.5) were loaded as double cantilever beams where the external forces are calculated from the equilibrium. Due to rotational friction in the loading arrangement, which was eliminated in subsequent tests, the loading ratios in tests AT0 (0.5/0.5) and AT200 (0.5/0.5) were 0.58/0.42 rather than 0.5/0.5 as intended. In subsequent tests, the loading ratios were as specified including beam BT 200 (0.5/0.5) which was identical to beam AT200 (0.5/0.5) apart from a minor difference in concrete strength.

Table 4.17: Summary of the results for series A

Beam ID	f'_c (MPa)	f_t (MPa)	ρ_v (%)	$V_{failure}$ RHS (KN)			V_{flex} RHS (KN)
				Inner	Outer	Total	
AC0 (0.5/0.5)	29.8	2.505	0	269.4	269.4*	538.8	885
AC200 (0.5/0.5)	30.3	2.608	0.201	370.9	370.9*	741.7	885
AT0 (0.5/0.5)	30.6	2.660	0	260.4	188.6*	449.0	795
AT200 (0.5/0.5)	31.2	2.764	0.201	425.3	308.0*	733.3	795

* indicates the critical shear plane

Table 4.17 shows that the outer failure load of comparable beams was consistently less for beams loaded on the tension than compression face with the difference greatest for beams without stirrups. The NLFE investigation in Chapter 7 suggests that the observed differences in strength for compression and tension face loading are real despite being within the range of scatter typically found in shear tests of identical beams. This scatter is most pronounced in beams without shear reinforcement but is somewhat difficult to quantify due to relative lack of repeat tests on identical beams. One way of quantifying the scatter is through statistical analysis of $P_{\text{test}}/P_{\text{calc}}$ calculated using refined analysis methods. For example, Sagaseta (2008) found the coefficient of variation (COV) in $P_{\text{test}}/P_{\text{calc}}$ to be around 11% for his STM of short shear span beams. A similar COV of 9% is obtained in this thesis for the NLFEA of the tested beams (see Table 6.5). This implies that the COV for scatter in the strength of notionally identical specimens is less than 10% since the calculation of $P_{\text{test}}/P_{\text{calc}}$ includes model uncertainty. Modes of failure and development of cracks

The development of cracks during testing and post-failure crack patterns are shown in Figure 4.8 and Figure 4.9 respectively (solid black lines representing post failure cracks).

Crack patterns in Series A are shown in Figure 4.9. Red, green blue and pink colours are used in this figure to define the first, second third and fourth cracks observed in the test. Failure occurred in the right hand shear span of all beams as intended. In all the four beams, the critical shear crack extended from the inner edge of the support plate to the inner edge of the outer loading plate. Hence, shear failure was not critical between the inner loading plate and the support. Minor flexural cracks were also observed in locations of maximum bending moments. These cracks are more observable in the crack strains obtained with the DIC (See Figure 5.16).

Beam AC0 (0.5/0.5), without shear reinforcement, was loaded in the compression face. The critical crack initiated at mid height of the beam and propagated from there towards the outer load plate and the adjacent support. The development of the critical crack was followed by a sudden brittle failure characterised by crushing of the concrete at the outer loading plate.

Beam AC200 (0.5/0.5), with shear reinforcement, was also loaded on its compression face. Two secondary cracks developed prior to the critical diagonal crack. The shear failure was relatively ductile compared to AC0 (0.5/0.5) owing to the presence of the shear reinforcement. At failure, concrete crushing occurred at the outer loading plate as in beam

AC0 (0.5/0.5). Subsequently, the cover to the compression reinforcement was lost between the loading plates after peak load due to reinforcement buckling. The critical diagonal crack in beam AC200 (0.5/0.5) was cranked as shown in Figure 4.9 rather than straight as in beam AC0 (0.5/0.5).

Beams AT0 (0.5/0.5) and AT200 (0.5/0.5), without and with shear reinforcement respectively, were loaded on their tension face. Beam AT0 (0.5/0.5) failed suddenly in a brittle manner due to concrete crushing in the compression zone. The failure was preceded by opening of the critical diagonal crack running between the edges of the support and outer loading plate. In the case of beam AT200 (0.5/0.5), a secondary crack developed prior to the critical diagonal crack which ran between the near loading plate and the support. At failure, several smeared cracks developed between the support and the far loading plates with the critical crack being less obvious to distinguish. The beam exhibited severe concrete crushing at failure with the height of the crushed zone greater than one third of the beam depth (see Figure 4.9).

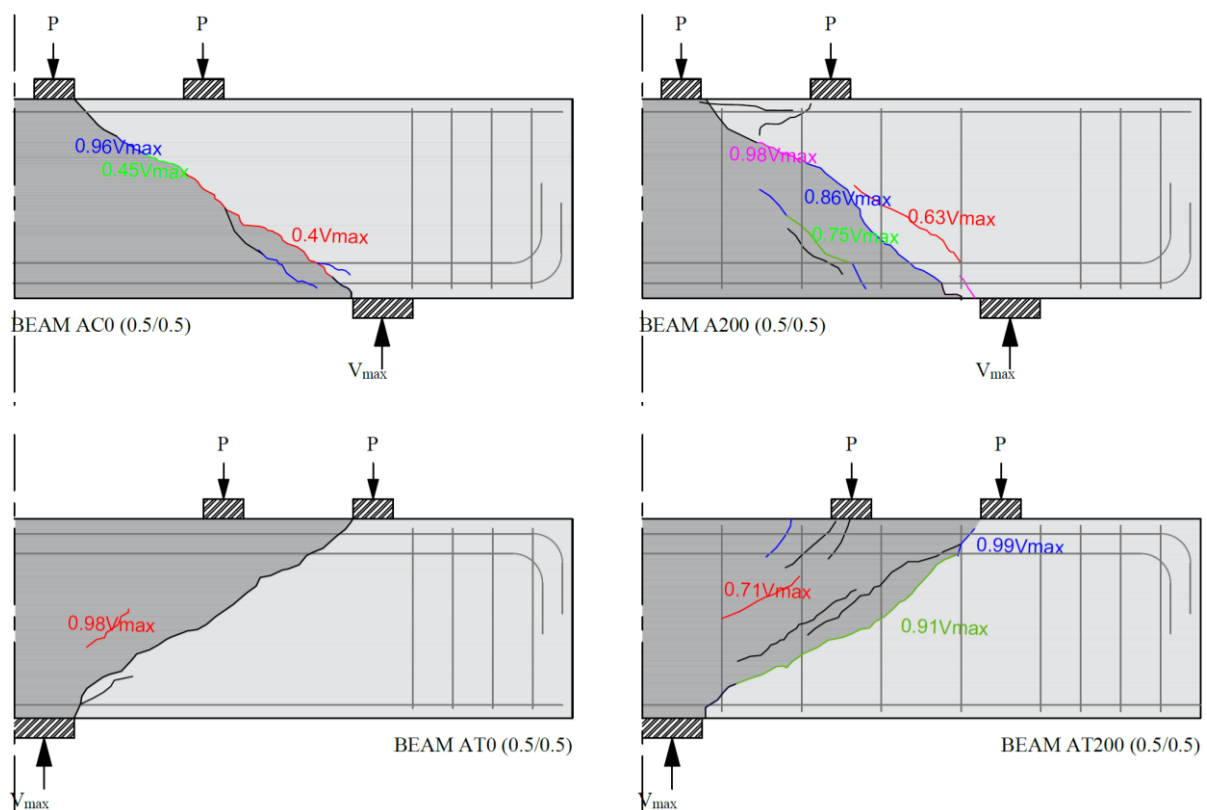


Figure 4.8: Development of the cracks during the test – Series A

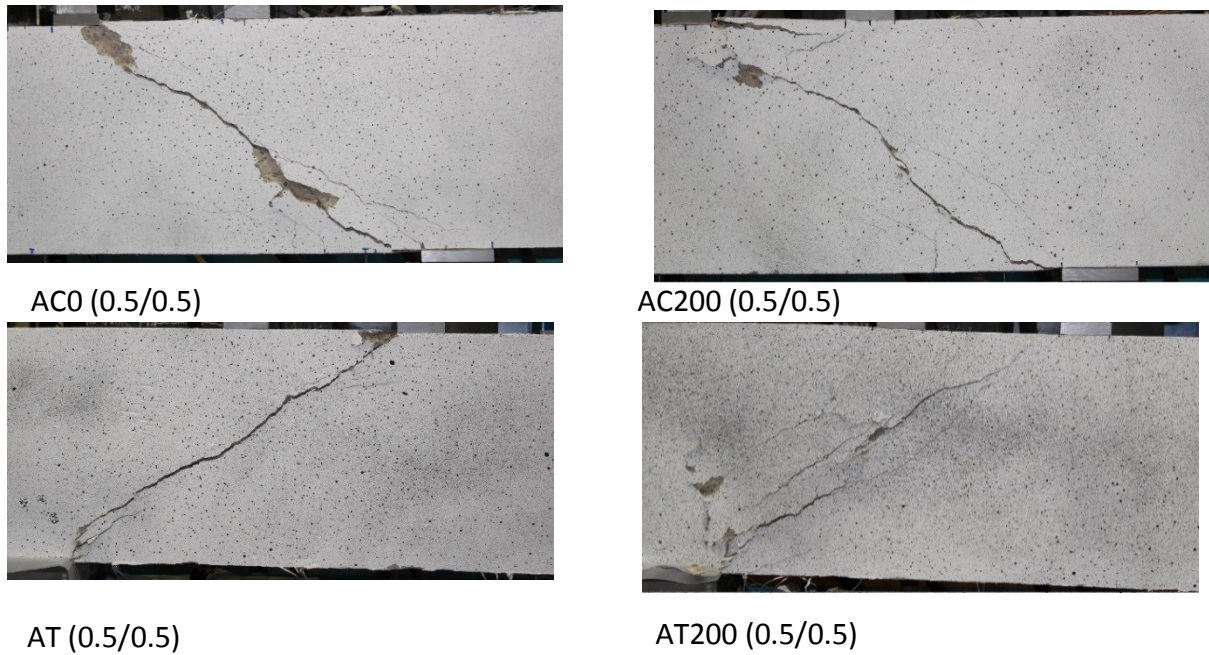


Figure 4.9: Crack patterns (post-peak) for Series A

4.3.2. Concrete surface strains and crack kinematics

Crack kinematics were derived using DIC. Virtual gauges were placed along the critical crack with a typical gauge length ranging between 75mm to 150mm based on the sensitivity analysis conducted in Chapter 6. Two orthogonal virtual gauges were positioned at intervals of 25mm along the height of the crack (Figure 4.10). Gauges limits were checked to ensure each gauge intersected only the critical crack. Gauges limits at the top and bottom of the crack were also checked to ensure end-points lie within the beam. The gauge length or gauge location were modified if the gauge intersected more than one crack or if its ends fell outside the beam boundaries.

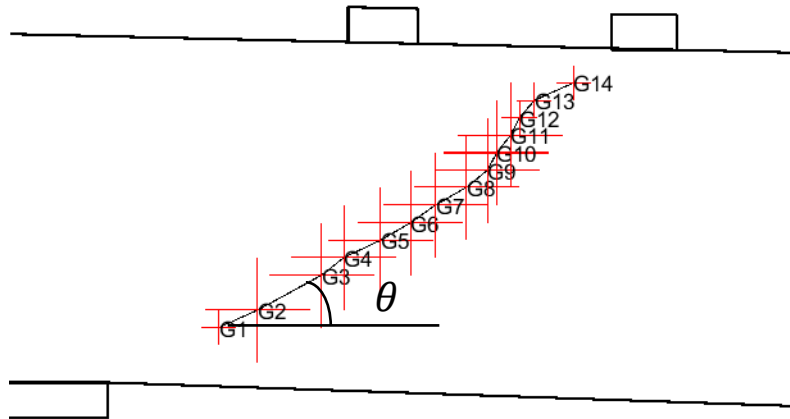


Figure 4.10: Typical virtual gauges along the critical crack (Beam BT200 (0.5/0.5))

Crack opening and sliding were obtained at steps of $0.1P_u$ where P_u is the total failure load applied to the failing side of the beam. The maximum crack opening and sliding displacements along the crack at peak load are shown in Table 4.18 for the beams in Series A. Also shown in Table 4.18 are the locations of maximum crack displacement as well as the crack orientation at these positions.

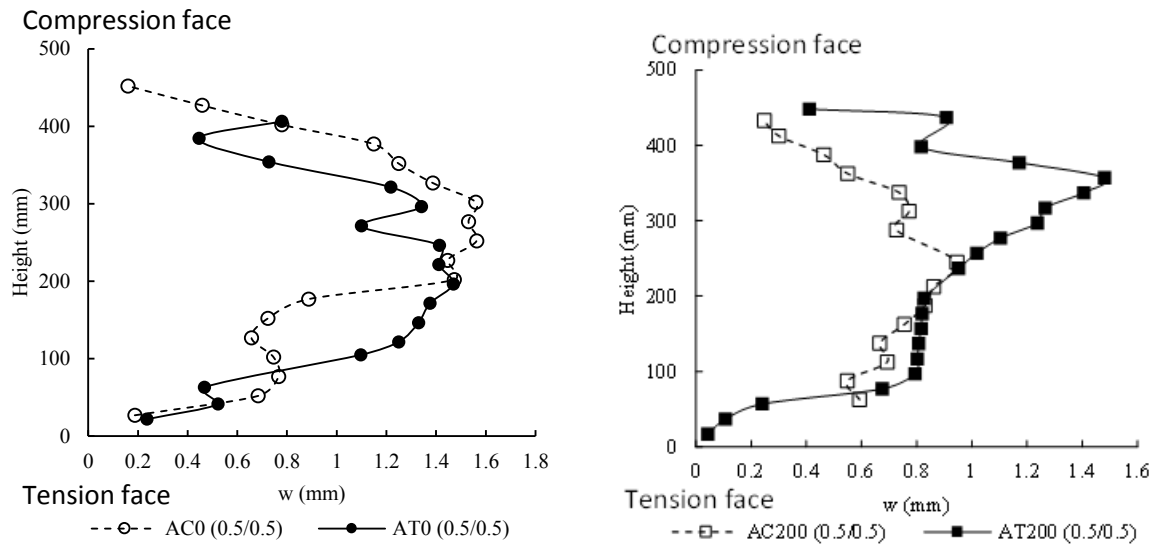
Table 4.18: Maximum crack opening and sliding for the beams in series A at peak load.

Beam	Max. opening (mm)	Height (mm)	Angle* (Degrees)	Max. sliding (mm)	Height (mm)	Angle* (Degrees)
AC0 (0.5/0.5)	1.56	252.1	-44.9	0.60	352.1	19.9
AC200 (0.5/0.5)	0.95	245.2	-45.9	0.24	162.6	28.6
AT0 (0.5/0.5)	1.47	253.4	27.6	1.28	145.7	59.9
AT200 (0.5/0.5)	1.48	167.9	23.1	1.28	87.9	42.8

* Positive angle (θ) is the angle between the horizontal axis and the critical crack measured counter-clockwise as in Figure 4.10.

The variation, over the depth of the beam, in the critical shear crack opening and sliding displacements is shown at failure in Figure 4.11. In the beams without shear reinforcement, the crack opening displacements are similar for tension and compression face loading. For beams with shear reinforcement, where failure was ductile, crack opening was greater in beam AT200 (0.5/0.5) than AC200 (0.5/0.5). Sliding displacements are noticeably higher for the beams loaded on the tension face.

a) Cracks opening



b) Cracks Sliding

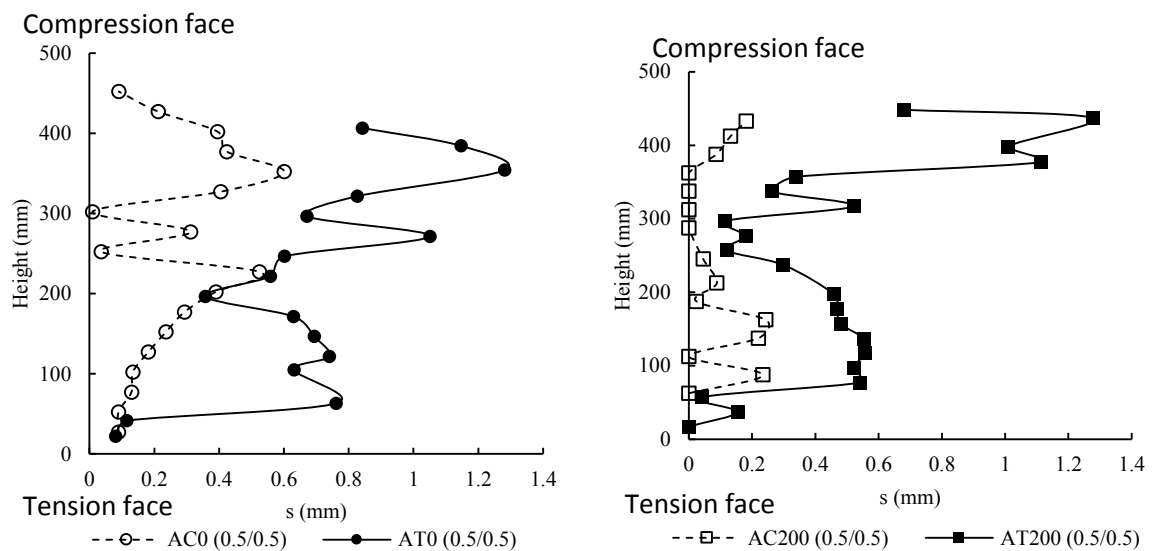
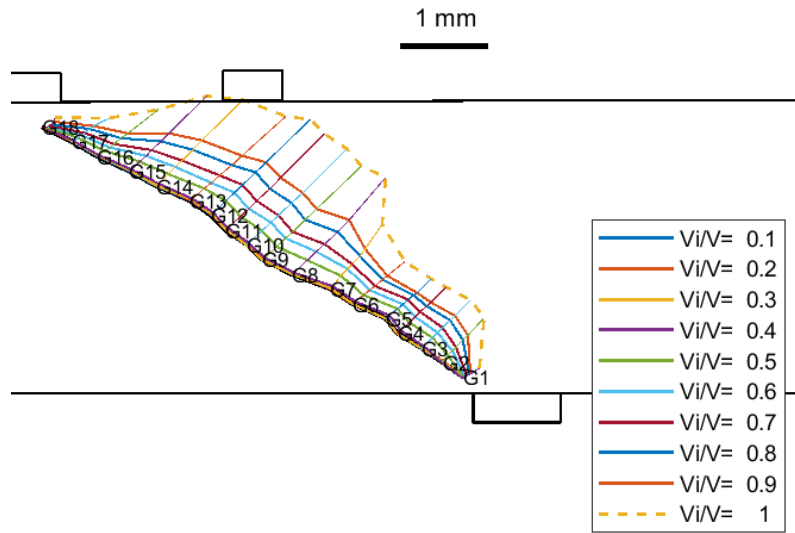
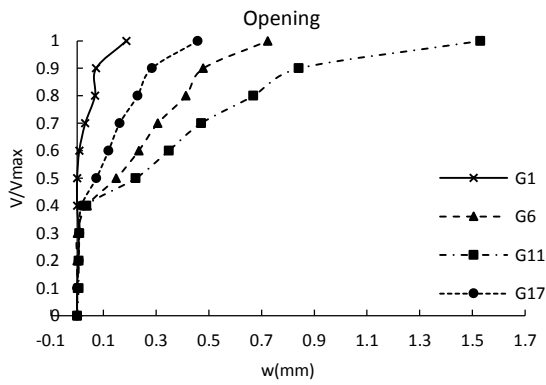


Figure 4.11: a) Crack opening and b) sliding along the beam heights at failure for series A

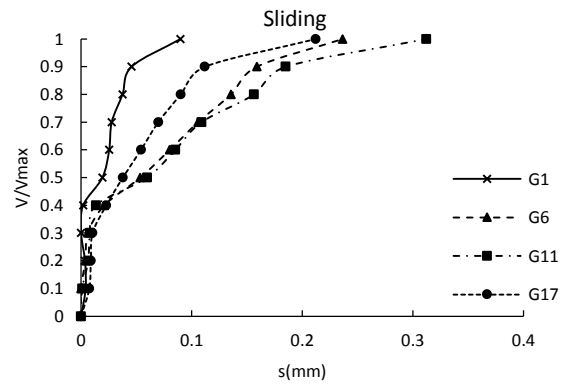
The crack kinematics during the tests are presented in Figure 4.12 to Figure 4.15 from which the crack development can be deduced. For instance, the sudden failure of beam AT0 (0.5/0.5) is evident in Figure 4.14 since crack displacements are zero until crack formation at 90% of the failure load. Post-failure crack kinematics were not obtained in all the beams due to spalling of the concrete in the compression face after failure, which disturbed the surface measurements of the DIC. The “-” sign in front of the load step indicates post failure load, if applicable (e.g. Figure 4.14 - a)



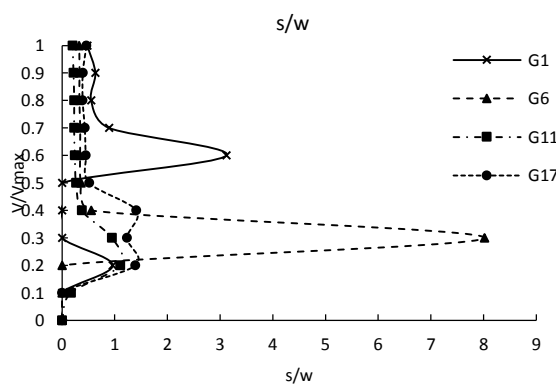
(a) crack kinematics



(b) crack opening

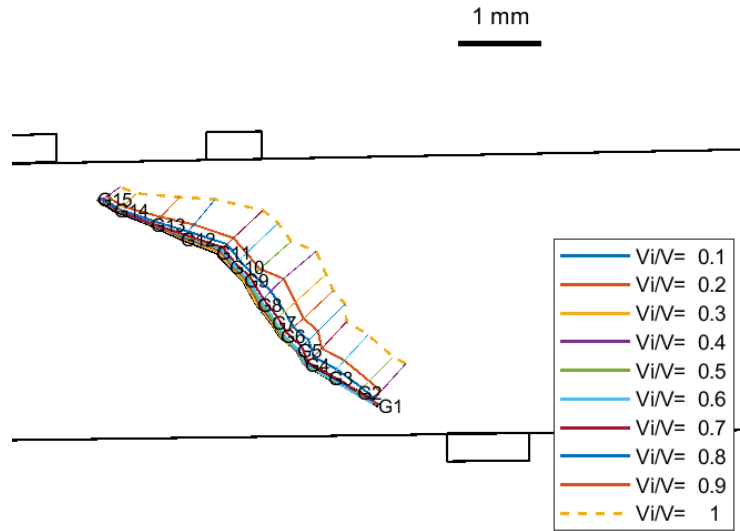


(c) crack sliding

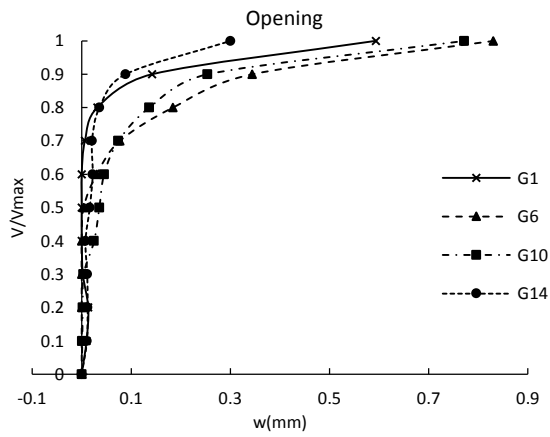


(d) crack sliding/opening

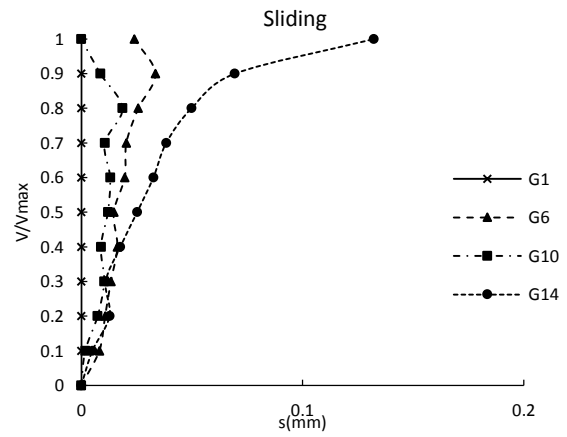
Figure 4.12: Crack Kinematics for beam AC0 (0.5/0.5)



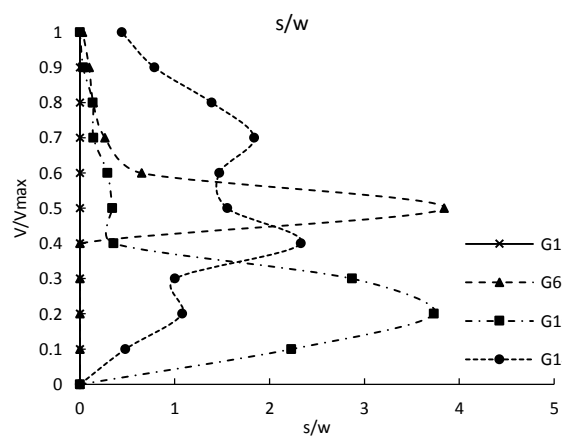
(a) crack kinematics



(b) crack opening

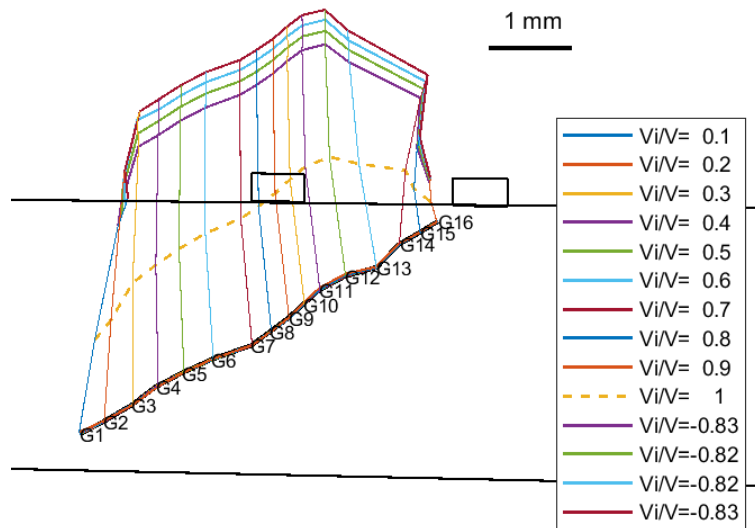


(c) crack sliding

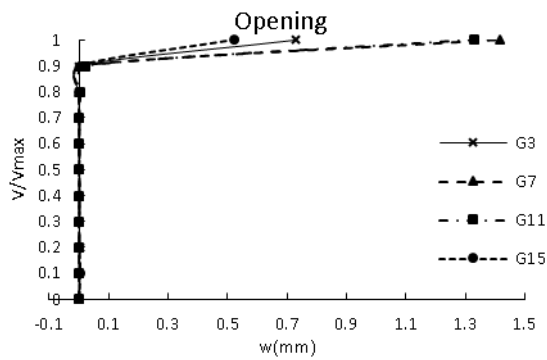


(d) crack sliding/opening

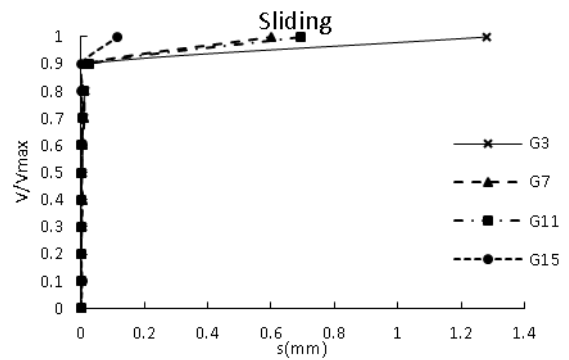
Figure 4.13: Crack Kinematics for beam AC200 (0.5/0.5)



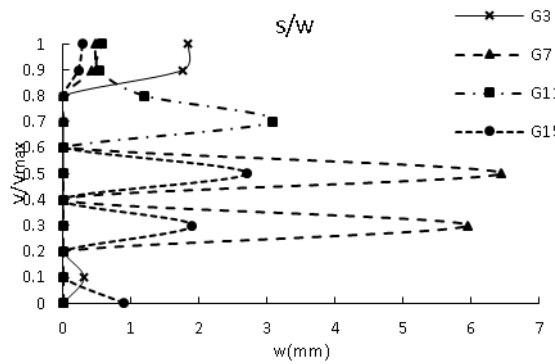
(a) crack kinematics



(b) crack opening

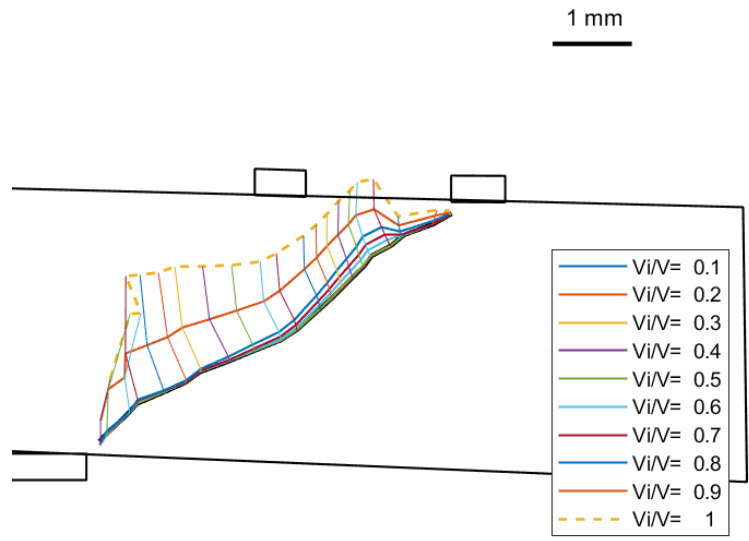


(c) crack sliding

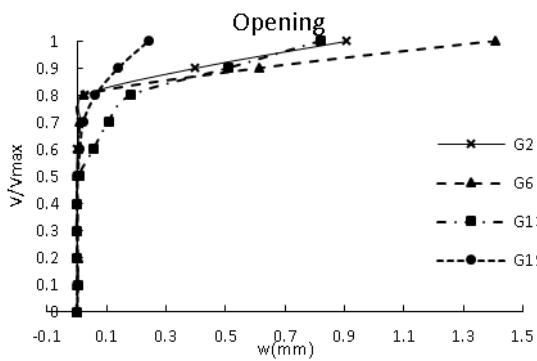


(d) crack sliding/opening

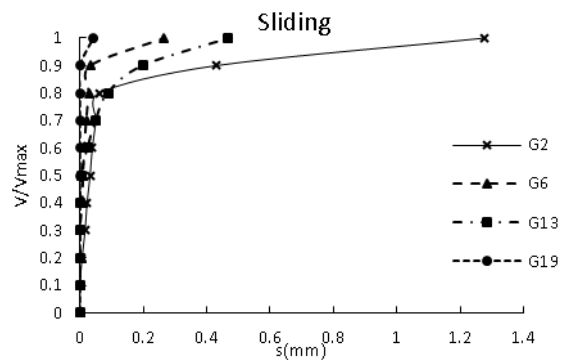
Figure 4.14: Crack Kinematics for beam AT0 (0.5/0.5)



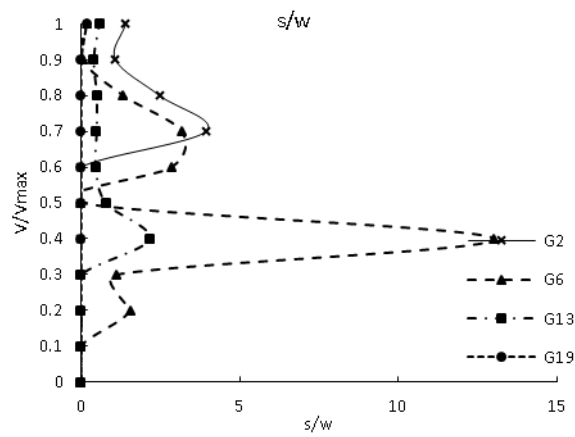
(a) crack kinematics



(b) crack opening



(c) crack sliding



(d) crack sliding/opening

Figure 4.15: Crack Kinematics for beam AT200 (0.5/0.5)

Comparison of the crack patterns and kinematics gives useful insights into the difference between the beams of Series A loaded on the tension and compression face. Figure 4.16 uses superposition to compare the crack patterns of comparable beams loaded on the tension and compression face. The crack patterns are inverted for the beams loaded on the tension face. Figure 4.16 shows that the crack patterns were very similar in the beams loaded on the tension and compression faces despite the apparent reduced strength of beams loaded on the tension face. However, the crack kinematics are different for the two cases. The reduction of strength is discussed later in Chapter 7.

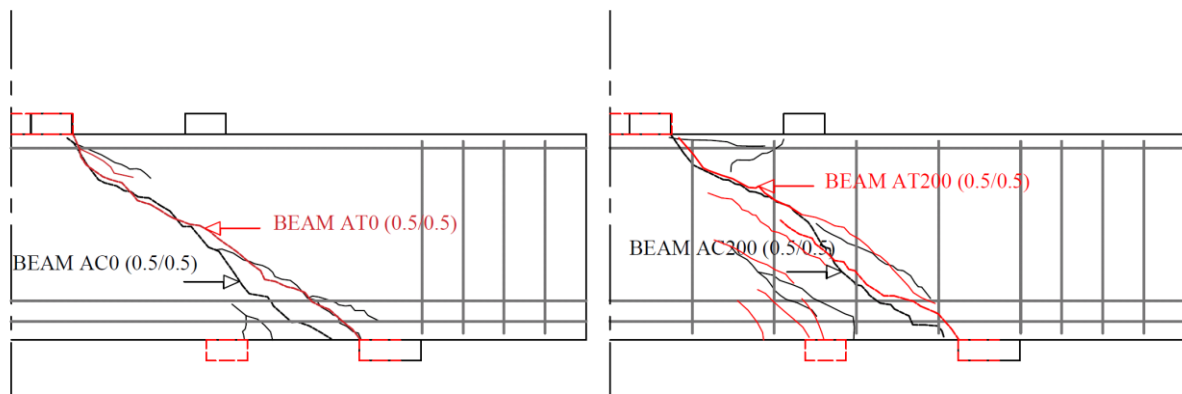


Figure 4.16: Crack patterns for comparable beams in Series A a) beams AC0 (0.5/0.5) and AT0 (0.5/0.5), b) beams AT200 (0.5/0.5) and AC200 (0.5/0.5).

4.3.3. Load-deflection response

The load-deflection response was recorded using LVDTs as described in section 3.5.3. LVDT#5 was positioned under the beams at mid span of the simply supported beams and at the ends of the cantilever beams (See Figure 4.17). Due to the limited available length between the uprights of the loading rig, the deflection of the beams loaded in tension was measured at a distance of 50 mm from their bottom corner.

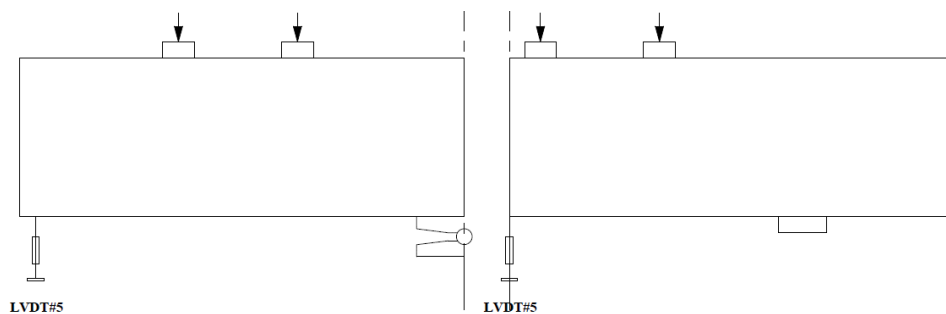


Figure 4.17: Location of the transducer (LVDT#5) in series A

Vertical displacement of the balanced cantilever beams was restrained at the centreline of the left hand actuator by setting the actuator displacement to zero while loading the RHS actuator in displacement control. Hence, the recorded end displacement of the RHS includes the deflection of the LHS. To determine the load deflection response of the RHS, displacements at LVDT#5 were corrected for the rotation of the beam around the bottom support roller as shown in Figure 4.18. The vertical displacement measured by LVDT#5 (named here $dy\#5$ shown in Figure 4.17) was reduced by the vertical displacement dy (θ shown in Figure 4.18) caused by a global rotation (θ) of the beam around the roller support.

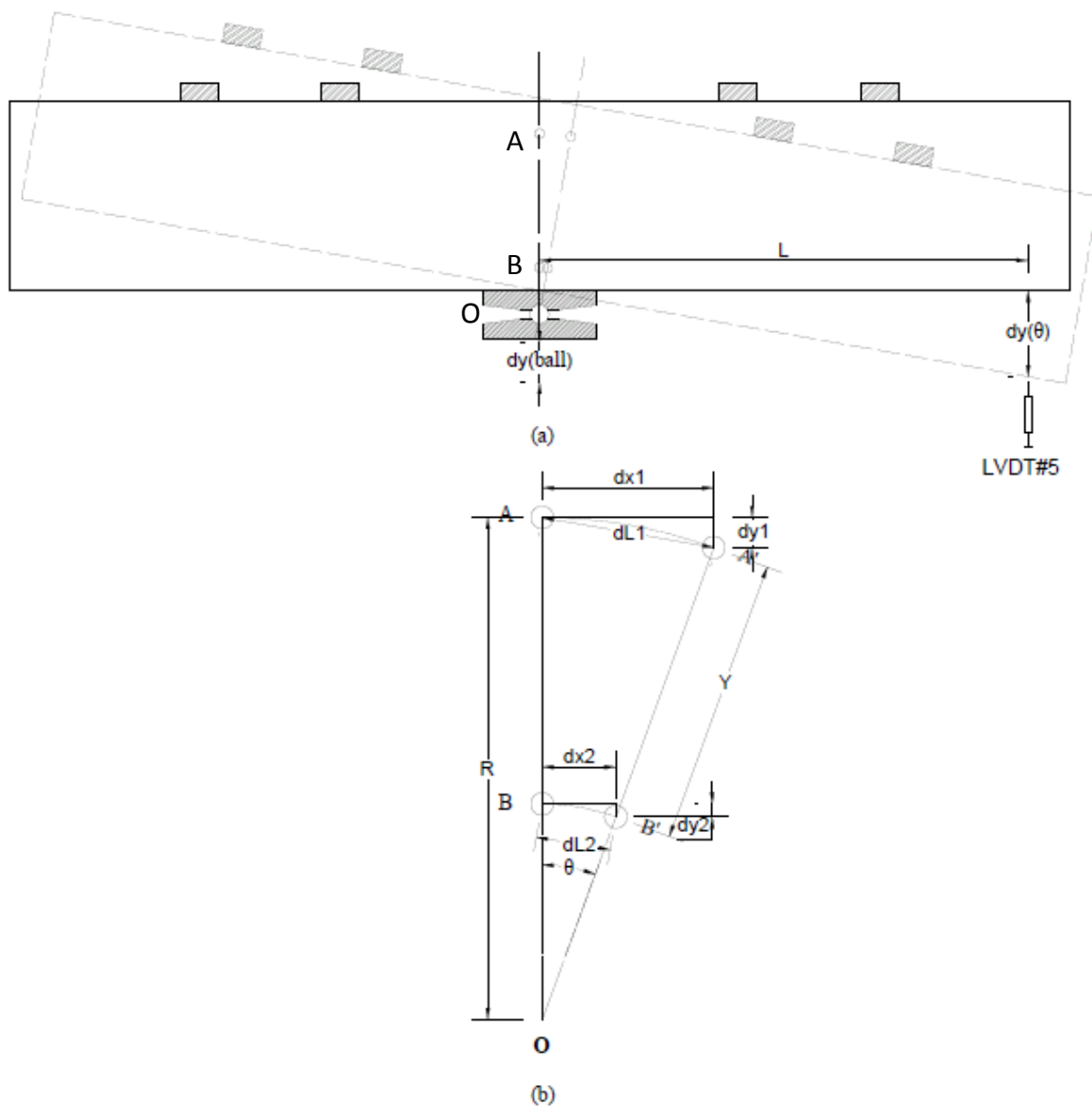


Figure 4.18: Vertical end displacement due to the rotation of the beam

The displacement due to the beam rotation at the support ($dy(\theta)$) was determined as follows from the relative displacements of (A) and (B) in Figure 4.18 – b that were determined using DIC:

$$R = \frac{Y}{1 - \frac{dL_2}{dL_1}} \quad \text{Equation 4.1}$$

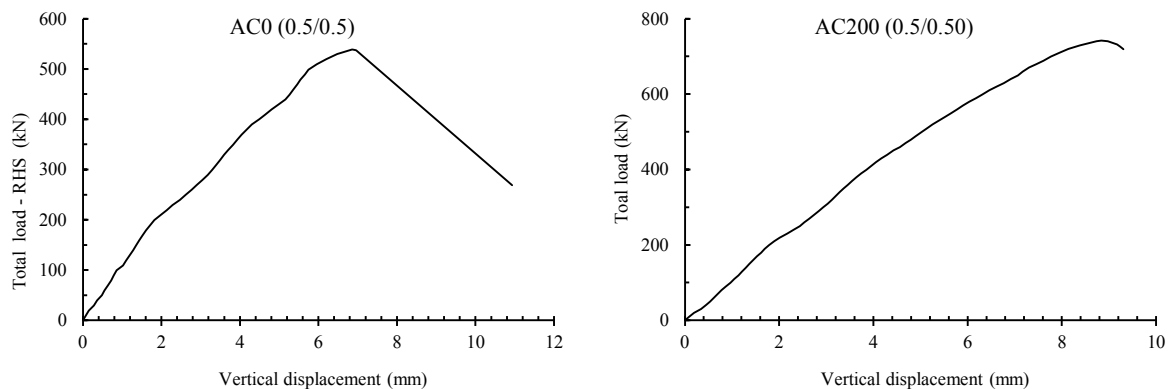
$$\tan \theta = \frac{dL_1}{R} \quad \text{Equation 4.2}$$

$$dy(\theta) = L \cdot \tan \theta \quad \text{Equation 4.3}$$

$$dy_{corrected} = dy(LVDT\#5) - dy(\theta) \quad \text{Equation 4.4}$$

In the above approximation, dl_2 is assumed to be zero since DIC showed the horizontal displacement dx_2 to be negligible. The centre of rotation o was assumed to be at the centre of the roller support.

Deflections in the cantilever beams have been corrected to allow for the rotation at the central support. The resulting load-displacement responses of the four beams are shown in Figure 4.19



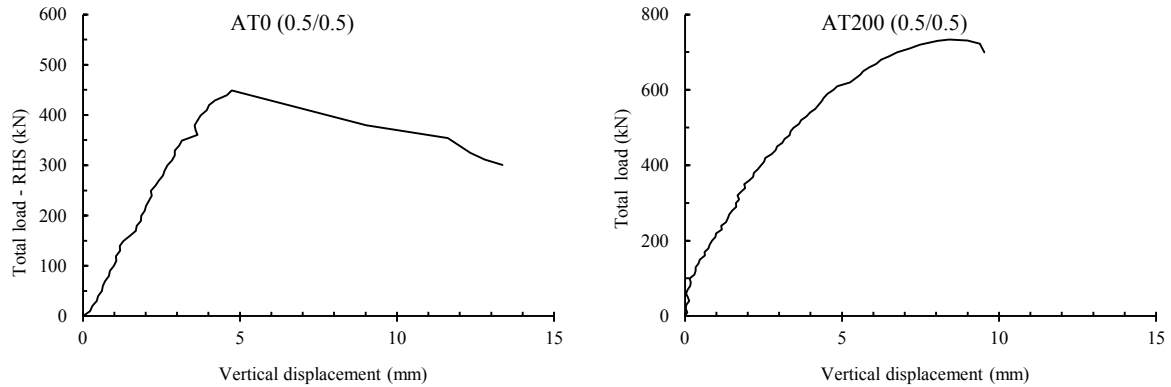


Figure 4.19: Load-deflection response for beams of series A

As mentioned earlier, the ratio of inner to outer loads was 58:42 in the Series (A) tension face tests rather than 50:50 as intended. The difference in loads resulted from rotational friction in the loading arrangement, which was eliminated in later tests. Comparison of the load deflection responses for beams with/without shear reinforcement shows that the presence of the shear reinforcement increases both the ultimate load and the stiffness of the beams loaded on the compression face (Figure 4.20). The increase in the failure load due to the presence of the shear reinforcement in beams loaded in the tension face (62%) was significantly greater than for beams loaded on the compression face (38%).

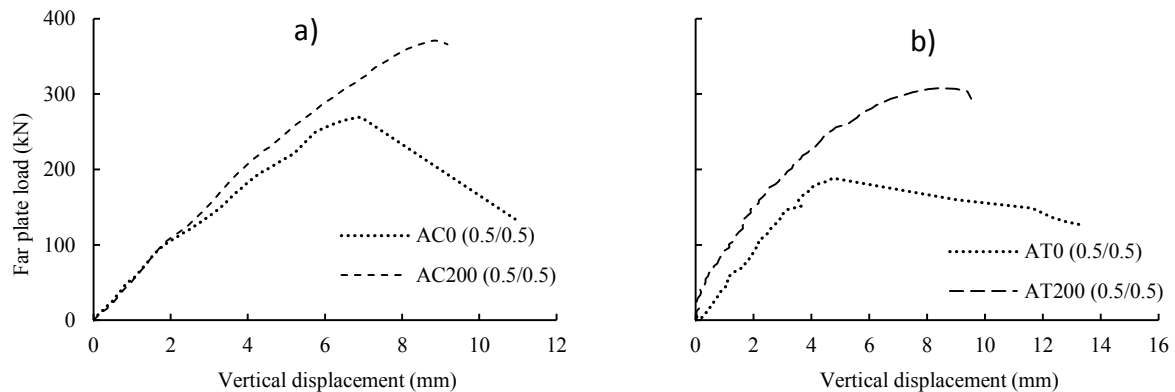


Figure 4.20: Influence of shear reinforcement on the behaviour of series A for beams loaded on the a) compression and b) tension face.

Comparison of load-deflection curves in Figure 4.21 shows that the shear force at the failure of the critical outer shear span was noticeably least for comparable beams of Series A loaded on the tension face. Possible reasons for this are discussed in Chapter 7.

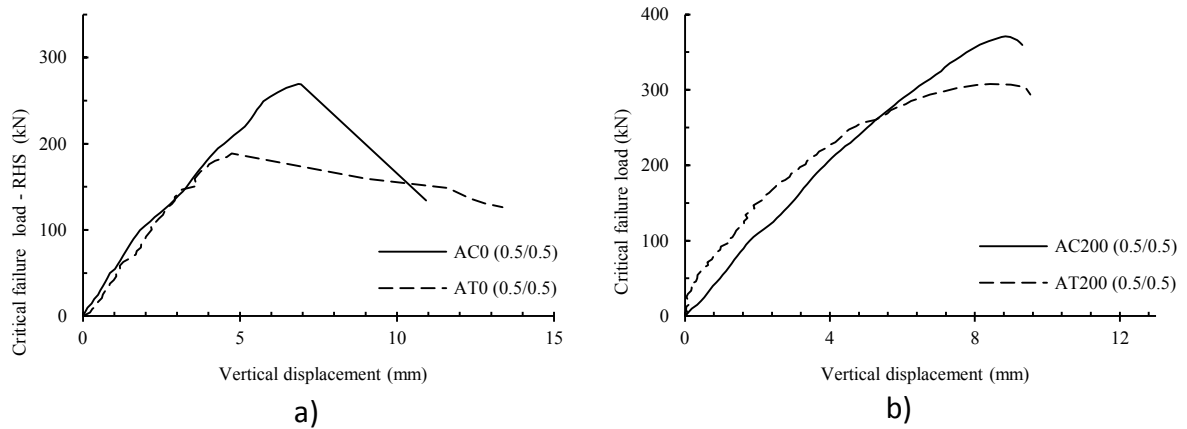


Figure 4.21: Influence of Comparison of load-displacement response for beams a) without and b) with shear reinforcement.

4.3.4. Reinforcement strains

Strain gauges were used to obtain strains in the longitudinal and shear reinforcement during loading. Strains were measured at locations of maximum moment (tensile or compressive), at positions of estimated maximum strain in shear reinforcement, adjacent to supports and loading plates and near the start of the bend in flexural reinforcement. Strain gauges locations and labels for beams in the series A are given in Figure 4.22 (faulty gauges are given in red).

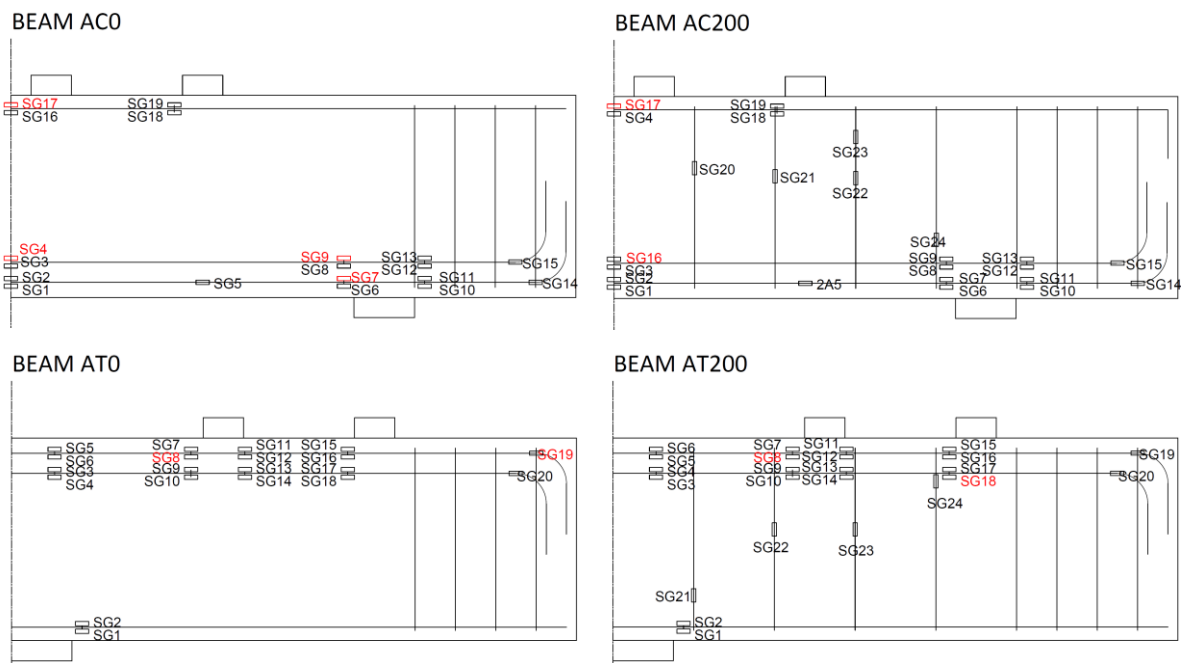


Figure 4.22: Strain gauges locations and labelled for beams series A

Strain gauges were placed in mainly pairs on the sides of the longitudinal bars (see section 3.5.2) to minimise the loss in the cross-sectional area and to minimise disturbance of

bond between the reinforcement and concrete. In locations where flexure in the bar due to dowel action was of interest, strain gauges were placed on the top and bottom of the bar to measure changes in strain due to flexure. Axial strains in longitudinal bars were obtained by averaging strains in pairs of the strain gauges. Fixing the strain gauges on the top and bottom required grinding parts of the ribs and the bar itself, thereby marginally reducing the bar cross sectional area as well as affecting bond between the concrete and the reinforcement bar. Less grinding of the ribs maintains better bond but jeopardises the adhesion of the gauge due to unevenness of the bar surface. Hence, a balance must be achieved between ensuring adhesion of the gauge and maintaining bond as well as bar cross-sectional area.

The axial strains in the reinforcement bars are presented in Figure 4.23, which shows that the tensile flexural reinforcement almost yielded at failure in beams AC200 (0.5/0.5) and AT200 (0.5/0.5).

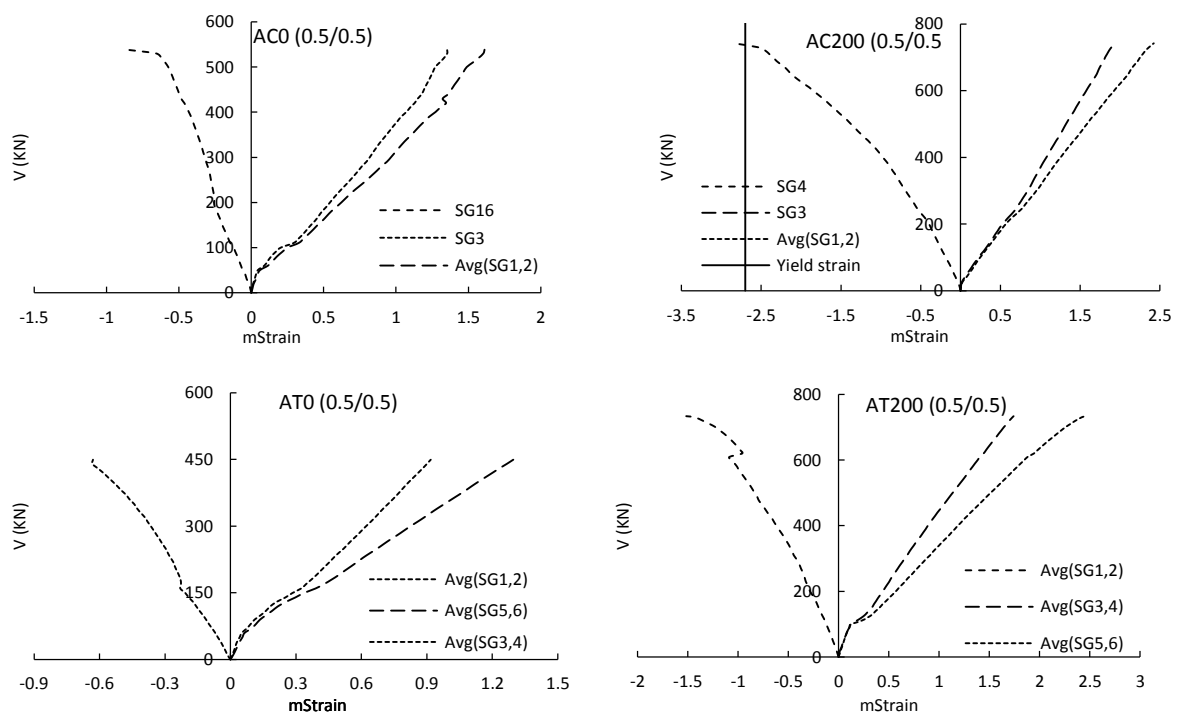


Figure 4.23 Flexural reinforcement strains for beams of series A

The influence of dowel action on reinforcement strain is presented in Figure 4.24. Results are unavailable for beam AC0 (0.5/0.5) due to gauge malfunction. One strain gauge was also lost on the compression reinforcement of beam AC200 (0.5/0.5). The strain readings show that there were noticeable differences in the axial strains at the top and bottom of the bars especially near failure. The difference in strain between the top and bottom gauges of the

tension bars was more significant for compression face loading (Beam AC200 (0.5/0.5)) than for tension face loading (Beams AT0 (0.5/0.5) and AT200 (0.5/0.5)) (see Figure 4.24).

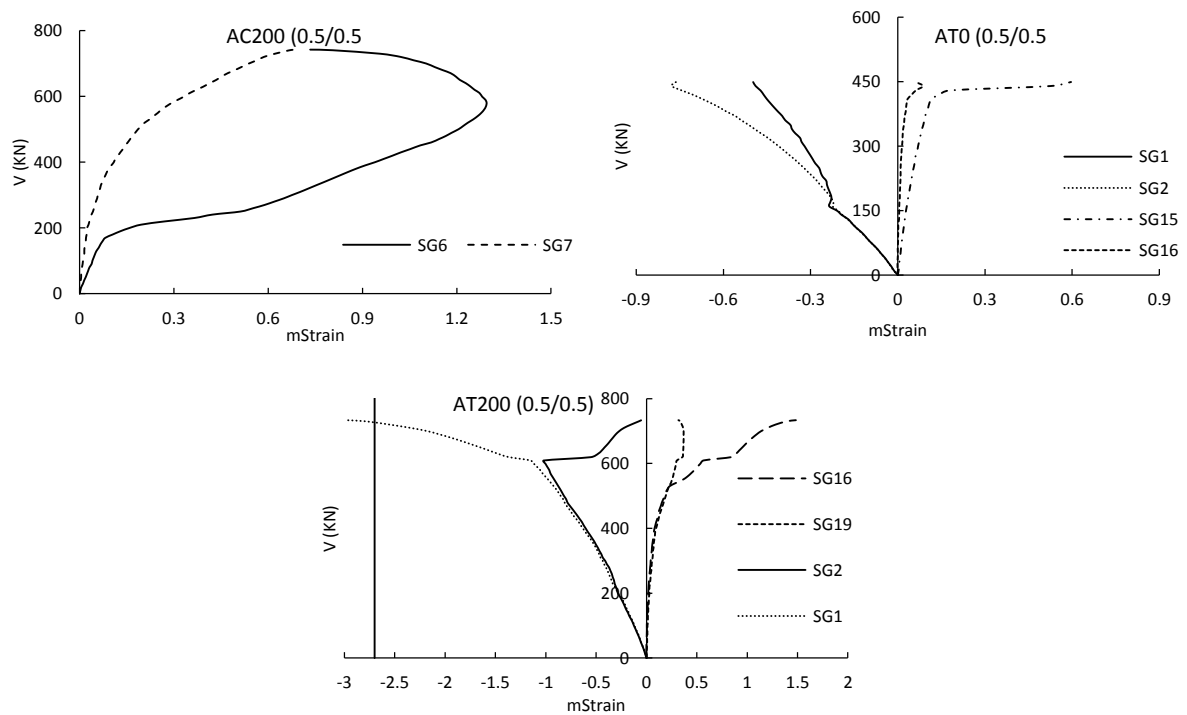
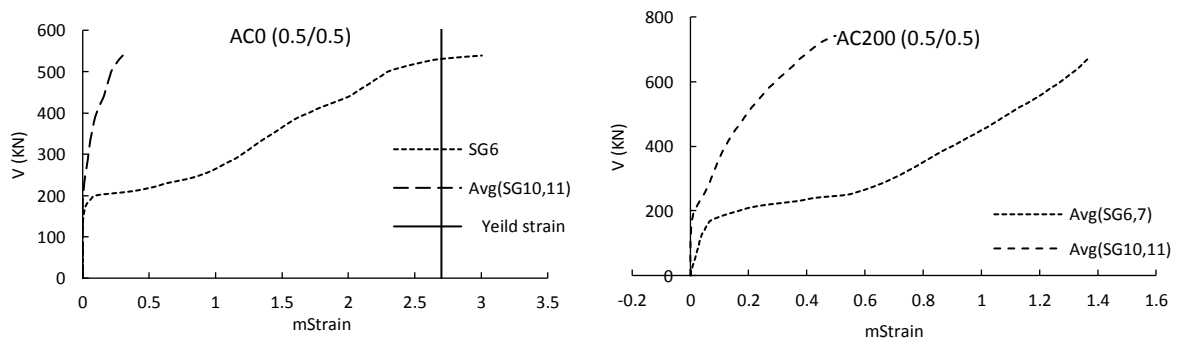


Figure 4.24 Dowel effect on the reinforcement strains for beams in series A

To study the effect of transverse pressure on reinforcement anchorage, strain gauges were fixed to the longitudinal tension reinforcement to either side of supports/loading plates. The results show a very significant reduction in tensile reinforcement strain due to the presence of transverse confinement. This reduction in strain across supports/loading plates was greater for beams loaded on the compression face than the tension face as shown in Figure 4.25. The influence of transverse pressure in confinement is discussed further in Chapter 7.



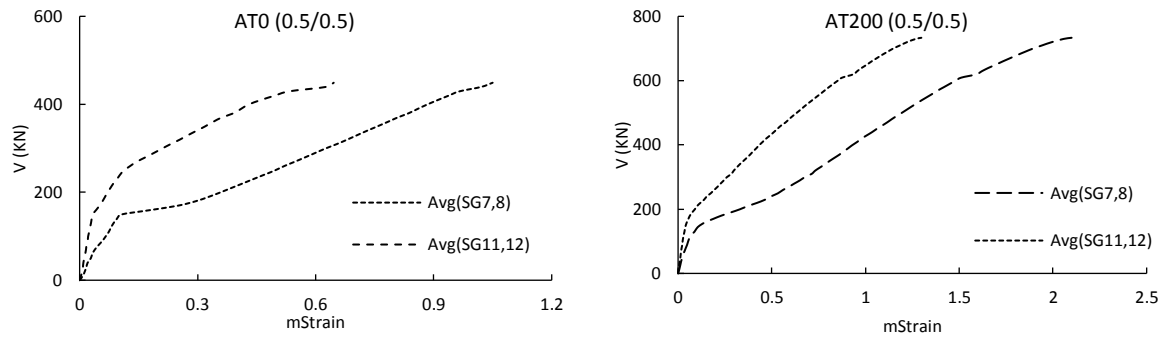


Figure 4.25 Reduction in the longitudinal reinforcement strain due to the presence of transverse confinement in series A

Shear reinforcement strains for series A are presented in Figure 4.26. The strains indicate that yielding occurred in at least some stirrups before failure. It should not be concluded that stirrups did not yield if not indicated in Figure 4.26 since the location of strain gauges did not necessarily coincide with the position of maximum strain. Other methods of estimating the reinforcement strains (FEA and Sigrist model (Sigrist, 1995) using DIC results) are discussed later in Chapter 7.

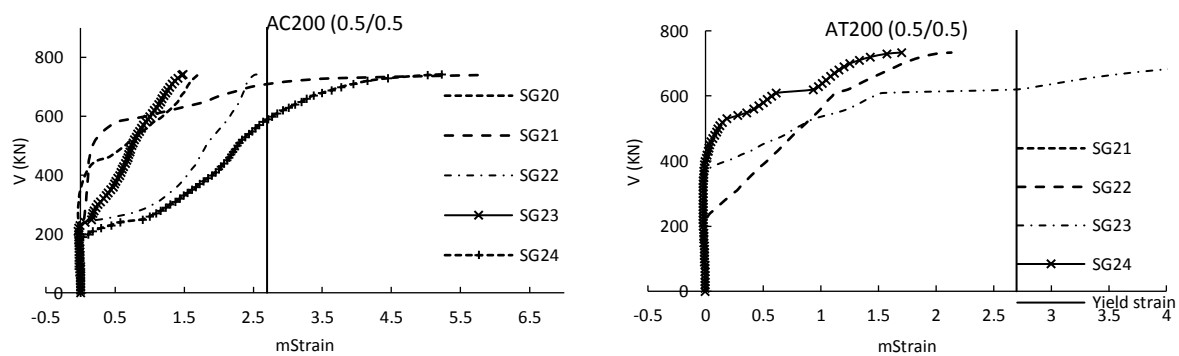


Figure 4.26: Shear reinforcement strains for series A

4.4. Results of Series B

4.4.1. Summary of test results

This series contained four beams (BT200 (0.5/0.5), BT200 (1.0/0), BT200 (0/1.0) and BT200 (0.3/0.7)) which were tested as balanced cantilevers. The critical shear span of all the beams was reinforced with B8 stirrups at 200 mm centres in their critical span. All the beams failed on the intended side (RHS). Results of this series are summarised in Table 4.19. The maximum deflection was obtained by correcting the displacement at LVDT#5 using the procedure illustrated in Figure 4.18.

A comparison of the capacity of the outer shear span can be seen by comparing the outer failure loads (P_2) of beams BT200 (0/1.0), BT200 (0.5/0.5) and BT200 (0.3/0.7). Beam BT200 (0/1.0) was loaded at the outer plate only while beams BT200 (0.5/0.5) and BT200 (0.3/0.7) were loaded at both of the plates in different ratios. Shear failure of beams BT200 (0.5/0.5) and BT200 (0.3/0.7) was critical in the outer shear plane with reduced failure loads P_2 of 324.15 kN and 396.53 kN respectively compared with 423.1 kN for beam BT200 (0/1.0). These results suggest that the application of the inner load P_1 reduced the failure load of the outer shear span P_2 . Further analysis of this is available in Chapter 7.

Table 4.19: Summary of the results for the series B

Beam ID	f'_c MPa	f_t MPa	Load Ratio		$V_{failure}$ RHS kN			V_{flex} kN	δ_{max} mm (LDTV#5)
			R1	R2	Inner	Outer	Total		
BT200 (0.5/0.5)	28.4	2.58	0.5	0.5	324.2	324.2*	648.3	795	34.1
BT200 (1.0/0)	28.9	2.72	1	0	610.3*	0	610.3	1079	29.8
BT200 (0/1.0)	29.2	2.82	0	1	0	423.1*	423.1	630	24.3
BT200 (0.3/0.7)	28.8	2.68	0.3	0.7	158.4	369.5*	527.9	720	25.9

* indicates the critical shear plane

4.4.2. Modes of failure and development of cracks

The development of cracks and the modes of failure in Series B is illustrated in Figure 4.27 and Figure 4.28 respectively. Figure 4.27 shows the development of cracking while Figure 4.28 shows the final crack pattern. The cause of failure is most evident in Figure 4.28. Similar to Figure 4.8 red and green blue colours are used to define the first, second third and fourth cracks (if present) in Figure 4.27. Minor flexural cracks were also observed in locations of maximum bending moments. These cracks are more observable in the crack strains obtained with the DIC (See Figure 5.16).

In beam BT200 (0.5/0.5) loaded with four equal point loads, the first crack initiated at the inner loading plate and extended downwards towards the support. At 80% of the failure load, a new diagonal crack, which became the critical shear crack, developed from the outer loading plate to the bottom support plate.

In beam BT200 (1.0/0), in which the load was applied only to the inner loading plate, the first diagonal crack initiated at the edge of the loading plate. Subsequently, a diagonal crack developed at the support plate. Near failure, the upper diagonal crack extended downwards and joined up with the lower crack forming the critical diagonal crack.

In beam BT200 (0/1.0) load was only applied to the outer loading plate. In this beam, the critical diagonal crack initiated at mid-height of the beam. As the load increased, the crack extended each way to the top and bottom plates. A secondary crack branched out of the critical crack near failure at the centre of the beam.

In beam BT200 (0.3/0.7), where the greatest load was applied at the outer support, the first crack initiated at the inner loading plate, while the critical crack developed subsequently and extended between the outer loading plate and the support.

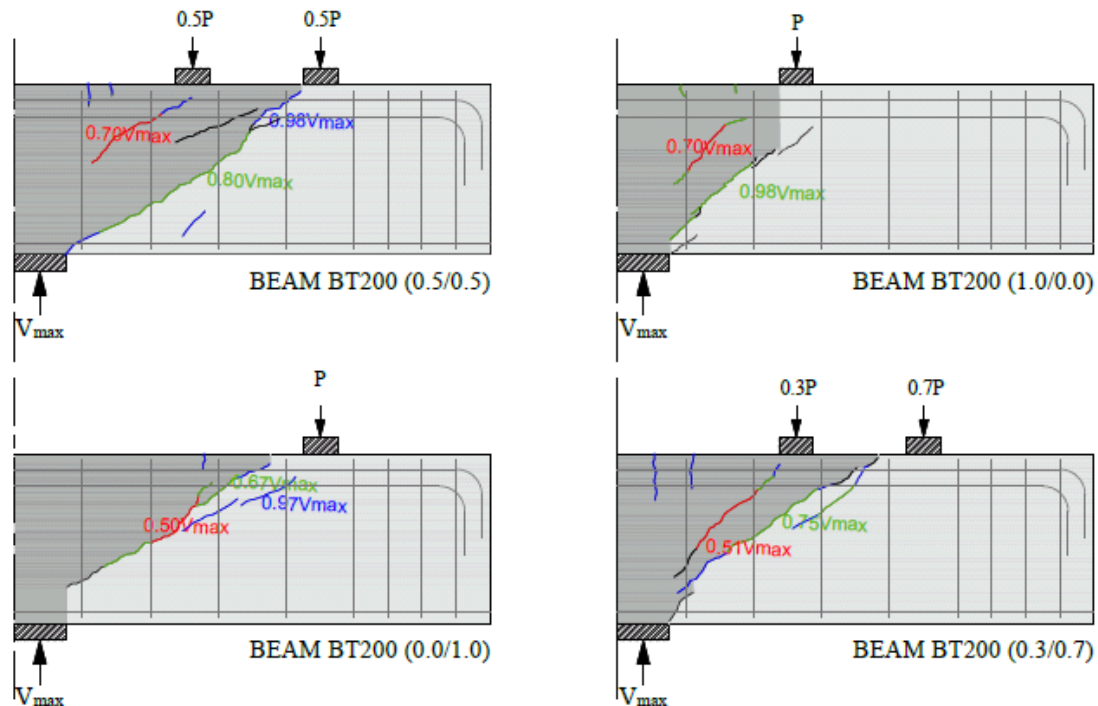


Figure 4.27: Development of the cracks during the test – series B

A common feature of the cracking pattern in beams loaded on their tension face at the inner plate was that a secondary crack developed around 50–70% of the total failure load between the inner load and support plates. This was also the case for beam AT200 (0.5/0.5) in series A. This secondary crack was not critical in any of the beams including BT200 (1.0/0) but had an effect of the deformation pattern as discussed later in Chapter 5. Failure in series B was typically initiated by penetration of the critical diagonal crack into the flexural compression

zone. In beams, loaded at the outer loading plate, failure was characterised by crushing of concrete within the flexural compression zone as in series A. In beam BT200 (1.0/0) there is evidence of concrete crushing along the complete length of the critical diagonal shear crack.

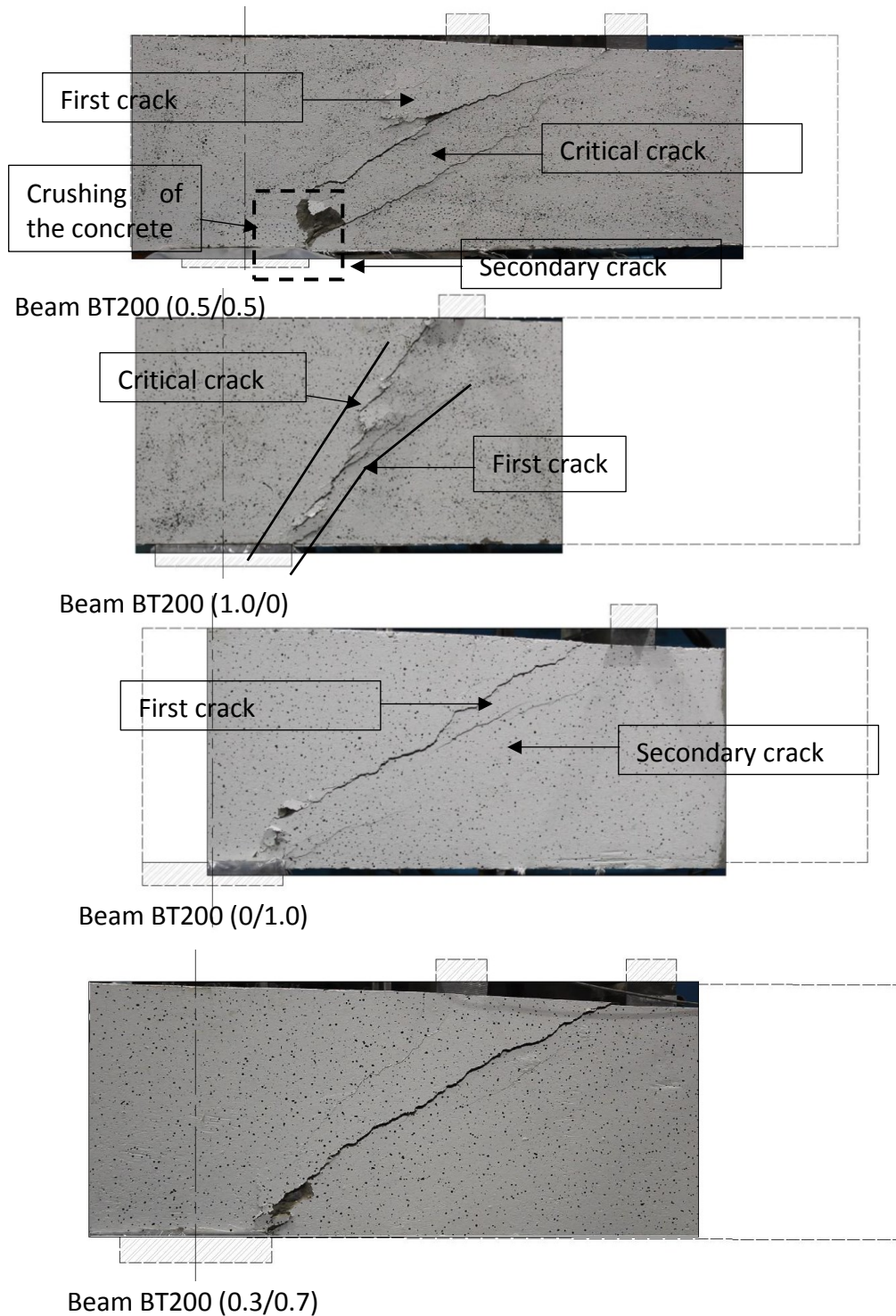


Figure 4.28: Failure modes and crack patterns (post-peak) for series B

Figure 4.29 superimposes the critical shear crack in all the beams of Series B as well as beam AT200 (0.5/0.5) from Series A, which was similar to beam BT200 (0.5/0.5) apart from the

applied load ratio being 0.58/0.42 rather than 0.5/0.5 as intended. Two types of crack path, dependent on the loading arrangement, are evident in Figure 4.29. The crack path is convex in beams BT200 (0.5/0.5) and AT200 (0.58/0.42) but almost straight in beams BT200 (0/1.0) and (0.3/0.7). This suggests that the crack path is diverted by the inner load once it exceeds around 40% of the total failure load but further data are required to confirm this.

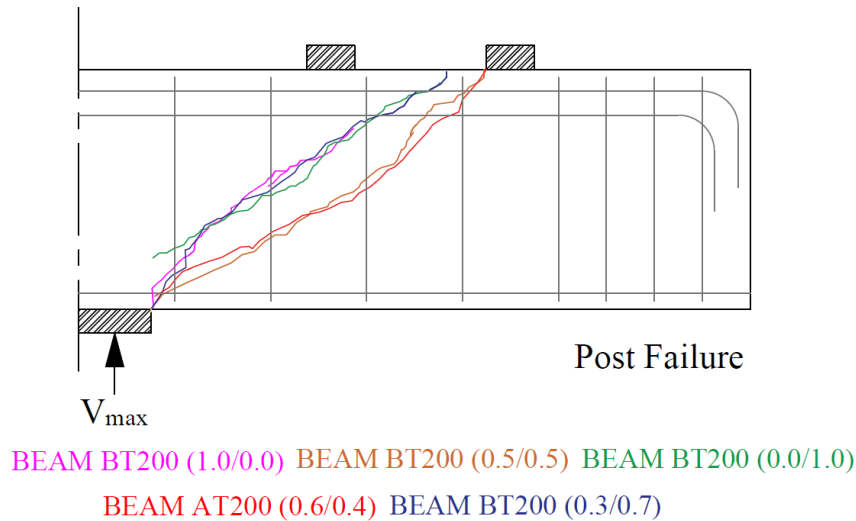
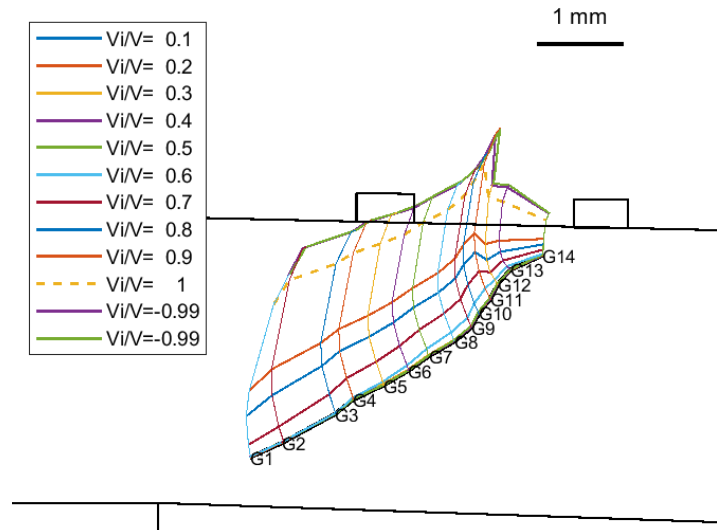


Figure 4.29: Critical shear cracks for series B a) at 95% of V_{max} and b) post failure

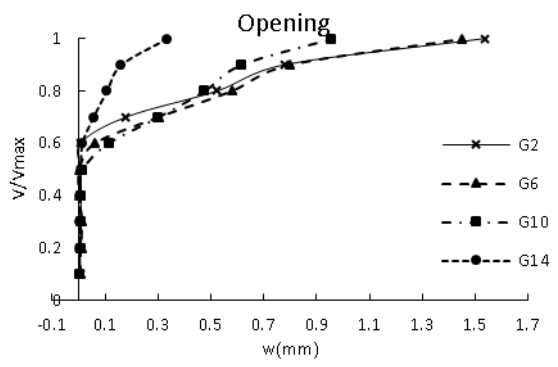
4.4.3. Concrete surface strains and crack kinematics

Similar procedures to series A were followed here. Crack kinematics were obtained from DIC with typical virtual gauges and crack orientation as given in Figure 4.10. The maximum crack opening and sliding displacements at peak load, corresponding height from the bottom of the beam and crack orientation are shown in Table 4.20 for Series B.

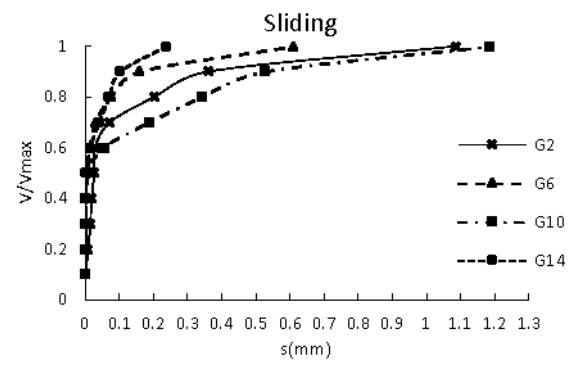
Figure 4.30 through to Figure 4.33 describe the crack opening and sliding for beams in series B. Cracks generally initiated from the mid-height of the beams and propagated to the tension and compression face until failure. Crack sliding was dominant at early stages of loading while crack opening was dominant near and at failure. Crack displacements were generally larger in the compression zone than in the tension zone, except for beam BT200 (0.3/0.7).



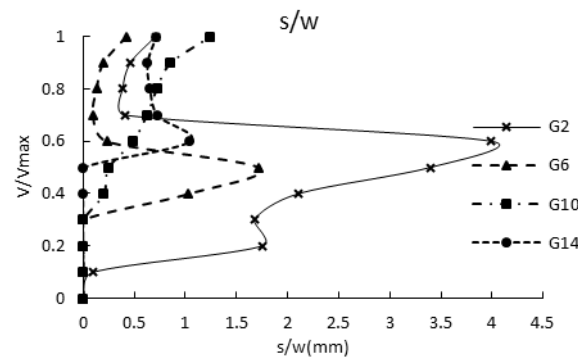
(a) crack kinematics



(b) crack opening



(c) crack sliding



(d) crack sliding/opening

Figure 4.30: Crack Kinematics for beam BT200 (0.5/0.5)

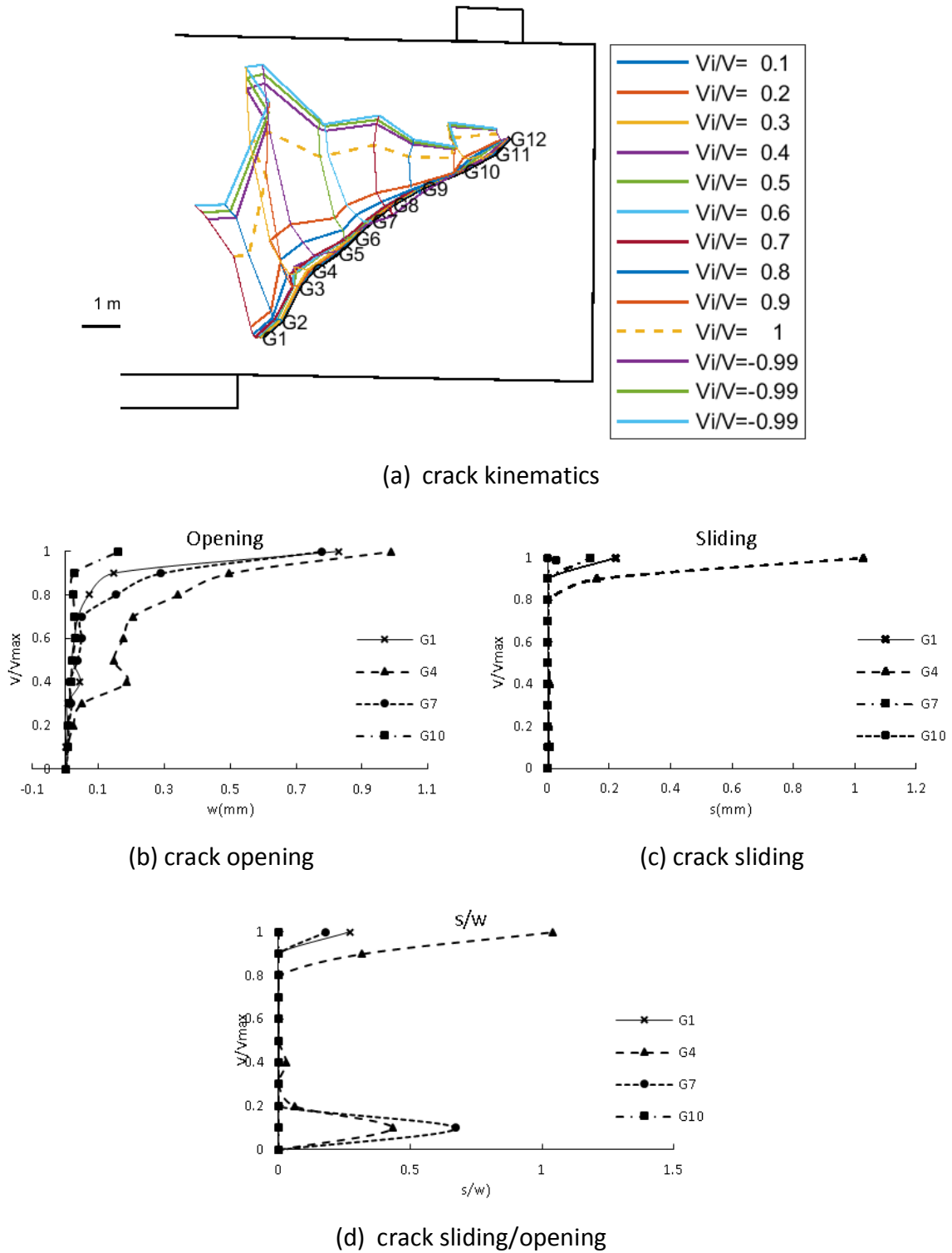
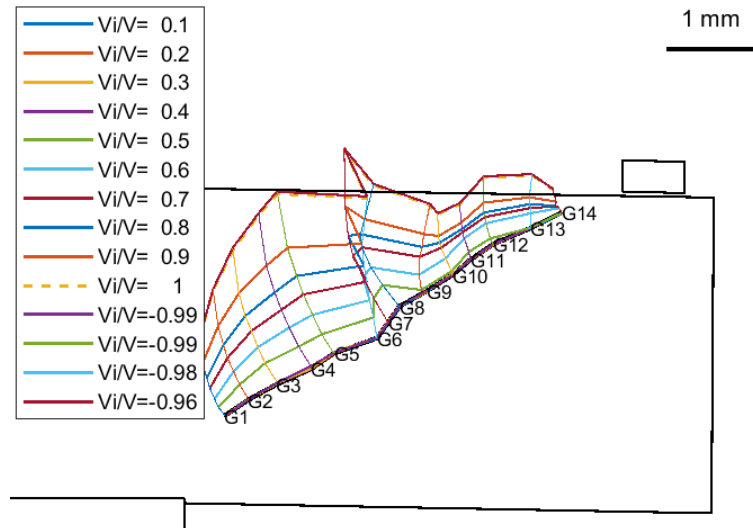
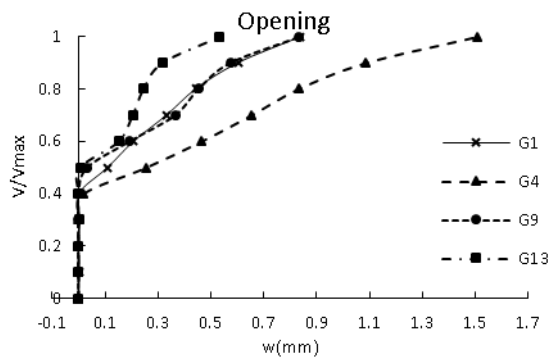


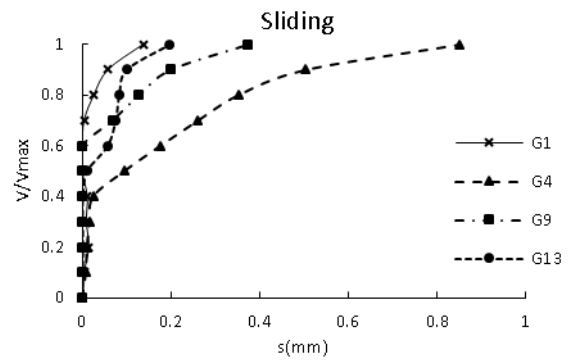
Figure 4.31: Crack Kinematics for beam BT200 (1.0/0)



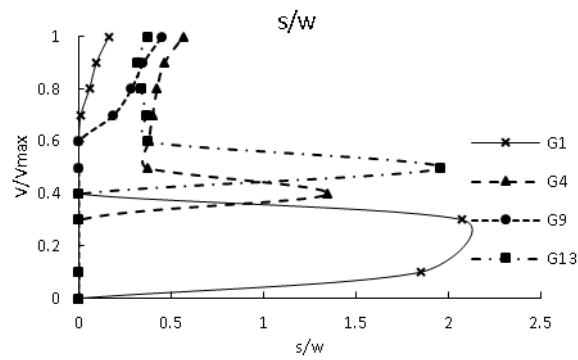
(a) crack kinematics



(b) crack opening

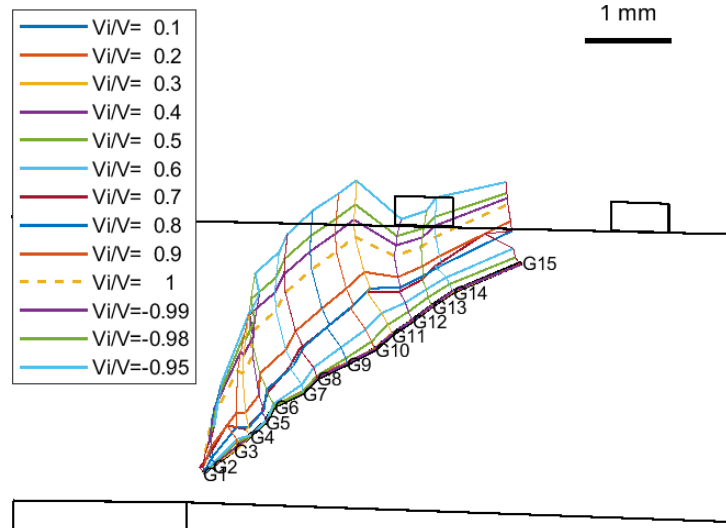


(c) crack sliding

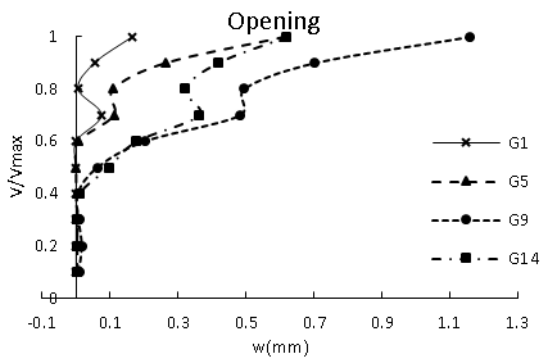


(d) crack sliding/opening

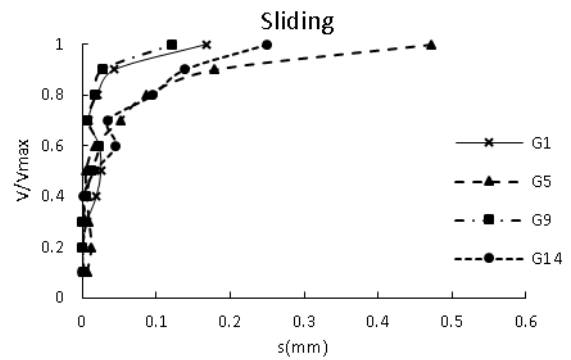
Figure 4.32: Crack Kinematics for beam BT200 (0/1.0)



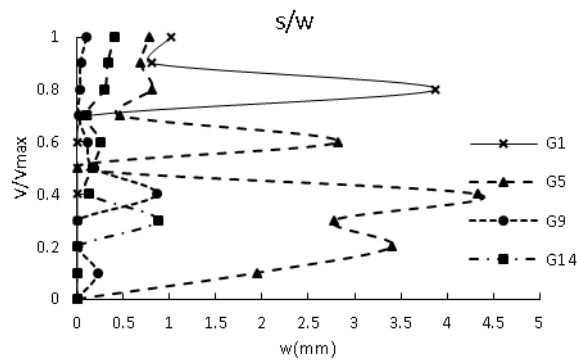
(a) crack kinematics



(b) crack opening



(c) crack sliding



(d) crack sliding/opening

Figure 4.33 Crack Kinematics for beam BT20 (0.3/0.7)

Table 4.20: Maximum crack opening and sliding for the beams in the series B at peak load

Beam	Max. opening (mm)	Height (mm)	Angle* (Degrees)	Max. sliding (mm)	Height (mm)	Angle* (Degrees)
BT(0.5/0.5)	1.54	41.9	32.6	1.32	241.9	62.7
BT(1.0/0)	1.34	143.6	45.0	1.03	116.9	72.2
BT(0/1.0)	1.80	116.9	22.0	1.24	166.9	55.0
BT(0.3/0.7)	1.17	231.3	36.3	0.56	56.3	35.2

* Positive angle (θ) is the angle between the horizontal axis and the critical crack measured counter-clockwise as in Figure 4.10.

4.4.4. Load-deflection response

The load-deflection response of beams in series B was measured using LVDTs positioned as described in section 3.5.3. Load-deflection responses of the beams were described by readings of the LVDT#5 bottom transducer as illustrated in Figure 4.34. All the beams in series C were loaded as balanced cantilevers with the LHS actuator displacement fixed to zero, which allows direct comparison of deflections without correction for beam rotations. Load-deflection response for beams of series B is given in terms of the total RHS and critical plane - load versus LVDT#5 deflection in Figure 4.35.

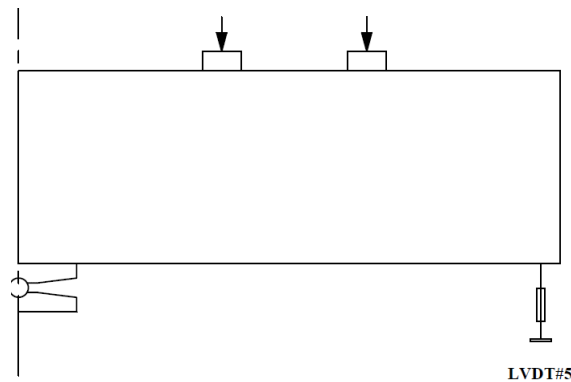


Figure 4.34: Location of LVDT#5 in series B

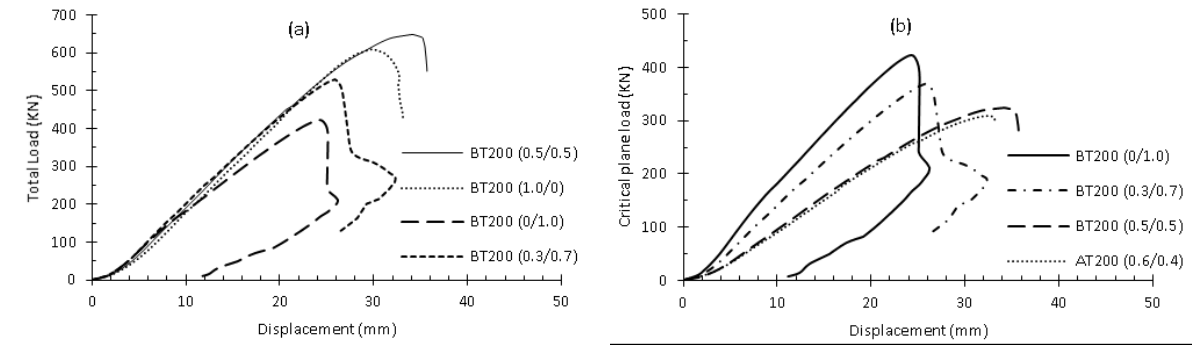
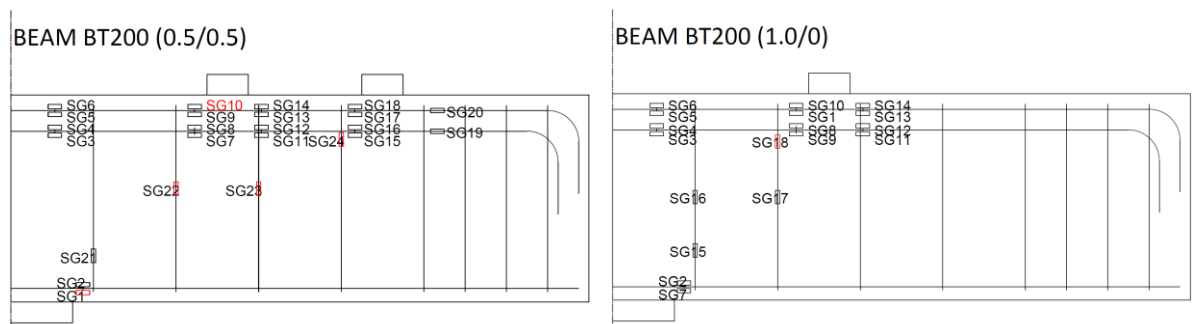


Figure 4.35: Load-deflection response for beams of series B (a) RHL vs deflection and b) Critical plane load vs deflection)

The load-deflection response is presented in two different forms. First, in Figure 4.35a, as the total applied load (P) on the RHS of the beams versus displacement and second, in Figure 4.35b, as the outer load (P_2) versus displacement. Results are shown in Figure 4.35b for all beams with tension face loading failing at the outer load plate within $2d$ of the face of the support including beam AT200(0.5/0.5). All these beams failed along the outer shear plane. Figure 4.35b shows that failure load (P_2) was greatest for beam BT200 (0/1.0) and reduced as the inner load (P_1) increased. The effect of the loading ratio on the capacity of the outer critical section is analysed further in Chapter 7.

4.4.5. Reinforcement strains

As in series A, strain gauges were used to record selected strains in the longitudinal reinforcement and stirrups. The strain gauge locations and numbering system are depicted in Figure 4.36 for series B. Labels of faulty gauges are indicated in red while gauges where reinforcement yielded were drawn in red.



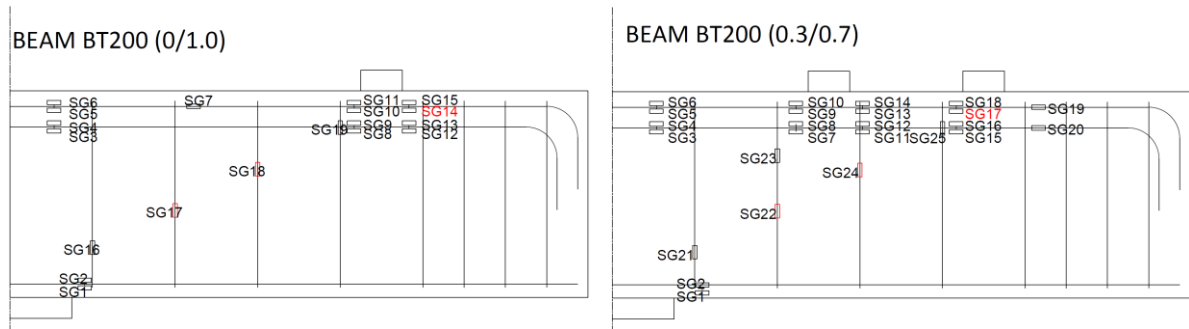


Figure 4.36: Strain gauges locations and labels for beams series B

The tensile and compressive strains in the longitudinal reinforcement of beams in series B are plotted in Figure 4.37. The strain gauge readings indicate that the compressive reinforcement yielded at failure in beam BT200 (0.5/0.5). This was also the case for beam AT200 (0.5/0.5) in series A which was similar to beam BT200 (0.5/0.5) apart from the loading ratio unintentionally being (0.58/0.42). As Figure 4.28 shows, beams exhibited severe concrete crushing at failure, and hence, the yielding of the compressive reinforcement could be related to the buckling of the reinforcement as stated earlier.

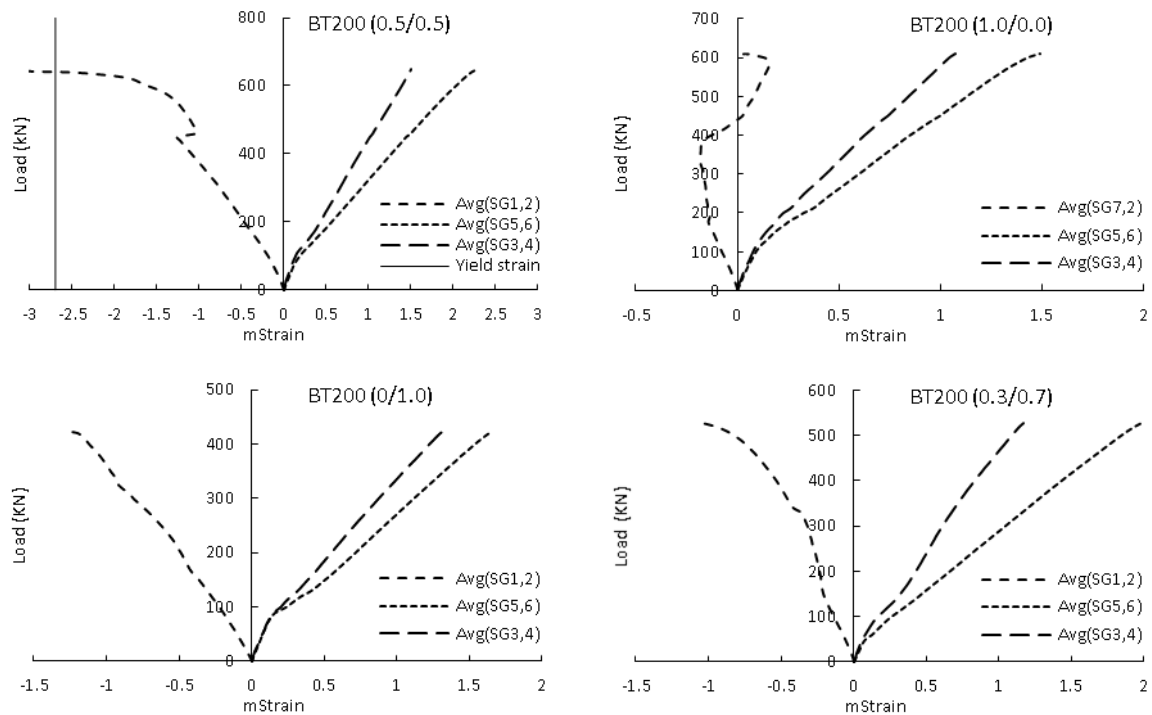


Figure 4.37: Longitudinal reinforcement strains series B

To study dowel action in the tension and compression reinforcement, two strain gauges were placed on the bottom and top of the compression reinforcement and four other gauges were

placed on the tensile flexural reinforcement were dowel was anticipated to happen. The crack was predicted to form between the support and the outer load plate for beams in series B, except where a single point load was applied at the inner plate (i.e. beam BT200 (1.0/0) and strain gauges were placed accordingly.

Flexure in the compression reinforcement, due to dowel action, was captured in all of the beams of series B. However, strain gauge SG17 in beam BT200 (0.3/0.7) was damaged during concrete casting so the dowel effect was measured for the bottom layer of tensile reinforcement of this beam. Flexure due to the dowel action changed the sign of strain from compression to tension in the bottom reinforcement of beams BT200 (0.5/0.5) and BT200 (1.0/0). Flexure due to dowel action also induced significant changes in tensile strain of the top longitudinal reinforcement in beams BT200 (1.0/0) and BT200 (0/1.0). The change in strain of the tensile reinforcement appeared to depend on whether the crack intercepted the top and bottom layers of the flexural reinforcement at locations of strain gauges.

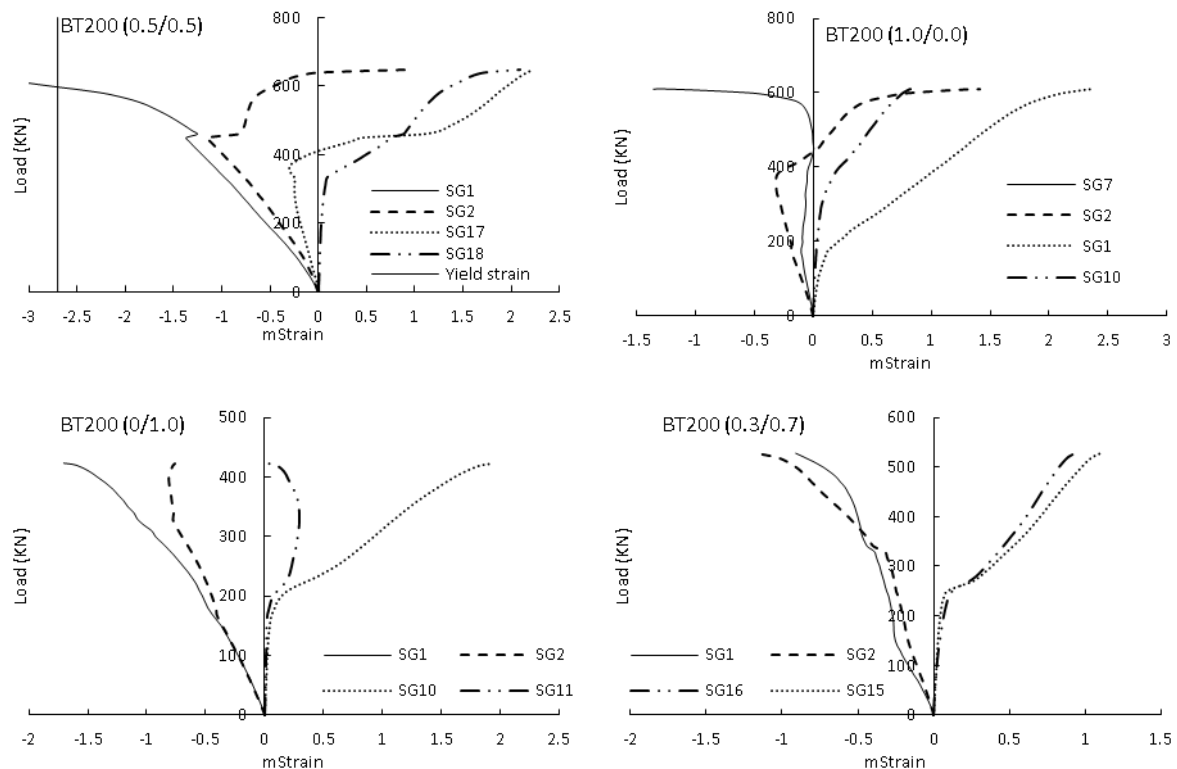


Figure 4.38: Reinforcement strains at dowel locations – Series B

The enhancement in bond caused by the transverse pressure from the loading plate was investigated by comparing reinforcement strains before and after the plate. The comparison showed significant reductions in strain over the support width particularly for beams loaded

with two point loads. In beam BT200 (0.3/0.7) where the SG17 was lost, the change in strain was obtained using the lower reinforcement layer. The results of the four beams are presented in Figure 4.39. Enhancement of the bond due to lateral confinement is discussed in details in Chapter 7.

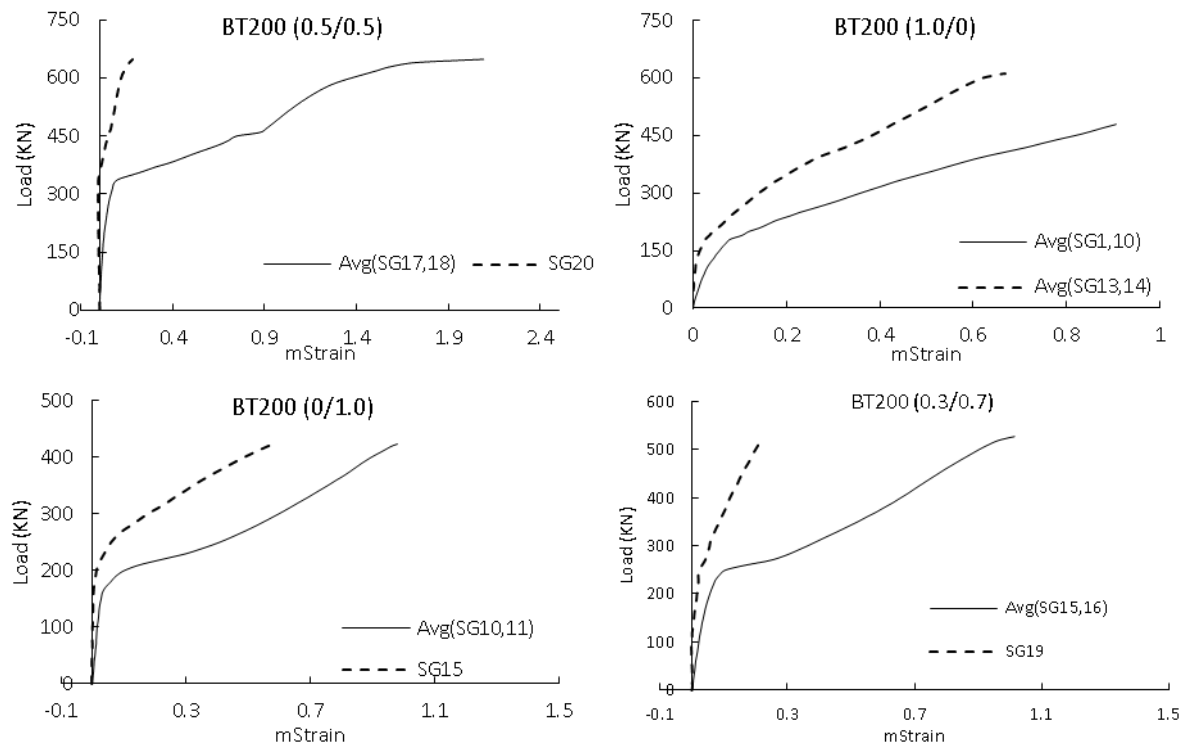


Figure 4.39: Reduction in the longitudinal reinforcement strain due to the presence of transverse confinement in series B

Strains in the shear reinforcement were obtained using strain gauges located in positions of predicted maximum stress. Results of the shear reinforcement strains for series B are presented in Figure 4.40. Yielding of shear reinforcement depends on the location of cracks relative to the reinforcement as well as the crack kinematics. For example, the stirrup closest to the flexural compression zone did not yield in any of the tests. However, at least one stirrup yielded in each test with some stirrups experiencing very high strains. However, strains were typically greater than measured in the stirrups since gauges were not typically positioned at the location of maximum strain, which depended on the crack pattern.

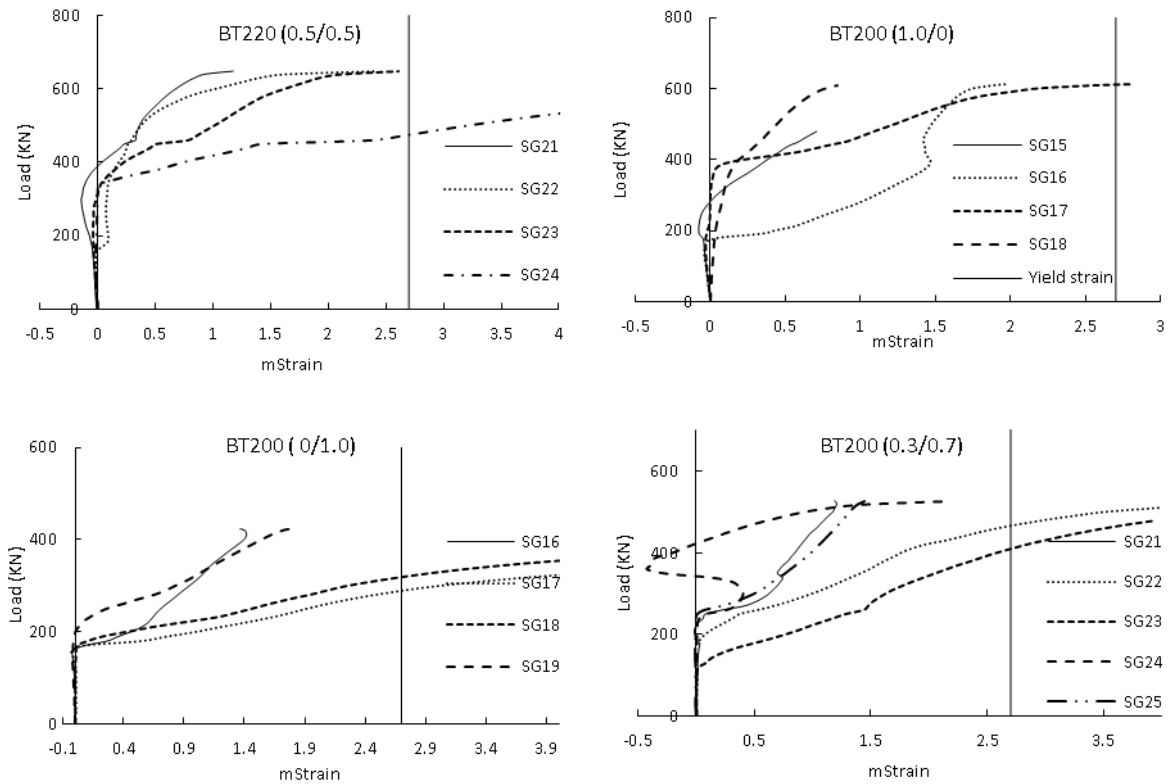


Figure 4.40: Shear reinforcement strains for series B

4.5. Results of Series C

4.5.1. Summary of the results

Series C investigated the influence on the shear strength of applying part of the load within and part outside $2d$ of the face of the support. The beam geometry, reinforcement arrangement and loading configuration are described in (3.2.3). Beams CT0 (1.0/0) and CT200 (1.0/0) were loaded with a single point load located at $1.66d$ from the centreline of the support. Beams CT0 (0.6/0.4) and CT200 (0.6/0.4) were loaded with point loads located at $1.66d$ and $3.0d$ from the centreline of the support.

Beam CT0 (0.6/0.4), without shear reinforcement, failed in the outer shear span while beam CT200 (0.6/0.4) failed in the inner shear span like beams CT0 (1.0/0) and CT200 (1.0/0). Results of Series C are summarised in Table 4.21. The total failure load of the beams loaded at $1.66d$ and $3.0d$ is seen to be slightly less than that of the companion beam loaded at just $1.66d$ with the percentage difference greatest for the beams without shear reinforcement.

Table 4.21: Summary of the results for series C

Beam ID	f'_c (MPa)	f_t (MPa)	ρ_v (%)	$V_{failure}$ RHS (KN)			$\frac{a_{v1}}{d}$	$\frac{a_{v2}}{d}$	V_{flex}
				Inner	Outer	Total			
CT0 (1.0/0)	26.9	2.59	0	441.0*	0	441.0	1.23	0	698
CT200 (1.0/0)	28.0	2.59	0.201	542.8*	0	542.8	1.23	0	698
CT0 (0.6/0.4)	28.9	2.60	0	227.0	151.3*	378.3	1.23	2.64	541
CT200(0.6/0.4)	28.3	2.60	0.201	301.0*	200.6	501.6	1.23	2.64	541

* indicates the critical shear plane

4.5.2. Modes of failure and development of cracks

The crack patterns of the beams in series C are shown in Figure 4.41 and Figure 4.42. In beams loaded at 1.66d alone, the critical diagonal crack ran directly from the inner edge of the load plate to the inner edge of the support, although secondary cracks also developed as shown in Figure 4.42. Minor flexural cracks were also observed in locations of maximum bending moments. These cracks are more observable in the crack strains obtained with the DIC (See Figure 5.16).

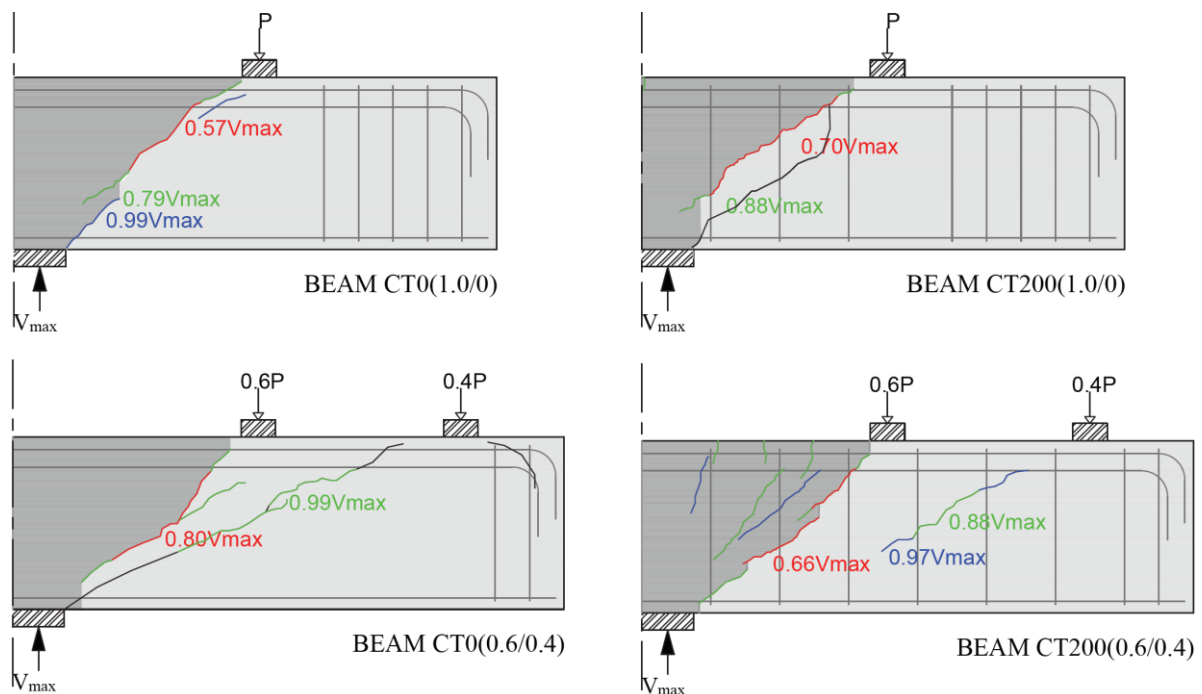


Figure 4.41: Development of the cracks during the test – series C

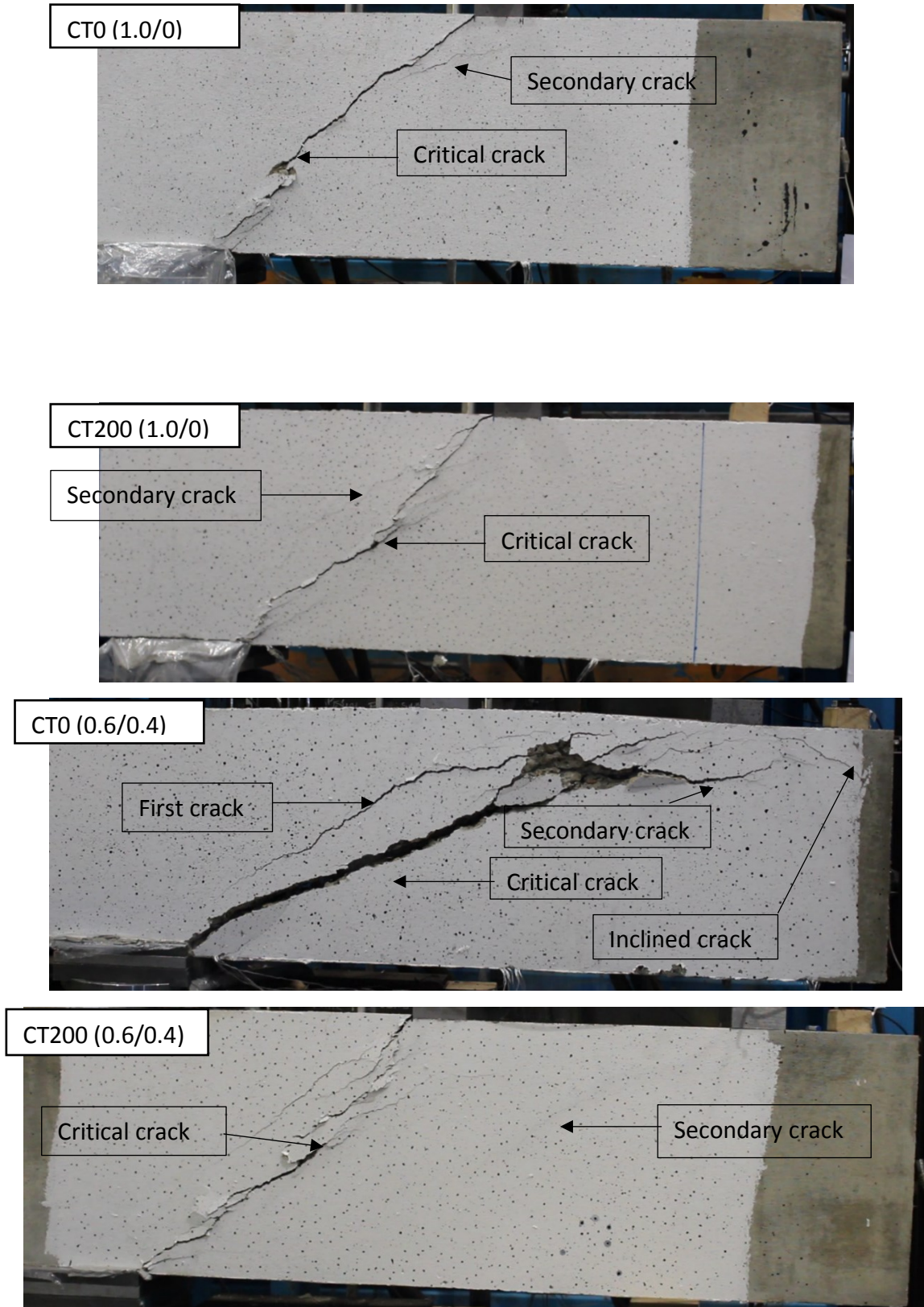


Figure 4.42: Modes of failure for beams of series C

The first crack in CT0 (0.6/0.4) ran between the support and the inner load plate. The critical diagonal crack formed just before failure. It ran between the outer loading plate and the

support. At failure, this crack extended along the flexural reinforcement to the right of the outer loading plate and propagated around the bend in the reinforcement (see Figure 4.42). In CT200 (0.6/0.4), the first two cracks developed at mid-depth of the beam and extended between the inner loading plate and the support. As the load approached failure, multiple cracks developed in the inner support shear span, which eventually coalesced to form the critical crack. The crack pattern in beams CT0 (0.6/0.4) and CT200 (0.6/0.4) were similar prior to failure but the failure plane was different as shown in Figure 4.42.

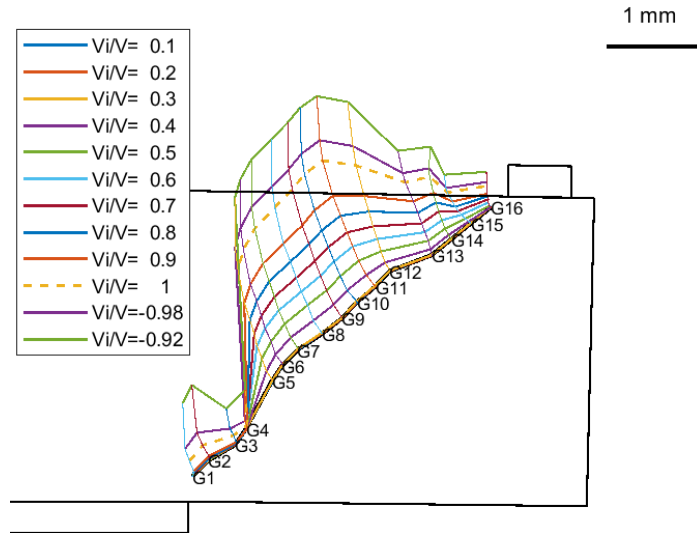
4.5.3. Concrete surface strains and crack kinematics

The maximum crack opening and sliding displacements for series C are presented in Table 4.22 along with the corresponding height from the bottom of the beam and crack orientation at peak load.

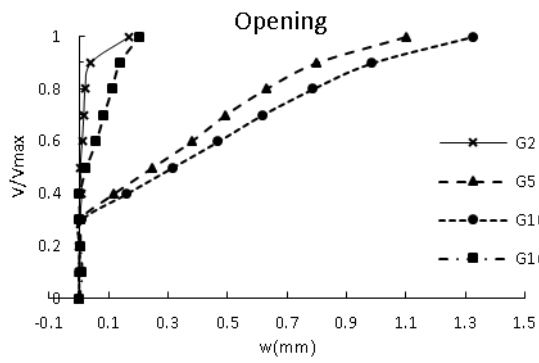
Table 4.22: Maximum crack opening and sliding for the beams in series C at peak load

Beam	Max. opening (mm)	Height (mm)	Angle* (Degrees)	Max. sliding (mm)	Height (mm)	Angle* (Degrees)
CT0(1.0/0)	1.39	241.9	33.2	0.85	191.9	59.9
CT200(1.0/0)	0.11	266.3	49.9	0.12	316.9	43.0
CT0(0.6-0.4)	1.08	341.9	29.2	0.61	293.6	46.5
CT200(0.6/0.4)	1.17	207.3	29.5	0.72	232.3	54.2

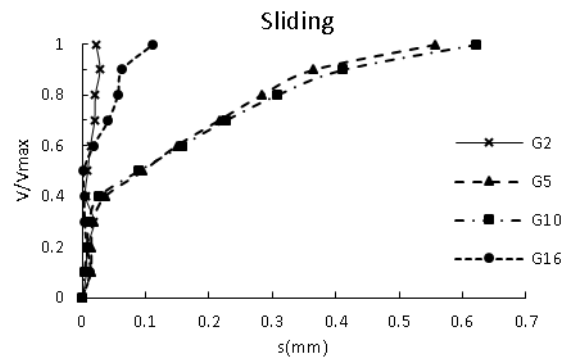
The crack kinematics for beams in series C are presented in Figure 4.43 to Figure 4.46. Three out of the four beams failed in the inner shear plane. Crack displacements in beams where the inner shear plane was critical were greatest at mid-height of the beams and reduced towards the crack ends. Figure 4.47 shows that the crack patterns were similar in the beams that failed along the inner shear plane particularly for beams CT200 (1.0/0) and CT200 (0.6/0.4) with shear reinforcement. Figure 4.47 also shows that the final crack pattern between the inner loading plate and support was similar in beam CT0 (0.6/0.4) and CT200 (0.6/0.4) despite CT0 (0.6/0.4) failing along the outer shear plane.



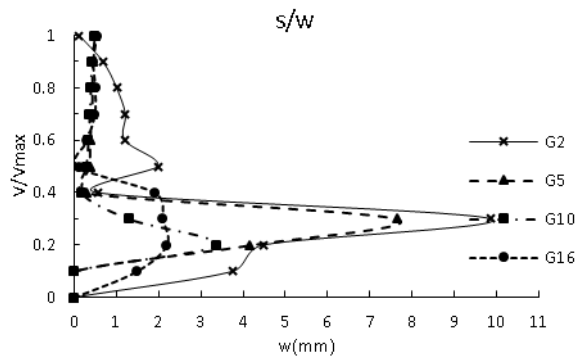
(a) crack kinematics



(b) crack opening

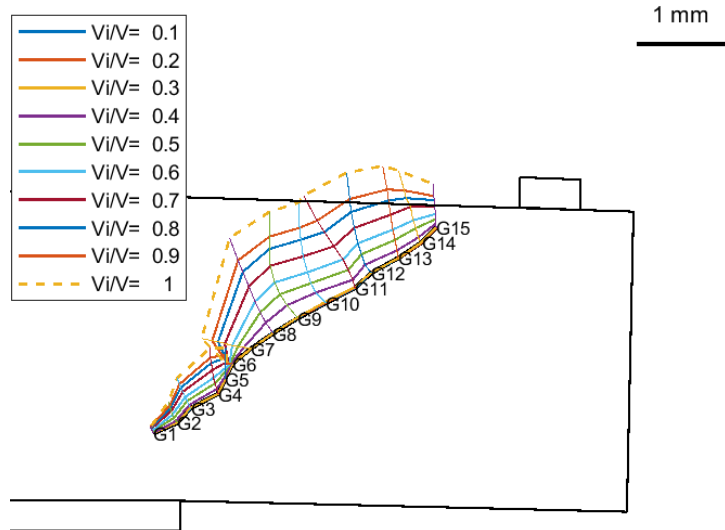


(c) crack sliding

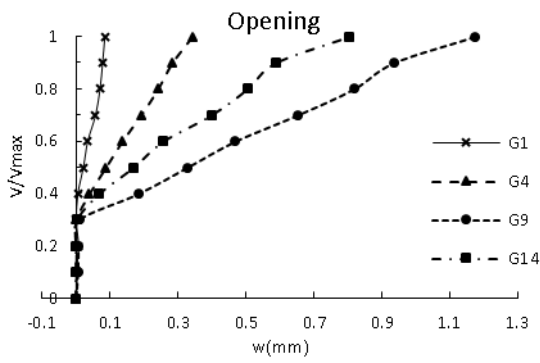


(d) crack sliding/opening

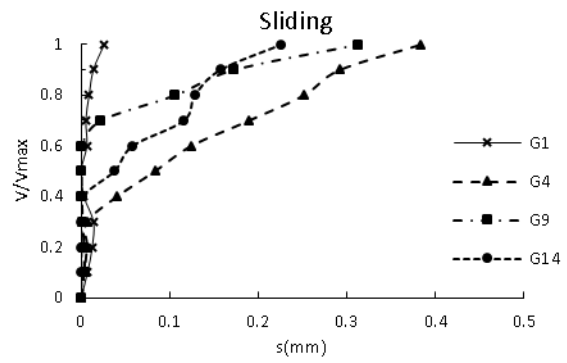
Figure 4.43: Crack Kinematics for beam CT0 (1.0/0)



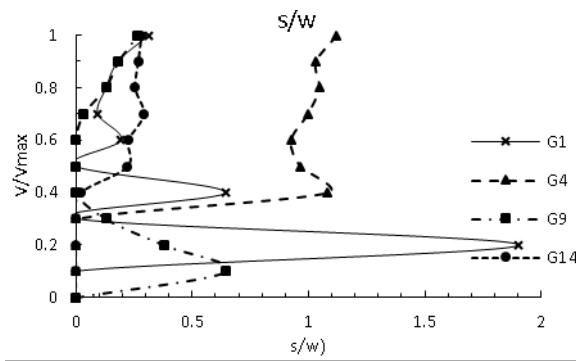
(a) crack kinematics



(b) crack opening

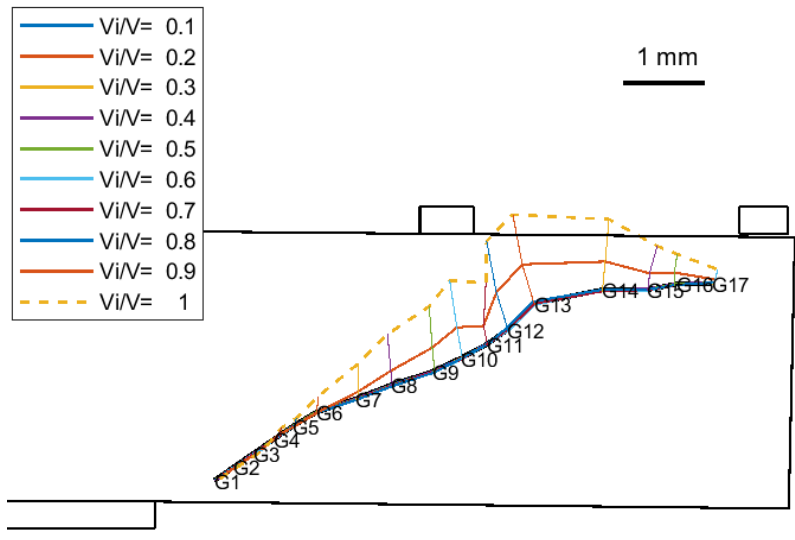


(c) crack sliding

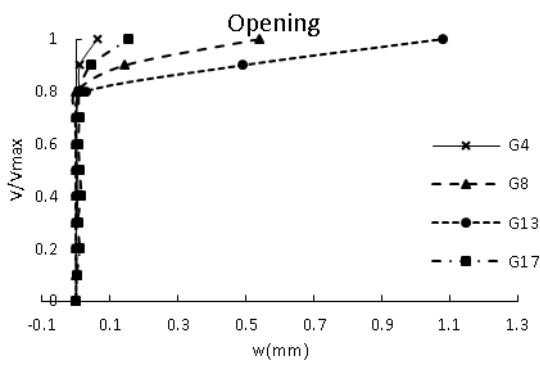


(d) crack sliding/opening

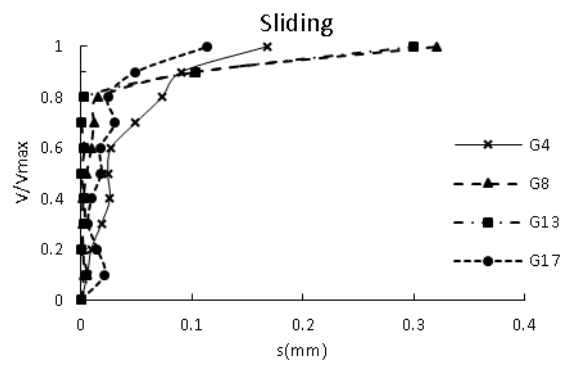
Figure 4.44: Crack Kinematics for beam CT200 (1.0/0)



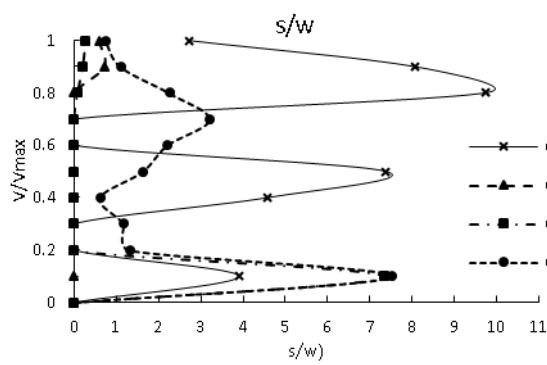
(a) crack kinematics



(b) crack opening



(c) crack sliding



(d) crack sliding/opening

Figure 4.45: Crack Kinematics for beam CT0 (0.6/0.4)

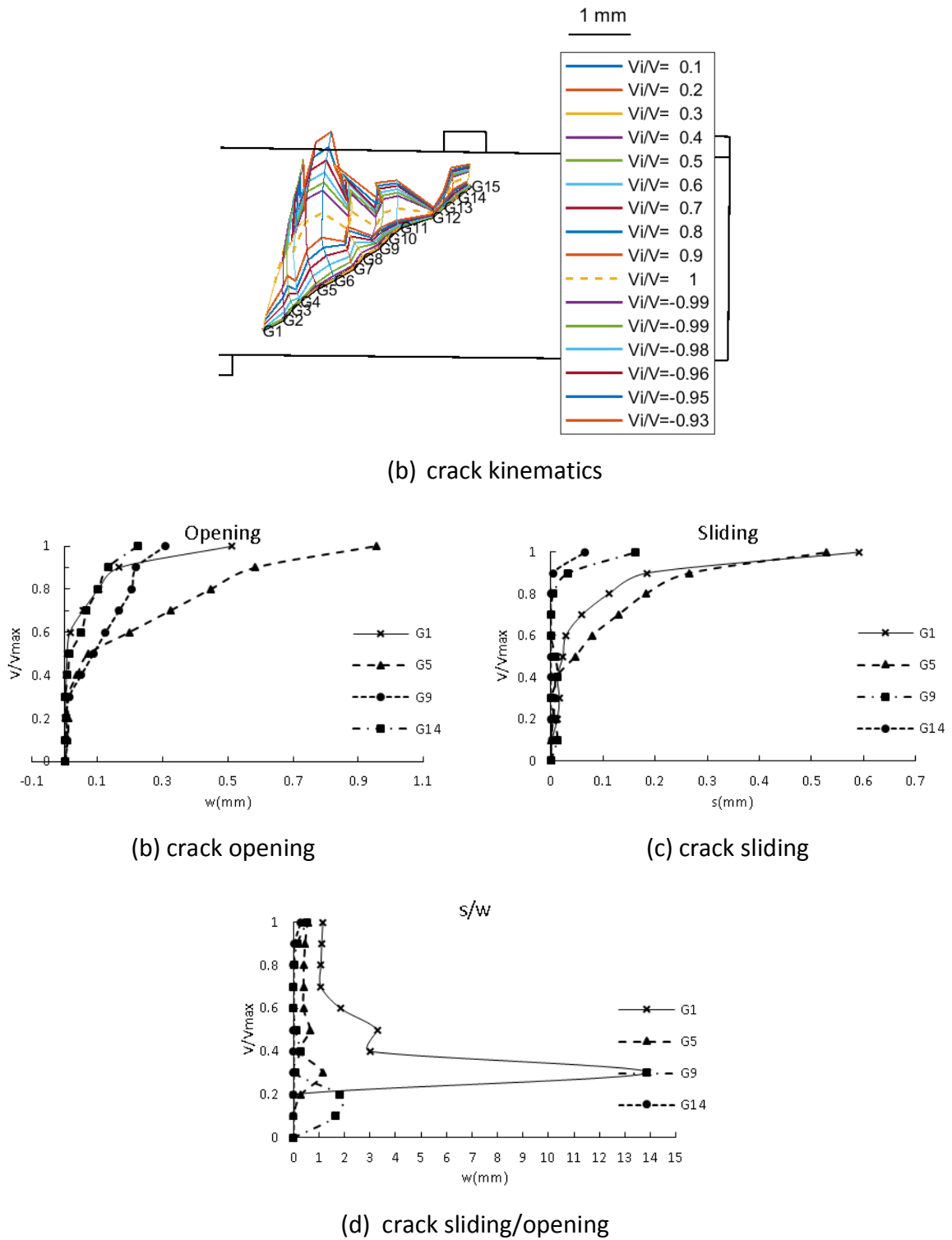


Figure 4.46: Crack Kinematics for beam CT200 (0.6/0.4)

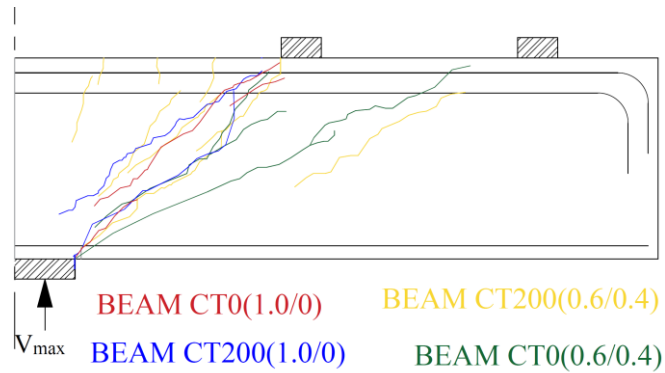


Figure 4.47: Overlapped crack patterns for beams in series C

4.5.4. Load-deflection response

Two different loading configurations were used in this series. Beams partially loaded outside the shear enhancement zone were asymmetric as described in section 3.4.3. Therefore, deflections from the two different loading arrangements are not directly comparable at LVDT#5 as shown in Figure 4.48. Hence, deflections were compared at LVDT#7, which measured displacement on the top of the beam at the inner loading plate. The position of LVDT#7 relative to the central support was the same for all the beams in series C. The load-deflection responses of the beams are shown in Figure 4.49

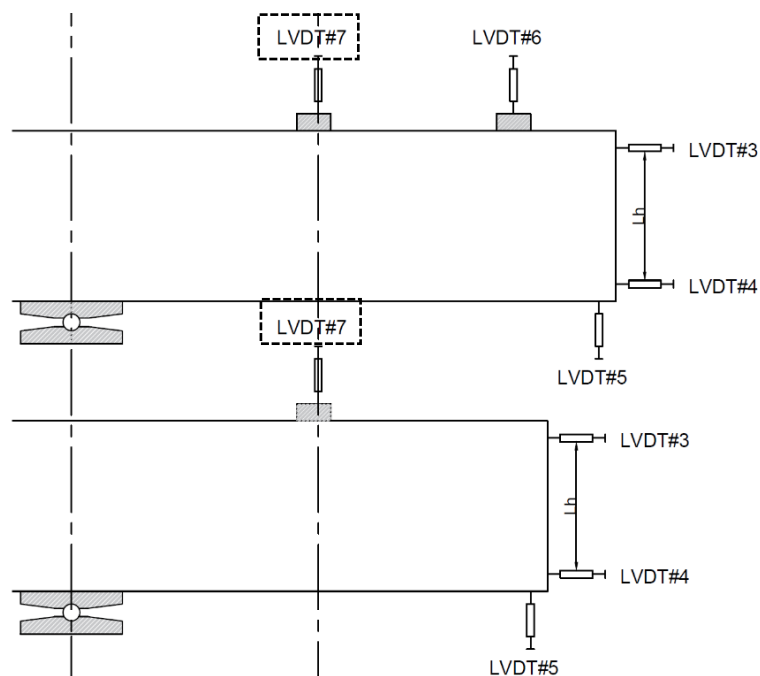


Figure 4.48: Location of the transducer (LVDT#7) in series C

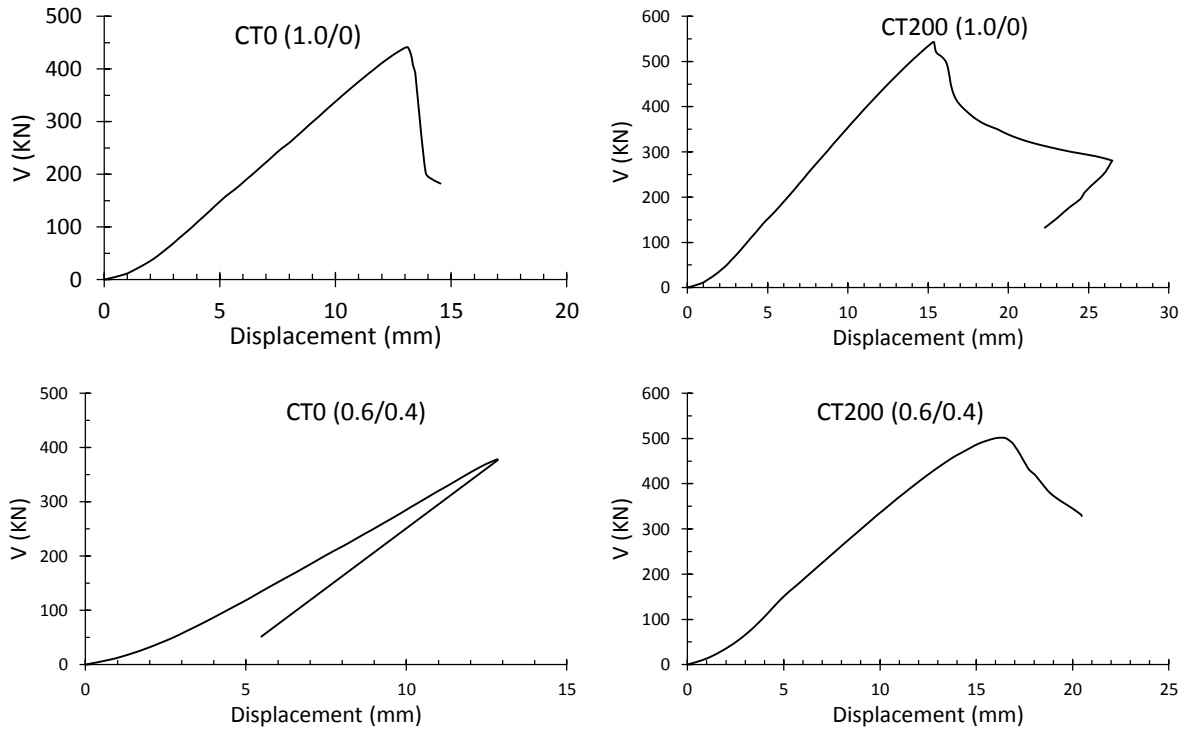


Figure 4.49: Load-deflection response for beams of series C

Figure 4.50 compares deflections in the pairs of beams without and with shear reinforcement. It shows that applying part of the load outside the shear enhancement zone at $3.0d$ reduced the total failure load compared with the companion beams just loaded at $1.66d$ from the support centreline. The reduction in strength is most significant for the beams without shear reinforcement.

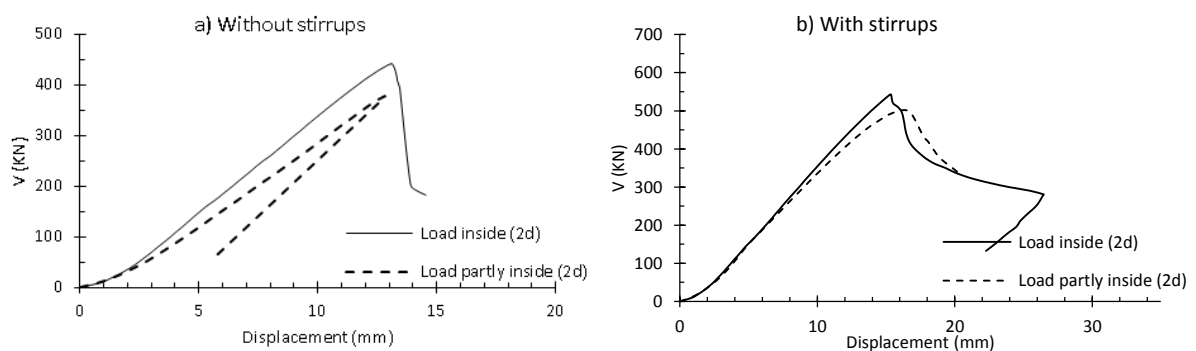


Figure 4.50: Effect of partially applying the load partially outside ($2d$) for beams a) without shear reinforcement and b) with shear reinforcement.

Figure 4.51 shows the influence of shear reinforcement on the displacement and failure load of beams loaded both entirely within and partly outside the shear enhancement zone. The figure shows the increase in strength provided by the shear reinforcement is noticeable for both cases.

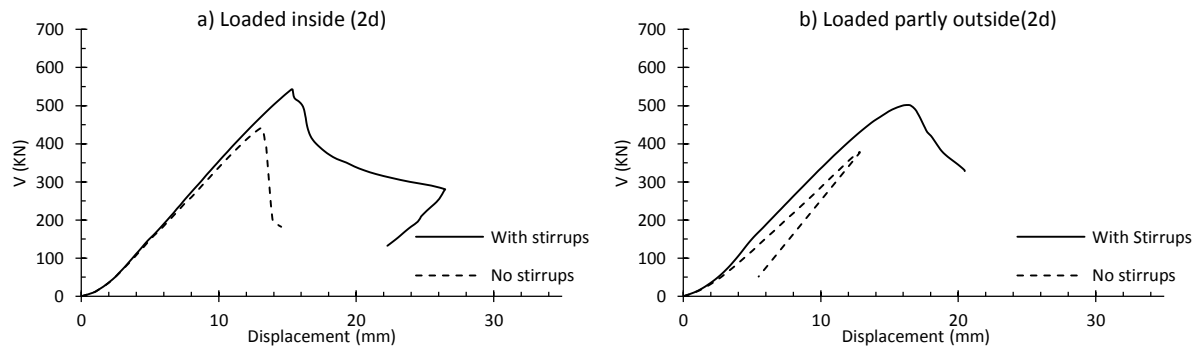


Figure 4.51: Effect shear reinforcement in beams loaded a) inside ($2d$) and b) partially outside ($2d$)

4.5.5. Reinforcement strains

Strain gauges were used to measure strain in the longitudinal reinforcement at the locations indicated in Figure 4.52. The strains in the longitudinal reinforcement of beams in series C are shown in Figure 4.53. No yielding occurred in the flexural tensile reinforcement of any of the beams. Only beam CT200 (0.6/0.4) experienced yielding of the compressive reinforcement at failure.

Strain gauges were placed on the top and bottom longitudinal bars to either side of the loading plates. Since these gauges were subject to damage during casting or loading, three strain gauges were placed at the inside edge of the loading plate where dowel action is significant. Two gauges were placed on the top and bottom of the bar as previously with an additional gauge placed on the side of the bar. This enabled meaningful results to be obtained if either the top or bottom gauges was lost as was the case for beam CT0 (1.0/0). The strains at edges of loading and support plates are shown in Figure 4.54.

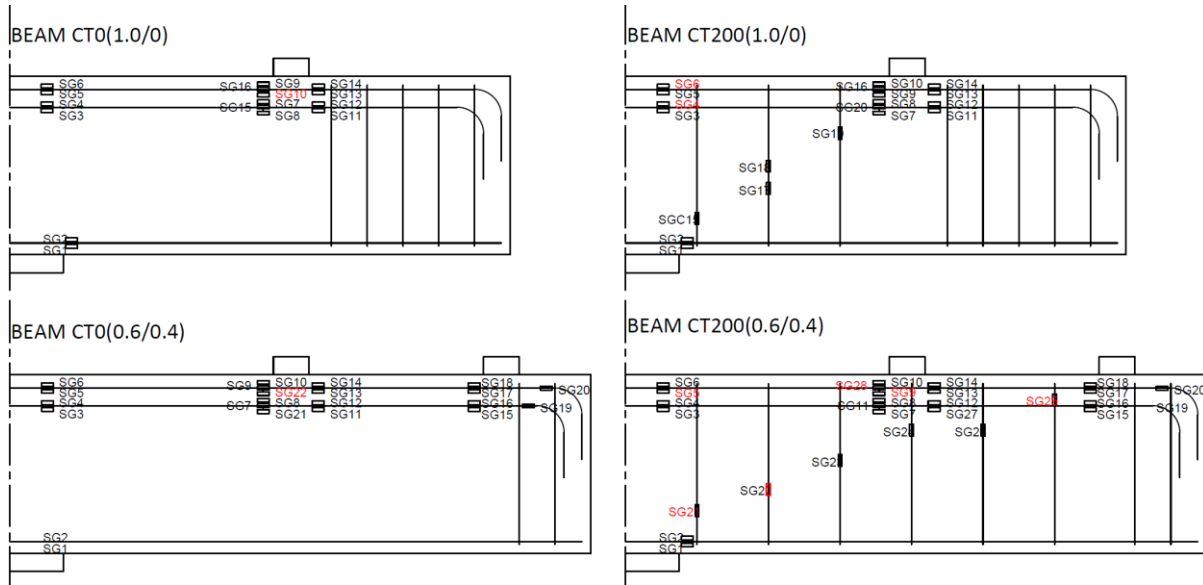


Figure 4.52: Strain gauges locations and labels for beams series C

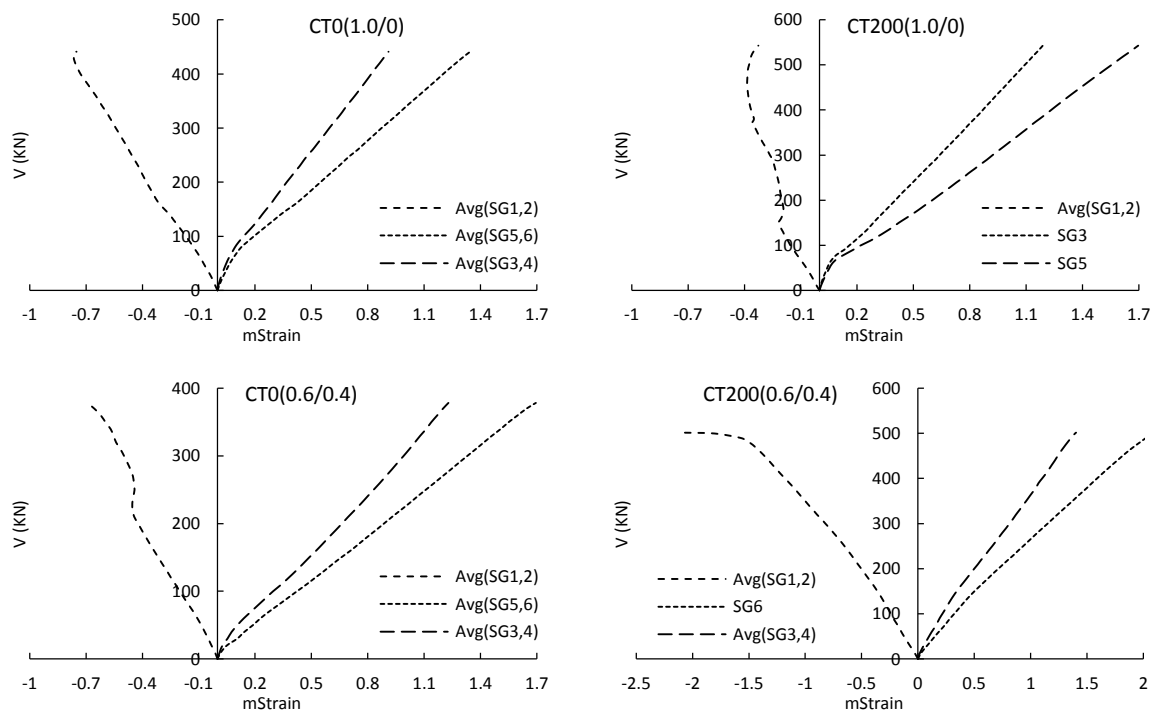


Figure 4.53: the flexural tensile and compressive strains of series C of beams

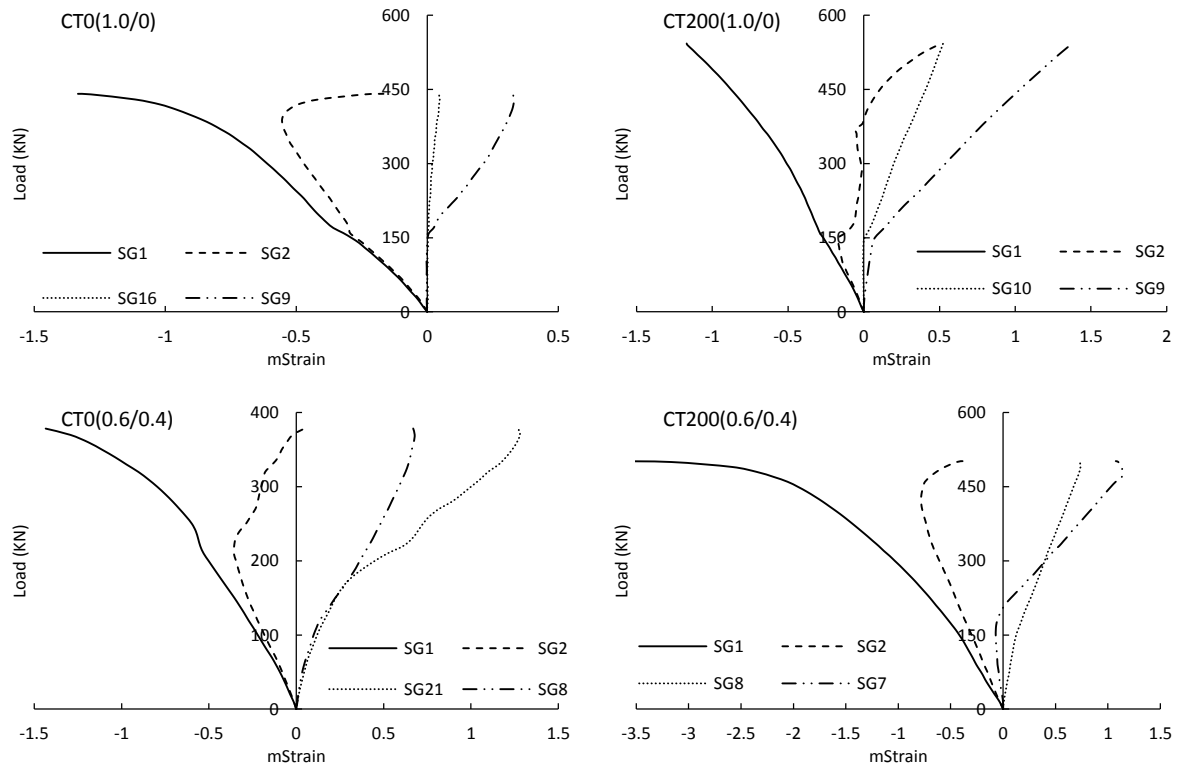


Figure 4.54 Reinforcement strains at dowel locations – series C

Although three strain gauges were used at locations of dowel action, two strain gauges malfunctioned in one of the tensile reinforcement of beam CT200 (0.6/0.4). The measurement of stirrup strain was also affected in beam CT200 (0.6/0.4) by the failure plane being wrongly predicted by the NLFEA. This difference between actual and expected failure plane also influenced the stirrup strains as discussed later.

The difference in longitudinal reinforcement strain to either side of the loading plates depends on the bond stress, which is enhanced by transverse confinement from the loading plate. This reduction in reinforcement strain across the width of the loading plate was greatest in beams loaded with single point load. This reduction was calculated based on the strains in the top reinforcement layer as shown in Figure 4.55. However, for beam CT0 (0.6/0.4) it was calculated for the lower reinforcement layer as the upper reinforcement gauge malfunctioned earlier.

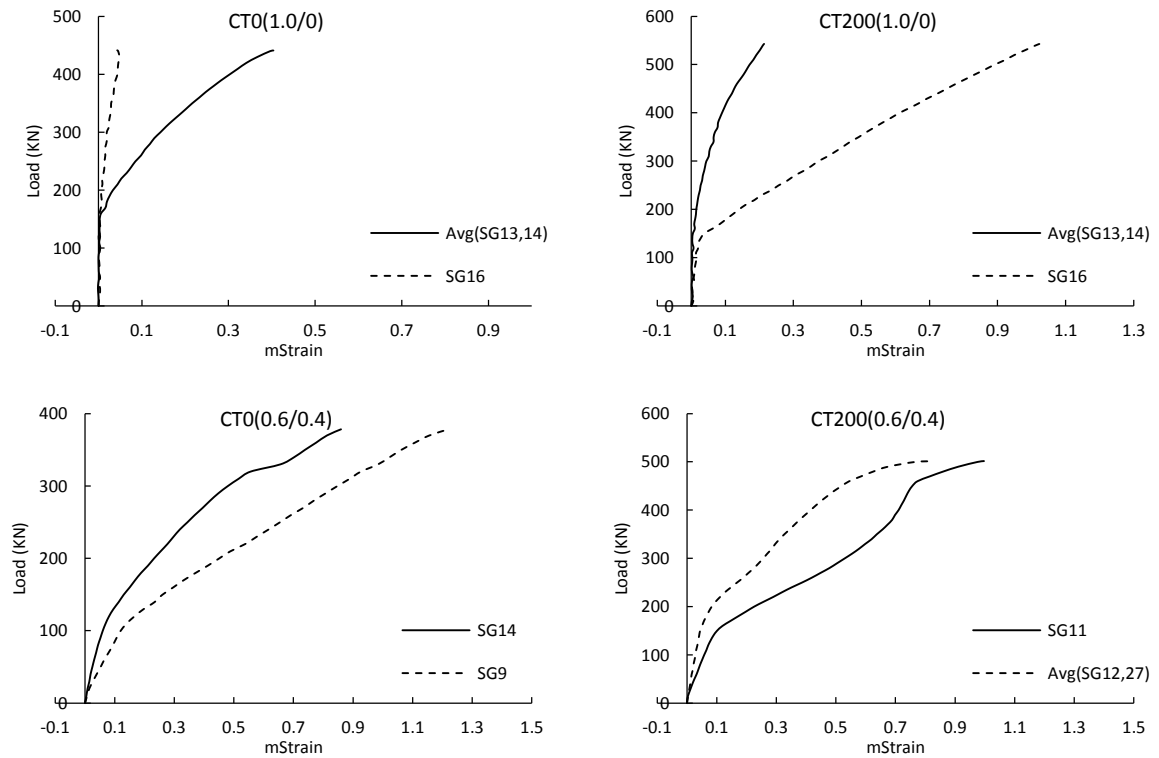


Figure 4.55: Reduction in the longitudinal reinforcement strain due to the presence of transverse confinement in series C

Two beams in series C contained shear reinforcement. Readings of strain gauges indicated that yielding occurred only in one strain gauge out of the successful eight gauges attached to the shear reinforcement in these two beams. Although this does not necessarily mean the reinforcement did not yield, it indicates that the stress levels in the shear reinforcement were lower for this series of beams.

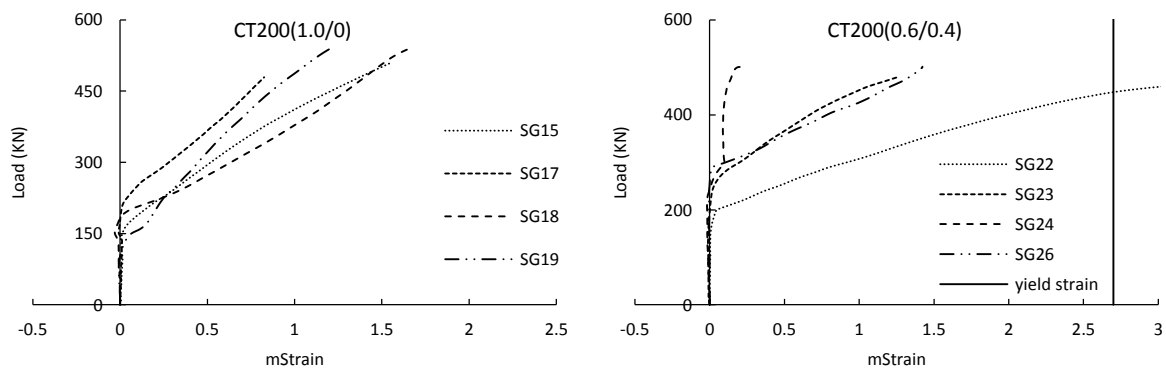


Figure 4.56: Shear reinforcement strains for series C

4.6. Conclusions

The results of the twelve beams tested in this research are presented in this chapter. Presented results include material strengths, beam failure loads and load-deflection response, crack development and kinematics and reinforcement strains.

The beams were cast in three groups of four with each group cast from a single batch of ready-mixed concrete specified to have strength class C25/30, consistency class S3 and limestone aggregate with a maximum size of 20mm. A total of 18 (36 for Series A) 100 mm cubes, 12 cylinders (100 mm diameter \times 200 mm long) for compressive strength, and 12 cylinders (150 mm diameter \times 300 mm long) for split cylinder tensile strength were cast with each series of beams. Half the specimens were cured in water at 20°C with the remainder cured in air alongside the beams. Cubes were tested at regular intervals to establish the development of compressive strength with time as well as the cube strength at the time of testing each beam. The cylinders were tested on the same day as the first and last beam test of each series. Compressive cylinder strengths were estimated for intermediate beam tests by interpolation making use of the strength development curve obtained from the cube tests. The reinforcement properties were obtained from tensile tests in which the axial strain was measured using a digital video extensometer.

The beams were loaded in displacement control to capture the post-failure behaviour. Series A considered the influence of loading face for matching pairs of beams without and with shear reinforcement. Due to rotational friction in the loading arrangement, which was eliminated in subsequent tests, the loading ratios in tests AT0 (0.5/0.5) and AT200 (0.5/0.5) were 0.58/0.42 rather than 0.5/0.5 as intended. The results for this series showed that the shear force at failure of the critical outer shear span was noticeably least for comparable beams of Series A loaded on the tension face.

Series B investigated the influence of the loading ratio for pairs of loads applied within $2d$ from the face of the support on the shear capacity. The result suggest that the application of the load inside $2d$ of the support reduced the failure load of the critical outer shear plane. The reduction in failure load of the outer shear plane increased with increasing inner load.

Series C examined the effect of partially loading beams both within and outside $2d$ from the face of the support. The results showed that applying an additional point load outside the shear enhancement zone ($2d$) reduced the shear strength of the beam. The critical shear

plane was the outer for the beam without shear reinforcement while the shear plane was the inner for the beam with the shear reinforcement.

The Influence of tension face loading on shear resistance, the prediction of critical failure plane for tested beams, the effect of the loading ratio on the failure plane and the effect of the transfer compression on the bond force are further discussed in details in Chapter 7.

CHAPTER 5. CRACKS KINEMATICS AND SHEAR TRANSFER MECHANISMS

5.1. Introduction

Various models have been developed to describe the deformation and crack kinematics of beams loaded in shear (Mihaylov et al., 2013, Mihaylov et al., 2015, Vecchio and Collins, 1986, Mihaylov, 2015). Of these, the Two Parameter Kinematic Theory (2PKT (Mihaylov et al., 2013)) and the Five-Spring Model (Mihaylov, 2015) provide simple procedures for estimating the deformation, crack kinematics, contribution of each shear transfer action and ultimate strength of deep beams loaded in shear. However, the provisions of the 2PKT and the five-spring model are derived for simply supported beams and are not directly applicable to the case of beams loaded with multiple point loads. Modifications are made in this chapter to the 2PKT and the five-Spring model to enable them to be applied to the tested beams.

Subsequently, deformation measurements obtained using DIC and LVDTs are used to assess the ability of the 2PKT and the five-spring model to describe the deformations of the tested beams. The estimated ultimate strength, load-deflection curves and crack kinematics obtained from the five-spring model are also compared with the experimental results. Finally, the contribution of each shear resisting mechanism to resistance is calculated using the five-spring model as well as crack displacements derived from DIC measurements. The latter contributions are evaluated using a range of models from the literature, which are reviewed in Chapter 2.

5.2. Description of Beams Deformation Using 2PKT

The 2PKT gives acceptable estimations of the full displacement fields of simply supported deep beams during tests (Mihaylov et al., 2013). The accuracy of the predictions depends on the accuracy of the obtained deformation measurements and the model assumptions. Using DIC increases the accuracy of the measured deformations and allows the use of finer deformation grids than originally employed by Mihaylov (2013). In this section, the two

parameters of the theory (the average strain $\varepsilon_{t,avg}$ and the shear displacement Δ_c) are derived from DIC and LVDT measurements obtained during the tests as shown in Figure 5.1. The 2PKT and the five-spring model make use of the same assumptions and methodology to evaluate beam deformations (the parameters $\varepsilon_{t,avg}$ and Δ_c). This is discussed below for the two configurations shown in Figure 5.1.

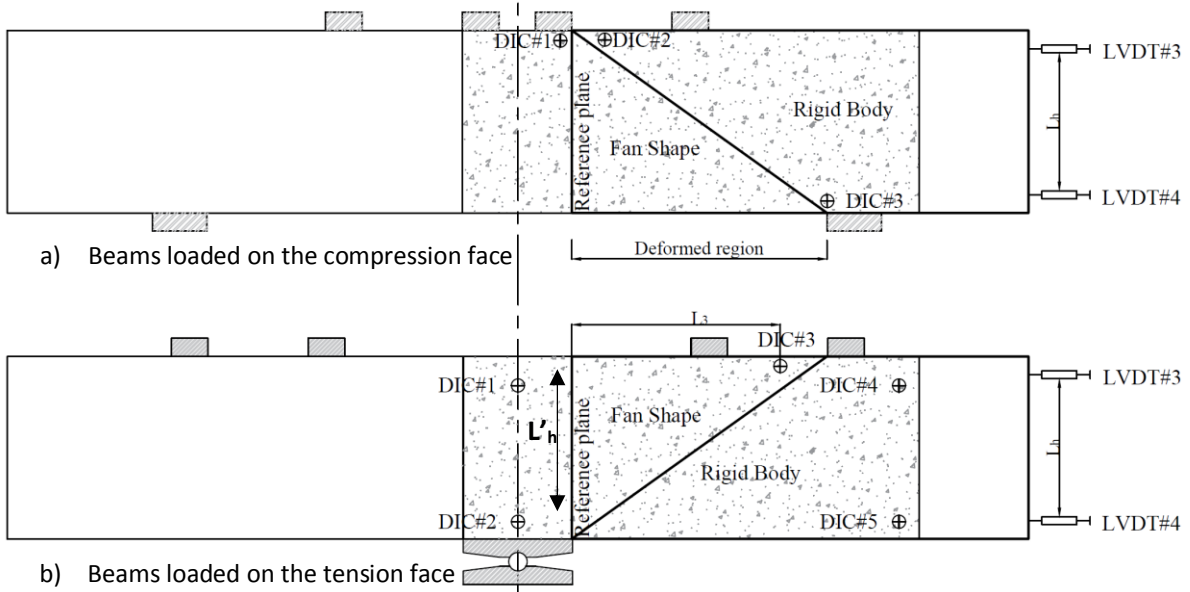


Figure 5.1: Instrumentation used to calculate parameters of the 2PKT for beams loaded on a) the compression face and b) the tension face.

5.2.1. Deformation of beams loaded on the compression face

Apart from the second point load, this case is similar to the original configuration assumed in the 2PKT (Mihaylov et al., 2013). To calculate the average strain $\varepsilon_{t,avg}$, the rotation of the rigid body φ_{block} was first determined as follows:

$$\varphi_{block} = \frac{(LVDT\#3 - LVDT\#4)}{L_h} \quad \text{Equation 5.1}$$

In which LVDT#3 and #4 depict the horizontal displacements measured at these transducers (see Figure 5.1) and L_h is the vertical distance between the two transducers. The block rotation φ_{block} and the crack angle (α) can be used to calculate the average strain in the tension reinforcement ($\varepsilon_{t,avg}$) (Kueres, 2018) as follows:

$$\varepsilon_{t,avg} = \varphi_{block} \cdot \frac{d}{l_t} \quad \text{Equation 5.2}$$

$$l_t = d \cot \alpha + S_{cr} \quad \text{Equation 5.3}$$

$$S_{cr} = \frac{\phi h}{40\rho_l d} \quad \text{Equation 5.4}$$

The spacing between the radial cracks S_{cr} (named S_{max} in the 2PKT) is expressed in terms of the longitudinal reinforcement ration ρ_l ; the effective depth d and the diameter of the bar ϕ (refer to Figure 2.17 in Chapter 2 for the description of l_t , ϕ_{block} , S_{cr} etc.). The relative vertical displacement between DIC#1 and DIC#2 constitutes the shear displacement Δ_c for beams loaded on the compression face.

A grid with an element size of 50mm was used to assess the ability of the 2PKT to describe the experimentally observed deformed shape of beams loaded on the compression face. To eliminate free body displacements, the measured deformations for compression face loading were corrected as follows:

1. The 2PKT assumes the reference plane (shown in Figure 5.1) remains vertical with no flexural rotation. Test measurements showed that this reference plane rotated in the tests (refer to Figure 5.2). Measured rotations and displacements were corrected for beams loaded in the compression face by tracking two points in the original reference plane to calculate the correction angle (see Figure 5.2). Correction for the balanced cantilever beams is described later in section 5.2.2

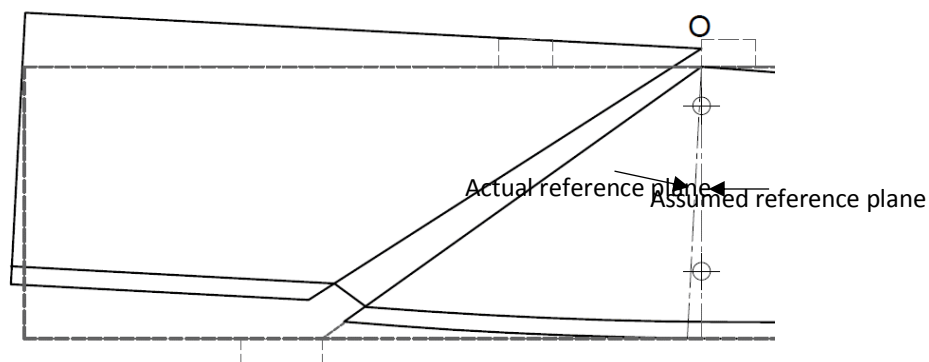


Figure 5.2: Correction of the rotation for beams loaded on the compression face

2. While the bottom support should ideally be fixed in the vertical direction, small vertical displacements were recorded during the test (in location DIC#3 for beams loaded in the compression), which indicated a max settlement of the support (between 0.7 to 1.23 mm). This settlement was subtracted from the measured vertical deformations to obtain the beam deformation relative to the support.

Using measured parameters $\varepsilon_{t,avg}$ and Δ_c , the deformed shape can be evaluated using the 2PKT as described by Equation 2.81 to Equation 5.5: (see section 2.4.2 of Chapter 2)

- For points below the crack (Fan part with radial cracks – refer to Figure 2.18 in Chapter 2)

$$\delta_x(x, z) = \varepsilon_{t,avg} \cdot x \quad \text{Equation 5.2}$$

$$\delta_z(x, z) = \frac{\varepsilon_{t,avg} \cdot x^2}{h - z} \quad \text{Equation 5.3}$$

- For points above the crack (Rigid body block – refer to Figure 2.18 in Chapter 2)

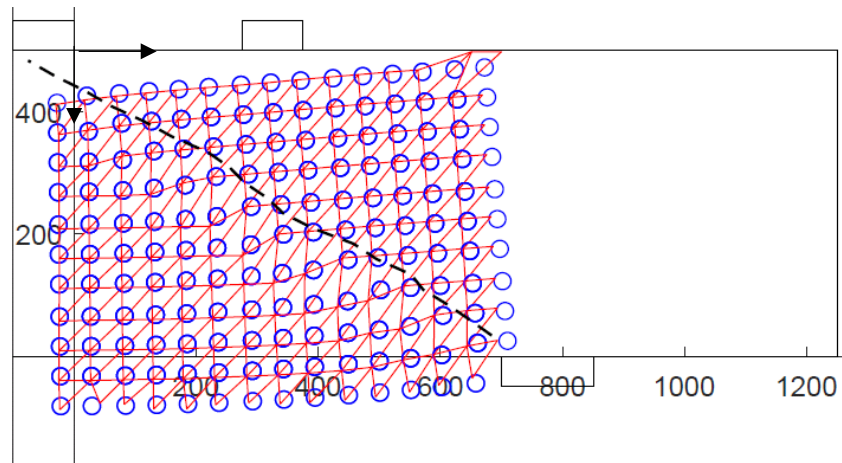
$$\delta_x(x, z) = \varepsilon_{t,avg} \cdot (h - z) \cot \alpha \quad \text{Equation 5.4}$$

$$\delta_z(x, z) = \varepsilon_{t,avg} \cdot x \cot \alpha + \Delta_c \quad \text{Equation 5.5}$$

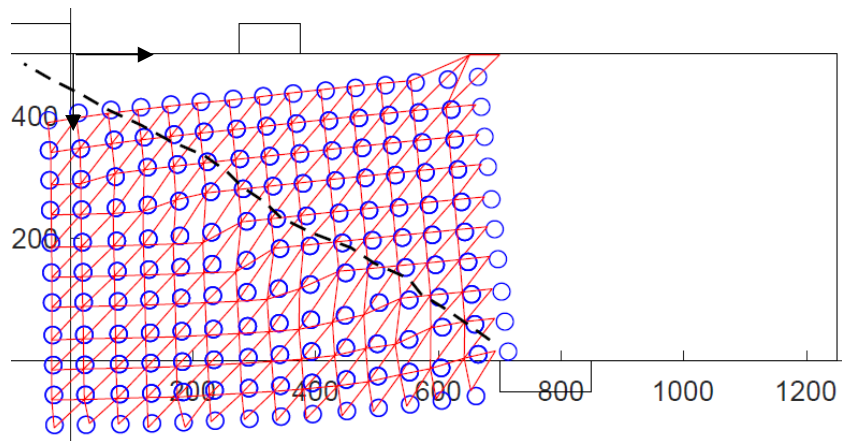
Comparisons were made at three different load stages:

1. After the appearance of first visual cracks (around 0.5 to $0.6V_{max}$),
2. An intermediate point between the first crack and the failure load (around $0.75V_{max}$),
3. Just prior to failure (around $0.95V_{max}$).

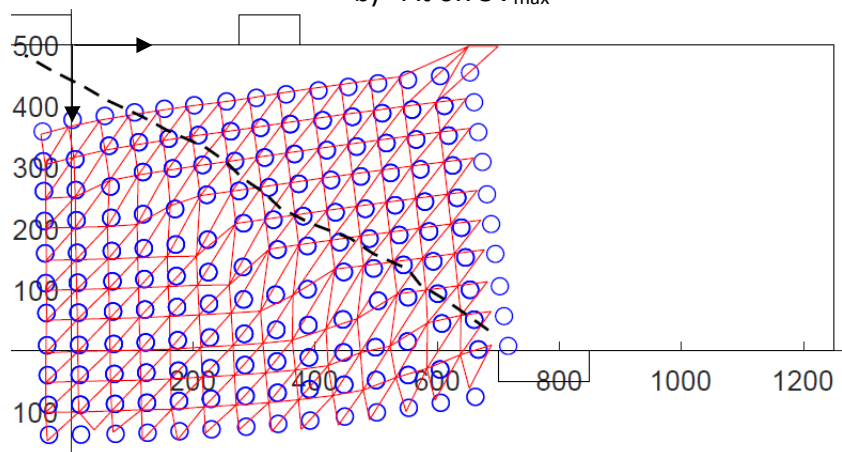
The measured and predicted displacements are compared below in Figure 5.3 for beam AC0 (0.5/0.5) which was loaded on the compression face. The measured deformation (deformation $\times 30$) obtained from the DIC was drawn as shown in Figure 5.3. The deformed locations of the grid calculated using the 2PKT was plotted in blue circle (deformation $\times 30$). As seen from the figure, predictions given by the 2PKT were reasonably accurate for beams loaded on the compression face, particularly for stages (1) and (2) described above where the average error between predicted and measured deformation was around $\mp 10\%$. For stage (3), where more flexural and shear cracks appeared, the error increased to around $\mp 20\%$. The 2PKT also gave accurate predictions for the maximum deformation. As cracks widen, errors in predicted displacements increase in the cracked concrete as shown in Figure 5.3 – c. It can be seen that for beams loaded on the compression face, the deformations were reasonably accurately predicted for up to 95% of the maximum failure load, particularly for the rigid body where no flexural cracks appeared.



a) At $0.50V_{max}$



b) At $0.75V_{max}$



c) At $0.95V_{max}$

Figure 5.3: Comparison between the 2PKT and the measured deformation for beam AC0 (0.5/0.5) – Deformation X30

The maximum measured resultant deformation at location (0,-500) obtained using the DIC system during the test was plotted against the deformation predicted using the 2PKT for beams AC0 (0.5/0.5) and AC200 (0.5/0.5) loaded on their compression face. Comparison in Figure 5.4 shows good agreement between the measured and predicted deformation with the 2PKT slightly overestimating the deformation at early stages of the load and underestimating it at near failure.

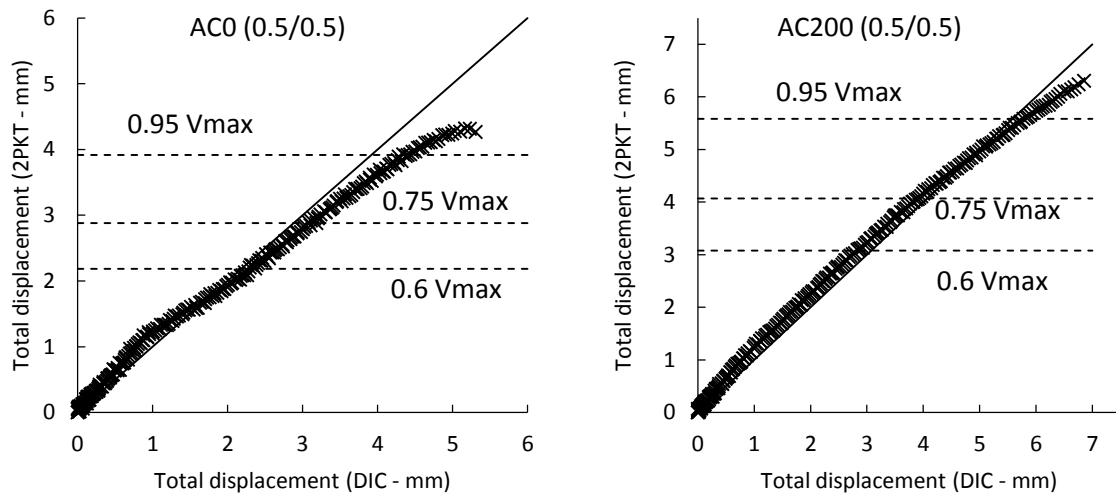


Figure 5.4: Comparison between measured and predicted maximum deformation at location (0,-500) of beams loaded on the compression face

5.2.2. Deformation of beams loaded on the tension face

For the double cantilever beams, the block rotation φ_{block} obtained using Equation 5.1 should be corrected to account for the global rotation φ_{global} of the beam due to the test configuration as mentioned earlier in Chapter 4. Corrections regarding both the rotation and measured displacements due to the global rotation were carried out as follows.

The global rotation φ_{global} can be obtained from (refer to Figure 5.1 – b).

$$\varphi_{global} = \frac{(DIC\#1 - DIC\#2)}{L'_h} \quad \text{Equation 5.6}$$

In which $DIC\#1$ and $DIC\#2$ measure the horizontal displacement at the centre of the beam. Length L'_h is the vertical distance between $DIC\#1$ and $DIC\#2$. In a few occasions, measurements LVDT#3 or #4 were not available and hence the block rotation φ_{block} was alternatively calculated using $DIC\#4$ and $\#5$. It can be seen from Figure 5.5 that these two methods give similar results.

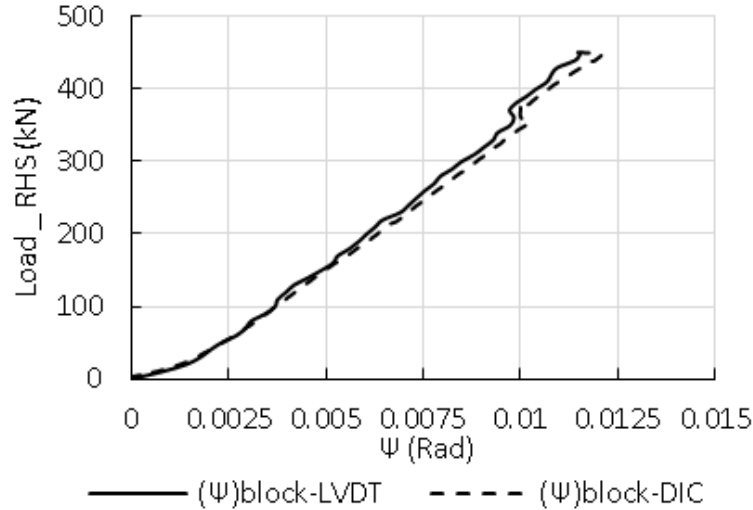


Figure 5.5: Block rotation calculated using LVDTs and DIC for beams AT0 (0.5/0.5)

The corrected block rotation φ'_{block} is the difference between the total block rotation and the global rotation of the beam:

$$\varphi'_{block} = \varphi_{block} - \varphi_{global} \quad \text{Equation 5.7}$$

The shear displacement for the double cantilever beams was calculated using the provisions given by Kueres (2018) described in Figure 5.6. The shear deformation δ_t (equivalent to Δ_c in this work) is the difference between the corrected total measured displacement δ_{total} and the flexural displacement $\delta_{flexural}$, or:

$$\Delta_c = \delta_{total} - \varphi'_{block} \cdot x_{\Delta_c} \quad \text{Equation 5.8}$$

In which x_{Δ_c} is the distance from the origin to the location where $\delta_{flexural}$ is measured. In this research, corrected total displacement was measured using LDTV#7 or DIC#3 positioned at a distance x_{Δ_c} from the support, as shown in Figure 5.7. The corrected total displacement δ_{total} was calculated using Equation 5.9 below. The second term in this equation is the deformation resulting from the global rotation (Δ_{supp} is the support displacement).

$$\delta_{total} = \text{LDTV\#7 (or DIC\#3)} - \varphi_{global} \cdot x_{\Delta_c} - \Delta_{supp} \quad \text{Equation 5.9}$$

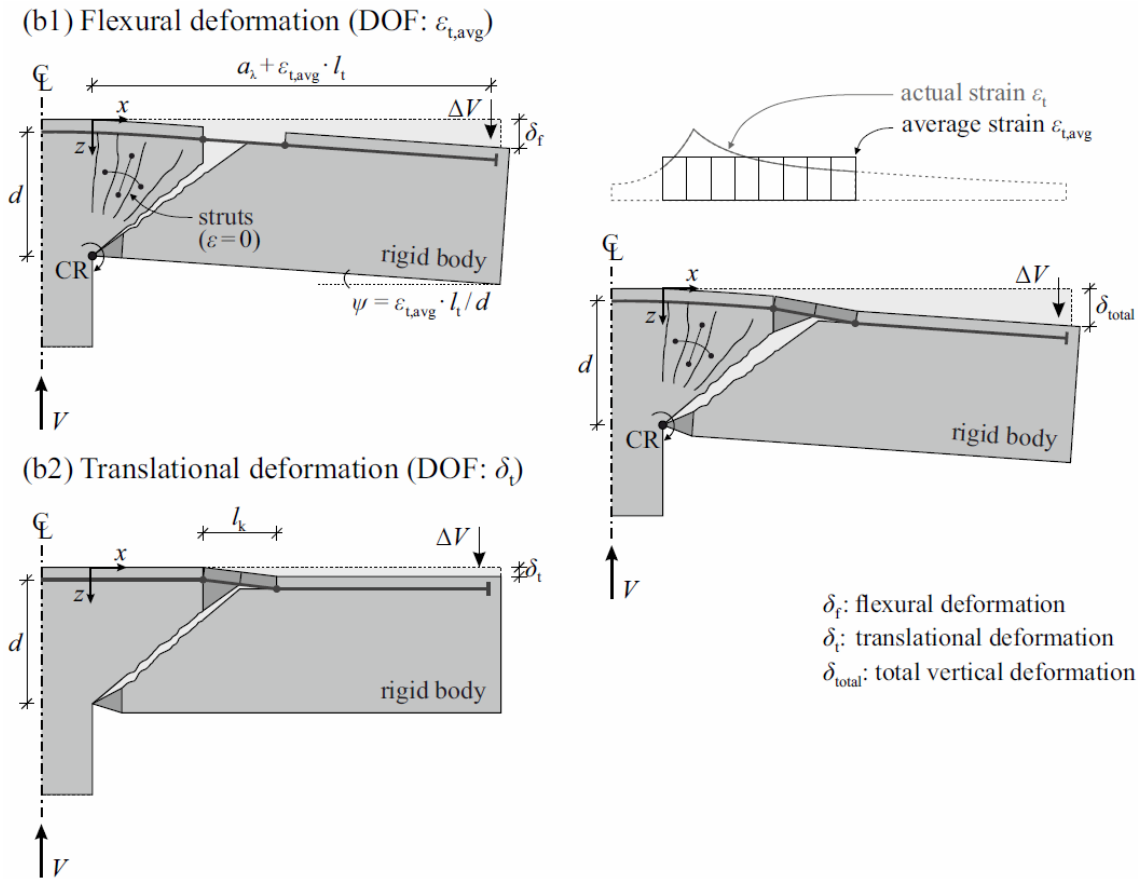


Figure 5.6: Calculations of the degrees of freedom for double cantilever beams (Kueres, 2018). Figure reproduced with permission of the rights holder, KUERES, D. A.

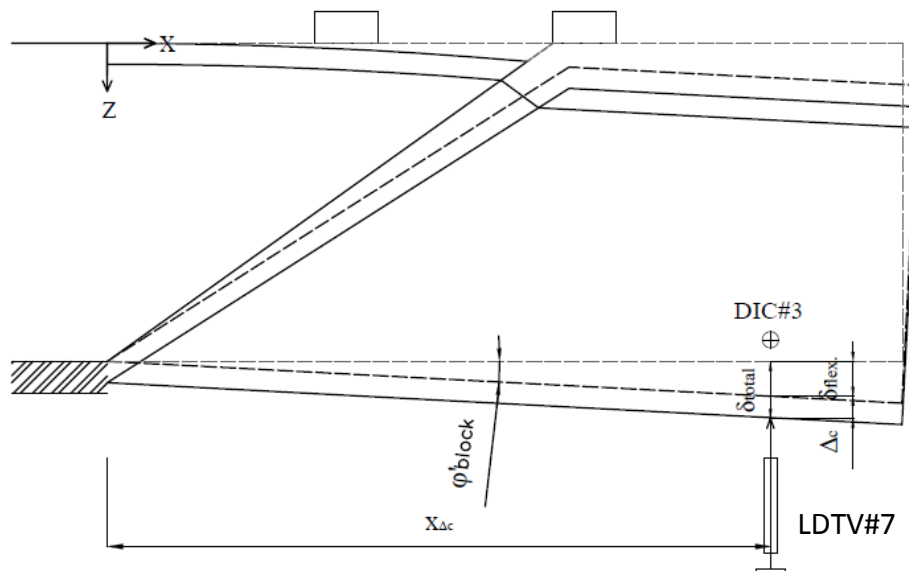


Figure 5.7: Calculation of the shear displacement for corrected double cantilever beams

If the original provisions of the 2PKT for calculating the deflected shape are used for beams loaded on their tension face, the resulting displacements are less accurate than obtained for

beams loaded on their compression face. Figure 5.8 shows the deformation of beam CT0 (0.6/0.4) loaded on its tension face. The significant appearance of the blue lines particularly from the inner shear span to the edge of the beam shows a noticeable reduction in the accuracy of predictions compared to Figure 5.3, where almost no blue lines appeared. The source of this error is investigated in the next section where a refinement is proposed to the 2PKT for the tested cantilever beams, with two point loads in the shear span.

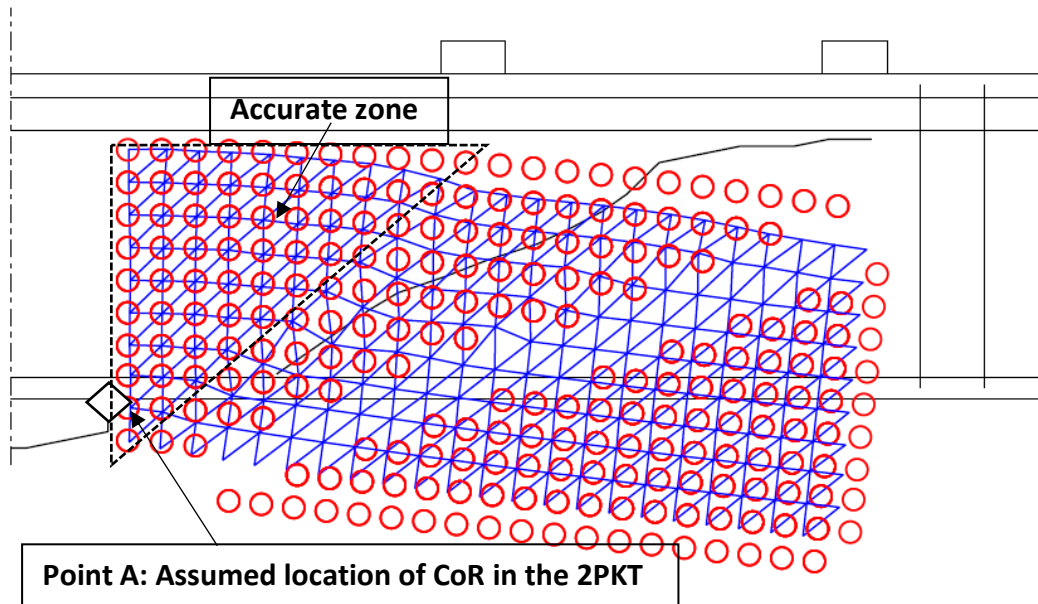


Figure 5.8: The Deformed shape of beam CT0 (0.6/0.4) obtained with original 2PKT at $0.95 V_{max}$ (deformation X30)

5.2.3. Modification of the 2PKT's description of the deformation for the double cantilever beams

Kueres (2018) reported that in his slab test, which had a comparable configuration to the setup of the balanced cantilever beams; the centre of rotation (CoR) of the rigid body is not at the centre of the loading point (Point A) in Figure 5.8 as assumed in the 2PKT which partially corrects for this by introducing a shear displacement at A.

Kueres (2018) determined the centre of rotation for reinforced concrete slabs with variable thicknesses failing in punching. He found that the experimentally observed location of the CoR varies dependent on the slenderness of the slabs (or the span to effective depth ratio). For regular slender slabs, the location of the CoR is approximately at the crack tip; however, this was not the case for compact slabs and footings. This assumption has been examined for

beams loaded on the tension face using the methodology given by Kueres and described as follows:

The deformed location of the bottom corner (x'_{out}, z'_{out}) is given by the intersection of the lines $z_w(x)$ and $z_r(x)$ (see Figure 5.9). Kueres showed that the equation of the deformed horizontal line $z_w(x)$ can be expressed as:

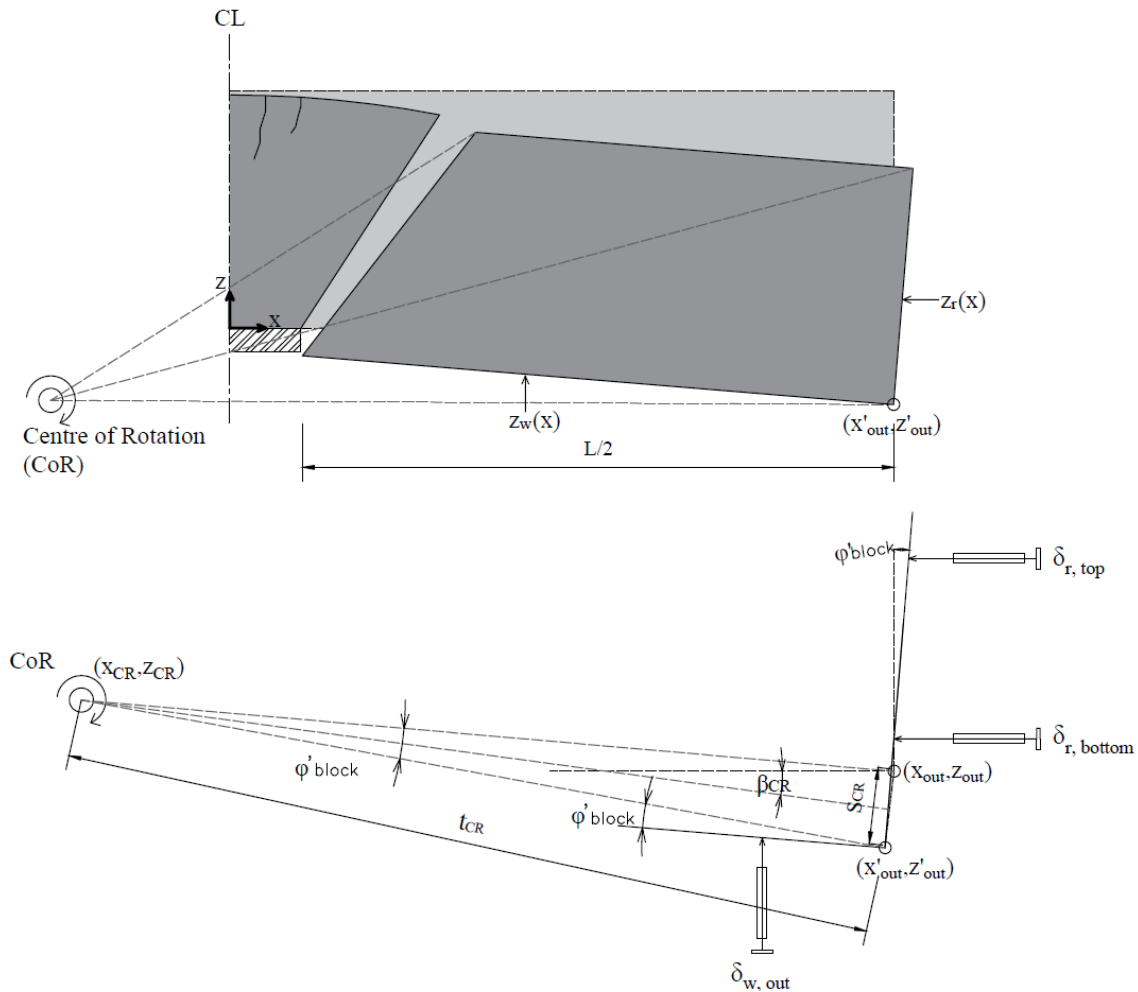


Figure 5.9: Location of the centre of rotation based on measured deformation (Kueres, 2018). Figure reproduced with permission of the rights holder, KUERES, D. A.

$$z_w(x) = a_w x + b_w \quad \text{Equation 5.10}$$

$$a_w = -\tan(\varphi'_{block})$$

$$b_w = -\delta_{w,out} - a_w \cdot x_{w,out}$$

While the equation of the deformed vertical line can be expressed as:

$$z_r(x) = a_r x + b_r \quad \text{Equation 5.11}$$

$$a_r = \cot(\varphi'_{block})$$

$$b_r = z_{r,bottom} - a_r \cdot (l/2 + \delta_{bottom})$$

The corrected rotation φ'_{block} (refer to Figure 5.7) was calculated with Equation 5.7. Deformation $\delta_{w,out}$ is the vertical displacement near the bottom edge at the location $(x_{w,out})$, while δ_{top} and δ_{bottom} are the top and bottom horizontal deformations at the end of the beam. $z_{r,bottom}$ is the vertical ordinate of the bottom horizontal LVDT. The previously mentioned measured displacement was corrected for the global rotation φ_{block} . Solving the above equations yields the following location of the bottom corner after rotation

$$x'_{out} = \frac{b_w - b_r}{a_r - a_w} \quad \text{Equation 5.12}$$

$$z'_{out} = a_r \left(\frac{b_w - b_r}{a_r - a_w} \right) + b_r \quad \text{Equation 5.13}$$

Kueres showed that the dimensions S_{CR}, t_{CR} and the angle β_{CR} shown in Figure 5.9 can be obtained as (Kueres, 2018):

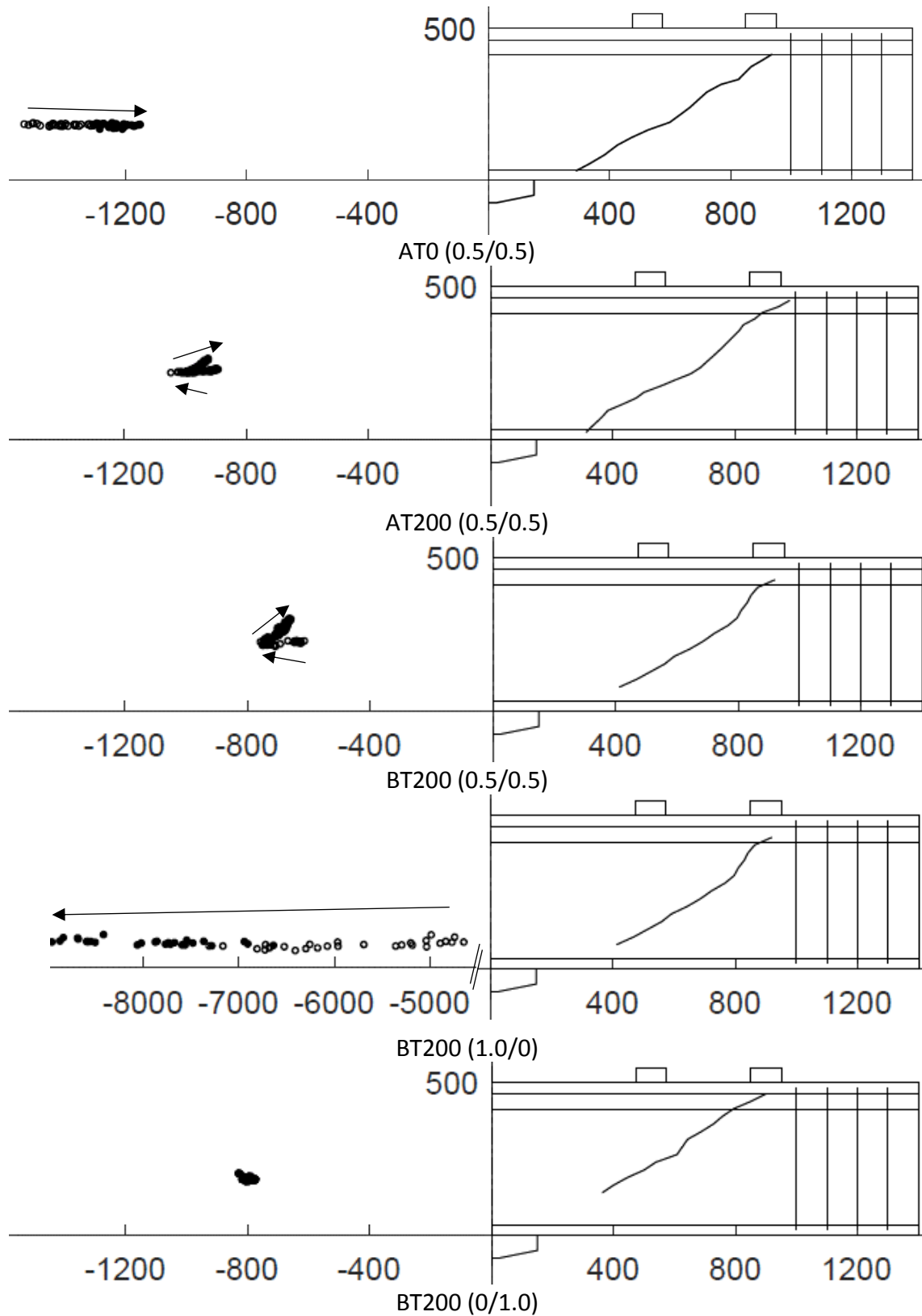
$$S_{CR} = \sqrt{\left(\frac{L}{2} - x'_{out}\right)^2 + (z'_{out})^2} \quad \text{Equation 5.14}$$

$$t_{CR} = \frac{S_{CR}}{2 \cdot \tan\left(\frac{\varphi'_{block}}{2}\right)} \quad \text{Equation 5.15}$$

$$\beta_{CR} = \arctan\left(\frac{(L/2 - x'_{out})}{-z'_{out}}\right) \quad \text{Equation 5.16}$$

The actual location of the CoR of the rigid region of beams loaded on their tension face can be obtained using Equation 5.10 to Equation 5.16. The position varies as shown in Figure 5.10 for the tested cantilever beams. The results in Figure 5.10 show that the CoR was located above its assumed location in the 2PKT (black dots in the figure indicate locations of the CoR for loads greater than 60% of the failure load and the arrow describes the direction of the movement of the CoR during the test). The consequence of the CoR being positioned above the x-axis was that a clockwise rotation of the rigid body is associated with a global horizontal displacement of the rigid body to the left. This horizontal shift was also noted by Kueres (2018) in his analysis of compact punching specimens. The great shift of the CoR in the horizontal displacement of beam BT200 (1.0/0), loaded with a single point load closer to the support,

indicated that the shear displacement was dominant, which agrees with the load configuration.



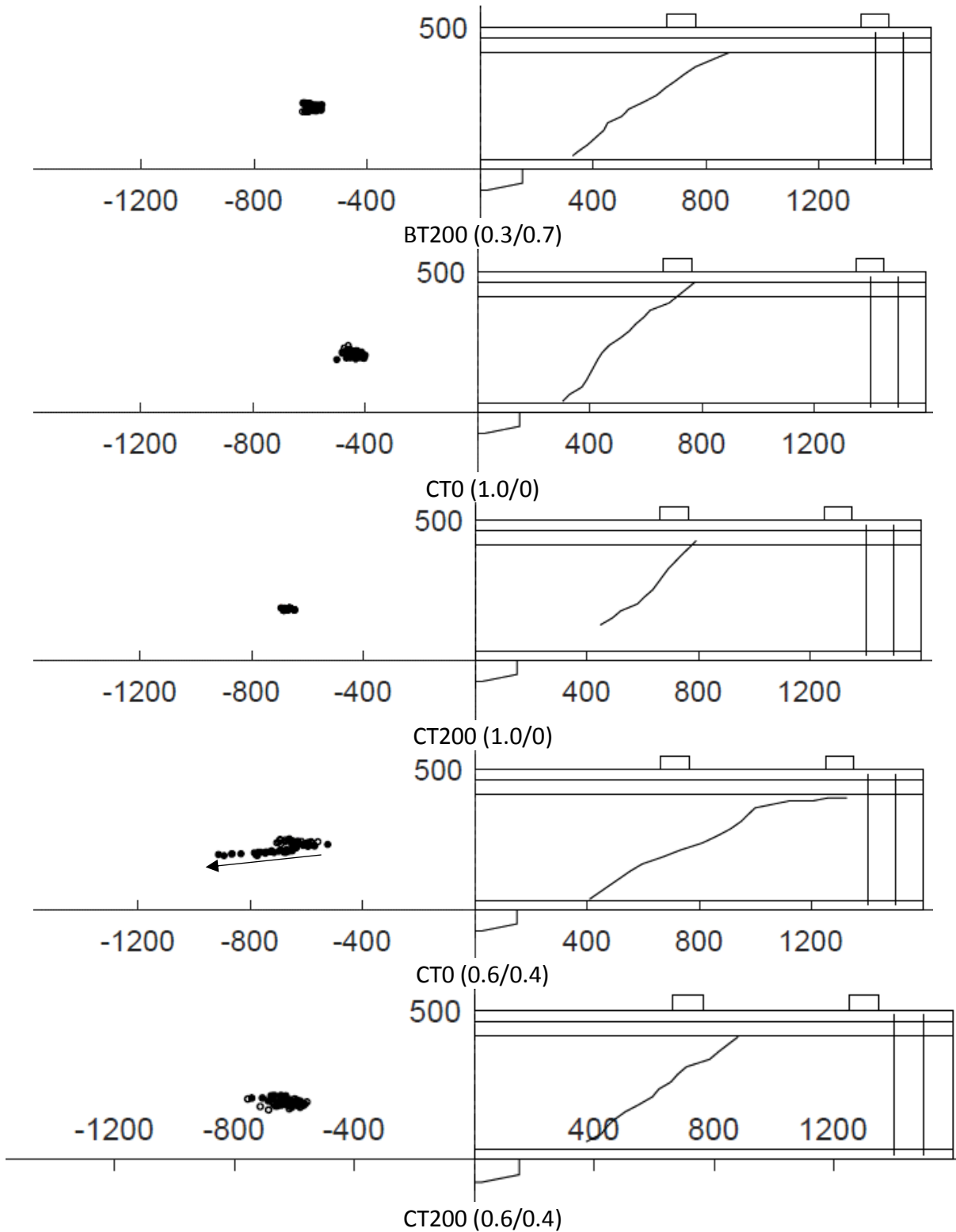


Figure 5.10: CoR for beams loaded as double cantilever beams

As discussed previously, the vertical shift of the CoR above the x-axis evident in Figure 5.10 indicates that a clockwise rotation of the rigid body below the diagonal failure crack introduces a global horizontal displacement of the rigid body to the left. This movement is

not captured by the 2PKT, which assumes that the CoR of the rigid body is positioned at point A in Figure 5.8. To illustrate the effect of the upwards shift in CoR, the variation of corrected horizontal displacement is plotted in Figure 5.11 at $0.95V_{max}$ for beam CT0 (1.0/0). The horizontal displacements are plotted along vertical planes positioned at $x = -150, 0, 50, 150$ and 350mm . The horizontal displacement is seen to be zero at the reference vertical plane at the centreline of the support ($x = -150\text{ mm}$) as required as well as at $x = 0$. The displacement at the lowest ordinate of $z = 50\text{ mm}$ is mainly due to axial shortening of the flexural compression zone of the beam. The positions of the CoR in Figure 5.10 are based on horizontal displacements measured using DIC along the line at $x = -150$. Consequently, the positions of the CoR shown in Figure 5.11 relate to the horizontal displacement of the bottom of the free body at $x = 0$ in Figure 5.11.

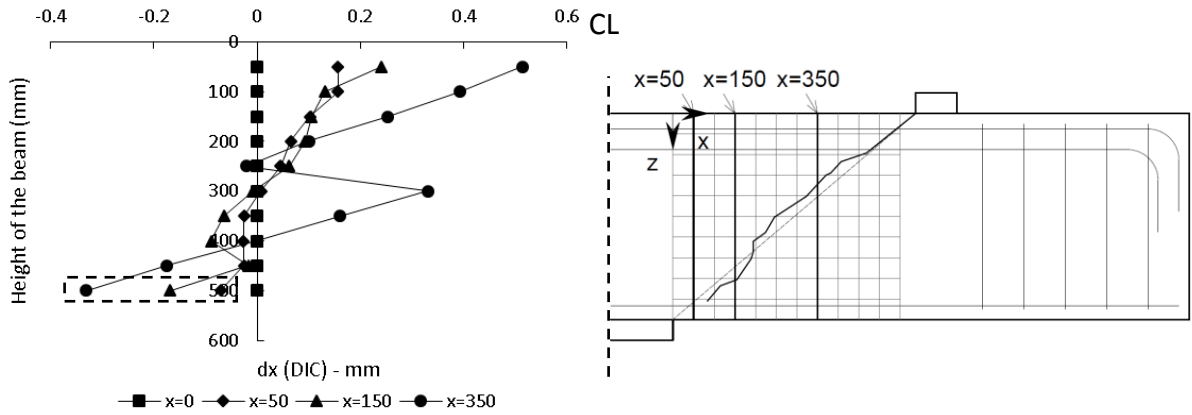


Figure 5.11: The variation of corrected horizontal displacement along the height of beam CT0 (1.0/0)

The 2PKT defines the deformation of the rigid body below the shear crack, in Figure 5.8, in terms of a rotation about the intersection of the diagonal failure crack with the extreme flexural compression fibre (point A in Figure 5.8) and a uniform vertical shear displacement. Comparison of the measured and calculated displacements in Figure 5.3 and Figure 5.8 shows that the displacements calculated using these kinematics are more accurate for the compression face loaded beams of Series A than for CT0 (0.6/0.4), which is representative of the tension face loaded beams with two point loads. Furthermore, the shear displacement is not zero throughout the fan zone as assumed in the 2PKT, neither is the distribution of tensile strain in the reinforcement is uniform as assumed in the 2PKT. As shown below, the rigid body

coordinates are better estimated if calculated in terms of rotations about the true CoR shown in Figure 5.10. In this approach, deformations of the rigid body in the x and z directions are calculated as:

$$\delta x = \varphi'_{block} \cdot (z + z_{CoR}) \quad \text{Equation 5.17}$$

$$\delta z = \varphi'_{block} \cdot (x + x_{CoR})$$

Where x_{CoR} and z_{CoR} define the position of the CoR.

Figure 5.12 shows the resulting deformations of the rigid body coordinates of beam CT0 (0.6/0.4) calculated again at $0.95V_{max}$. The displacement of the rigid body is seen to be well predicted by this approach with predictions much better than in Figure 5.8.

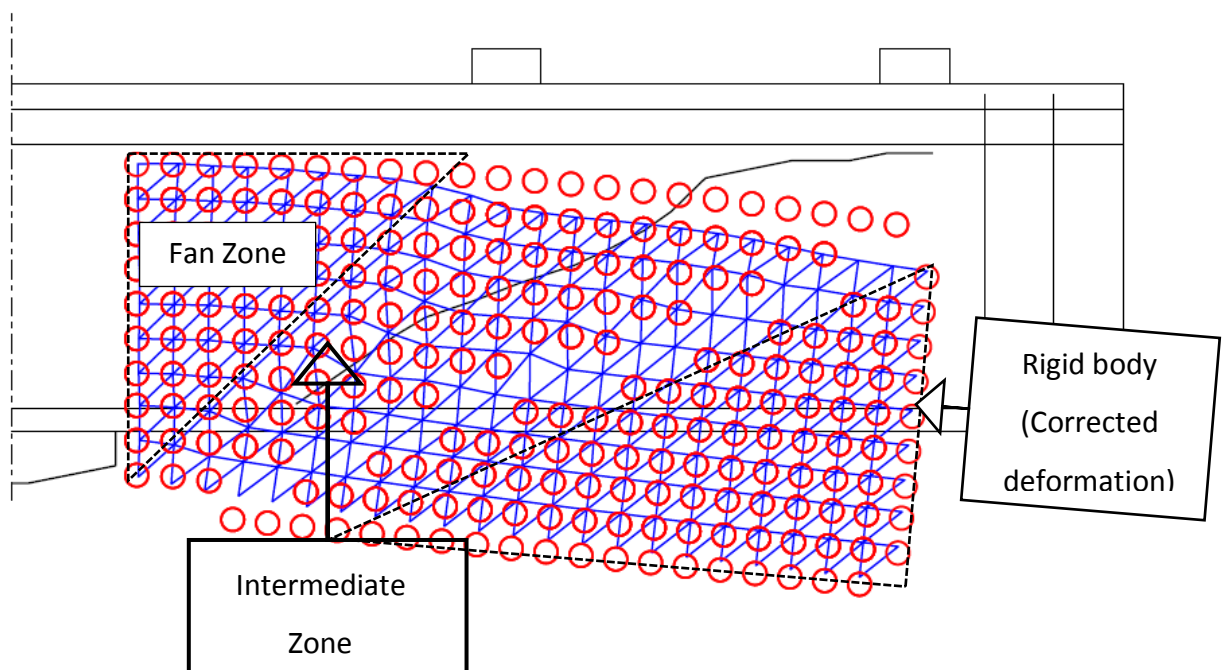


Figure 5.12: Corrected deformation of beam CT0 (0.6/0.4) calculated using actual CoR at $0.95 V_{max}$ (deformation X30)

Unlike the 2PKT, which divides the deformed shape into a fan shaped arrangement struts and a rigid body, Figure 5.12 suggests that the deformed shape of beams loaded in two-point loads on their tension face can be divided into three parts: the fan zone, the rigid body and an intermediate zone. The fan zone is similar to the one defined in the 2PKT and its deformation can be described in terms of the average strain $\varepsilon_{(t,avg)}$ using equations Equation 2.81 and Equation 5.3 from the 2PKT. The deformation of the rigid body can be described solely in terms of the rotation about the actual CoR as shown above.

Figure 5.8 shows that the deformation of the intermediate zone in Figure 5.12 is not well predicted if calculated using Equation 2.81 and Equation 5.3 of the 2PKT. The reason for this is explained by the DIC displacements, which show that, for beams with two-point loads applied on the tension face, an additional secondary crack propagates inside the fan shape between the support and the inner shear plane. Although this crack was not critical, it introduced a “partial” shear displacement (Δ'_c) for this zone (see Figure 5.13) which needs to be included in the equation of its vertical deformation.

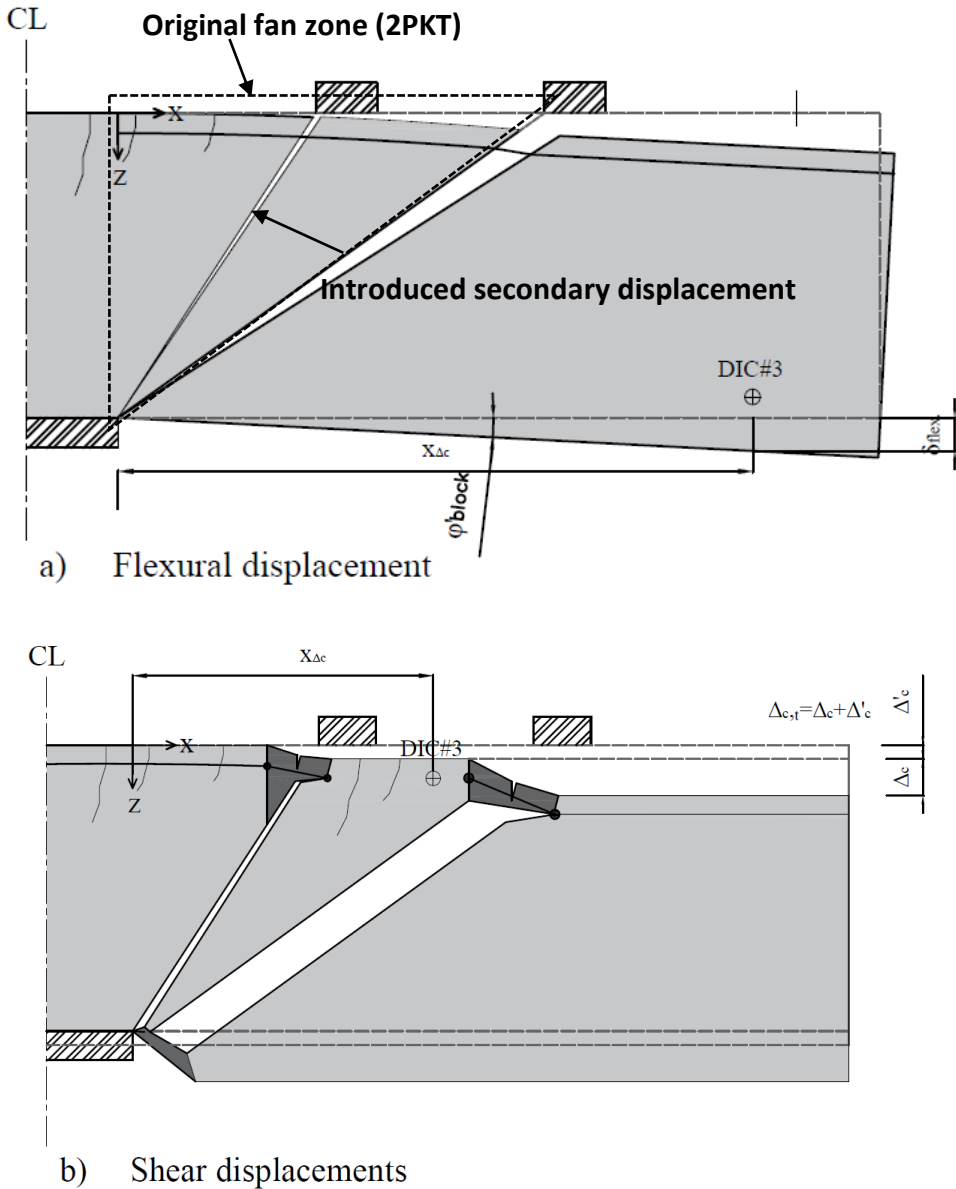


Figure 5.13: Suggested deformation of beams with two-point loads on the tension face

To validate this assumption, Figure 5.14 shows the variation of the measured vertical deformation with height in the critical shear span of beam CT0 (0.6/0.4) from $x = 50$ to $x =$

1200 mm. Two clear shifts in the vertical deformations can be distinguished in Figure 5.13. These shifts correspond to the locations of the two shear cracks in the beam and support the idea of introducing a vertical shear displacement into the equation of vertical displacement for the intermediate zone. Hence, to describe the deformation of the intermediate zone, which is treated as a fan shape in the original model, a constant shear displacement is introduced as follows:

$$\delta_x(x, z) = \varepsilon_{t,avg} \cdot x \quad \text{Equation 5.18}$$

$$\delta_z(x, z) = \frac{\varepsilon_{t,avg} \cdot x^2}{h - z} + \Delta'_c \quad \text{Equation 5.19}$$

Where Δ'_c is the first shear displacement shown in Figure 5.14. To evaluate Δ'_c , locations of DIC#3 and L_3 shown in Figure 5.1 were used instead of LVDT#7 and x_{out} used to estimate Δ_c earlier in Equation 5.8.

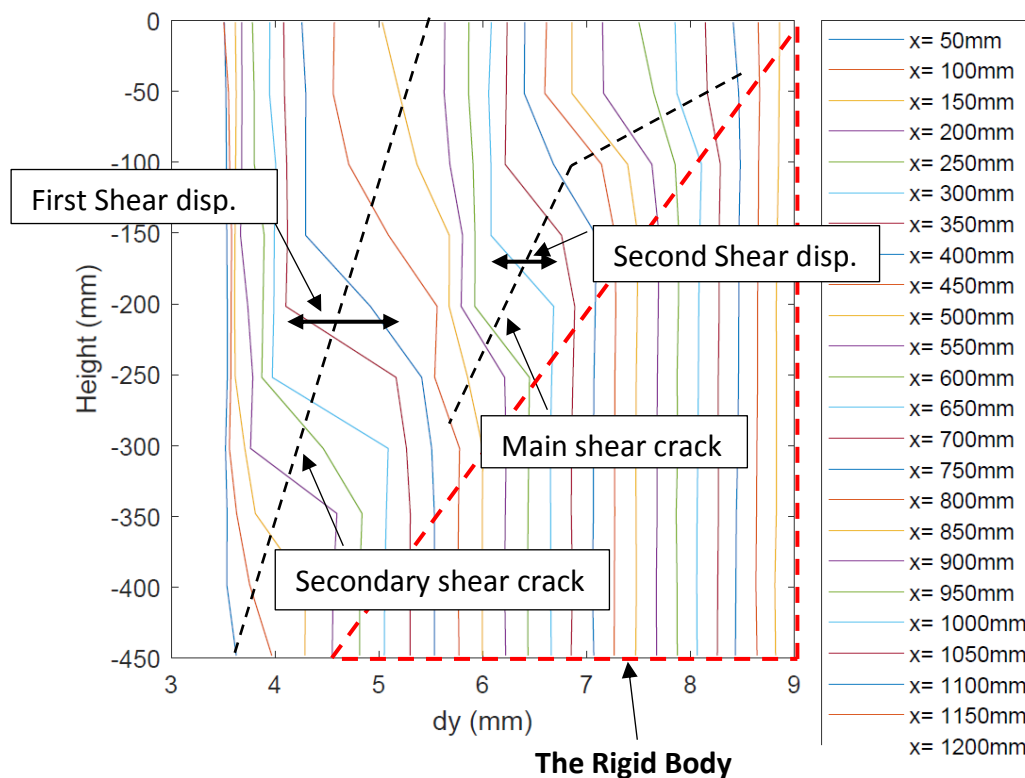


Figure 5.14: Variation of vertical deformation in the shear span with the height of double cantilever beams with two-point loads

Figure 5.14 also validates the assumption of the rigid body made by Mihaylov in the 2PKT (2013). The figure shows that the vertical deformation is constant in the rigid zone for a given horizontal distance (x). The final deformed shaped of beam CT0 (0.6/0.4) after introducing this modification is shown in Figure 5.15. It can be seen that the accuracy of the predictions

is enhanced significantly for the intermediate and rigid zones after introducing these modifications. The predictions for the other cantilever beams at $0.95V_{max}$ are presented in Figure 5.16.

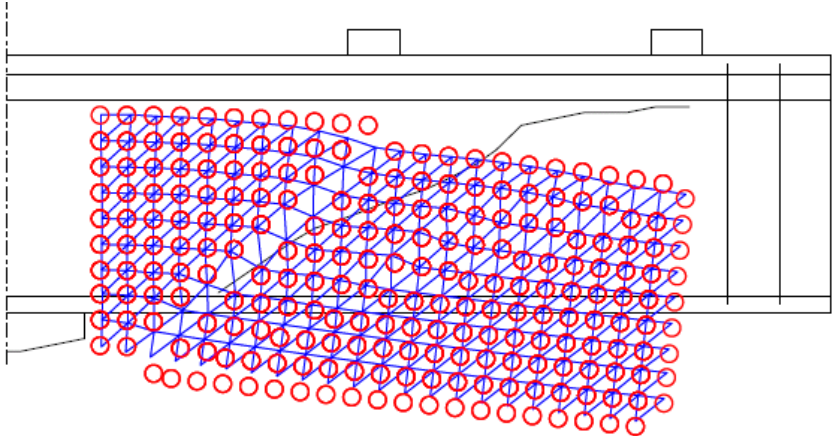
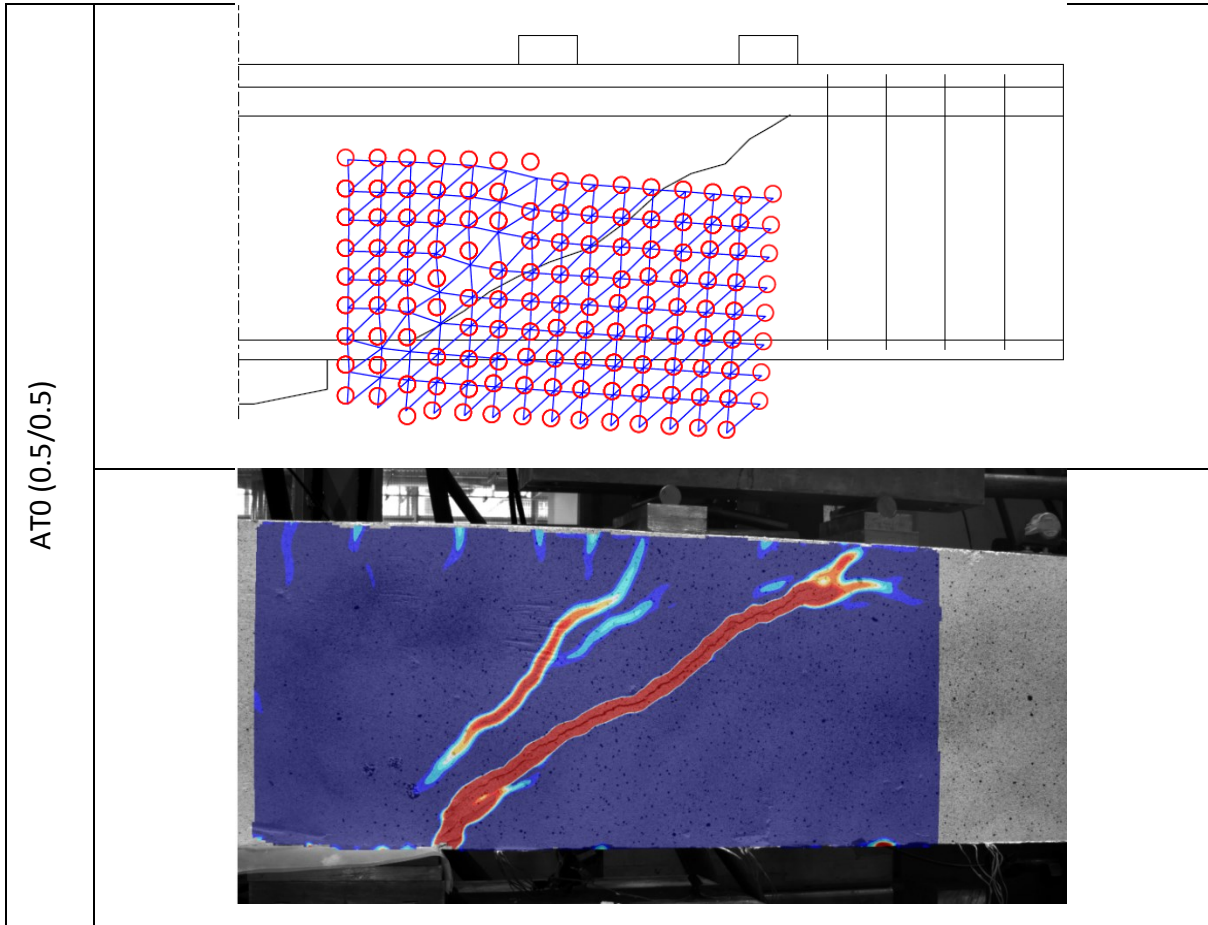
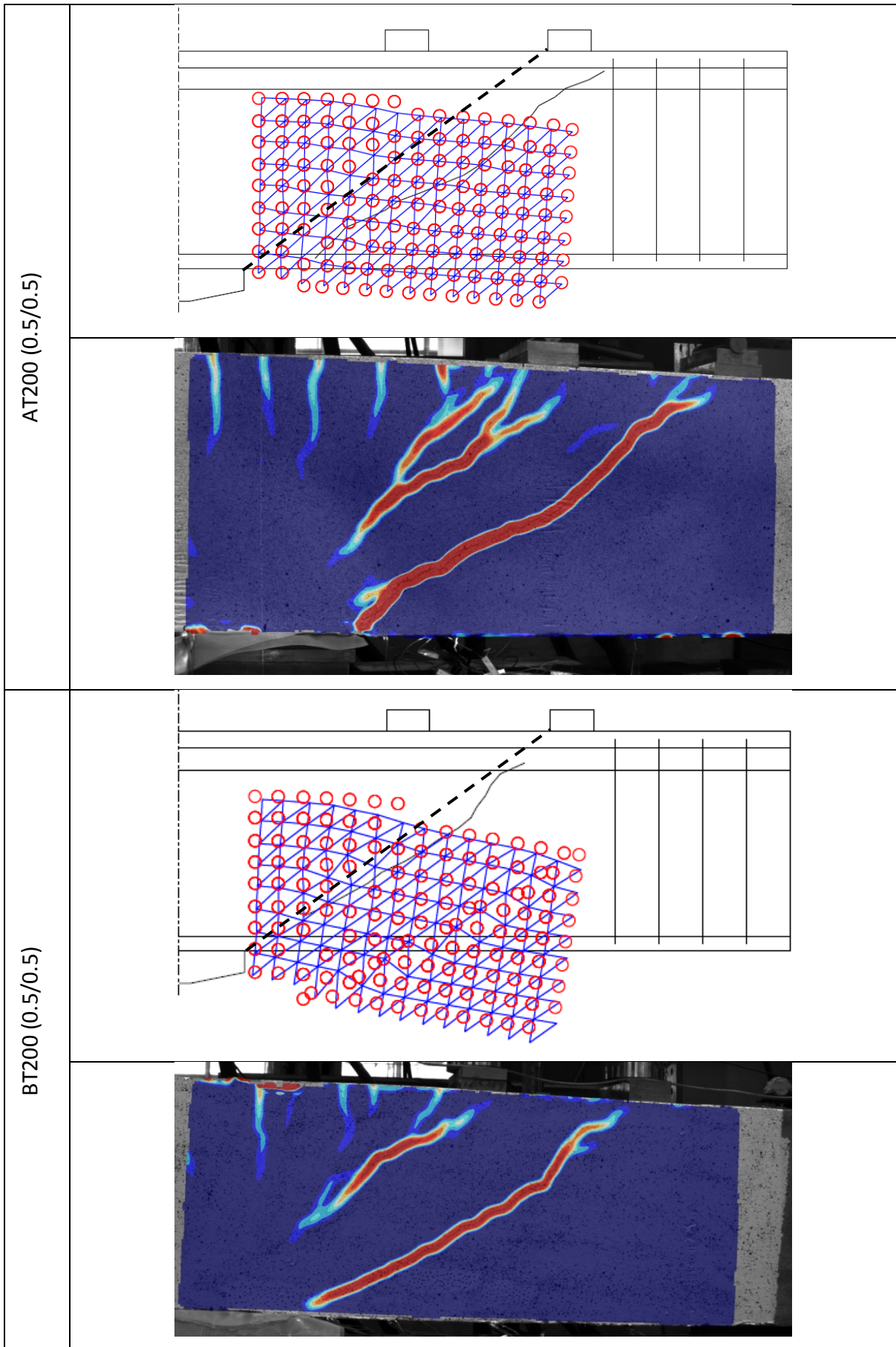
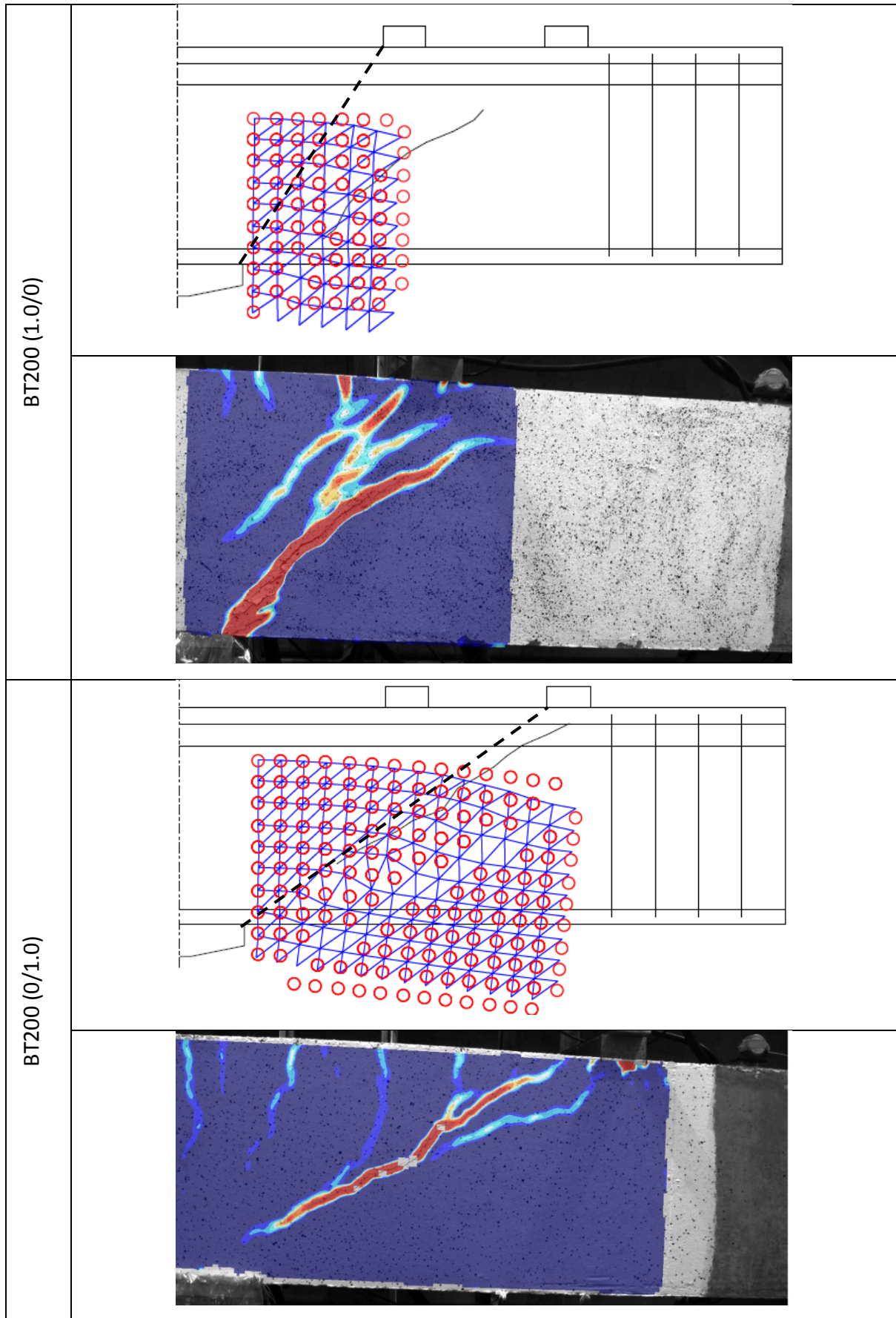
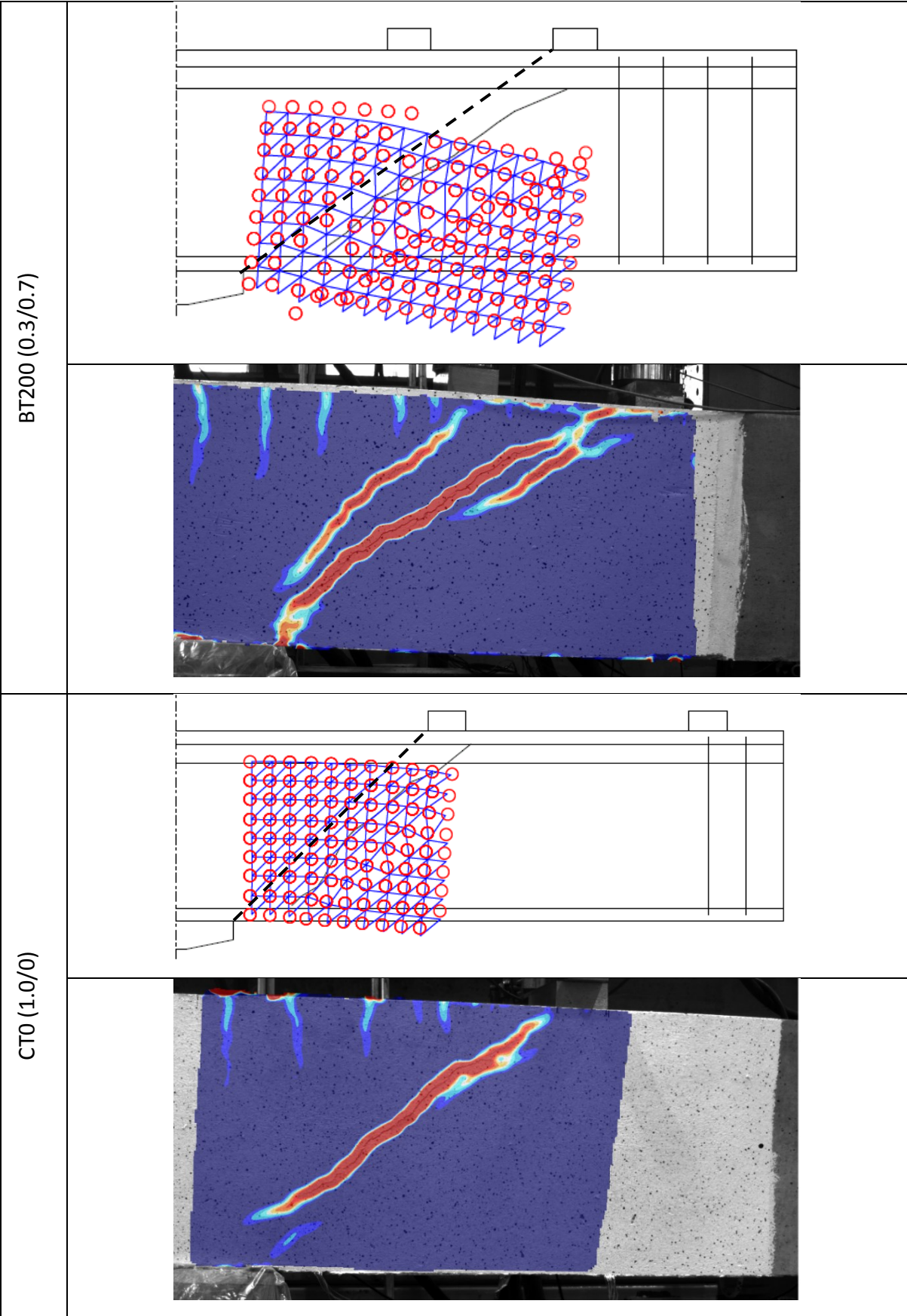


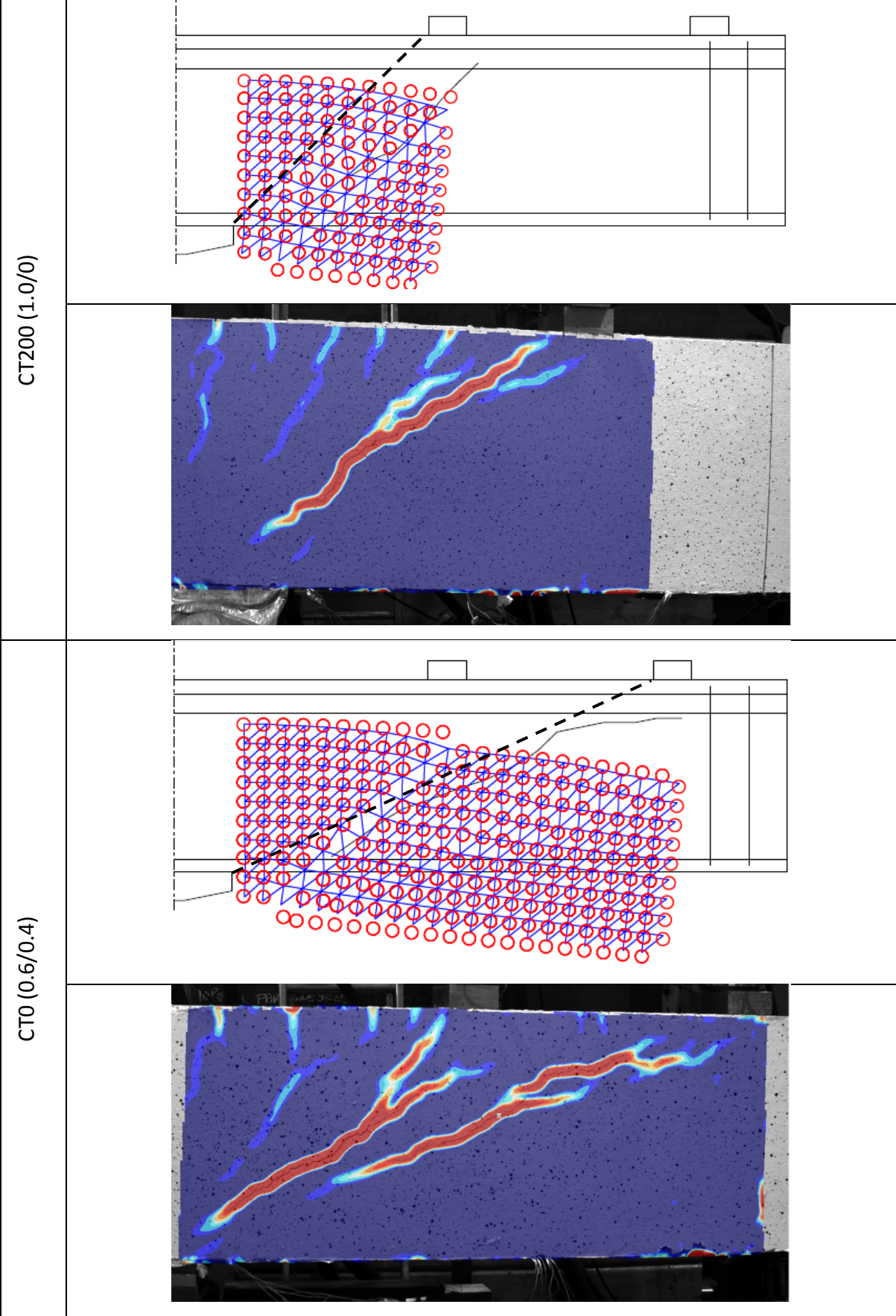
Figure 5.15: Final corrections for the deformed shaped of beam CT0 (0.6/0.4) at $0.95V_{max}$ calculated using modified 2PKT (deformation X 3)











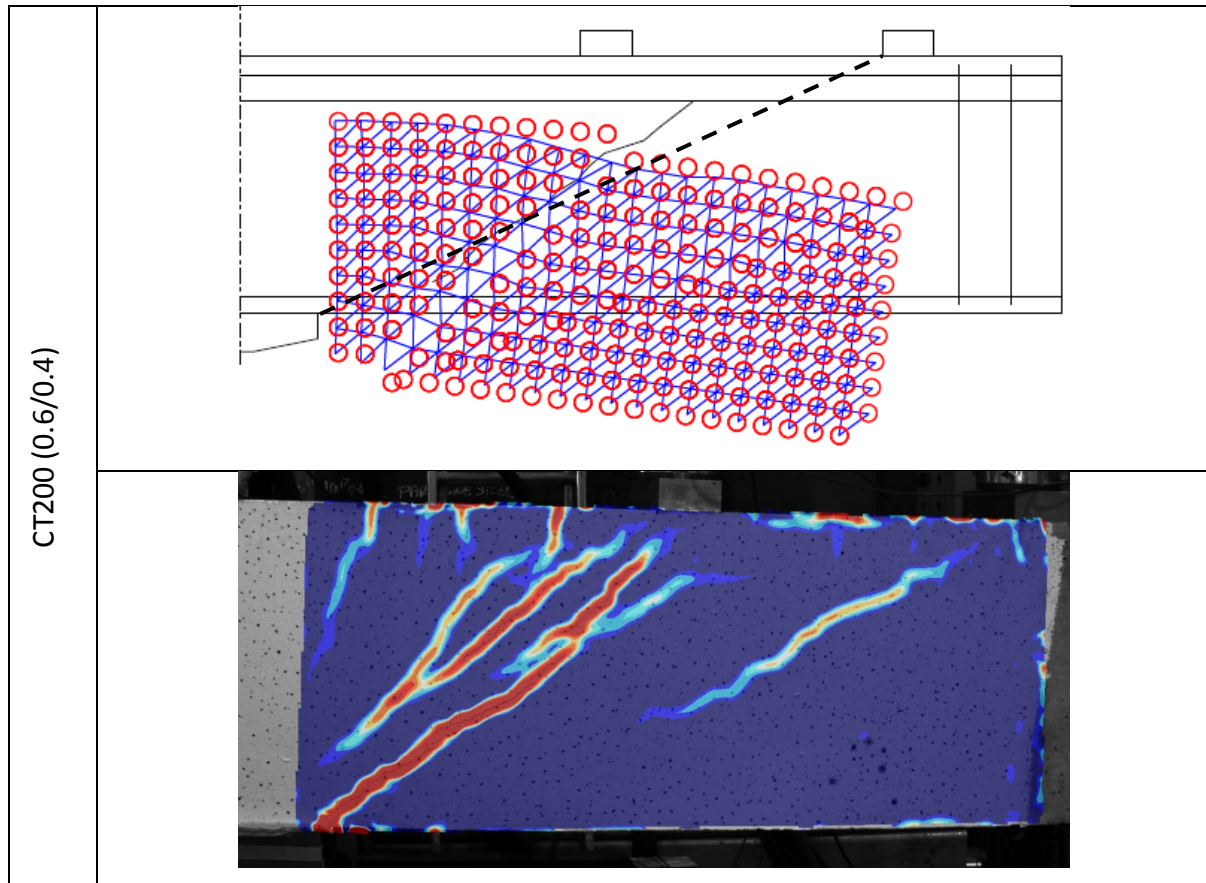
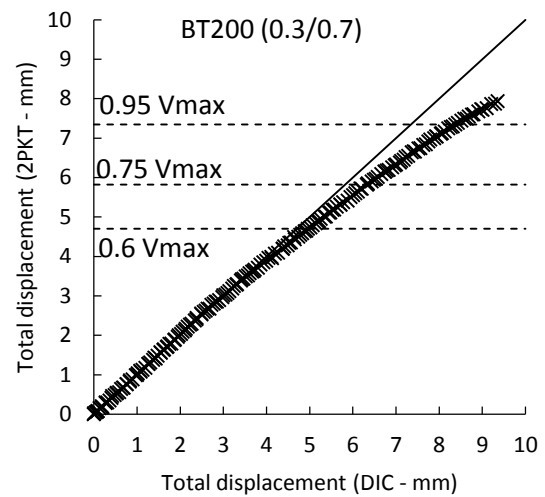
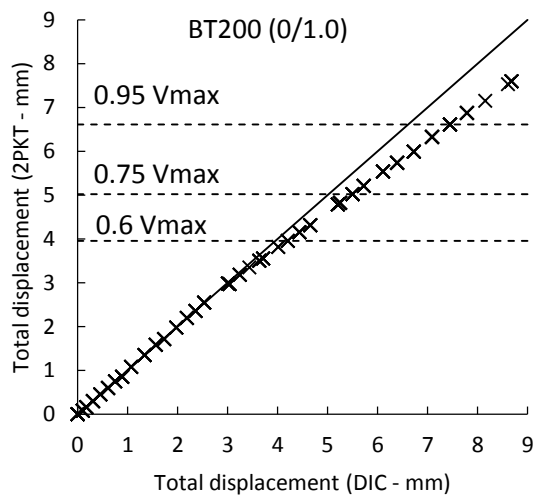
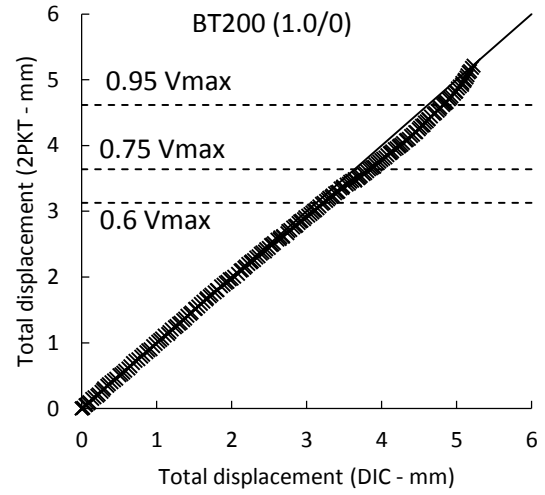
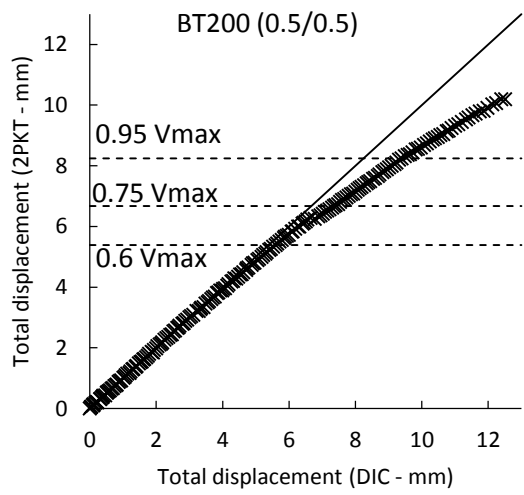
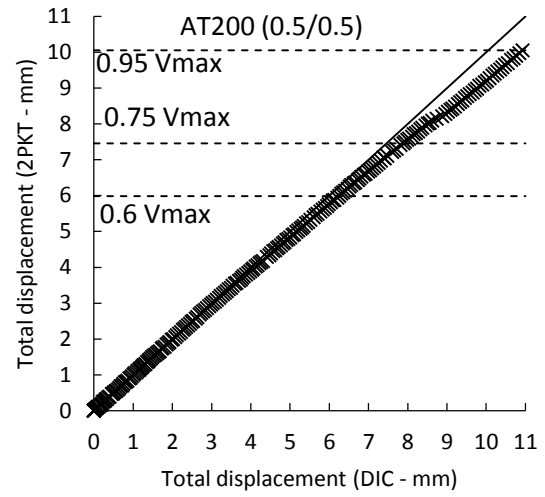
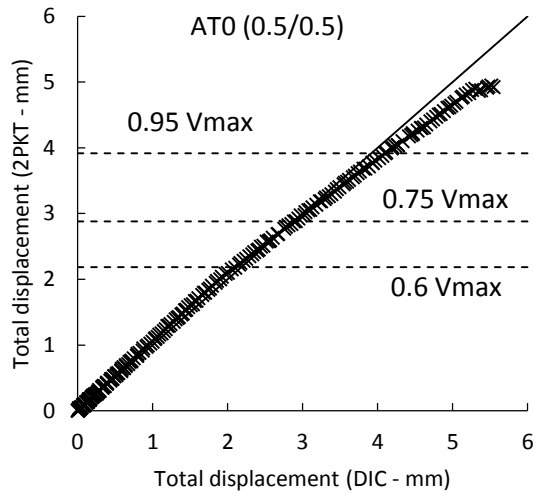


Figure 5.16: Comparison between the 2PKT and the measured deformation ($\times 30$) for beams loaded on their tension face at $0.95V_{max}$

The maximum vertical displacement at ($a_{v,crt} - 500$) of the shear span measured using the DIC system was compared to displacement calculated using the modified provisions of the 2PKT for beams loaded as double cantilevers. The comparison shown in Figure 5.17 shows good agreement between the measured and predicted displacements with the modified provisions slightly underestimating the displacement near failure.



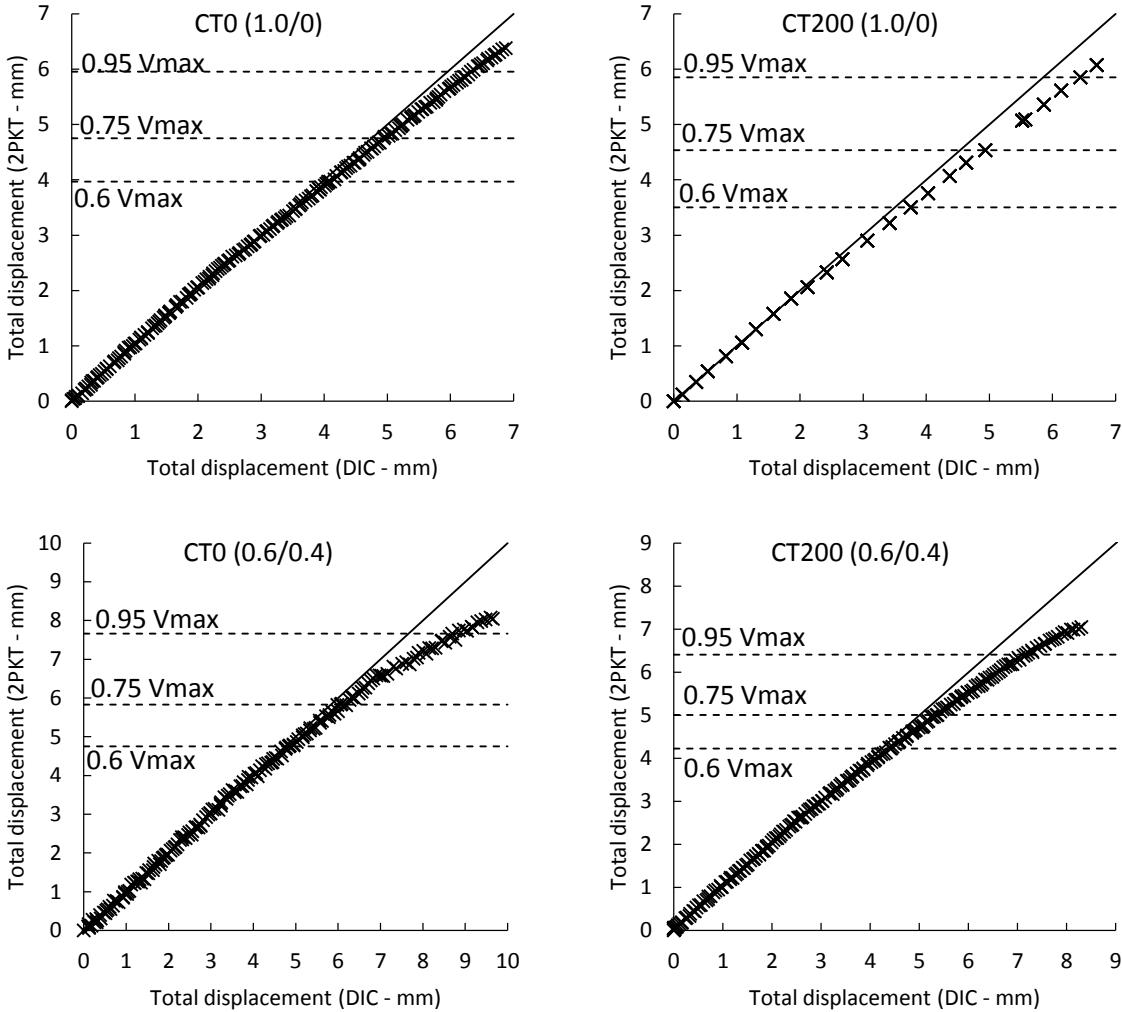


Figure 5.17: Comparison between measured and predicted maximum deformation of beams loaded as a double cantilever

Overview

As demonstrated in Figures 5.10 to 5.12, the 2PKT does not fully describe the observed displacement of the double cantilever beams tested in this research. This is particularly the case for beams with two-point loads where a shear displacement developed within the fan shaped region of the 2PKT that is not accounted for in the 2PKT. Additionally, the location of the CoR of the rigid body below the diagonal failure crack was found to lie vertically above the x-axis. This implies that the rigid body displaced horizontally to the left as it rotated as previously observed in compact punching specimens by Kueres and Hegger (2018). Comparisons of Figure 5.8 (without corrections) and Figure 5.12 (with corrections) for beam CT0 (0.6/0.4) shows that these modifications improved the predicted deformation significantly compared to the original provisions. Further confirmation is provided by Figure

5.16 and Figure 5.17, which show that the 2PKT produced reasonable estimates of the measured displacements when modified to account for the intermediate shear displacement and upwards shift of the CoR.

5.3. **Assessing Beam Strength and Shear Transfer Actions Using the Five – Spring Model**

The five-spring model provides a full description of the beam deformation, ultimate strength and load-deflection response (Mihaylov, 2015). Deformations are obtained based on the two parameters $\varepsilon_{t,avg}$ and Δ_c and failure is governed by crushing of the concrete in the critical loading zone (CLZ). While the procedures described in the five-spring model are relatively simple and give accurate estimations, these procedures need modifications to be applicable for beams with multiple point loads. This section highlights these differences and suggests some modifications.

For beams with two-point loads near the support, failure can theoretically occur along either the inner or outer shear plane. In order to estimate the failure load and to predict the load-deflection response, both of the shear planes should be investigated to determine the critical plane. Some terms in the model depend on the strains in particular locations, like the flexural tensile force, the crack opening and the dowel contribution. For one point load within the shear span, the five-spring model assumes $\varepsilon_{t,avg}$ to be uniform along the shear span. However, the equation for average strain requires modification when a second point load is introduced within the shear span (see Table 5.1 for the step strain profile). Equations to estimate strains, flexural tensile forces and shear strength are modified consequently as shown in Table 5.1.

Using the provisions given in Table 5.1, the ultimate load, load-deflection response and the shear transfer mechanisms can be estimated. As mentioned earlier, the shear strength of beams with two-point loads in the shear span must be evaluated for both shear planes to find the critical section. The 2PKT assumes the minimum and maximum reinforcement tensile forces T_{min} and T_{max} are equal, while the five-spring model reduces T_{max} due to the contribution of the stirrups. The strain for beams with a pair of point loads varies based on the load configuration, hence, for simplicity; the reduction of the strain due to the contribution of the stirrups is ignored in these calculations. The solution procedure for

estimating the ultimate shear strength is summarized in Figure 5.18 below with further details given in Chapter 2. Table 5.2 shows the predictions of the shear strength and failure plane for test beams using the five-spring model. The strength of beams with two-point loads was taken as the least corresponding to failure along each shear plane (depicted as predicted failure load in Table 5.2). The failure load was also calculated based on the “actual” shear failure plane observed in the tests. It can be seen that the model correctly predicts the failure planes for the majority of beams loaded with two-point loads except for two beams (namely AT200 (0.5/0.5) and BT200 (0.5/0.5)), which are notionally similar. The accuracy of the strength predictions is very good, particularly for beams with two-point loads. Interestingly, the estimated failure loads were also good for beams where the critical shear plane was falsely predicted. The accuracy of the predictions for beams with single point load was good (Mean = 0.88 and COV = 10) but less accurate compared to predictions of beams with two-point loads (Mean = 0.97 and COV = 11). Table 5.2 also compares the measured and predicted maximum displacement for the tested beams. It can be seen that the 2PKT underestimated the total displacement for all the tested beams.

Table 5.1: Modification of the five-spring model to account for beams with multiple point loads

Beams loaded on the tension face		Beams loaded on the compression face	
Failure of the outer shear span			
$\varepsilon_{t,avg}$ $= \frac{\varepsilon_{t,1}a_1 + \varepsilon_{t,2} \cdot (a_2 - a_1)}{a_2}$	Equation 5.20		
$T_1 = \frac{P(R_1a_1 + R_2a_2)}{0.9d}$	Equation 5.21	$T_1 = \frac{P(a_2 - R_1(a_2 - a_1))}{0.9d}$	Equation 5.22
$\alpha_\varepsilon = \frac{\varepsilon_{t,2}}{\varepsilon_{t,1}}$ $= \frac{PR_2a_2}{P(R_1a_1 + R_2a_2)}$	Equation 5.23	$\alpha_\varepsilon = \frac{\varepsilon_{t,2}}{\varepsilon_{t,1}} = 1.0$	Equation 5.24
$V_{flex} = \frac{0.9d \cdot T_1}{R_1a_1 + R_2a_2}$	Equation 5.25	$V_{flex} = \frac{0.9d \cdot T_1}{a_2 - R_1(a_2 - a_1)}$	Equation 5.26
$L_{b1e} = R_2L_{b1}$	Equation 5.27	$L_{b1e} = L_{b1}$	Equation 5.28

Failure of the inner shear span			
$V_{flex} = \frac{0.9d \cdot T_1}{R_1 a_1 + R_2 a_2}$	Equation 5.29	$V_{flex} = \frac{0.9d \cdot T_1}{a_1}$	Equation 5.30
$L_{b1e} = L_{b1}$	Equation 5.31	$L_{b1e} = L_{b1}$	Equation 5.32

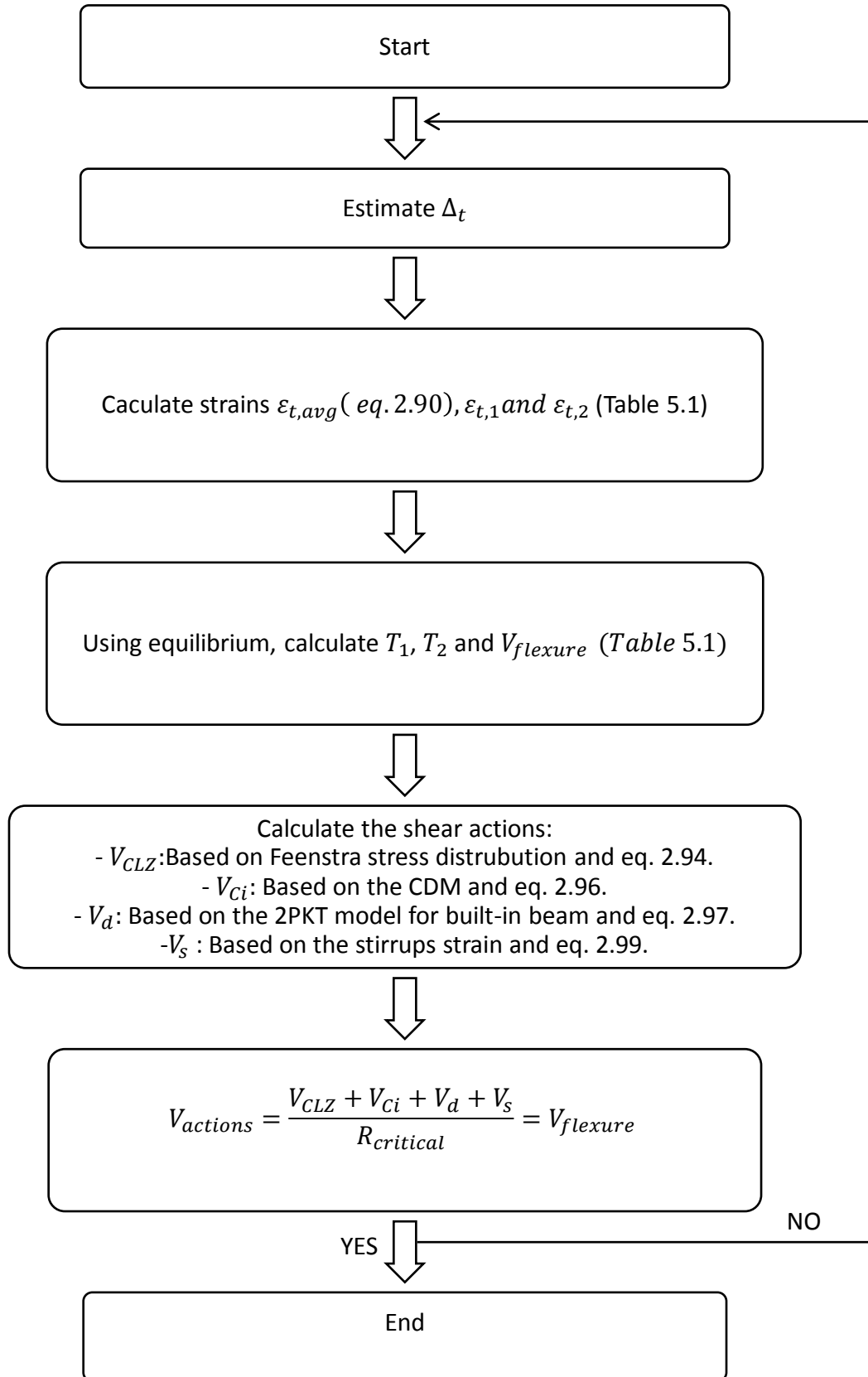


Figure 5.18: Solution procedures for estimating the ultimate shear strength using the five-spring model

Table 5.2: Predictions of the shear strength and failure plane for test beams using the five-spring models

Beam		V_{test} (kN)	Failure plane		$V_{Predicted}/V_{test}$		$\delta_{2PKT,predicted}$	
			Predicted	Actual	Predicted plane	Actual plane	δ_{test}	
Single point load	BT200 (1.0/0)	610	-	-	1.01	1.01	0.68	
	BT200 (0/1.0)	423	-	-	0.78	0.78	0.84	
	CT0 (1.0/0)	441	-	-	0.91	0.91	0.99	
	CT200 (1.0/0)	543	-	-	0.83	0.83	0.80	
Multiple point loads	AT0 (0.5/0.5)	449	Outer	Outer	1.24	1.24	0.81	
	AT200 (0.5/0.5)	733	Inner*	Outer	0.92	1.01	0.76	
	BT200 (0.5/0.5)	648	Inner*	Outer	0.94	0.94	0.60	
	BT200 (0.3/0.7)	528	Outer	Outer	0.89	0.89	0.51	
	CT0 (0.6/0.4)	378	Outer	Outer	0.87	0.87	0.48	
	CT200 (0.6/0.4)	502	Inner	Inner	0.93	0.93	0.82	
	AC0 (0.5/0.5)	539	Outer	Outer	1.01	1.01	0.74	
	AC200 (0.5/0.5)	742	Outer	Outer	0.89	0.89	0.67	
					Mean	0.93	0.94	0.73
					SD	0.11	0.11	0.14
					COV	12.05	12.13	19.24

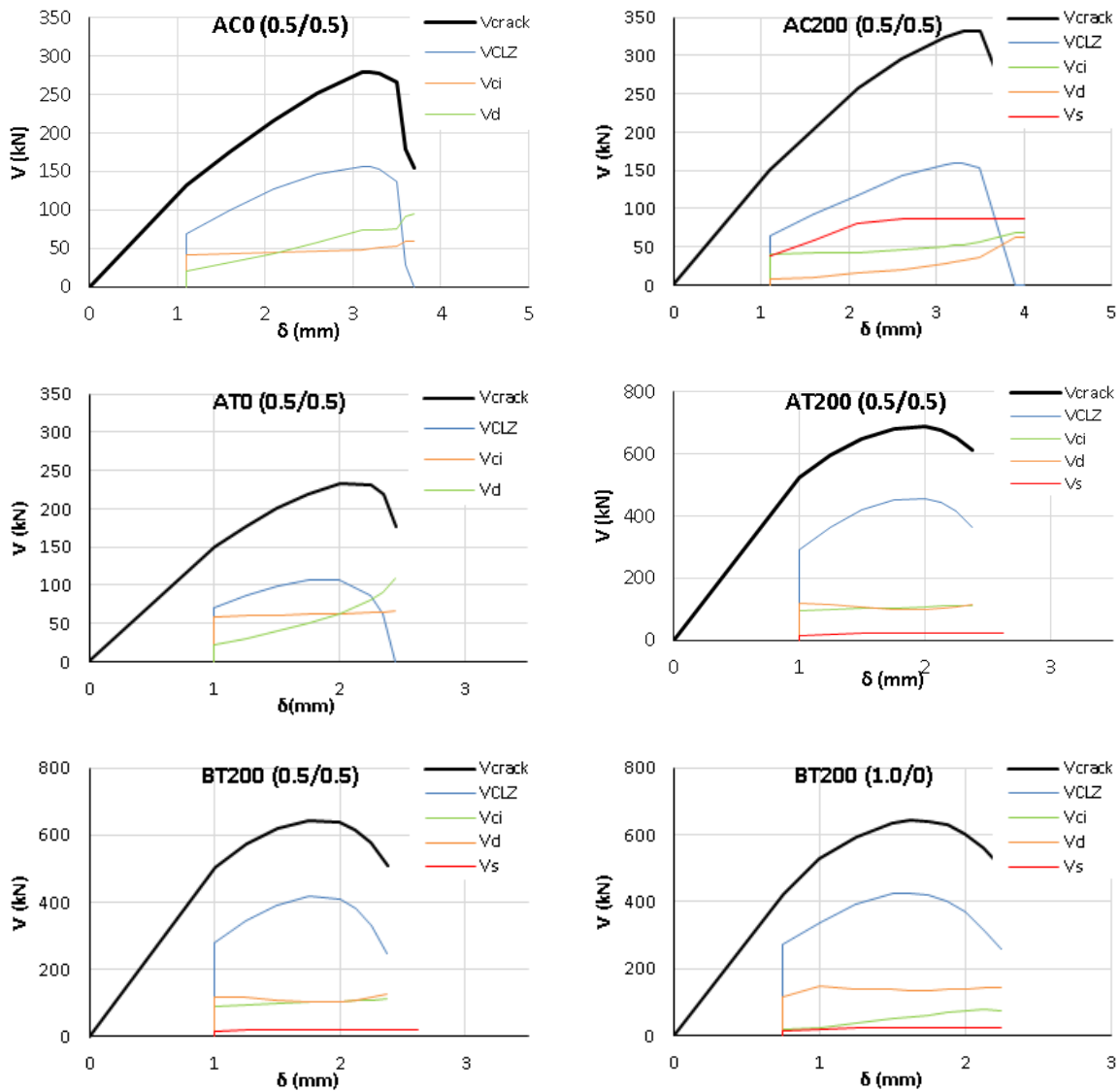
* Falsely predicted failure plane.

The shear force transferred through the crack by the various shear transfer mechanisms was evaluated using the five-spring model. The model assumes a tri-linear response with three distinctive points: i) flexural cracking of the concrete, ii) formation of the first diagonal shear crack and iii) the sectional capacity of the beam using Level of Approximation III of MC2010 (See Section 2.3.3). After diagonal shear cracking, the capacity of the beam is determined from consideration of the shear transfer mechanisms. This is based on the assumption that the shear transfer mechanisms are activated after the critical diagonal shear crack has formed. In this work, the third point of the tri-linear response (the sectional capacity of the MC2010) was disregarded, as the failure loads given by MC2010 for the majority of the beams were greater than the load required to form the critical crack in the tests. Hence, the response cannot be linear up to the MC2010 sectional capacity. To estimate the contribution of the shear transfer mechanisms and the load-deflection response, the following iterative procedure can be used (for an imposed displacement Δ):

- a) Calculate the flexural crack load $V_{cr,flex}$ and the load forming the first diagonal crack $V_{cr,sh}$ with their corresponding deflection to plot the bilinear response.
- b) Estimate Δ_t and calculate $\Delta_c = \Delta - \Delta_t$.
- c) Calculate strains $\varepsilon_{t,avg}$, $\varepsilon_{t,1}$ and $\varepsilon_{t,2}$ using Table 5.1.
- d) Calculate equilibrium components (T_1 , T_2 and V_{flex}).
- e) Find the contribution of the shear transfer actions. To calculate V_{CLZ} , the user needs to choose a stress-strain formula for the compressive response of the concrete. Using Δ_c , $\varepsilon_{c,max}$ can be calculated from Equation 2.93. In this work, the Feenstra model (1993) was adopted for concrete compressive behaviour.
- f) If the difference between the summation of the shear transfer actions $V_{actions}$ and the corresponding shear force from equilibrium V_{flex} is less than the acceptable error, the imposed displacement Δ and the shear force V_{flex} will be plotted in the non-linear part of the curve. Otherwise, return to step b) to estimate a different value of Δ_t .
- g) Increase Δ and repeat steps (b) to (f) until the full load-deflection response is obtained, including the post-peak response.

The contributions of the different shear transfer mechanisms estimated using the five-spring model are presented in Figure 5.19. The dominant component was the contribution of the CLZ and the least effective component was the dowel contribution. The upper limits of the

dowel and shear reinforcement mechanisms governed their contribution for the majority of the beams. The selected model for the aggregate interlock (the Contact Density Model (Li, 1989)) relates the shear resistance provided by aggregate interlock to the ratio γ between the crack sliding and opening displacements (detailed description of the model is available in Chapter 2). The crack opening is proportional to the sliding in the five-spring model; this resulted in a nearly constant value of γ . The contribution of the CLZ is related to the selection of the stress-strain relationship of the concrete uniaxial compressive strength. The choice of stress-strain relationship for the concrete in the CLZ is not specified in the five-spring model. In this work, the parabolic stress distribution described later in Chapter 6 (Feenstra, 1993) was selected to model this behaviour.



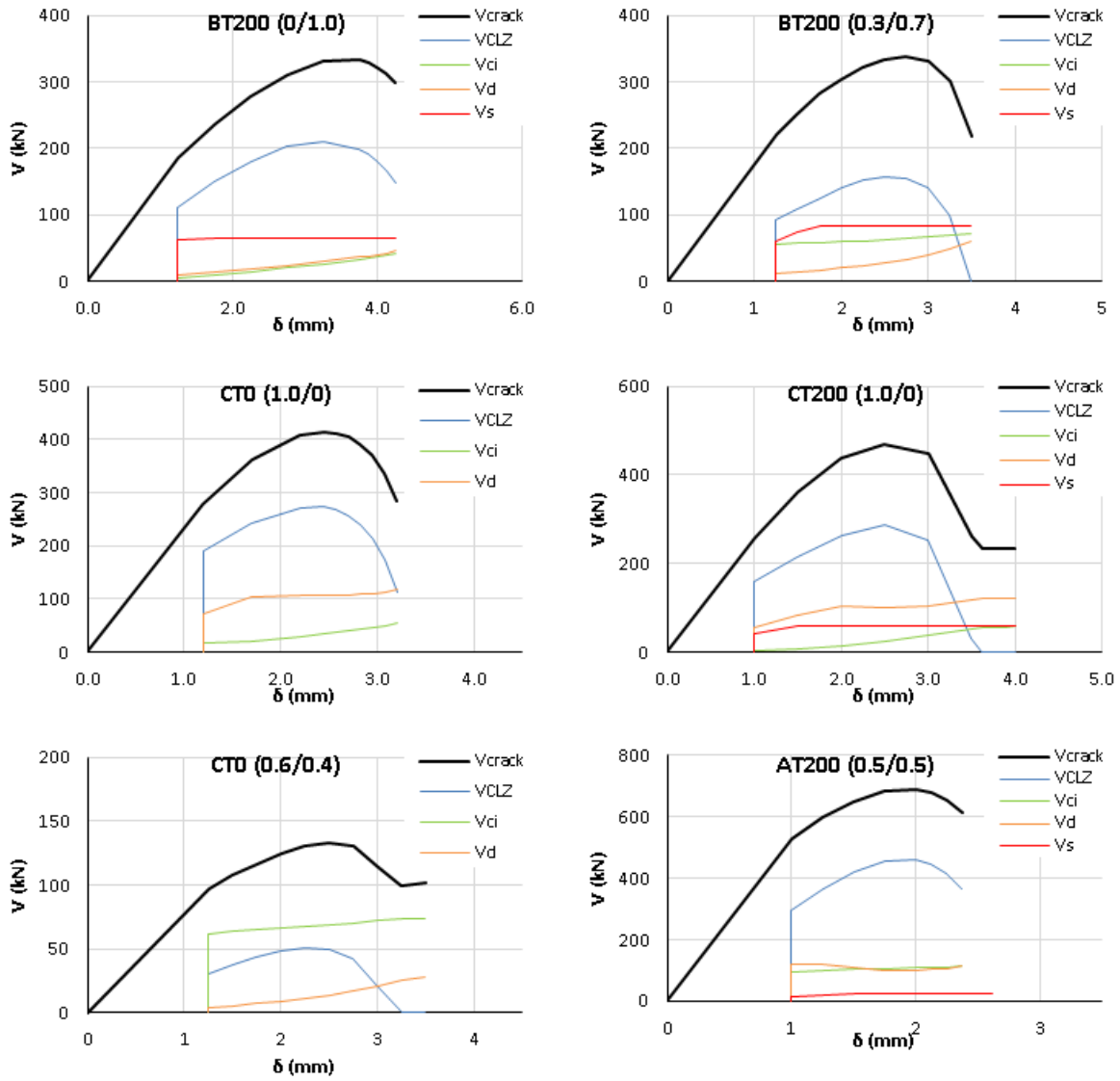
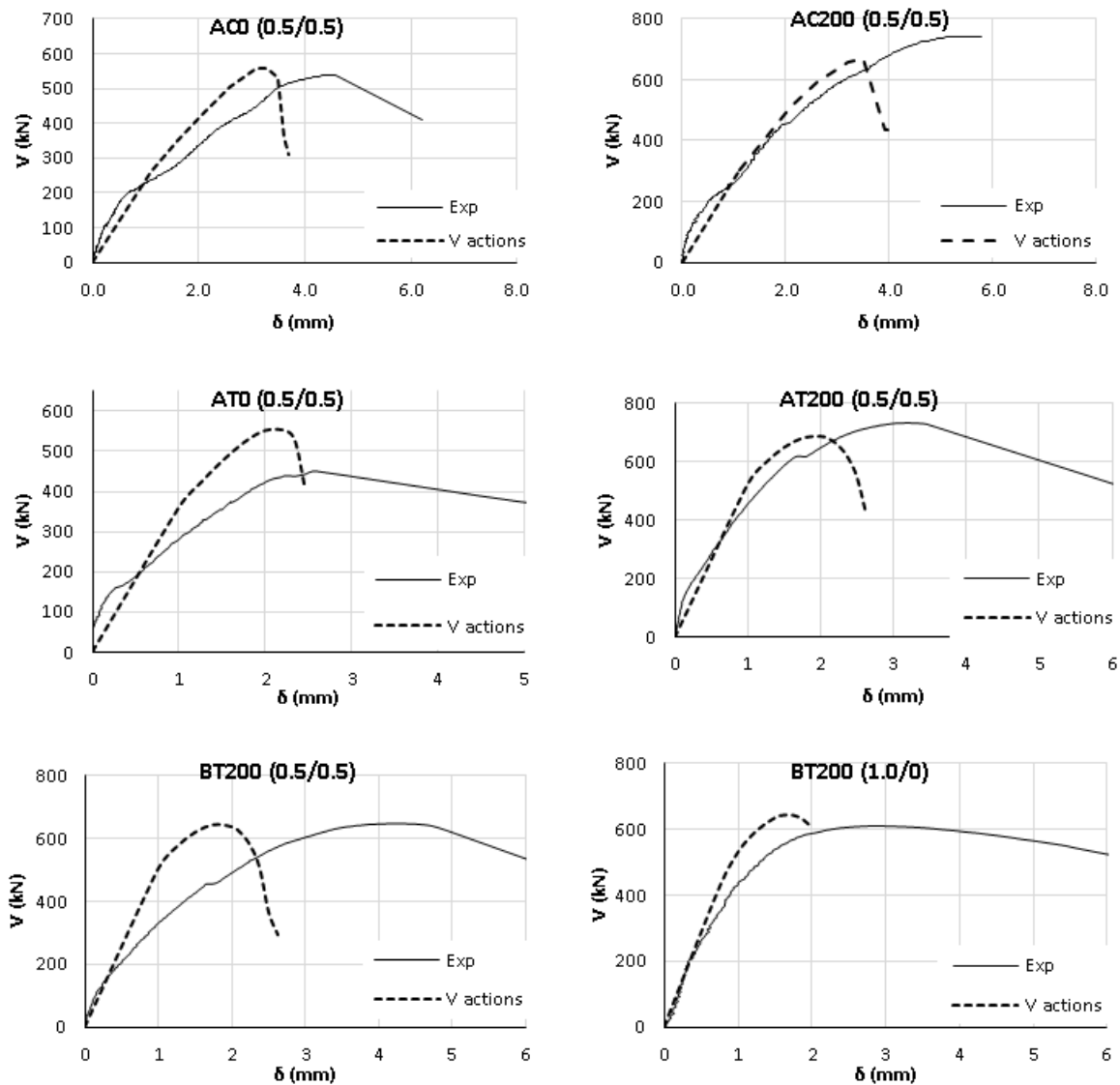


Figure 5.19: Shear transfer mechanisms evaluated using the five-spring model

Figure 5.19 shows that, with the exception of CT0 (0.6/0.4), the greater part of the shear force is resisted by the CLZ with the other contributions relatively independent of load post cracking. In the post-peak phase of the response, the contribution of the CLZ reduced while the rest of the components remained almost constant. In beam CT0 (0.6/0.4), which failed outside the shear enhancement zone without shear reinforcement, the dominant contribution was aggregate interlock. The dowel contribution was limited and the contribution of the shear reinforcement increased as the shear span to effective depth increased. As well as prediction of the ultimate load and critical shear plane, the five-spring model was used to evaluate the load-deflection response for the tested beams. For double cantilever beams, to obtain the value of the absolute deflection, corrections described in

Section 5.2.2 were implemented. For beams where the predicted failure plane was different from the actual ones, load-deflection curves based on the predicted failure plane were compared to the actual deformation at the corresponding plane obtained from the DIC to facilitate the comparison.

Figure 5.20 compares the measured load-deflection responses of the tested beams with those obtained using the five-spring model. It can be seen from the figure that the five-spring model gives reasonable predictions of the response, especially for the pre-peak response. The post-peak part of the load-deflection response was poorly modelled for the majority of the beams. As shown later, the post-peak of the load-deflection response in the five-spring model is mainly governed by the CLZ.



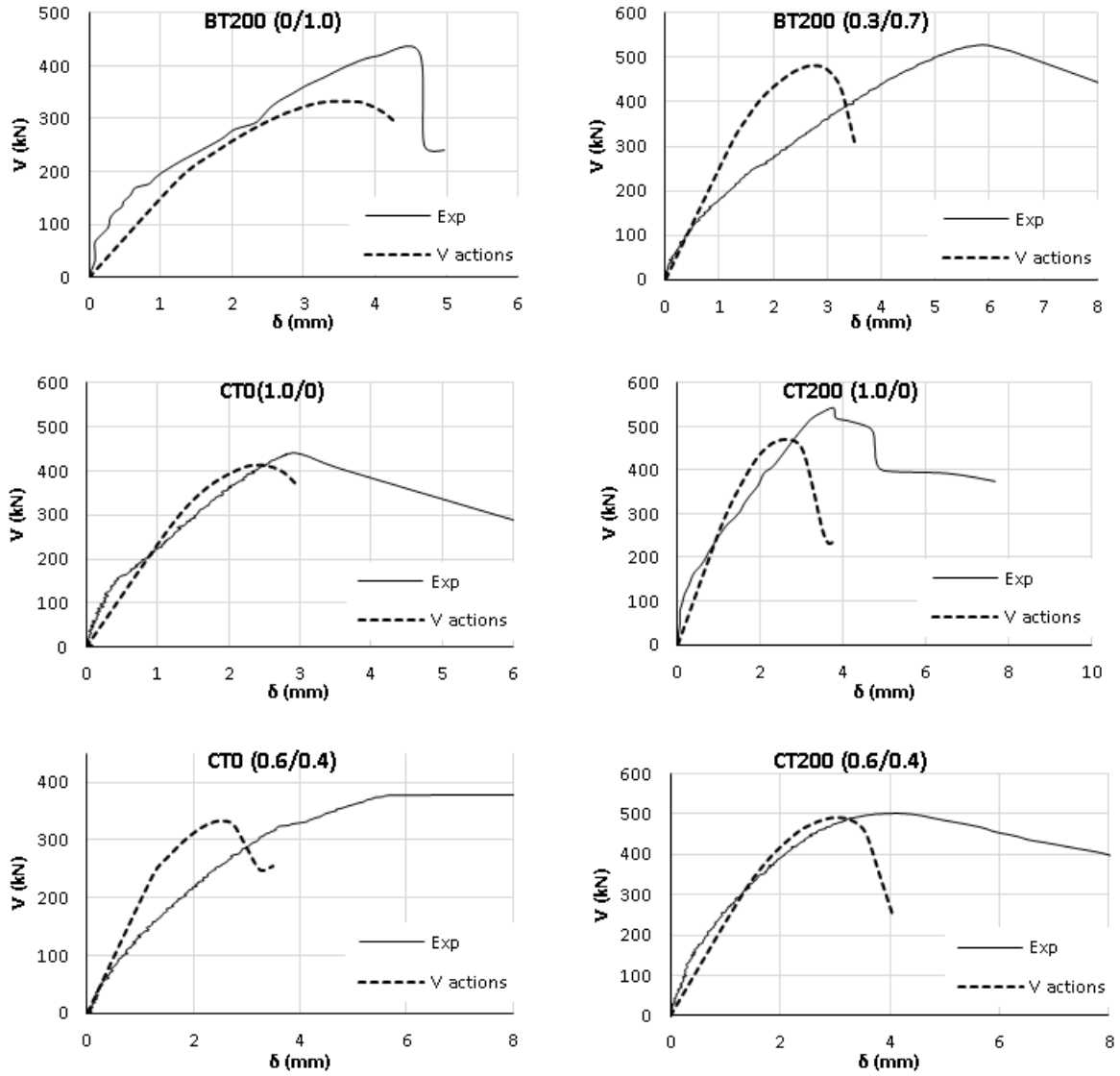
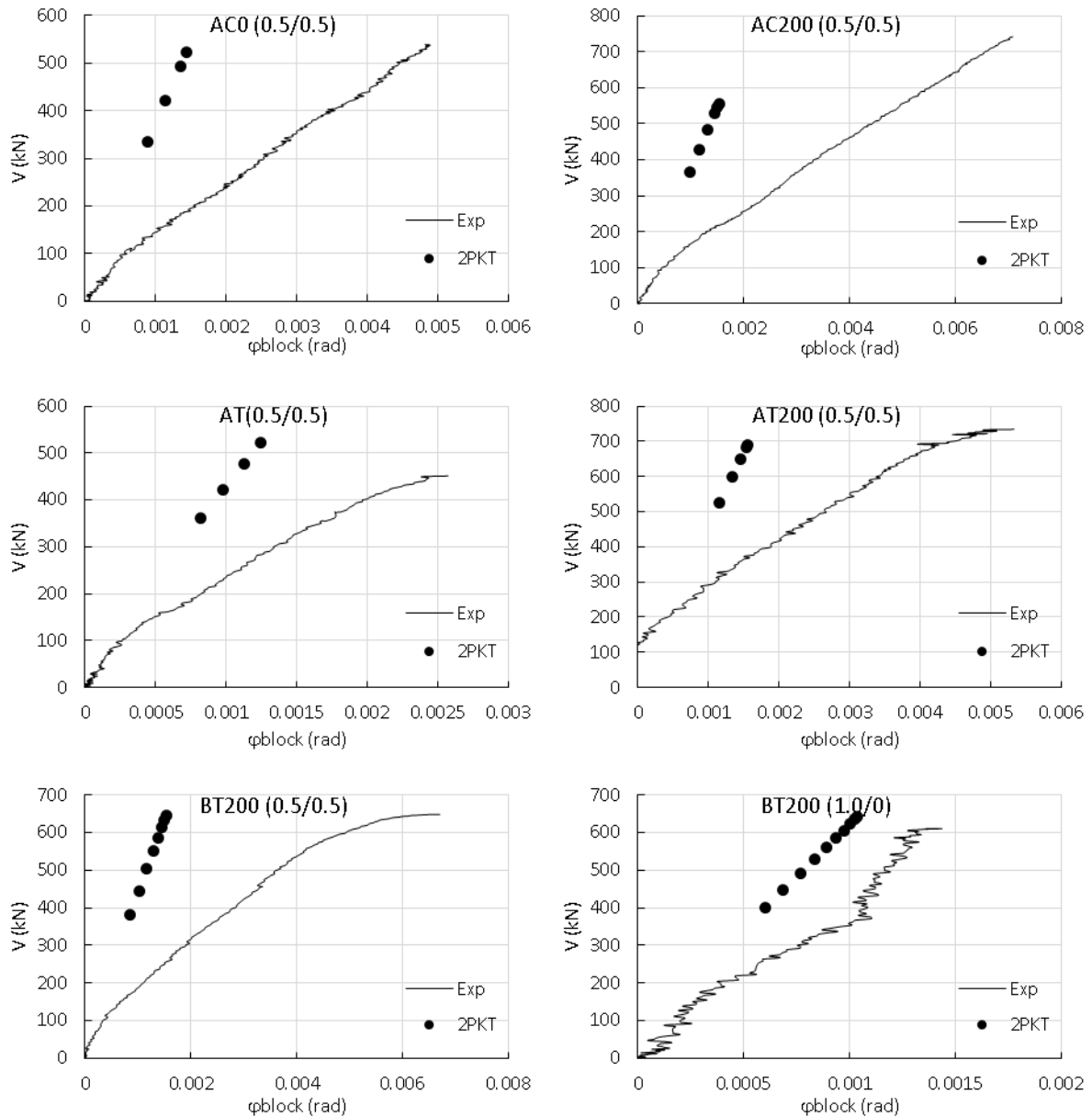


Figure 5.20: Predictions of the load-deflection response of the test beams using the five-spring model

5.4. Validation of Crack Kinematics Assumed in the 2PKT and the Five – Spring Model

Section 5.2 assessed the ability of the 2PKT model to describe the experimentally observed deformations of the beams in terms of experimentally derived values of φ_{block} and $\varepsilon_{t,avg}$. The experimentally measured rotation of the rigid body φ_{block} was used to calculate the two parameters of the theory as described in the literature (Mihaylov et al., 2013, Kueres, 2018). However, when estimating the ultimate load and deflection in 5.3, the rotation φ_{block} and the shear displacement Δ_c were outputs of the solution procedure. The measured block

rotation and shear displacement were compared with the estimated values from the 2PKT. Experimentally measured rigid body rotations of double cantilever beams and shear displacements were corrected to account for the global rotation of the beam about the support. Figure 5.21 compares the measured and estimated rotation φ_{block} of the rigid body in the 2PKT.



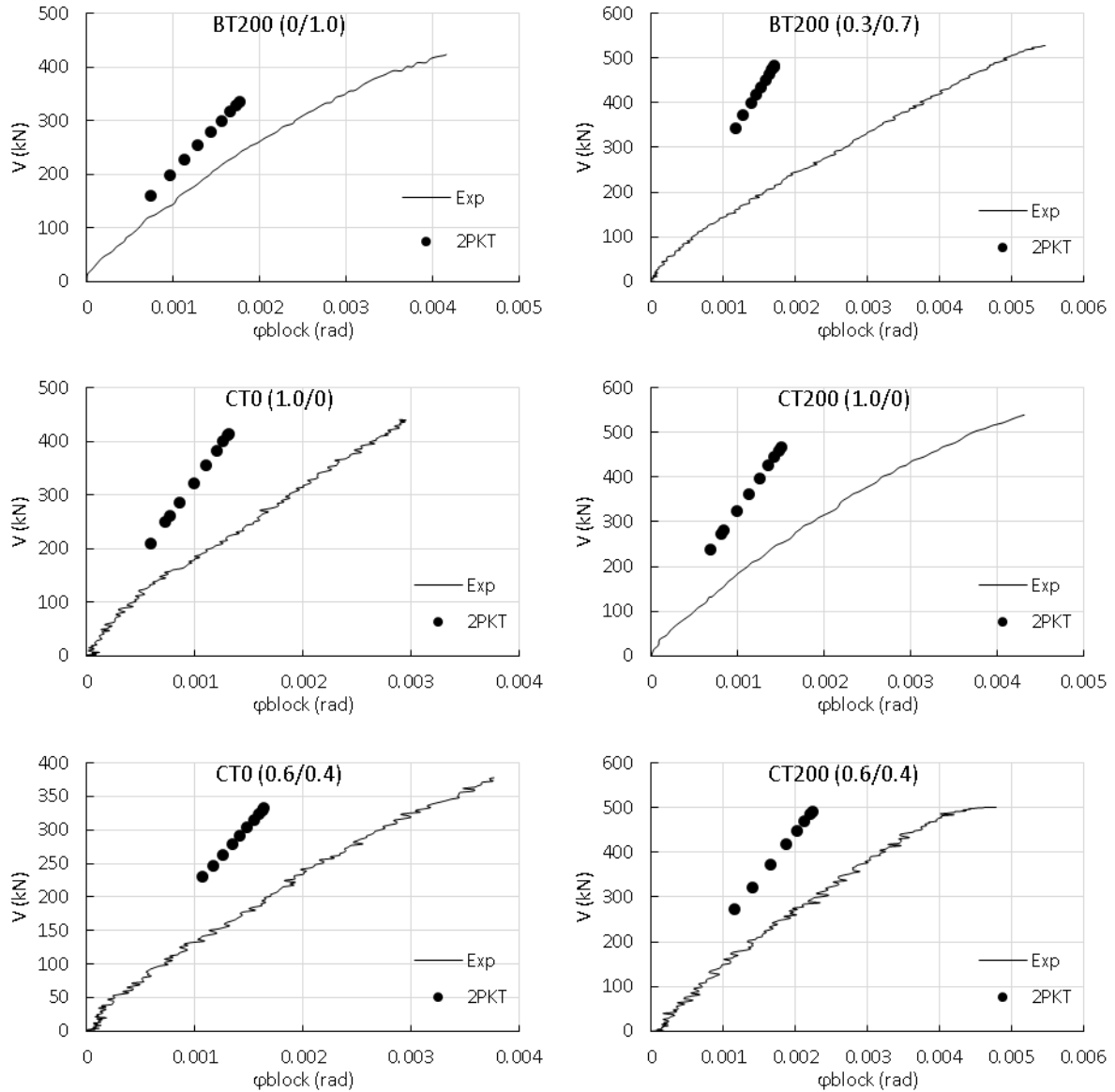


Figure 5.21: Comparison between the measured and estimated rotation of the rigid body in the 2PKT

Figure 5.21 shows that the 2PKT consistently underestimates the measured rotation of the rigid body. Despite this, the 2PKT broadly captures the measured trend of experimental behaviour well in term of the rotation of the rigid body. This is illustrated in Figure 5.22 (a) and (b) which show, respectively, rigid body rotations of beams in series A obtained experimentally and from the 2PKT. Both the measured and predicted rotations are greater for the beams of Series A loaded on the compression face than tension face. In addition, there are negligible differences in rotation, both experimental and predicted, between beams with and without shear reinforcement with the difference least for beams loaded on the compression face (beams AC0 (0.5/0.5) and AC200 (0.5/0.5)). The 2PKT relates the flexural

displacement to the average tensile strain in the rebar for a given crack angle. The average tensile strain is calculated based on the flexural equilibrium of the free body, hence, for a similar load configuration, the rotation will be the same for a given beam regardless of the presence of the shear reinforcement. This is due to the assumption that $T_{min} \approx T_{max}$, which neglects the reduction on the tensile force due to the presence of stirrups for beams without shear reinforcement.

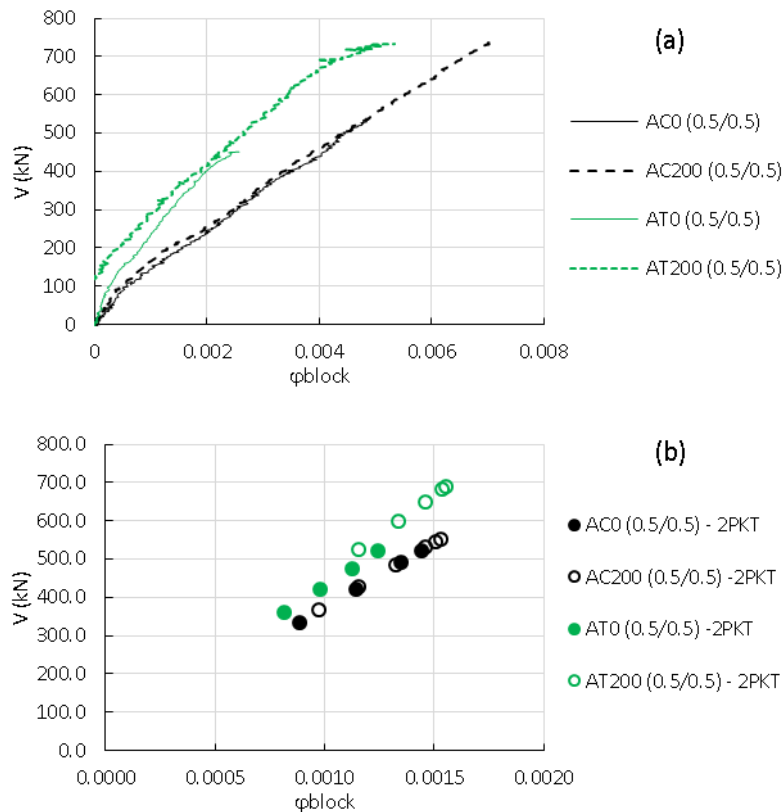


Figure 5.22: Rotation of the rigid body of beams in series A obtained (a) experimentally and (b) from the 2PKT

The negligible influence of shear reinforcement on the rigid body rotation evident in Figure 5.22, particularly for compression face loading, is also apparent in Figure 5.23 for beams CT0 (1.0/0) and CT200 (1.0/0), without and with shear reinforcement respectively. Both these beams were loaded with a single point load. The rigid body rotations were also very similar for beams CT0 (0.6/0.4) and CT200 (0.6/0.4) without and with shear reinforcement respectively. Beam CT0 (0.6/0.4) failed in the outer shear plane while beam CT200 (0.6/0.4) failed in the inner shear plane. Hence, the rotation of the rigid bodies was slightly different. This difference was reflected in the experimental rotation and was captured

by the 2PKT as can be seen in Figure 5.23 – b. In the 2PKT, the rotation of the rigid body increases with the decrease of the crack angle, hence, it is expected to see the rotation of the rigid body of beam CT0 (0.6/0.4), failing in the outer shear span, greater than the rotation in beam CT200 (0.6/0.4) failing in the inner shear span.

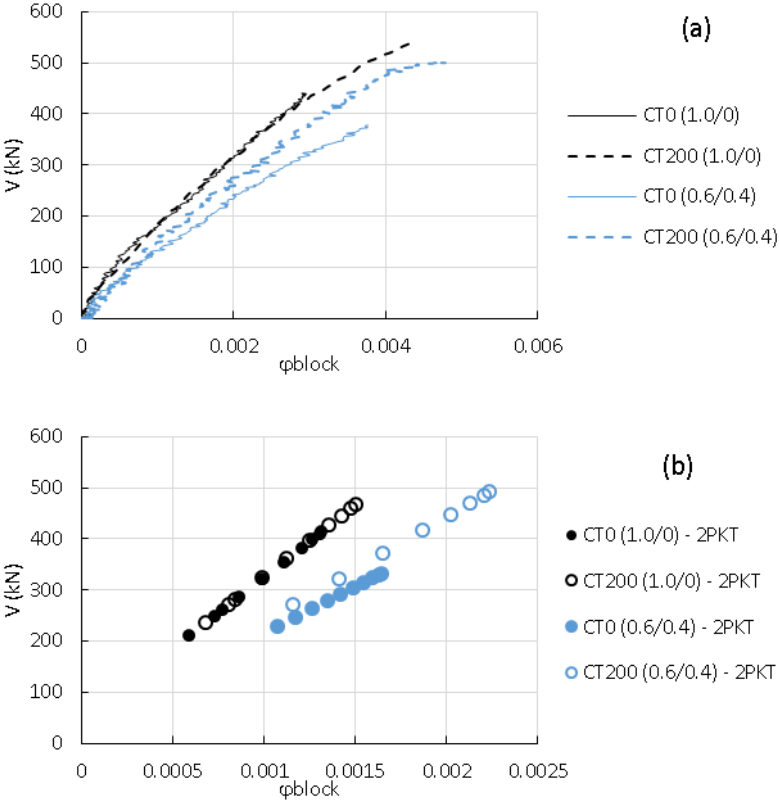
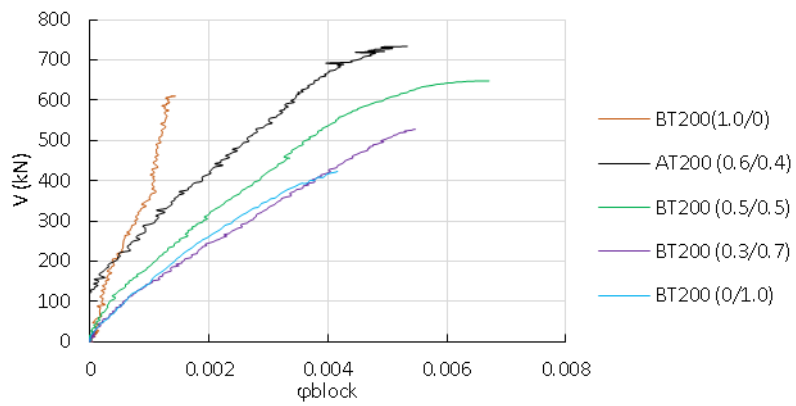
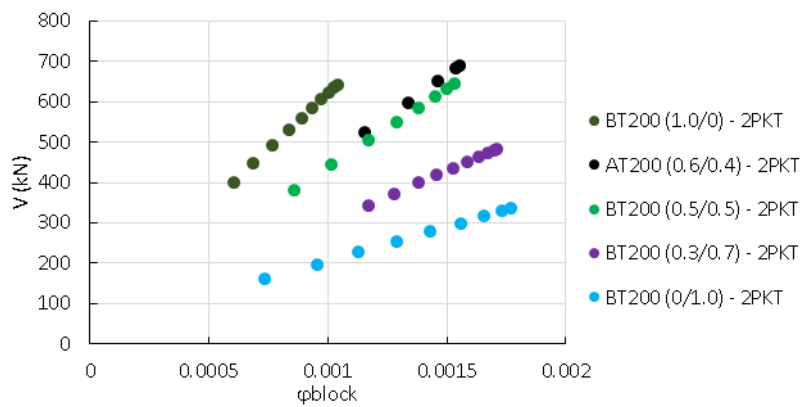


Figure 5.23: Rotation of the rigid body of beams in series C obtained (a) experimentally and (b) from the 2PKT

The effect of applying loads on the outer shear plane of beams in series B (in addition to beam AT200 (0.5/0.5) depicted here as AT200 (0.6/0.4) to reflect the actual, rather than intended, loading ratio) was studied using the 2PKT kinematics. Applying loads in the outer shear plane increased the rotation of the rigid body due to the increase in the flexural displacement; this increment was proportional to the amount of the load applied in the outer shear plane. While the 2PKT clearly demonstrated this increment in rotation in Figure 5.24 – b, the observed increment in the rotations from the test (Figure 5.24 – a) was less noticeable for higher values of loads in the outer shear plane.



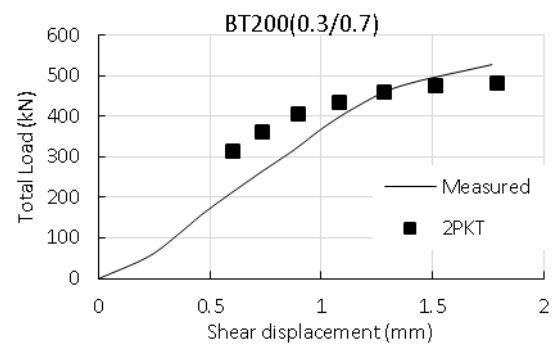
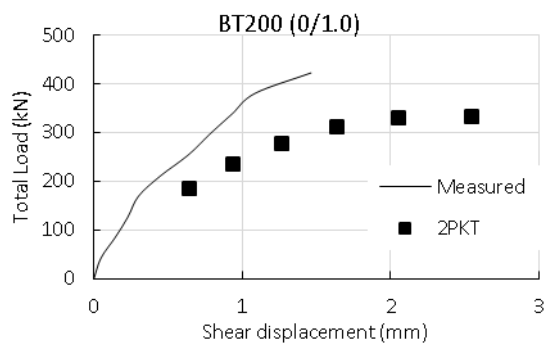
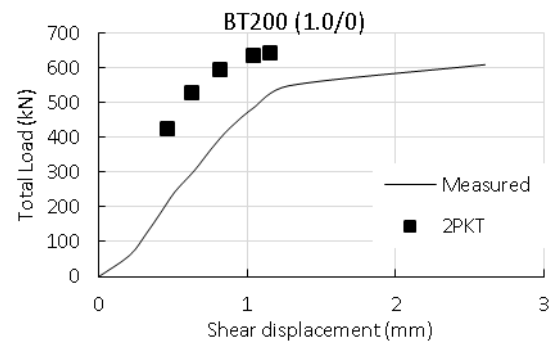
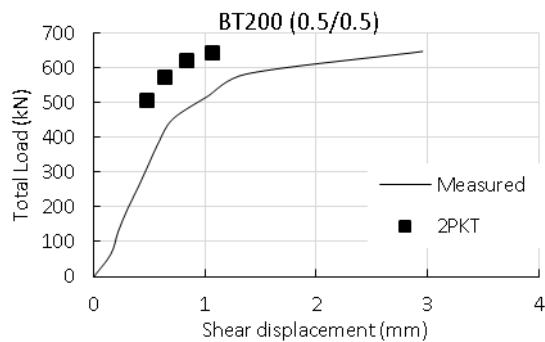
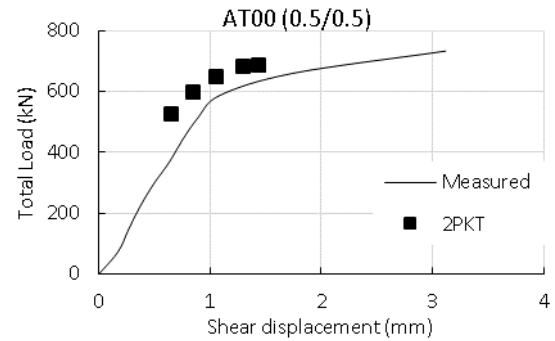
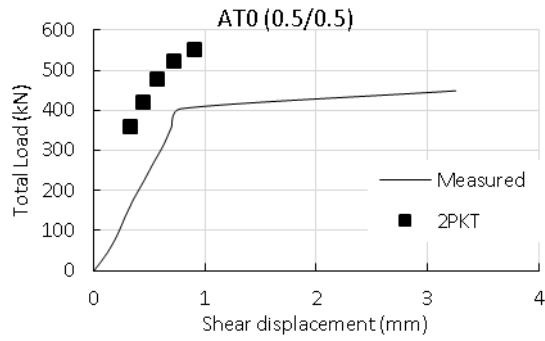
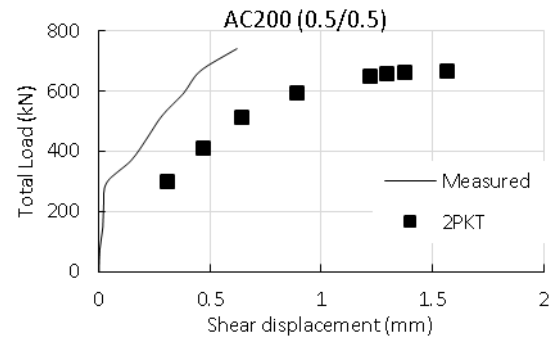
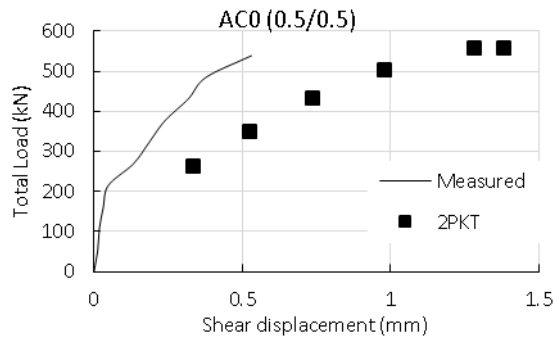
(a)



(b)

Figure 5.24: Rotation of the rigid body of beams in series B obtained (a) experimentally and (b) from the 2PKT

Figure 5.25 compares the measured and estimated shear displacement in the 2PKT. Unlike the rotation of the rigid body, which was underestimated by the 2PKT. Figure 5.25 shows that the estimated shear displacements were sometimes greater than the measured ones during the test (in four beams) and sometimes greater at late stages of the tests. The estimated shear displacement were more accurate compared to the estimated rotations particularly for beams AT200 (0.5/0.5), BT200 (0.5/0.5), BT200 (0.3/0.7), CT200 (1.0/0) and CT200 (0.6/0.4), which all had shear reinforcement. The Interaction between the estimated block rotation and shear displacement with the estimated crack kinematics is discussed next.



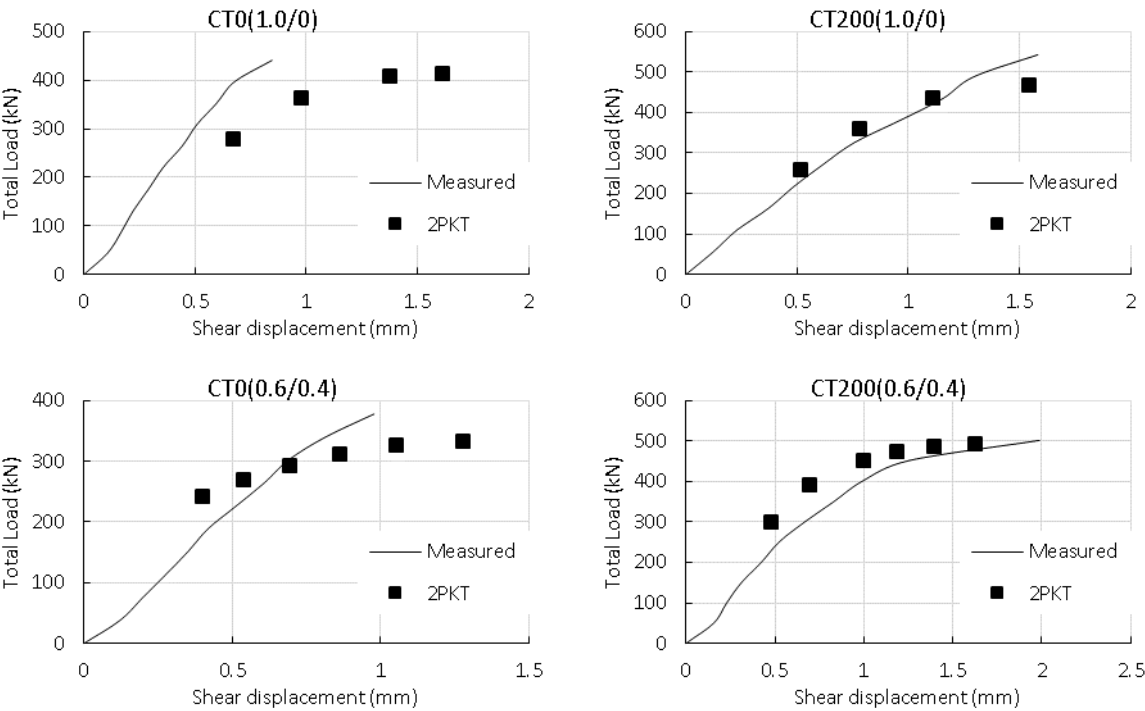
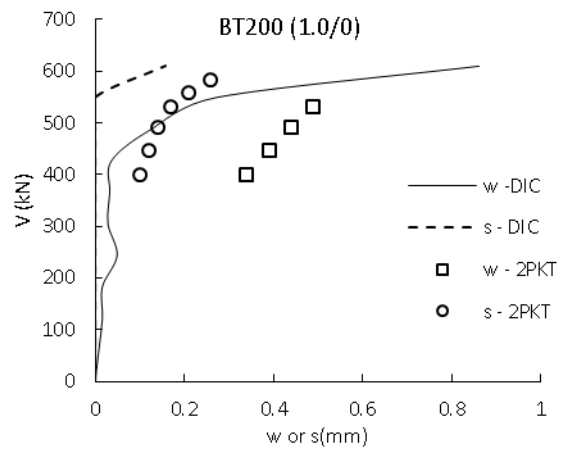
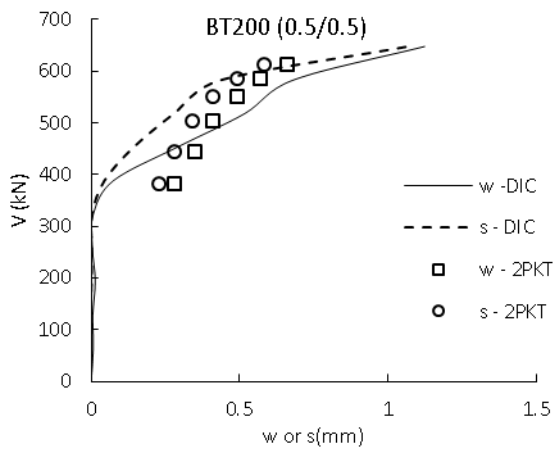
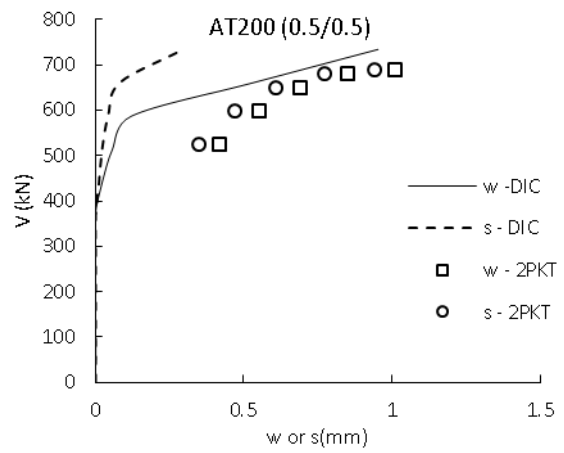
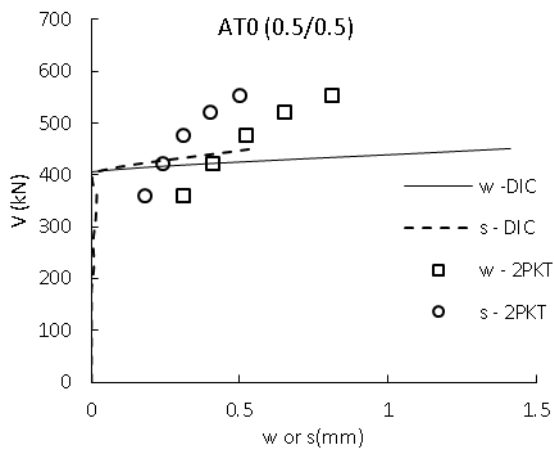
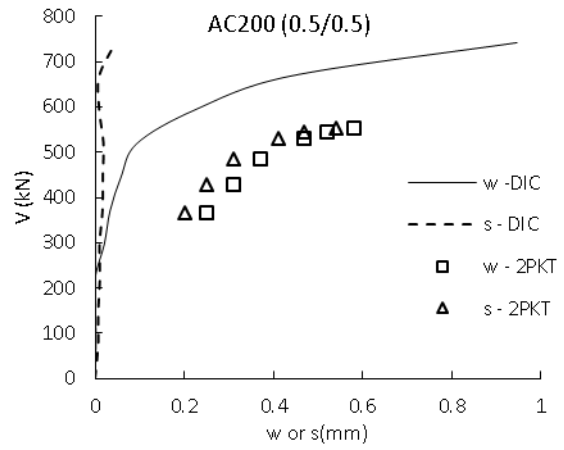
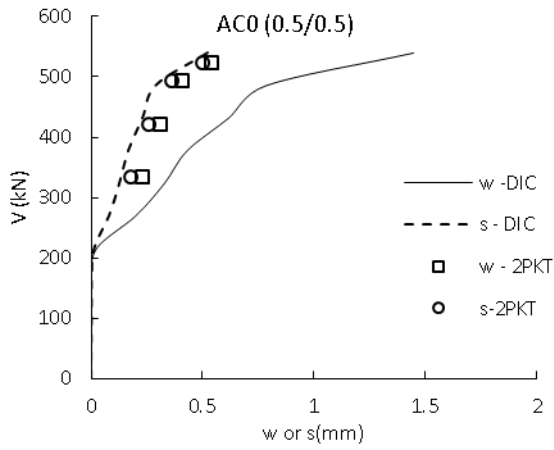


Figure 5.25: Comparison between the measured and estimated shear displacement in the 2PKT

The underestimation of the rotation of the rigid body by the 2PKT suggests that the crack displacements might be underestimated by the 2PKT. As stated in Chapter 2, the crack opening in the 2PKT varies linearly along the length of the crack while the crack sliding due to the shear displacement is constant. However, the observed kinematics reported in Chapter 4 do not support this. The crack opening takes a parabolic shape which is in agreement with similar tests and suggested formula for the crack opening (Poldon et al., 2019). In order to facilitate the comparison, measured crack opening and sliding at mid-height of the crack were compared to the mid-height values calculated using the 2PKT. The crack opening and sliding in the 2PKT are given by Equation 2.91 and Equation 2.92 in Chapter 2. The comparison between measured and estimated crack displacements is presented for the test beams in Figure 5.26.



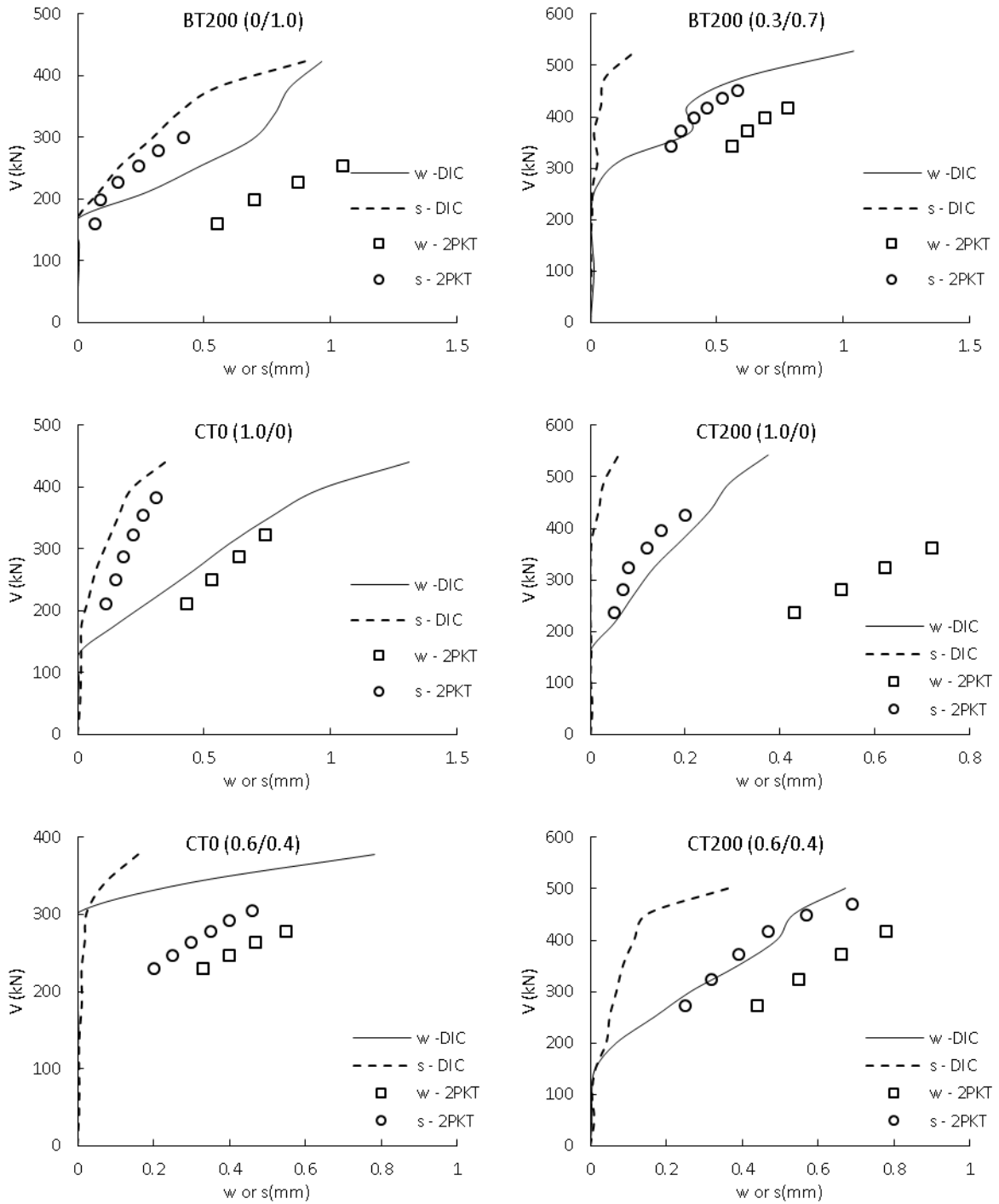


Figure 5.26: Comparison between measured and estimated kinematic using the 2PKT for the test beams

Although the calculated block rotations were less than the measured ones (see Figure 5.21), the comparison in Figure 5.26 shows that the estimated crack opening and sliding were greater than measured ones at the mid-height of the beam. This is largely due to the dominant contribution of the shear displacement, which was typically close to or greater than the

measured displacement, as shown in Figure 5.25. However, the calculations of the crack opening and sliding depend on the crack orientation, whether these were obtained from the DIC (Campana et al., 2013) or calculated using the 2PKT. For DIC calculations, crack kinematics at the mid-height of the beam were obtained using the actual orientation of the crack at that location, while a fixed angle α was used in the 2PKT based on the assumption that the crack runs directly between the support and the critical loading plate. To investigate the effect this assumption on the crack kinematics, the observed and assumed crack patterns were compared for the tested beams. For example, the actual and assumed orientation of the critical diagonal crack are compared in Figure 5.27 for beam BT200 (0.5/0.5). Figure 5.27 shows that the assumed orientation can vary noticeably from the observed one, which can have a significant influence of the magnitude of the crack opening and sliding displacements as shown in Figure 5.28.

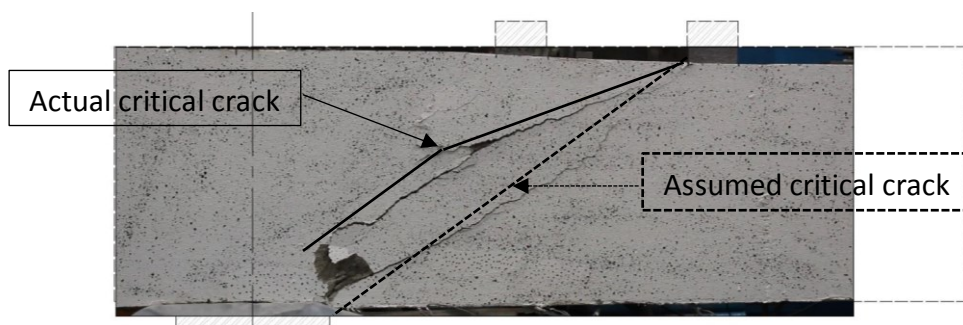


Figure 5.27: Comparison of the orientation of the actual critical crack and the 2PKT assumed critical crack – Beam BT200 (0.5/0.5)

Figure 5.28 assesses the sensitivity of the crack kinematics of the 2PKT to the crack angle for beam BT200 (0.5/0.5). In Figure 5.28, the crack opening and sliding were calculated using equations of the 2PKT and varying the crack angle α . The figure demonstrates that, for a given load step, block rotation and shear displacement, the crack kinematics varies significantly depending on the value of the crack orientation. Hence, it is possible that, even if the measured block orientation and shear displacement were greater than the calculated ones, the measured crack opening and sliding can be less than the calculated one, based on the crack orientation at mid-height of the beam.

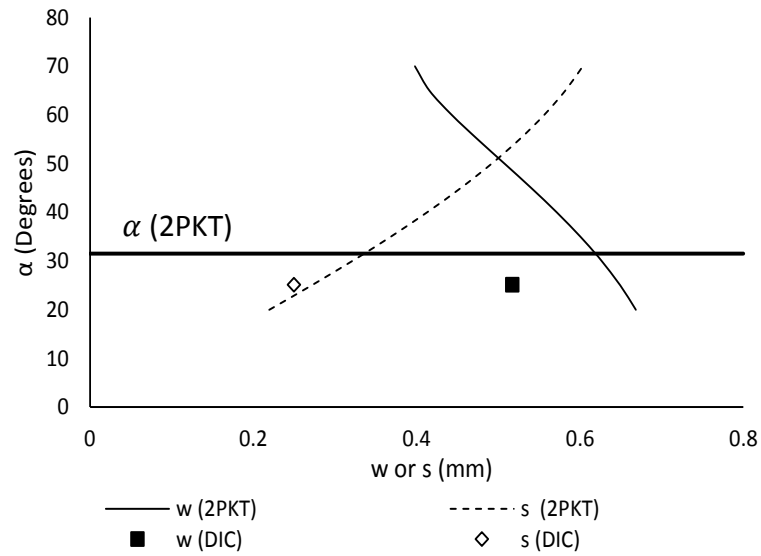


Figure 5.28: Sensitivity of the crack kinematics at mid height to the selection of the crack angle for beam BT200 (0.5/0.5) at $0.8V_{max}$

To study the effect of using the mid-height crack displacements to determine the contribution of aggregate interlock, the measured and predicted variation of the critical shear crack displacements were compared over height of the tested beams. Typical results are shown for beam BT200 (0.5/0.5) in Figure 5.29 at $0.8V_{max}$. This comparison suggests that the 2PKT values are overestimated.

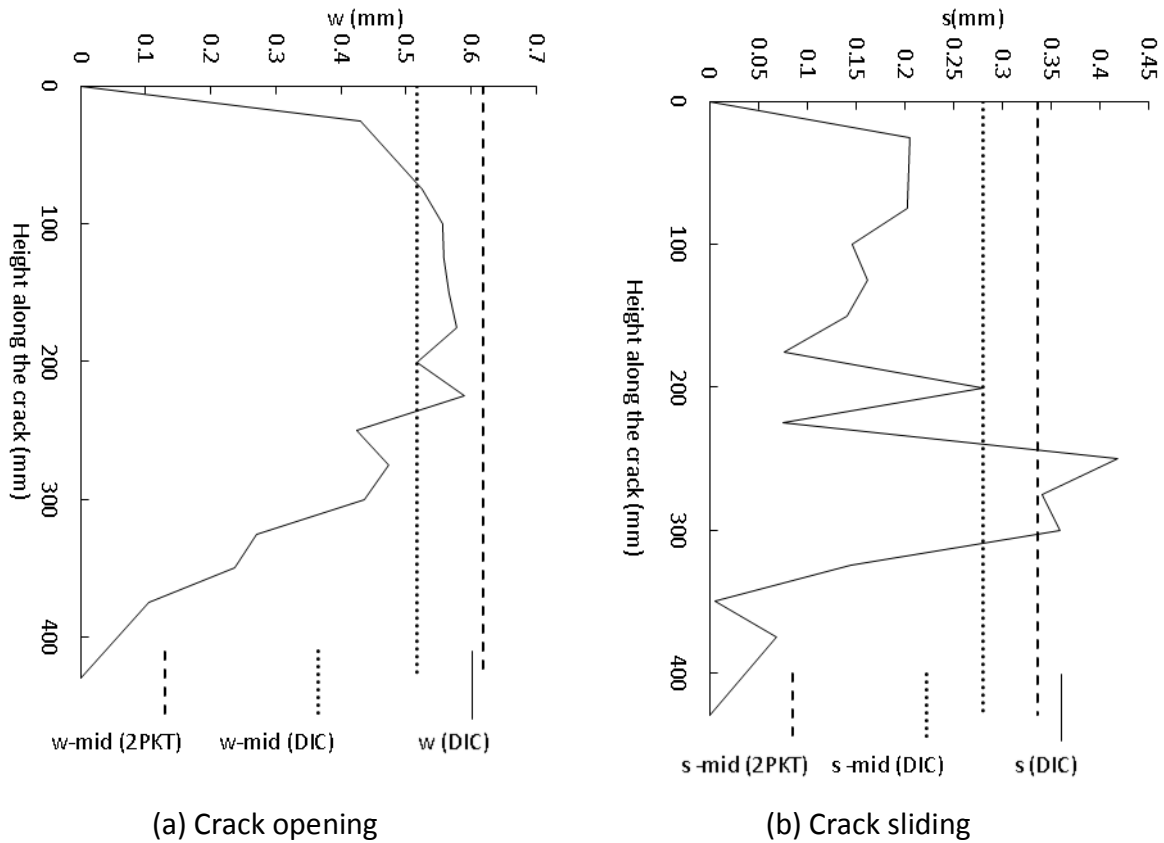


Figure 5.29: Variation of the crack kinematics along the height of the critical crack of beam BT200 (0.5/0.5) at $0.8V_{max}$

The CDM was used to calculate the shear stress along the critical diagonal crack in terms of the displacements along the crack. The results are shown in Figure 5.30 for beam BT200 (0.5/0.5) at $0.8V_{max}$. Figure 5.30 also shows shear stresses calculated in terms of the measured and calculated mid-height crack displacements shown in Figure 5.29. The total vertical shear force along the crack was found to be 35.7 kN by summing the contribution of each crack segment. Calculating the shear force in terms of the mid-height shear stress determined from measured crack displacements gives a very similar shear force of 38.0 kN. Use of the calculated mid-height crack displacements gives a slightly higher shear force of 45.68 kN.

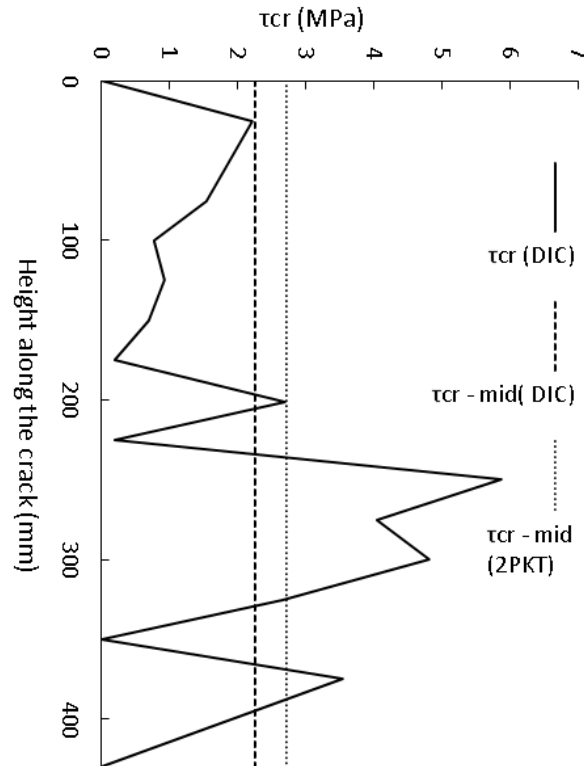


Figure 5.30: Shear stress along the crack calculated using variable and mid-height crack kinematics at $0.8V_{max}$ – Beam BT200 (0.5/0.5)

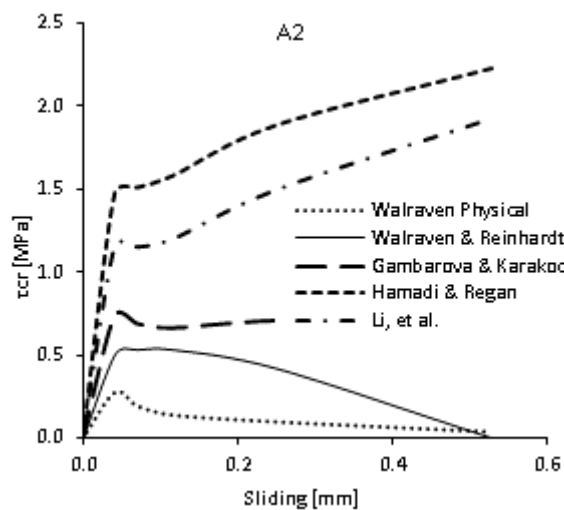
5.5. Shear Transfer Actions Based on Other Models in the Literature

The shear strength calculated using the five-spring model is the summation of the contributions of the shear transfer mechanisms. The calculated strength depends on the crack kinematics and the assumed constitutive models for shear transfer actions. There were noticeable differences between the measured and estimated rotations and crack kinematics as shown earlier. Yet, the five-spring model gave accurate estimations for the ultimate loads and deformations of the test beams.

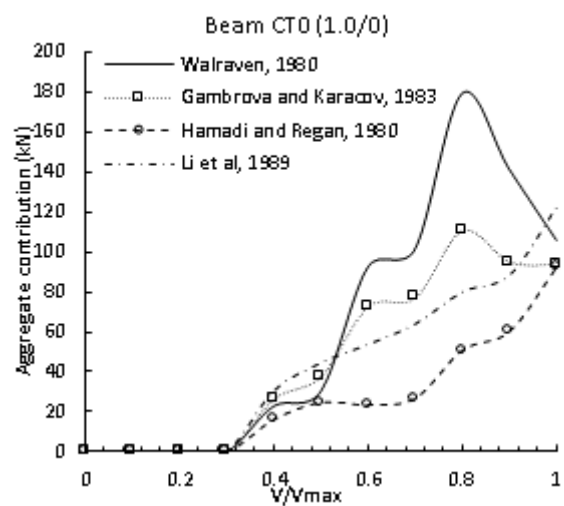
Equilibrium is always ensured in the five-spring model since the sum of the contributions of the shear transfer mechanisms is equated to the shear force derived from moment equilibrium in the shear span. The deformation parameters Δ_c and $\varepsilon_{t,avg}$ link the shear resisting contributions to the external force. The model can give good predictions, even if the

contributions of individual mechanisms are not well predicted, so long as the various errors compensate for each other.

Determination of the individual contributions of each shear resisting mechanism is subject to error resulting from inaccuracies in measured crack kinematics and modelling assumptions. These uncertainties have been investigated by the author (Elwakeel et al., 2018) for similar short span beams with multiple point loads (Fang, 2013) as well as the beams tested in this research. This study shows that implementing different models for the same shear transfer mechanism can lead to significant differences in the estimations. In extreme cases, the differences can be up to a factor of ten as shown in Figure 5.31. A merit of the five-spring model over simply summing the contributions of each shear resisting mechanism determined from measured crack displacements and measured strains is that equilibrium is always satisfied in the five-spring model as discussed above.

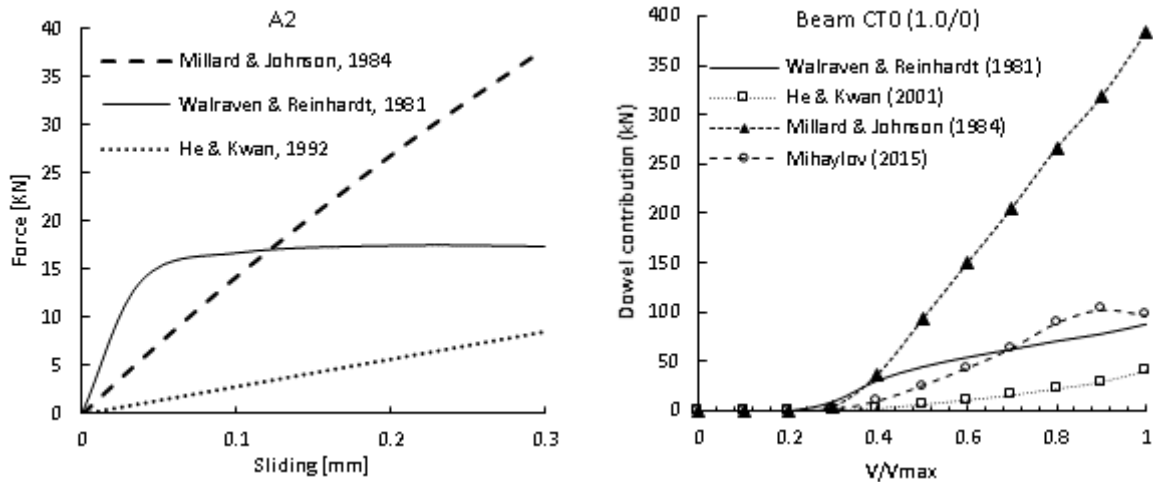


Beam A2 from Fang (2013)(Elwakeel et al., 2018)



Beam CT0 (1.0/0)

a) Different models of aggregate interlock



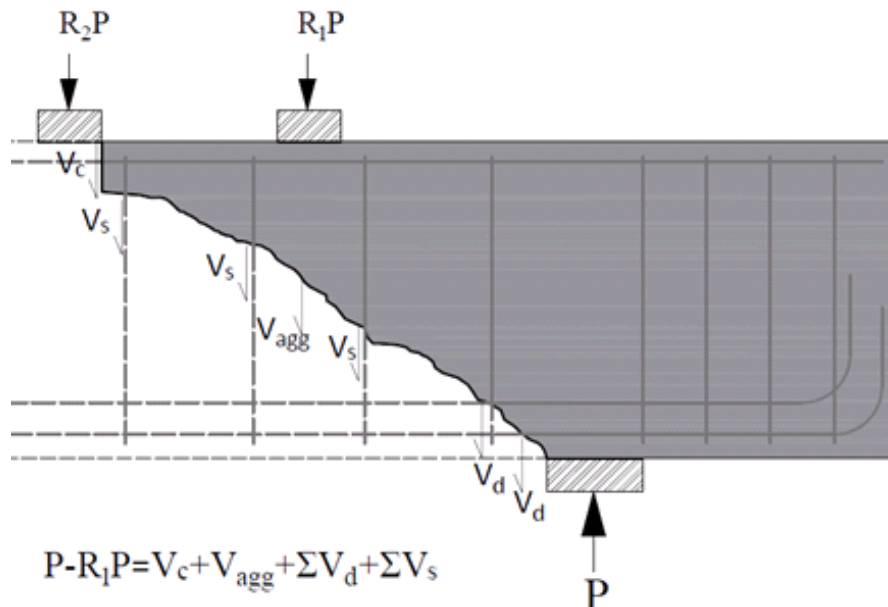
Beam A2 from Fang (2013)(Elwakeel et al., 2018)

Beam CT0 (1.0/0)

b) Different models of dowel contribution

Figure 5.31: Aggregate interlock and dowel contributions estimated using different models

The shear transfer actions were calculated from consideration of free body diagrams like that shown Figure 5.32. In beams loaded with two-point loads, the sum of the shear forces acting on the failure plane should ideally be equal to the load applied on the outer plate as shown in Figure 5.32.



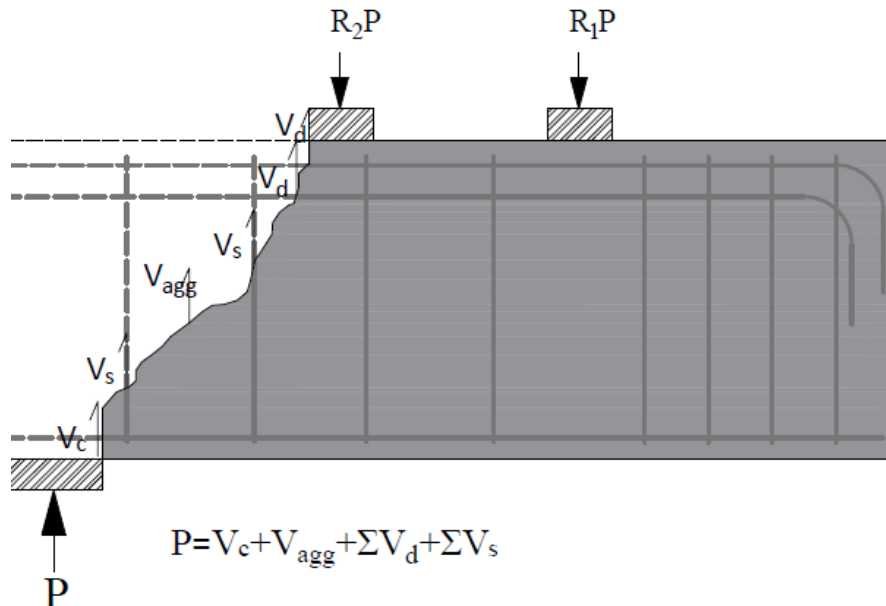


Figure 5.32: Shear transfer actions in a free body diagram of a beam with two-point loads

5.5.1. S-w curves of the tested beams

The shear transfer actions in the tested beams were estimated again using alternative shear resisting models from the literature and the actual crack shape and kinematics. For this purpose, the two-phase Walraven model was used to determine the contribution of aggregate interlock. This model is widely used and has been studied by several researchers (Campana et al., 2013, Ulaga, 2003, Guidotti, 2010). As mentioned in Chapter 2, the model assumes that the crack sliding (s) occurs after the full development of the crack opening (w). Guidotti (2010) suggested that only part of the crack opening (w_0) is necessary for the sliding to initiate, after which both the crack opening and sliding increase at an angle ($\gamma = \arctan(w_f/\delta)$) where $w_f = w - w_0$. Ulaga (2003), on the other hand, assumed that cracks initiate at an angle (γ) with $w_0 = 0$. The reader is referred to Chapter 2 for further discussion of the crack kinematic models.

This discussion has been revisited for the test beams. From the test results, the angle γ of the s-w curves depended on the location along the crack where the kinematics were measured. For instance, the crack sliding was more dominant for gauges near the compression face. This was the case for beams loaded on both the tension and compression face as shown in Figure 5.33, which shows the crack kinematics obtained using the DIC for beam AC0 (0.5/0.5) and AT200 (0.5/0.5).

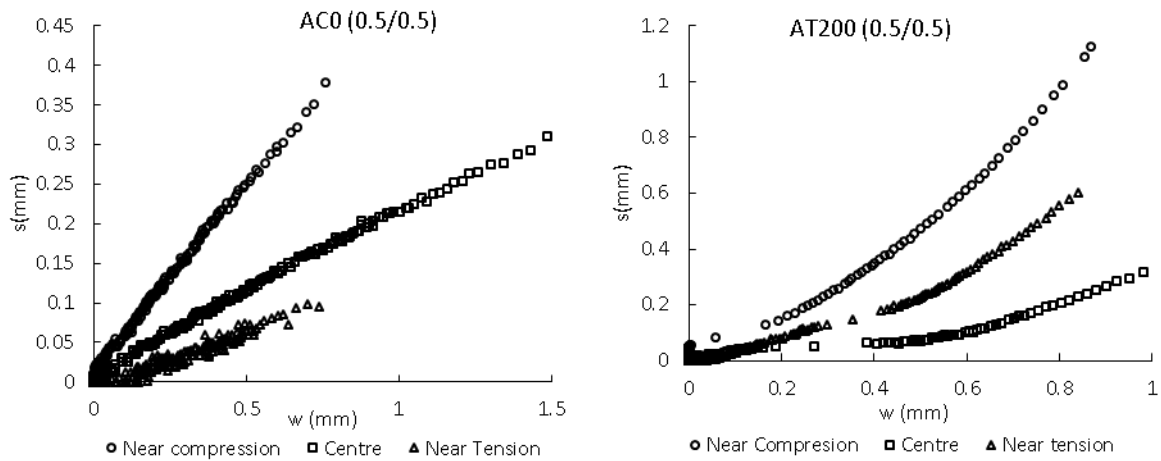
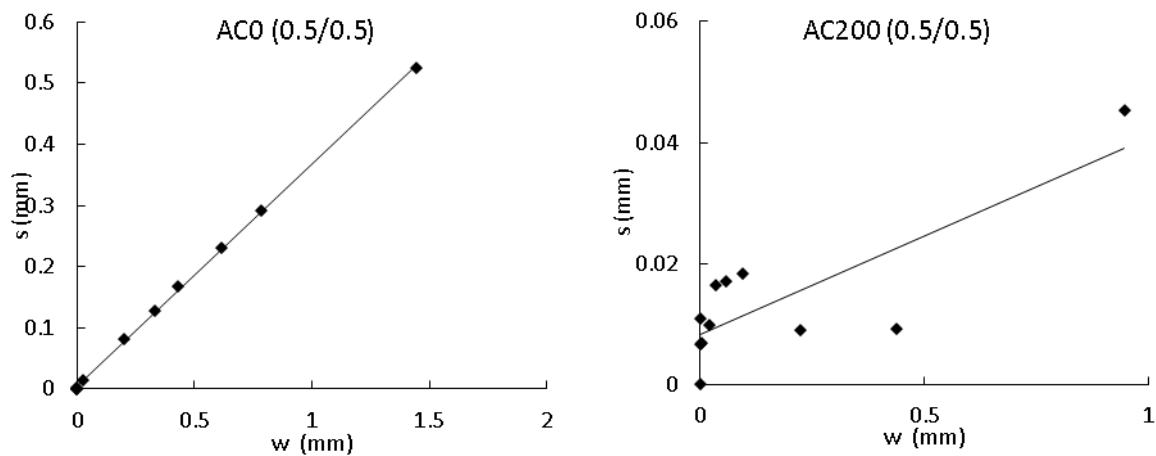
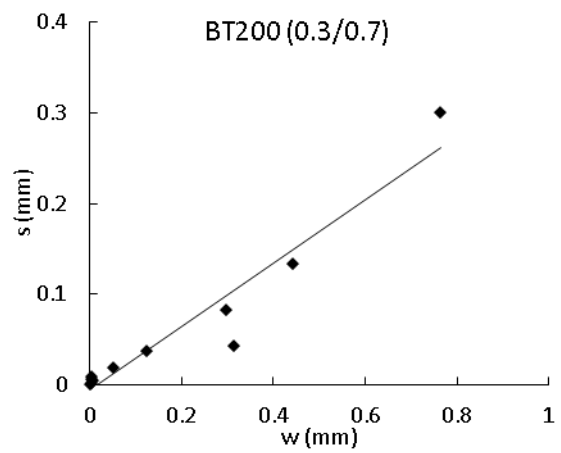
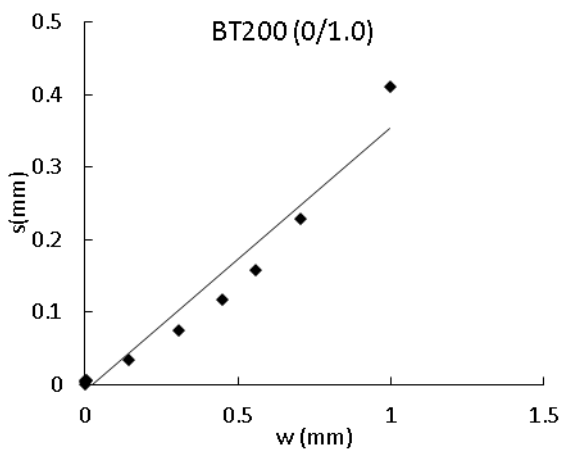
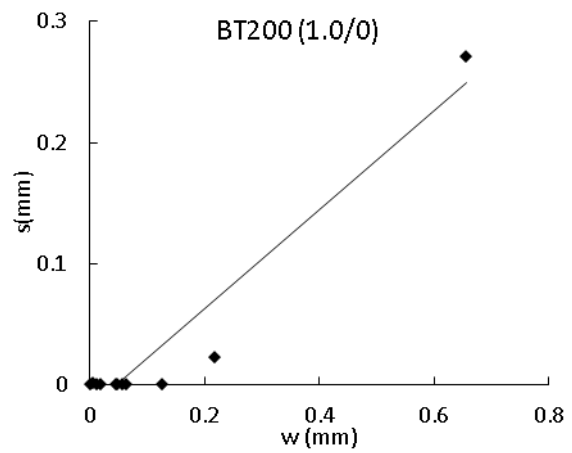
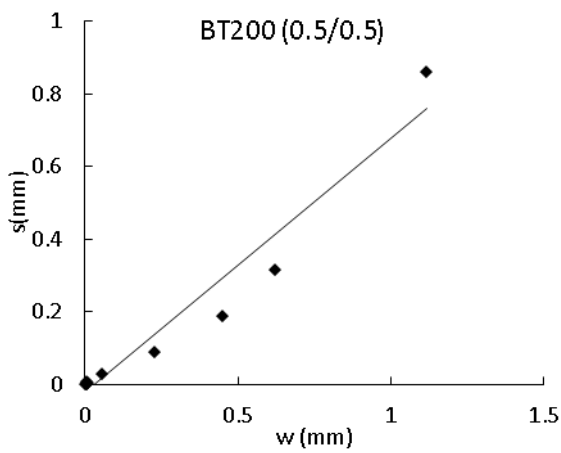
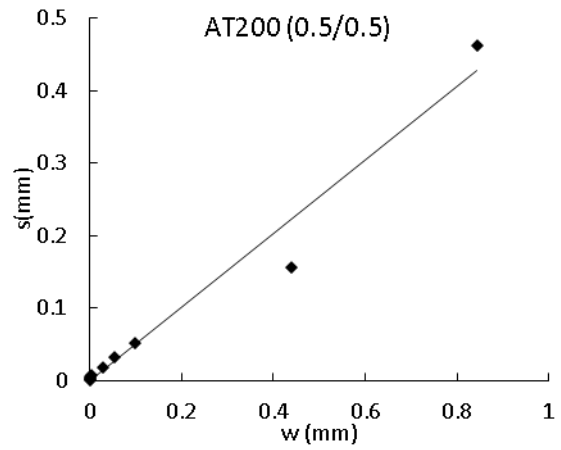
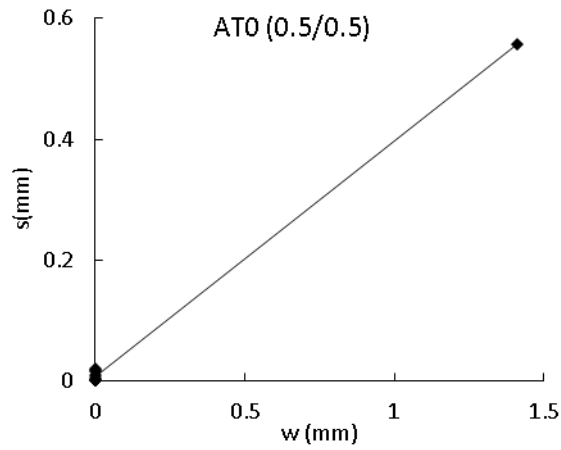


Figure 5.33: s - w curves for beam AC0 (0.5/0.5) and AT200 (0.5/0.5)

Figure 5.33 also shows that for some locations along the crack, the kinematics can lead to an initial crack opening w_0 before the crack sliding initiates, while for other locations in the same beam the initial crack opening w_0 is not clearly defined. Instead of using all the images processed during the test with a frequency of 0.2 Hz as in Figure 5.33, the initial crack opening w_0 and angle α were obtained along the crack length at steps of $0.1V_{max}$, as described earlier in Chapter 4. The results are shown in Figure 5.34 below.





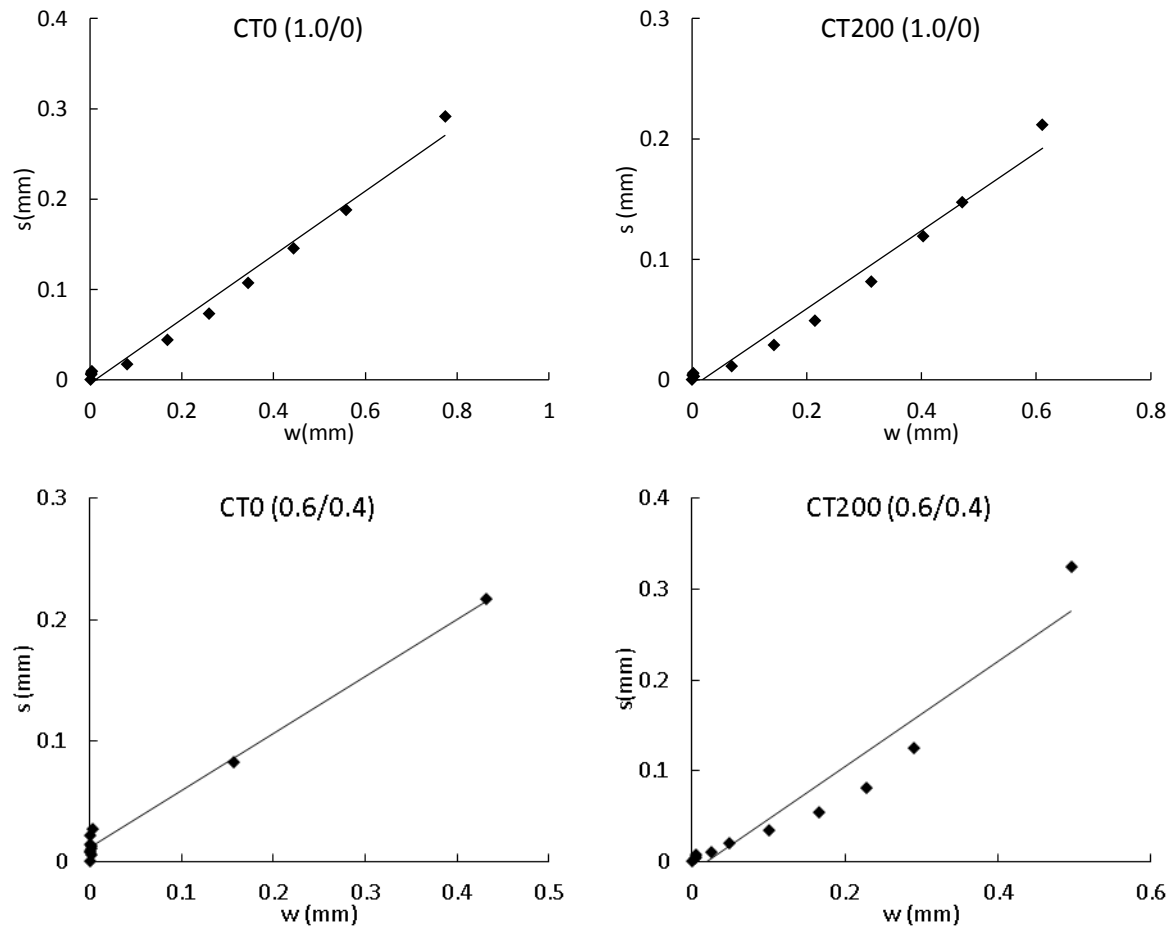


Figure 5.34: s - w curves for the test beams based on average readings

The majority of the beams in Figure 5.34 had an initial crack opening w_0 , prior to sliding, as suggested by Guidotti (2010). However, the initial crack opening was very small for the majority of the beams; hence, it is safe to assume that the Ulaga description (2003) fits the observed kinematics. The results of some of the beams (beams AC0 (0.5/0.5), AC200 (0.5/0.5), AT0 (0.5/0.5) and CT0 (0.6/0.4)) suggested that these beams had an initial crack sliding prior to crack opening. This unrealistic finding is attributed to the fact that the kinematics in Figure 5.31 are based on averaging results of the gauges along the crack length and the fit line can be affected by scattering of the response, particularly near failure. In conclusion, the kinematics assumed by Walraven in his original model do not match the measured kinematics. Furthermore, the angle γ of the s - w curves was influenced by the location along the crack where the kinematics were measured.

The kinematics described by Walraven and Ulaga are special cases of those described by Guidotti (Guidotti, 2010). If the angle γ of the s - w curve is set to zero in the Guidotti model,

the kinematics follow the original Walraven model while if w_0 is set to zero, the kinematics follow Ulaga's provisions. For the test results shown in Figure 5.34, the kinematics of Ulaga are closest to the observed behaviour. The influence of γ on the shear resistance provided by aggregate interlock was investigated by calculating the shear resistance provided by aggregate interlock along the failure crack using the methods of Walraven, Ulaga and Guidotti. Figure 5.35 shows that there are only minor differences between the predictions of Walraven, Ulaga and Guidotti for beams AC0 (0.5/0.5) and BT200 (1.0/0) despite the two beams having very different s-w curves. No significant crack opening occurred before sliding in beam AC0 (0.5/0.5) unlike BT200 (1.0-0) where w_0 was significant. As shown in Figure 5.35, the original Walraven model provides an upper limit while the kinematics proposed by Ulaga represent a lower limit, as also shown by (Campana et al., 2013). The behaviour shown in Figure 5.32 is representative of that in the other tested beams.

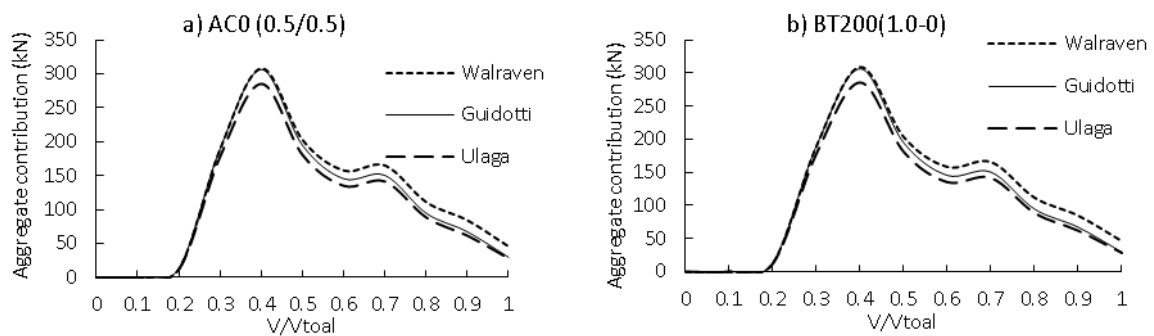
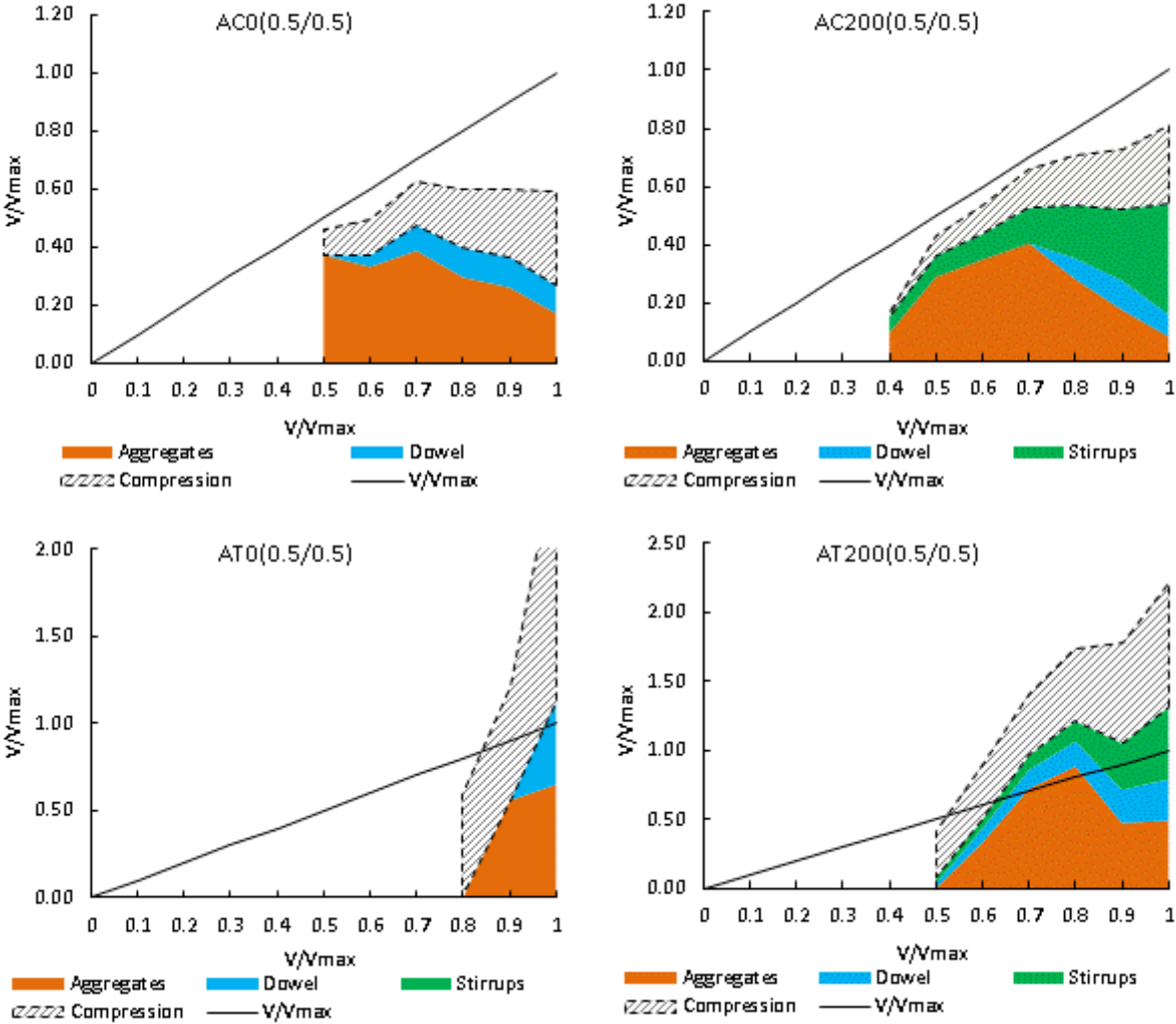


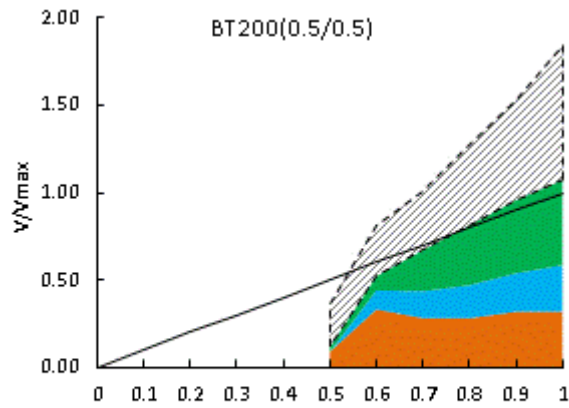
Figure 5.35: Contribution of the aggregate interlock calculated using provisions suggested by Walraven, Guidotti and Ulaga for a) beam AC0 (0.5/0.5) and b) BT200 (1.0-0).

5.5.2. Results of the shear transfer actions

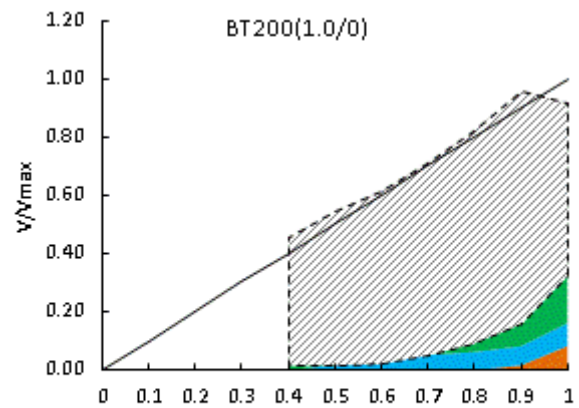
For the shear transfer mechanisms, the Walraven model (1980) was selected to estimate the contribution of aggregate interlock in the tested beams. The contribution of aggregate interlock was calculated by integrating the vertical component of the crack shear stress and normal stress along the failure shear crack. The total aggregate volume of the concrete was taken as 0.75 of the total volume of the concrete as suggested by Walraven (1980) while the coefficient of friction was taken as 0.4. As stated earlier in Chapter 3, the maximum aggregate size was 20mm. For consistency, the dowel contribution was calculated using the model of (Walraven and Reinhardt, 1981) which is a refinement of that originally proposed by Walraven (1980). The shear displacements at locations where the diagonal crack intersected the flexural

reinforcement as well as the crack opening parallel to the direction of the stirrups were obtained using DIC. These measurements were used to obtain the dowel force and the stirrups contributions respectively. The contribution of the shear reinforcement was estimated using the Sigrist two-step bond model (1995) while the contribution of the critical loading zone was estimated using the five-spring model (2015). Figure 5.36 shows the shear transfer actions for the test beams during the tests.

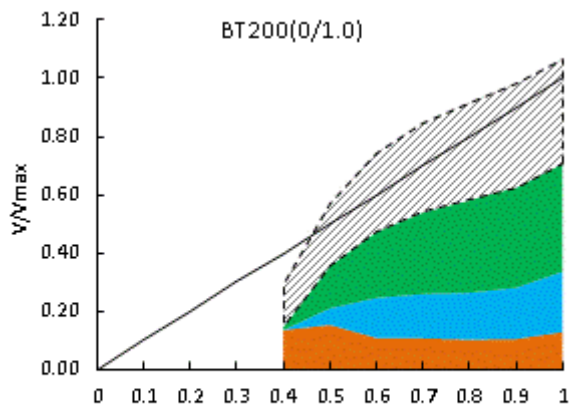




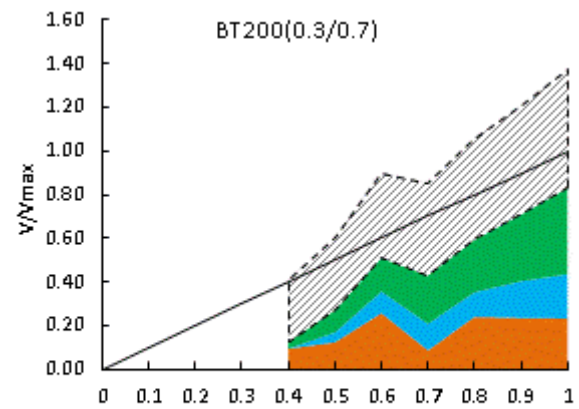
■ Aggregates ■ Dowel ■ Stirrups
 Compression V/V_{max}



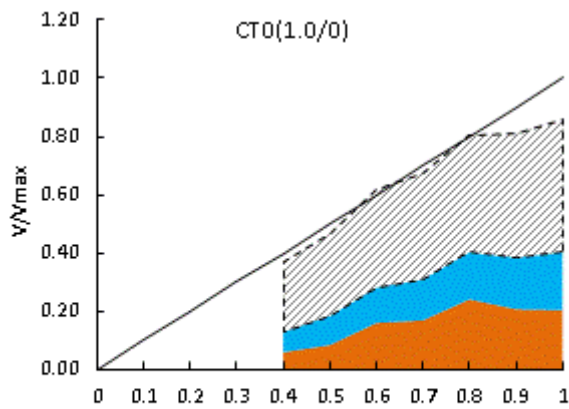
■ Aggregates ■ Dowel ■ Stirrups
 Compression V/V_{max}



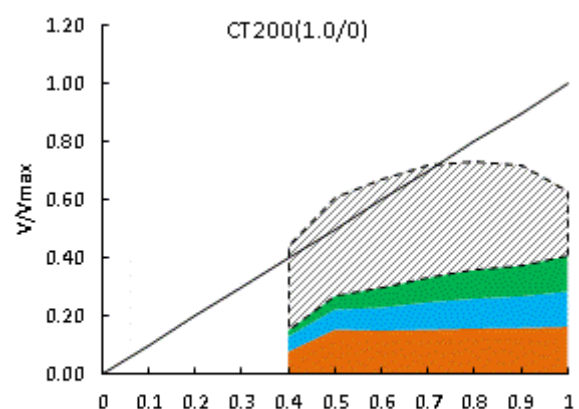
■ Aggregates ■ Dowel ■ Stirrups
 Compression V/V_{max}



■ Aggregates ■ Dowel ■ Stirrups
 Compression V/V_{max}



■ Aggregates ■ Dowel
 Compression V/V_{max}



■ Aggregates ■ Dowel ■ Stirrups
 Compression V/V_{max}

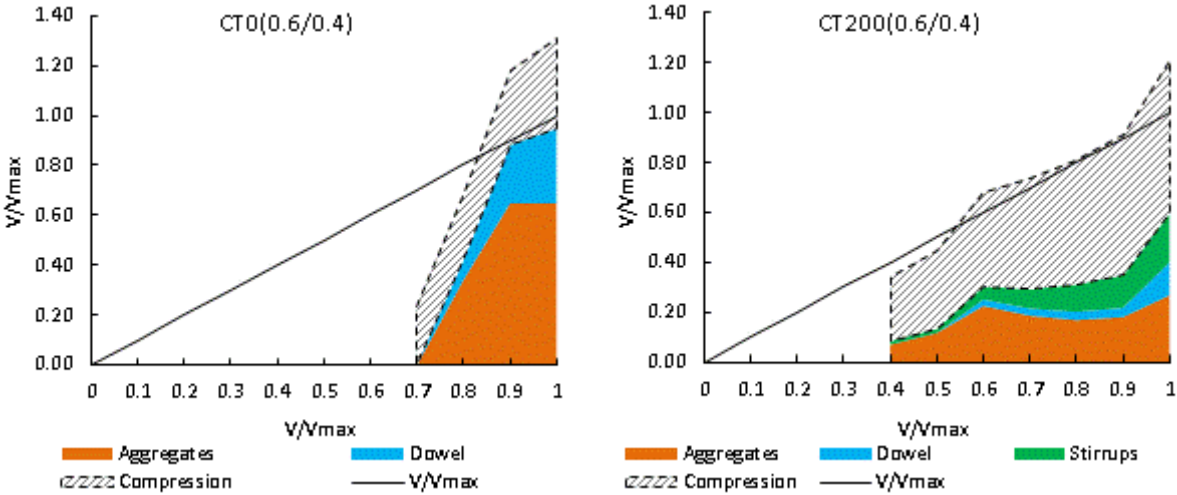
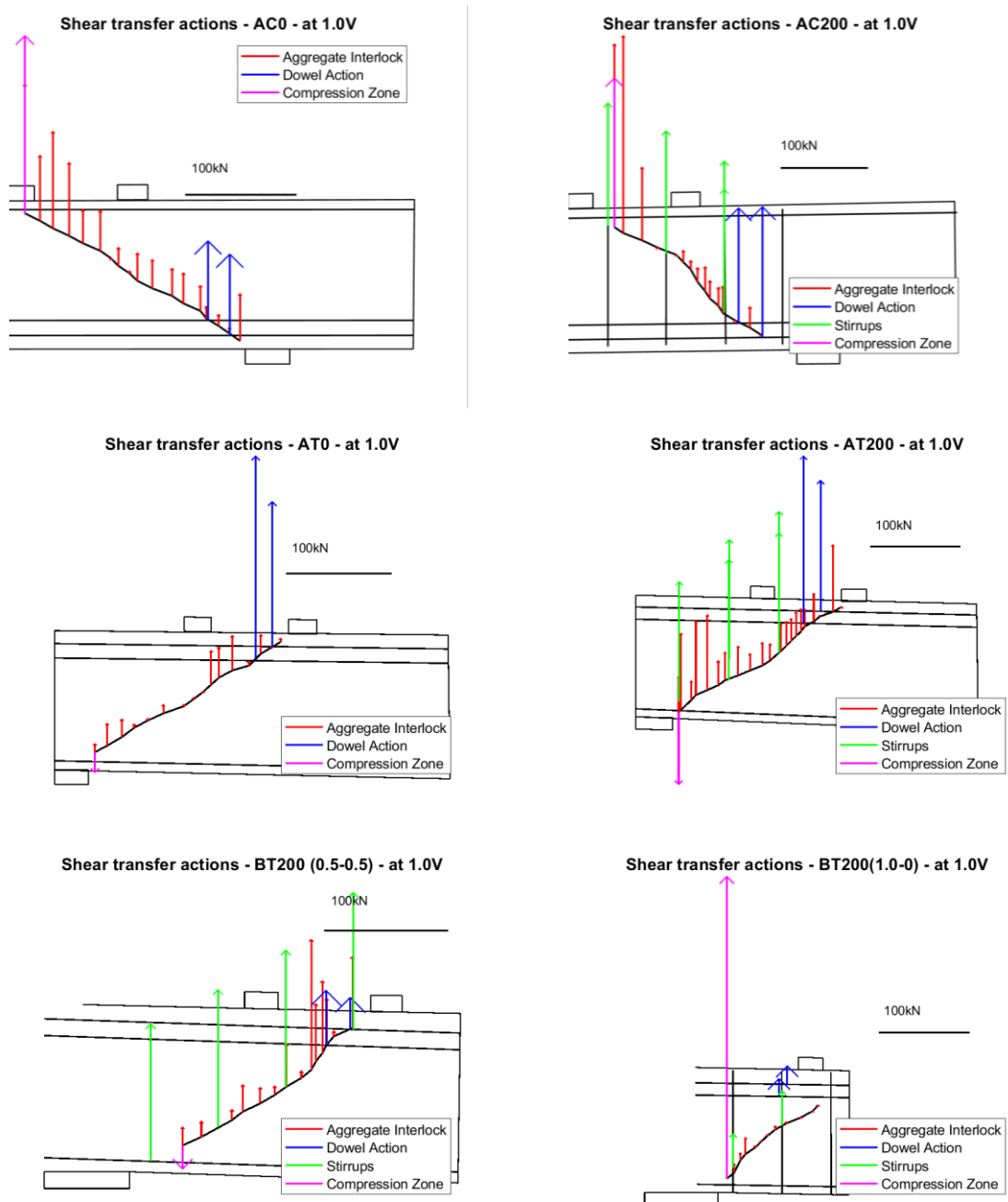


Figure 5.36: Shear transfer actions for test beams

It can be seen that, unlike the five-spring model, the summation of the mechanisms can lead to a shear resistance greater than the actual applied shear force in the majority of the tests. In beams AT0 (0.5/0.5), AT200 (0.5/0.5) and BT200 (0.5/0.5) the estimated resultant shear force carried by aggregate interlock, dowel action and the stirrups (if applicable) was greater than the total applied load. Although these three beams are similar to beams AT0 (0.5/0.5) without shear reinforcement, this overestimation cannot be directly linked to one mechanism. While the contribution of the aggregate interlock seems overestimated for beams AT0 (0.5/0.5) and AT200 (0.5/0.5), the contribution of the stirrups seems noticeably higher in beam BT200 (0.5/0.5). As mentioned earlier, these differences can occur even for identical beams because of the sensitivity of the models to the crack kinematics and orientation. Generally, the contribution of the shear reinforcement and dowel action increased with the increase of the shear span to depth ratio, while the contribution of the flexural compression zone was greater for beams with shorter span to depth ratios and when greater loads were applied closer to the support.

5.5.3. Shear transfer actions based on equilibrium

As appears in Figure 5.36, the total shear force calculated with different models can sometimes be greater than the actual total shear force. To maintain vertical equilibrium, the contribution of the compression zone is sometimes defined from the vertical equilibrium of the rigid body as the force not expressed by the other mechanisms (Fang, 2013, Elwakeel et al., 2018). The contribution of the compression zone in Figure 5.37 was calculated based on vertical equilibrium considering the free body shown in Figure 5.32.



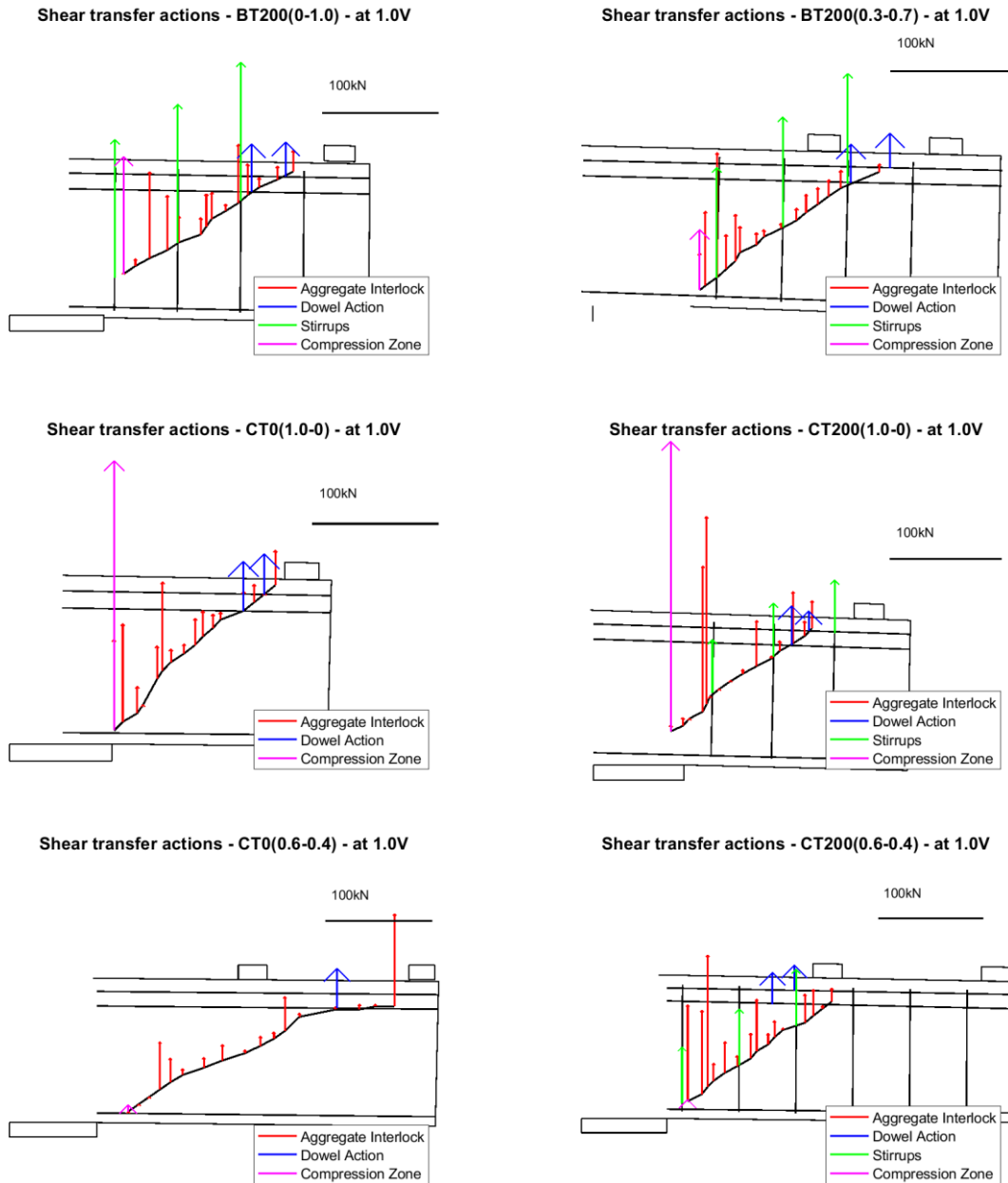


Figure 5.37: Shear transfer actions at failure based on equilibrium

The behaviour of beams with pairs of point loads loaded on the tension and compression face (the first four beams) is compared below in terms of their shear transfer mechanisms. The contributions of dowel action and aggregate interlock were greater in beams loaded on the tension face. The increased contribution of the aggregate interlock and dowel action for tension face loading resulted from the higher values of the crack sliding compared to beams loaded on their compression face. The dowel action contribution was obtained by adding the contributions of each layer of reinforcement calculated independently. This requires further

consideration but maybe an overestimate as the model used for the dowel contribution assumes dowel action to be of minor importance and does not provide an upper limit for it (Walraven and Reinhardt, 1981). Other models, for example, the five-spring model, limit the contribution to either formation of plastic hinges in the bar or failing of the concrete cover. For beams of series B, Beam BT200 (1.0/0), where the load was only applied near to the support, the majority of the applied force was carried by arching action as shown in Figure 5.36 with negligible contribution from other shear actions. For beams failing in the outer shear plane in series B (Beams BT200 (0.5/0.5), BT200 (0.3/0.7) and beam BT200 (1.0/0)), the proportion of load resisted by aggregate interlock increased as the load applied near the support increased. This can be attributed to the increase in the normal stress due to the confinement provided by the inner load. Figure 5.38 presents the crack kinematics for beams in series B failing in the outer shear plane for $a_{v2} < 2d$. The legend shows the percentage of the load applied closer to the support (P_1/P) to the load applied in the outer shear plane (P_2/P). Increasing the load on the inner plate reduced displacements in the critical shear crack leading to a greater contribution of aggregate interlock. The contribution of the aggregate interlock for these beams during the test are presented in Figure 5.39.

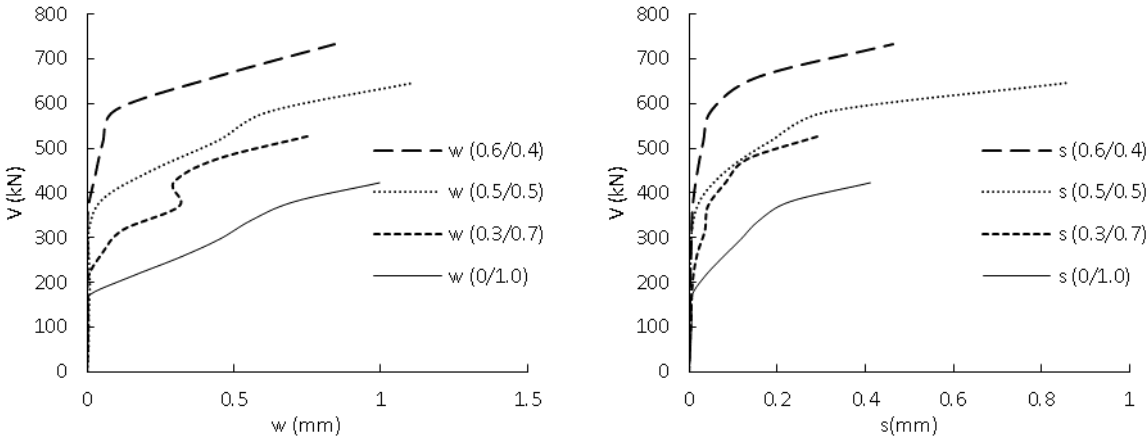


Figure 5.38: Comparison of the crack kinematics for beams failing in outer shear plane inside (2d)

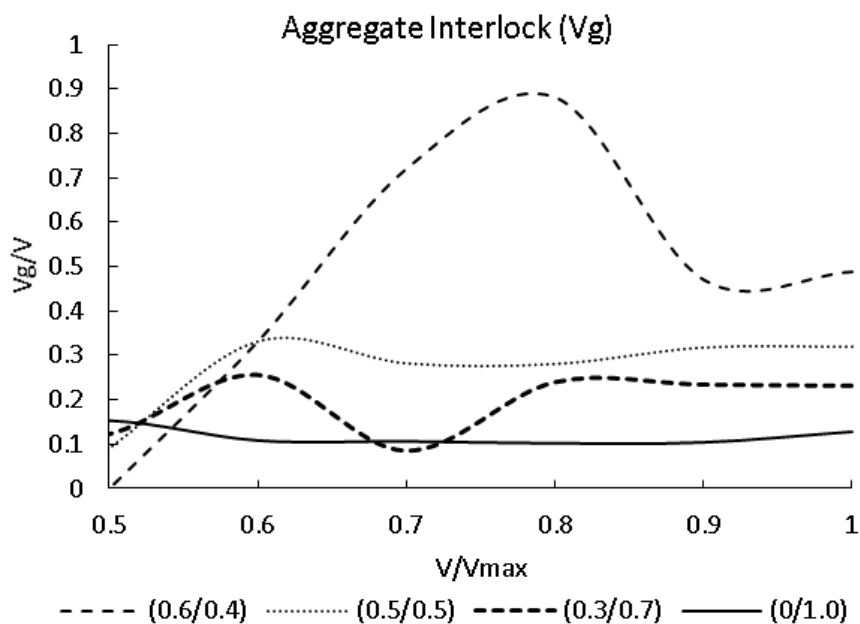


Figure 5.39: The contribution of the aggregate interlock for beams in series B during the test.

5.6. Conclusions

The use of DIC facilitated the validation of the provisions given by the 2PKT to predict the full displacement field of the shear span during tests. The two parameters of the theory were experimentally obtained using either actual or virtual LVDTs to examine the proposed deformation given by the 2PKT. Using measured rotation (φ_{block}) and shear displacement (Δ_c), the 2PKT gave accurate predictions of the deformation for beams loaded on the compression face and less accurate predictions for beams loaded on the tension face. Modifications of the theory for beams loaded on the tension face were introduced to account for the shear displacement resulting from the secondary shear crack and the actual location of the CoR. The modified approach gave significantly better predictions of the deformation for beams loaded on the tension face.

The strength, load-deflection responses and the shear transfer mechanisms of the test beams were evaluated using the five-spring model. The model provided very good predictions with an average accuracy of the predictions for beams with two-point loads = 0.97 and COV = 11, while the average accuracy of the predictions for beams with single point load = 0.88 and COV = 10. The load-deflection response was governed by the CLZ as the rest of the contributions were either restricted to an upper limit or nearly constant. In the post-peak response, the

contribution of the CLZ reduced significantly, while the rest of the components remained constant, and hence, the post-peak response was more softened than what was experimentally observed.

The contributions given by the five-spring model for the tested beams were generally sensible. The governing contribution for all of the short beams was the contribution of the CLZ as expected, while for beam CT0 (0.6/0.4), which failed outside the shear enhancement zone without shear reinforcement, the dominant contribution was the aggregate interlock. The dowel contribution was limited and the contribution of the shear reinforcement increased as the shear span of the critical failure increased. The two kinematic parameters estimated by the model were assessed using the test results. It appeared that there were noticeable differences between the measured and estimated rotations and crack kinematics. Yet, the five-spring model gave accurate estimations for the ultimate loads and deformations of the test beams.

The contributions of the mechanisms were also calculated using various models available in the literature. The Walraven model (1980) was used to estimate the contribution of the aggregate interlock and the dowel contribution. The contribution of the shear reinforcement was estimated using the two steps bond model (Sigrist, 1995) while the contribution of the critical loading zone was estimated using the five-spring model (2015).

The contributions of dowel action and aggregate interlock were greater in beams loaded on the tension face. These increased contributions resulted from crack sliding being greater than in comparable compression face loaded beams. The contribution of the aggregate interlock for beams failing in the outer shear span increased as the load applied closer to the support increased. This was linked to the increase in the normal stress due to the confinement provided by the inner load, which was experimentally observed. The contribution of the dowel action was the least significant while the stirrups were more effective as the shear span to effective depth increased.

Determination of individual contribution of the different mechanisms included some uncertainties associated with the accuracy of the obtained crack kinematics and the model assumptions. Regardless of this, these models can still be used to compare the contributions of the shear mechanisms in test beams as long as the same model for each component has been used for all of the beams.

CHAPTER 6. NON-LINEAR FINITE ELEMENT (NLFE) METHODOLOGY

6.1. Introduction

Experimental investigation is essential for the development of improved design methods for reinforced concrete beams loaded in shear. However, experimental investigation is expensive and time-consuming with benefit subject to adequate selection of loading and boundary conditions. Properly calibrated nonlinear finite element analysis (NLFEA) can be used to identify key parameters influencing behaviour such as loading arrangement, beam geometry, concrete strength and support conditions. This helps in deciding on the critical parameters to be investigated in laboratory investigations thereby significantly reducing costs and enhancing the usefulness of test results. NLFEA can be further refined after testing to conduct parametric studies on non-investigated parameters.

This chapter provides a brief background to NLFEM with emphasis on the smeared crack model and the software used in this research (DIANA v10.2 (DIANA, 2017)). Relevant material models available in DIANA are discussed for concrete (compressive, tensile and shear behaviour) and reinforcement (embedded and bond-slip reinforcement models). Meshing considerations are also discussed (element types, mesh size and modelling of loading plate) along with the solution procedures used.

6.2. Discrete and Smeared Crack Modelling

Cracked concrete is usually modelled using either discrete or smeared crack models. In discrete models, cracks are modelled as displacement discontinuities which can be simulated using interface element to separate adjacent elements. Conversely, smeared crack models treat cracked concrete as a continuum and the stress-strain relationships are derived accordingly (Rots, 1991).

The respective advantages and disadvantages of discrete and smeared crack models have been much discussed since the early beginnings of crack modelling. The discrete crack model was introduced in 1967 (Ngo and Scordelis, 1967). It reflects the physical nature of the crack by identifying the crack as a true discontinuity. However, this representation does not readily fit within the finite element method as crack formation requires the introduction of a displacement discontinuity in the finite element mesh. Another drawback of the discrete

crack model is that it forces the crack to follow a predefined path along the element edges. Even so, the discrete crack can still be used in engineering problems where the crack path can be pre-imagined (e.g. notched specimens).

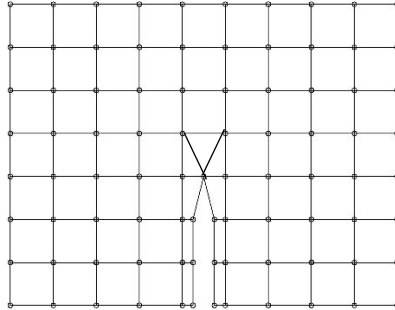


Figure 6.1: Nodal separation in Smearred crack model

The concept of smeared crack modelling was firstly introduced in the late 1960s by Rashid (Rashid, 1968) as an alternative to the discrete crack model. As mentioned earlier, the smeared crack model deals with cracked concrete as a continuum rather than introducing a physical discontinuity in the mesh. Although continuity is favourable in terms of mesh topology, and does not impose any restrictions on the crack path, it contradicts the physical nature of the material discontinuity in cracks.

The principle of smeared cracks is justified by the existence of bands of micro-cracks in the concrete due to the concrete heterogeneity and the presence of the reinforcement. These bands of microcracks have even been recognised as a material property (Bažant, 1983). It is only at late stages of loading that those cracks link up to form macro cracks (Borst et al., 2004). Furthermore, in particular cases, the macrocracks take the form of smeared cracks as in large scale shear walls or panels with dense reinforcement.

6.3. Smeared Crack Model

In the smeared crack model, the initial isotropic stress-strain relationship is replaced by an orthotropic relationship after crack formation. This orthogonality not only permits a free orientation of the initial crack but also preserves the topology of the finite element mesh.

The axis of orthotropy is determined from the initial crack orientation. After crack formation, shear stress can be transferred across cracks through aggregate interlock, and hence, the principal stress direction may no longer align with the initial orientation of the crack. The orientation of the crack is assumed to be either fixed following the initial crack orientation

“fixed-crack model” or the crack may be allowed to co-rotate with the axis of the principal strain “rotating-crack model”. A hybrid model between the rotating and fixed crack model is the “multi-direction crack model”.

6.3.1. Fixed smeared crack model

In fixed crack models, the crack orientation along the crack path is fixed to the initial crack orientation. As mentioned before, when a crack propagates, forces can develop in the crack surface as the angle of principal stresses deviates from the initial crack orientation.

In the early days of smeared crack modelling the normal and shear stiffness moduli were set to zero upon crack formation in the stiffness matrix causing the crack normal and shear force to disappear once the crack is initiated. This not only ignores the tensile and shear forces transmitted through cracks but also introduces numerical difficulties imposed by the strong discontinuity due to this sudden switch (Rots and Blaauwendraad, 1989).

Accordingly, values other than zero for the stiffness moduli after crack formation have been introduced by many researchers with different reduction approaches for both shear and normal stiffness. Further details regarding direct and shear stiffness reduction factors are explained in sections (6.4.1) and (6.4.3).

One of the main merits of the fixed crack model is its consideration of the force transmitted through crack surfaces. This is particularly important for members without shear reinforcement where a significant portion of the shear force may be transferred through cracks (Campana et al., 2013, Mihaylov et al., 2013, Mihaylov et al., 2015). However, determining the optimum shear model and its associated values (e.g. the shear retention factor) can be troublesome (De Borst and Nauta, 1985, Sagaseta, 2008).

6.3.2. Multi-directional fixed smeared crack model

In a multi-directional fixed smeared crack model, the crack orientation is fixed to the initial crack orientation and the angle of the principal stresses axis is permitted to rotate up to a limiting criterion. After this criterion is violated, a new crack is initiated following the rotation of the principal stress, giving rise to the term multi-directional crack model.

In order to fully formulate a constitutive multi-direction crack model; criteria for the crack initiation should be defined along with the stress-strain relationship. A crack is initiated when the following two criteria are violated simultaneously:

- The principal tensile stress exceeds the tensile strength of the concrete, and
- The angle between the crack orientation and the axis of the principal stresses exceeds a threshold angle.

On violation of these criteria, a new crack is initiated and the previous crack data are erased from memory, unlike the fixed crack model where the initial crack preserves its orientation up to the end of the analysis (DIANA, 2017).

In order for the above two conditions to occur simultaneously, it is possible that the principal tensile stress may temporarily become significantly larger than the tensile strength before the angle between the crack orientation and the axis of the principal stresses exceeds the threshold angle (De Borst and Nauta, 1985). Therefore, attention should be paid when defining the threshold angle. An angle of 60° has been found to give reasonable predictions (DIANA, 2017, De Borst and Nauta, 1985, Sagaseta, 2008).

The approach of multi-directional cracks is suitable for cases where the fracture is initiated in tension and subsequently proceeds in tension-shear. In this case, the initial crack orientation remains fixed for a certain period after which the crack angle rotates.

The stress-strain relationship is generally defined in smeared crack models in terms of cracked concrete without any distinction between cracks and the solid concrete between cracks. Forces transmitted through a crack can better be studied using the crack strain instead of the total strain. For that reason, many researchers recognise the importance of decomposing the total strain (ε) into solid strain (ε^{con}) and cracked strains (ε^{cr}) in the so-called principle of strain decomposition (Borst et al., 2004, Rots and Blaauwendraad, 1989, Bažant, 1983).

$$\Delta\varepsilon = \Delta\varepsilon^{cr} + \Delta\varepsilon^{con} \quad \text{Equation 6.1}$$

One advantage of strain decomposition is that it allows the use of a separate decomposed crack model, which is a step closer to a discrete crack model. Decomposed crack models can also be used in combination with other nonlinear phenomena (e.g. plasticity, creep and shrinkage) (Rots and Blaauwendraad, 1989, De Borst and Nauta, 1985).

Another important advantage of strain decomposition is that it allows the decomposed crack strain to be further sub-decomposed into a system of non-orthogonal cracks meeting in a sampling point (De Borst, 1987)

$$\Delta\varepsilon^{cr} = \Delta\varepsilon_1^{cr} + \Delta\varepsilon_2^{cr} + \dots \quad \text{Equation 6.2}$$

6.3.3. Rotating smeared crack model

As mentioned earlier, the axis of the principal stresses in a smeared model usually rotates after the formation of the initial crack. An alternative version of the smeared crack model is the rotating crack model which was first introduced by Cope (Cope et al., 1980) who suggested aligning the rotation of the material orthotropy with the crack orientation. A well-known example of the rotating crack model is the modified compression field theory (Vecchio and Collins, 1986) which adopts the concept of coaxiality.

Introducing material orthotropy directly causes misalignment of the principal stress and strain axes (Bažant, 1983). Therefore, the direct use of the stress-strain relationship is inconsistent without any correction of this misalignment. To enforce the coaxiality, a key condition must be satisfied regarding the tangential shear modulus G_{12} as follows:

$$G_{12} = \frac{(\sigma_{11} - \sigma_{22})}{2(\varepsilon_{11} - \varepsilon_{22})} \quad \text{Equation 6.3}$$

Where σ_{11} and σ_{22} are the initial principal stress and ε_{11} and ε_{22} are the initial principal strains in the 1, 2 directions. This condition is derived by maintaining the same change in rotations of the principal stress and strain axes in Mohr's circle following a small strain increment (De Borst and Nauta, 1985).

The concept of the rotating crack model can be extended to a multi-directional crack model by setting the threshold angle to zero with no tensile strength criterion and ignoring the previous crack history as new cracks form. Although this method is similar to the rotating crack method, it allows the use of the strain decomposition as in the multi-directional crack model.

Overall, the fixed cracked model allows force to be transmitted through the crack surface by reducing the normal and tangential stiffness moduli after cracking. However, previous studies show that the choice of optimum shear retention model is not a straightforward task with investigation needed to determine which model and its associated variables are most suitable (Sagaseta, 2008, Amini Najafian et al., 2013). The multi-direction fixed crack model updates the crack orientation when the difference between the crack orientation and the principal stress exceeds a predefined threshold angle. This is of a great significance especially for tension-shear types of failure where the crack initiates in tension and then tends to rotate. Nevertheless, attention should be taken when deciding the threshold angle as poor choice

can cause the principal tensile stress to exceed the tensile strength of the concrete. In rotating crack models there are no restrictions on the crack orientation which is updated continuously in each load step. The main shortcomings of the concept of coaxiality as introduced in this model are that it fails to simulate behaviour in structures where shear slip or shear transfer along cracks is predominant (Vecchio, 2000), besides ignoring forces carried along the crack surface.

6.4. NLFEA Using DIANA

DIANA 10.2 classifies smeared crack models described in section (6.3) into two main categories:

1. Total strain crack model which includes the fixed and rotating crack models without strain decomposition.
2. The multi-directional crack model which involves strain decomposition.

This section will briefly describe the different material models available in DIANA for its fixed and rotating total strain crack models. As described earlier the fixed crack model is suitable for cases where shear transfer through cracks is important (e.g. deep beams) and it has been reported to give good predictions in similar cases (Fang, 2013, Sagaseta, 2008).

6.4.1. Compressive behaviour of concrete

The total strain crack models in DIANA provide several constitutive models to simulate the compressive behaviour of the concrete beside the simple models (i.e. the linear elastic and multilinear models). Three material models for the compressive behaviour of the concrete are discussed in this section and their relevant equations are presented. These models are Hognestad parabolic curve (1951), Thorenfeldt curve (1987) and Feenstra parabolic curve (1993).

The compressive behaviour of structural concrete depends mainly on the isotropic stress and lateral cracking. Models adopted in DIANA for the effect of lateral confinement and cracking will be discussed at the end of this section.

Hognestad parabolic compression curve

The axisymmetric parabolic curve proposed by Hognestad (1951) was one of the earliest compressive curves to take into account the softening behaviour of the concrete in compression. The whole stress-strain diagram in this curve is stress-dependent only with one defining parameter (the strain corresponding to the maximum compressive stress α_p). Equations describing this model are given below:

$$f = -f_c \left(2 \frac{\alpha}{\alpha_p} - \left(\frac{\alpha}{\alpha_p} \right)^2 \right) \quad \text{Equation 6.4}$$

$$\alpha_p = -2 \frac{f_c}{E} \quad \text{Equation 6.5}$$

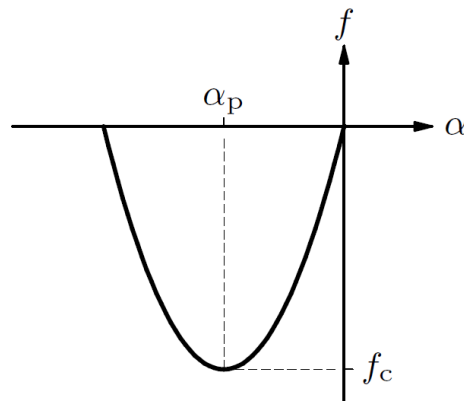


Figure 6.2: Hognestad compression curve in DIANA (DIANA, 2017) - figure reproduced with permission of the rights holder, TNO-DIANA.

Thorenfeldt compression curve

Thorenfeldt (1987) modified the simple compressive curve proposed by Popovic (1973) to also account for high strength concrete, especially in the post-peak response. The Thorenfeldt compression curve is presented in Figure 6.3.

The relationship between the compressive stress f and the strain α is given as follows (notations are as described in Figure 6.3 above):

$$f = -f_p \frac{\alpha}{\alpha_p} \left(\frac{n}{n - \left(1 - \frac{\alpha}{\alpha_p} \right)^{nk}} \right) \quad \text{Equation 6.6}$$

In which $n = 0.8 + \frac{f_{cc}}{17}$ and $k = \begin{cases} 1 & \text{for } \alpha_p < \alpha < 0 \\ 0 & \text{for } \alpha \leq 0 \end{cases}$

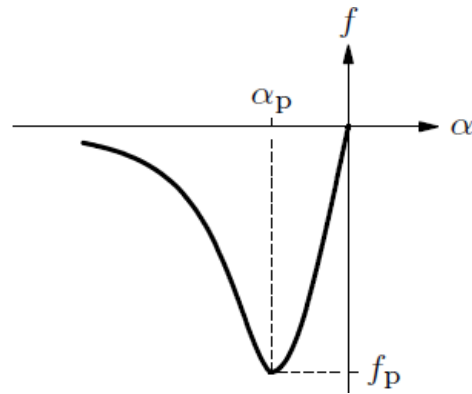


Figure 6.3: Thorenfeldt compression curve in DIANA (DIANA, 2017) - figure reproduced with permission of the rights holder, TNO-DIANA.

Feenstra parabolic compression curve

Feenstra (1993) proposed a material model for plain and reinforced concrete in which the failure mechanism is related to the growth of cracks at the micro-level. The internal damage caused by microcracks is modelled using internal parameters generally related to inelastic strains. The parabolic curve described by Feenstra is shown in Figure 6.4 below.

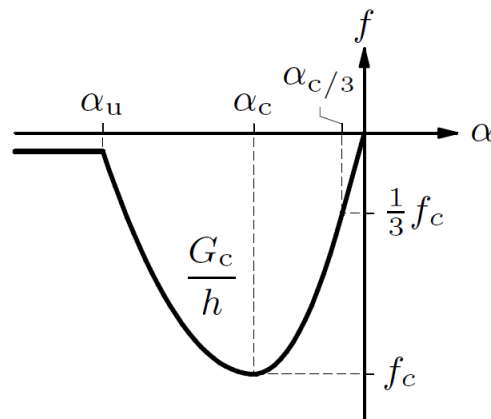


Figure 6.4: Feenstra parabolic curve in DIANA (DIANA, 2017) - figure reproduced with permission of the rights holder, TNO-DIANA.

The stress-strain relationship in Figure 6.4 above is defined with three characteristic strain values: the strain $\alpha_c/3$ at which the stress in the concrete f is third of the concrete compressive strength f_c , the strain α_c at which the stress in the concrete reaches the compressive strength and the strain α_u at which the concrete is fully softened in compression. Equations for these strains are stated below:

$$\left(\frac{\alpha_c}{3}\right) = -\frac{1}{3} \frac{f_c}{E} \quad \text{Equation 6.7}$$

$$\alpha_c = -\frac{5f_c}{3E} = 5\left(\frac{\alpha_c}{3}\right) \quad \text{Equation 6.8}$$

$$\alpha_u = \alpha_c - \frac{3G_c}{2hf_c} \quad \text{Equation 6.9}$$

As can be seen from the above equations, the stress-strain relationship is independent of the compressive fracture energy G_c up to the maximum concrete strength. After that, the strain depends on the fracture energy and the element size (h). The stress-strain relationship is given by:

$$f = \begin{cases} -f_c \frac{\alpha}{\alpha_c/3} & \text{for } \alpha_c/3 < \alpha \leq \\ -f_c \frac{1}{3} \left(1 + 4 \left(\frac{\alpha - \alpha_c/3}{\alpha_c - \alpha_c/3} \right) - 2 \left(\frac{\alpha - \alpha_c/3}{\alpha_c - \alpha_c/3} \right)^2 \right) & \text{for } \alpha_c < \alpha \leq \alpha_t \\ -f_c \left(1 - \left(\frac{\alpha - \alpha_c}{\alpha_u - \alpha_c} \right)^2 \right) & \text{for } \alpha_u < \alpha \leq \alpha \\ 0 & \text{for } \alpha \leq \alpha_u \end{cases} \quad \text{Equation 6.10}$$

A significant advantage of the Feenstra model is that the compression softening behaviour depends on the compressive fracture energy G_c thereby introducing a degree of mesh independency. The compressive fracture energy is usually obtained as a multiple of the tensile fracture energy G_f . Feenstra used a value of $100 G_f$ for the compressive fracture energy (Feenstra, 1993) and DIANA suggests a value in the range of (50-100) G_f (DIANA, 2017).

Compression behaviour with lateral confinement

The strength and ductility of concrete are highly affected by the level of confinement provided (Binici, 2005). This was first recognised by Richart who studied the failure in concrete subject to uniaxial, biaxial and tri-axial stress (Richart et al., 1928). Figure 6.5 below shows the increment of the compressive stress with the level of confinement. The failure surface cannot be reached at high tri-axial stresses.

In experimental works, concrete under loading plates is usually subject to tri-axial stress. In 2D plane stress elements, this confinement effect can be simulated in DIANA using the model proposed by Selby and Vecchio (Selby and Vecchio, 1997). This model is based on Hsieh-Ting-Chen failure surface model which is used to evaluate the required compressive stress in the major direction in a biaxial or triaxial stress state.

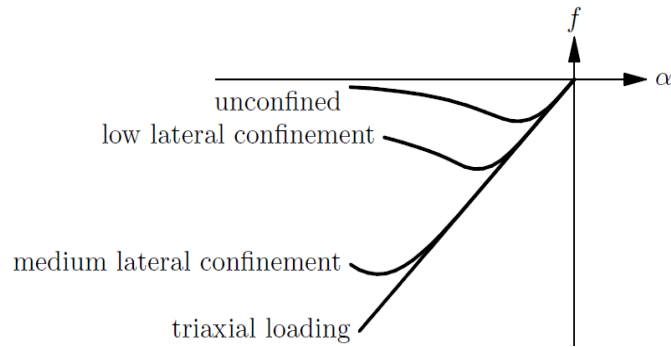


Figure 6.5: influence of lateral confinement (DIANA, 2017) - figure reproduced with permission of the rights holder, TNO-DIANA.

One of the suggested solutions to simulate the confinement effect is to add out of plane reinforcement in the concrete adjacent to loading plates. However, this can result in numerical instabilities in the FEM (Selby and Vecchio, 1997). Another approach to deal with this effect is to increase the concrete strength locally beneath loading plates. This was done by Fang (2013) who found that adoption of Selby and Vecchio's model in DIANA did not prevent premature failure of the concrete adjacent to loading plates (Fang, 2013). Premature failure of the concrete adjacent to loading plates can also be avoided by providing an interface element between the loading plates and the concrete beneath as discussed in section 6.5

Influence of lateral cracking on the compressive strength

Vecchio and Collins (Vecchio and Collins, 1986) showed that the principal compressive stress in cracked concrete depends not only on the principal compressive strain but also on the co-existing principal tensile strain. Cracked concrete experiences a reduction in both compressive strength and stiffness compared to its cylinder behaviour when subject to high tensile strains in a direction normal to the compression (Vecchio and Collins, 1986).

Many strain softening models are proposed in the literature of which DIANA adopts the models of the Japanese Society of Civil Engineering model (2007), Vecchio and Collins (1986) and Vecchio and Collins (1993). These three models are briefly reviewed below.

Japanese Society of Civil Engineering

Transverse tensile strain and associated cracking reduces the concrete compressive strength. DIANA simulates this reduction by introducing stress and strain reduction factors $\beta_{\sigma cr} = \beta_{\sigma cr}(\alpha_{lat})$ and $\beta_{\epsilon cr} = \beta_{\epsilon cr}(\alpha_{lat})$. The parameter (α_{lat}) takes account of the internal damage caused by lateral cracking. Figure 6.6 shows the lateral reduction model proposed by the Concrete Standard Specification for Concrete Structures by the JSCE. The internal damage

parameter (α_{lat}) here represents the total maximum tensile strain. The strain reduction factor $\beta_{\sigma_{cr}}$ is taken as 1.0.

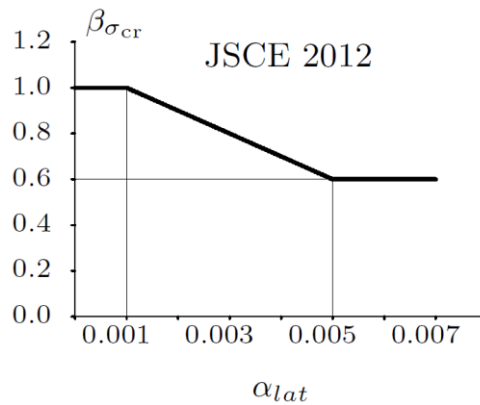


Figure 6.6: Lateral reduction model - JSCE(DIANA, 2017) - figure reproduced with permission of the rights holder, TNO-DIANA.

Vecchio and Collins (1986)

This is based on the Hognestad parabolic stress-strain relationship described earlier in section (6.4.1). The lateral reduction effect solely depends on the principal tensile strain ϵ_1 . The tensile strain ϵ_0 is also kept unchanged here. The equation describing this model is presented below:

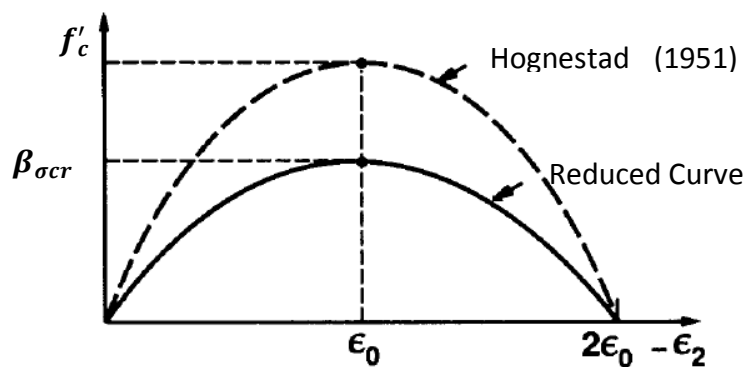


Figure 6.7: Lateral reduction model - (Vecchio and Collins, 1986). . Figure reproduced with permission of the rights holder, ACI Structural Journal.

$$\beta_{\sigma_{cr}} = \frac{1}{0.85 - 0.27 \frac{\alpha}{\alpha_{lat}}} \leq 1 \tag{Equation 6.11}$$

$\beta_{\sigma_{cr}}$ is the compressive strength softening parameter due to lateral cracking and α_{lat} is the lateral strain.

Vecchio and Collins (1993)

Vecchio and Collins extended their 1986 model for use with high and low strength concrete by changing the compression curve into the Thorenfeldt curve described in section (6.4.1). The Thorenfeldt curve was adopted since it gives a better correlation for high and low strength concrete (Vecchio and Collins, 1993).

Vecchio and Collins (1993) proposed two alternative strength reduction factors. Approach A relates the reduction factor to both principal tensile and compressive strain while Model B just accounts for principal tensile strain. DIANA adopts Model B which can be described as:

$$\beta_{\sigma cr} = \frac{1}{1 + K_c} \leq 1 \quad \text{Equation 6.12}$$

$$K_c = 0.27 \left(-\frac{\alpha_{lat}}{\varepsilon_0} - 0.37 \right) \quad \text{Equation 6.13}$$

In this study, the model proposed by Vecchio and Collins (Vecchio and Collins, 1993) is used as it provided good estimates for similar studies (Sagaseta, 2008, Fang, 2013) based on the sensitivity analysis performed in section 6.8.3.

6.4.2. Tensile behaviour of the concrete

Concrete is usually treated as a softening material in both tension and compression. The stress-strain relationship is modelled in tension assuming elastic behaviour up to the tensile strength followed by a softening branch as in Figure 6.8 below (Hordijk et al., 1986). In the tension softening phase, the stress distribution in the concrete in the vicinity of the crack tip is associated with the deformation and softening characteristics.

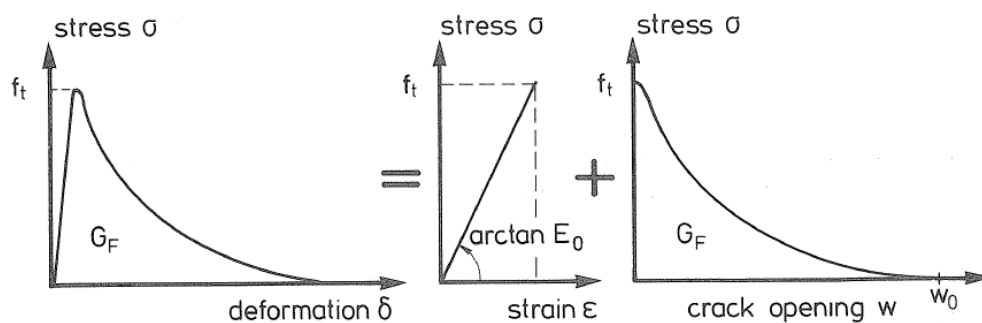


Figure 6.8: tensile behaviour of the concrete (Hordijk, 1992)

In DIANA, the relation between crack stress (σ_{nn}^{cr}) and the crack strain (ε_{nn}^{cr}) in the softening branch is written as:

$$\sigma_{nn}^{cr}(\varepsilon_{nn}^{cr}) = f_t \cdot y\left(\frac{\varepsilon_{nn}^{cr}}{\varepsilon_{nn,ult}^{cr}}\right) \quad \text{Equation 6.14}$$

In which f_t is the tensile strength of the concrete and $y(\varepsilon_{nn}^{cr}/\varepsilon_{nn,ult}^{cr})$ represents the general softening function. The softening function depends mainly on the tensile fracture energy (G_f) – the energy required to form a unit area of a crack – and element size characterized by the crack bandwidth (h). The fracture energy is modelled in DIANA using the following expression:

$$G_f = h \int_{\varepsilon_{nn}^{cr}=0}^{\varepsilon_{nn}^{cr}=\infty} \sigma_{nn}^{cr}(\varepsilon_{nn}^{cr}) \cdot d\varepsilon_{nn}^{cr} \quad \text{Equation 6.15}$$

It can be seen from Equation 6.15 above that the tensile fracture energy, and hence the tensile softening behaviour depends on the element size (or the crack bandwidth). The crack bandwidth was first introduced by Bazant (Bažant, 1983) as the width of a strip along the element representing the crack in which the strain is constant and equal to the crack strain. DIANA gives the user the option of calculating the crack bandwidth based on the element size automatically using formulae given by Rots (1988) or Govindjee (1995). Alternatively, the user may define the value of the crack bandwidth manually. The most common approach, however, is to use Rots approximation where the crack bandwidth is calculated in a two-dimensional configuration as the square root of twice the total element size (Fang, 2013, Sagaseta, 2008).

Tensile behaviour can be modelled in DIANA using the 16 alternative models shown in Figure 6.9. Details are presented below of the Hordijk model (Hordijk, 1992) which is used in this research. Details of the other models can be found in the DIANA Material library (DIANA, 2017).

Hordijk tensile softening model

The nonlinear softening model of Hordijk (1992) has widely been used in NLFEA over the past two decades due to its good performance (Hendriks and A. de Boer, 2017, Fang, 2013). It is characterised by the ultimate crack strain ($\varepsilon_{nn,ult}^{cr}$) at which the stress reduces to zero, and the reduced tensile strength (f_t) as follows:

$$\frac{\sigma_{nn}^{cr}(\varepsilon_{nn}^{cr})}{f_t} = \begin{cases} \left(1 + \left(c_1 \frac{\varepsilon_{nn}^{cr}}{\varepsilon_{nn,ult}^{cr}}\right)^3\right) e^{-c_2 \frac{\varepsilon_{nn}^{cr}}{\varepsilon_{nn,ult}^{cr}}} - \dots & \text{for } 0 < \varepsilon_{nn}^{cr} < \varepsilon_{nn,ult}^{cr} \\ \frac{\varepsilon_{nn}^{cr}}{\varepsilon_{nn,ult}^{cr}} (1 + c_1^3) e^{-c_2} & \text{for } \varepsilon_{nn,ult}^{cr} < \varepsilon_{nn}^{cr} < \infty \\ 0 & \text{for } \varepsilon_{nn,ult}^{cr} < \varepsilon_{nn}^{cr} < \infty \end{cases} \quad \text{Equation 6.16}$$

With $c_1 = 3$ and $c_2 = 6.93$. The ultimate strain ($\varepsilon_{nn,ult}^{cr}$) and the reduced tensile strength (f_t) are given by:

$$\varepsilon_{nn,ult}^{cr} = 5.136 \frac{G_f}{f_t h} \quad \text{Equation 6.17}$$

$$f_t = \left(0.739 \frac{G_f E}{h}\right)^{\frac{1}{2}} \quad \text{Equation 6.18}$$

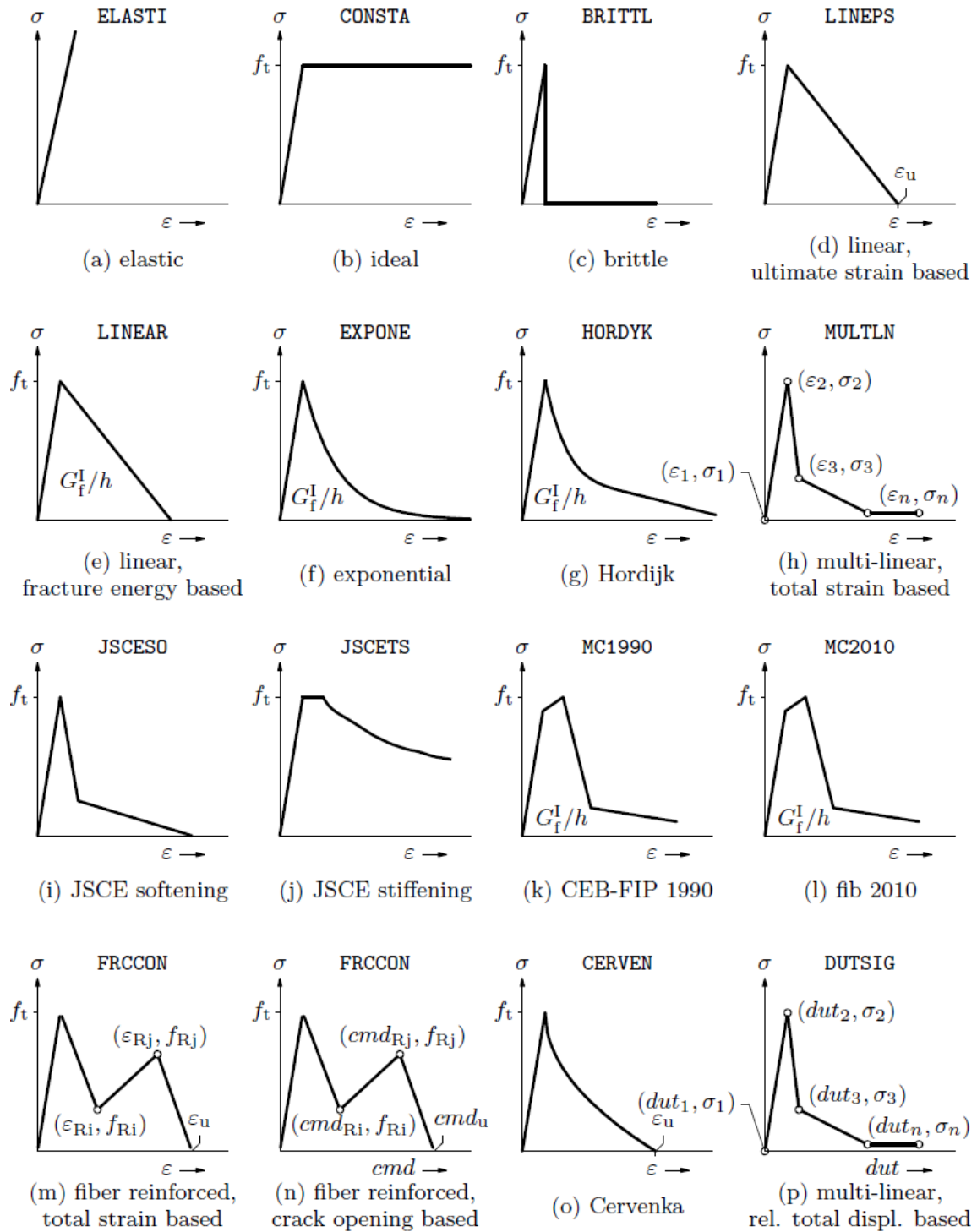


Figure 6.9: predefined tension softening for Total Strain crack models (DIANA, 2017) - figure reproduced with permission of the rights holder, TNO-DIANA.

6.4.3. Shear behaviour of the concrete

In a fixed smeared crack model, the shear force can be transmitted through the crack surface by means of aggregate interlock and dowel action. As mentioned earlier in section (6.3.1), the shear stiffness is reduced in the FEA to consider the reduction in the shear strength due to the formation of cracks. This reduction can be modelled in DIANA using either constant or variable shear retention models.

Constant shear retention models

The constant shear retention model is commonly used to simulate the concrete behaviour in shear. It assumes a constant reduction based on a user-defined value for the shear retention factor (β) – Figure 6.10 with a typical range of 0.1 to 0.2 (Rots, 1988, Sagaseta, 2008).

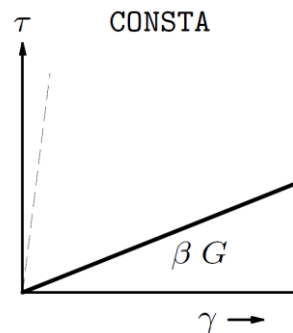


Figure 6.10: Constant shear retention for total strain crack model (DIANA, 2017) - figure reproduced with permission of the rights holder, TNO-DIANA.

Varying the shear retention factor can influence strength and stiffness noticeably. Several researchers conducted sensitivity studies to investigate this effect on the results of FEA in both 2D and 3D models. According to these studies (Fang, 2013, Eder et al., 2010, Rots and Blaauwendraad, 1989, Khwaounjoo et al., 2000) the shear strength and ductility increase with increasing shear retention factor. Experimental evidence suggests that the shear stiffness does not remain constant after cracking and reduces as the crack opens (Fang, 2013).

Variable shear retention models

Besides the constant shear retention model, DIANA offers several variable shear retention models where the shear stiffness reduces with the increase of the crack width. The Multi-linear shear stress-strain model and the multi-linear shear retention strain model are solely user-defined models in which the key points of the diagram need to be defined by the user. The Damage based shear retention model is built on the work done by Selby and Vecchio (Selby and Vecchio, 1993) on modelling three dimensional reinforced concrete elements

where they consider the effect of lateral expansion. In the aggregate size based shear retention model, introduced by Hendriks in 2012, the shear stiffness tends to zero as the crack opens wider than half the mean aggregate diameter (d_{agg}). The shear retention factor is given by (Belletti et al., 2012, DIANA, 2017),:

$$\beta = 1 - \left(\frac{2}{d}\right) \varepsilon_{nn}^{cr} h \quad \text{Equation 6.19}$$

DIANA includes various variable shear retention models including the Contact Density model (Li et al., 1989) and Maekawa Decay of Shear Transfer model (Maekawa et al., 2003). The Contact Density model (CDM) defines different relationships between the crack shear stress and the normalised crack strain for every crack shear direction in cases of loading or unloading. In DIANA, it is advisable to define a minimum value for the shear retention factor $\beta_{min} \leq 0.01$. If no value is assigned to β_{min} , this can yield a zero value for the shear stiffness. The Maekawa Decay of Shear Transfer model is identical to the Contact Density model but the crack shear stress obtained from the Contact Density model (τ^{cr}) is further reduced if the crack shear strain (γ_{cr}) exceeds a limiting value ($\gamma_{cr,ult}$). The reduced crack shear stress is given by:

$$\tau_{DST}^{cr} = \tau^{cr} \left(\frac{\gamma_{cr,ult}}{\gamma_{cr}}\right)^c \quad \text{Equation 6.20}$$

The same recommendations regarding the minimum shear retention factor apply here also. DIANA also includes the variable shear retention model proposed by Al-Mahaidi (al-Mahaidi, 1978) who linked the shear retention factor linearly to the total strain (ε_{nn}) as follows:

$$\beta = 0.4 \frac{f_t}{E \varepsilon_{nn}} \quad \text{Equation 6.21}$$

Where f_t is tensile strength and E is the elastic modulus of the concrete.

Discussion regarding the concrete shear behaviour in FEA

The choice of the shear retention model has a significant influence on the behaviour of the FEM (Khwaounjoo et al., 2000). Although the constant shear retention model is often used in NLFEA, experimental evidence supports the use of variable shear retention models particularly for beams without shear reinforcement where the behaviour after cracking is governed by the crack roughness and kinematics. A constant shear retention model implies that the shear stiffness is constant after cracking regardless of the increase in the crack opening. On the other hand, several researchers claim that variable shear retention models

return overly high values for the shear retention factor resulting in overly stiff responses (Rots and Blaauwendraad, 1989, Sagaseta, 2008). However, these studies did not include any of the variable shear retention models adopted by DIANA. Using a constant shear factor is inconsistent with the experimental observation that the stiffness of shear transfer through aggregate interlock reduces with increasing crack width.

6.4.4. Reinforcement modelling

The interaction between the concrete and reinforcement in reinforced concrete is highly complex and depends on bond-slip between the reinforcement and concrete. There are two main approaches to model reinforcement in DIANA: embedded reinforcement and bond-slip model.

Embedded reinforcement models

Embedded reinforcement is modelled by adding stiffness to the mother concrete element in which the reinforcement is embedded. The embedded element does not have any extra degrees of freedom and its strain is obtained from the total strain of the mother element. This implies a perfect bond relationship between the embedded reinforcement and the surround mother elements (concrete).

Embedded reinforcement can be modelled with either discrete embedded elements (bar reinforcement) or continuous embedded elements (grid reinforcement). Bar reinforcement is suitable for structural elements with widely dispersed reinforcement (e.g. beams without/with low shear reinforcement), whereas grid reinforcement is preferred in cases of large areas of evenly distributed reinforcement (e.g. solid slabs and beams highly reinforced for shear).

The optimum selection of embedded reinforcement model (smeared or discrete) is case dependent. While the smeared model reduces the running time significantly, it fails to predict the actual crack patterns if used to model elements where the location of the critical crack is important such as short beams for example. This is due to the “smearing” of tensile stress within the shear span as reported by Sagaseta - Figure 6.11 (Sagaseta, 2008). Apart from predicting crack patterns. Sagaseta concluded that both of the embedded models discussed can be used to model short shear span beams failing in shear (Sagaseta, 2008).

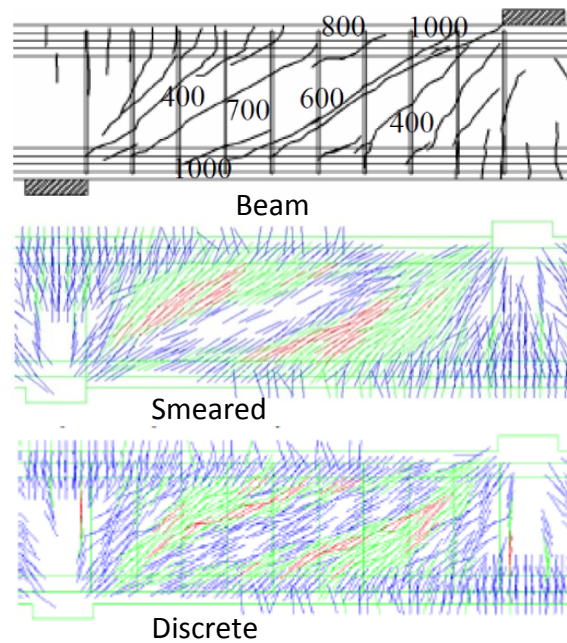


Figure 6.11: Smeared and discrete models for reinforcement (Sagasetta, 2008) . Figure reproduced with permission of the rights holder, Sagasetta J.

DIANA provides various material models for reinforcement of which the Von Mises Plasticity is most applicable for non-cyclic loading. A powerful feature that has been introduced in DIANA 10.2 for reinforcement modelling is the ability to input the full stress-strain curve data obtained from the tensile test of the reinforcement.

Bond-slip reinforcement models

As well as perfect bond, DIANA provides five alternative bond-slip reinforcement models in which the interaction between the reinforcement and the concrete (bond-slip relationship) can be defined. The cubic bond-slip relationship proposed by Dorr (DÖRR 1980) is a polynomial function with a shear limit when the slip reach a certain value Δu_t^o . The power law proposed by Naokowski (Noakowski 1978) is a stick-slip model of the shear-slip relationship. Similar to this model are the two models proposed by Shima et al. (Shima al. 1987).

Bond-slip models can provide a realistic description of the interaction between the reinforcement and surrounding concrete, which is influenced by transverse and longitudinal cracks. Yet, as shown by Fang in Figure 6.13, the response of reinforced concrete beams can be realistically simulated assuming perfect bond between the reinforcement and surrounding concrete (Fang, 2013).

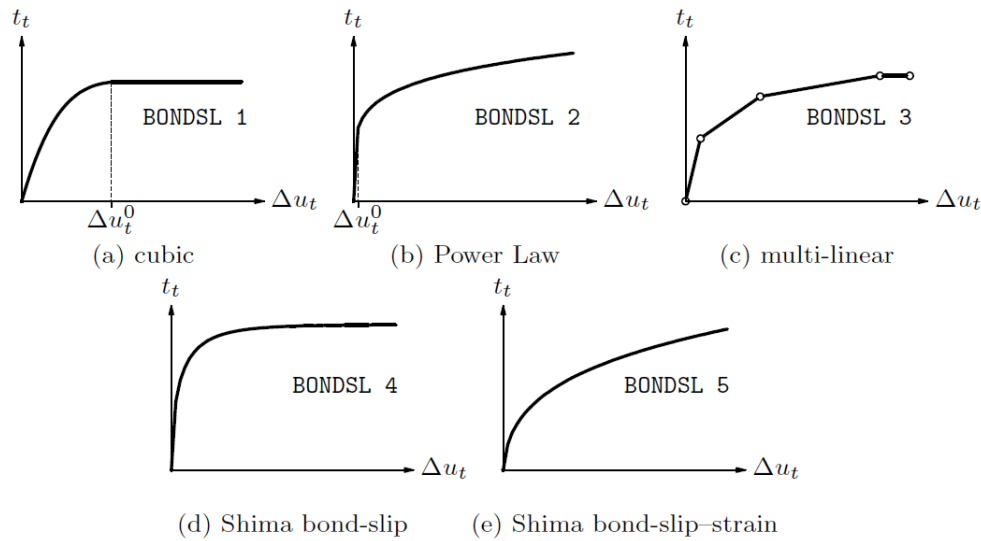


Figure 6.12: Bond-slip reinforcement models (DIANA, 2017) - figure reproduced with permission of the rights holder, TNO-DIANA.

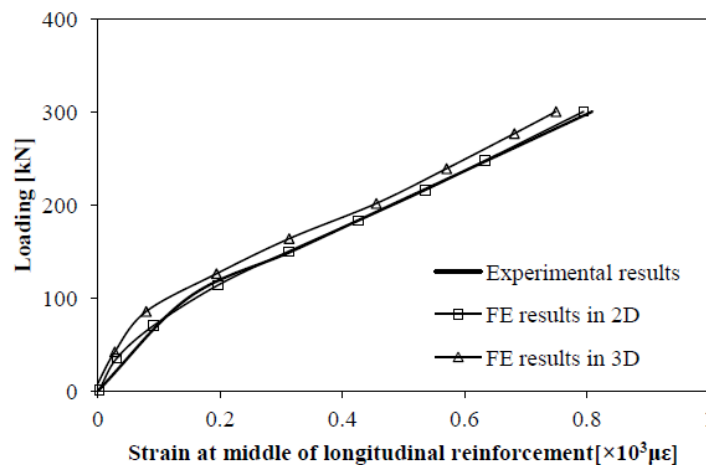


Figure 6.13: Strain predictions in the reinforcement using the Von Mises plasticity model (Fang, 2013)

6.4.5. Solution procedures for non-linear systems

When concrete cracks, the relationship between the force and displacement vectors become nonlinear leading to a system of the nonlinear equations. Unless very small load steps are used, a purely incremental solution will often lead to inaccurate results (DIANA, 2017). In order to achieve equilibrium between external and internal forces, an incremental-iterative solution must be used. A typical iterative solution algorithm is shown in Figure 6.14 below. In an iterative process, the external load step f_{ext} is applied while the total displacement increment Δu is kept to zero initially. The iterative displacement increment δu is obtained

using the out of balance force vector g . After obtaining the new internal force f_{int} , if the error is within the assumed limit, the increment ends, otherwise, the out of balance force g is used again to calculate the iterative increment δu .

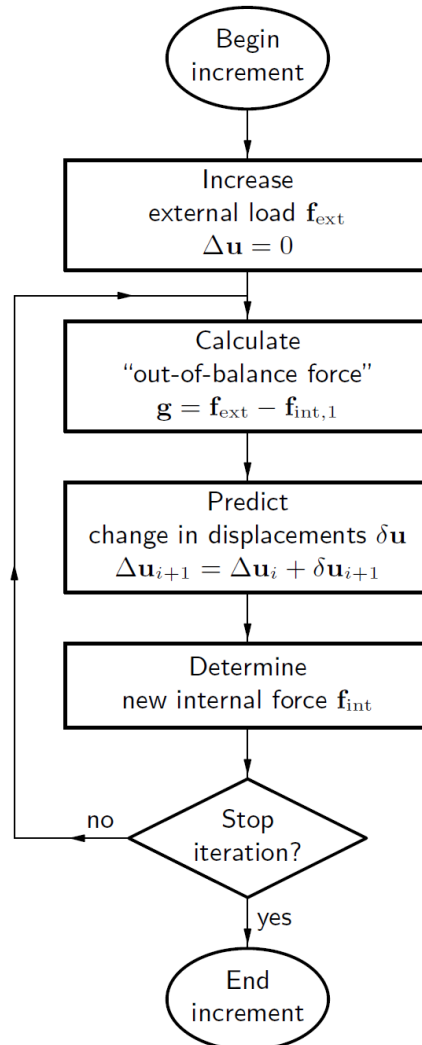


Figure 6.14: Typical iterative process in NLFEA (DIANA, 2017) - figure reproduced with permission of the rights holder, TNO-DIANA.

DIANA presents three numerical methods for predicting the displacement increment (δu_i) and constructing the stiffness matrix. These methods are Newton–Raphson, Quasi-Newton and the Constant Stiffness method. The Newton-Raphson method has two subclasses: regular Newton-Raphson and modified Newton-Raphson. In the regular method, the stiffness matrix is updated at each iteration, which increases the processing time per iteration. However, convergence is obtained in relatively few iterations. The modified Newton-Raphson evaluates the stiffness matrix at the start of each load increment. This reduces the processing time per

iteration, yet, leads to a relatively higher number of iterations to converge. The Quasi-Newton method – also called the Secant method – evaluates the stiffness matrix from the last known position at the equilibrium path, unlike the previous Newton-Raphson methods. This sustains a balance between the number of iterations needed to reach convergence and iterations time consumption.

The constant stiffness method can be used if the above methods fail to converge after a number of successive iterations. This method uses the stiffness matrix obtained from the last increment. If this method is used from the start of the analysis, it starts with a linear stiffness matrix. This method obtains the slowest convergence time (DIANA, 2017).

In this research, the Quasi-Newton (Secant) method is used to solve the system of nonlinear equations as it resulted in both reasonable numbers of iterations to converge and reasonable iteration running time.

The iteration process performed with one of the above methods needs to be combined with a convergence criteria to stop the process. DIANA provides three convergence norms: Force, Displacement and Energy norms. The use of proper norms depends on the type of analysis. In this research, an Energy norm is used as it showed good predictions in similar cases (Sagaseta, 2008, Fang, 2013, Khwaounjoo et al., 2000). Based on sensitivity studies, a relatively strict tolerance of 1×10^{-3} is adopted in this research owing to the softening response of concrete in compression and tension.

The iteration process stops when the convergence criteria are satisfied. Besides, the analysis also stops if the number of iterations reaches a pre-defined maximum number. Lastly, the analysis may also stop if divergence occurs, although divergence of the solution does not necessarily relate to structural failure as it can occur due to numerical difficulties especially for brittle materials (De Borst and Nauta, 1985).

Newton's method is very efficient in solving mechanical problems for materials that do not exhibit a "snap-through" or a "snap back" resulting from buckling or work softening near failure (Vasios, 2015). The proper identification of structural failure of concrete can only be verified by tracing the post-peak response. Newton methods alone cannot accurately predict the solution if a snap-through or a snapback occurs (see Figure 6.15).

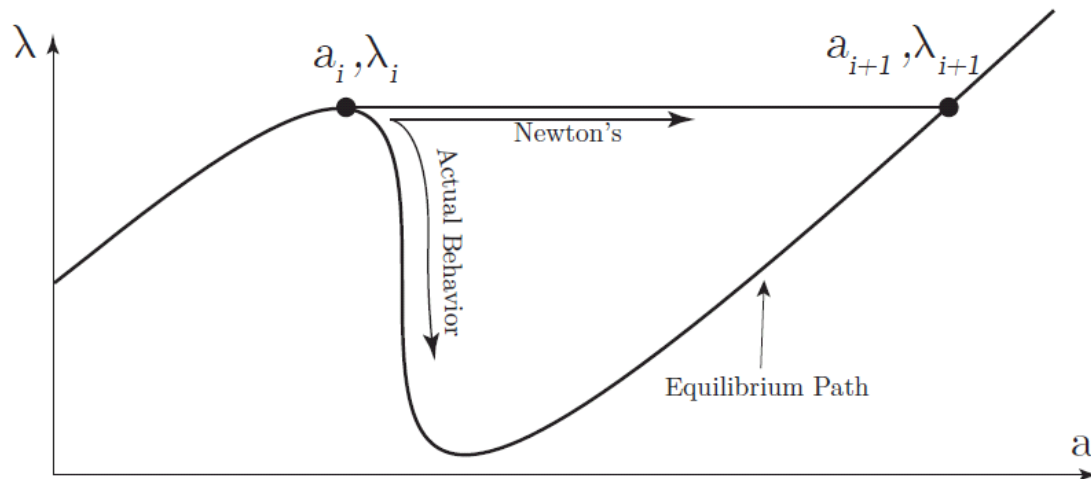


Figure 6.15: Difference between the actual behaviour and Newton's solution

Snap through and snap back can be followed using the arc-length technique (Figure 6.16), which was introduced by Riks (Riks, 1979) and modified by several scholars since then. The advantage of the arc length method over Newton's is that it captures the post-peak behaviour and ensures that the analysis does not stop because of any numerical difficulties near failure in finding the next point of the equilibrium path.

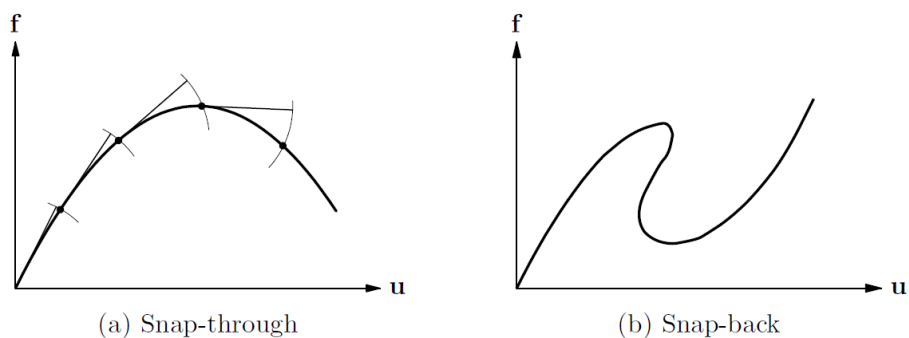


Figure 6.16: Arc-length control (DIANA, 2017) - figure reproduced with permission of the rights holder, TNO-DIANA.

The effect of introducing the arc-length technique to the analysis is demonstrated in Figure 6.17 for beam AT200 (0.5/0.5) where only arc length control captured the snap through. The analysis without arc length control stopped prematurely as a result of the analysis failing to converge at the point of snap through. Further examples are presented in section 6.6.

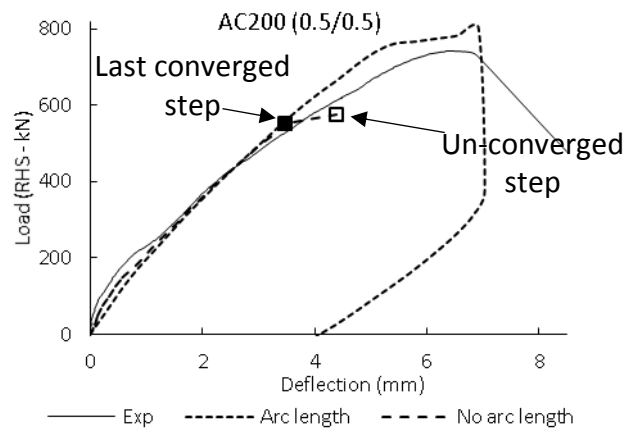


Figure 6.17: The effect of introducing the arc-length technique to the analysis of beam AT200 (0.5/0.5)

6.4.6. Elements and mesh considerations

Shear failure in reinforced concrete is typically modelled using either 2D plane stress elements or 3D solid elements. Plane stress elements “also called membrane elements” must satisfy three conditions: i) the coordinates of their nodes must be in a flat plane, ii) the thickness should be relatively small compared to other dimensions and iii) the load must be applied at the plane of the elements (DIANA, 2017).

Fang (Fang, 2013) examined the sensitivity of the results obtained using a lower order element of four nodes which is based on a linear integration (Q8MEM) compared to the higher-order element CQ16M in DIANA. The use of the lower element reduces the running time for the model, however, the higher element was reported to give better results. Besides, using linearly interpolated elements in a non-linear analysis can cause parasitic shear and volumetric locking to occur (DIANA, 2017).

In this research, an eight-node quadrilateral isoparametric plane stress element (CQ16M) is used to model the behaviour of beams in shear – Figure 6.18. This element is based on a quadratic interpolation and a default 2×2 Gaussian integration scheme.

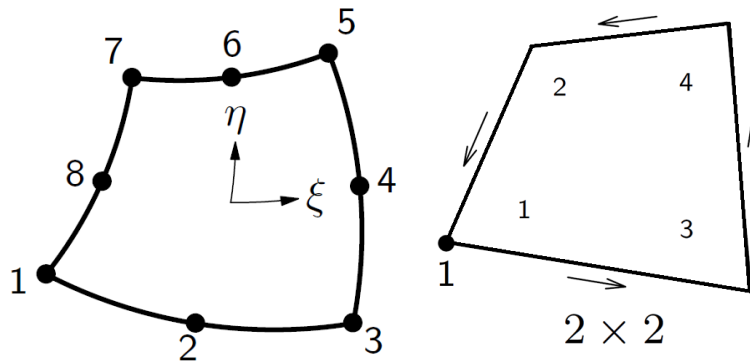


Figure 6.18: 2D Plane stress element used in the FEM (DIANA, 2017) - figure reproduced with permission of the rights holder, TNO-DIANA.

As mentioned in section (6.4.4), reinforcement can be modelled using embedded reinforcement bars. These bars consist of several particles (Figure 6.19) that must completely be inside structural elements. The location points in the bars define the position of the particles which is determined automatically by the software.

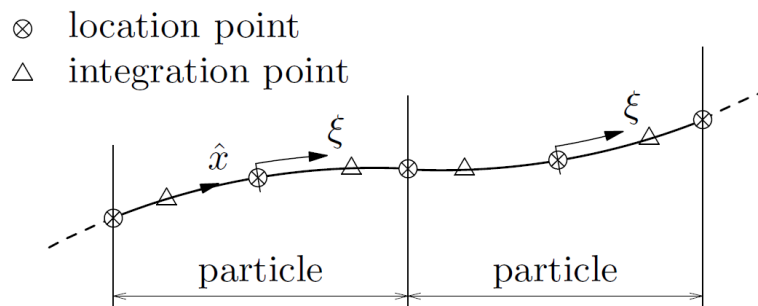


Figure 6.19: The topology of a reinforcement bar (DIANA, 2017) - figure reproduced with permission of the rights holder, TNO-DIANA.

6.5. Model Calibration and Baseline Parameters

In this research, the NLFEA was initially calibrated using similar previous studies on short span beams (Fang, 2013, Sagaseta, 2008), of which, the beams tested by Fang (2013) with multiple point loads were the most pertinent beams for this experimental program in the currently available literature. This section reviews the FEA procedure used by Fang in his analysis of his tested short shear span beams. Fang's analysis is replicated and attempts to address difficulties reported by Fang are described. The calibrated model and relevant modifications are considered as the baseline model for the sensitivity analysis following later and are validated using test results presented in Chapter 4.

6.5.1. Description of NLFEA performed by Fang

Fang tested 12 beams in two series of six (see Table 6.4). The first series contained beams with single point loads (B1-25 and B1-50), beams with two point loads (B2-25 and B2-50) and beams with four point loads (beams B3-25 and B3-50) applied to the compression face, all without shear reinforcement. The second series contained beams with two point loads (A-1, S1-1 and S2-1) and beams with four point load (A-2, S1-2 and S2-2). Beams A-1 and A-2 were without shear reinforcement while the other four beams contained shear reinforcement. The beams tested by Fang (2013) are comparable to the author's beams in terms of shear span, shear reinforcement, test configuration for beams loaded on the compression face and cross sectional dimensions, apart from the width of the beam.

Fang used DIANA (DIANA v9.4) for his NLFEA. Regarding material models; Fang used the parabolic compression curve for concrete suggested by Feenstra (Feenstra, 1993) with the lateral reduction factor proposed by Vecchio and Collins (Vecchio and Collins, 1993). The Hordijk tension softening model (Hordijk, 1992) was adopted for the tensile behaviour of the concrete. A constant shear retention model was used with a shear retention factor of 0.25 for all of the beams. The reinforcement was modelled using Von-Mises plasticity model with no strain hardening. A linear elastic model was assumed for the loading plates. In the solution algorithm, an automatic load stepping of a force-control analysis was performed with a Newton-Raphson solver. An energy based convergence criteria was adopted with iterations to stop at an energy norm less than 1%. Table 6.1 gives details of the material properties he used in his analyses which were either calculated in terms of the concrete compressive strength (E_c using EC2 2004, G_f using MC2010) or obtained from material tests (f'_t , E_s and f_y). Poisson's ratio was assumed to be zero for concrete and 0.3 for the reinforcement and steel plates. More details of Fang's work can be found elsewhere (Fang, 2013).

Table 6.1: Properties of materials used in the FEA for beams tested by Fang (Fang, 2013)

Beam	f'_c (MPa)	f'_t (MPa)	E_c (MPa)	E_s (GPa)	G_f (N/mm)	$f_{y,tension}$ (MPa)	$f_{y,comp.}$ (MPa)	$f_{y,w}$ (MPa)
B1-25	45.7	2.23	36426	200	0.085312	520	-	-
B1-50	45.7	2.23	36426	200	0.085312	520	-	-
B2-25	45.7	2.23	36426	200	0.085312	520	-	-
B2-50	45.7	2.23	36426	200	0.085312	520	-	-
B3-25	45.7	2.23	36426	200	0.085312	520	-	-
B3-50	45.7	2.23	36426	200	0.085312	520	-	-
A-1	33.1	1.90	33613	200	0.070722	560	540	540
A-2	34.6	1.94	33971	200	0.072493	560	540	540
S1-1	33.7	1.92	33767	200	0.071483	560	540	540
S1-2	36	1.98	34321	200	0.074246	560	540	540
S2-1	35.2	1.96	34122	200	0.073247	560	540	540
S2-2	36.7	2.00	34468	200	0.074992	560	540	540

Fang restrained the beams vertically at the centre of the supporting plates. Horizontal restraint was provided at the central node of the left hand bearing plate. A mesh of 8-node quadrilateral plane stress elements with element size of 25 mm was used to model both the concrete and steel plate elements as shown in Figure 6.20. Loads were applied directly on the top of the loading plates as a pressure load.

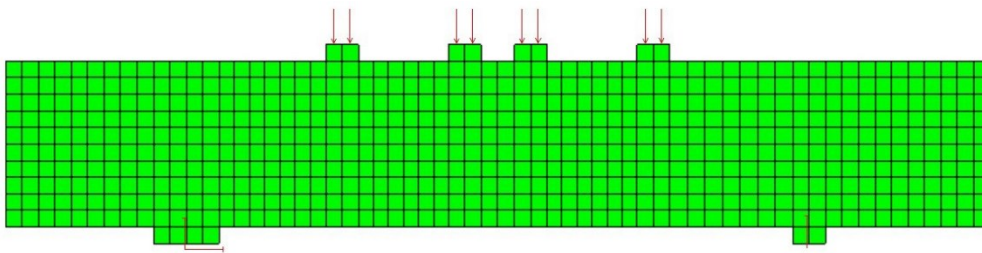


Figure 6.20: Geometry, mesh, boundary conditions and loading of beam S1-1 (Fang, 2013)

6.5.2. Challenges faced Fang and model enhancements

Fang reported several issues related to the modelling of his beams. The most significant issue was the premature failure occurring in a quarter of his beams, arising from stress concentrations below the loading plates. Other difficulties encountered were numerical difficulties arising from the brittle behaviour of concrete, selection of user-defined parameters for the different concrete models and the slightly stiff response of the FE models.

The author repeated the NLFEA of Fang using the same model parameters and solution procedures. The results were very similar to those obtained by Fang with the same issues of premature failure and overly stiff response. A major drawback of the FE presented by Fang is the failure to simulate the post peak behaviour, which gives rise to concerns that the analysis might not have continued to failure. To capture the descending part of the post peak response, arc length control is used in this research. This enables the descending branch of the load deflection response to be captured. It is also worth mentioning that convergence is better achieved using the Quasi-Newton Raphson solver instead of the Newton Raphson solver used by Fang. A more strict energy convergence tolerance of 0.001 was used with a maximum number of iterations of 300. Fang attributed the premature failure of his analyses to localised stress concentration near the loading plates. Therefore, an interface element was introduced between loading plates and concrete beams in this research as described later in the modelling of the loading plates (section 6.7).

6.5.3. Enhanced results and baseline model parameters

This section summarizes the enhanced procedure adopted by the author to replicate the FEA of the beams tested by Fang. The final parameters from this study were adopted as a baseline for the sensitivity analysis of the author's beams presented in Section 6.8.

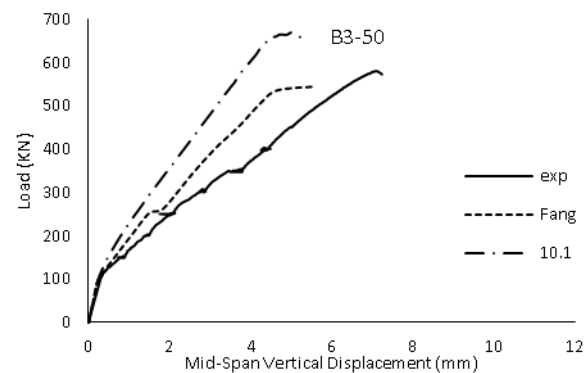
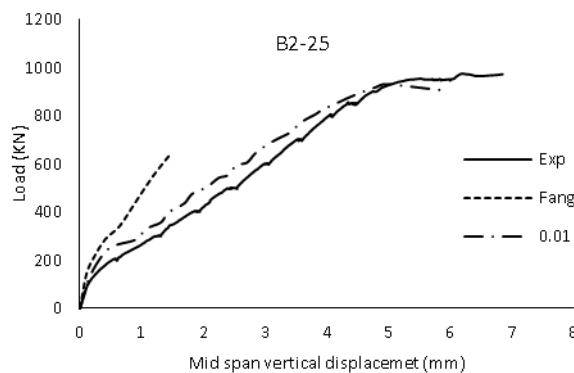
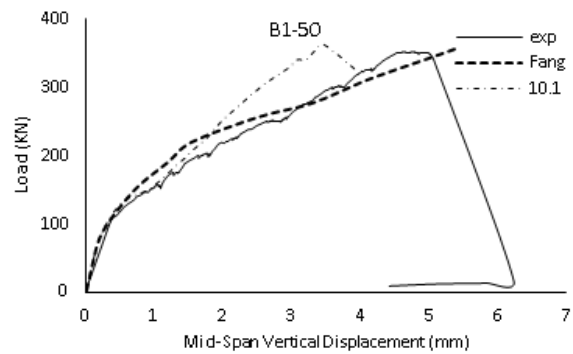
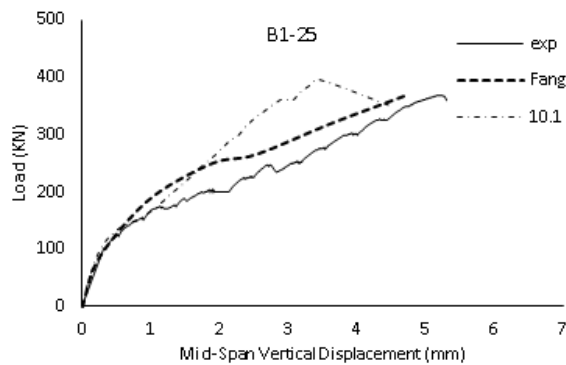
The parabolic compressive stress strain response of Feenstra was adopted in conjunction with a fixed crack model. A baseline constant shear retention factor of 0.25 was adopted. The DIANA default value of 0.15 for Poisson's ratio was used as recommended for similar cases (DIANA, 2017) instead of zero as used by Fang. This had a slight effect on the stiffness of the response. The Hordjik tensile model was adopted for tensile behaviour. Reinforcement was modelled using the Von-Mises Plasticity model with strain hardening. Elastic behaviour was assumed for the steel loading and support plates. Regarding the solution procedures, explicit load steps were used (maximum step size of 0.05 of the total load) with an arc length technique to capture the descending part of the load deflection response. The quasi Newton Raphson solution algorithm was used with an energy norm of 0.001.

Overall, these assumptions were found to give reasonable predictions for the response of Fang's beams. Introducing interface elements and arc-length techniques overcame the issue of premature failure and enabled simulation of the post peak response. The final results for the FE of the beams are presented in Figure 6.21 and Table 6.2. The failure loads are in

reasonable agreement with the test results and on average better than obtained by Fang. The accuracy of displacement prediction is variable with predictions tending to be overly stiff. Surprisingly, given the similarity in input parameters, the load deflection responses are in some cases significantly stiffer than obtained by Fang.

Table 6.2: Comparison of the FE results obtained by Fang (2013) and in this work

Beam	Failure Load	Fang (2013) – DIANA v9.4		Author (DIANA v10.1)	
		FE Load	FE/Exp.	FE Load	FE/Exp.
B1-25	368	371	1.01	397	1.08
B1-50	352	359	1.02	363	1.03
B2-25	977	646	0.66	930	0.95
B2-50	929	737	0.79	847	0.91
B3-25	480	609	1.27	646	1.35
B3-50	580	546	0.94	670	1.16
A1	823	640	0.78	829	1.01
A2	350	469	1.34	370	1.06
S1-1	1000	810	0.81	703	0.70
S1-2	601	625	1.04	660	1.10
S2-1	1179	828	0.70	1200	1.02
S2-2	820	662	0.81	960	1.17
Average			0.93		1.04
CoV			23.0		14.96



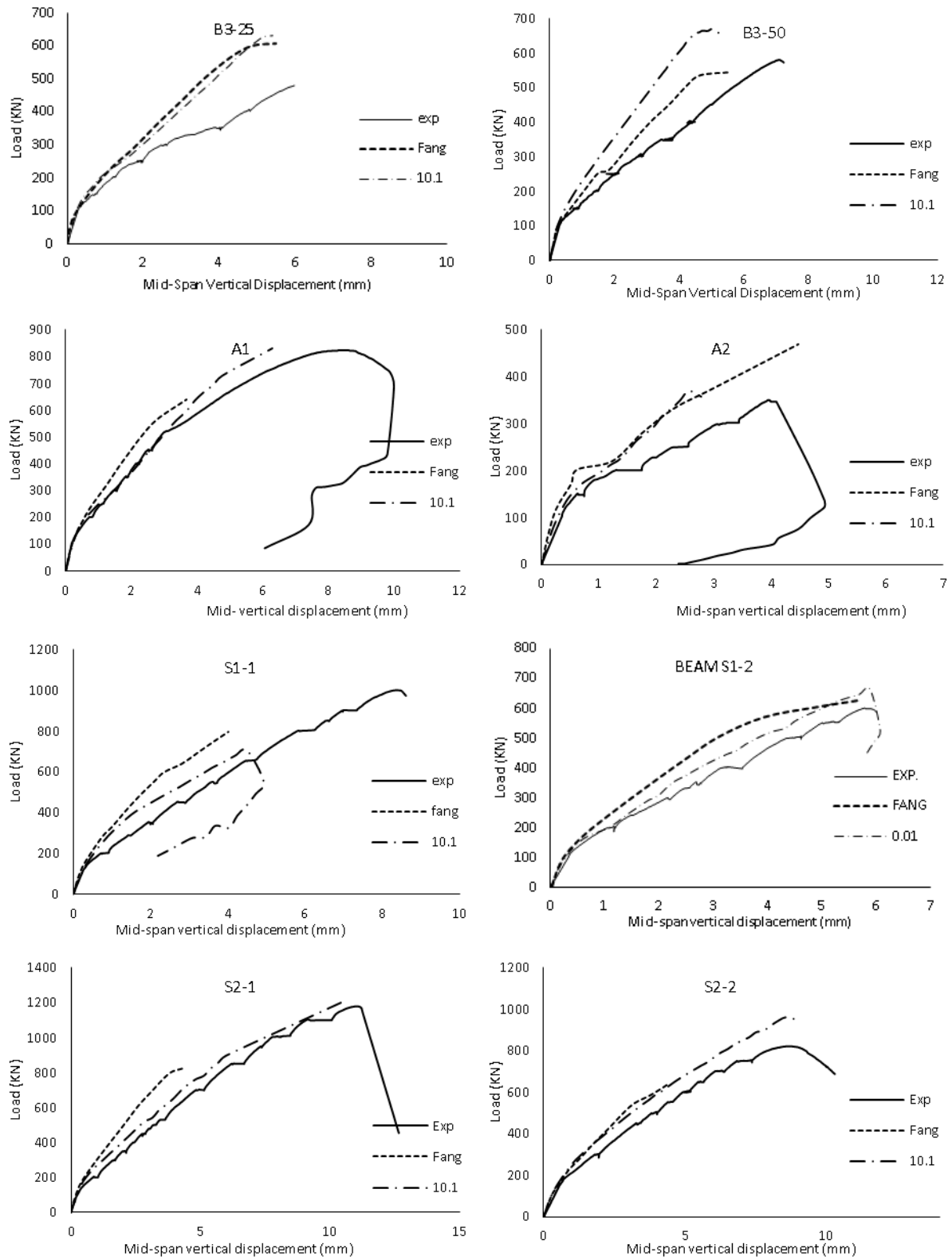
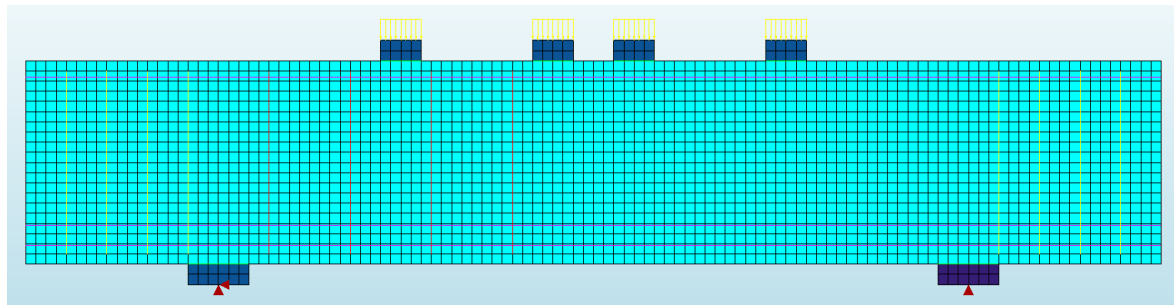


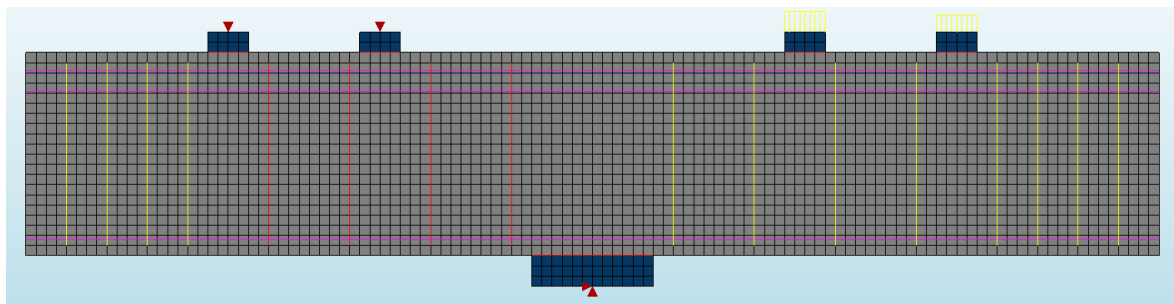
Figure 6.21: Replication and comparison of Fang's beams FEA

6.6. Constructing the FE Models for the Tested Beams

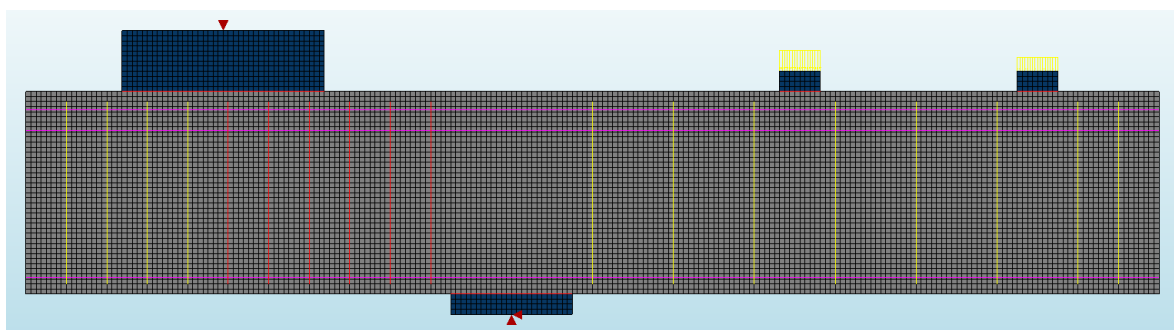
This section describes the FE mesh, loads and boundary conditions used to model beams tested in this research. Regarding the model mesh, an element size of 25 mm was used for the majority of the beams with a few beams modelled with an element size of 12.5mm to maintain regular mesh when geometrical constraints are present. The model mesh, load and support configurations are presented in Figure 6.22.



(a) Beams Loaded in the compression face.



(b) Beams Loaded in the tension face.



(c) Beams Loaded partly outside (2d) in the tension face.

Figure 6.22: Finite element mesh, loading and boundary conditions of beam

For beams loaded on the compression face, loads were applied linearly on all of the top plates with a roller and a hinge on the right and left hand support plates respectively (see Figure 6.22 – a). For balanced cantilevers (see Figure 6.22 b and c), the load was applied linearly on the

RHS top plates while rollers were placed on the top LHS plates. The bottom support of the balanced cantilevers was modelled as a hinge support.

Although these configurations were adopted in the FEA to simulate the exact test setup in the laboratory, the partial movement between the rig parts observed in the test resulted in a global rotation for the balanced cantilever beams. In the FEA, however, the vertical displacement in the LHS of the beams were almost zero. The measured deflections presented in this section are all corrected for global rotation about the support as described in section 4.3.3.

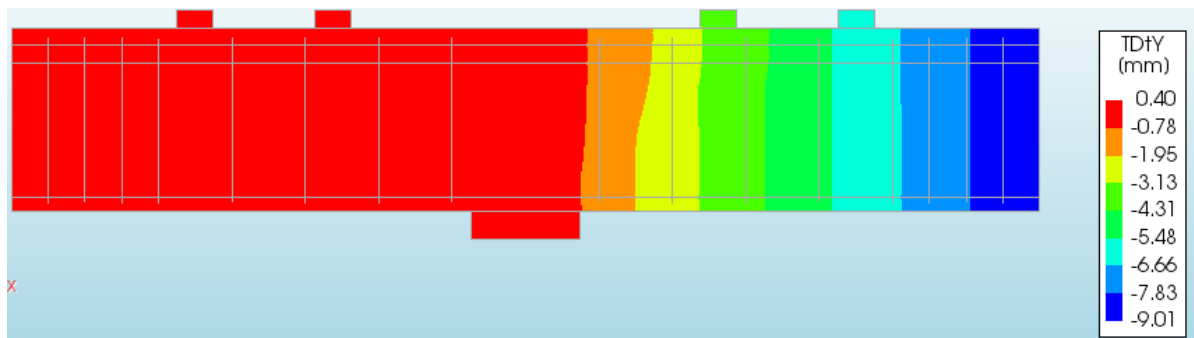


Figure 6.23: Vertical displacement of beam AT200 (0.5/0.5)

6.7. Modelling of the Loading Plates

Stress concentration under loading plates has been reported in previous studies of short and deep beams (Sagasetta, 2008, Fang, 2013). This stress concentration is believed to cause premature failure in FEA and has previously been overcome by increasing the concrete strength beneath the loading plates or decreasing the thickness of the loading plate (Sagasetta, 2008, Fang, 2013) – Figure 6.24.

Failure of short span and deep beams is mainly associated with crushing of the concrete in the flexural compression zone which is depicted by the presence of significant plastic strains in these locations. While increasing the concrete strength beneath loading plates mitigates the stress concentration problem, it also changes the behaviour of the concrete in the compression zone. To overcome this, a structural interface element between the concrete beam and loading plates is used in this research. The structural interface element describes the interface behaviour in terms of a relation between the normal and shear tractions and the normal and shear relative displacements across the interface.

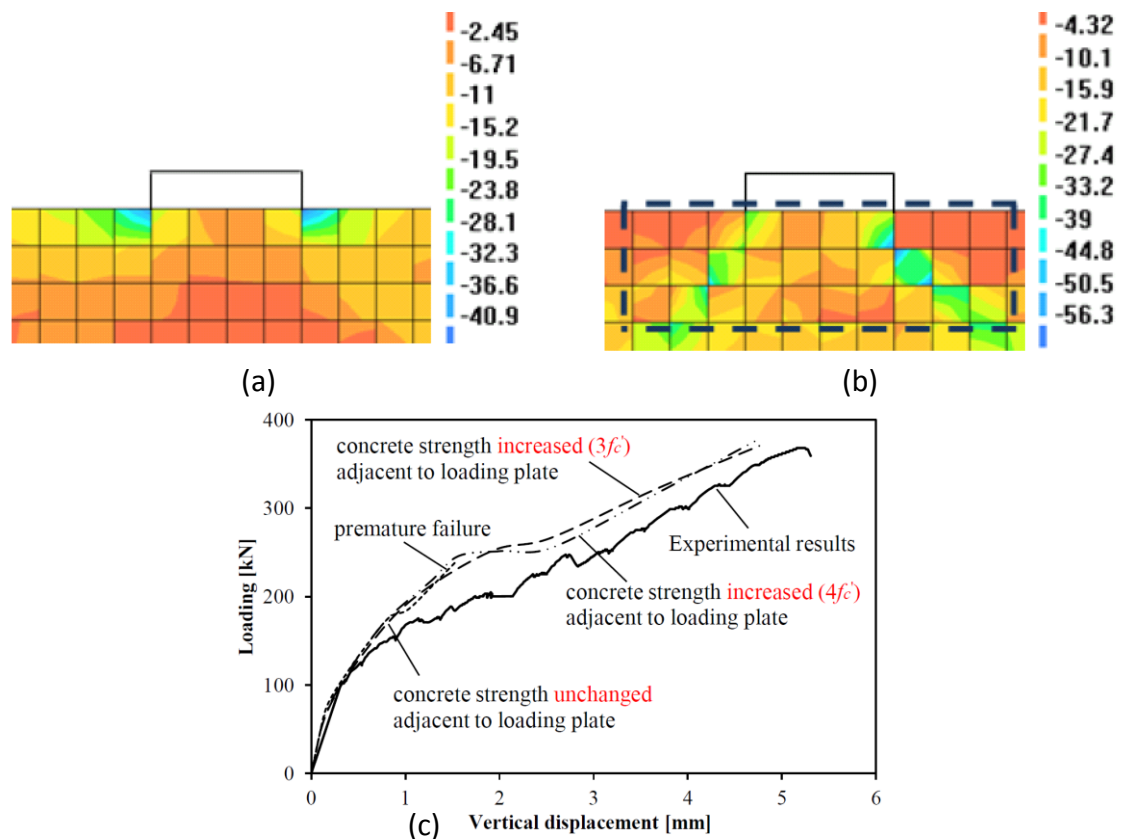


Figure 6.24: Stress concentration below loading plates a) no strength enhancement b) strength enhanced c) load-deflection response (Fang, 2013)

The interface element used in this research was an elastic interface element depicted CL121. An interface with normal and shear stiffness of $1 \times 10^7 \text{ N/mm}^3$ and $1 \times 10^5 \text{ N/mm}^3$ respectively was used as recommended for similar cases (DIANA, 2017). Beam B2-25 modelled by Fang (2013) was re-modelled using the same parameters as he adopted in his work but without and with interface elements. Introducing interface elements was found to significantly improve the prediction of both ultimate load and stiffness. The ratio of predicted to actual failure load increased from 0.66 (Fang, 2013) to 0.96 when using interface elements. Additionally, the introduction of interface elements eliminated the stress concentration under the loading plate (Figure 6.26) visible in Figure 6.24 – a.

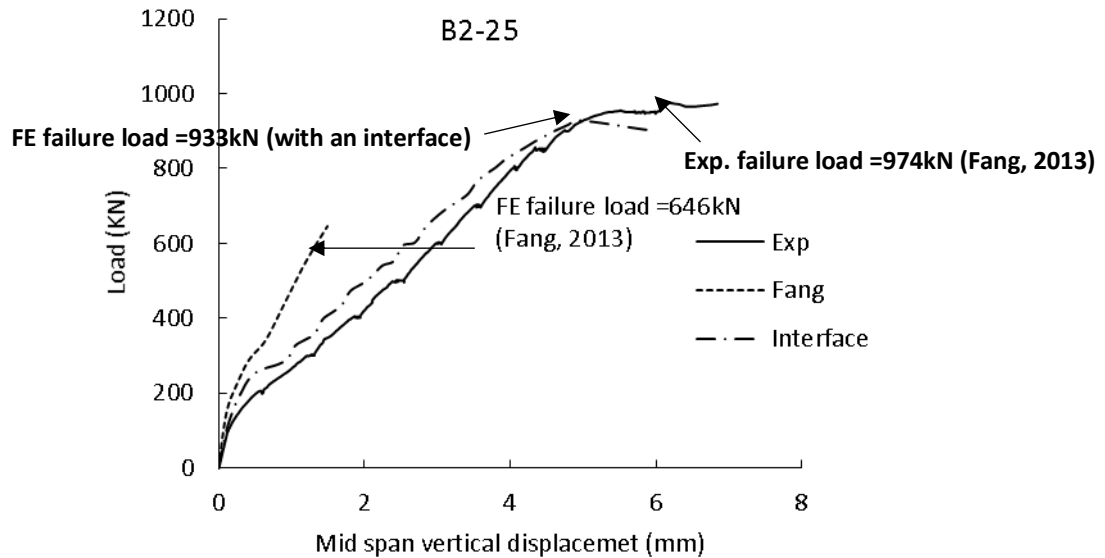


Figure 6.25: Enhancement of the response of beam B2-25 due to the interface element

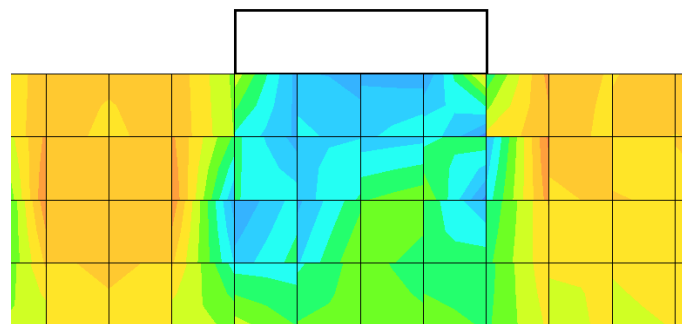


Figure 6.26: Stress variation under the loading plate with the use of an interface element.

6.8. Sensitivity Analysis of the Model

In this section, the test results presented in Chapter 4 are used to calibrate the NLFEA and to conduct sensitivity analysis of several parameters. The sensitivity of the analysis to the parameters of the base model presented in the previous section is investigated here.

6.8.1. Element size

The results of the NLFEA depend on the element size. Previous NLFEA suggests the use of elements size of 50mm (Sagasetta, 2008, Fang, 2013). However, it has also been reported that finer mesh enhances the performance of the NLFEA, yet, increases the running time (Fang, 2013). In this research, a sensitivity analysis was performed to examine the sensitivity of the FE to the element size. Elements with sizes (100mm, 50mm, 25mm and 12.5mm) were investigated and the analysis showed that results were similar for a mesh of an element size

25mm and smaller (see Figure 6.27). Hence, an element size of 25 mm was used for the majority of the beams with a few beams modelled with an element size of 12.5mm to maintain regular mesh when geometrical constraints are present.

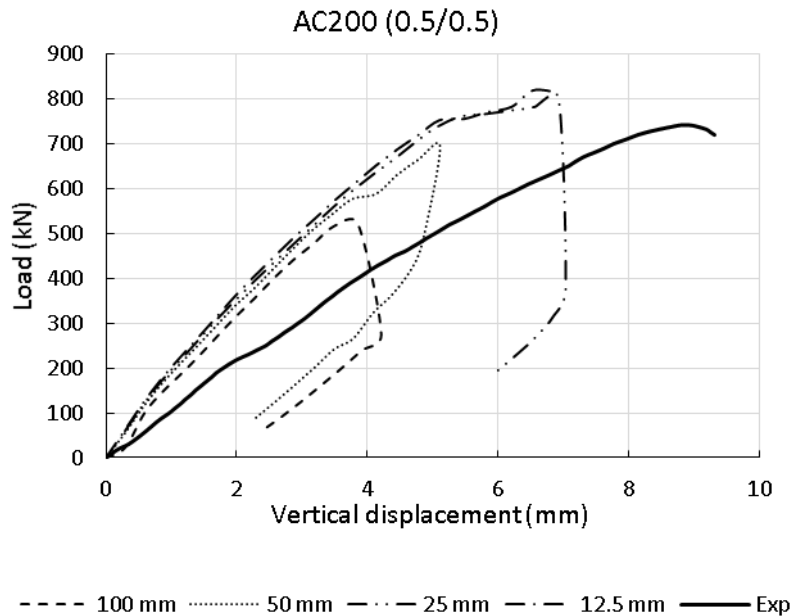


Figure 6.27: Sensitivity of the FEA to the element size (Beam AC200 (0.5/0.5))

6.8.2. Fixed and rotating crack model

For deep beams where the direction of crack propagation from the load to the support is almost predefined, the use of a fixed crack model is advocated by several previous studies (Sagasetta, 2008, Fang, 2013). To validate this assumption, the tested beams were modelled using the fixed, rotating and fixed to rotating crack models of to examine the sensitivity of the analysis to the model selection and to compare the observed and predicted crack pattern. Results are shown in Figure 6.28 for beams AC0 (0.5/0.5) and AC200 (0.5/0.5) without and with shear reinforcement respectively. The crack pattern is possibly most realistically captured with the fixed crack model but differences in crack patterns are minor.

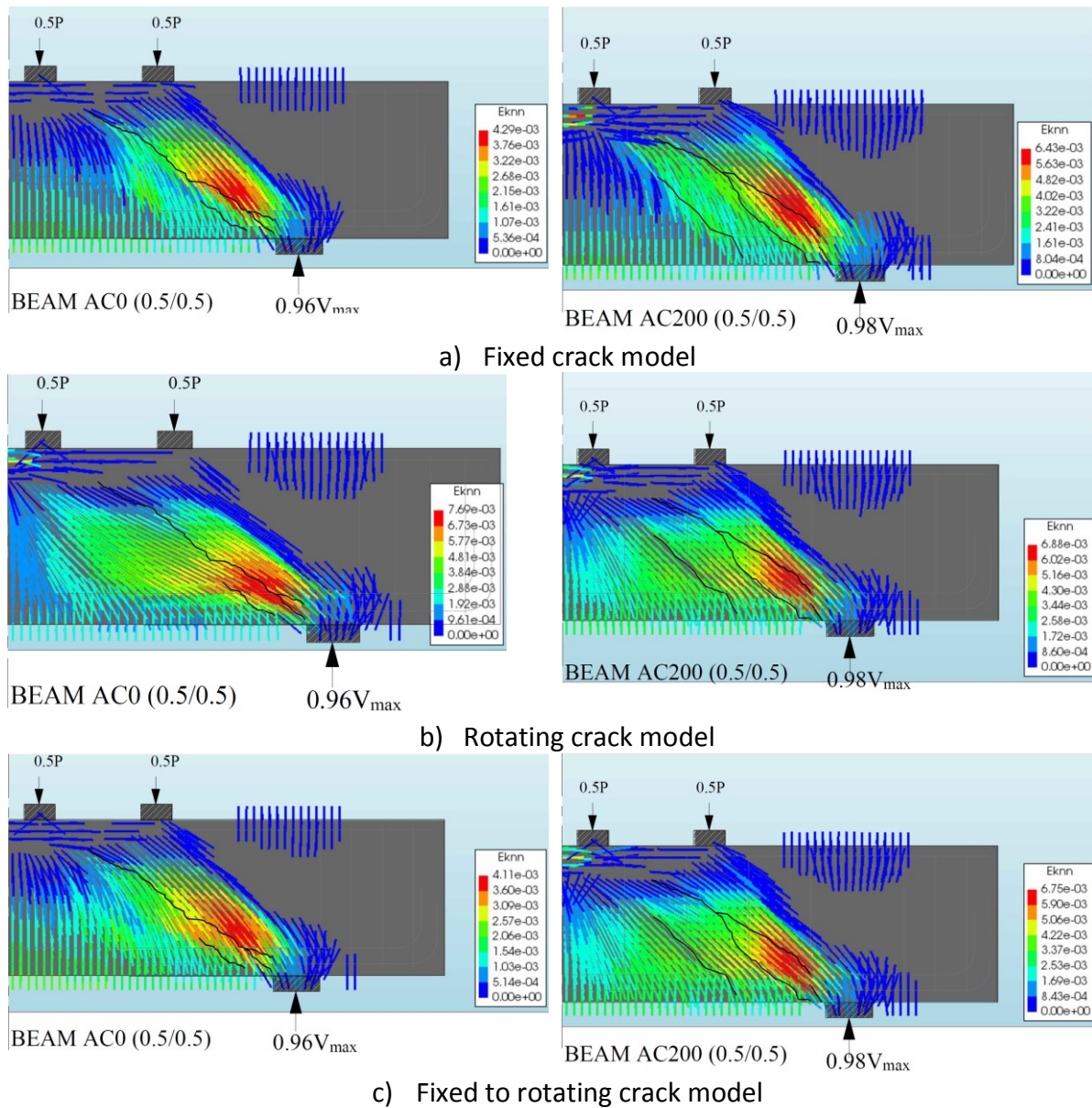


Figure 6.28: Crack patterns obtained using FEA with a) fixed, b) rotating and c) fixed to rotating crack models

Figure 6.29 shows the sensitivity of the load deflection response to the crack model for beams AC0 (0.5/0.5) without shear reinforcement and for beam AC200 (0.5/0.5) with shear reinforcement. Although the results are similar, the fixed crack model gives the best estimate of the ultimate shear resistance. The disadvantage of the fixed crack model is that it is sensitive to the choice of shear retention model. Beam AC0, without shear reinforcement, was modelled using a variable shear retention model while beam AC200 (0.5/0.5), with shear reinforcement, was modelled used a constant shear retention model. More details regarding the selection of the shear retention model are provided in section 6.8.5.

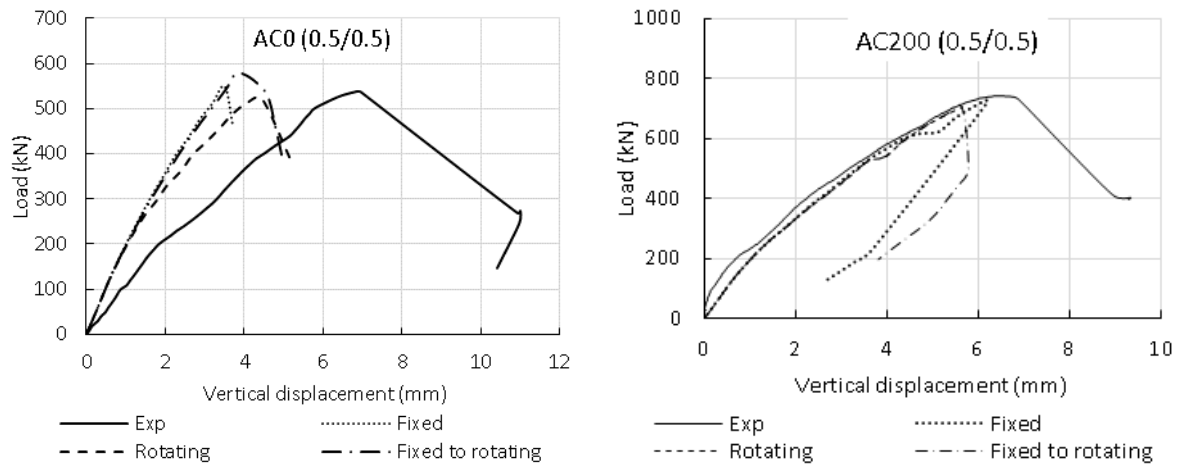


Figure 6.29: Sensitivity of the FEA to the crack model

6.8.3. Compressive behaviour of the concrete

The Feenstra model (1993) was adopted in the author’s baseline FEM on the basis of calibration studies described earlier and the previous NLFEA studies of deep beams using DIANA (Sagasetta, 2008, Fang, 2013). Of the models considered, Feenstra’s compressive model gave noticeably the best responses for the tested beams. A comparison between different constitutive models for the compressive behaviour of the concrete is shown in Figure 6.30 for comparable beams loaded on the compression (AC200 (0.5/0.5)) and tension face (BT200 (0.5/0.5)).

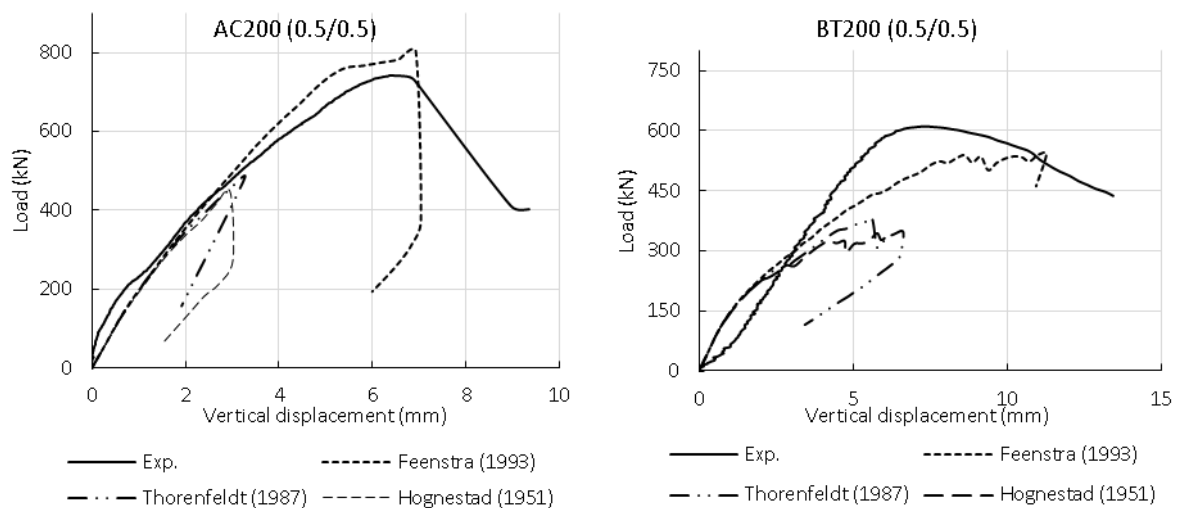


Figure 6.30: Comparison of the different compressive models in FEA for the concrete in predicting the failure

6.8.4. Compressive fracture energy

Several studies indicate that there is no general agreement on the ideal value of the compressive fracture energy G_{fc} (Ožbolt and Reinhardt, 2002, Sagaseta, 2008). However, the compressive behaviour of the selected compressive model depends significantly on it (Feenstra, 1993). A reasonable justification for this is that the effect of the compressive fracture energy on the post-peak stiffness is case dependent (Sagaseta, 2008).

Several values have been suggested for G_{fc} as a multiple of the fracture energy G_f . Commonly adopted values are $50 G_f$, $100 G_f$ and $200 G_f$ (Fang, 2013). Figure 6.31 shows that the FE analysis carried out using the baseline parameters was less sensitive to the value of the compressive fracture energy. Accordingly a value of $100 G_f$ was used as it gave the best estimates consistently and it has also been reported to provide good predictions in similar cases (Sagaseta, 2008, Fang, 2013).

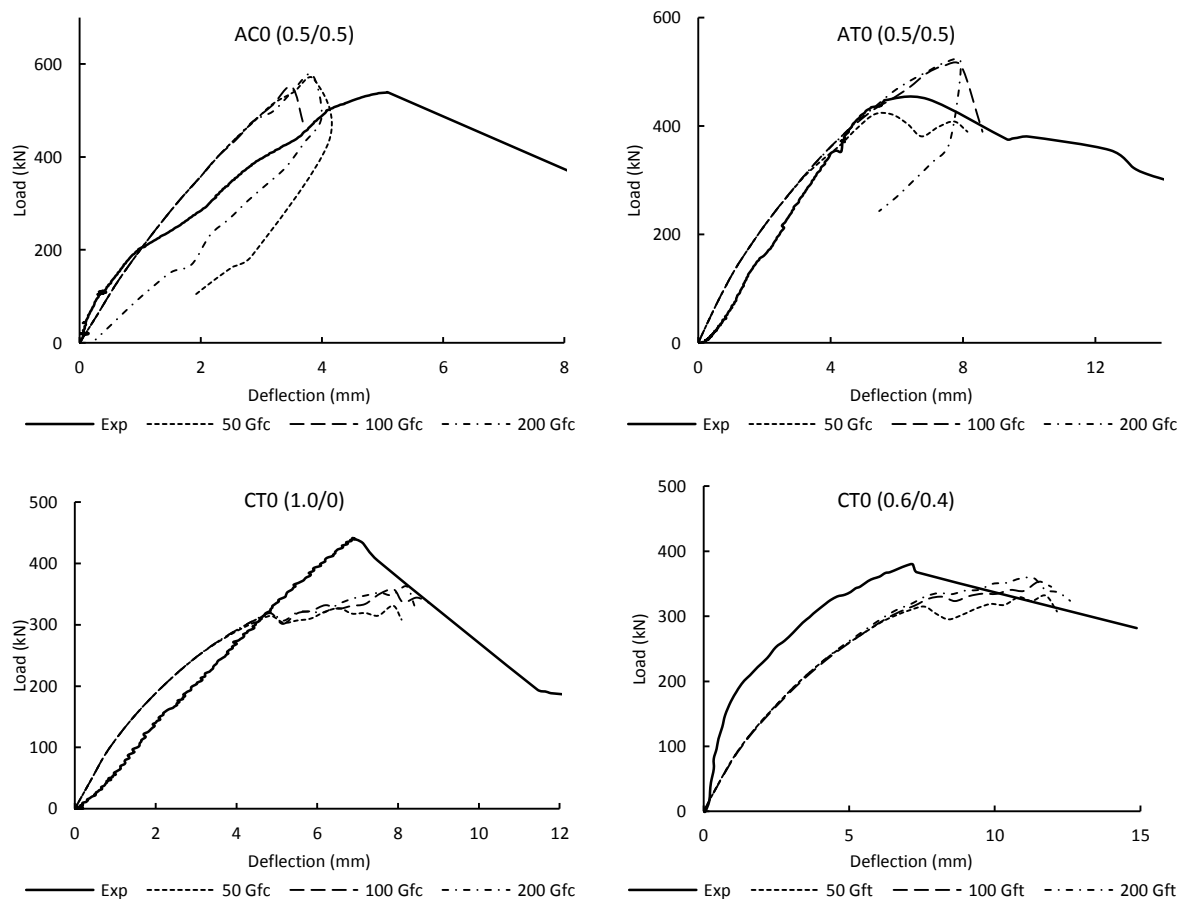


Figure 6.31: The sensitivity of the FE analysis to the compressive fracture energy for beams without shear reinforcement

6.8.5. Shear retention model

As mentioned in section (6.4.3) earlier, the concrete shear behaviour is affected by the choice of shear retention model, particularly for beams without shear reinforcement. The sensitivity of the analysis to the shear retention model for beams without shear reinforcement is examined in Figure 6.32. Generally, the aggregate size-based model gives the highest strengths, while the damage based model (Selby and Vecchio, 1993) gives the lowest strengths. The decay shear transfer model (Maekawa et al., 2003) provides the best strength estimates with an average FE/Exp

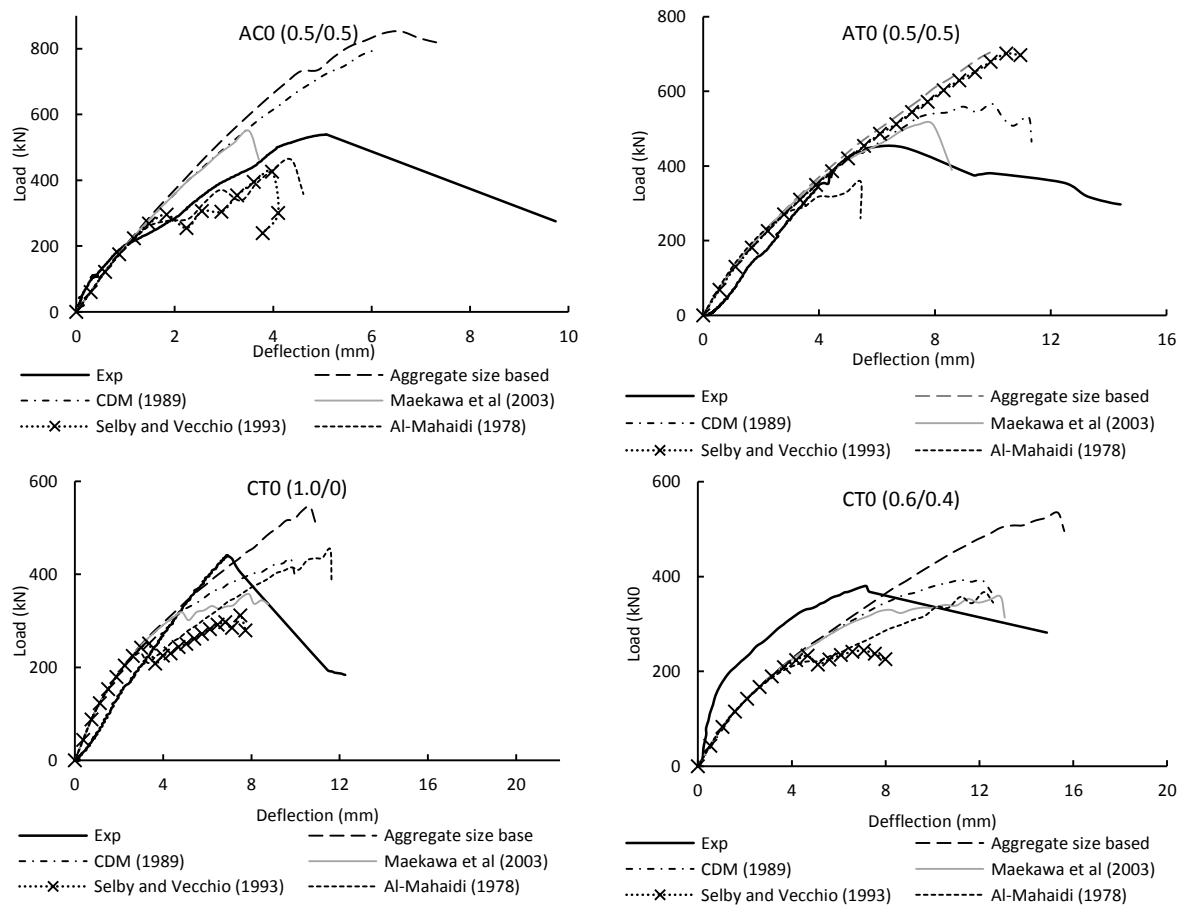


Figure 6.32: Sensitivity of the FEA to the shear retention models for beams without shear reinforcement (Beam AC0 (0.5/0.5))

For beams with shear reinforcement, a constant shear retention model was used with a $\beta=0.25$ which gave the best estimates for the test beams with shear reinforcement and in previous studies (Fang, 2013, Sagaseta, 2008). This the sensitivity of the analysis to the constant shear retention value is presented in Figure 6.33

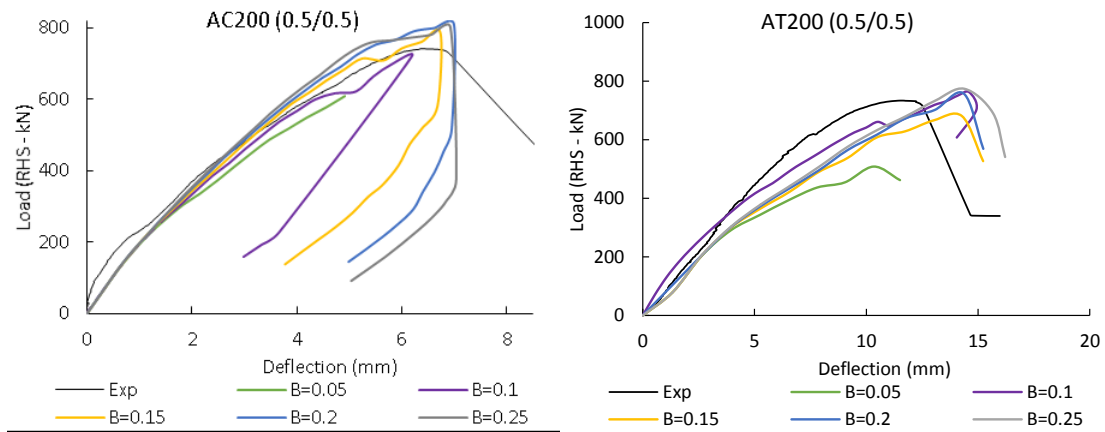


Figure 6.33: Sensitivity of the analysis to the constant shear retention value

6.9. Finally Adopted Parameters

The final choice of modelling parameters was based on the sensitivity analyses described in section 6.8 as well as calibration studies made using the author's test results. The chosen constitutive models and associated parameters are summarised in Table 6.3 below. The material properties used in the NLFEA are summarised Table 6.4. The concrete fracture energy and elastic modulus were calculated in accordance with EC2 and MC2010 using the equations below:

$$G_f = G_{f0} \left(\frac{f_{cm}}{f_{cm0}} \right)^{0.7} \quad \text{Equation 6.22}$$

$$G_{f0} = 0.0204 + 6.625 \times 10^{-4} D_{max}^{0.95} \quad \text{Equation 6.23}$$

$$E_{cm} = 22 \left(\frac{f_{cm}}{10} \right)^{0.3} \quad \text{Equation 6.24}$$

D_{max} is the maximum aggregate size, f_{cm} is the mean concrete compressive strength and $f_{cm0}=10\text{MPa}$.

Table 6.3: Material models and properties used in the FEA

Material Type	Materials Model	Parameters
Concrete	Compressive strength:	f_{ck}
	Parabolic	G_{fc}
		E_c
		Compressive strength reduction: Vecchio and Collins (1993)
		Confinement effect: Selby and Vecchio (1997)
	Tensile Strength: Hordjik	f_t (Obtained from the Brazilian tests)
		G_f
		Poisson ratio ($\nu = 0.15$)
		Poisson Reduction: Damaged based
	Shear retention (Constant)	$\beta = 0.25$
	Shear retention (Variable)	β from (!!! INVALID CITATION !!!)
Reinforcement	Linear Elasticity	$E_s = 210,000$ MPa
	Von Mises Plasticity (Total strain hardening)	$f_y = 570$ MPa
Steel Plates	Linear Elasticity	$E_s = 210,000$ MPa
		Poisson ratio ($\nu = 0.3$)
Interface element	Linear Elasticity (2D line interface)	Normal stiffness= $1.00E+07$ N/mm ³
		Shear stiffness= $1.00E+05$ N/mm ³

Table 6.4: Material properties used in the NLFEA

Beam	f_{cm} (MPa)	f_{tm} (MPa)	E_c (MPa)	G_f (N/mm)	G_{fc} (N/mm)
AC0 (0.5/0.5)	29.80	2.505	32784.63	0.08068	8.07
AC200 (0.5/0.5)	30.30	2.608	32914.12	0.08143	8.14
AT0 (0.5/0.5)	30.60	2.660	32991.26	0.08187	8.19
AT200 (0.5/0.5)	31.20	2.764	33144.27	0.08276	8.28
BT200 (0.5/0.5)	28.43	2.58	32423.54	0.07862	7.86
BT200 (1.0/0)	28.89	2.72	32545.82	0.07932	7.93
BT200 (0/1.0)	29.24	2.82	32638.15	0.07984	7.98
BT200 (0.3/0.7)	28.78	2.68	32516.68	0.07915	7.91
CT0 (1.0/0. 0)	26.90	2.59	32008.87	0.07630	7.63
CT200 (1.0/0)	28.04	2.59	32319.01	0.07803	7.80
CT0 (0.6/0.4)	28.90	2.60	32548.47	0.07933	7.93
CT200 (0.6/0.4)	28.33	2.60	32396.81	0.07847	7.85

A quasi-Newton solution method was used with a user-specified step maximum size of 0.05 of the total measured failure load in conjunction with arc length control. This maximum step size is automatically reduced if the analysis failed to converge in late stages of the analysis. An energy convergence criterion was used with a convergence tolerance of 0.001 and a maximum iteration limit of 300. The importance of using arc length control was highlighted earlier in section 6.4.5. Figure 6.34 shows the effect of introducing the arc-length technique for the analysis of the beams in series (A) which includes beams with/without shear reinforcement loaded on the compression/tension face. The inclusion of arc length control is seen to capture the post-peak responses and result in enhanced predictions of the failure load.

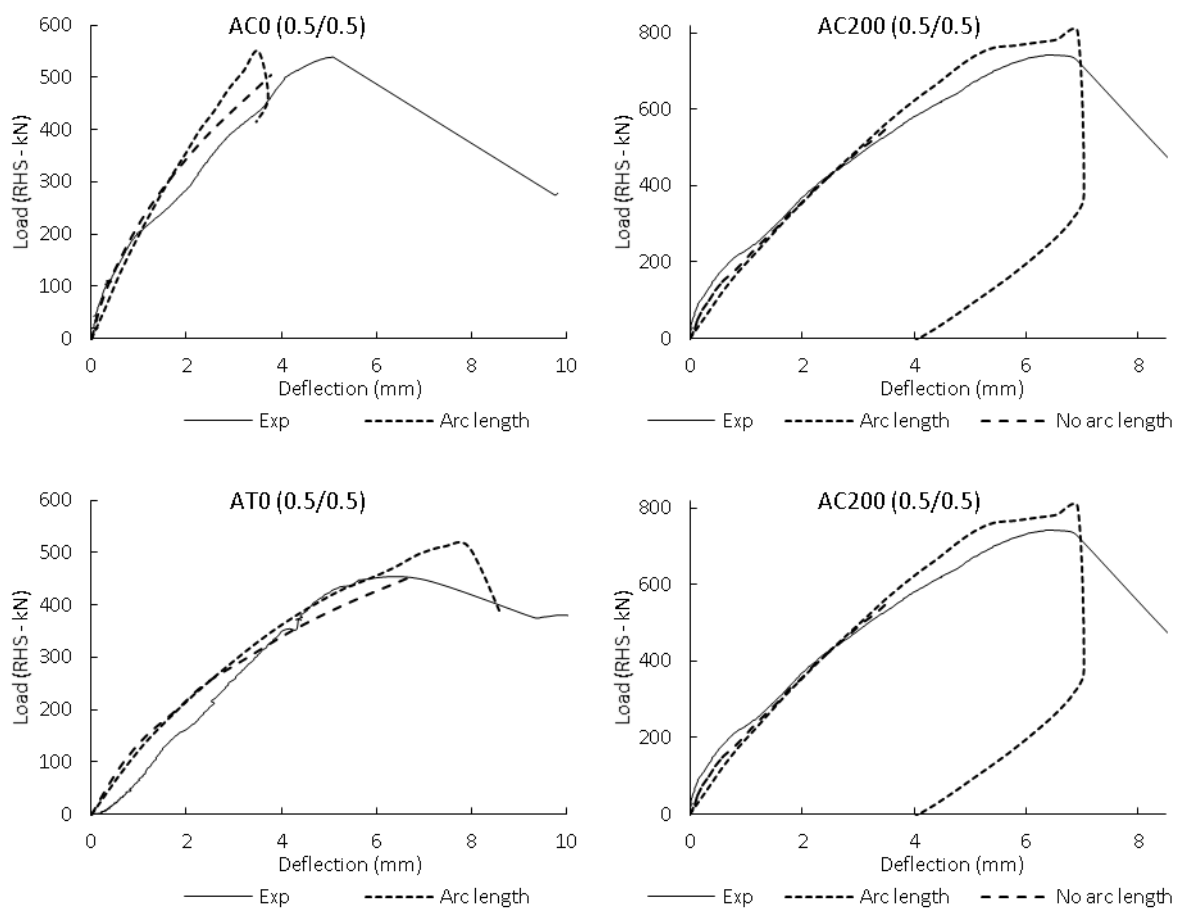


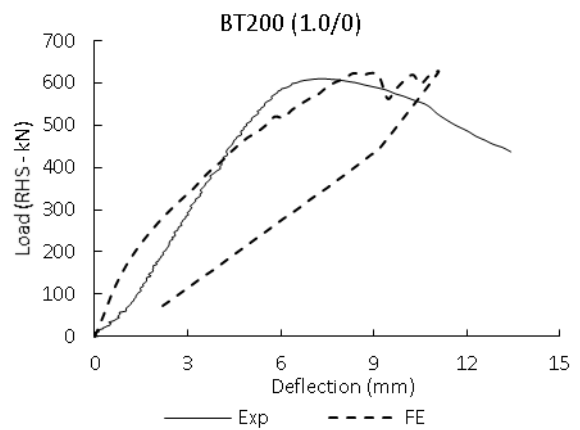
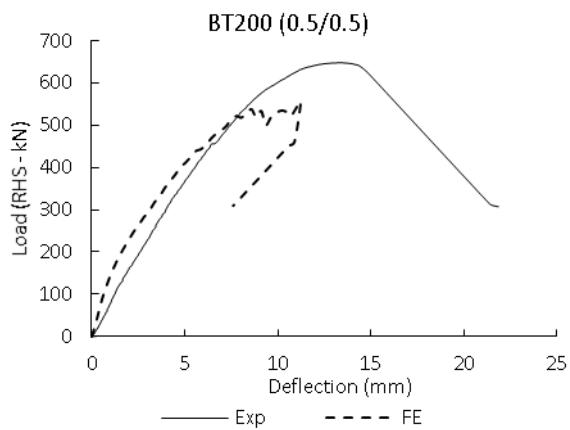
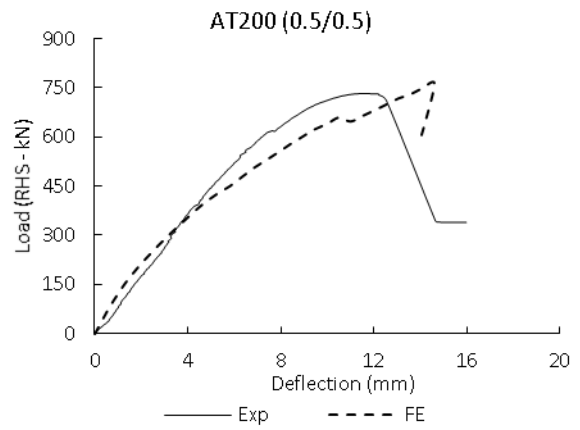
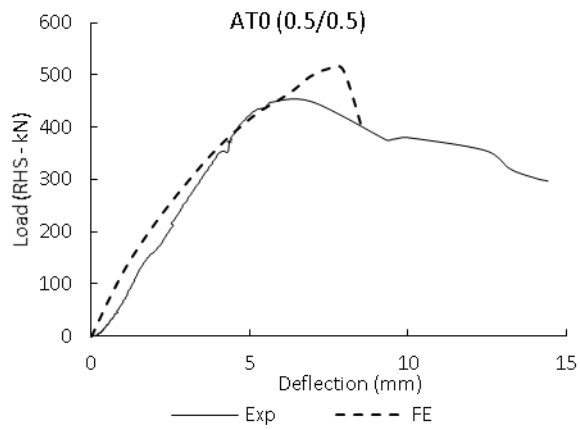
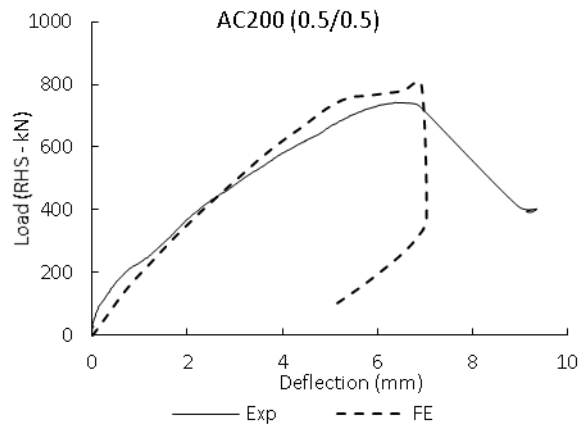
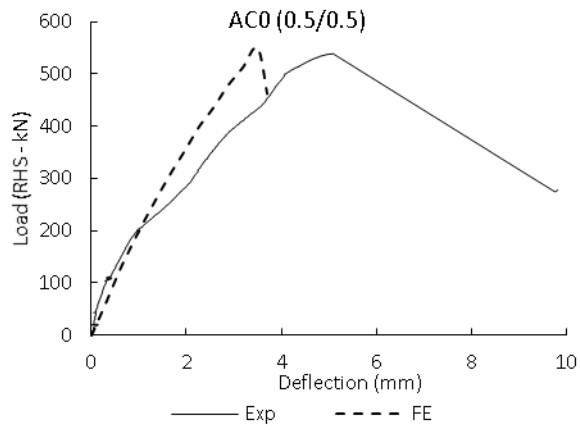
Figure 6.34: Effect of introducing the arc-length technique to the analysis of the beams in series A

6.10. Results of the FEA

Test results presented in Chapter 4 were used to calibrate the baseline FEA as described earlier to give a best fit of the predictions for all the tested beams. The selected models and solution procedures discussed above were used to model the test beams. A summary of the FE results is presented in Table 6.5. The analysis accurately predicted the failure loads of the beams with an average FE to actual failure load of 1.0 and a COV of 9. As shown in Figure 6.35, the FEA gave reasonable predictions of maximum displacement for the majority of the beams tested in this research.

Table 6.5: Summary of the results of the FEA

Beam	FE/Exp.	
	Load	Disp.
AC0 (0.5/0.5)	1.02	0.69
AC200 (0.5/0.5)	1.08	1.09
AT0 (0.5/0.5)	1.14	1.07
AT200 (0.5/0.5)	1.04	1.27
BT200 (0.5/0.5)	0.86	0.84
BT200 (1.0/0)	1.03	1.53
BT200 (0/1.0)	1.12	1.39
BT200(0.3/0.7)	0.98	1.07
CT0 (1.0/0)	0.81	1.15
CT200 (1.0/0)	1.02	1.03
CT0 (0.6/0.4)	0.95	1.80
CT200 (0.6/0.4)	1.01	1.15
Average	1.00	1.17
St Dev	0.09	0.28
COV %	9.19	24.22



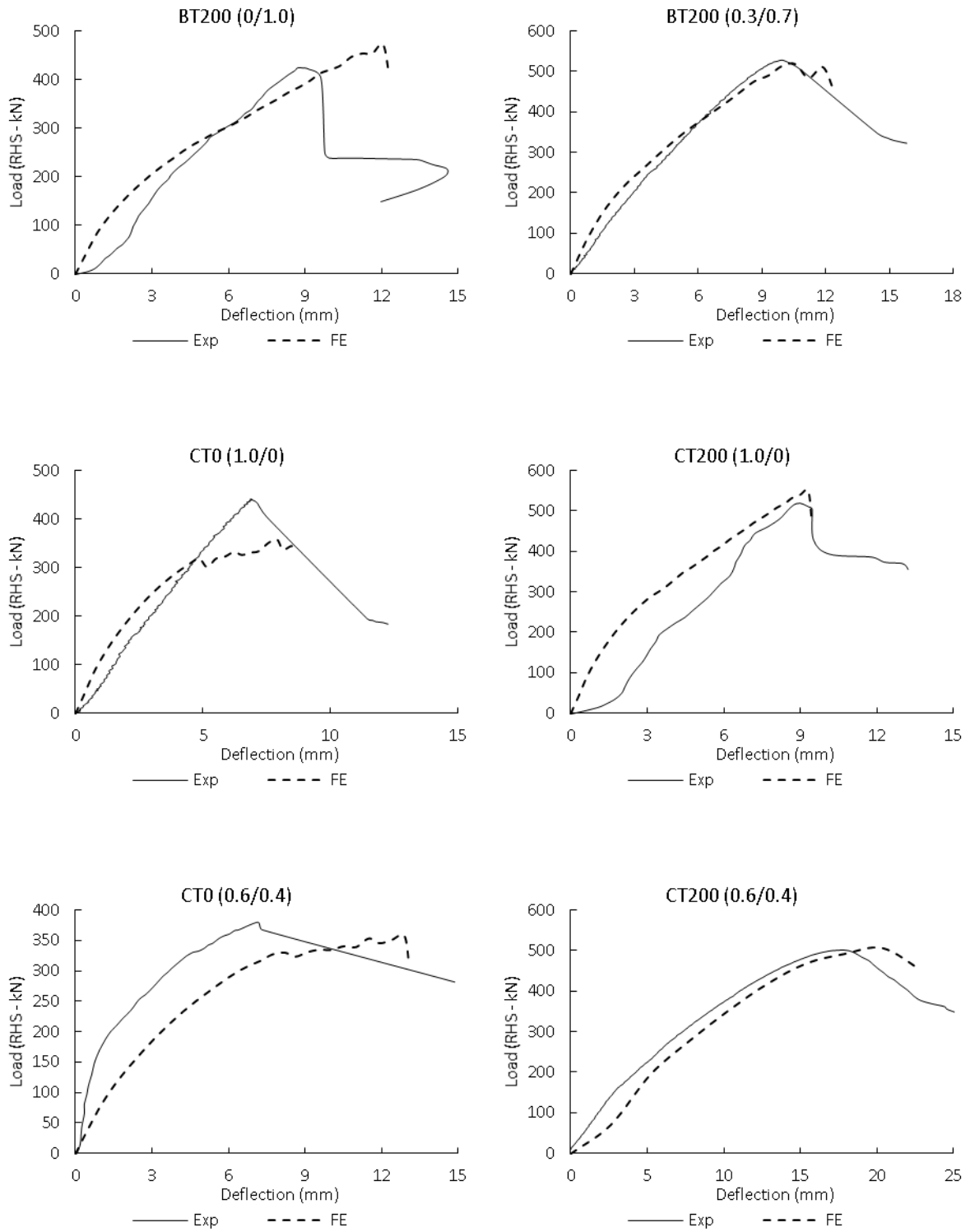


Figure 6.35: Prediction of the load-deflection using FEA

6.11. Conclusions

This chapter describes the NLFEA used in this research. An overview of discrete and smeared cracking models is given with a particular focus on the various types of the smeared crack model available in DIANA. The concrete and reinforcement material models available in DIANA are critically reviewed. The models adopted in this research are justified on the basis of sensitivity analyses and comparisons of measured and predicted responses for beams tested by Fang (2013) as well as the author.

A fixed crack approach is used in this work. To model the concrete behaviour in compression, the Feenstra parabolic curve (1993) is used with a compressive fracture energy of $100G_{f,t}$. The models of Selby and Vecchio (1997) and Vecchio and Collins (1993) are used to model the effect of lateral confinement and cracking respectively on the compressive behaviour of concrete. The Hordijk tensile model (1992) is used to model the tension softening behaviour of concrete. Following a sensitivity analysis, the variable shear retention model suggested by Maekawa (2003) is used for beams without shear reinforcement while the constant shear retention model with $\beta = 0.25$ is used for beams with shear reinforcement. Interface elements are introduced between the beam and the loading/support plates to prevent the development of localised stress concentrations at the plate corners. This in turn prevents premature failure. Reinforcement is modelled using embedded bars and Von Mises plasticity with strain hardening.

Regarding the solution procedure, a user-specified maximum step size of 0.05 of the total load with an arc length technique is used. To solve the system of the nonlinear equations, a quasi-Newton method is used with an energy convergence criterion. A convergence tolerance of 0.001 is used with a maximum number of iterations of 300.

The authors test results were utilised to calibrate the FEA. The resulting NLFEA modelling procedure predicted the failure loads of the beams with an average FE to actual failure load of 1.0 and COV of 9%. The FEA was also able to predict the maximum displacement and the load-deflections response fairly good for the majority of the beams.

CHAPTER 7. ANALYSIS OF EXPERIMENTAL RESULTS

7.1. Introduction

The shear strength of RC beams is significantly enhanced by arching action when loads are applied within around twice the beam effective depth ($2d$) of supports. Apart from the tests of Brown and Bayrak (2007) and Vollum and Fang (2014), little attention has been given to the case of beams with multiple point loads applied to the flexural compression face within $2d$ of supports. This research considers shear enhancement in cantilever beams with multiple point loads applied to the tension face.

Shear enhancement in beams loaded within $2d$ of supports is most simply modelled using simplified semi-empirical methods such as that of EC2 (BSI, 2004), the superseded UK code BS8110 (BSI, 1997) and fib Model Code 2010 (fib, 2013). The test results presented in Chapter 4 show some differences in the strength of comparable beams loaded on the flexural tension and compression faces. However, current design provisions for shear enhancement do not distinguish between beams loaded on the flexural tension and compression faces.

Alternatively, and more rationally, shear enhancement can be modelled with mechanically based models such as the strut and tie method (Sagasetta and Vollum 2010, Vollum and Fang, 2015). The STM of Vollum and Fang (2015) is applicable to short shear span beams with pairs of loads applied to the compression face within $2d$ of the support. Refined STMs can be developed on the basis of compressive stress fields determined using NLFEA. The analysis shows that stress fields determined with NLFEA are different for comparable beams of series A, described earlier in section 3.2.1 and Figure 3.3, loaded on the flexural compression and tension faces. As discussed previously, tension face loading can arise in structures like crosshead girders and continuous beams.

This chapter considers the test results presented in Chapter 4 and assesses the practical significance of differences in shear strength arising from tension and compression face loading. The shear strength of the tested beams is assessed in this chapter using the provisions given in various design codes, strut-and-tie models and NLFEA.

7.2. Assessment of Beam Strength Using Codified Sectional Methods

This section considers the shear enhancement design methods given in the superseded UK code BS8110 (BSI, 1997), EC2 (BSI, 2004) and fib Model Code 2010 (MC2010) (fib, 2013). These methods apply to beams loaded on the top face within $a_v \leq 2d$. EC2 and MC2010 reduce the contribution to the design shear force of loads applied within $a_v \leq 2d$ by the multiple $\beta = \frac{a_v}{2d}$. The multiple β is limited to a minimum value of 0.25 in EC2 and 0.5 in MC2010. Unlike EC2 and MC2010, BS 8110-97 enhances the shear resistance provided by concrete $v_{Rd,c}$ for beams loaded within $a_v \leq 2d$ by the multiple $\beta = \frac{2d}{a_v} \geq 0.5$. The design methods of BS8110 and EC2 are only equivalent of: i) a single load is applied within a distance of $a_v \leq 2d$ from the support and ii) the shear resistance is not increased by shear reinforcement. In addition, the application of the design provisions for the shear enhancement in EC2 is unclear for beams with shear reinforcement and multiple point loads applied within $a_v \leq 2d$ as discussed by Vollum and Fang (2015). Further details regarding codes provisions are provided in Chapter 2. Vollum and Fang (2015) introduced some modifications to the equations of shear capacity provided in EC2, BS8110 and MC2010 to account for shear enhancement in beams with two-point loads applied within $2d$ of the support. The basic assumption was to investigate two different failure planes as illustrated in Figure 2.14. For a beam with two-point loads within $a_v \leq 2d$, failure is checked in BS8110 for each of the failure planes shown in Figure 2.14 as follows (equations shown are for BS8110):

$$V_{Ed} \leq V_{Rd,c} \cdot \frac{2d}{a_{v1}} + n_{av1} A_{sw} f_{yd} \frac{d}{a_{v1}} \quad \text{Equation 7.1}$$

$$R_2 V_{Ed} \leq V_{Rd,c} \cdot \frac{2d}{a_{v2}} + n_{av2} A_{sw} f_{yd} \frac{d}{a_{v2}} \quad \text{Equation 7.2}$$

In which V_{Ed} is the design shear force, $V_{Rd,c}$ is the shear strength without shear reinforcement and n_{avi} is the number of the stirrups within shear span i . In BS8110, the shear resistance V_{Ed} is checked for both the shear planes indicated in Figure 2.14.

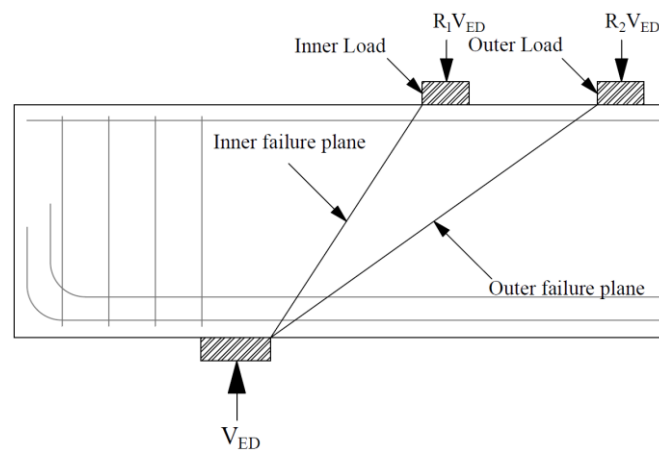


Figure 7.1: Expected failure planes for beams loaded with two points within $2d$

EC2 does not explicitly define the enhanced shear strength of a beam loaded with multiple point loads within $2d$ of supports. However, neglecting self-weight, a natural interpretation (Vollum and Fang, 2015) of the code requirements for a symmetrically loaded beam with two-point loads within $2d$ of each support is to take the failure load as the most critical of:

$$\beta_1 P_1 + \beta_2 P_2 \leq V_{Rd1} = \max(V_{Rd,c}, V_{Rd,s1}) \quad \text{Equation 7.3}$$

$$\beta_2 P_2 \leq V_{Rd2} = \max(V_{Rd,c}, V_{Rd,s2}) \quad \text{Equation 7.4}$$

In which P_1 and P_2 are the loads applied in the inner and outer load plates. The shear resistances $V_{Rd,c}$ and $V_{Rd,s}$ are defined in Section 2.3 of EC2.

Vollum and Fang (2015) showed that taking the total failure load (P_1+P_2) as the least of the values corresponding to equations 7.3 and 7.4 gives nonsensical results for beams with shear reinforcement where $V_{Rd,s2} > V_{Rd,c}$. This is the case because of the application of an infinitesimally small load P_1 causes the shear resistance to reduce from $V_{Rd,s2}$ to $\max(V_{Rd,c}, V_{Rd,s1})$ which is less than $V_{Rd,s2}$.

To circumvent this, Vollum and Fang (2015) proposed replacing equation 7.3 for failure along the inner plane with the interaction equation below:

$$\frac{\beta_1 P_1}{\max(V_{Rd,c}; n_{av1} A_{sw} f_{yd})} + \frac{\beta_2 P_2}{\max(V_{Rd,c}; n_{av2} A_{sw} f_{yd})} \leq 1.0 \quad \text{Equation 7.5}$$

MC2010 defines the control section for shear as the most critical of d from the face of the support or d from the face of the load. In MC2010, the shear resistance depends on the reinforcement strain as described in Section 2.3.3 of Chapter 2. The reinforcement strain due to flexure is enhanced by shear but cannot exceed the reinforcement strain at the section of maximum moment. Therefore, the strain given by equation 2.41 was limited to a maximum

of $\frac{M_{max}}{2E_sA_sZ}$ in the analysis of the tested beams. This limit governed for the tension face loaded beams where M_{max} was calculated at the centreline of the support. For beams loaded on the tension face the critical section for shear is consequently at d from the face of the inner load unless $a_v < d$ in which case MC2010 suggests that the shear resistance should be calculated as if the load were at d from the face of the support. For members loaded on the tension face, where $a_v < d$, the control section was taken at the support face where the flexural reinforcement strain is greatest. For beams loaded in the compression face, when $a_v < d$, the control section was taken at d from the face of the support as if the load was applied at a distance $(d + \text{load plate width}/2)$ – see Figure 7.2 a.

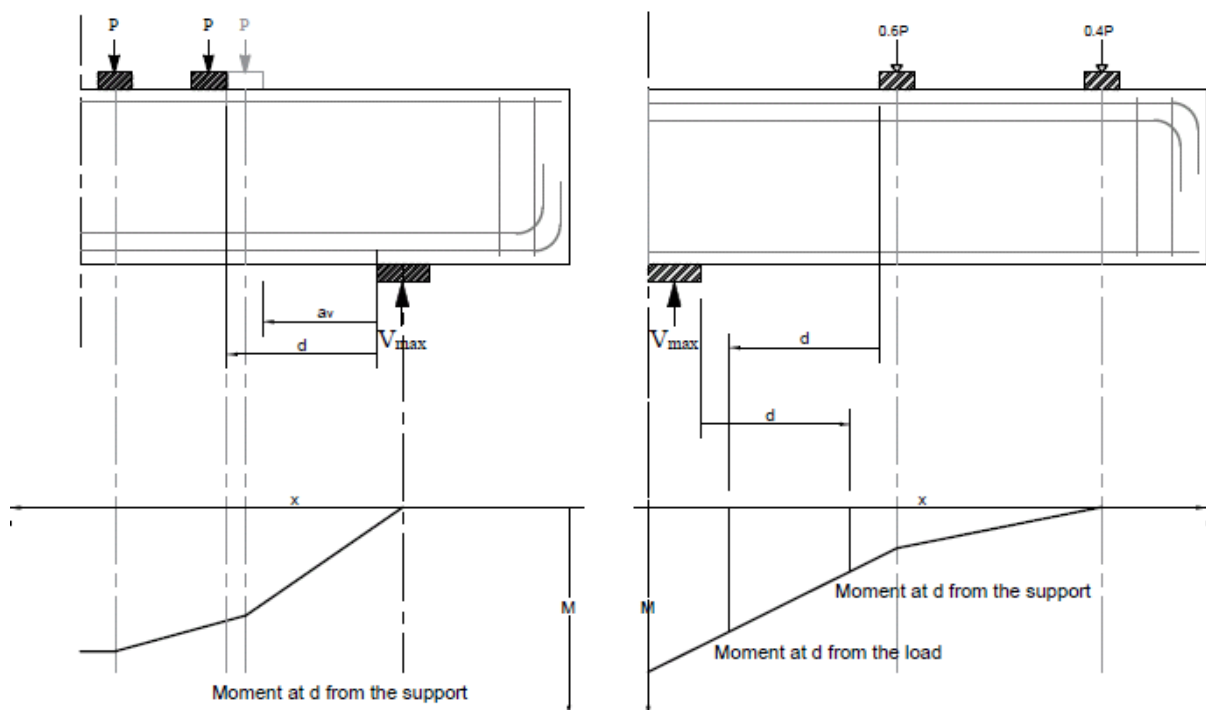


Figure 7.2: Control section for cases where a) $a_v < d$ and b) control section at d from the face of the concentrated load.

The EC2, BS8110 and MC2010 strength predictions are presented in Table 7.1, which shows that the predictions are all safe and rather conservative. The EC2 shear strengths of beams with two point loads in the shear span were calculated using equations 7.3 and 7.4 as suggested by Vollum and Fang (2015). For purposes of comparison, V_{Rdc} was calculated with EC2 when applying the BS 8110 shear enhancement method. Overall, MC2010 level of accuracy (LoA) III gave the best estimates with an average of 0.75 and a COV of 0.18 and EC2 gave the worst estimates. One point to highlight here is that none of the considered design

methods explicitly accounts for the influence of loading face (i.e. whether the load is applied on the flexural tension or compression face of the beam). Unlike BS8110 and EC2, MC2010 relates shear resistance to the flexural reinforcement strain. Consequently, the calculated shear resistance given by MC2010 is different for notionally identical beams with the AC (0.5/0.5) and AT (0.5/0.5) loading arrangements.

Table 7.1: Predictions of the shear strength of the test beams calculated with different design codes

Beams	Exp.	BS 8110	EC2	MC 2010	
				Exp./LoA.II	Exp./LoA.III
AC0 (0.5/0.5)	539	0.58	0.40	0.38	0.55
AC200 (0.5/0.5)	742	0.66	0.41	0.48	0.61
AT0 (0.5/0.5)	449	0.75	0.51	0.47	0.70
AT200 (0.5/0.5)	733	0.67	0.42	0.49	0.64
BT200 (0.5/0.5)	648	0.74	0.46	0.53	0.70
BT200 (1.0/0)	610	0.79	0.54	0.75	0.98
BT200 (0/1.0)	423	0.69	0.53	0.65	0.92
BT200(0.3/0.7)	528	0.79	0.55	0.59	0.79
CT0 (1.0/0)	441	0.47	0.47	0.47	0.71
CT200 (1.0/0)	543	0.64	0.52	0.68	0.92
CT0 (0.6/0.4)	378	0.56	0.44	0.44	0.67
CT200 (0.6/0.4)	502	0.70	0.60	0.58	0.80
	Average	0.67	0.49	0.54	0.75
	SD	0.09	0.06	0.11	0.13
	COV	0.14	0.11	0.20	0.18

Table 7.2 shows an assessment of the code predictions in Table 7.1. The results are indicative and should be treated with caution due to the limited extent of test data.

Table 7.2: Assessment of code predictions of the strength of beams tested in this program

Beams with single point load (No of beams = 4)				
	Exp./BS8110	Exp./EC2	Exp./MC2010(II)	Exp./MC2010(III)
Average	0.65	0.52	0.64	0.88
SD	0.14	0.03	0.12	0.12
COV	0.21	0.07	0.19	0.14
Beams with multiple point loads – All beams (No of beams = 8)				
Average	0.68	0.47	0.50	0.68
SD	0.08	0.07	0.07	0.08
COV	0.12	0.16	0.14	0.12
Beams with multiple point loads -Stirrups (No of beams = 5)				
Average	0.71	0.49	0.53	0.71
SD	0.06	0.08	0.05	0.08
COV	0.08	0.17	0.09	0.11
Beams with multiple point loads - No stirrups (No of beams = 3)				
Average	0.63	0.45	0.43	0.64
SD	0.11	0.06	0.04	0.06
COV	0.17	0.13	0.10	0.12
Beams with multiple point loads - compression face (No of beams = 2)				
Average	0.62	0.41	0.43	0.58
SD	0.05	0.01	0.07	0.04
COV	0.09	0.02	0.17	0.07
Beams with multiple point loads - Tension face (No of beams = 6)				
Average	0.70	0.50	0.52	0.72
SD	0.08	0.07	0.06	0.06
COV	0.12	0.14	0.12	0.09

Overall the MC2010 (LoA III) predictions are best but the BS8110 predictions are also reasonable. EC2 and MC2010 LoAII gave the most conservative estimations particularly for beams loaded on the compression face with multiple point loads as reported previously by Fang (Fang, 2013). For beams with multiple point loads, strength estimates were less conservative for beams with shear reinforcement than without shear reinforcement but there are insufficient results to draw firm conclusions. However, this trend is also evident in Fang's

strength estimations of his beams with multiple loads within the shear span (Fang, 2013). The better estimates for tension face loaded beams results from the lower observed shear strengths of the beams loaded in the tension face. The significance of this is explored in section 7.4.5.

7.3. Evaluation of the Shear Strength Using Strut-and-tie Models

The strut-and-tie method (STM) is a popular tool for estimating the strength of discontinuity regions in which plane sections do not remain plane. Several design codes suggest using STM to account for shear strength enhancement in deep beams (BSI, 2004, ACI-Committee, 2014, CSA, 2004, fib, 2010).

The model developed by Sagaseta and Vollum (Sagaseta and Vollum, 2010) (depicted here as STM1) for beams with vertical shear reinforcement simplifies the principal of nodal subdivision. To avoid considering stirrups individually, the stirrups can be replaced by a single tie, positioned at the centroid of the effective stirrups, with the same cross sectional area as the effective stirrups. This model (presented here in Figure 2.32) has been used and modified by several researchers (Amini Najafian et al., 2013, Vollum and Fang, 2015).

This model (STM1) was developed to calculate the strength of simply supported short shear span beams with either a central point load or two symmetrically positioned point loads applied to the compression face of the beam. Clearly, the model is also applicable if the beam shown in Figure 7.3 if turned upside down to represent a cantilever beam with a single point load applied to the tension face. The load is transmitted to the supports in this model through a combination of a direct strut (Strut I) and a truss (Strut II and strut III) equilibrated by vertical stirrups. Strut I carries λP while the remainder of the load $(1 - \lambda)P$ is carried by the vertical stirrups. The shear reinforcement is assumed to yield at failure unless preceded by flexural failure or disappearance of the direct strut. Stirrups within the central $\frac{3}{4}$ of the shear span are considered effective. The direct strut resists a proportion β of the total tensile force in the reinforcement at the bottom node. Once λ and β are known, the geometry of the nodes can be defined.

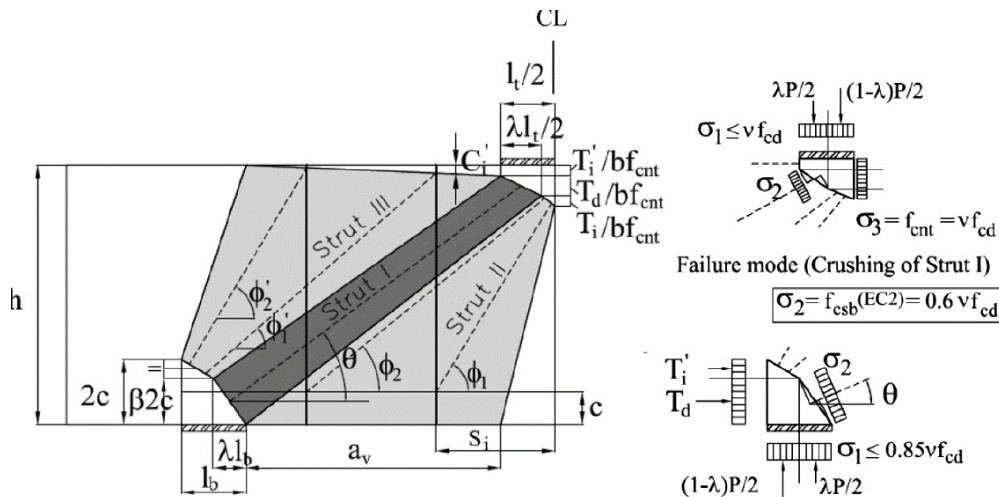


Figure 7.3: Sagaseta and Vollum model for deep beams with vertical shear reinforcement (Sagaseta and Vollum, 2010)

When using the STM design recommendations of EC2, the stresses under the load plate (the CCC node) and the support plate (the CCT node) are limited to $v' f_{cd}$ and $0.85v' f_{cd}$ respectively, where $v' = (1 - \frac{f_{ck}}{250})$. The stress at the rear face of the CCC node is limited to $v' f_{cd}$ while no check is made on the stress at the rear face of the CCT node as permitted by EC2. Failure is assumed to occur at the lowest load corresponding to bearing failure at either the top or bottom node, crushing of strut I at either the top or the bottom node to strut interface or flexure. The strength of Strut I is reduced due to the presence of the cracks and transverse tensile strain. EC2 accounts for this with a strength reduction factor of $0.6v'$. Further details of the STM geometry and solution algorithm can be found elsewhere (Sagaseta, 2008).

Sagaseta and Vollum (2010) used STM1 to assess the strength of 47 deep beams with a shear span to effective depth ranging between 1 and 2. This was done with the strength of the direct strut calculated using both the EC2 and the MCFT provisions. Overall, the STM was found most accurate for beams with stirrups and gave the most consistent results if the strength of the direct strut was calculated using the provisions of the MCFT.

A similar approach to STM1 was adopted by Mihaylov et al. (2013) who proposed the STM shown in Figure 7.4. The model can be seen as a simplification of STM1 proposed by Sagaseta (2008) with the strut D representing the resultant of the struts I and III in STM1. A merit of this model is its simplicity, which does not greatly jeopardise the accuracy of results compared with STM1.

Figure 7.5 compares beam strengths calculated using STM1 and the model provided by Mihaylov et al. (2013) for the tested beams with a single point load with EC2 provisions. The results show both models gave conservative estimations of the failure load with SMT1 providing slightly higher estimates. Results were calculated based on the measured concrete strength of the beams.

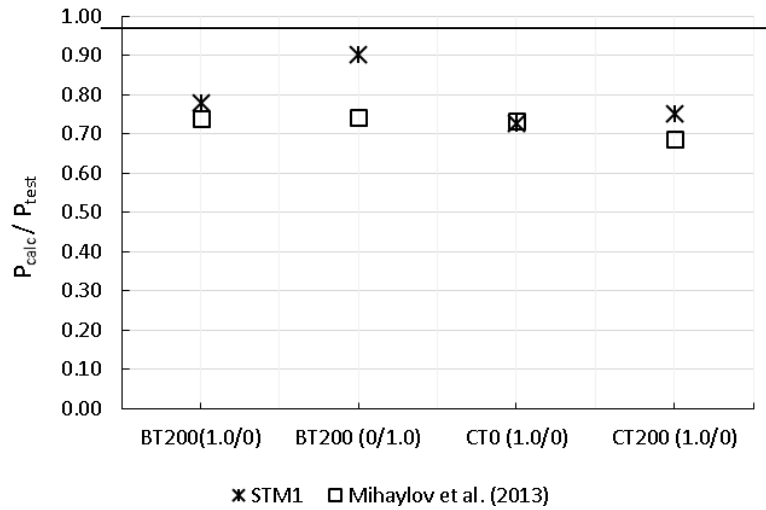
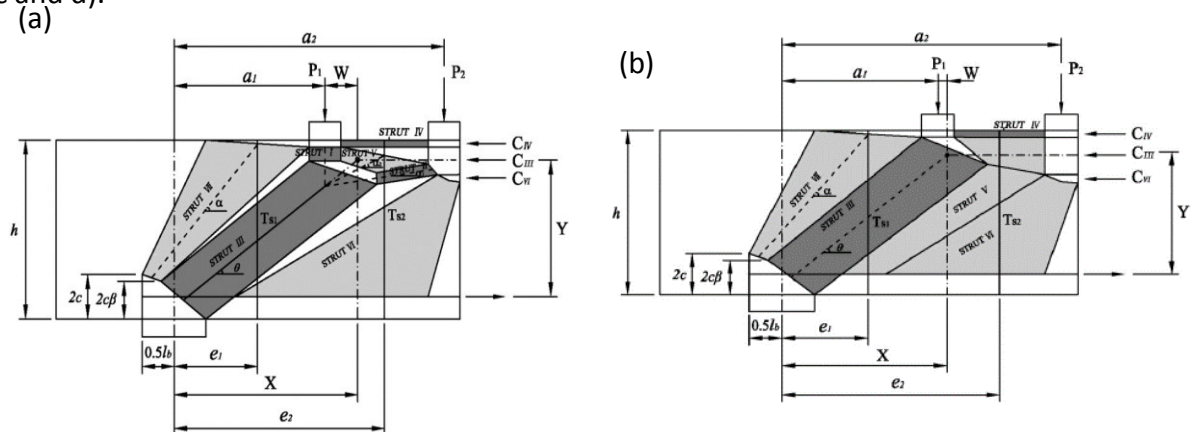


Figure 7.5: Comparison of the strength calculated using STM1 and the model provided by Mihaylov (2013) for beams with single-point load.

STM1 is unsuitable for estimating the shear strength of beams with multiple point loads within the shear span. Fang (2013) developed the STM shown in Figure 2.33 for simply supported deep beams that are symmetrically loaded with four-point loads as in tests AC0 (0.5/0.5) and AC200 (0.5/0.5). The model is depicted STM2 in this work and is applicable to beams without and with shear reinforcement. The reason for adopting STM2 in this research for beams loaded on the compression face was the good agreement between the stress fields obtained with NLFEA and the assumed strut orientation in STM2 (see Figure 2.33 c and d).



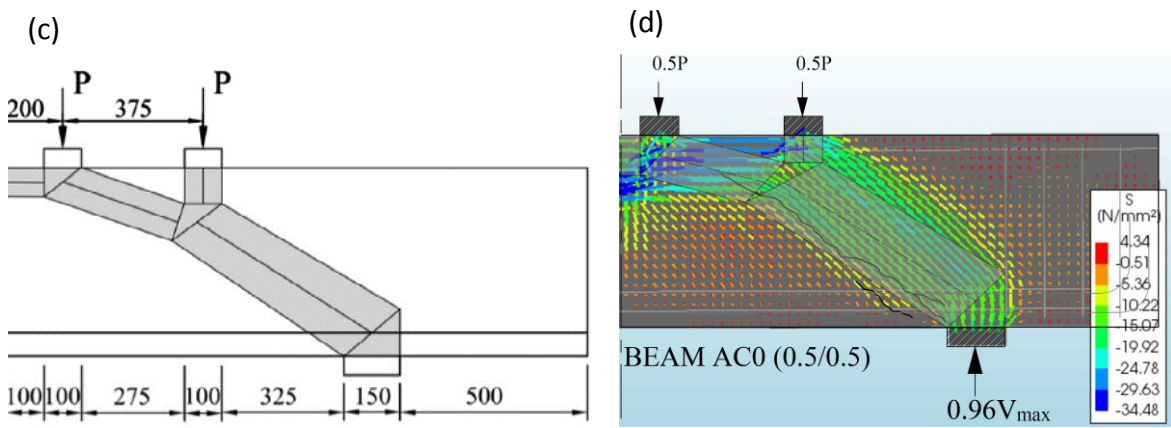


Figure 7.6: STMs proposed by Fang for beams with four-point loads (Fang, 2013): a) $P_2 < T_{s1} + T_{s2}$, b) $P_2 < T_{s1} + T_{s2}$, c) no shear reinforcement and d) stress fields of beam AC0 (0.5/0.5)

For beams with shear reinforcement, the geometry of the model depends on whether the total shear force $T_{s1} + T_{s2}$ resisted by the stirrups is less or greater than the applied force P_2 (Figure 2.33 a and b). The load is carried out in this model through a combination of direct struts and an indirect truss mechanism equilibrated by shear reinforcement. Similar to STM1, the direct strut resists a proportion β of the tensile force in the reinforcement at the bottom node. Forces C_{III} , C_{IV} and C_{VI} are the horizontal components of the forces in struts III, IV and VI respectively. The depth of the compression zone at P_2 can be obtained from flexural equilibrium assuming that the stress at the rear face of the node equals the strength of the CCC (i.e. v_{fcd} in EC2). Stirrups within the clear shear span (a_{v1}) and between the point loads are replaced by ties T_{s1} and T_{s2} with resistance $T_{si} = f_y n_i A_{sw}$, where n_i is the number of stirrups in tie T_{si} .

The failure load of STM2 is the least of the flexural capacity, the crushing strength of strut III or the bearing capacity at the plates. Further details about the STM geometry and solution algorithm is available elsewhere (Fang, 2013, Vollum and Fang, 2014).

7.3.1. STM for beams loaded in the tension face (STM3)

STM2 is not applicable for cases where multiple loads are applied to the tension face of the beam within the shear span, as it is not compatible with the reinforcement arrangement. This is reflected in differences in the observed behaviour and strength of notionally identical beams loaded on the tension and compression faces as well as the FE results presented in Section 7.4.

The STM shown in Figure 7.7 (depicted STM3) was developed by the author for the analysis of the cantilever beams tested in this program with two-point loads applied to the critical shear span. The total load (P) applied to the tension face is divided into loads $R_2 \cdot P$ applied to the outer load plate and load $R_1 \cdot P$ applied to the inner plate. The inner load ($R_1 P$) is transferred directly from the inner plate to the support through direct strut (4) as shown in Figure 7.7. The outer load ($R_2 \cdot P$) is transferred through a combination of a direct strut (2) and an indirect truss mechanism that is equilibrated by the vertical stirrups.

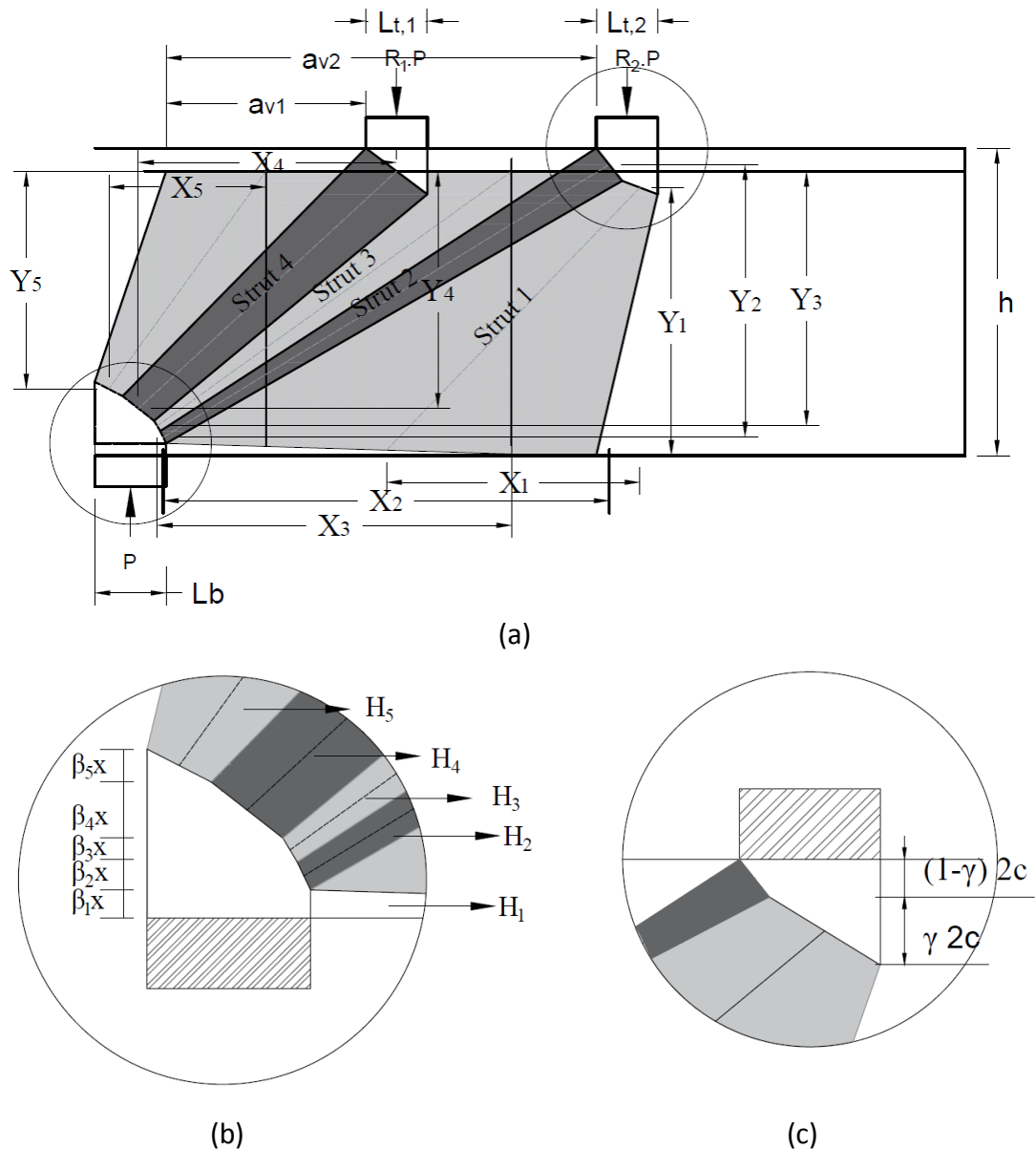


Figure 7.7: STM3 for beams loaded in the tension face. a) Geometry, b) bottom CCC node and c) top outer CCT node

The two discrete vertical ties shown in Figure 7.7 represent the centroid of the stirrups placed within the inner and outer shear spans, which are assumed to be at $0.25a_{v2}$ and $0.75a_{v2}$ respectively for the tested loading arrangement. Nodes in this model were assumed non-hydrostatic. The stress distribution is assumed uniform at the node boundaries. The geometry of the CCC node at the central support is defined by the horizontal components (H_i) of the force in struts associated with the nodes and the width of the support. As shown in Figure 7.7 – b, the height of the compression zone x calculated from equilibrium is divided into several parts corresponding to the proportions of the horizontal components of the struts in the CCC node. The geometry of the CCT nodes under the loads is defined by the distance to the centroid of the flexural reinforcement and width of the loading plates. Force in the outer loading plate is transferred to the bottom plate through a combination of the direct strut 2 and the truss of the stirrups in the outer shear span and struts 1 and 3. The STM is defined by the following equations of geometry and equilibrium (X_i and Y_i are the horizontal and vertical projections of strut i and $l_{t1} = l_{t2} = l_t$):

Strut (1)

$$X_1 = 0.5a_{v2} + l_t \left(1 - \frac{0.5(T_{s1} + T_{s2})}{P_2}\right) \quad \text{Equation 7.11}$$

$$Y_1 = h - 2d' + \gamma d' - 0.5\beta_1 x \quad \text{Equation 7.12}$$

$$H_1 = \frac{X_1}{Y_1} (T_{s1} + T_{s2}) \quad \text{Equation 7.13}$$

$$\beta_1 = H_1 / C \quad \text{Equation 7.14}$$

$$\gamma = \frac{H_1}{H_1 + H_2} \quad \text{Equation 7.15}$$

Strut (2)

$$X_2 = a_{v2} + 0.5 \frac{P_2 - (T_{s1} + T_{s2})}{P_1 + P_2} l_b + 0.5 \left(1 - \frac{T_{s1} + T_{s2}}{P_2}\right) l_t \quad \text{Equation 7.16}$$

$$Y_2 = h - (\beta_1 + 0.5\beta_2)x - d'(1 - \gamma) \quad \text{Equation 7.17}$$

$$H_2 = \frac{X_2}{Y_2} (P_2 - T_{s1} - T_{s2}) \quad \text{Equation 7.18}$$

$$\beta_2 = H_2/C \quad \text{Equation 7.19}$$

Strut (3)

$$X_3 = 0.75a_{v2} + \frac{(P_2 - T_{s1} - 0.5T_{s2})}{P_1 + P_2} l_b \quad \text{Equation 7.20}$$

$$Y_3 = h - (\beta_1 + \beta_2 + 0.5\beta_3)x \quad \text{Equation 7.21}$$

$$H_3 = \frac{X_3}{Y_3} T_{s2} \quad \text{Equation 7.22}$$

$$\beta_3 = H_3/C \quad \text{Equation 7.23}$$

Strut (4)

$$X_4 = a_{v1} + 0.5l_t + \frac{0.5P_1 + P_2 - T_{s1}}{P_1 + P_2} l_b \quad \text{Equation 7.24}$$

$$Y_4 = d - (\beta_1 + \beta_2 + \beta_3 + 0.5\beta_4)x \quad \text{Equation 7.25}$$

$$H_4 = \frac{X_4}{Y_4} P_1 \quad \text{Equation 7.26}$$

$$\beta_4 = H_4/C \quad \text{Equation 7.27}$$

Strut (5)

$$X_5 = 0.25a_{v1} + l_b \left(1 - \frac{T_{s1}}{P_1 + P_2}\right) \quad \text{Equation 7.28}$$

$$Y_5 = d - (\beta_1 + \beta_2 + \beta_3 + \beta_4 - 0.5\beta_5)x \quad \text{Equation 7.29}$$

Moment equilibrium

$$M = P_2a_2 + P_1a_1 - 0.5(P_1 + P_2)l_b \quad \text{Equation 7.30}$$

$$\frac{x}{d} = 1 - \sqrt{1 - 2k} \quad \text{Equation 7.31}$$

$$k = \frac{M}{bd^2 f_{ck}} \quad \text{Equation 7.32}$$

$$w = l \sin \theta + u \cos \theta \quad \text{Equation 7.33}$$

In the above equations, β_i is the contribution of the horizontal component of the force in strut (i) to the total compression force in the flexural compression zone, C is the flexural compressive force at the central support and T_{si} is the tensile force carried by stirrups set i . Failure in STM3 is governed by the crushing either strut (2) or (4). The strut width (w) is calculated using Equation 7.33 in terms of the vertical and horizontal projections of the strut normal to its centreline at the top and bottom nodes. The vertical and horizontal projections of the strut to node interface are given in Table 7.3 for each strut at its top and bottom ends. The axial resistance of each direct strut was calculated in accordance with the recommendations of EC2 and the Modified Compression Field Theory (Vecchio and Collins, 1986). Following the example of Sagaseta and Vollum (2010) and Collins and Mitchell (1991), different concrete strengths were adopted at the intersection of struts with CCC and CCT nodes as described in Table 7.3.

If the total tensile force carried by the stirrups ($T_{s1} + T_{s2}$) is greater than the outer load (R_2P), as was the case in beam CT200 (0.6/0.4), the force in strut 2 is set to zero and the failure is governed by crushing of strut 3 or 1 at top. In this case, the stirrups do not yield at failure.

Table 7.3: Height and width of struts 2 and 4

	Strut 2		Strut 4	
	Top	Bottom	Top	Bottom
Width	$\frac{P_2 - T_{s1} - T_{s2}}{P_2} l_t$	$\frac{P_2 - T_{s1} - T_{s2}}{P_1 + P_2} l_b$	l_t	$\frac{P_1}{P_1 + P_2} l_b$
Height	$2d'(1 - \gamma)$	$\beta_2 x$	$2d'$	$\beta_4 x$
EC2 strut strength	$0.6 \left(1 - \frac{f_{ck}}{250}\right) f_{ck}$	$\alpha \left(1 - \frac{f_{ck}}{250}\right) f_{ck}$	$0.6 \left(1 - \frac{f_{ck}}{250}\right) f_{ck}$	$\alpha \left(1 - \frac{f_{ck}}{250}\right) f_{ck}$
MCFT strut strength	$\frac{f_{ck}}{(0.8 + 170\varepsilon_1)}$	$0.85 f_{ck}$	$\frac{f_{ck}}{(0.8 + 170\varepsilon_1)}$	$0.85 f_{ck}$

7.3.2. Solution procedure for STM3

The shear resistance in STM3 can be readily obtained using a nonlinear equation solver like the Generalized Reduced Gradient (GRG) solver in Microsoft Excel or an iterative procedure like the following:

1. Estimate an initial value of P and calculate P_1 and P_2 where $P_1 = R_1 \times P$ and $P_2 = P_2 \times P$. R_1 and R_2 and known.
2. Calculate the compression depth x from Equation 7.31 and calculate the total compressive force (C) respectively.
3. Assume stirrups yield and calculate X_1 , X_2 , X_3 and X_4 using equations: Equation 7.11, Equation 7.16, Equation 7.20 and Equation 7.24.
4. Estimate unknowns H_1 , H_2 , H_3 , H_4
5. Calculate β_1 , β_2 , β_3 , β_4 , γ using equations: Equation 7.14, Equation 7.19, Equation 7.23, Equation 7.27 and Equation 7.15.
6. Vary H_1 , H_2 , H_3 , H_4 in solver until estimated and calculated values are equal (use Equation 7.13, Equation 7.18, Equation 7.22 and Equation 7.26 for the calculating H_i).
7. Vary P until strut (2) or strut (4) fails.

STM3 reduces to STM1 if the inner load is not present in which case strut (4) vanishes.

7.3.3. Results of the STM

The tested beams were analysed with the appropriate STM as indicated in Table 7.4, which presents failure loads for strut strengths calculated with both EC2 and the MCFT. STM3 is applicable to all the tested cantilever beams since it reduces to STM1 for the beams with single point loads in the shear span. All the stirrups in the clear shear span were assumed to yield, which is reviewed later in section 7.4.2, unless the resulting direct strut force was negative in which case the stirrup force was calculated from equilibrium assuming that the direct strut force was zero.

Results are presented in Table 7.4 for STM 3 EC2 with $\alpha = 1.0$ (as adopted by Sagaseta and Vollum (2010) and Vollum and Fang (2015) for beams loaded on their compression face) and $\alpha = 0.85$ which gives improved predictions for STM3 where failure at the CCC node governs (where $\alpha \left(1 - \frac{f_{ck}}{250}\right) f_{ck}$ defines the strength of struts 2 and 4 at the CCC node (see Table 7.3)). As

shown in Table 7.4, the overall accuracy of the STM predictions is good particularly if strut strengths are calculated using EC2 with $\alpha = 0.85$ (mean/covariance of $P_{calc}/P_{test} = 0.87/17\%$). STM3 EC2 gives good estimates of failure load for the 10 cantilever beams (including 4 with single point loads for which STM3 reduces to STM1). Only the strength of beam AT0 (0.5/0.5) is significantly overestimated with $P_{calc}/P_{test} = 1.2$. For the six cantilever beams with two point loads, the mean/covariance of P_{calc}/P_{test} are 0.97/13% for EC2 ($\alpha = 0.85$) and 0.84/23% for MCFT. STM3 EC2 with $\alpha = 0.85$ correctly predicts shear failure to occur in the outer shear span due to crushing of strut 2 for all relevant beams except CT200 (0.6/0.4).

Table 7.4: Experimental failure load and estimations of P_{calc}/P_{test} using STMs and FEA

Beam ID	STM	RHS Failure loads (kN)	STM P_{calc}/P_{test} (total)			five - spring model P_{calc}/P_{test}	FE Test
			EC2		MCFT		
			$\alpha = 1$	$\alpha = 0.85$			
AC0(0.5/0.5)	2	539	0.74	0.74	0.61	1.01	1.02
AC200(0.5/0.5)	2	742	0.70	0.70	0.70	0.78	1.08
AT0(0.5/0.5)	3	449	1.43	1.20	1.15	0.91	1.14
AT200(0.5/0.5)	3	733	0.94	0.86	0.83	0.83	1.04
BT200(0.5/0.5)	3	648	1.05	0.87	0.88	1.24	0.86
BT200(1.0/0)	1/3	610	0.78	0.78	0.91	1.01	1.03
BT200(0/1.0)	1/3	423	0.90	0.90	0.77	0.94	1.12
BT200(0.3/0.7)	3	528	1.03	1.01	0.88	0.89	0.98
CT0(1.0/0)	1/3	441	0.73	0.73	0.63	0.87	0.81
CT200(1.0/0)	1/3	543	0.75	0.75	0.72	0.93	1.02
CT0(0.6/0.4)	3	378	0.93	0.93	0.60	1.01	0.95
CT20 (0.6/0.4)	3	502	0.94	0.94	0.67	0.89	1.01
Average			0.91	0.87	0.78	0.94	1.0
SD			0.20	0.14	0.16	0.12	0.09
COV			0.22	0.17	0.21	0.13	0.09

The accuracy of the models presented earlier is compared in Figure 7.8 below. STM1 proposed by Sagaseta (2008) was used to estimate the strength of beams with single point load (BT200(1.0/0), BT200 (0/1.0), CT0 (1.0/0) and CT200 (1.0)) while the STM2 (Vollum and Fang, 2014) was used to estimate the strength of beams AC0 (0.5/0.5) and AC200 (0.5/0.5) loaded with two point loads on the compression face. The strength of the remaining six beams loaded with two point loads on the tension face was calculated using STM3. Figure 7.8 shows the accuracy of the estimated strength for the tested beams obtained using relevant STM in terms of the mean and the range of predictions. It can be seen that the proposed STM3 gives the best estimates if the provisions of the MCFT are used to estimate the strength of the strut.

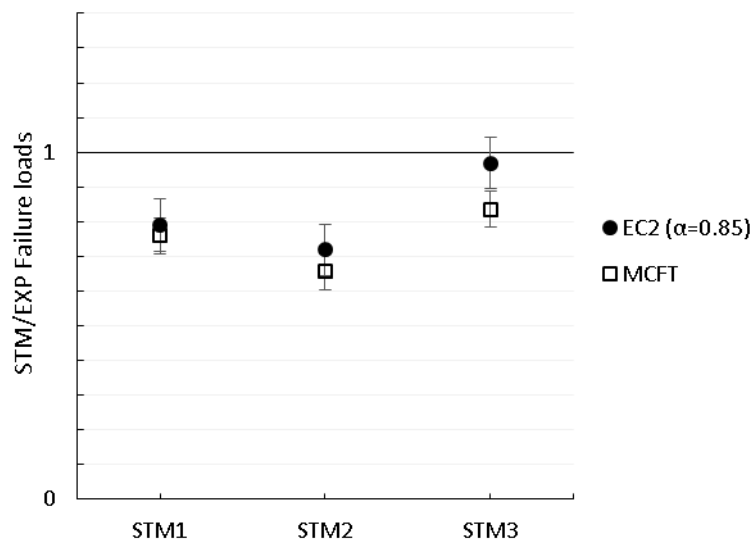


Figure 7.8: Comparison of STM results obtained using the MCFT and EC2 with $\alpha = 0.85$.

STM3 can be readily adapted for the analysis of beams loaded on the compression face like beams AC0 (0.5/0.5) and AC200 (0.5/0.5). The required STM modification is illustrated in Figure 7.9 below for beam AC0 (0.5/0.5). Also shown in Figure 7.9 is STM3 for beam AT0 (0.5/0.5) which was loaded on its tension face. In each case, strut 2 was critical with failure occurring at the interface with the CCT node as shown in the figure. For purposes of comparison STM3 is drawn for beam AT0 (0.5/0.5) with the intended loading ratio of (0.5/0.5) rather than the actual loading ratio of (0.6/0.4). The concrete strengths of both beams were assumed to equal that of beam AC0 (0.5/0.5) for purposes of analysis. STM3 incorrectly estimates the strength of beam AC0 (0.5/0.5), loaded on the compression face ($V_{STM3}=382/279$ KN for EC2 and MCFT), to be slightly less than the strength of beam AT0

(0.5/0.5) loaded on the tension face ($V_{SMT3}=399/300$ KN for EC2/MCFT). The predicted strength of beam AT0 (0.5/0.5) is greater than AC0 (0.5/0.5) since the width of strut 2 perpendicular to the strut centreline at the CCT node is greatest for AT0 (0.5/0.5) due to its greater bearing length (100 mm compared with 75 mm). In reality, the tests suggest that the strength of tension face loaded beams like AT0 (0.5/0.5) is less than compression face loaded beams like AC0 (0.5/0.5). As discussed later in Section 7.4.5, this is predicted by NLFEA but not STM, which appears to be overly sensitive to node dimensions as suggested by Vollum and Fang (2015).

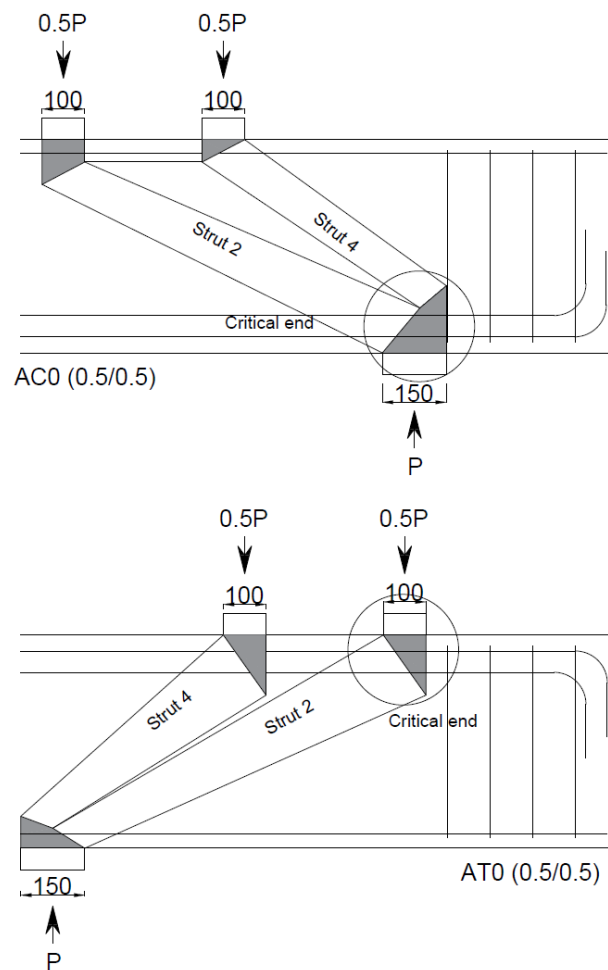
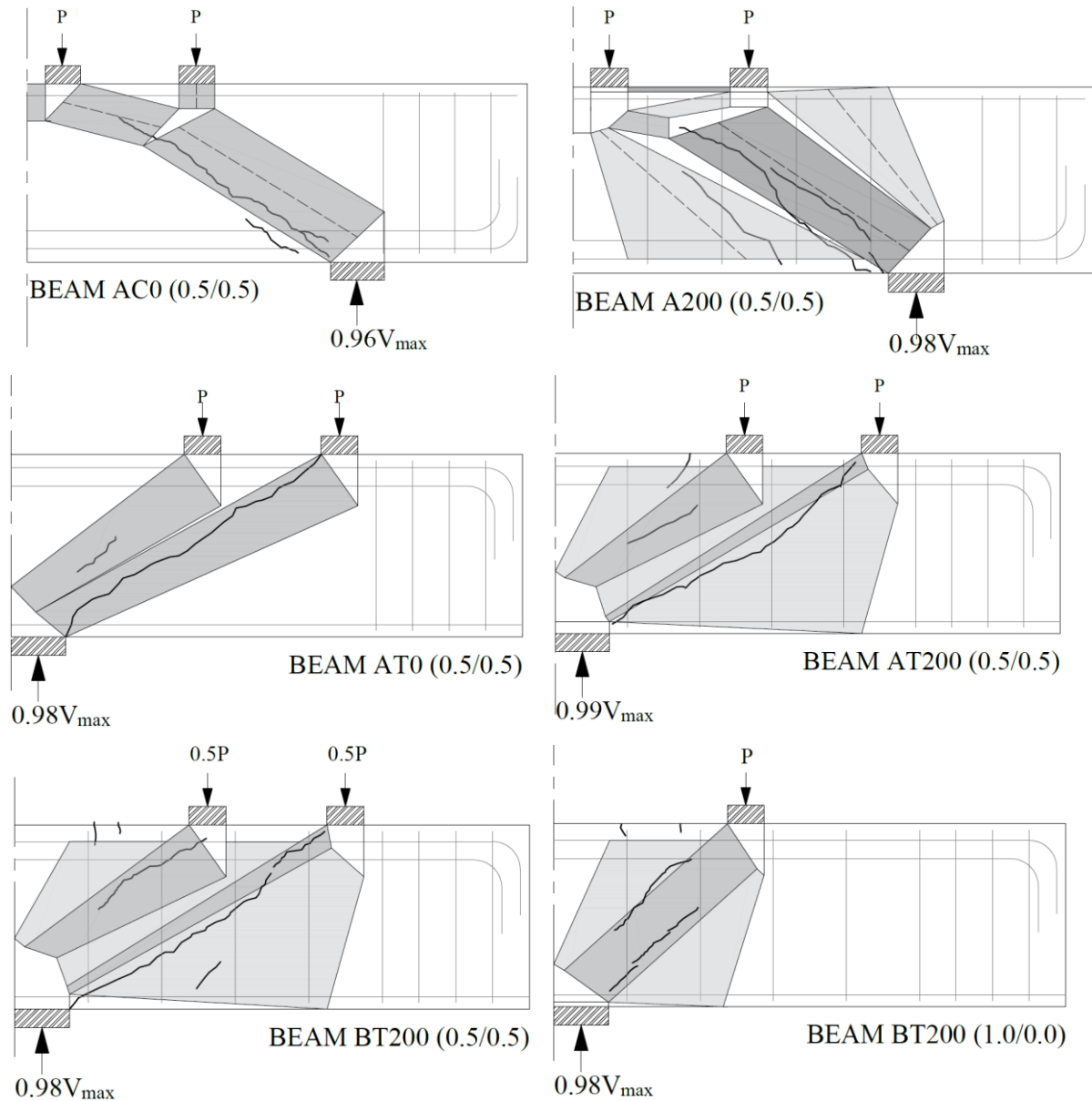


Figure 7.9: STM3 adopted for beam AC0 (0.5/0.5) loaded on the compression face

7.3.4. The geometry of the STM of the tested beams

In this section, the geometry of the implemented STMs is shown in Figure 7.10 superimposed onto the major crack patterns observed prior to failure. These STM geometries shown in

Figure 7.10 were obtained using the measured concrete strengths. Figure 7.10 shows that in most cases the STM geometry is consistent with the stress flow assumed in the STMs. Typically, a diagonal crack passes through the direct struts of the STMs. This supports the earlier assumption that the strength of the direct struts is reduced due to crack penetration.



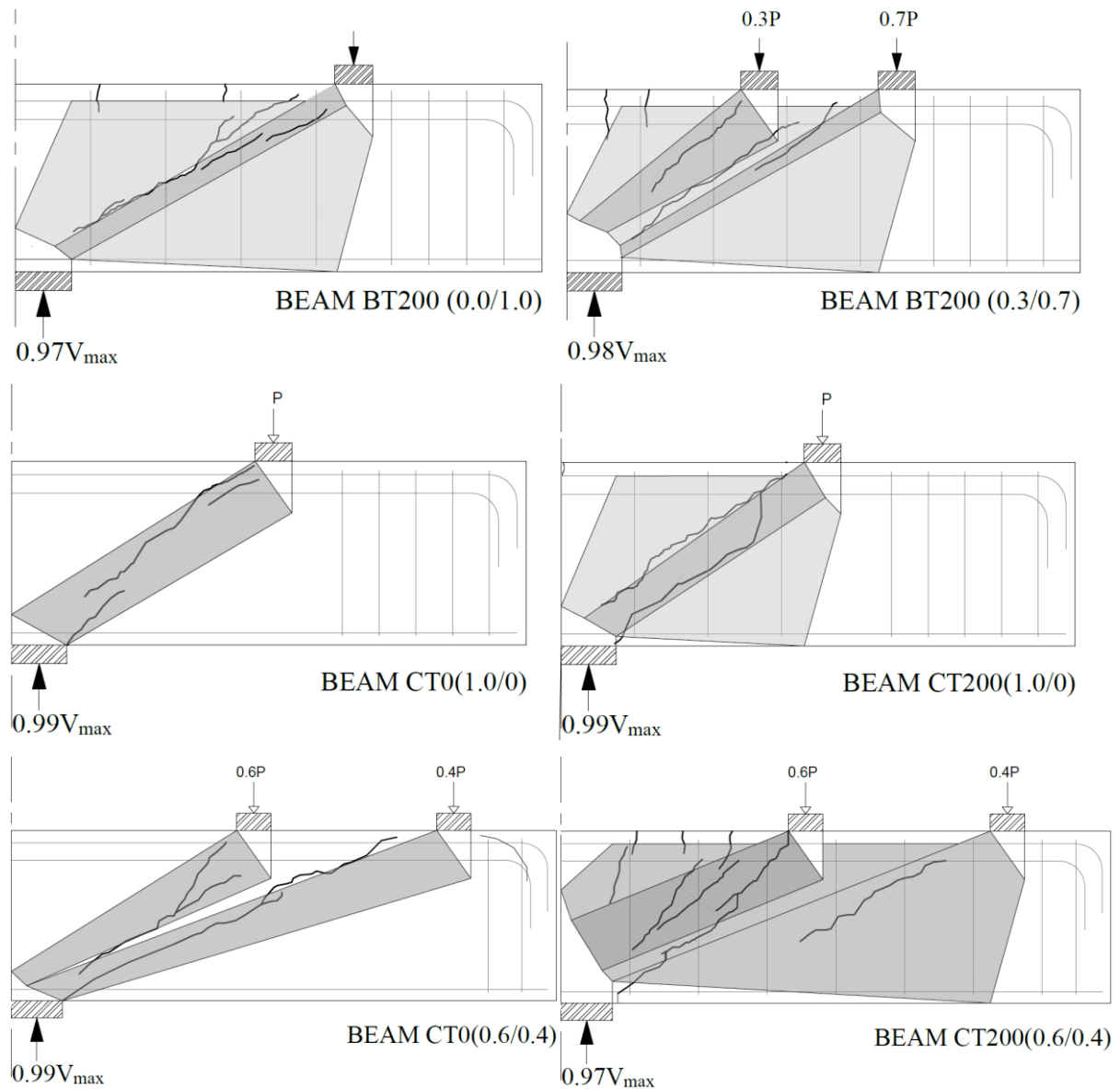


Figure 7.10: Overlay of the STMs on the major crack pattern for test beams

7.4. Comparison between STM, Test Behaviour and NLFEA.

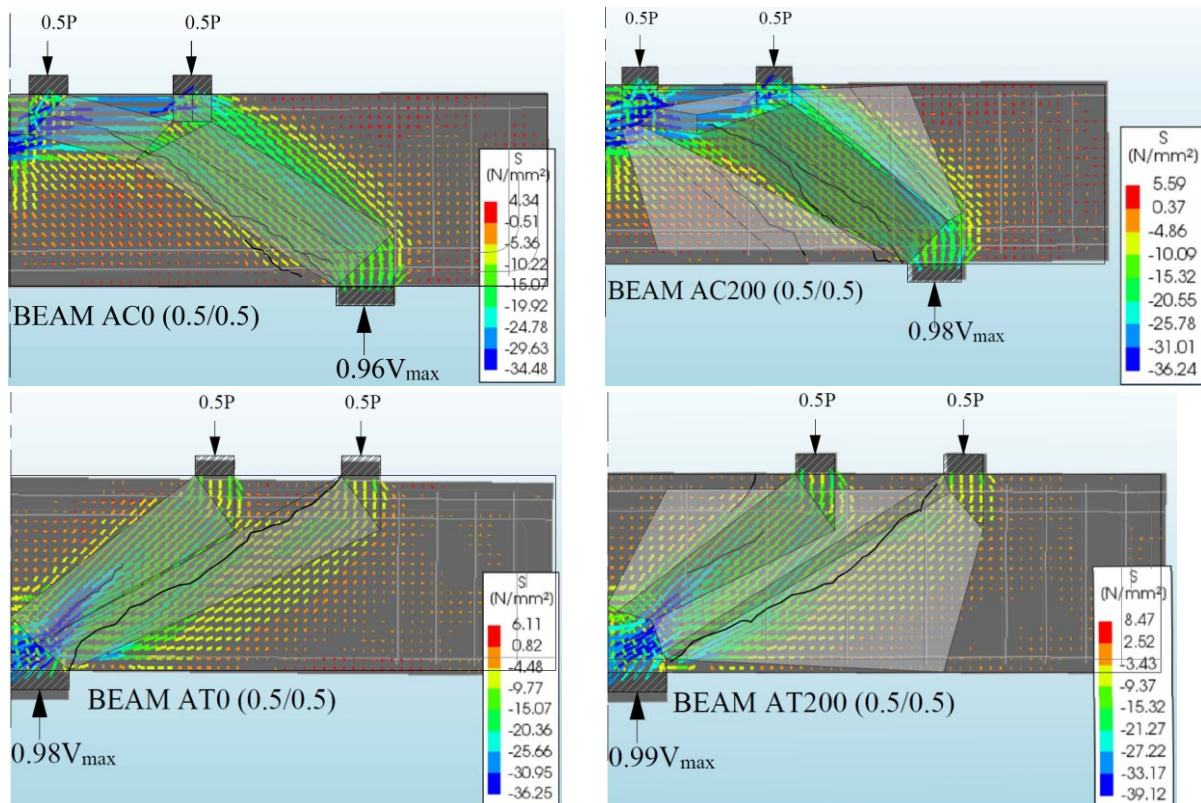
Nonlinear finite element analysis (NLFEA) was performed using DIANA finite element analysis software (v10.2) to estimate the shear strength of the test beams and to conduct parametric studies. Further details about the software, models used, calibration and sensitivity analysis are found in Chapter 6 and in Diana Users' Manual (DIANA, 2017). The analysis was carried out with an Intel® core™ i7 processor and an installed RAM memory of 64GB. Predictions of failure loads and load-deflection response obtained using the NLFEA were presented in Chapter 5. Furthermore, beam strength has been estimated in this chapter using design codes

and STMs. As shown in Table 7.4 the NLFEA predictions were most accurate of the considered assessment methods (STMs and design codes) while the design codes provided the most conservative estimates.

7.4.1. Comparison of the stress fields and crack patterns

This section compares the stress fields assumed in the STM with those obtained with NLFEA at peak load. The geometry of the STMs varies dependent on the concrete strength provisions used. While EC2 relates the strength of the cracked strut to the compressive strength only, the MCFT relates its strength to the state of the strain of associated reinforcement and to the strut inclination. The geometry of STMs was calculated based on the MCFT, as the results were similar for the MCFT and EC2 (with $\alpha = 0.85$).

The principle stress vectors obtained from the FEA were overlaid on the STMs and experimental crack patterns as shown in Figure 7.11 and Figure 7.13. The strut locations of the proposed STM coincide well with the stress fields, particularly for beams without shear reinforcement where the stress field is most clearly defined. Clear differences can be seen in the NLFEA stress fields for beams loaded on the tension and compression face (e.g. Beams AC0 (0.5/0.5) and AT0 (0.5/0.5)).



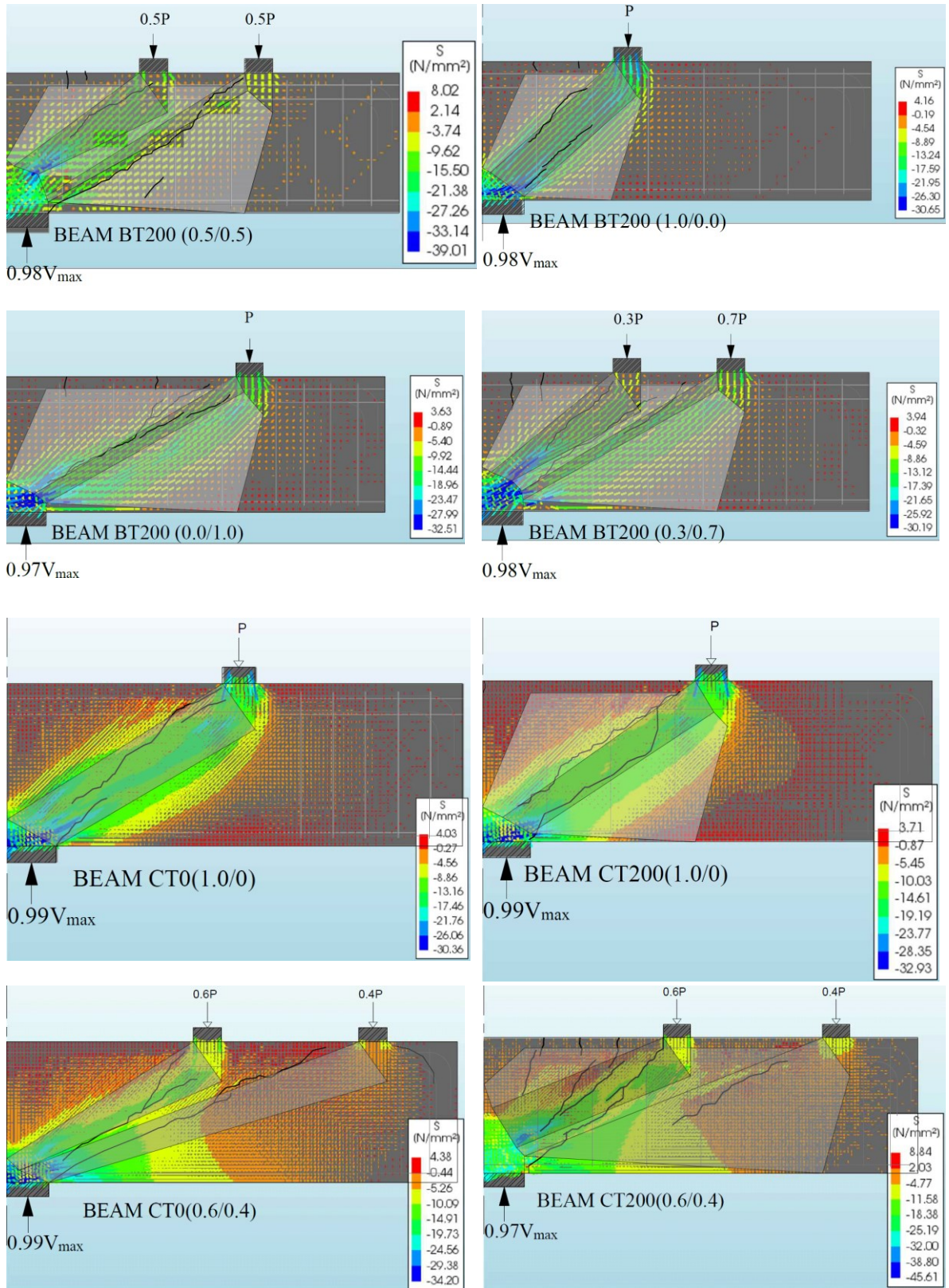


Figure 7.11: FEA principal stress, STMs and experimental cracks for the test beams

Failure in the STMs presented in this work is assumed to be due to concrete crushing in the struts. This assumption was investigated by examining the plastic strains in the concrete at failure obtained from the NLFEA. Figure 7.12 below shows the plastic strains in beams AC200 (0.5/0.5) and BT200 (0.5/0.5), which indicated crushing of the concrete in these locations. Beam AC200 (0.5/0.5) was loaded on the compression face with multiple point loads, and hence, its strength was evaluated using STM2 (Fang, 2013). STM2 assumes plastic stresses to develop at the back of the top CCC and the governing failure criteria was crushing of strut *III*. The appearance of plastic strains in strut *III* and at the back of the top CCC node is consistent with the assumed failure load and the use of the plastic strength for the CCC node. Similar conclusions also apply to STM3 for beams loaded on the tension face as shown in Figure 7.13 for beam BT200 (0.5/0.5). Failure of SMT3 is assumed to occur due to crushing of either strut 2 or 4 depending on the loading ratio.

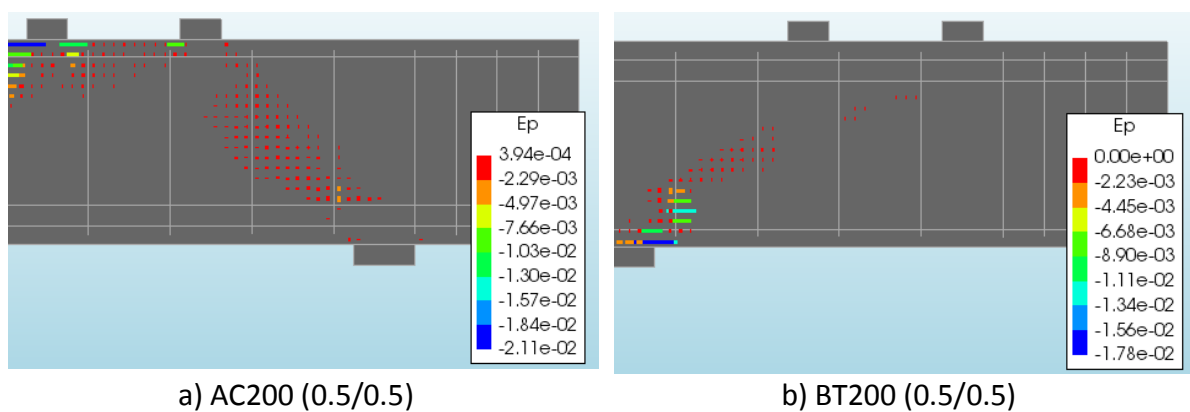
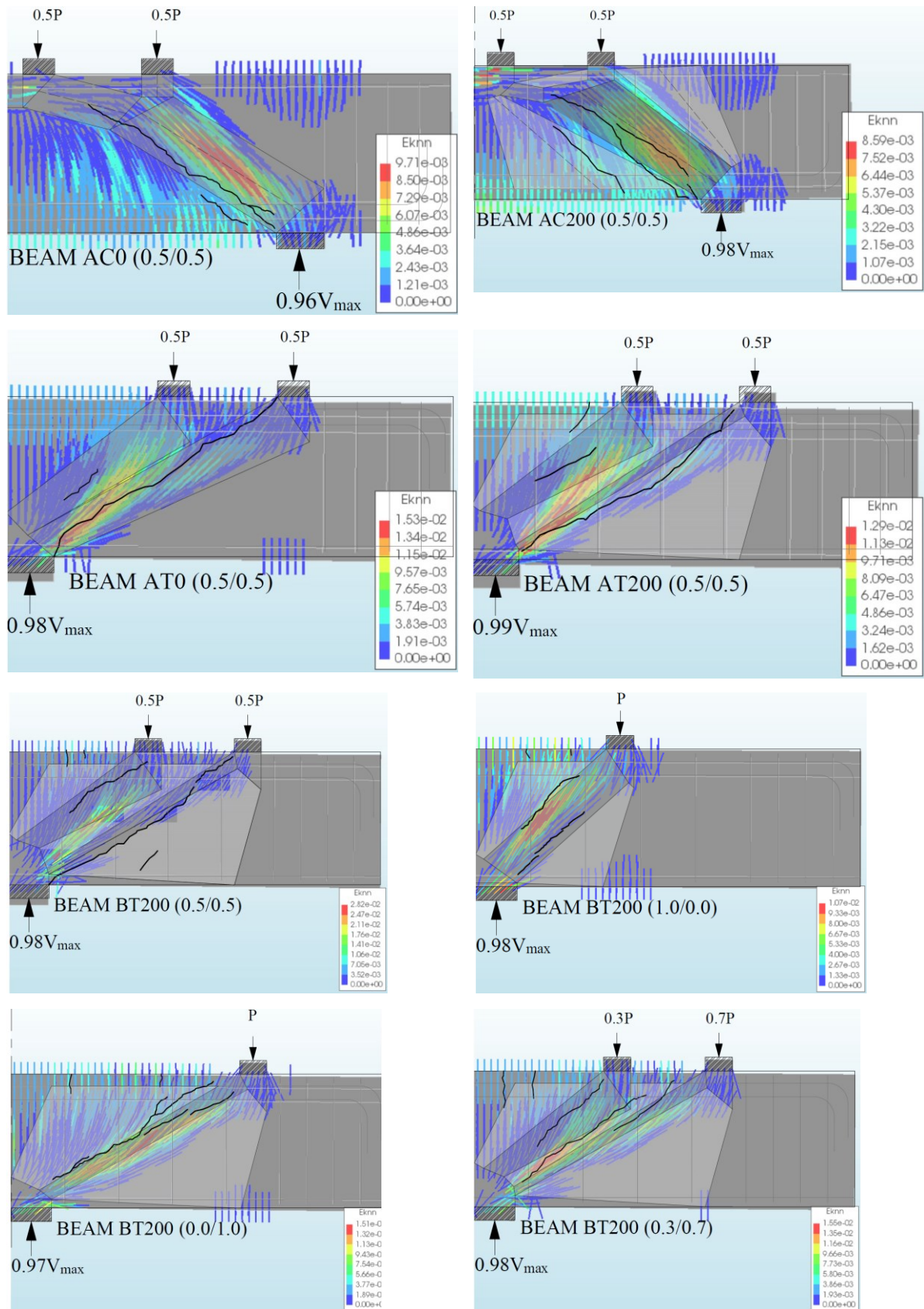


Figure 7.12: Plastic strain at failure for beams a) AC200 (0.5/0.5) and b) BT200 (0.5/0.5)

Figure 7.13 shows the crack normal strains and the experimentally observed crack patterns for the tested beams. For beams loaded on the compression face (i.e. beams AC0 (0.5/0.5) and AC200 (0.5/0.5)), the FE predicted the cracks to propagate at a steeper angle than observed between the bottom support and the inner load plate. In the tests, only the lower part of the crack was oriented at the crack angle determined by the FEA. At later stages of testing, the inclination of the crack in the top half of the beam became shallower forming a dogleg as shown in Figure 7.13. A more detailed description of the development of cracking in beams AC0 (0.5/0.5) and AC200 (0.5/0.5) can be found in Chapter 4. The crack pattern in beams loaded on the tension side was consistent with the NLFEA crack normal strains for the majority of the beams. For beams loaded with multiple point loads, the two cracks observed

on the tests between the inner and the outer loading plate and the support were observed in the FEA.



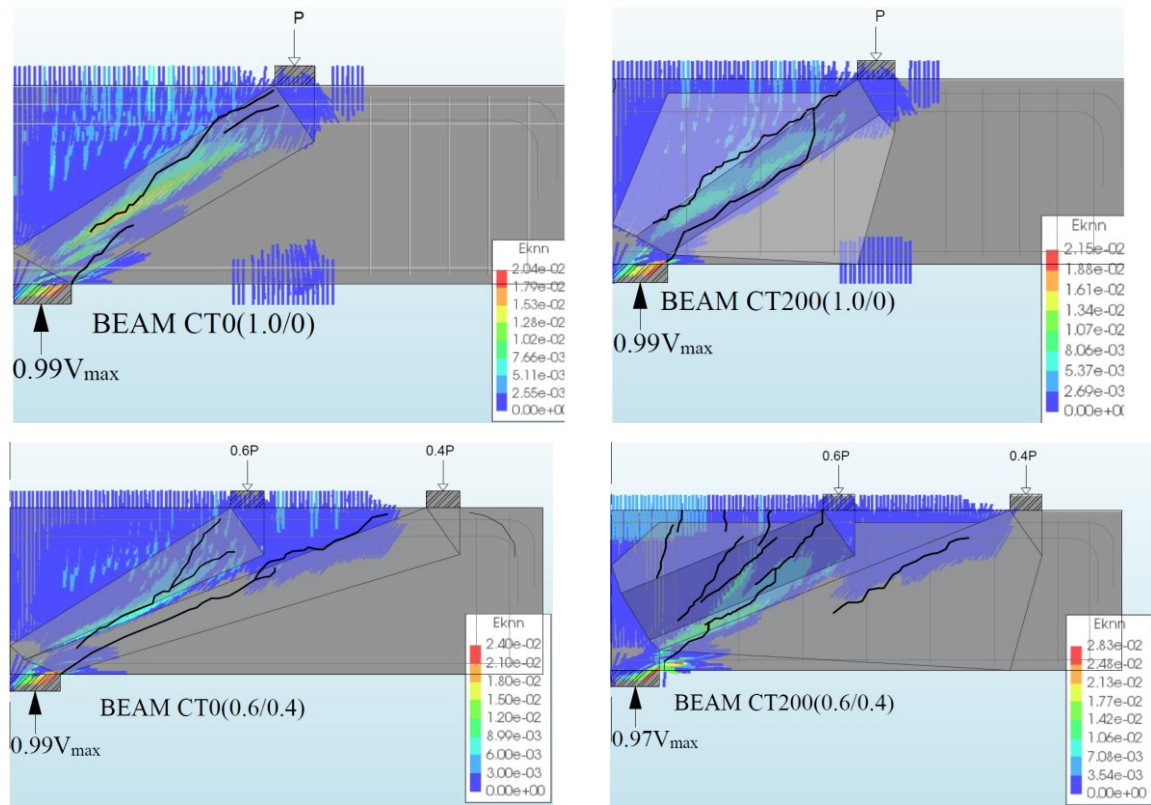


Figure 7.13: FEA principal strains, STMs and experimental cracks for the test beams

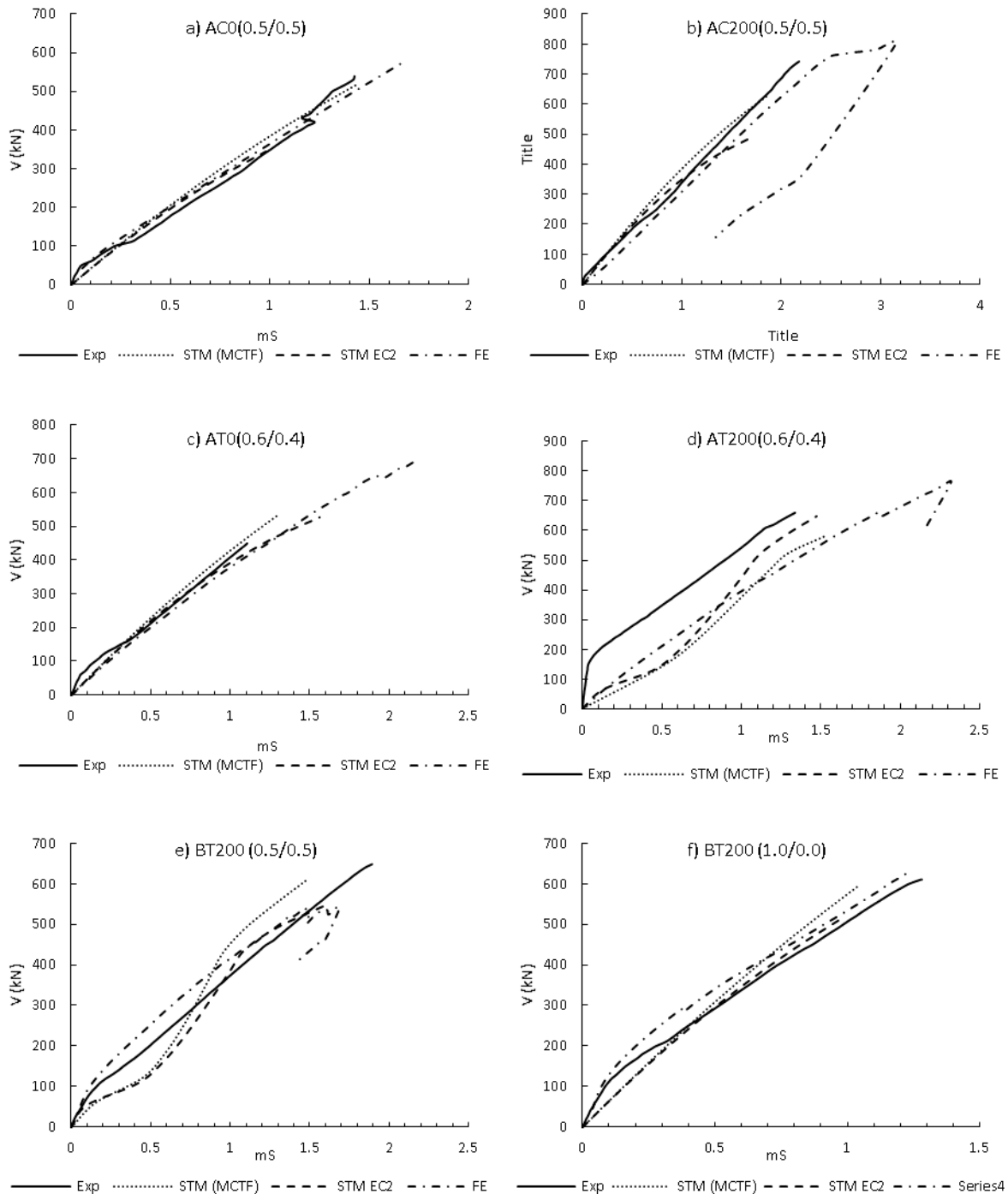
7.4.2. Comparison of measured, STM and NLFEA reinforcement strains

This section compares the strains measured during the tests using strain gauges with those predicted using NLFEA and STM if applicable. These comparisons include flexural strains and stirrup strains. The strains at the supports and loading plates are discussed separately in section 7.4.3

Flexural strains

Flexural tensile strains obtained from the experimental program were compared to strains obtained from STM for both EC2 and MCFT strut strength provisions. Maximum experimental flexural strains were obtained by averaging readings of strain gauges SG1, SG2, SG3 and SG4 for beams loaded on the compression and tension face. Strain gauges SG1 and SG2 measured the strains in the extreme flexural layer while SG3 and SG4 measured strains of the inner reinforcement layer (more detail regarding positioning of strain gauges (see Figure 3.25, Figure 4.22, Figure 4.36 and Figure 4.52) and strain measurements are available in Chapters 3 and 4). A similar approach was adopted regarding the strains in the FEA, which were extracted at the same positions as the strain gauges in the tests. The measured strains in the

two layers of flexural reinforcement were averaged to facilitate comparison with the STM strain. These results were also compared to the results obtained from the FEA as shown in Figure 7.14. This figure shows that both STM and FEA strains were comparable to the experimental results. Strains obtained with STM were sometimes greater than obtained from the tests but that is to be expected, since the STM does not take tension stiffening from the concrete into consideration.



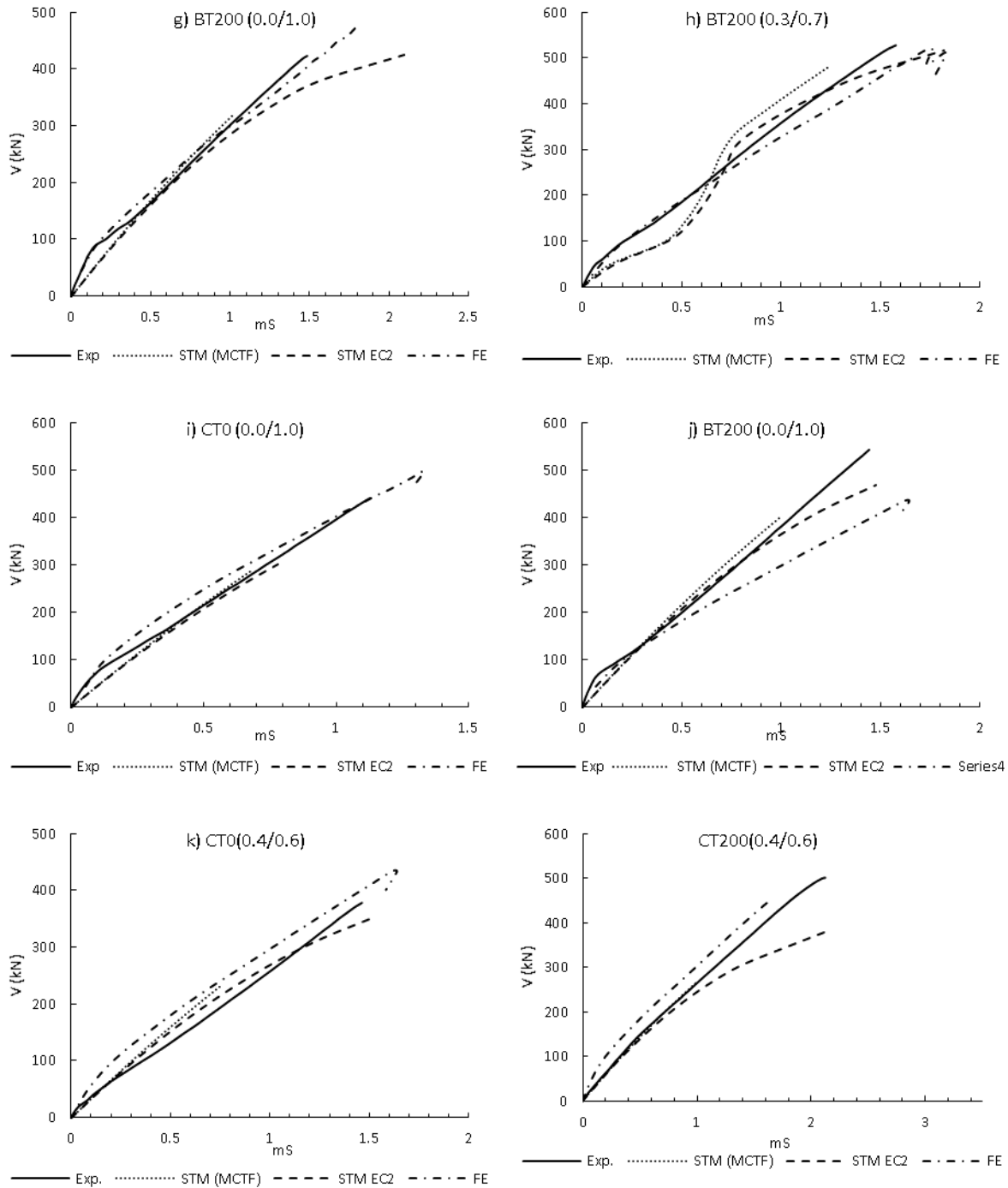


Figure 7.14: Maximum flexural tensile strains obtained from the experimental program, STM3 (EC2 and MCFT) and FEA

Stirrup strains

In the STM, the direct strut contribution is calculated assuming that the stirrups yield. The validity of this assumption was investigated by examining the strains measured in selected stirrups of each beam as well as the results of the NLFEA simulations. Strain gauges were

positioned on all the stirrups between the support and outer load at locations where NLFEA suggested strains would be greatest. Additionally, stirrup strains were estimated from measured crack widths using the method proposed by Sigrist (Sigrist, 1995) as described in Chapter 2. In this model, all the tension force is transferred by the stirrups at locations where cracks intercept the stirrups and reduce in regions of bonded concrete. In the elastic zone of the stirrups, the bond is assumed constant and equal to twice the concrete tensile strength. The bond reduces to the concrete tensile strength if the stirrups yield. The stresses and forces of the stirrups in this work was estimated based on the measured crack widths and crack locations. In practice, the strain gauge positions did not always coincide with the critical shear cracks in the tested beams due to differences between the observed and estimated crack patterns. Therefore, the peak strains would usually have been greater than measured. The difference between observed and NLFEA crack patterns is to be expected since the geometry of the critical shear crack varies randomly between notionally identical beams. Despite this, the measured and calculated strains agree reasonably well as shown in Figure 7.16 for beams with shear reinforcement. Table 7.5 summarises the number and position of stirrups that yielded in each test according to the measured strains, Sigrist (Sigrist, 1995) and NLFEA. Based on the greatest of the measured and NLFEA strains, at least one stirrup yielded in all the beams. By way of comparison, it is assumed in the STM that all the stirrups yield apart from beam CT200 (0.6/0.4) where stirrups only yield within the inner clear shear span a_{v1} . Despite this, the STM gives reasonable yet conservative estimates of beam strength as shown in Table 7.4.

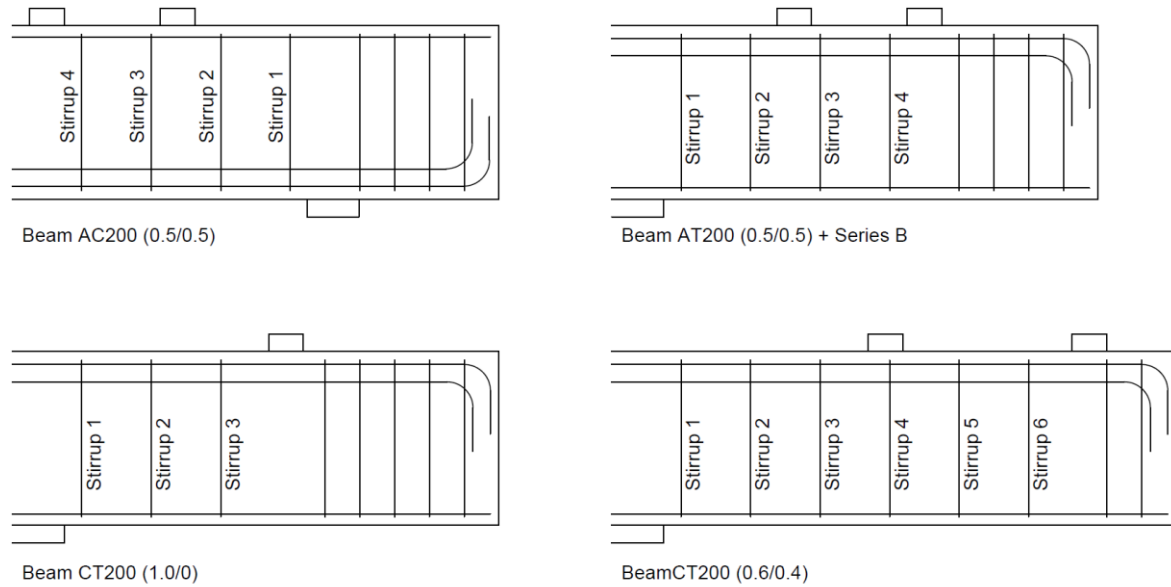
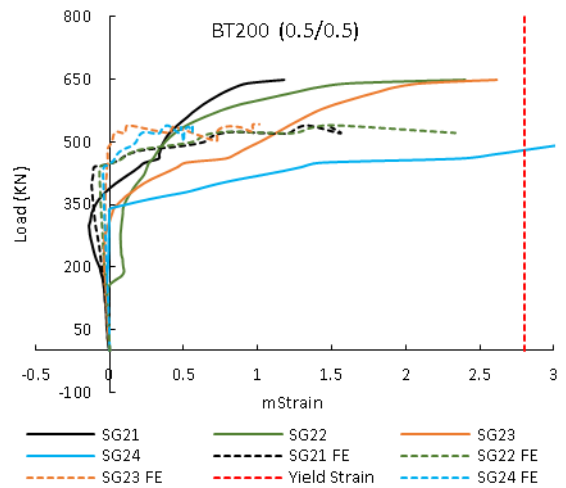
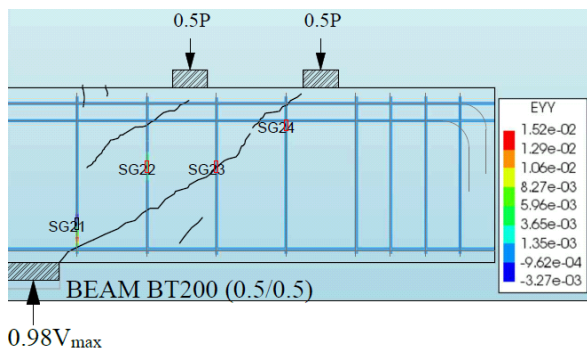
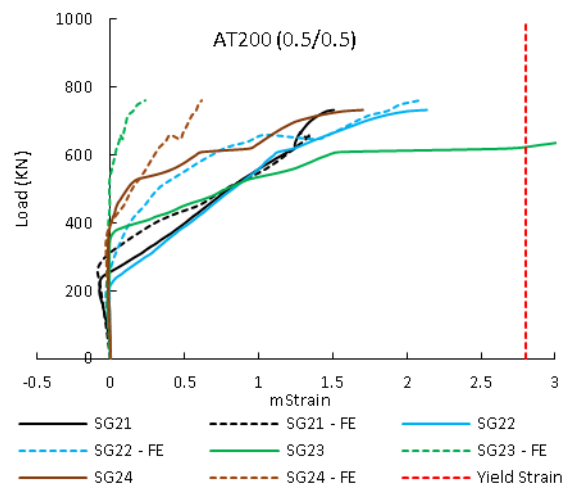
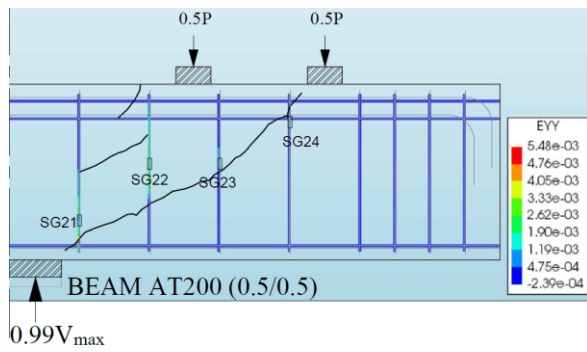
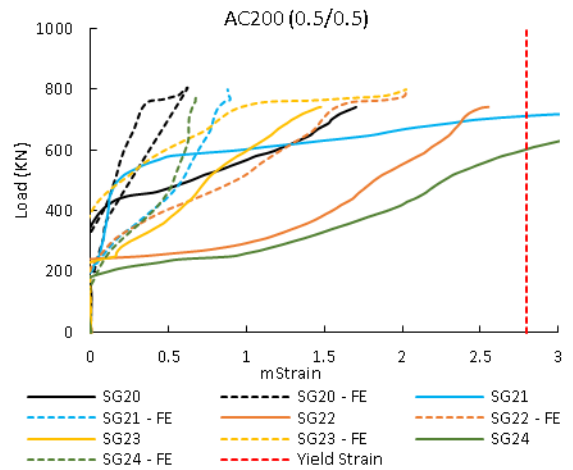
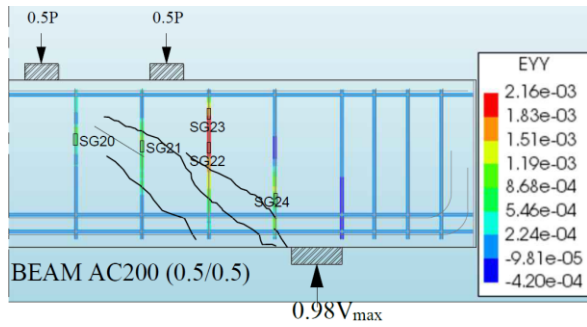


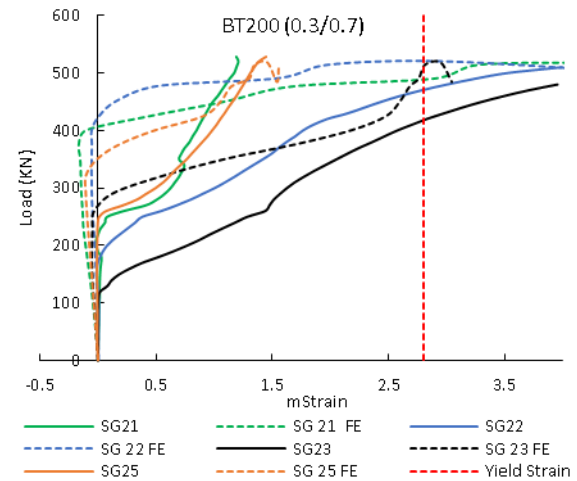
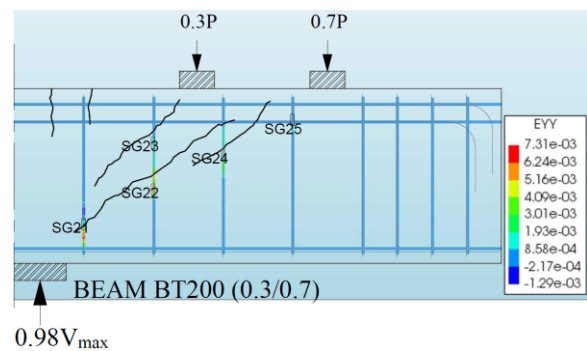
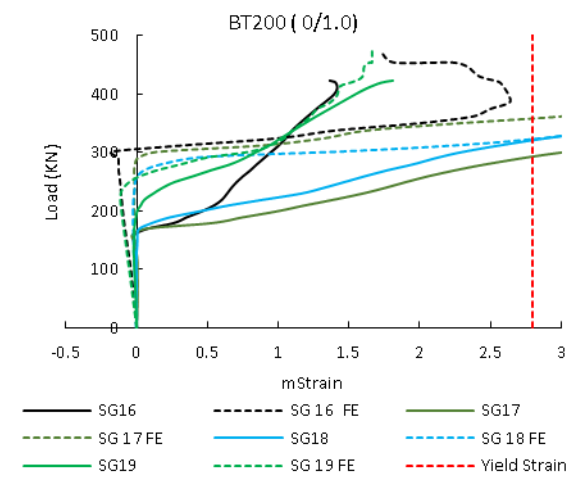
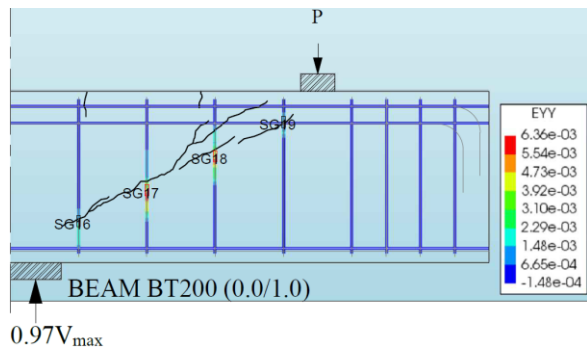
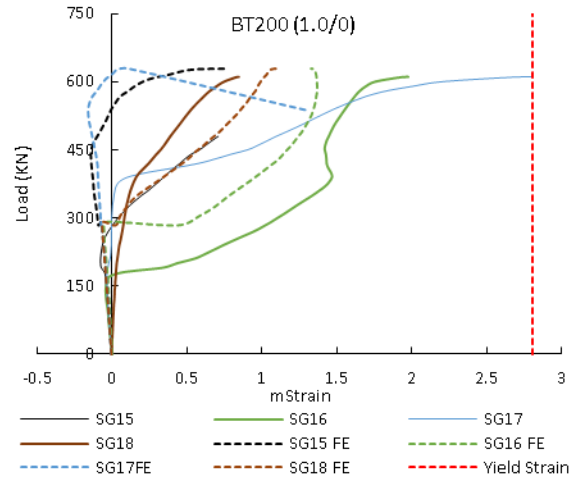
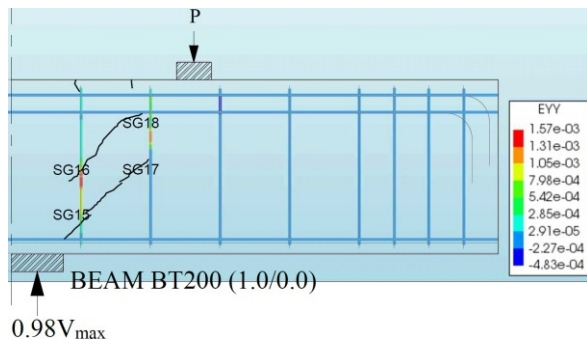
Figure 7.15: Locations and names of stirrups in the tested beams

Table 7.5: Location and number of stirrups yielded in the test and NLFEA

Beam ID	Total No. of stirrups in shear span	Location of stirrups that yielded (STR 1 near to the support)		
		Strain Gauges	Sigrist	NLFEA
AC200 (0.5/0.5)	4	STR 2, 3	-	-
AT200 (0.5/0.5)	4	STR 3	STR 3	-
BT200 (0.5/0.5)	4	STR 2, 3, 4	STR 2, 3	STR 1
BT200 (1.0/0)	2	STR 2	STR 1	-
BT200 (0/1.0)	4	STR 2, 3	STR 2, 3	STR 1, 2, 3
BT200 (0.3/0.7)	4	STR 2,3	STR 2	STR 1, 2, 3
CT200 (1.0/0)	3	-	-	STR 1, 2
CT200 (0.6/0.4)	6	STR 2	STR 2	STR 2

The strain gauge measurements presented in Table 7.5 and Figure 7.16 show that the majority of the yielded stirrups are the ones in the middle of the shear span, which was previously reported on fibre optics strain measurements of short span beams (Poldon et al., 2019). This finding is supported by the strains obtained from the observed crack kinematics except for beam BT200 (1.0/0) where STR1 yielded based on Sigrist model (1995).





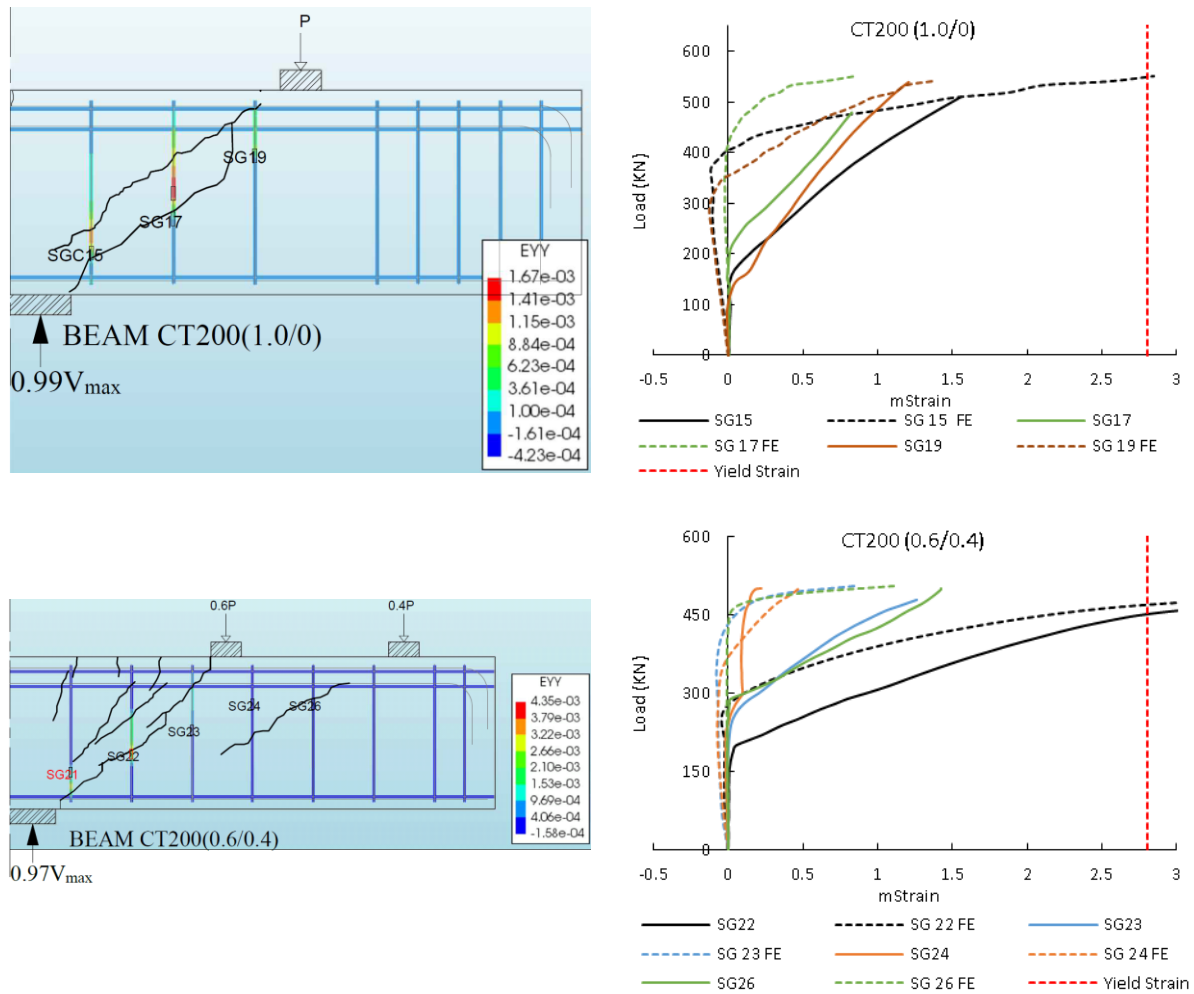


Figure 7.16: Comparison between FE and experimentally obtained shear reinforcement strain

7.4.3. The effect of the transfer compression on the bond force

The presence of transverse pressure (or confinement) increases the bond strength between the reinforcement and the concrete in two ways: it delays the splitting failure which occurs in planes perpendicular to the applied stress and it increases the friction force in the interface between the concrete and the reinforcing bar (Cairns et al., 2015).

The rate of increase in bond strength due to lateral confinement is most pronounced at low transverse pressures where an increase of confinement delays splitting. At high transverse pressures, the increase in bond strength with increasing pressure is less pronounced since increasing the transverse pressure only serves to prevent the pull through by increasing friction. A schematic representation of this is shown in Figure 7.17

The increase in bond strength (or the reduction of bond length) due to applied pressure is particularly beneficial at the supports of deep beams and at loading points of corbels. In this

research, strain gauges were positioned to measure the axial force before and after the support/load plates in the flexural tension face. In Figure 7.18, the applied pressure is assumed uniform along the load/support plate and fans at an angle 45° until it intersects the reinforcing bar. The transfer pressure P_{tr} is then given as:

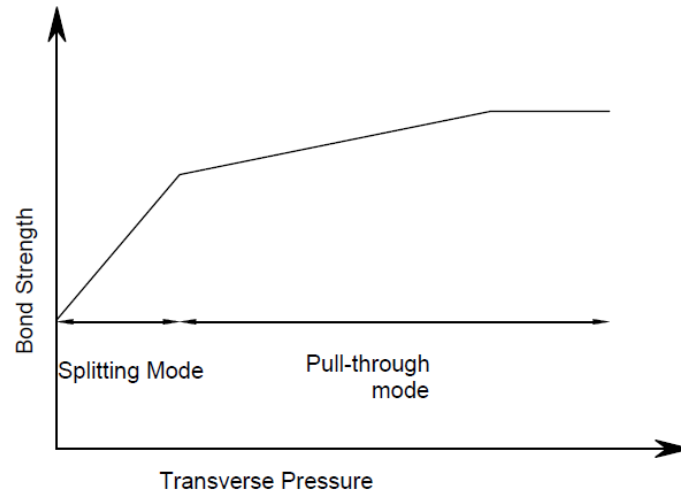


Figure 7.17: The influence of transverse pressure on the bond strength during loading – adapted from MC2010

$$p_{tr} = \frac{P}{bL_{comp}} \quad \text{Equation 7.34}$$

In which P is the load acting on the load/support plate, b is the beam width and L_{comp} is the length of the reinforcement bar over which the load is spread.

Strain gauges were attached to the reinforcement bars to either side of the load/support plates at a spacing L_{SG} . The bar force at these gauges reduces from F_{max} to F_{min} through bond between the reinforcement and concrete.

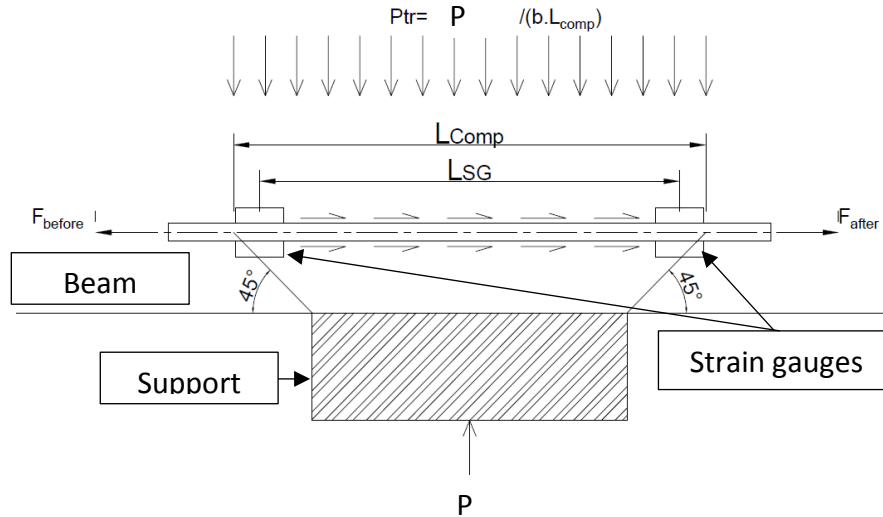


Figure 7.18: Measurement of reduction in axial force along the support/load plates

MC2010 and EC2 account for this enhancement differently. MC2010 explicitly relates the enhanced bond strength to the transverse pressure whereas EC2 reduces the required anchorage length by a multiple α_5 , which depends on the transverse pressure. Although these two approaches look different, they can be put into the same format by rearranging the EC2 equations. EC2 estimates the design value of the ultimate bond stress f_{bd} as:

$$f_{bd} = 2.25\eta_1\eta_2f_{ctd} \quad \text{Equation 7.35}$$

The coefficient η_1 relates to the quality of the bond condition and the position of the bar during concreting and is taken as 1.0 in this work, while η_2 depends on the bar diameter ϕ and is taken as 1.0 for $\phi < 32\text{mm}$. f_{ctd} is the design value of concrete tensile strength.

The basic anchorage length $l_{b,rqrd}$ is calculated in terms of f_{bd} as:

$$l_{b,rqrd} = \frac{\phi}{4} (\sigma_{sd} / f_{bd}) \quad \text{Equation 7.36}$$

In which σ_{sd} is the applied stress and ϕ is bar diameter.

The required anchorage length l_{bd} is given by the product of the basic anchorage length $l_{b,rqrd}$ and the multiple $\alpha_1\alpha_2\alpha_3\alpha_4\alpha_5$, in which the coefficients α_1 to α_5 account for the shape of the bar, concrete cover, confinement by transverse reinforcement, confinement by welded reinforcement and the effect of transverse pressure respectively. The design anchorage length l_{bd} can be expressed in terms of α_5 as follows:

$$l_{bd} = k\alpha_5l_{b,rqrd} \quad \text{Equation 7.37}$$

In which $k = \alpha_1\alpha_2\alpha_3\alpha_4$.

The maximum design force that can be developed by the bond over an anchorage length l_{bd} is given by:

$$F_{bd} = \frac{l_{bd}\pi\phi f_{bd}}{k\alpha_5} \quad \text{Equation 7.38}$$

Equation 7.38 can be expressed in terms of the transverse pressure f_{tp} as:

$$F_{bd} = \frac{l_{bd}}{k} \pi\phi f_{bd} \left(1 + \frac{f_{tp}}{f_{bd}}\right) \quad \text{Equation 7.39}$$

$$\frac{f_{tp}}{f_{bd}} = \left(\frac{1}{\alpha_5} - 1\right) \quad \text{Equation 7.40}$$

EC2 gives the coefficient α_5 as:

$$\alpha_5 = 1 - 0.04p_{tr} \leq 0.7 \quad \text{Equation 7.41}$$

Where p_{tr} is the transverse pressure. Hence, the enhanced bond strength is given by:

$$f_{bd,enhanced} = \frac{f_{bd}}{k} \left(1 + \frac{0.04p_{tr}}{1 - 0.04p_{tr}}\right)$$

Unlike EC2, estimating the enhanced bond strength due to transverse pressure is straightforward in MC2010 as can be seen in:

$$f_{bd} = (\alpha_2 + \alpha_3)f_{bd,0} - 2p_{tr} < 2f_{bd,0} - 0.4p_{tr} < 1.5\sqrt{f_{ck}} \quad \text{Equation 7.42}$$

The coefficients α_2 and α_3 account for the passive confinement from the cover and the transverse reinforcement and $f_{bd,0}$ is the basic bond strength. Further details regarding the effect of the other parameters on the bond strength can be found in the design codes (fib, 2010, BSI, 2004).

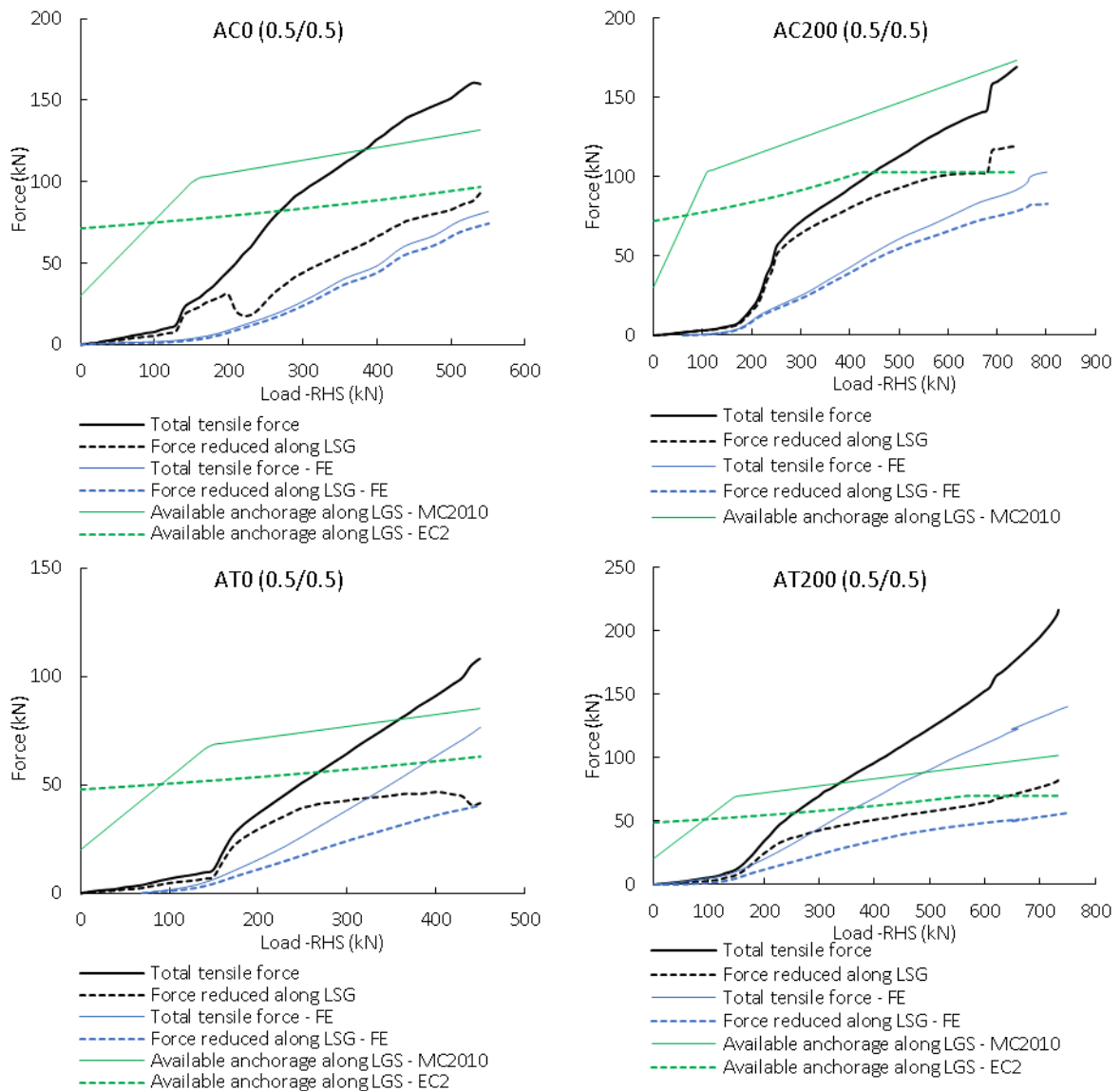
Strain measurements were obtained to either side of the support for the beams loaded on the compression face and to either side of the load plates for beams loaded in the tension side. Due to malfunctioning of strain gauges, results are not available for beams BT200 (1.0/0), BT200 (0/1.0) and CT0 (1.0/0).

To evaluate the reduction of the axial force along the length L_{SG} , results from the FE analysis were also used. Figure 7.19 shows the maximum tensile force at the plate edge and the reduction along the length L_{SG} (i.e. $F_{before} - F_{after}$) for the tested beams. Results are presented for forces determined from the measured strains as well as FEA at the same locations. Figure 7.15 also shows the maximum available bond force along the length L_{SG} calculated using both EC2 and MC2010. These forces were calculated with partial factors

equal to 1.0. It is worth mentioning that L_{SG} is larger for beams loaded on the compression face, and hence, the change in force along it is also larger.

Generally, there was reasonable agreement between the trends of measured and NLFEA tensile forces but the measured forces were consistently greater than calculated. However, for beams loaded on the compression face, the FE suggested that the majority of the tensile force was anchored along the length L_{SG} while test results show otherwise. This is reasonable given that the FE assumes a perfect bond between the concrete and the reinforcement.

Regarding the code estimations, the maximum design force that can be developed along the length L_{SG} is greater than the measured change in force for all of the beams when calculated using MC2010. This was also the case for EC2 apart from beams AT200 (0.5/0.50) and CT200 (1.0/0) where the maximum transferred force was slightly greater than the code limit.



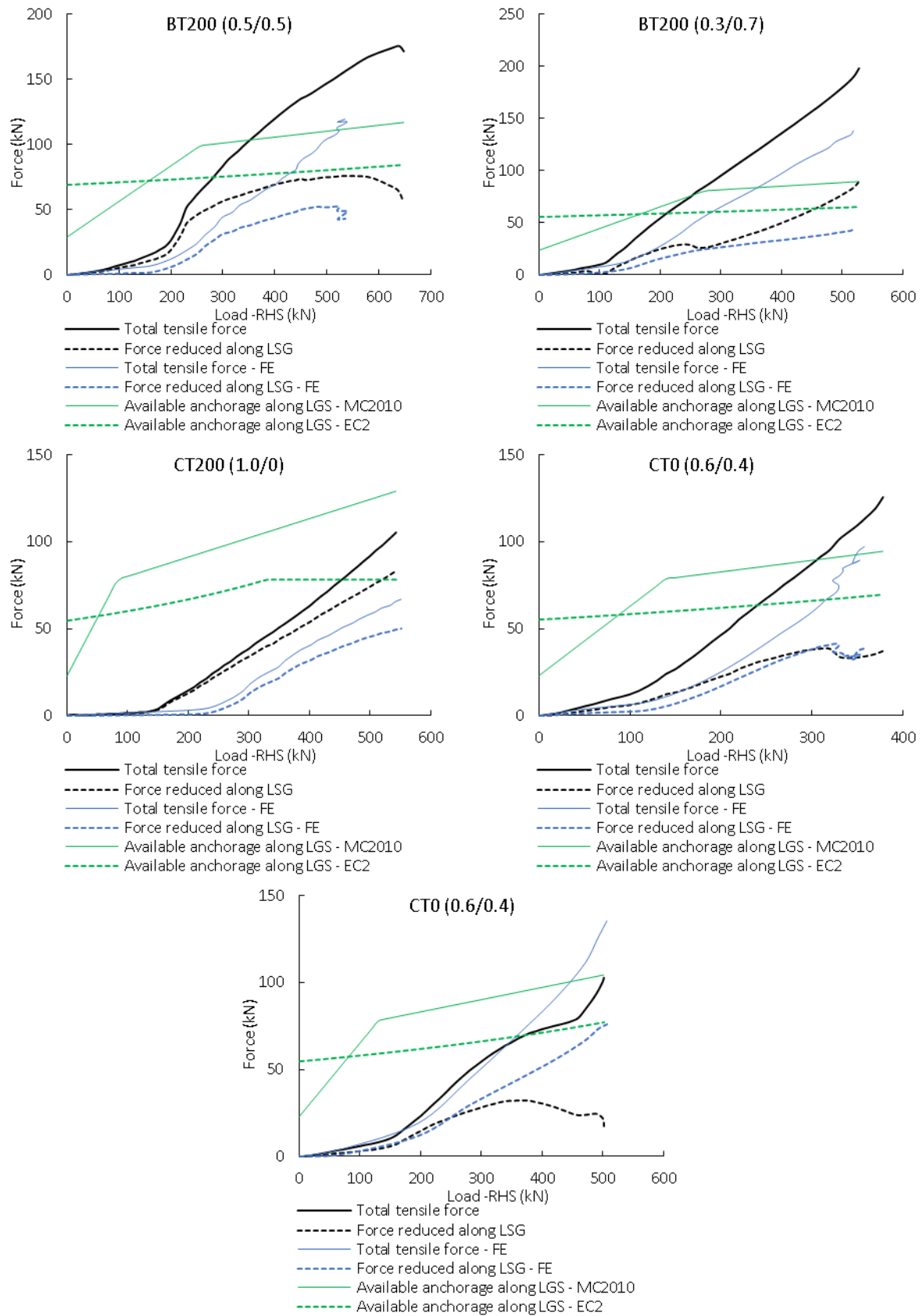


Figure 7.19: Effect of transverse pressure on the bond strength for the tested beams

The basic bond strength given by MC2010 is around half that calculated with EC2 but, the influence of transverse pressure is significantly greater according to MC2010 than EC2. Consequently, the maximum force developable along the length L_{SG} is always greater for MC2010 than EC2. The MC2010 pull-through mode bond strength was not critical in any of the tested beams. However, in some cases the maximum force transferred along L_{SG} exceeded the design strength given by EC2. There was no visible evidence of bond failure in any of these tests.

7.4.4. Prediction of critical failure plane for tested beams

In this research, the shear strength of beams loaded with multiple point loads was estimated using several methods (the five-spring model discussed in Chapter 5, NLFEA described in Chapter 6, design codes and STM). Dependent on the ratio between the inner (P_1) and outer (P_2) loads, beams loaded with two point loads can fail in shear along the inner or outer shear planes depicted in Figure 2.14. This section reviews the accuracy of these methods in predicting the failure plane and their sensitivity to the ratio between P_1 and P_2 .

As mentioned earlier, the shear strength of beams with two-point loads calculated using the five-spring model must be evaluated for both shear planes to find the critical section. Both EC2 and BS8110 indicate the location of the critical shear plane while the maximum shear force is always critical with MC2010. Two different STMs were used to estimate the strength of beams with pairs of point loads. STM2, which used for beams loaded on their compression face, does not indicate a failure plane as it assumes shear failure to occur due to crushing of strut III at its bottom end – see Figure 2.33. Contrarily, in STM3 the outer shear span is critical when the failure load is governed by strut 2 (Figure 7.7). The situation is less clear with the NLFEA, which does not give any direct indication of the critical failure plane. In the tests, failure occurred in the outer shear span of all specimens except CT200 (0.6/0.4). Table 7.1 compares the predicted failure plane obtained using different methods. For beams with multiple point loads, the strength for failure along the outer and inner shear planes was estimated using equations Equation 7.4 and Equation 7.5 for EC2, following the recommendations of Vollum and Fang (2014).

Table 7.6: Predicted and actual failure plane for different models

Beam	Actual failure plane	Predicted failure plane				
		Five-Spring	STM3 (EC2)	STM3 (MCFT)	BS 8110	EC2
AC0 (0.5/0.5)	Outer	Outer	N/A	N/A	Outer	Inner
AC200 (0.5/0.5)	Outer	Outer	N/A	N/A	Inner	Inner
AT0 (0.5/0.5)	Outer	Outer	Outer	Outer	Inner	Inner
AT200 (0.5/0.5)	Outer	Inner	Outer	Inner	Inner	Inner
BT200 (0.5/0.5)	Outer	Inner	Outer	Inner	Inner	Inner
BT200 (0.3/0.7)	Outer	Outer	Outer	Outer	Outer	Inner
CT0 (0.6/0.4)	Outer	Outer	Outer	Outer	Inner	Inner
CT200 (0.6/0.4)	Inner	Inner	Inner	Inner	Inner	Inner

STM3 (EC2) correctly predicts the failure plane for all relevant beams while STM3 (MCFT) and the five-spring model fail to predict the failure plane of beams AT200 (0.5/0.5) and BT200 (0.5/0.5), which are notionally identical. EC2 falsely predicted shear failure to be critical in the inner shear span for all specimens with two-point loads apart from CT200 (0.6/0.4). BS8110 similarly fails to predict the correct failure plane with the exception of beams AC0 (0.5/0.5) and BT200 (0.3/0.7).

The influence of P_1/P on the measured and predicted failure loads P_2 is illustrated in (Figure 7.20 – a) for series B and beam AT200 (0.5/0.5). The predicted failure mode is depicted in (Figure 7.20– a) by open symbols for failure in the inner shear span and solid symbols for failure in the outer shear span. Figure 7.20a shows that the shear resistance of the critical outer shear span P_2 reduced as P_1 was increased while Figure 7.20b shows the maximum shear force P increased with increasing P_1/P despite the reduction in shear resistance P_2 of the outer shear span. This interaction between P_1 and P_2 is most realistically captured by STM3 EC2 ($\alpha = 0.85$) and NLFEA but all the strength predictions are reasonable.

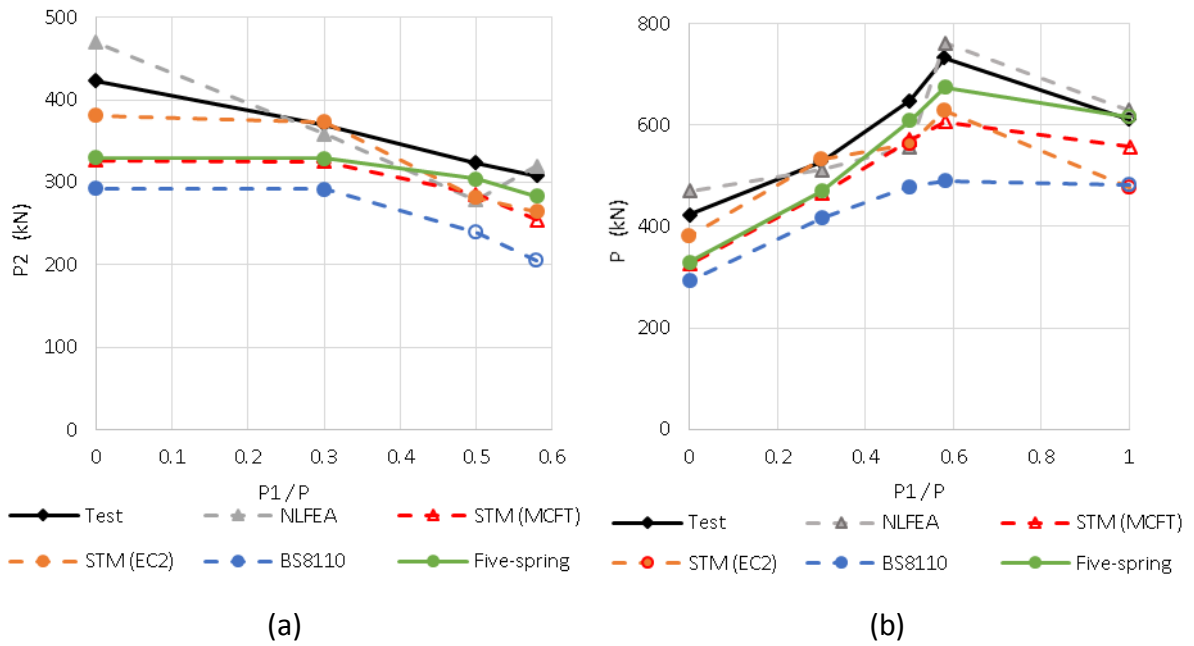


Figure 7.20: Influence of P_1/P on normalised failure loads a) P_2 and b) P for Series B

Figure 7.21a and b show the influence of P_2/P on the measured and predicted failure loads according to BS8110 and EC2 respectively. Strengths are shown in each figure for beams without and with shear reinforcement. Failure is predicted to occur at the least of the loads corresponding to failure along the inner and outer shear planes. Figure 7.21 also shows the measured strengths of beams in Series A and B in which the outer shear plane was always critical in the tested beams.

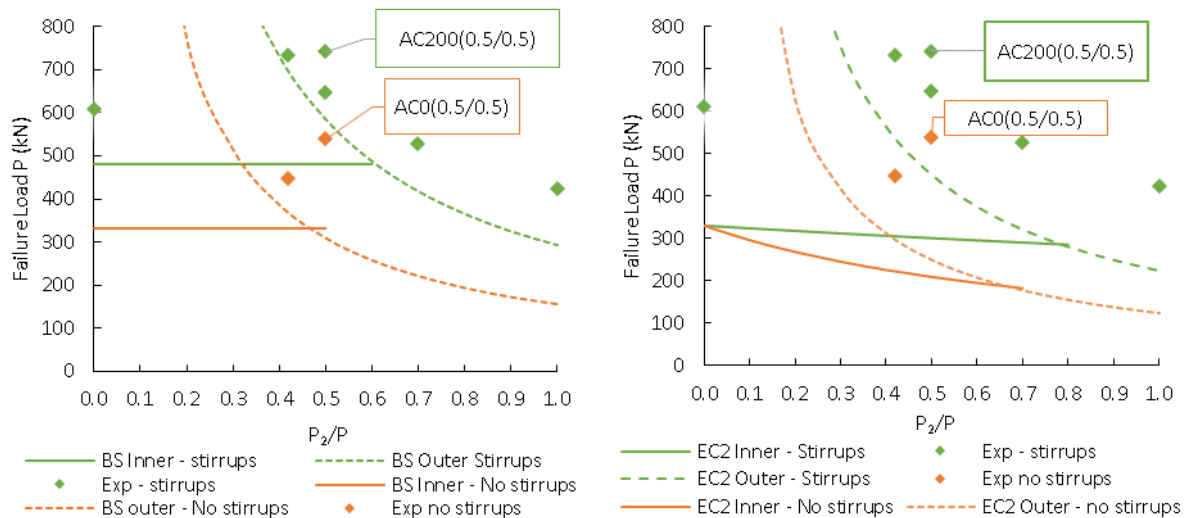


Figure 7.21: Influence of failure plane for series A and B according to a) BS8110 and b) EC2

Beams loaded on the compression face (i.e. beams AC0 (0.5/0.5) and AC200 (0.5/0.5) are identified in the graphs. All other beams were loaded on the tension face. For both BS8110 and EC2, the experimental failure load corresponds most closely to the predicted failure load for failure along the outer shear span. The overall failure load is underestimated because both codes underestimate the shear resistance for failure along the inner shear plane.

7.4.5. Influence of tension face loading on shear resistance

The predicted influence of compression/tension face loading was investigated by comparing the resistance of matching pairs of beams, with four-point loads, identical to those tested in Series A but with all specimens having the same concrete strength of $f_c = 30$ MPa. Partial factors were taken as 1.0 for steel and concrete. Beam strengths were calculated for both tension and compression face loading using NLFEA, the 5 spring model and STM3 EC2 (with $\alpha = 0.85$ for beams without shear reinforcement (i.e. strut strength at CCC node equals $0.85(1 - f_{ck}/250)f_{ck}$) and $\alpha = 1$ for beams with shear reinforcement). The geometrical arrangements for the tension and compression face loading were the same as adopted in test series A. Consequently, the width of the loading plates was 100 mm irrespective of whether the load was applied to the flexural tension or compression face. Similarly, the width of the support plate was 300 mm for cantilever beams and 150 mm for simply supported beams. The consequence of this is that the node geometries of beams with loading ratios (1.0/0) and (0/1.0) are different for tension and compression face loading. This is reflected in the STM results as discussed further below. The strength of tension face loaded beams was calculated with STM3, which is equivalent to STM1 for loading ratios of (1.0/0) and (0/1.0) so long as the inner load is assumed zero. Compression face loaded strengths were calculated with STM1 or STM2 as appropriate. The measured and predicted failure loads P are plotted in Figure 7.22a and b for beams without and with shear reinforcement respectively. The experimental and NLFEA results in Figure 7.22 suggest that tension face loaded beams have lower shear resistance than comparable compression face loaded beams. However, the five - spring model and STM incorrectly predict the shear resistance of the tension face loaded beams to be greater than that of comparable compression face loaded beams. It appears that the adopted STM are overly sensitive to variations in node dimensions as found by Vollum and Fang (2015) as discussed later.

Of previous tests with compression face loading, only those of Vollum and Fang (2015) are comparable with the current campaign. Vollum and Fang (2015) tested five simply supported beams with pairs of concentrated loads applied within $2d$ of supports. The geometry and loading arrangement of these beams were almost identical to beams AC0 (0.5/0.5) and AC200 (0.5/0.5) apart from the beam width being 165 mm instead of 250 mm. A straightforward method of assessing the influence of loading face on shear enhancement is to compare $P_{\text{test}}/P_{\text{calc}}$ for the tests of Vollum and Fang as well as this campaign using BS8110 which of the code methods gives the most consistent predictions of strength. In total, there are seven beams with pairs of equal loads on the compression face and three beams with pairs of equal loads on the tension face. The mean value of $P_{\text{test}}/P_{\text{calc}}$ for BS8110 is 1.50 for all beams loaded on the compression face and 1.39 for all beams loaded on the tension face. Whilst inconclusive, this suggests that the influence of loading face is sufficiently small that it can be neglected in practical design.

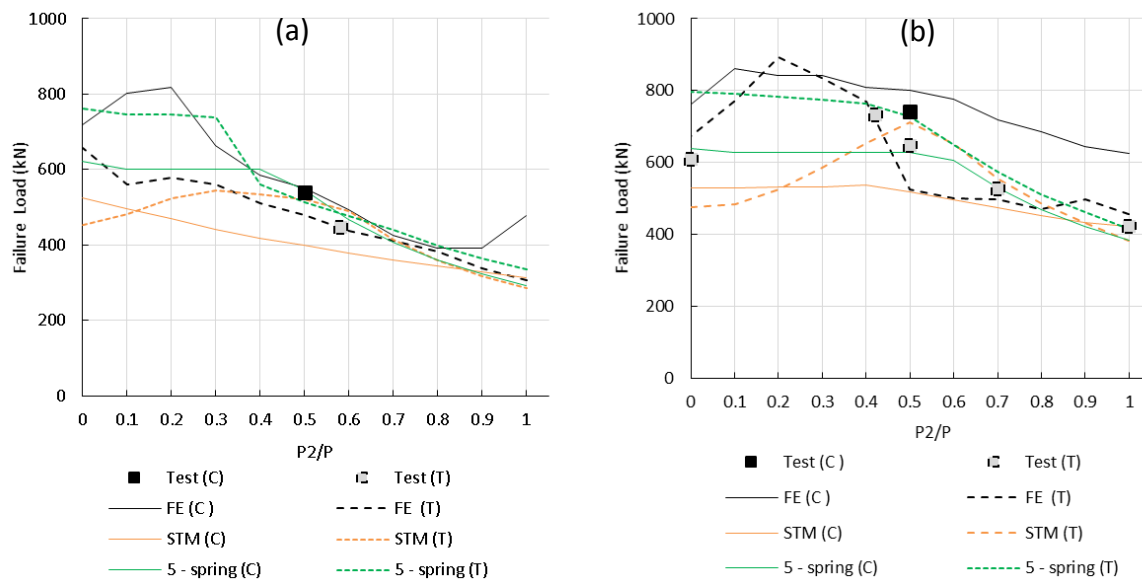


Figure 7.22: Influence of loading face on measured and predicted shear resistance for beams a) without and b) with shear reinforcement

(Note: T refers to beams loaded on the tension face while C refers to beams loaded on the compression face).

Neglecting the effect of self-weight, which is minimal, the differences in strength predictions for compression and tension face loading in Figure 7.22 for $P_2/P = 0$ and 1.0 arise because of differences in the widths of the load/support plates. In the case of compression face loading, the width of the supports (CCT nodes) is 150 mm while the loading plates are 100

mm wide (CCC nodes). For tension face loading, the support is at a CCC node and the loading plates at CCT nodes. Despite the clear shear span being unchanged, the NLFEA and STM predict different strengths for tension and compression face loading. The differences in strength can be attributed to differences in the width of the loading and support plates for tension and compression face loading of otherwise identical beams as discussed earlier in section 7.3.4

For the tested beams, the STM3 predictions for tension face loading are more accurate than those of STM2 for compression face loading. Figure 7.22 shows that STM2 gives lower strength predictions for compression face loading than STM3 for tension face loading whereas the test data suggests the opposite. Compared with STM, the five - spring model is simpler to implement if just used ultimate strength. Furthermore, the five – spring model is a powerful tool if used to estimate the load-deflection response and contributions of the shear transfer actions.

The data in Figure 7.22 are explored in more detail below. To illustrate the effect of varying the load ratio within the shear span, the test results of beams containing shear reinforcement are plotted against P_2/P for tension face loading in Figure 7.23 a. The test results indicate that the total failure load (P) increased as the load ratio P_2/P increased from 0 to 0.4. Subsequently, the total failure load reduced as P_2/P was increased from 0.4 to 1.0. Test results are unavailable for load ratios P_2/P between 0 and 0.4. Figure 7.22a also shows predicted strengths. The change in slope of the STM3 results at $P_2/P = 0.5$ is associated with the predicted failure plane switching from outer to inner for $P_2/P \leq 0.5$. In reality, the transition would have occurred for the tested beams at $P_2/P < 0.4$. In general, the ratio P_2/P at which the failure plane switches from outer to inner depends on the shear reinforcement ratio since shear reinforcement has a greater influence on the strength of the outer than inner shear plane. Figure 7.23 a also shows that the general trend of the observed behaviour was captured by the NLFEA, STM and five - spring model.

Figure 7.23 b, c and d show the predicted effect on resistance of varying the load ratio (P_2/P) tension (T) and compression (C) face loading of beams with stirrups (S) and without stirrups (NS). Predicted strengths are shown for FEA, STM and the five – spring model. For the FEA, it can be seen that the maximum strength occurs at $P_2/P = 0$ for tension face loading of beams without shear reinforcement. The FEA gives greater strengths for compression than tension

face loading for beams both with and without shear reinforcement with the difference most pronounced for beams with stirrups.

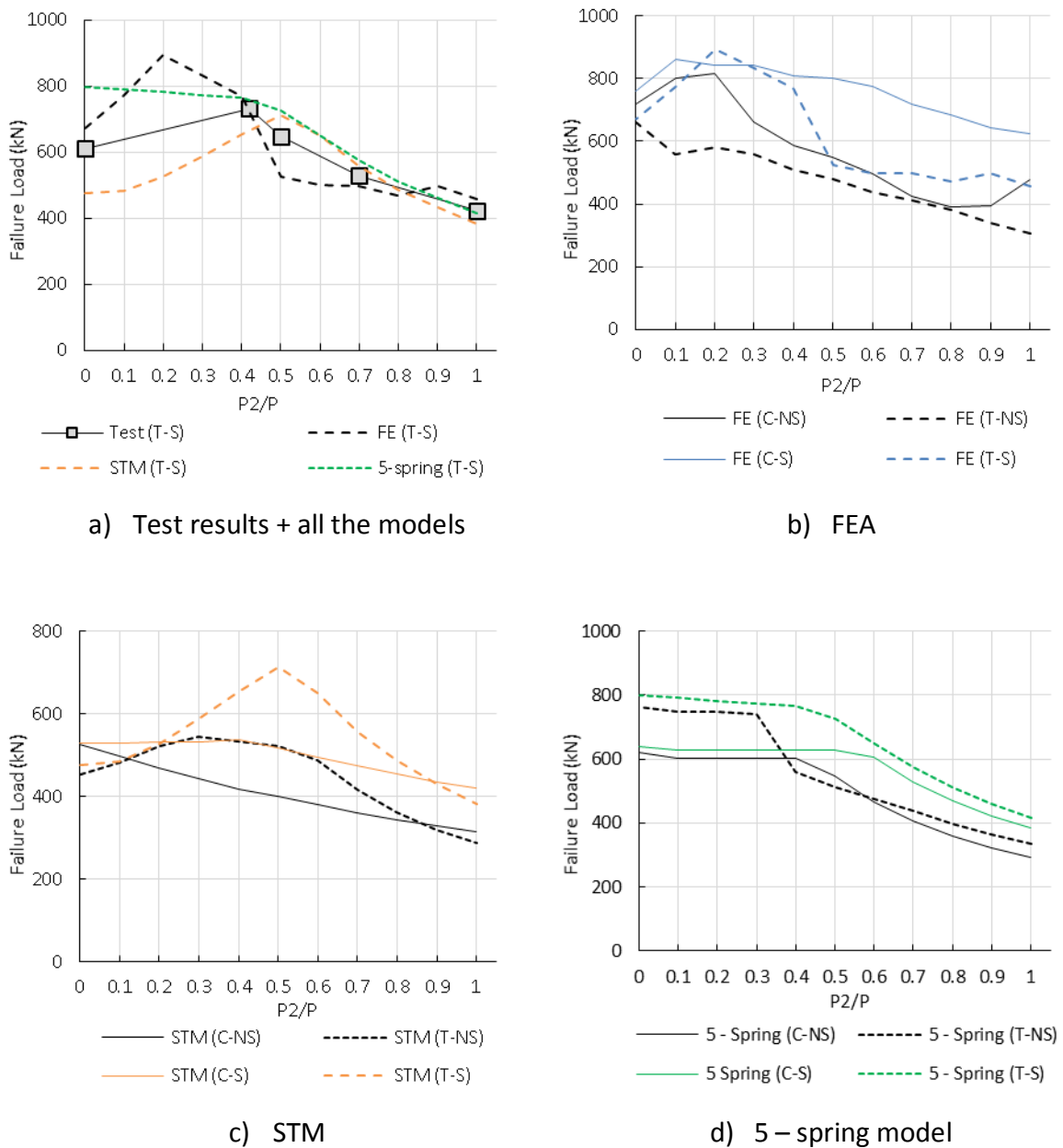


Figure 7.23: The effect of varying the load ratio within the shear enhancement zone for beams loaded on the tension face predicted using several models

Figure 7.23a shows that STM3 captured the general trend of the test data for tension face loaded beams with shear reinforcement. However, the reduction in P as P_2/P reduces from 0.5 to 0 is overestimated. STM2 gives lower strengths for compression face loading than given by STM3 for tension face loading for load ratios P_2/P between 0.2 and 0.8, which is inconsistent with the experimental data shown in Figure 7.22.

When using the five - spring model to assess the resistance of beams with two point loads within the shear span, it is necessary to assess the strength of both shear planes. For cases where higher load ratios are applied on the inner loading plate with $P_1/P \geq 0.7$, the strength of the inner shear plane governs the capacity of the beam. As mentioned in Chapter 5, the dominant shear transfer mechanism in the five - spring model is the contribution of the critical loading zone (CLZ), particularly for small ratios of a_v/d . When the inner shear plane governs, the effective width of the CLZ (L_{b1e}) for beams loaded on the tension face (150mm) is greater than that of beams loaded on the compression face (100mm). Hence, when the inner shear plane governs, the predicted strength of beams loaded on the tension face were greater. The effect of changing L_{b1e} on the strength of a beam with $P_1/P = 1$ is shown in Figure 7.24 (a) for beams with and without shear reinforcement, where the increase of the failure load is proportional to the increase of L_{b1e} .

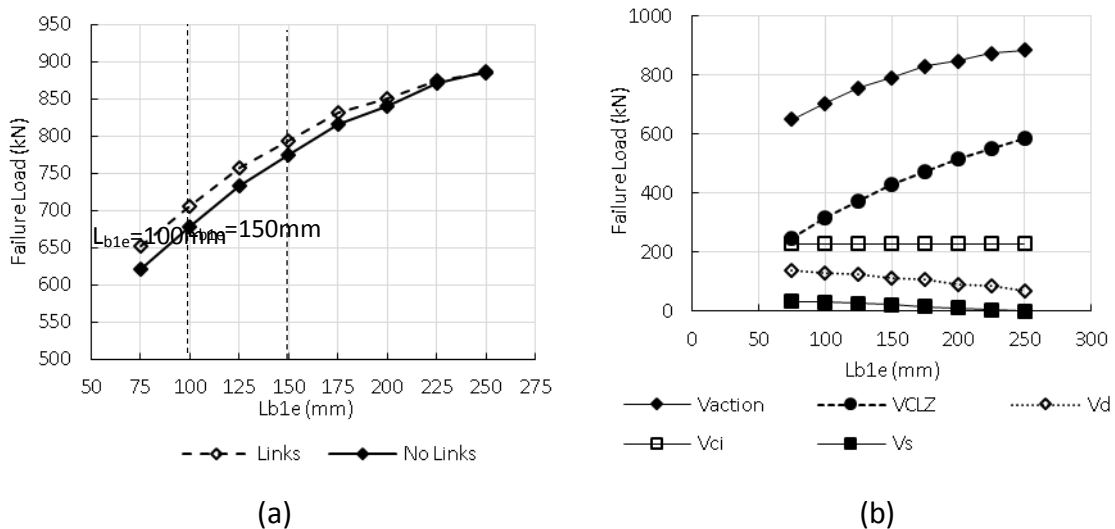


Figure 7.24: The effect of changing L_{b1e} on the strength of a beam with $P_1/P = 1$

The contributions of the other mechanisms are either constant or reduce with increasing L_{b1e} as shown in Figure 7.24 (b), which is drawn for a beam with shear reinforcement. The contribution of the shear reinforcement diminishes for higher values of L_{b1e} as the effective number of stirrups reduces due to the reduction in clear shear span.

When the outer failure plane governs, the difference in the predicted strength reduces for tension and compression face loading. The reason for this is that for beams loaded on the tension face; the effective width of the CLZ (L_{b1e}) reduces from L_{b1} to $R_2 L_{b1}$ when the outer plane governs. Accordingly, the contribution of the CLZ reduces ($L_{b1} = 150$ mm). A schematic

representation is presented in Figure 7.25 below, which shows the change of the effective width and the contribution of the CLZ as the failure plane changes. The effective width L_{b1e} for beams loaded on the compression face is constant for both failure planes and equal to 100mm.

The strength predictions are sensitivity to the dimension of the CLZ in the five-spring model. This is in agreement with the above investigation and with the observations in the original five – spring model (Mihaylov, 2015). Due to this over sensitivity, the five-spring model, as well as the STM, gives higher strengths for beams loaded on the tension face than compression face, whereas the test results and NLFEA suggest the opposite.

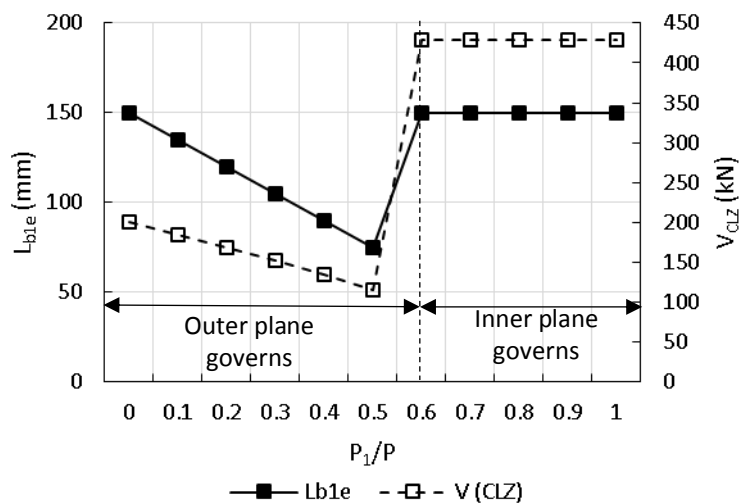


Figure 7.25: Change of the effective width and the contribution of the CLZ with the change of the failure plane

7.5. Conclusions

This chapter investigates the test results presented in Chapter 4 using design codes, STM and NLFEA. A STM, depicted STM3, is developed for tension face loading. Comparisons are made between these methods to assess how they perform for various load arrangements and loading ratios. Good predictions of shear resistance were obtained with NLFEA, the five-spring model and STM with the former most accurate. However, it should be noted that the NLFEA was calibrated using the test data while no such calibration was required for either the 5 spring model or STM.

Regarding design codes, the strengths of the tested beams were compared with the predictions of BS8110, EC2, and MC2010. These methods do not differentiate between tension and compression face loading or boundary conditions. The code predictions were all safe and with EC2 particularly conservative. Overall, MC2010 LoA III gave the best strength estimates with an average of 0.75 and a COV of 18% and EC2 the worst.

For beams loaded on the tension face with two-point loads, the ratio of the inner load (P_1) to the outer load (P_2) point loads was varied in the tests. Investigations of the beams in series B in addition to beam AT200 (0.5/0.5) showed that the shear resistance of the outer shear span reduced as the inner load was increased but the total failure load increased as the ratio of inner to outer load increased.

Beams loaded with pairs of loads, positioned within around $2d$ of supports, may fail along either the inner or outer shear plane both running between the support and load. Failure occurred in the outer shear span of all the tested beams except CT200 (0.6/0.4). The influence of P_1 on the shear resistance of the outer shear span is captured by STM3 and NLFEA but not by BS8110, EC2 or MC2010. Among the design methods, the suggested strut-and-tie model (STM3) was the only method to correctly predict the failure plane for all relevant beams. BS8110 and EC2 underestimate the maximum shear resistance and consequently falsely predict shear failure to occur along the inner shear plane in the majority of the tests with two-point loads within the shear span.

The shear resistance of short shear span beams may be reduced if loads are applied to the flexural tension face rather than compression face. The reduction appears greatest for beams without shear reinforcement but the difference does not appear sufficient to be considered in practical design.

Test results and FE were also used to study the effect of the transverse pressure on the enhancement of the bond strength along the width of the load or support plate (L_{SG}) and to assess the relevant provisions given in the EC2 and MC2010. Generally, there was good agreement between the measured and predicted tensile force using FEA with the FE predictions being consistently lower. The basic bond strength given by MC2010 is around half that calculated with EC2 but, the influence of transverse pressure is significantly greater according to MC2010 than EC2. Consequently, the maximum force developable along the length L_{SG} is always greater for MC2010 than EC2. The MC2010 pull-through mode bond

strength was not critical in any of the tested beams. However, in some cases the maximum force transferred along L_{SG} exceeded the design strength given by EC2. There was no visible evidence of bond failure in any of these tests.

CHAPTER 8. CONCLUSIONS AND RECOMMENDATIONS

This thesis considers the influence of loading arrangement and boundary conditions on shear enhancement in beams loaded on either their flexural compression or tension face. Shear enhancement occurs when beams are loaded on their top face within around twice the beam effective depth of supports. The vast majority of tests on short span beams have been done on top loaded simply supported beams where the top face is in compression. Such tests are also representative of the end supports of beams on simple supports. However, in practice, beams are typically continuous with moment restraint at end supports. In this case, the top face is in tension as in the cantilever beams tested in this program. The study includes laboratory investigation, nonlinear finite element analysis, analysis using the 2PKT of Mihaylov et al (2013) and strut-and-tie modelling. The main parameters investigated in this work are the influence of loading face, the ratio of the loads applied within the shear enhancement zone ($2d$ from the face of the support) and the influence of loading the beam partly within and partly outside of the shear enhancement zone. This chapter provides a summary of this research, highlights key conclusions, design recommendations and suggested further work.

8.1. Background Overview

The shear strength of RC deep beams remains a subject of considerable research. The literature presented in Chapter 2 describes key studies relevant to this research and identifies pertinent gaps in the literature, as summarized below.

- Cracked concrete can resist applied shear through different shear transfer actions. These actions, namely aggregate interlock, dowel contribution, residual tensile strength, the contribution of the compression zone and stirrups if present are highly dependent on the kinematics and shape of the shear cracks. Evaluation of these contributions includes two levels of uncertainties: the accuracy of the obtained crack kinematics and the validity of the models used. In recent years, several researchers have re-evaluated currently available design models in light of detailed measurements of crack kinematics obtained using digital image correlation (DIC) systems.
- While the majority of code provisions are based on empirical equations (e.g. EC2 for members without shear reinforcement, BS8110 and ACI-318), a few have recently

adopted physical models for the prediction of the shear strength (MC2010 and AASHTO _LRFD). The shear strength of RC beams exhibits significant enhancement when loads are applied close to the support due to arching action. Design codes express shear strength enhancement of beams loaded within $2d$ from the support in terms of the shear span a_v to effective depth d ratio. BS 8110 enhances the shear resistance provided by the concrete for beams loaded within $a_v \leq 2d$ by the multiple $\frac{2d}{a_v}$. Conversely, EC2 and MC2010 reduce the contribution to the design shear force of loads applied within $a_v \leq 2d$ by the multiple $\beta = \frac{a_v}{2d}$ where β is limited to a minimum of 0.25 in EC2 and 0.5 in MC2010. Although these approaches appear similar, there can be significant differences between the enhanced shear resistances given by EC2, MC2010 and the BS8110. Moreover, application of the EC2 shear enhancement design provisions are unclear for beams with shear reinforcement and multiple point loads applied within $a_v \leq 2d$ as discussed by Vollum and Fang (2015). These sectional methods are also not sensitive to the load application face or the boundary conditions.

- The modified compression field theory (MCFT) is one of the earliest and most comprehensive theories for describing the behavior of RC panels under membrane action. The method can be implemented into finite element programs or sectional analysis programs like Response 2000 (Bentz and Collins, 2000) for the calculation of shear resistance in sections where plane sections remain plane. The two-parameter kinematic theory (2PKT) (Mihaylov et al., 2013) and the associated five-spring model (Mihaylov, 2015) are pertinent to the analysis of deep beams. They can predict the full displacement field of the shear span during loading but are case sensitive needing modifications to account for variations in load arrangement and boundary conditions.
- A popular method for estimating the shear capacity of members with discontinuity regions is the strut-and-tie model. The model developed by Sagaseta and Vollum (2010) for the stress fields utilizes the principle of nodal sub-division and has been used and modified by several researchers to account for different loading arrangements (Amini Najafian et al., 2013, Vollum and Fang, 2015). Vollum and Fang (2015) developed an STM for beams with two concentrated loads applied to the flexural compression face within $2d$ of supports. The STM geometry was based on the

geometry of the compressive stress field determined with NLFEA. The STM of Vollum and Fang is only valid for compression face loading of simply supported beams since the assumed dog-leg geometry of the direct strut is incompatible with the reinforcement arrangement for tension face loading. Furthermore, the orientation of the compressive stress field changes for tension face loading of cantilever beams loaded with pairs of loads within $2d$ of supports. The research in this thesis was motivated by these differences in stress field for compression and tension face loading which were confirmed by preliminary FE investigation prior to the experimental investigation.

8.2. Description of the Experimental Program and Summary of the Test Results

The experimental program of this research consists of 12 beams designed to investigate the effect of loading arrangement and loading face on shear enhancement in top-loaded beams. All the beams measured 2800 mm long by 250mm wide by 500mm deep. The flexural tension reinforcement, in all the beams, consisted of two layers of three bars of 25 mm diameter ($\rho = 2.36\%$). The effective depth measured to the centroid of the tension reinforcement was 429.5 mm. Two 16 mm diameter bars were provided in the flexural compression zone of all beams ($\rho' = 0.322\%$). In all the tests, additional shear reinforcement was provided in the left-hand shear span to ensure that failure occurred in the right-hand shear span. Where provided, shear reinforcement in the critical shear span consisted of high strength (Grade 500) 8 mm diameter links at 200 mm centres.

The beams were cast in three groups of four, depicted A to C, with each group cast from a single batch of ready-mixed concrete specified to have strength class C25/30, consistency class S3 and limestone aggregate with a maximum size of 20mm. Each series of four tests had separate objectives. Series A was designed to investigate the influence of loading the tension or compression face of otherwise identical beams without and with shear reinforcement. Series B examined the effect of varying the ratio between the inner and outer loads on the shear strength of balanced cantilever beams with stirrups. Series C compared the shear resistance of beams loaded inside and partly outside the shear enhancement zone. The beams were loaded in displacement control to capture the post-failure response. Detailed

measurements of displacements and crack kinematics were obtained by means of Digital Image Correlation (DIC). Transducers were also used as a cross-check on displacements calculated with DIC. Up to 24 strain gauges were fixed to the reinforcement at locations selected based on nonlinear finite element analysis. The results of the experimental program are summarized below:

Series A consisted of two beams loaded with an equal pair of loads on the compression face and comparable two beams loaded on the tension face. The load ratios of beams loaded on the tension face were slightly unequal (0.58/0.42 instead of 0.5/0.5) due to rotational friction in the loading arrangement, which was eliminated in subsequent tests. All the four beams failed on the outer shear span. The test results showed that the shear force at the failure of the critical shear span of comparable beams was less for tension face loading. This suggests that the shear resistance of top face loaded short span beams may be reduced if loads are applied to the flexural tension face rather than compression face. The reduction appears greatest for beams without shear reinforcement but the difference does not appear sufficient to be considered in practical design. When crack patterns of comparable beams loaded on the tension and compression face were superimposed (crack patterns were inverted for the beams loaded on the tension face), the patterns were very similar in the beams loaded on the tension and compression faces despite the apparent reduced strength of beams loaded on the tension face.

Series B investigated the effect of loading ratio for loads applied within the shear enhancement zone of beams loaded on the tension face. In all the tests, the first crack developed in the inner shear span but the crack causing failure extended from the support to the outermost loading plate. Failure of beams in Series B was typically characterised by concrete crushing in the compression zone. The result of this beam in addition to the last beam from series A, with identical geometry and shear reinforcement but a different loading ratio, suggested that the shear resistance of the outer critical shear span reduced as the inner load was increased for beams failing in the outer shear span.

Series C contained four beams, the first two beams were with and without shear reinforcement loaded with a single point load applied at an equivalent lever arm to that of two equal point loads loaded on the tension face. In the other two beams of series C, another point was applied outside $2d$ for the beams with and without shear reinforcement. The

critical shear plane was the outer for the beam without shear reinforcement while the shear plane was the inner for the beam with the shear reinforcement. The results showed that applying an additional point load outside the shear enhancement zone ($2d$) reduced the shear strength of the beam. Results also showed that the strength of beams loaded with a pair of equal point loads within $2d$ of the support was greater than the strength of beams loaded with a single point load positioned at the centroid of the pair of loads.

8.3. Analysis of the Results and Shear Transfer Actions

The experimental results described earlier were used to study the deformation of the beams and the shear transfer actions. Strengths of the tested beams were evaluated using the five-spring model, codes provisions (BS8110, EC2 2004 and MC2010), nonlinear FEA and strut and tie models.

The following conclusions were reached regarding deformed shapes and shear transfer mechanisms:

- Results obtained using the DIC were used to validate the provisions given by the 2PKT to predict the full displacement field of the shear span during tests. These results were used to calculate crack kinematics, rotation of the free body of the beams and the shear displacement of the 2PKT. The 2PKT gave accurate predictions of the deformation for beams loaded on the compression face and less accurate predictions for beams loaded on the tension face. Modifications of the theory for beams loaded on the tension face were introduced to account for the shear displacement resulting from the secondary shear crack and the actual location of the centre of rotation of the free body. The modified approach gave significantly better predictions of the deformation for beams loaded on the tension face.
- Modifications were also introduced to the five-spring model in order to obtain shear strength, load-deflection responses and the shear transfer mechanisms of the tested beams with two-point loads within the shear span. The modified model provided very good strength predictions for beams with two-point loads. In all beams loaded within $2d$ of supports, the load-deflection response was largely governed by the response of the critical loading zone (CLZ) as the rest of the contributions were either curtailed by their upper limit or nearly constant. In the post-peak response, the contribution of the

CLZ reduced significantly, while the rest of the components remained constant. Consequently, the post-peak response softened more rapidly than experimentally observed.

- The dowel contribution was limited in the 2PKT by the formation of plastic hinges in the bar. The contribution of the shear reinforcement to shear resistance increased with increasing shear span due to the mobilisation of more stirrups. The two kinematic parameters (block rotation $\varepsilon_{t,avg}$ and shear displacement Δ_c) of the five-spring model were evaluated using the DIC measurements. This revealed noticeable differences between the measured and estimated values. Although the calculated block rotations were less than the measured ones, the estimated crack opening and sliding were greater than measured ones at the mid-height of the beam. This is largely due to the dominant contribution of the shear displacement, which was typically close to or greater than the measured displacement. Despite this, the five-spring model gave accurate estimations for the ultimate loads and deformations of the test beams.
- The only beam in which the CLZ response did not govern was beam CT0 (0.6/0.4), without shear reinforcement, which failed outside the shear enhancement zone. In this case, aggregate interlock was the dominant contribution.
- The shear transfer actions were also determined using various models available in the literature. The models of Walraven were used to estimate the contribution of the aggregate interlock (Walraven, 1980) and the dowel contribution (Walraven and Reinhardt, 1981). The contribution of the shear reinforcement was estimated using the two-step bond model (Sigrist, 1995) while the contribution of the flexural compression zone was estimated using the CLZ model from the five-spring model (Mihaylov, 2015). The contributions of dowel action and aggregate interlock were greater in beams loaded on the tension face than comparable compression face loaded beams. These increased contributions resulted from crack sliding being greater in the tension face loaded beams than in comparable compression face loaded beams. Further beam tests are required to determine the generality of this finding due to scattering in test results for notionally identical beams. The total contribution of aggregate interlock to the shear resistance of beams failing in the outer shear span increased as the load applied closer to the support increased. With increasing ratio of

shear span to effective depth, the relative contribution of dowel action reduced while that of stirrups increased. Determination of the individual contribution of the different mechanisms includes some uncertainties associated with the accuracy of the obtained crack kinematics and the shear resisting model assumptions. Regardless of this, consistent use of shear resisting models for analysis of tested beams gives useful insights into the relative contributions of each shear resisting mechanism.

Apart from the five-spring model, the shear strength of the tested beams was estimated using design codes, STM and NLFEA. Comparisons were made between these methods to assess how they perform for the different load arrangements and ratios. The following conclusions were drawn from this analysis.

- Overall, the best predictions of shear resistance were obtained with NLFEA, the five spring model and STM. The enhanced beam shear predictions of EC2 were overly conservative.
- Regarding design codes, the strength of the tested beams was compared with the predictions of BS8110, EC2, and the MC2010. These methods do not differentiate between tension and compression face loading or boundary conditions. The code predictions were all safe and rather conservative. Overall, MC2010 gave the best estimates while EC2 gave the worst.
- For beams loaded on the tension face with two-point loads, the ratio of the load applied in the inner load plate to the outer load plate was varied in the tests for five identical beams containing shear reinforcement. All beams loaded with two-point loads inside the shear enhancement zone failed along the outer shear span. These results showed that the shear resistance of the critical outer shear span reduced consistently as the inner load increased.
- The influence of the inner load on the shear resistance of the outer shear span is captured by the newly developed strut and tie model (STM3), the modified five-spring model and the NLFEA but not by the BS8110, EC2 or MC2010. Of the considered design methods, only the suggested strut and tie model (STM3) was the only method to correctly predict the failure plane for all relevant beams. BS8110 and EC2 underestimate the maximum shear resistance and consequently falsely predict shear

failure to occur along the inner shear plane in the majority of the tests with two-point loads within the shear span.

- Strain gauge measurements and NLFEA were used to study the effect of the transverse pressure on the enhancement of bond strength along the width of the load or support plate. Generally, there was a reasonable agreement between measured and predicted variation in tensile forces near the load/support plates, but the FEA predictions were consistently lower than measured. The average bond stress across the load/support plates was compared with the bond strengths given EC2 and MC2010.
- The basic bond strength given by MC2010 is around half that calculated with EC2 but the influence of transverse pressure is significantly greater according to MC2010 than EC2. Consequently, the maximum force developable along the length L_{SG} is always greater for MC2010 than EC2. The MC2010 pull-through mode bond strength was not critical in any of the tested beams. However, in some cases, the maximum force transferred along L_{SG} exceeded the design strength given by EC2. There was no visible evidence of bond failure in any of these tests.

8.4. Design Observations and Recommendations

Engineers and practitioners commonly use design codes, strut-and-tie models and in certain cases, NLFEA to design and check deep beams for shear. This research considers the influence of tension face loading on shear enhancement in short shear span beams loaded with pairs of point loads. The following design recommendations are suggested based on the work conducted in this thesis:

1. Of the design codes, BS8110 and MC2010 LoAIII gave the best strength predictions. The accuracy of the BS8110 predictions was relatively uniform for all the tested beams. The method was slightly more conservative for tension face than compression face loading but the difference is sufficiently small not to be considered significant for practical design. The accuracy of the MC2010 LoAIII predictions was more variable with results most accurate for beams with single-point loads and least accurate for compression face loaded beams with multiple point loads. EC2 gave the most conservative estimations. For beams with multiple point loads, estimates were better

across the board for beams with shear reinforcement than without shear reinforcement.

2. The observed reduction in shear resistance of short shear span beams loaded on the flexural tension face does not appear sufficient to be considered in practical design but further investigation is suggested to confirm this finding.
3. STM3 developed in this research is a practical tool for estimating the shear strength of short shear span cantilever beams loaded with pairs of point loads. The method is readily extendable to the calculation of enhanced shear resistance at internal supports of continuous beams. Additionally, the model can be readily modified in the future to deal with more than two-point loads. STM3 correctly predicts the failure plane of the relevant tested beams. The assumed stress field is shown to be consistent with the experimentally observed crack patterns and stress fields obtained with NLFEA. The strut and tie models developed for beams loaded with pair of load provided acceptable predictions with a relatively easy procedure to follow, particularly if the EC2 provisions were used to evaluate the strength of the strut. The calculations of the ultimate strength using the 5-spring model are easier. However, the five – spring model is a powerful tool if used to evaluate the load-deflection response and the shear transfer actions during the tests, which is tedious particularly for beams loaded with pair of load.

Although the NLFEA provided the best estimates of the shear capacity of the tested beams, the FEA was sensitive to the adopted modelling parameters and required careful calibration against test results before use in design. Some modelling recommendations from this work, which are thought to be generally useful for similar cases, are summarized below:

1. For shear critical elements such as deep beams, the FEA can be very sensitive to the selection of shear retention model and associated input parameters. Based on this work, the use of a variable shear retention factor is suggested for modelling beams without shear reinforcement as recommended in the Dutch Guidelines for NLFEA (Hendriks et al., 2017). For beams with shear reinforcement, the best strength predictions were obtained using a constant shear retention factor of 0.25.

2. When modelling loading and support plates, introducing an interface element overcomes the reported issue of stress concentration at plate corners. Interface elements give better stress distribution under the plates without the need to introduce out of plane reinforcement or to enhance the concrete strength beneath the plates, which changes the properties of the modelled member.
3. Using the arc-length technique in load controlled modelling captures localised snap-through as well as the post-peak response. This avoids premature numerical failure as well as demonstrating that the peak load has been reached.

This research is the first research to consider the application of multiple point loads applied within and partly outside the shear enhancement zone on the tension face. It will be of great value to the available shear database and sheds lights on the importance of this load configuration. However, as the first piece of research for such configuration, some of the findings are not comprehensive and need further investigation to support them.

8.5. Suggestions for Further Work

Recommendations for further work include:

1. The observed reduction of the shear strength for beams loaded on the tension face was relatively small but was also predicted by NLFEA. Further experimental investigation is required to quantify the reduction in strength more definitively but the difference appears sufficiently small that it can be neglected in practice. However, as codes become more refined it may become necessary to differentiate between tension and compression face loading in top-loaded beams.
2. The beam tests show that a pair of equal point loads applied within $2d$ from the face of the support can conservatively be treated as an equivalent point load. Nevertheless, it was also shown in this research that the shear strength of the critical outer shear plane reduces with the increase of the load at the inner loading plate. Hence, generalizing this finding for pairs of unequal point loads is questionable and merits further experimental investigations.

3. Test results showed that pairs of equal point loads applied within $2d$ from the face of the support can conservatively be treated as an equivalent point load applied at the centroid of the two loads. This observation was made by comparing beams CT0 (1.0/0) and CT200 (1.0/0) with beams AT0 (0.5/0.5) and AT200 (0.5/0.5). However, confirmation of the generality of this finding requires further experimental and numerical investigation.
4. The double cantilever case discussed in this research is a simpler form of a continuous beam. STM3 presented in this work can be modified to calculate the enhanced shear resistance at internal supports of continuous beams loaded both within and outside $2d$ of supports.
5. A common case of the double cantilever beams is the bridge crosshead girders. These structures sometimes contain more than two-point load. The proposed design methods should be extended to general solutions that deal with any numbers of point loads.

REFERENCES

- AASHTO-LRFD 2008. Bridge design specifications, customary US units, with 2008 interim revisions. Washington, DC.
- AASHTO-LRFD 2012. Bridge Design Specifications 2012 Washington. DC, USA American Association of State Highway and Transportation Officials.
- ACCIAIOLI, A., LIONELLO, G. & BALEANI, M. 2018. Experimentally Achievable Accuracy Using a Digital Image Correlation Technique in measuring Small-Magnitude ($< 0.1\%$) Homogeneous Strain Fields. *Materials*, 11, 751.
- ACI-COMMITTEE 2014. Building Code Requirements for Structural Concrete (ACI 318-14) and Commentary. ACI, Farmington Hills, United States.
- AL-MAHAIDI, R. S. H. 1978. *Nonlinear finite element analysis of reinforced concrete deep members*, Cornell University, May.
- AMINI NAJAFIAN, H., VOLLUM, R. L. & FANG, L. 2013. Comparative assessment of finite-element and strut and tie based design methods for deep beams. *Magazine of Concrete Research*, 65, 970-986.
- ASTM 2017. Standard Test Method for Splitting Tensile Strength of Cylindrical Concrete Specimens. West Conshohocken, USA: ASTM International
- BAUMANN, T. & RÜSCH, H. 1970. *Versuche zum studien der verdübelungswirkung der biegezugbewehrung eines stahlbetonbalkens (German)*, Berlin, Ernst.
- BAŽANT, Z. 1985. Mechanics of fracture and progressive cracking in concrete structures. *Fracture mechanics of concrete: Structural application and numerical calculation*. Springer.
- BAŽANT, Z. P. 1983. Comment on orthotropic models for concrete and geomaterials. *Journal of Engineering Mechanics*, 109, 849-865.
- BAZANT, Z. P. & GAMBAROVA, P. G. 1980. Rough crack models in reinforced concrete. *Journal of Structural Engineering, ASCE*, 4, 23.
- BELLETTI, B., ESPOSITO, R. & WALRAVEN, J. 2012. Shear capacity of normal, lightweight, and high-strength concrete beams according to Model Code 2010. II: Experimental results versus nonlinear finite element program results. *Journal of Structural Engineering*, 139, 1600-1607.
- BENTZ, E. C. & COLLINS, M. 2000. Response 2000 manual. Retrieved April, 10, 2007.
- BENTZ, E. C., VECCHIO, F. J. & COLLINS, M. P. 2006. Simplified modified compression field theory for calculating shear strength of reinforced concrete elements. *ACI Structural Journal*, 103, 614.
- BENTZ, M. P. C. E. C. X., EDWARD G SHERWOOD LIPING 2008. AN ADEQUATE THEORY FOR THE SHEAR STRENGTH OF REINFORCED CONCRETE STRUCTURES. *Magazine of Concrete Research*, 60, 15.
- BINICI, B. 2005. An analytical model for stress-strain behavior of confined concrete. *Engineering Structures*, 27, 1040-1051.
- BORST, R. D., REMMERS, J. J., NEEDLEMAN, A. & ABELLAN, M. A. 2004. Discrete vs smeared crack models for concrete fracture: bridging the gap. *International Journal for Numerical and Analytical Methods in Geomechanics*, 28, 583-607.
- BOYAN, I. M., EVAN, C. B. & MICHAEL, P. C. 2013. Two-Parameter Kinematic Theory for Shear Behavior of Deep Beams. *Structural Journal*, 110.

- BROWN, M. D. & BAYRAK, O. 2007. Investigation of deep beams with various load configurations. *ACI Structural Journal*, 104, 611.
- BSI 1997. 8110: Structural use of concrete—code of practice for design and construction. London, UK.
- BSI 2004. *Eurocode 2: Design of Concrete Structures: Part 1-1: General Rules and Rules for Buildings*, British Standards Institution.
- CAIRNS, G. L. B. J., ELIGEHAUSEN, R., LETTOW, S., METELLI, G., PANTAZOPOULOU, S. & PLIZZARI, G. A. 2015. Bond and anchorage of embedded steel reinforcement in fib Model Code 2010. *fib Bulletin* fib - International Federation for Structural Concrete.
- CAMPANA, S., RUIZ, M. F., ANASTASI, A. & MUTTONI, A. 2013. Analysis of shear-transfer actions on one-way RC members based on measured cracking pattern and failure kinematics. *Magazine of Concrete Research*, 65, 386-404.
- CAVAGNIS, F., FERNÁNDEZ RUIZ, M. & MUTTONI, A. 2015. Shear failures in reinforced concrete members without transverse reinforcement: An analysis of the critical shear crack development on the basis of test results. *Engineering Structures*, 103, 157-173.
- CAVAGNIS, F., FERNÁNDEZ RUIZ, M. & MUTTONI, A. 2017. An analysis of the shear-transfer actions in reinforced concrete members without transverse reinforcement based on refined experimental measurements. *Structural Concrete*, 16.
- CHOI, K.-K., HONG-GUN, P. & WIGHT, J. K. 2007. Unified shear strength model for reinforced concrete beams-Part I: Development. *ACI Structural Journal*, 104, 142.
- COLLINS, M. P., BENTZ, E. C., SHERWOOD, E. G. & XIE, L. 2008. An adequate theory for the shear strength of reinforced concrete structures. *Magazine of Concrete Research*, 60, 635-650.
- COPE, R., RAO, P., CLARK, L. & NORRIS, P. Modelling of reinforced concrete behaviour for finite element analysis of bridge decks. Proceedings of the International Conference on Numerical Methods for Non-linear Problems, 1980.
- CSA 2004. *Design of concrete structures*, Canadian Standard Association.
- DE BORST, R. 1987. Smeared cracking, plasticity, creep, and thermal loading—A unified approach. *Computer methods in applied mechanics and engineering*, 62, 89-110.
- DE BORST, R. & NAUTA, P. 1985. Non-orthogonal cracks in a smeared finite element model. *Engineering Computations*, 2, 35-46.
- DE WILDER, K., LAVA, P., DEBRUYNE, D., WANG, Y., DE ROECK, G. & VANDEWALLE, L. 2015. Experimental investigation on the shear capacity of prestressed concrete beams using digital image correlation. *Engineering Structures*, 82, 82-92.
- DELATTE JR, N. J. Beyond failure: Forensic case studies for civil engineers. 2008. American Society of Civil Engineers.
- DIANA, T. 2017. Manual, DIANA User's Material library. *DIANA finite element analysis user's manual, release*.
- DULACSKA, H. Dowel action of reinforcement crossing cracks in concrete. Journal Proceedings, 1972. 754-757.
- EDER, M. A., VOLLUM, R. L., ELGHAZOULI, A. Y. & ABDEL-FATTAH, T. 2010. Modelling and experimental assessment of punching shear in flat slabs with shearheads. *Engineering Structures*, 32, 3911-3924.
- ELEIOTT, A. F. 1974. *An experimental investigation of shear transfer across cracks in reinforced concrete*, Cornell University, June.

- ELWAKEEL, A., FANG, L., ABDELSALAM, M. & VOLLUM, R. L. 2018. Contribution of the Shear Transfer Actions in Short Span Beams. *fib Bulletin 85: Towards a rational understanding of shear in beams and slabs*, 85, 15.
- FANG, L. 2013. *Shear enhancement in reinforced concrete beams*. PhD Thesis or dissertation, Imperial College London.
- FEENSTRA, P. H. 1993. *Computational aspects of biaxial stress in plain and reinforced concrete*. TU Delft, Delft University of Technology.
- FERNÁNDEZ RUIZ, M., MUTTONI, A. & SAGASETA, J. 2015. Shear strength of concrete members without transverse reinforcement: A mechanical approach to consistently account for size and strain effects. *Engineering Structures*, 99, 360-372.
- FIB 2010. MC 2010 in fib Bulletin 56 2010. ISBN 978-2-88394-096-3.
- GAMBAROVA, P. & KARAKOÇ, C. A new approach to the analysis of the confinement role in regularly cracked concrete elements. Transactions of the 7. international conference on structural mechanics in reactor technology. Vol. H, 1983.
- GUIDOTTI, R. 2010. *Poinçonnement des planchers-dalles avec colonnes superposées fortement sollicitées (In French)*. EPFL.
- HAMADI, Y. & REGAN, P. 1980. Behaviour of normal and lightweight aggregate beams with shear cracks. *The Structural Engineer*, 58, 71-79.
- HE, X. & KWAN, A. 2001. Modeling dowel action of reinforcement bars for finite element analysis of concrete structures. *Computers & Structures*, 79, 595-604.
- HENDRIKS, M. A. N. & A. DE BOER, B. B. 2017. Guidelines for Nonlinear Finite Element Analysis of Concrete Structures. Rijkswaterstaat Centre for Infrastructure.
- HORDIJK, D., CORNELISSEN, H. & REINHARDT, H. 1986. Experimental determination of crack softening characteristics of normalweight and lightweight concrete. *HERON*, 31 (2), 1986.
- HORDIJK, D. A. 1992. Tensile and tensile fatigue behaviour of concrete; experiments, modelling and analyses. *Heron*, 37.
- HUBER, P., HUBER, T. & KOLLEGER, J. 2016. Investigation of the shear behavior of RC beams on the basis of measured crack kinematics. *Engineering Structures*, 113, 41-58.
- HUBER, T., HUBER, P. & KOLLEGER, J. 2019. Influence of aggregate interlock on the shear resistance of reinforced concrete beams without stirrups. *Engineering Structures*, 186, 26-42.
- JAMES K. WIGHT, J. G. M. 2012. *Reinforced Concrete: Mechanics and Design*, Pearson.
- KANI, G. N. J. 1964. The Riddle of Shear Failure and its Solution. *Journal Proceedings*, 61.
- KHWAOUNJOO, Y. R., FOSTER, S. J., GILBERT, R. I. & FOSTER, M. A. 2000. *3D Finite Element Modelling of Punching Type Problems Using Diana*, School of Civil Environmental Engineering University of New South Wales.
- KUERES, D. & HEGGER, J. 2018. Two-parameter kinematic theory for punching shear in reinforced concrete slabs without shear reinforcement. *Engineering Structures*, 175, 201-216.
- KUERES, D., RICKER, M., CLASSEN, M. & HEGGER, J. 2018. Fracture kinematics of reinforced concrete slabs failing in punching. *Engineering Structures*, 171, 269-279.
- KUERES, D. A. 2018. *Two-parameter kinematic theory for punching shear in reinforced concrete slabs*. Doctor of Engineering, University of Aachen
- LAVISION 2017. Product-Manual for DaVis 8.4. Göttingen, Germany
- LAVISION 2018. DaVis 10.0 Software. In: GMBH, L. (ed.).

- LEE, C., TAKE, W. A. & HOULT, N. A. 2011. Optimum accuracy of two-dimensional strain measurements using digital image correlation. *Journal of Computing in Civil Engineering*, 26, 795-803.
- LEONDARDT, F. 1965. Reducing the shear reinforcement in reinforced concrete beams and slabs. *Magazine of Concrete Research*, 17, 187-198.
- LI, B. 1989. Contact density model for stress transfer across cracks in concrete. *Journal of the Faculty of Engineering, the University of Tokyo*, 9-52.
- LIU, J. & MIHAYLOV, B. I. 2016. A comparative study of models for shear strength of reinforced concrete deep beams. *Engineering Structures*, 112, 81-89.
- MAEKAWA, K., OKAMURA, H. & PIMANMAS, A. 2003. *Non-linear mechanics of reinforced concrete*, CRC Press.
- MAEKAWA, K. & QURESHI, J. 1996. Computational model for reinforcing bar embedded in concrete under combined axial pullout and transverse displacement. *Doboku Gakkai Ronbunshu*, 1996, 227-239.
- MATAMOROS, A. B. & WONG, K. H. 2003. Design of simply supported deep beams using strut-and-tie models. *ACI Structural Journal*, 100, 704-712.
- MIHAYLOV, B. 2015. Five-spring model for complete shear behaviour of deep beams. *Structural Concrete*, 16, 71-83.
- MIHAYLOV, B. I., BENTZ, E. C. & COLLINS, M. P. 2013. Two-Parameter Kinematic Theory for Shear Behavior of Deep Beams. *Structural Journal*, 110.
- MIHAYLOV, B. I., HUNT, B., BENTZ, E. C. & COLLINS, M. P. 2015. Three-Parameter Kinematic Theory for Shear Behavior of Continuous Deep Beams. *ACI Structural Journal*, 112, 47-57.
- MILLARD, S. & JOHNSON, R. 1984. Shear transfer across cracks in reinforced concrete due to aggregate interlock and to dowel action. *Magazine of Concrete Research*, 36, 9-21.
- MÖRSCH, E. 1922. Der eisenbetonbau (reinforced concrete construction) - In German. *Verlag von Konrad Witwer, Stuttgart, Germany*.
- MUTTONI, A. & FERNÁNDEZ RUIZ, M. 2007. Concrete cracking in tension members and application to deck slabs of bridges. *Journal of Bridge Engineering*, 12, 646-653.
- MUTTONI, A. & FERNÁNDEZ RUIZ, M. 2008. Shear strength of members without transverse reinforcement as function of critical shear crack width. *ACI Structural Journal*, 2, 163-172.
- NGO, D. & SCORDELIS, A. C. 1967. Finite Element Analysis of Reinforced Concrete Beams. *Journal Proceedings*, 64, 12.
- OŽBOLT, J. & REINHARDT, H. Numerical study of mixed-mode fracture in concrete. IUTAM Symposium on Analytical and Computational Fracture Mechanics of Non-Homogeneous Materials, 2002. Springer, 367-376.
- PAN, B., XIE, H., WANG, Z., QIAN, K. & WANG, Z. 2008. Study on subset size selection in digital image correlation for speckle patterns. *Optics express*, 16, 7037-7048.
- PARK, H.-G., CHOI, K.-K. & WIGHT, J. K. 2006. Strain-based shear strength model for slender beams without web reinforcement. *ACI Structural Journal*, 103, 783.
- PASTORE, M. V. F. & VOLLUM, R. L. An analysis of the shear transfer actions in RC short span beams using crack kinematics recorded via DIC. Proceedings of the fib Symposium 2019: Concrete - Innovations in Materials, Design and Structures, 2019a. 1755-1762.
- PASTORE, M. V. F. & VOLLUM, R. L. Shear enhancement in RC beams with concomitant loads near and far from supports. Proceedings of the fib Symposium 2019: Concrete - Innovations in Materials, Design and Structures, 2019b. 1763-1770.

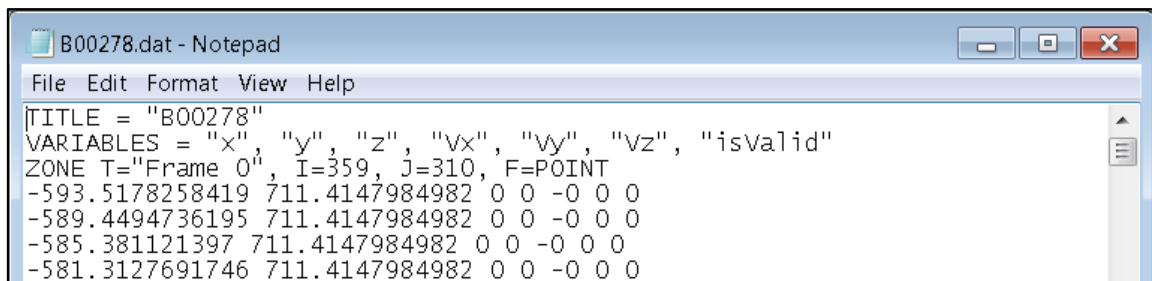
- PAULAY, T. & LOEBER, P. 1974. Shear transfer by aggregate interlock. *Special Publication*, 42, 1-16.
- POLDON, J., BENTZ, E. & HOULT, N. Measuring and modelling shear crack widths and slips in a shear test of a member with stirrups. Proceedings of the fib Symposium 2019: Concrete - Innovations in Materials, Design and Structures, 2019. 1858-1865.
- RASHID, Y. 1968. Ultimate strength analysis of prestressed concrete pressure vessels. *Nuclear engineering and design*, 7, 334-344.
- RICHART, F. E., BRANDTZAEG, A. & BROWN, R. L. 1928. A study of the failure of concrete under combined compressive stresses. University of Illinois at Urbana Champaign, College of Engineering. Engineering Experiment Station.
- RIKS, E. 1979. An incremental approach to the solution of snapping and buckling problems. *International journal of solids and structures*, 15, 529-551.
- ROTS, J. G. 1988. *Computational modeling of concrete fracture*. Delft University of Technology.
- ROTS, J. G. 1991. Smeared and discrete representations of localized fracture. *International Journal of Fracture*, 51, 45-59.
- ROTS, J. G. & BLAAUWENDRAAD, J. 1989. Crack models for concrete, discrete or smeared? Fixed, multi-directional or rotating? *HERON*, 34 (1), 1989.
- RUIZ, M. F., MUTTONI, A. & GAMBAROVA, P. 2007. Analytical modeling of the pre-and postyield behavior of bond in reinforced concrete. *Journal of Structural Engineering*, 133, 1364-1372.
- RUIZ, M. F., MUTTONI, A. & KUNZ, J. 2010. Strengthening of flat slabs against punching shear using post-installed shear reinforcement. *ACI Structural Journal*, 107, 434.
- RUSSO, G., VANIR, R. & PAULETTA, M. 2005. Reinforced Concrete Deep Beams--Shear Strength Model and Design Formula. *ACI Structural Journal-American Concrete Institute*, 102, 429-437.
- SAGASETA, J. & VOLLUM, R. L. 2010. Shear design of short-span beams. *Magazine of Concrete Research*, 62, 267-282.
- SAGASETA, J. & VOLLUM, R. L. 2011. Influence of aggregate fracture on shear transfer through cracks in reinforced concrete. *Magazine of Concrete Research*, 63, 119-137.
- SAGASETA, J. A. 2008. *The influence of aggregate fracture on the shear strength of reinforced concrete beams*. PhD Thesis, Imperial College London.
- SAS, G., BLANKSVÄRD, T., ENOCHSSON, O., TÄLJSTEN, B. & ELFGREN, L. 2012. Photographic strain monitoring during full-scale failure testing of Örnsköldsvik bridge. *Structural Health Monitoring*, 11, 489-498.
- SCHLAICH, J. & SCHAFFER, K. 1991. Design and detailing of structural concrete using strut-and-tie models. *Structural Engineer*, 69, 113-125.
- SCHLAICH, J., SCHÄFER, K. & JENNEWEIN, M. 1987. Toward a consistent design of structural concrete. *PCI journal*, 32, 74-150.
- SELBY, R. & VECCHIO, F. 1997. A constitutive model for analysis of reinforced concrete solids. *Canadian Journal of Civil Engineering*, 24, 460-470.
- SELBY, R. G. & VECCHIO, F. J. 1993. *Three-dimensional constitutive relations for reinforced concrete*, [Toronto], University of Toronto, Dept. of Civil Engineering.
- SHIMA, H., CHOU, L.-L. & OKAMURA, H. 1987. Micro and macro models for bond in reinforced concrete. 32.
- SIGRIST, V. 1995. Zum Verformungsvermögen von Stahlbetonträgern (In German). Birkhäuser.

- SOLTANI, M., AN, X. & MAEKAWA, K. 2003. Computational model for post cracking analysis of RC membrane elements based on local stress–strain characteristics. *Engineering Structures*, 25, 993-1007.
- SOROUSHIAN, P., OBASEKI, K. & ROJAS, M. C. 1987. Bearing strength and stiffness of concrete under reinforcing bars. *ACI Materials Journal*, 84.
- STAMENKOVIC, H. 1977. Inflection points as statical supports are responsible for structural failure of AMC warehouse in Shelby, Ohio, 1955. *Matériaux et Construction*, 10, 375-384.
- THORENFELDT, E., TOMASZEWICZ, A. & JENSEN, J. Mechanical properties of high-strength concrete and application in design. Proceedings of the symposium utilization of high strength concrete, 1987. Tapir Trondheim Norway, 149-159.
- TUREYEN, A. K. & FROSCHE, R. J. 2003. Concrete shear strength: another perspective. *ACI Structural Journal*, 100.
- VASIOS, N. 2015. *The Arc Length Method: Formulation, Implementation and Applications*. PhD, University of Harvard.
- VECCHIO, F. 2000. Disturbed stress field model for reinforced concrete: formulation. *Journal of structural engineering*, 126, 1070-1077.
- VECCHIO, F. J. & COLLINS, M. P. 1986. The modified compression-field theory for reinforced concrete elements subjected to shear. *ACI Structural Journal*, 83, 219-231.
- VECCHIO, F. J. & COLLINS, M. P. 1993. Compression response of cracked reinforced concrete. *Journal of Structural Engineering*, 119, 3590-3610.
- VOLLUM, R. L. & FANG, L. 2014. Shear enhancement in RC beams with multiple point loads. *Engineering Structures*, 80, 389-405.
- VOLLUM, R. L. & FANG, L. B. 2015. Shear enhancement near supports in RC beams. *Magazine of Concrete Research*, 67, 443-458.
- WALRAVEN, J. & REINHARDT, H. 1981. Theory and experiments on the mechanical behaviour of cracks in plain and reinforced concrete subjected to shear loading. *HERON*, 26 (1A), 1981.
- WALRAVEN, J. C. 1980. *Aggregate interlock: a theoretical and experimental analysis*. TU Delft, Delft University of Technology.
- YANG, K.-H. & ASHOUR, A. F. 2010. Strut-and-tie model based on crack band theory for deep beams. *Journal of Structural Engineering*, 137, 1030-1038.
- YANG, K. H. & ASHOUR, A. F. 2008. Code modelling of reinforced-concrete deep beams. *Magazine of Concrete Research*, 60, 441-454.
- ZARARIS, P. D. 2003. Shear strength and minimum shear reinforcement of reinforced concrete slender beams. *Structural Journal*, 100, 203-214.

APPENDIX I

This appendix describes the procedures followed to obtain crack kinematics from the digital images correlation (DIC) system. DIC captures images at a predefined frequency during the test and calculates displacements of subset in the two directions. In order to obtain the crack opening and sliding from these results, a post processing procedures were used as described below (This description is based on Davis 10.0 provided by LaVision, and may vary according to software used):

1. Export the deformation files for each frame from the DIC software as a B***.dat file. The file contains the X, Y and Z coordinates of each subset and associated deformations (see Figure I.1)

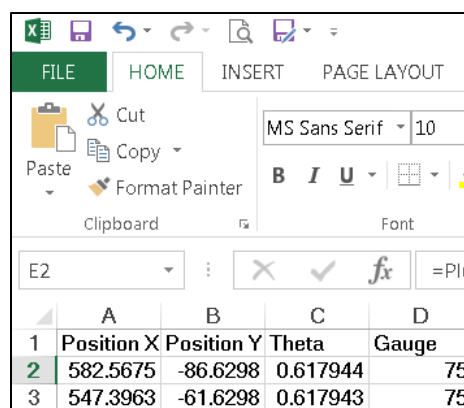


```

B00278.dat - Notepad
File Edit Format View Help
|TITLE = "B00278"
VARIABLES = "x", "y", "z", "vx", "vy", "vz", "isValid"
ZONE T="Frame 0", I=359, J=310, F=POINT
-593.5178258419 711.4147984982 0 0 -0 0 0
-589.4494736195 711.4147984982 0 0 -0 0 0
-585.381121397 711.4147984982 0 0 -0 0 0
-581.3127691746 711.4147984982 0 0 -0 0 0
  
```

Figure I.1: Sample of deformation file exported from Davis 10

2. Export a reference image from the DIC. Scale and reference it in AutoCAD to obtain coordinates of the beams boundaries, locations of reinforcement, crack points and plates.
3. Using a suitable number of station points to define the crack (e.g. 25 points along the length of the crack), generate the crack ordinates file CrackXYs.xls shown in Figure I.2 below.



	A	B	C	D
1	Position X	Position Y	Theta	Gauge
2	582.5675	-86.6298	0.617944	75
3	547.3963	-61.6298	0.617943	75

Figure I.2: File CrackXYs.xls

4. Generate the file 'Beam Geometry.xls' that contains the boundary and plates coordinates. This is used in plotting and in ensuring that the virtual demecs are placed corrected fit inside the beam before the calculations start.

E	F	G	H	I	J	K	L
Name	Position X	Position Y			Name	Position X	Position Y
Beam Bou	-189.113	379.6381			Plates	-198.982	379.6381
Beam Bou	-207.661	-113.774			Plates	-101.405	379.6381
Beam Bou	1158.172	-113.414			Plates	174.8467	383.158
Beam Bou	1162.119	383.9492			Plates	275.7381	383.5313
					Plates	599.4968	-113.533
					Plates	747.6589	-113.533

Figure I.3: 'Beam Geometry.xls'

5. Use the MATLAB code provided below to obtain the crack opening and sliding.

% This script calculates the crack opening and sliding using DIC data

clear all

clc

File='BT(0.5-0.5)'; %Beam Name

D=date;

Crack_Points = readtable('CrackXYs.xls'); %Reads cracks coordinates. See Figure I.2

O=0;% DEMEC orientation 0 or pi()/4 ONLY. (0 for horz and vert gauges)

DEMECs=size(Crack_Points,1); %Number of points along the crack

%% Generating the DEMEC's point matrix (DEMECxys)

DEMECxys(DEMECs,8)=zeros;

for pt=1:DEMECs

L=Crack_Points(pt,4); % Read gauge length for each point(mm)

DEMECxys(pt,1)=Crack_Points(pt,1)-L/2*cosd(O);%X1

DEMECxys(pt,2)=Crack_Points(pt,2)-L/2*sind(O);%Y1

DEMECxys(pt,3)=Crack_Points(pt,1)+L/2*sind(O);%X2

DEMECxys(pt,4)=Crack_Points(pt,2)-L/2*cosd(O);%Y2

DEMECxys(pt,5)=Crack_Points(pt,1)+L/2*cosd(O);%X3

DEMECxys(pt,6)=Crack_Points(pt,2)+L/2*sind(O);%Y3

DEMECxys(pt,7)=Crack_Points(pt,1)-L/2*sind(O);%X4

DEMECxys(pt,8)=Crack_Points(pt,2)+L/2*cosd(O);%Y4

end

%% Plot Crack and Gauge lines at first step to check

% This is not necessary and is not of the core code

%Properties of the plot

Gridweight=0.4;

Testlineweight=0.5;

axislabelfont=12 ;

```

Titlefont=12;
axisnumberingfont=12;
Legendfont=12;
axis equal
% Plotting the beam
Beam=xlsread('Beam Geometry.xls','f2:h5'); % Reads beams edges during the test, See Figure
I.3
% Constructing loading plates
Plates(1:2,:)=xlsread('Beam Geometry.xls','k2:l3');
Plates(3,:)=Plates(2,:)+[0,50];
Plates(4,:)=Plates(1,:)+[0,50];
Plates(5,:)=Plates(1,:);
Plates(6:7,:)=xlsread('Beam Geometry.xls','k4:l5');
Plates(8,:)=Plates(7,:)+[0,50];Plates(9,:)=Plates(6,:)+[0,50];
Plates(10,:)=Plates(6,:);
Plates(11:12,:)=xlsread('Beam Geometry.xls','k6:l7');
Plates(13,:)=Plates(12,:)-[0,50];Plates(14,:)=Plates(11,:)-[0,50];
Plates(15,:)=Plates(11,:);
BeamPlot1=plot(Beam(:,1),Beam(:,2),'k-','LineWidth',1,'HandleVisibility','off');
axis equal
hold on
plot(Plates(1:5,1),Plates(1:5,2),'k-','LineWidth',1,'HandleVisibility','off');
axis equal
hold on
plot(Plates(6:10,1),Plates(6:10,2),'k-','LineWidth',1,'HandleVisibility','off');
axis equal
hold on
plot(Plates(11:15,1),Plates(11:15,2),'k-','LineWidth',1,'HandleVisibility','off');
hold on
plot(Crack_Points(:,1),Crack_Points(:,2),'-k');
set(gca,'fontsize',axisnumberingfont);
set(gca,'gridlinestyle',':');
set(gca,'LineWidth',Gridweight)
xlabel('X (mm)','fontsize',axislabelfont,'fontname','Times New
Roman','fontweight','bold','color','k');
ylabel('Y (mm)','fontsize',axislabelfont,'fontname','Times New
Roman','fontweight','bold','color','k');
axis equal
hold on
% Writing point names on the plot
min_y=min(Beam(:,2));
for i= 1:DEMECs
x = [DEMECxys(i,1) DEMECxys(i,5)];
y = [DEMECxys(i,2) DEMECxys(i,6)];
x2 = [DEMECxys(i,3) DEMECxys(i,7)];
y2 = [DEMECxys(i,4) DEMECxys(i,8)];
plot(x,y,'r');

```

```

plot(x2,y2,'r');
text(Crack_Points(i,1),Crack_Points(i,2),['G',num2str(i)],'FontSize',8);
Demecs_highths(i,1)=Crack_Points(i,2)-min_y;
hold on
end
hold off
axis off
saveas(BeamPlot1,['Beam ',num2str(File),'-',num2str(D),'SGs.png']);

%% Extracting the closest points from the DIC subsets in the first image
files=dir ('B*.dat');
numfiles=size(files,1);
filename=files(1).name;
A=dlmread(filename, ' ',3,0);
A=real(A);
Arows=size(A,1);
for j=1:DEMECs
DEMECxy1=DEMECxys(j,1:2);
dist2=(A(:,1)-DEMECxy1(1)).^2+(A(:,2)-DEMECxy1(2)).^2;
[mind2,DEMEC1(j)]=min(dist2);
DEMECxy2=DEMECxys(j,3:4);
dist2=(A(:,1)-DEMECxy2(1)).^2+(A(:,2)-DEMECxy2(2)).^2;
[mind2,DEMEC2(j)]=min(dist2);
DEMECxy3=DEMECxys(j,5:6);
dist2=(A(:,1)-DEMECxy3(1)).^2+(A(:,2)-DEMECxy3(2)).^2;
[mind2,DEMEC3(j)]=min(dist2);
DEMECxy4=DEMECxys(j,7:8);
dist2=(A(:,1)-DEMECxy4(1)).^2+(A(:,2)-DEMECxy4(2)).^2;
[mind2,DEMEC4(j)]=min(dist2);
X1(1,j)=A(DEMEC1(j),1);
X2(1,j)=A(DEMEC2(j),1);
X3(1,j)=A(DEMEC3(j),1);
X4(1,j)=A(DEMEC4(j),1);
Y1(1,j)=A(DEMEC1(j),2);
Y2(1,j)=A(DEMEC2(j),2);
Y3(1,j)=A(DEMEC3(j),2);
Y4(1,j)=A(DEMEC4(j),2);
Lh0(j) = sqrt((X3(1,j)-X1(1,j))^2+(Y3(1,j)-Y1(1,j))^2); % initial length of horizontal gauge
Lv0(j) = sqrt((X4(1,j)-X2(1,j))^2+(Y4(1,j)-Y2(1,j))^2); % initial length of vertical gauge
end
%% Extracting points from the rest of the images
step=1;%Here the script will read a file every (step)files
n=1;
Load=abs(dlmread('Load.dat', ' ',3,0)); % Read loads from the load file exported from DIC
[MaxL,lastimg]= max(abs(Load(:,3)));
for i=1:step:numfiles
files=dir ('B*.dat');

```

```

filename=files(i).name;
A=dlmread(filename, ',3,0);
Arows=size(A,1);
for j=1:DEMECTs
dx1(i,j) = A(DEMEC1(j),4);dx3(i,j)=A(DEMEC3(j),4);
dx2(i,j)=A(DEMEC2(j),4);dx4(i,j)=A(DEMEC4(j),4);
dy1(i,j)=A(DEMEC1(j),5);dy3(i,j)=A(DEMEC3(j),5);
dy2(i,j)=A(DEMEC2(j),5);dy4(i,j)=A(DEMEC4(j),5);
a1=[1 0 -Y1(j);...
    0 1 X1(j);...
    1 0 -Y4(j);...
    0 1 X4(j)];
c1=[dx1(i,j);dy1(i,j);dx4(i,j);dy4(i,j)];
r1=(inv(transpose(a1)*a1))*(transpose(a1)*c1);
w1=[r1(1,1)-r1(3,1)*Crack_Points(j,2);r1(2,1)+r1(3,1)*Crack_Points(j,1)];
a2=[1 0 -Y2(j);...
    0 1 X2(j);...
    1 0 -Y3(j);...
    0 1 X3(j)];
c2=[dx2(i,j);dy2(i,j);dx3(i,j);dy3(i,j)];
r2=(inv(transpose(a2)*a2))*(transpose(a2)*c2);
w2=[r2(1,1)-r2(3,1)*Crack_Points(j,2);r2(2,1)+r2(3,1)*Crack_Points(j,1)];
W=w1-w2;
sc = 150;
dx(i,j) = W(1);
dy(i,j) = W(2);
X_Coord(n,j) = Crack_Points(j,1) + W(1)*sc;
Y_Coord(n,j) = Crack_Points(j,2) + W(2)*sc;
Theta=Crack_Points(j,3);
w(i,j)=-W(1)*sin(Theta)+W(2)*cos(Theta);
s(i,j)=W(1)*cos(Theta)+W(2)*sin(Theta);
if w(n,j)<0.001 %excluding values less than the threshold
    w(n,j)=0; %excluding negative values
end
if s(n,j)<0.001
    s(n,j)=0;
end
Header1(1,j)={'DEMEC'};
Header2(1,j)=(j);
end
Proc_files(n,1)=i;
LStep(n,1)=abs(Load(i,3));
Vi(n,1)=round(LStep(n,1)/MaxL,2); % Rounds load factor to 2 dicimals to use it in the steps of
0.1Vmax (next step)
n=n+1;
end
% By this steps, crack opening matrix (w) and sliding (s) marices have been

```

```

% generated for all of the crack points and load steps. If needed, next
% section will generate a reduced form in steps of 0.1Vmax.
%% Steps of 0.1V max
for i=1:10
Ratio_in_tens(i,1)=i/10;
end
% Addin pre-peak kinematics
k=1;
for i=1:size(Ratio_in_tens,1)
  LR=Ratio_in_tens(i,1);
for j=1:lastimg
  if Vi(j,1)==LR
    Final_w(k,1)=Vi(j,1);Final_s(k,1)=Vi(j,1);
    Final_w(k,2:size(w,2)+1)=w(j,1:size(w,2));
    Final_s(k,2:size(s,2)+1)=s(j,1:size(s,2));
    Final_X(k,1)=Vi(j,1);Final_Y(k,1)=Vi(j,1);
    Final_X(k,2:size(w,2)+1)=X_Coord(j,1:size(w,2));
    Final_Y(k,2:size(w,2)+1)=Y_Coord(j,1:size(w,2));
    k=k+1;
  end
end
end
% Adding post-peak kinematics
i=1;
for j=1:numfiles-lastimg+1
  if Vi(lastimg-1+j,1)==1
  else
    postFinal_w(i,1)=Vi(lastimg-1+j,1);postFinal_s(i,1)=Vi(lastimg-1+j,1);
    postFinal_w(i,2:size(w,2)+1)=w(lastimg-1+j,1:size(w,2));
    postFinal_s(i,2:size(s,2)+1)=s(lastimg-1+j,1:size(s,2));
    postFinal_X(i,1)=Vi(lastimg-1+j,1);postFinal_Y(i,1)=Vi(lastimg-1+j,1);
    postFinal_X(i,2:size(w,2)+1)=X_Coord(lastimg-1+j,1:size(w,2));
    postFinal_Y(i,2:size(w,2)+1)=Y_Coord(lastimg-1+j,1:size(w,2));
    Ratio_in_tens(10+i,1)=-postFinal_w(i,1);
    i=i+1;
  end
end
% As the load factor Vi is rounded up to two decimals, it is expected to
% have several images with the same load factor of a multiple of 0.1V. Here,
% the script averages load factors for the same multiple of 0.1V.

% Pre-failure
k=1; q=0;
for i=1:10
  count=0;
  for j=1:size(Final_w,1)
    if Final_w(j,1)==i/10

```



```

    count=count+1;
end
Count(i,1)=count;
end
Count(i,2)=q+1;
Count(i,3)=q+Count(i,1);
q=Count(i,3);
KINEMATICS_w(i,1)=i/10;
KINEMATICS_s(i,1)=i/10;
KINEMATICS_X(i,1)=i/10;
KINEMATICS_Y(i,1)=i/10;
if Count(i,1)==1;
KINEMATICS_w(i,2:size(Final_w,2))=Final_w(Count(i,2),2:size(Final_w,2));
KINEMATICS_s(i,2:size(Final_s,2))=Final_s(Count(i,2),2:size(Final_w,2));
KINEMATICS_X(i,2:size(Final_X,2))=Final_X(Count(i,2),2:size(Final_w,2));
KINEMATICS_Y(i,2:size(Final_Y,2))=Final_Y(Count(i,2),2:size(Final_w,2));
else
KINEMATICS_w(i,2:size(Final_w,2))=mean(Final_w(Count(i,2):Count(i,3),2:size(Final_w,2)));
KINEMATICS_s(i,2:size(Final_s,2))=mean(Final_s(Count(i,2):Count(i,3),2:size(Final_s,2)));
KINEMATICS_X(i,2:size(Final_X,2))=mean(Final_X(Count(i,2):Count(i,3),2:size(Final_X,2)));
KINEMATICS_Y(i,2:size(Final_Y,2))=mean(Final_Y(Count(i,2):Count(i,3),2:size(Final_Y,2)));
end
end
%% Post-failure
KINEMATICS_w(11:size(postFinal_X,1)+11-1,:)=postFinal_w;
KINEMATICS_s(11:size(postFinal_Y,1)+11-1,:)=postFinal_s;
KINEMATICS_X(11:size(postFinal_X,1)+11-1,:)=postFinal_X;
KINEMATICS_Y(11:size(postFinal_Y,1)+11-1,:)=postFinal_Y;
%% Maximum crack kinematics
strat_high(1:size(Crack_Points(:,2),1),1)=16.9-Crack_Points(1,2);
DEMEC_h=Crack_Points(:,2)+strat_high;
for i=1:10
Max_Kin(i,1)=KINEMATICS_s(i,1);
Max_Kin(i,2)=max(KINEMATICS_w(i,2:size(KINEMATICS_w,2)));
[~,demec_maxw]= max(KINEMATICS_w(i,2:size(KINEMATICS_w,2)));
Max_Kin(i,3)=DEMEC_h(demec_maxw,1);
Max_Kin(i,4)=Crack_Points(demec_maxw,3)*180/pi();
Max_Kin(i,5)=max(KINEMATICS_s(i,2:size(KINEMATICS_w,2)));
[~,demec_maxs]= max(KINEMATICS_s(i,2:size(KINEMATICS_s,2)));
Max_Kin(i,6)=DEMEC_h(demec_maxs,1);
Max_Kin(i,7)=Crack_Points(demec_maxs,3)*180/pi();
end
%% Plotting strain gauges
figure
set(gca, 'Visible', 'off')
axis equal

```

```

BeamPlot=plot(Crack_Points(:,1),Crack_Points(:,2),'k-', 'LineWidth',2,'HandleVisibility','off');
hold on
X_Coord=KINEMATICS_X(:,2:size(Final_X,2));
Y_Coord=KINEMATICS_Y(:,2:size(Final_Y,2));
crack_locxt=transpose(X_Coord);
crack_locyt=transpose(Y_Coord);
for c=1:size(Ratio_in_tens,1)-3
Vi2(c)=Ratio_in_tens(c);
    if Vi2(c)==1.000
        plot(crack_locxt(:,c),crack_locyt(:,c),'--','LineWidth',1.25)
        axis equal
        hold on
    else
        plot(crack_locxt(:,c),crack_locyt(:,c),'LineWidth',1.0)
        axis equal
        hold on
    end
end
legend(strcat('Vi/V=',num2str(Vi2)),'Location','northwest');
for c=1:DEMECs
plot(X_Coord(1:size(Ratio_in_tens,1)-3,c),Y_Coord(1:size(Ratio_in_tens,1)-3,c),'HandleVisibility','off');
hold on
end
one_mm=[475,475;475+1*sc,475];
plot(one_mm(:,1),one_mm(:,2),'k-', 'LineWidth',2,'HandleVisibility','off');
hold on
text(500,525,'1 mm')
% Plotting the beam
Beam=xlsread('Beam Geometry.xls','f2:h5');
% Constructing loading plates
Plates(1:2,:)=xlsread('Beam Geometry.xls','k2:l3');
Plates(3,:)=Plates(2,:)+[0,50];
Plates(4,:)=Plates(1,:)+[0,50];
Plates(5,:)=Plates(1,:);
Plates(6:7,:)=xlsread('Beam Geometry.xls','k4:l5');
Plates(8,:)=Plates(7,:)+[0,50];Plates(9,:)=Plates(6,:)+[0,50];
Plates(10,:)=Plates(6,:);
Plates(11:12,:)=xlsread('Beam Geometry.xls','k6:l7');
Plates(13,:)=Plates(12,:)-[0,50];Plates(14,:)=Plates(11,:)-[0,50];
Plates(15,:)=Plates(11,:);
plot(Beam(:,1),Beam(:,2),'k-', 'LineWidth',1,'HandleVisibility','off')
hold on
plot(Plates(1:5,1),Plates(1:5,2),'k-', 'LineWidth',1,'HandleVisibility','off')
hold on
plot(Plates(6:10,1),Plates(6:10,2),'k-', 'LineWidth',1,'HandleVisibility','off')
hold on

```

```

plot(Plates(11:15,1),Plates(11:15,2),'k-', 'LineWidth',1, 'HandleVisibility','off')
for i= 1:DEMECs
text(Crack_Points(i,1),Crack_Points(i,2),['G',num2str(i)], 'FontSize',8);
Demecs_hights(i,1)=Crack_Points(i,2)-min_y;
hold on
end
axis off
axis off
saveas(BeamPlot,['Beam ',num2str(File),'-',num2str(D),'Full Crack_plot.png']);
%% Writing the kinematics as an excel sheet
Header3={'Vi/Vmax'};
xlswrite(['Reduced      Crack      Kinematics      ',num2str(File),'-',num2str(D),'
Processed.xlsx'],Proc_files,'Processed files');
xlswrite(['Reduced      Crack      Kinematics      ',num2str(File),'-',num2str(D),'
Processed.xlsx'],LStep,'Processed files','b1');
xlswrite(['Reduced      Crack      Kinematics      ',num2str(File),'-',num2str(D),'
Processed.xlsx'],Header1,'Opening - full','b1');
xlswrite(['Reduced      Crack      Kinematics      ',num2str(File),'-',num2str(D),'
Processed.xlsx'],Header1,'Sliding - full','b1');
xlswrite(['Reduced      Crack      Kinematics      ',num2str(File),'-',num2str(D),'
Processed.xlsx'],Header2,'Opening - full','b2');
xlswrite(['Reduced      Crack      Kinematics      ',num2str(File),'-',num2str(D),'
Processed.xlsx'],Header2,'Sliding - full','b2');
xlswrite(['Reduced      Crack      Kinematics      ',num2str(File),'-',num2str(D),'
Processed.xlsx'],Header3,'Opening - full','a1');
xlswrite(['Reduced      Crack      Kinematics      ',num2str(File),'-',num2str(D),'
Processed.xlsx'],Header3,'Sliding - full','a1');
xlswrite(['Reduced      Crack      Kinematics      ',num2str(File),'-',num2str(D),'
Processed.xlsx'],round(transpose(Vi),2),'Opening - full','a3');
xlswrite(['Reduced      Crack      Kinematics      ',num2str(File),'-',num2str(D),'
Processed.xlsx'],round(transpose(Vi),2),'Sliding - full','a3');
xlswrite(['Reduced      Crack      Kinematics      ',num2str(File),'-',num2str(D),'
Processed.xlsx'],round(w,3),'Opening - full','b3');
xlswrite(['Reduced      Crack      Kinematics      ',num2str(File),'-',num2str(D),'
Processed.xlsx'],round(s,3),'Sliding - full','b3');
% Reduced
xlswrite(['Reduced      Crack      Kinematics      ',num2str(File),'-',num2str(D),'
Processed.xlsx'],Header1,'Opening Reduced','b1');
xlswrite(['Reduced      Crack      Kinematics      ',num2str(File),'-',num2str(D),'
Processed.xlsx'],Header1,'Sliding Reduced','b1');
xlswrite(['Reduced      Crack      Kinematics      ',num2str(File),'-',num2str(D),'
Processed.xlsx'],Header2,'Opening Reduced','b2');
xlswrite(['Reduced      Crack      Kinematics      ',num2str(File),'-',num2str(D),'
Processed.xlsx'],Header2,'Sliding Reduced','b2');
xlswrite(['Reduced      Crack      Kinematics      ',num2str(File),'-',num2str(D),'
Processed.xlsx'],KINEMATICS_w,'Opening Reduced','a3');

```

```
xlswrite(['Reduced      Crack      Kinematics      ',num2str(File),'-',num2str(D),'
Processed.xlsx'],KINEMATICS_s,'Sliding Reduced','a3');

xlswrite(['Reduced      Crack      Kinematics      ',num2str(File),'-',num2str(D),'
Processed.xlsx'],'w_max','Max Kinematics','b1');
xlswrite(['Reduced      Crack      Kinematics      ',num2str(File),'-',num2str(D),'
Processed.xlsx'],'s_max','Max Kinematics','c1');
xlswrite(['Reduced      Crack      Kinematics      ',num2str(File),'-',num2str(D),'
Processed.xlsx'],Max_Kin,'Max Kinematics','a2');
```

APPENDIX II

Figure No.	Page	Source of the work	Copyright holder	Request Date	Permission granted	Remarks
Figure 1.1	37	COLLINS, M. P., BENTZ, E. C., SHERWOOD, E. G. & XIE, L. 2008. An adequate theory for the shear strength of reinforced concrete structures. Magazine of Concrete Research, 60, 635-650.	Magazine of Concrete Research	10/10/2019	Yes	10/10/2019
Figure 2.2	45	CAMPANA, S., RUIZ, M. F., ANASTASI, A. & MUTTONI, A. 2013. Analysis of shear-transfer actions on one-way RC members based on measured cracking pattern and failure kinematics. Magazine of Concrete Research, 65, 386-404.	Magazine of Concrete Research	10/10/2019	Yes	10/10/2019
Figure 2.6	48	BAZANT, Z. P. & GAMBAROVA, P. G. 1980. Rough crack models in reinforced concrete. Journal of Structural Engineering, ASCE, 4, 23.	Journal of Structural Engineering	09/10/2019	Yes	02/10/2019
Figure 2.8	54	CAMPANA, S., RUIZ, M. F., ANASTASI, A. & MUTTONI, A. 2013. Analysis of shear-transfer actions on one-way RC members based on measured cracking pattern and failure kinematics. Magazine of Concrete Research, 65, 386-404.	Magazine of Concrete Research	10/10/2019	Yes	10/10/2019
Figure 2.10	57	PARK, H.-G., CHOI, K.-K. & WIGHT, J. K. 2006. Strain-based shear strength model for slender beams without web reinforcement. ACI Structural Journal, 103, 783.	ACI Structural Journal	09/10/2019	Yes	14/11/2019
Figure 2.11	60	CAVAGNIS, F., FERNÁNDEZ RUIZ, M. & MUTTONI, A. 2017. An analysis of the shear-transfer actions in reinforced concrete members without transverse reinforcement based on refined experimental measurements. Structural Concrete, 16.	Structural Concrete	07/10/2019	Yes	07/10/2019
Figure 2.11	60	HUBER, T., HUBER, P. & KOLLEGGGER, J. 2019. Influence of aggregate interlock on the shear resistance of reinforced concrete beams without stirrups. Engineering Structures, 186, 26-42.	Engineering Structures	07/10/2019	Yes	07/10/2019
Figure 2.12	61	COLLINS, M. P., BENTZ, E. C., SHERWOOD, E. G. & XIE, L. 2008. An adequate theory for the shear strength of reinforced concrete structures. Magazine of Concrete Research, 60, 635-650.	Magazine of Concrete Research	10/10/2019	Yes	10/10/2019
Figure 2.14	68	FANG, L. 2013. Shear enhancement in reinforced concrete beams. PhD Thesis or dissertation, Imperial College London.	L. Fang	-	Yes	Creative Commons Attribution Non-Commercial No Derivatives licence

Figure 2.15	71	VECCHIO, F. J. & COLLINS, M. P. 1986. The modified compression-field theory for reinforced concrete elements subjected to shear. ACI J., 83, 219-231.	ACI Structural Journal	09/10/2019	Yes	14/11/2019
Figure 2.26	72	VECCHIO, F. J. & COLLINS, M. P. 1986. The modified compression-field theory for reinforced concrete elements subjected to shear. ACI Structural Journal., 83, 219-231.	ACI Structural Journal	09/10/2019	Yes	14/11/2019
Figure 2.17	74	MIHAYLOV, B. I., BENTZ, E. C. & COLLINS, M. P. 2013. Two-Parameter Kinematic Theory for Shear Behavior of Deep Beams. ACI Structural Journal, 110.	ACI Structural Journal	09/10/2019	Yes	14/11/2019
Figure 2.18	75	MIHAYLOV, B. I., BENTZ, E. C. & COLLINS, M. P. 2013. Two-Parameter Kinematic Theory for Shear Behavior of Deep Beams. ACI Structural Journal, 110.	ACI Structural Journal	09/10/2019	Yes	14/11/2019
Figure 2.19	76	MIHAYLOV, B. I., BENTZ, E. C. & COLLINS, M. P. 2013. Two-Parameter Kinematic Theory for Shear Behavior of Deep Beams. ACI Structural Journal, 110.	ACI Structural Journal	09/10/2019	Yes	14/11/2019
Figure 2.21	79	KUERES, D., RICKER, M., CLASSEN, M. & HEGGER, J. 2018. Fracture kinematics of reinforced concrete slabs failing in punching. Engineering Structures, 171, 269-279.	Engineering Structures	07/10/2019	Yes	07/10/2019
Figure 2.22	80	MIHAYLOV, B. 2015. Five-spring model for complete shear behaviour of deep beams. Structural Concrete, 16, 71-83.	Structural Concrete	07/10/2019	Yes	07/10/2019
Figure 2.23	80	MIHAYLOV, B. 2015. Five-spring model for complete shear behaviour of deep beams. Structural Concrete, 16, 71-83.	Structural Concrete	07/10/2019	Yes	07/10/2019
Figure 2.24	83	SCHLAICH, J., SCHÄFER, K. & JENNEWEIN, M. 1987. Toward a consistent design of structural concrete. PCI journal, 32, 74-150.	SCHLAICH, J., SCHÄFER, K. & JENNEWEIN, M.	10/10/2019	Awaiting response	Copy rights rest with authors, no response yet.
Figure 2.25	85	SCHLAICH, J., SCHÄFER, K. & JENNEWEIN, M. 1987. Toward a consistent design of structural concrete. PCI journal, 32, 74-150.	SCHLAICH, J., SCHÄFER, K. & JENNEWEIN, M.	10/10/2019	Awaiting response	Copy rights rest with authors, no response yet.
Figure 2.26	86	SCHLAICH, J., SCHÄFER, K. & JENNEWEIN, M. 1987. Toward a consistent design of structural concrete. PCI journal, 32, 74-150.	SCHLAICH, J., SCHÄFER, K. & JENNEWEIN, M.	10/10/2019	Awaiting response	Copy rights rest with authors, no response yet.
Figure 2.27	86	SCHLAICH, J., SCHÄFER, K. & JENNEWEIN, M. 1987. Toward a consistent design of structural concrete. PCI journal, 32, 74-150.	SCHLAICH, J., SCHÄFER, K. & JENNEWEIN, M.	10/10/2019	Awaiting response	Copy rights rest with authors, no response yet.
Figure 2.28	87	SCHLAICH, J., SCHÄFER, K. & JENNEWEIN, M. 1987. Toward a consistent design of structural concrete. PCI journal, 32, 74-150.	SCHLAICH, J., SCHÄFER, K. & JENNEWEIN, M.	10/10/2019	Awaiting response	Copy rights rest with authors, no response yet.

Figure 2.30	89	YANG, K.-H. & ASHOUR, A. F. 2010. Strut-and-tie model based on crack band theory for deep beams. Journal of Structural Engineering, 137, 1030-1038.	Journal of Structural Engineering	07/10/2019	Yes	07/10/2019
Figure 2.31	90	JAMES K. WIGHT, J. G. M. 2012. Reinforced Concrete: Mechanics and Design, Pearson.	JAMES K. WIGHT	10/10/2019	Yes	14/10/2019
Figure 2.32	91	SAGASETA, J. & VOLLUM, R. L. 2010. Shear design of short-span beams. Magazine of Concrete Research, 62, 267-282.	Magazine of Concrete Research	10/10/2019	Yes	10/10/2019
Figure 2.33	91	FANG, L. 2013. Shear enhancement in reinforced concrete beams. PhD Thesis or dissertation, Imperial College London.	L. Fang	-	Yes	Creative Commons Attribution Non-Commercial No Derivatives licence
Figure 2.34	93	BSI 2004. Eurocode 2: Design of Concrete Structures: Part 1-1: General Rules and Rules for Buildings, British Standards Institution.	British Standards Institution	-	Yes	Open Access
Figure 5.6	199	KUERES, D. A. 2018. Two-parameter kinematic theory for punching shear in reinforced concrete slabs. Doctor of Engineering, University of Aachen	KUERES, D. A	10/10/2019	Yes	31/10/2019
Figure 5.9	201	KUERES, D. A. 2018. Two-parameter kinematic theory for punching shear in reinforced concrete slabs. Doctor of Engineering, University of Aachen	KUERES, D. A	10/10/2019	Yes	31/10/2019
Figure 6.2	263	DIANA, T. 2017. Manual, DIANA User's Material library. DIANA finite element analysis user's manual, release.	TNO DIANA	10/10/2019	Yes	14/10/2019
Figure 6.3	263	DIANA, T. 2017. Manual, DIANA User's Material library. DIANA finite element analysis user's manual, release.	TNO DIANA	10/10/2019	Yes	14/10/2019
Figure 6.4	264	DIANA, T. 2017. Manual, DIANA User's Material library. DIANA finite element analysis user's manual, release.	TNO DIANA	10/10/2019	Yes	14/10/2019
Figure 6.5	265	DIANA, T. 2017. Manual, DIANA User's Material library. DIANA finite element analysis user's manual, release.	TNO DIANA	10/10/2019	Yes	14/10/2019
Figure 2.15	267	VECCHIO, F. J. & COLLINS, M. P. 1986. The modified compression-field theory for reinforced concrete elements subjected to shear. ACI J., 83, 219-231.	ACI Structural Journal	09/10/2019	Yes	14/11/2019
Figure 6.6	267	DIANA, T. 2017. Manual, DIANA User's Material library. DIANA finite element analysis user's manual, release.	TNO DIANA	10/10/2019	Yes	14/10/2019
Figure 6.9	270	DIANA, T. 2017. Manual, DIANA User's Material library. DIANA finite element analysis user's manual, release.	TNO DIANA	10/10/2019	Yes	14/10/2019
Figure 6.10	271	DIANA, T. 2017. Manual, DIANA User's Material library. DIANA finite element analysis user's manual, release.	TNO DIANA	10/10/2019	Yes	14/10/2019

Figure 6.11	274	SAGASETA, J. A. 2008. The influence of aggregate fracture on the shear strength of reinforced concrete beams. PhD Thesis, Imperial College London.	SAGASETA, J. A.	10/10/2019	Yes	17/10/2019
Figure 6.12	275	DIANA, T. 2017. Manual, DIANA User's Material library. DIANA finite element analysis user's manual, release.	TNO DIANA	10/10/2019	Yes	14/10/2019
Figure 6.13	275	DIANA, T. 2017. Manual, DIANA User's Material library. DIANA finite element analysis user's manual, release.	TNO DIANA	10/10/2019	Yes	14/10/2019
Figure 6.14	276	DIANA, T. 2017. Manual, DIANA User's Material library. DIANA finite element analysis user's manual, release.	TNO DIANA	10/10/2019	Yes	14/10/2019
Figure 6.16	278	DIANA, T. 2017. Manual, DIANA User's Material library. DIANA finite element analysis user's manual, release.	TNO DIANA	10/10/2019	Yes	14/10/2019
Figure 6.18	280	DIANA, T. 2017. Manual, DIANA User's Material library. DIANA finite element analysis user's manual, release.	TNO DIANA	10/10/2019	Yes	14/10/2019
Figure 6.19	280	DIANA, T. 2017. Manual, DIANA User's Material library. DIANA finite element analysis user's manual, release.	TNO DIANA	10/10/2019	Yes	14/10/2019
Figure 6.20	282	FANG, L. 2013. Shear enhancement in reinforced concrete beams. PhD Thesis or dissertation, Imperial College London.	L. Fang	-	Yes	Creative Commons Attribution Non-Commercial No Derivatives licence
Figure 6.24	288	FANG, L. 2013. Shear enhancement in reinforced concrete beams. PhD Thesis or dissertation, Imperial College London.	L. Fang	-	Yes	Creative Commons Attribution Non-Commercial No Derivatives licence
Figure 7.5	311	MIHAYLOV, B. I., BENTZ, E. C. & COLLINS, M. P. 2013. Two-Parameter Kinematic Theory for Shear Behavior of Deep Beams. ACI Structural Journal, 110.	ACI Structural Journal	09/10/2019	Yes	14/11/2019